

Local Probe Techniques for Hydrogen Measurement in Ultra-High Strength Steels

A Dissertation

Presented to the Faculty of the School of Engineering and Applied Science
University of Virginia

In Partial Fulfillment of the
Requirements for the Degree of
Doctor of Philosophy (Materials Science and Engineering)

by

Rebecca Filardo Schaller
May 2016

APPROVAL SHEET

The dissertation is submitted in partial fulfillment of the
requirements for the degree of
Doctor of Philosophy (Materials Science and Engineering)

Rebecca F. Schaller

(Author)

This dissertation has been read and approved by the examining Committee:

Dr. John R. Scully

(Thesis Advisor)

Dr. Rob G. Kelly

(Committee Chair)

Dr. James T. Burns

(Committee Member)

Dr. Elizabeth J. Opila

(Committee Member)

Dr. Gary M. Koenig

(Committee Member)

Accepted for the School of Engineering and Applied Science:



Dean, School of Engineering and Applied
Science

May 2016

Abstract

Hydrogen embrittlement (HE) is a concern specifically in ultra-high strength steels (UHSS) prevalent in key structural and vehicle components. Hydrogen production and uptake in high strength materials is well documented in many full immersion environments such as during cathodic protection. However, there is a lack of information regarding hydrogen production in atmospheric exposure conditions. Marine aerosols, industrial pollutants, and other environmental factors, such as UV and relative humidity, greatly affect atmospheric corrosion damage, where oxygen reduction (ORR) is the primary cathodic reaction. However, the hydrogen evolution reaction (HER) can produce atomic hydrogen. Hydrogen production and uptake that occurs on a metal surface is likely affected by many of the same environmental factors that cause high environmental severity since anodic and cathodic reactions are coupled during naturally occurring corrosion. An understanding of the effects of these various exposure conditions on hydrogen production and uptake in UHSS is necessary to develop new alloys with improved corrosion resistance as well as to anticipate and manage the effects of environment severity on embrittlement susceptibility of currently employed UHSS.

This thesis aims to obtain a better understanding of the corrosion processes generating hydrogen electrochemically and the factors controlling hydrogen production, uptake, and diffusible concentrations, at both the meso- and micrometer length scales during the atmospheric exposures of selected high performance alloys. Hydrogen production and uptake was investigated in three ferrous alloys, two ultra-high strength steels (UNS S46500 and UNS K92580), and one carbon steel (UNS G10180). Included in this study

are both traditional analysis of meso-scale H uptake under atmospheric exposure conditions using thermal desorption spectroscopy as well as pioneering local detection methods. The objective was to develop and demonstrate the utility and efficacy of the novel local hydrogen probes. The applications of the Scanning Kelvin Probe (SKP) and the Scanning Electrochemical Microscope (SECM) were explored. The detection of spatial distribution of the diffusible H concentration was demonstrated on pre-exposed metallic surfaces with the SKP and SECM. The application of these local scale techniques is shown to provide local and spatial information on H concentration pertinent to atmospheric corrosion and previously unattainable with meso-scale techniques. An understanding of the H severity at this local scale can be expanded to the meso-scale and provide significant information on severity of atmospheric exposure environments in terms of H production, uptake, and transport.

The SKP was explored as one viable option. Factors that may limit the feasibility to measure diffusible H concentrations using this method were assessed. An explanation for the measurement concept for H detection in the SKP and the controlling factors was developed. Moreover, a relationship between the measured SKP potential and the diffusible hydrogen concentration ($C_{H,Diff}$) was determined. Factors such as RH, size of charging area, and time were also explored. Finally, simulations of steady state H and H^+ diffusion verified experimental determination of local H concentrations produced from exposures.

A second novel technique for spatial, local H determination was explored; the SECM. The explanation of the measurement concept for H detection in the SECM and

controlling factors were rationalized. Optimization of solution, potential applied to the SECM microelectrode tip, the tip to sample height selection, scan rate, and scan size were presented. A correlation between H pre-charged materials and the effect on interrogating current measured was determined and a quantitative relationship between the current measured at the SECM tip and $C_{H,Diff}$ was presented. The effects of solution phase transport of species used in the redox competition mode were compared to solid state diffusion simulations to assess spatial resolution.

Both the SKP and SECM techniques were then extended towards the detection of local hydrogen concentrations sites on samples pre-exposed under atmospheric conditions (in $MgCl_2$). Electrochemical analysis of conditions present in atmospheric drops was investigated to better understand the basic roles of various environmental parameters such as pH, Cl^- type, and concentration. SKP and SECM scans of samples from controlled atmospheric pre-exposures are presented to demonstrate the application of these techniques to local detection of naturally absorbed H due to production and uptake from atmospheric corrosion processes.

The scientific contribution of this thesis is that it established novel local measurements of hydrogen concentrations during atmospheric exposures using local probes. Methods for not only hydrogen detection but accurate quantification on steel surfaces were established. The scientific basis for the SKP and SECM measurements, detection, resolution, and quantitative relationships between probe signal and H concentration, were developed. Explanations for the effects of hydrogen concentrations on these measurement techniques, methods for application, as well as suggestions for future work

are given to enhance the field of hydrogen embrittlement research through localized H detection. From the engineering perspective, a new method to quantify environmental severity and alloy susceptibility was developed.

Acknowledgements

I would first like to thank my advisor, Dr. John Scully, for his support and guidance while a graduate student at the University of Virginia. I will be forever grateful for the countless opportunities, he has given me. His guidance, mentorship, support, patience, and friendship have enabled me to pursue my degree and instilled in me lessons that will extend further in life. I would also like to acknowledge my other committee members, Dr. Rob Kelly, Dr. James Burns, Dr. Elizabeth Opila, and Dr. Gary Koenig for their assistance with my research.

I am grateful to Dr. Nick Birbilis and Dr. Sebastian Thomas from Monash University for their assistance and expertise with the scanning electrochemical microscope. In addition, I would like to thank Dr. Joseph Labukas at the Army Research Laboratories for his generous loan of their SECM. I appreciate the help and support of all of the faculty and students in the Materials Science Department who have helped me over the years and specifically the Center for Electrochemical Science and Engineering. In particular, I would like to thank Derek Horton, Andrew King, Sam Madden, and Mary Lyn Lim for their guidance and introduction to the labs and help with many experiments. I would like to thank Katie Lutton for her continued support, both in the lab and out as an undergraduate student and fellow graduate student. Finally, I would like to thank Veronica Rafla, Kat Gusieva, Brendy Rincon Troconis, and Leslie Bland for their continued moral support and for being great friends.

Most of all, I would like to thank my family. My parents, for continuing to push me towards what I want and for being the constant support I need to obtain my goals.

My sister, for consistently being there as the friend I need. And to TJ, for his continued support through both the ups and downs of this journey.

Table of Contents

Abstract.....	i
Acknowledgements	v
Table of Contents	vii
List of Tables	xii
List of Figures.....	xiv
CHAPTER 1. Introduction.....	36
1.1. Background	36
1.1.1. Hydrogen Detection Methods	37
1.1.2. Atmospheric Corrosion of Ferrous Alloys in Outdoor Environments	39
1.1.3. Materials of Interest	47
1.1.4. Hydrogen Behavior and Materials	51
1.1.5. Hydrogen Uptake in Pits and other Occluded Sites	62
1.1.6. Hydrogen Uptake in an Atmospheric Drop (Evans Cell)	65
1.1.7. Studies of Atmospheric Hydrogen Embrittlement	67
1.1.8. Local Scale Investigations of Hydrogen Uptake in Atmospheric Conditions	69
1.2. Critical Unresolved Issues	73
1.2.1. Engineering Perspective	73
1.2.2. Scientific Perspective	74
1.3. Objectives	77
1.4. References.....	81
1.5. Tables:	90
1.6. Figures:	95
CHAPTER 2. Characterization of Hydrogen Uptake in UHSS in Selected Full Immersion, Atmospheric, and LALT Environments	111
2.1. Abstract	111
2.2. Introduction and Background	112

2.3.	Experimental Procedures	118
2.3.1.	Materials.....	118
2.3.2.	Full Immersion Corrosion Characterization.....	118
2.3.3.	TDS Characterization of Material-Hydrogen Interactions.....	119
2.3.4.	Sample Preparation for Environmental Exposure.....	124
2.3.5.	Characterization of Salt Deposition and Calibration of Salt Coverage as a Function of Deposition Mode.....	126
2.3.6.	Exposures of Steel as a Function of Salt Deposition Method.....	130
2.3.7.	Post Exposure Characterization	131
2.4.	Experimental Results	134
2.4.1.	Electrochemical Characterization of the Corrosion Behavior of Materials of Interest	134
2.4.2.	Characterization of the Material-Hydrogen Interaction ..	135
2.4.3.	Salt Deposition and Pre-Exposure Imaging	137
2.4.4.	Corrosion Characterization	138
2.4.5.	Thermal Desorption Spectroscopy Analysis of Pre-exposed Samples.....	140
2.5.	Discussion.....	144
2.5.1.	Hydrogen Production and Uptake During Atmospheric Corrosion.....	145
2.5.2.	Hydrogen Production in an Isolated Droplet.....	146
2.5.3.	Basis for Hydrogen Uptake in Atmospheric Exposures: Effects of Environmental Parameters	149
2.5.4.	Relationship Between Hydrogen Uptake and Mass Loss.....	152
2.6.	Future Work	153
2.7.	Conclusions.....	154
2.8.	References.....	155
2.9.	Tables:.....	159
2.10.	Figures:	163
CHAPTER 3.	Spatial Determination of Diffusible Hydrogen Concentrations in UHSS from Uniform Pre-Charging Using the Scanning Kelvin Probe.....	205
3.1.	Abstract	205

3.2.	Introduction and Background	206
3.2.1.	SKP and Corrosion Characterization	207
3.2.2.	SKP as a Method for Local Hydrogen Characterization.....	213
3.3.	Experimental Procedures	215
3.3.1.	Materials.....	215
3.3.2.	Evaluation of the Effect of Electrochemical Hydrogen Pre-charging.....	216
3.3.3.	Electrochemical Impedance Spectroscopy Analysis.....	218
3.3.4.	Electrochemical Extraction of Hydrogen	219
3.3.5.	Measurements for SKP Calibration.....	221
3.3.6.	Calibration of the SKP Potential Versus $C_{H,Diff}$ Using Cathodically Pre-charged Samples	223
3.3.7.	Cross-sectioning method established for estimation of $D_{H,eff}$ in selected samples	225
3.4.	Experimental Results	226
3.4.1.	Evaluation of the Effect of Electrochemical Hydrogen Pre-charging on Anodic Polarization and E_{OCP}	226
3.4.2.	Evaluation of the Effect of Electrochemical Hydrogen Pre-charging using EIS	227
3.4.3.	Electrochemical Impedance Spectroscopy Analysis.....	227
3.4.4.	Effect of pre-charging: pH	228
3.4.5.	Electrochemical Extraction for $C_{H,Diff}$ determination: Effect of η_H and Temper	228
3.4.6.	Calibration of the SKP:	229
3.4.7.	Calibration of the SKP: Electrochemically Pre-charged Samples.....	232
3.4.8.	SKP Φ Measurements and $D_{H,eff}$ Calculations	233
3.5.	Discussion	236
3.5.1.	Origins of the H effect on the SKP Potential	237
3.5.2.	Limitations of H Detection in SKP	248
3.6.	Future Work	251
3.7.	Conclusions.....	253
3.8.	References.....	255

3.9.	Tables:.....	260
3.10.	Figures:	262
CHAPTER 4.	Spatial Determination of Diffusible Hydrogen Concentrations in UHSS from Uniform Pre-Charging Using the Scanning Electrochemical Microscope	310
4.1.	Abstract	310
4.2.	Introduction and Background	310
4.2.1.	SECM Modes and Corrosion Characterization	311
4.2.2.	SECM as a Method for Local Hydrogen Characterization	314
4.3.	Experimental Procedures	317
4.3.1.	Materials	317
4.3.2.	Electrochemical Evaluation of SECM Measurement Environment	318
4.3.3.	SECM Calibration: Determination of Optimal Measurement Electrolyte	320
4.3.4.	Measurements for SECM Calibration in the Case of H Pre-charged Materials	323
4.3.5.	Effect of Time: Pre and Post-Hydrogen Charging	326
4.3.6.	Diffusion Calculations: H^+ , H, and O_2 in Electrolyte and UHSS	327
4.4.	Experimental Results	328
4.4.1.	Corrosion Electrochemistry in the SECM Measurement Environment	328
4.4.2.	SECM Calibration and Optimization	330
4.4.3.	Diffusion Calculations: H^+ , H, and O_2 in Electrolyte and UHSS	335
4.5.	Discussion	337
4.5.1.	Origins of the H effect on the SECM tip current	337
4.5.2.	Limitations of H detection in the SECM	342
4.6.	Future Work	342
4.7.	Conclusions	343
4.8.	References	345
4.9.	Tables:	347

4.10.	Figures:	349
CHAPTER 5. Spatial determination of diffusible hydrogen concentrations proximate to pits formed under atmospheric exposure using the Scanning Kelvin Probe and Scanning Electrochemical Microscope.....388		
5.1.	Abstract	388
5.2.	Introduction and Background	389
5.3.	Experimental Procedures	390
5.3.1.	Materials	390
5.3.2.	Electrochemical Evaluation of Droplets	391
5.3.3.	Atmospheric Exposures and Imaging for Corrosion Characterization	391
5.3.4.	SKP of Atmospherically Exposed Samples	392
5.3.5.	SECM of Atmospherically Exposed Samples.....	394
5.3.6.	Diffusion modeling of H from an uptake “hot spot”	394
5.4.	Experimental Results	395
5.4.1.	Electrochemical Droplet Analysis.....	395
5.4.2.	Corrosion Evaluation of Droplets through Imaging.....	395
5.4.3.	SKP of Atmospherically Pitted Samples.....	396
5.4.4.	SECM of Atmospherically Pitted Samples	398
5.4.5.	H Diffusion Analysis.....	399
5.5.	Discussion	399
5.5.1.	Advantages/ Limitations of H Detection Atmospherically in the SKP and SECM.....	399
5.6.	Future Work	400
5.7.	Conclusions.....	402
5.8.	References	404
5.9.	Tables:.....	406
5.10.	Figures:	407

List of Tables

Table 1. Comparison of absorbed H concentration detection and quantification characterization techniques in metallic materials with advantages and disadvantages.	90
Table 2. Oxides and Hydroxides found on corroded iron.[13]	90
Table 3. Chemical Composition (wt%) of UNS S46500 Stainless Steel, UNS K92580, and UNS G10180.[75, 83, 142]	91
Table 4. Mechanical Properties of UNS S46500 Stainless Steel, as-annealed / CT and H900 Temper, UNS K92580 Peak-Aged, and UNS G10180.[75, 83, 90]	91
Table 5. Hydrolysis reactions with expressions for the equilibrium pH.[114]	91
Table 6. Calculated room temperature $D_{H,eff}$ data for iron, iron with primary alloying elements for the UHSS of interest, a martensitic Cr alloy, martensite, martensitic stainless steel, PH 13-8, and UNS K92580.....	92
Table 7. Typical hydrogen trap binding energies reported for ferrous alloys (kJ/mol)....	93
Table 8. Trap site binding energies and densities for precipitation hardened martensitic stainless steel (Fe-8.5Ni-12.7Cr-2.18Mo-1.13Al-0.036C-0.1Mn wt%).[125]	94
Table 9. Trap site binding energies and densities reported for UNS K92580.[125]	94
Table 10. Estimated ratio of $C_{H,Diff}$ to C_L based on probable $D_{H,eff}$	94
Table 11. Corrosion rates of carbon steels at atmospheric exposure sites and full immersion and the diffusible hydrogen concentration for these exposures.....	159
Table 12. Composition (wt. %).[1]	160
Table 13. Material Properties.[1]	160
Table 14. Exposure conditions at Birdwood golf course: Location: 38.04N, 78.53W..	160
Table 15. Salt density for various atmospheric exposures and environments.	161
Table 16. Table of corrosion products found with XRD and Raman. X indicates that the species was found with XRD, and R indicates that it was found with Raman. [41]	161
Table 17. Comparison of average atmospheric droplet spacing to H concentration at the same distance as droplet spacing relative to a corrosion site. Concentration profile is assumed uniform if overlap between hydrogen uptake spots occurs at $C_{x,t}/C_o \geq 0.5$	161
Table 18. Calculated diffusion distances for C_H equal to 90% C_o over a period of 10 days for different initial spherical H distributions. $D_{H,eff}$ used were $6.2 \times 10^{-9} \text{ cm}^2/\text{s}$, $6 \times 10^{-9} \text{ cm}^2/\text{s}$, and $1 \times 10^{-7} \text{ cm}^2/\text{s}$ for UNS S46500, UNS K92580, and UNS G10180 respectively.	162
Table 19. Calculated Q_{mass} (gravimetric) and $Q_{H,abs}$ (TDS) corrected with LECO calibration based on mass loss and $C_{H,total}$ for selected 10 day exposures. ^a	162
Table 20. UNS K92580 and UNS S46500 Composition (wt. %).[76]	260

Table 21. UNS K92580 and UNS S46500 Material Properties.[76]	260
Table 22. Experimental sequence for cathodic pre-charging followed by OCP and EIS to explore effect of solution and pre-charging environments.	260
Table 23. SKP and SKPFM Measurements: In-situ backside H detection.....	261
Table 24. Possible Oxidation Reactions and Their Nernst Potentials ($i_{ox} = i_c = i_{ORR}$).	261
Table 25. UNS K92580 and UNS S46500 Composition (wt. %).[31]	347
Table 26.UNS K92580 and UNS S46500 Material Properties.[31]	347
Table 27. List of Mediators and Non-Mediator Solutions and Reactions Obtained at the SECM ME Tip.[9, 15-17, 32, 33]	348
Table 28. UNS S46500 Composition (wt. %).[24]	406
Table 29.UNS S46500 Material Properties.[24]	406
Table 30. Comparison of absorbed H concentration detection and quantification characterization techniques applied in this dissertation.....	406

List of Figures

- Figure 1. The wide span of different length scales with relation to the material, pitting, and aerosols pertinent to atmospheric corrosion. SOURCE: University of Virginia, CESE, courtesy of Matthew R. Begley and Richard P. Gangloff, Hongbo Cong and J.R. Scully, Atmospheric Corrosion, Christopher Leygraf and Thomas E. Graedel, and I. Cole. [13, 60, 164] 95
- Figure 2. Average corrosion rate vs. chloride deposition rate for a range of studies of steels exposed under atmospheric field exposure conditions. Data compiled from various sources with UNS K92580 exposures at U.Va.[165]..... 96
- Figure 3. a) Equilibrium salt concentration for NaCl, MgCl₂, and CaCl₂ formed in an H₂O droplet with respect to relative humidity and 25 °C, [56, 57] and b) Calculated theoretically assumed uniform water layer thickness for varied RH and sodium chloride deposition densities ranging from 0 to 15 µg/cm² (field exposures have exhibited ranges from 0.22 to 10 µg/cm²/day for rural to severe marine sites[43, 44]) at room temperature assuming equilibrium salt level and perfect wetting. [55, 63] 96
- Figure 4. Pourbaix diagram in water at 25°C for a) Fe, b) Cr, c) Mo, and d) Ni. The range of passivity is indicated.[59] 97
- Figure 5. Mixed potential analysis of a differential aeration cell on identical iron electrodes with equal area a) assuming uniform constant solution concentration and b) with passivated cathode and acidified anode.[66] 98
- Figure 6. a) The Evans water drop experiment schematic [10, 114] and b) Schematic of process occurring at an actively growing pit in iron. [66] 99
- Figure 7. Pit morphologies produced in MgCl₂ 750 µg/cm² exposures on 304L Stainless steel at 38% RH for 24 h and 30°C at a) edge of droplet displaying satellite pits and b) center of droplet displaying spiral attack.[72] 99
- Figure 8. Scanning electron micrograph and Transmission electron micrograph of microstructural features in UNS K92580: a) martensite laths and b) coherent M₂C carbides.[74]..... 99
- Figure 9. a) 304 L SS, UNS S46500, UNS K92580 and 316L predicted maximum pit radii from the Kelly Shedd model. NaCl loading densities of exposures were 240 or 600 µg/cm² exposed at 90 or 95% RH. b) Repassivation potential vs charge density for UNS S46500 and UNS K92580 exposed in 0.6 M sodium chloride.[78]..... 100
- Figure 10. Scanning electron micrograph and Transmission electron micrograph of microstructural features in UNS S46500: a) banded martensite packets and b) Ni₃Ti Precipitates.[82] 100
- Figure 11. pH measured for crevices on Fe-Cr binary alloys with varying Cr composition, triangles: held at +0.300 V in 3.5 wt% NaCl Solution for 5 hours, and hatched region: samples exposed for 10 months to natural sea water at NRL Key West.[93]..... 101

- Figure 12. Optical image of UNS G10180 etched with 60mL H₂O + 40 mL HCl + 10 mL HNO₃. [166] 101
- Figure 13. Cathodic polarization data, experimental and calculated, for UNS K92580. Polarization scans were acquired at 0.167 mV/s in deaerated 0.6 M Cl⁻ electrolytes adjusted to pH of 1 and 6 and depict HER in 3 regimes. [100] 102
- Figure 14. Corrosion vs. Cr content showing weight loss for steels exposed for four years in either semirural, industrial, moderate marine, or severe marine atmospheres with a salt loading density ranging from 2 – 150 mg NaCl/m²d. [91] 102
- Figure 15. C_{H,Ddiff} values vs. hydrogen overpotential for UNS K92580 and AISI 4130. H pre-charged in saturated Ca(OH)₂ at 23°C. C_{H,Ddiff} values were calculated by the barnacle cell method. [7] 103
- Figure 16. C_{H,Ddiff} values vs. hydrogen overpotential a) UNS S46500 H900 H pre-charged in pH 8 borate buffer. C_{H,diff} values were calculated by the barnacle cell method using a D_{Heff} of 1.9x10⁻⁸ cm²/s. Results for UNS K92580 in pH 8 borate buffer are shown for comparison and b) reaction rate mechanism model results for UNS K92580 showing the relationship between C_{H,Ddiff}, η_H, as well as pH. [100] 103
- Figure 17. a) Threshold stress intensity for internal hydrogen embrittlement, K_{TH}, with a constant dK/dt of 2.2 x 10⁻⁴ MPa√m/s and varying diffusible H concentration. [10] b) Normalized K_{TH} vs E_{applied} for four high-strength steels (PH 13-8, 18 Ni 250, UNS K92580, and UNS S46500) where Kehler et al. employed the relationship of x² = 2.82G. [99, 109, 167] 104
- Figure 18. Schematic of electrochemical conditions at a crack tip/ pit due to anodic polarization. [100] 104
- Figure 19. a) Anodic polarization scans of PH 13-8 Mo in deaerated solutions of H₂SO₄ with 0.1 M Fe⁺², 0.018 M Cr⁺³, and 0.01 M Ni⁺². b) Polarization data for solutions of dissolved salts and deaerated 5 M H₂SO₄ with C_H vs potential for bulk charged, planar PH 13-8 Mo. [115] 105
- Figure 20. X_{crit}² vs gap data. Three regions are displayed, E_{H/H+}>E_{Pass}>E where no passivation occurs but H is produced, E_{H/H+}>E>E_{Pass} where H is produced but it is passive, and E>E_{H/H+}>E_{Pass} where no H is produced. [115] 105
- Figure 21. Example of effect of x²/G for anodic and cathodic polarizations, a) C_{H,Diff} vs. E_{applied} for a range of x²/G values for UNS K92580 charged in 0.6 M NaCl solution, bulk pH calculated using the minimum pH (i.e., average minus one standard deviation) for passivated and polished surfaces. b) Predicted K_{TH} vs applied potential for UNS K92580 using the Gerberich micromechanical model where predicted values were calculated assuming α = 1.0 MPa-m^{0.5}/atom fraction H and k_{IG} = 0.72 MPa-m^{1/2}. [100] 106
- Figure 22. An example Pourbaix diagram for conditions of a propagating crack in 4340 Steel in 0.6 M NaCl solution. [168] 106

- Figure 23. Potential, C_H and pit diameter versus pit depth from a rescaled experimental pit, 1500 μm diameter by 40 mm depth cylinder, which was exposed to 5 M H_2SO_4 + dissolved metal ions. $E_{\text{app}} = -0.60 \text{ V Hg/Hg}_2\text{SO}_4$. [169] 107
- Figure 24. Current densities observed for Zinc wires in-situ during repeat experiments with 1 μL seawater droplet exposures (a and b), and c) a 10 μL seawater droplet. The strong color intensities indicate the areas covered by the droplets. [117] 107
- Figure 25. Potential distribution across a) carbon steel sample with a 0.05 N NaCl droplet with reference to V_{SHE} . Colors indicated by pH indicators potassium ferricyanide and phenolphthalein (pink indicating formation of OH^- and blue indication formation of Fe^{2+}), thus the anode is the central area with a cathodic outer ring. b) SS 316 with a 0.5 M NaCl droplet after 30 min (closed circle), 2 h (open circle), and 18 h (closed triangle). c) Galvanized steel with a 0.5 g/L NaCl droplet. [118] 108
- Figure 26. Fracture stress vs. hydrogen content for hydrogen pre-charged steels (solid symbols) and steels corroded by cyclic atmospheric corrosion tests (open symbols). Diffusible H concentration was determined through TDS. [121] 109
- Figure 27. Comparison of the average H absorbed to the average mass loss per day for a 7 day driving atmospheric exposure test of steel (Fe-0.02C-0.01Si-0.15Mn-0.01P- $\leq 0.01\text{S wt\%}$). [123] 109
- Figure 28. Schematic of the polarization diagram for a rusted and wetted surface of steel that changes to a dry surface developed by Tsuru et.al and actual measurements during drying of a) permeation current and b) pH and potential for 0.5M NaCl solution. [30] 110
- Figure 29. a) SKP potential map of the Pd coated (100 mm) exit side of the galvanized steel sample. The sample was scribed on the entry side and exposed to 0.1 M NaCl aqueous electrolyte. b) Potential maps with time: the top map is 1 h, 3 h, 4 h and 15 h is the bottom map. With time, the hydrogen rich scribe at the back side disappears or becomes uniformly charged. [32] Potentials measured in the SKP are reported referenced vs. the onset of the binary point (bp). 110
- Figure 30. Thermal Desorption Spectroscopy chamber schematic 163
- Figure 31. A) A droplet array with 5 by 5 mm spacing between droplet centers of 1 M NaCl pH 6.5 solution 1 μL drops (average diameter of 500 μm) on UHSS and B) a Hirox optical image of a 1M NaCl pH 6.5 droplet on UHSS sample. 163
- Figure 32. Electrochemical testing of UNS S46500 as annealed/CT a) 1 h E_{OCP} followed by a polarization scans either b) anodic polarizations, from -30 mV vs E_{OCP} , at a scan rate of 0.1667 mV/s to 0.5 V_{SCE} or c) cathodic polarizations, from +30 mV vs E_{OCP} , at a scan rate of 0.1667 mV/s to -2 V_{SCE} in ambiently aerated and deaerated 0.05 M, 0.9 M, and 5.3 M NaCl. 165
- Figure 33. Electrochemical testing of UNS S46500 H900 a) 1 h E_{OCP} followed by a polarization scans either b) anodic polarizations, from -30 mV vs E_{OCP} , at a scan rate of 0.1667 mV/s to 0.5 V_{SCE} or c) cathodic polarizations, from +30 mV vs

- E_{OCP} , at a scan rate of 0.1667 mV/s to -2 V_{SCE} in ambiently aerated and deaerated 0.05 M, 0.9 M, and 5.3 M NaCl..... 167
- Figure 34. Electrochemical testing of UNS G10180 a) 1 h E_{OCP} followed by a polarization scans either b) anodic polarizations, from -30 mV vs E_{OCP} , at a scan rate of 0.1667 mV/s to 0.5 V_{SCE} or c) cathodic polarizations, from +30 mV vs E_{OCP} , at a scan rate of 0.1667 mV/s to -2 V_{SCE} in ambiently aerated and deaerated 0.05 M, 0.9 M, and 5.3 M NaCl..... 169
- Figure 35. Electrochemical testing of UNS K92580 a) 1 h E_{OCP} followed by a polarization scans either b) anodic polarizations, from -30 mV vs E_{OCP} , at a scan rate of 0.1667 mV/s to 0.5 V_{SCE} or c) cathodic polarizations, from +30 mV vs E_{OCP} , at a scan rate of 0.1667 mV/s to -2 V_{SCE} in ambiently aerated and deaerated 0.05 M, 0.9 M, and 5.3 M NaCl..... 171
- Figure 36. Electrochemical testing of UNS S46500 As Annealed/CT a) 1 h E_{OCP} followed by a polarization scans either b) anodic polarizations, from -30 mV vs E_{OCP} , at a scan rate of 0.1667 mV/s to 0.5 V_{SCE} or c) cathodic polarizations, from +30 mV vs E_{OCP} , at a scan rate of 0.1667 mV/s to -2 V_{SCE} in deaerated 0.05 M, 0.9 M, and 5.3 M NaCl and 0.05 M, 0.6 M, and 5.4 M $MgCl_2$ 173
- Figure 37. Electrochemical testing of UNS S46500 H900 a) 1 h E_{OCP} followed by a polarization scans either b) anodic polarizations, from -30 mV vs E_{OCP} , at a scan rate of 0.1667 mV/s to 0.5 V_{SCE} or c) cathodic polarizations, from +30 mV vs E_{OCP} , at a scan rate of 0.1667 mV/s to -2 V_{SCE} in deaerated 0.05 M, 0.9 M, and 5.3 M NaCl and 0.05 M, 0.6 M, and 5.4 M $MgCl_2$ 175
- Figure 38. Electrochemical testing of UNS G10180 a) 1 h E_{OCP} followed by a polarization scans either b) anodic polarizations, from -30 mV vs E_{OCP} , at a scan rate of 0.1667 mV/s to 0.5 V_{SCE} or c) cathodic polarizations, from +30 mV vs E_{OCP} , at a scan rate of 0.1667 mV/s to -2 V_{SCE} in deaerated 0.05 M, 0.9 M, and 5.3 M NaCl and 0.05 M, 0.6 M, and 5.4 M $MgCl_2$ 177
- Figure 39. Electrochemical testing of UNS K92580 a) 1 h E_{OCP} followed by a polarization scans either b) anodic polarizations, from -30 mV vs E_{OCP} , at a scan rate of 0.1667 mV/s to 0.5 V_{SCE} or c) cathodic polarizations, from +30 mV vs E_{OCP} , at a scan rate of 0.1667 mV/s to -2 V_{SCE} in deaerated 0.05 M, 0.9 M, and 5.3 M NaCl and 0.05 M, 0.6 M, and 5.4 M $MgCl_2$ 179
- Figure 40. A) TDS ramp rate tests of charged a) hydrogen over-potential of -1.0 V (-1.74 V_{SCE}) in pH 8.5 borate buffered solution) as-annealed / CT UNS S46500, b) Calculated saturation curves assuming various diffusion coefficients (lines) plotted with experimental results from TDS ramp rate tests of as annealed/CT UNS S46500 (squares)..... 179
- Figure 41. Isothermal TDS results at various temperatures for as-annealed / CT UNS S46500 stainless steel. a) Background subtracted H_2 pressure as a function of time, b) normalized H concentration egressed as a function of time. Specimens were H-charged for 14 days at room temperature at a hydrogen overpotential of -0.8 V in pH 10, 0.6M NaCl solution..... 180

- Figure 42. Arrhenius plot of D_H for as-annealed/CT UNS S46500 stainless steel, obtained from isothermal TDS tests shown with 95% confidence interval for regression indicated. 181
- Figure 43. TDS spectra for as-annealed/CT and H900 UNS S46500 at a ramp rate of 5 °C/min for a) unexposed samples and samples charged in pH 10, 0.6 M NaCl solution for 48 hours at η_H = b) -200 mV and c) -400 mV. 181
- Figure 44. Isothermal TDS results at various temperatures for H900 UNS S46500 stainless steel. a) Background subtracted H_2 pressure as a function of time, b) normalized H concentration egressed as a function of time. Specimens were H-charged for 14 days at room temperature at a hydrogen overpotential of -0.8 V in pH 10, 0.6 M NaCl solution. 182
- Figure 45. Arrhenius plot for H900 stainless steel, obtained from isothermal TDS tests shown with 95% confidence interval for regression. Data was corrected using an average heating time for the sample to reach the chamber temperature of 7.6 s. 182
- Figure 46. Calibration through conductivity measurements of average salt deposition per cm^2 for salt print, mist and droplets. a) Salt print, calibration was deposition versus print number, b) Salt spray, deposition versus spray number, c) Salt drops, deposition versus sample number (all samples were loaded with same number of droplets and average area coverage of 1.5 %) and d) ASTM B-117 standard versus sample number of parafilm substrates exposed for one hour. 183
- Figure 47. SEM and EDS analysis of dried 0.5 μ L salt droplets on Si substrate. Concentrations are different than those discussed previously, as higher concentrations were chosen to display salt morphology. 184
- Figure 48. SEM micrographs of a) NaCl and b) ASTM Seawater on Si. Samples were exposed on a Peltier stage with dry salts and imaged while temperature was decreased at the stage. This caused an increase in localized RH as the vapor pressure condensed about the stage as the temperature decreased and evaporated as it was increased. Simultaneous imaging shows the wetting and drying cycle for both salts, but as temperature changes were involved, the deliquescence points are different from those expected at room temperature. Also, in both cases, some hysteresis is observed. 186
- Figure 49. SEM images of unexposed samples with a) salt printing deposition of 1 M NaCl solution, producing about 161 μ g/ cm^2 on UHSS, b) 1 M NaCl salt solution, about 138 μ g/ cm^2 on UHSS, c) 1 M NaCl solution, about 220 μ g/ cm^2 on UHSS, and d) ASTM-B-117 after 1 h exposure. All samples allowed to dry 15 min prior to imaging. 187
- Figure 50. UNS S46500 Hirox optical imaging, SEM, and XRD of three exposure environments: ASTM B-117, Bidrwood Golf course atmospheric exposure, and ASTM artificial seawater spray exposed at 92 % RH. XRD unexposed spectra shown in purple and exposed in green. 188
- Figure 51. UNS K92580 Hirox optical imaging, SEM and XRD of three exposure environments: ASTM B-117, Bidrwood Golf course atmospheric exposure, and

- ASTM artificial seawater spray exposed at 92 % RH. XRD unexposed spectra shown in purple and exposed in green. 189
- Figure 52. UNS G10180 Hirox optical imaging, SEM and XRD of three exposure environments: ASTM B-117, Bidrwood Golf course atmospheric exposure, and ASTM artificial seawater spray exposed at 92 % RH. XRD unexposed spectra shown in purple and exposed in green. 190
- Figure 53. Example droplet exposures for 48 h at 99% RH with Universal pH indicator for a) UNS S46500, b) UNS K92580, and c) UNS G10180. Blue indicates alkaline areas, whereas orange indicates acidic areas. Droplet exposures were used to estimate size of anodic uptake areas across the various steels, 40 μm pits for UNS S46500 and 500 μm anodic areas for UNS K92580 and UNS G10180 applied for calculations in Figure 54. 191
- Figure 54. Relative H concentration for steady state radial diffusion of H from assumed dominant H uptake sites, for UNS S46500, assumed to be a pit of $d = 40 \mu\text{m}$, for UNS K92580 and UNS G10180, assumed to be an anodic site due to Evans cell formation of $d = 500 \mu\text{m}$. $D_{\text{H,eff}}$ assumed were $6.2 \times 10^{-9} \text{ cm}^2/\text{s}$, $6 \times 10^{-9} \text{ cm}^2/\text{s}$, and $1 \times 10^{-7} \text{ cm}^2/\text{s}$ respectively and exposure period was taken to be 10 days... 192
- Figure 55. C_{H} total determined by TDS analysis for a wide range of laboratory ALTs, field, and full immersion pre-charging exposures. C_{H} was determined from ramped TDS and calibrated with LECO analysis. 193
- Figure 56. TDS hydrogen partial pressure spectra and C_{H} total determined by TDS analysis for a select comparison of laboratory ALTs, field, and full immersion pre-charging exposures for UNS K92580 (a and c) and UNS S46500 (b and d). C_{H} was determined from ramp rate TDS and calibrated with LECO analysis. . 194
- Figure 57. Selected a) mass loss and b) $C_{\text{H,total}}$ for LALT and salt fog exposures..... 195
- Figure 58. C_{H} Total vs. Mass Loss: Total hydrogen concentration vs. mass loss varies across alloy type..... 195
- Figure 59. Within one similar environment, producing the same surface coverage, in this case ASTM –B-117 and modified B-117, $C_{\text{H Total}}$ can be compared and scaled with mass loss. a) TDS spectra for UNS K92580 and UNS G10180 exposures, b) Estimated $C_{\text{H,diff}}$ vs. mass loss for a ten day exposure period assuming $Q_{\text{HER}} = 0 \%$ Q_{C} , and that $D_{\text{L}} = 6 \times 10^{-5} \text{ cm}^2/\text{s}$ and $K = 1 \times 10^{-7} \text{ mol}/\text{cm}^3$ 196
- Figure 60. Schematic of a) Evans droplet cell and b) pitting droplet cell. Blue indicates alkaline pH, while red indicates acidic pH. 197
- Figure 61. a) pH map of using universal indicator of NaCl droplet on carbon steel exposed for 48 h at 99% RH, indicating Evans cell formation. b) Reaction rate model results for UNS K92580 showing the relationship between $C_{\text{H,diff}}$ and η_{H} . Area highlighted in blue predicts the range of $C_{\text{H,diff}}$ for the overpotentials shown in c. c) SKP potential across a NaCl drop on carbon steel as measured by Mansfeld et. al.[46] Green line indicates the cathodic current density due to hydrogen and the blue shaded area represents the hydrogen overpotential..... 198

- Figure 62. a) pH and potential map of UNS K92580 exposed to 5.3 M NaCl 1 μ L droplet for 900 min. pH was estimated using Figure 53-c. Potential measurements were taken in the SKP. b) η_H vs distance across the droplet area calculated from SKP potential. c) η_H and i_H vs distance across drop. Green line indicates the cathodic current density due to hydrogen. d) Predicted $C_{H,diff}$ from calculated η_H and estimated pH using data for electrochemical extraction measurements for UNS K92580.[42]..... 200
- Figure 63. a) pH and potential map of UNS S46500 exposed to 5.3 M NaCl 1 μ L droplet for 120 min. pH was estimated from Figure 53-a. Potential measurements were taken in the SKP. b) η_H vs distance across the droplet area calculated from SKP potential. c) η_H and i_H vs distance across drop. Green line indicates the cathodic current density due to hydrogen. d) Predicted $C_{H,diff}$ from calculated η_H and estimated pH using data for electrochemical extraction measurements for UNS S46500.[42]..... 202
- Figure 64. Droplet height and potential map over time of steel exposed to 5.3 M NaCl 1 μ L droplet at 78% RH. Potential measurements were taken in the scanning kelvin probe (SKP). a) peak aged UNS K92580 and b) UNS S46500 as annealed/CT. 203
- Figure 65. a) Graph of calculated Q_{mass} vs. $Q_{H, abs}$ based on mass loss and $C_{H,total}$ for selected exposures. B) Schematic of relationship/quantities of different charges.[16, 23, 59]..... 204
- Figure 66. Calibration of the Au tip, Corrosion potential measured in bulk solution vs. the difference of the SKP potentials for different metals covered with 1 mm of 1 M Na_2SO_4 .[26] 262
- Figure 67. a) Schematic of a two potential (V_1 and V_2) sample in the SKP with a, the distance from the potential interface, d, the distance from the probe tip to sample, and D, the probe diameter noted. b) Estimation of the difference in normalized potential between V_1 and V_2 ($\Delta E a, d$) based a with varied d. c) Calculation of the corrected lateral response, ΔL_{50} , based on d with varied D where the star indicates the test conditions in this study..... 263
- Figure 68. Schematic of SKP permeation measurement on Pd coated backside of a scribe in galvanized steel.[39] 264
- Figure 69. Image of Microcapillary cell. 264
- Figure 70. Schematic of the reactions during H at SKP measurement interface. The mixed potential in the red pre-charged zone represents a situation where the coupled potential is a H potential. 265
- Figure 71. Example of steady state diffusion of H in UNS S46500 over the 24 h pre-charging time period. 265
- Figure 72. Model of equivalent circuit applied for EIS fitting at OCP in 0.6 M NaCl and 5 mM NaCl. [46]..... 266
- Figure 73. a) SKP stage setup and b) schematic of H pre-charged sample with position of SKP line scan. 266

- Figure 74. a) Pre-charging current densities vs. time from 30 min cathodic polarization of UNS K92580 in deaerated 0.1 M NaOH. b) E_{OCP} measured initially post-charging vs. the pre-charging overpotential in 0.1 M NaOH. c) $C_{\text{H,Diff}}$ vs. E_{OCP} for UNS K92580. E_{OCP} determined from initial OCP measured post-charging for cathodic pre-charging tests, $C_{\text{H, diff}}$ determined from UNS K92580 reaction mechanism model for pH 10.[58] 267
- Figure 75. Anodic polarizations in 0.6 M NaCl, pH 5.5. Polarizations scanned at 0.1667 mV/s from -200 mV vs. OCP to 1 V vs OCP. Scans were taken post hydrogen pre-charging for 1 h in 0.6 M NaCl + NaOH pH 10 at hydrogen overpotentials of -200, -400, and -600 mV for a) As Annealed/CT UNS S46500, b) H900 UNS S46500, c) UNS K92580, and d) UNS G10180. 269
- Figure 76. E_{OCP} of As Annealed/CT UNS S46500 with 1 h hydrogen pre-charging, 1 h OCP, and no prior test a) in 0.6 M NaCl + NaOH pH 10 and b) in 0.6 M NaCl pH 5.5..... 270
- Figure 77. EIS of As Annealed/CT UNS S46500 with 1 h hydrogen pre-charging a) Nyquist, b) Bode, and c) Phase, 1 h OCP d) Nyquist, e) Bode, and f) Phase, and no prior test g) Nyquist, h) Bode, and i) Phase, in 0.6 M NaCl pH 10. 271
- Figure 78. EIS of As Annealed/CT UNS S46500 with 1 h hydrogen pre-charging a) Nyquist, b) Bode, and c) Phase, 1 h OCP d) Nyquist, e) Bode, and f) Phase, and no prior test g) Nyquist, h) Bode, and i) Phase, in 0.6 M NaCl pH 5.5. 272
- Figure 79. E_{OCP} of peak aged UNS K92580 with 1 h hydrogen pre-charging, 1 h OCP, and no prior test a) in 0.6 M NaCl + NaOH pH 10 and b) in 0.6 M NaCl pH 5.5. 274
- Figure 80. EIS of UNS K92580 with 1 h hydrogen pre-charging a) Nyquist, b) Bode, and c) Phase, 1 h OCP d) Nyquist, e) Bode, and f) Phase, and no prior test g) Nyquist, h) Bode, and i) Phase, in 0.6 M NaCl pH 10. 274
- Figure 81. EIS of UNS K92580 with 1 h hydrogen pre-charging a) Nyquist, b) Bode, and c) Phase, 1 h OCP d) Nyquist, e) Bode, and f) Phase, and no prior test g) Nyquist, h) Bode, and i) Phase, in 0.6 M NaCl pH 5.5. 275
- Figure 82. E_{OCP} of UNS G10180 with 1 h hydrogen pre-charging, 1 h OCP, and no prior test a) in 0.6 M NaCl + NaOH pH 10 and b) in 0.6 M NaCl pH 5.5. 277
- Figure 83. EIS of UNS G10180 with 1 h hydrogen pre-charging a) Nyquist, b) Bode, and c) Phase, 1 h OCP d) Nyquist, e) Bode, and f) Phase, and no prior test g) Nyquist, h) Bode, and i) Phase, in 0.6 M NaCl pH 10. 277
- Figure 84. EIS of UNS G10180 with 1 h hydrogen pre-charging a) Nyquist, b) Bode, and c) Phase, 1 h OCP d) Nyquist, e) Bode, and f) Phase, and no prior test g) Nyquist, h) Bode, and i) Phase, in 0.6 M NaCl pH 5.5. 278
- Figure 85. Summary of initial EIS taken after 1 h pre-charge, 1 h OCP, and no initial OCP in 0.6 M NaCl + NaOH, pH 5.5 and pH 10 for UNS S46500 As Annealed/CT a) Nyquist, b) Bode, and c) Phase, UNS K92580 d) Nyquist, e) Bode, and f) Phase, and UNS G10180 g) Nyquist, h) Bode, and i) Phase. 279

- Figure 86. Oxidation current density vs. time. Oxidation current density was calculated from EIS fitting for both 0.6 M NaCl + NaOH pH 10 exposures at E_{OCP} vs time and for a single exposure of 5 mM NaCl + NaOH pH 10 exposures. 280
- Figure 87. a) Cathodic pre-charging of As-Annealed/CT UNS S46500 in deaerated Borate Buffer solution pH 8.4 for 1 h, and b) E_{OCP} 2 h measurement in same solution for a pre-charged and uncharged sample. 280
- Figure 88. Pre-charging current densities in a) As Annealed/CT and b) H900 UNS S46500. UNS S46500 $C_{H,Diff}$ results from electrochemical H extraction i (A/cm^2) vs time (s) for each hydrogen overpotential (η_H), c) As Annealed/CT and d) H900. Comparison of the $\log(i)$ vs $\log(t)$ electrochemical extraction to the theoretical slope of $-1/2$ for e) As Annealed/CT and f) H900 UNS S46500. 282
- Figure 89. UNS S46500 $C_{H,Diff}$ results from electrochemical extraction. a) H extraction i (A/cm^2) vs time (s) for each hydrogen overpotential (η_H) and b) $C_{H,Diff}$ (wppm) vs. pre-charging η_H with E_{OCP} vs. pre-charging η_H . Samples were H pre-charged in 0.6 M NaCl + NaOH, pH 10 naturally aerated room temperature solution for 24 h at $\eta_H = -150$ to -1000 mV (-982 to -1832 mV_{SCE}). Extraction occurred in 0.1 M NaOH, pH 11.75 solution at $\eta_H = +330$ mV (-605 mV_{SCE}) for 1 h. $C_{H,Diff}$ values were determined from i at 1800 s. E_{ocp} was measured immediately post-charging in same solution for 1 hour, values shown above are those measured within the first 10 s after H charging. 282
- Figure 90. a) SKP potential line scans in 40, 60, 80, and 95% RH humid air across H pre-charged zones in as annealed/CT UNS S46500. Samples were pre-charged by cathodic polarization in an electrochemical flat cell with a 1 cm^2 opening and 0.6 M NaCl + NaOH, pH 10 with ambient aeration at room temperature for 24 h at $\eta_H = -200$ to -1000 mV (-1032 to -1832 mV_{SCE}). b) Pre-charging overpotential vs. SKP potential for samples H pre-charged and measured in the SKP at various RH. 283
- Figure 91. SKP Potential vs. time for ramped RH. Shown for the Au/Al calibration block as well as UNS S46500 in the As Annealed/ CT condition for an uncharged sample and samples H pre-charged at $\eta_H = -100$ and -800 mV for 24 h in 0.6 M NaCl + NaOH pH 10. 284
- Figure 92. SKP potential line scans in 57% RH humid air across H pre-charged zones in as annealed/CT UNS S46500. Samples were pre-charged by cathodic polarization in an electrochemical flat cell with a 1 cm^2 opening and 0.6 M NaCl + NaOH, pH 10 with ambient aeration at room temperature for 24 h at $\eta_H = -400$ mV (-1232 mV_{SCE}). a) Pre-charging overpotential vs. SKP potential for samples H pre-charged in a small aperture cell and measured post-charging in the SKP at various time. b) Initial SKP line scan of small aperture and 1 cm diameter aperture pre-charged samples. 285
- Figure 93. SKP potential line scans in 57% RH humid air across H pre-charged zones in as annealed/CT UNS S46500. Samples were pre-charged by cathodic polarization in full immersion coated with stop off lacquer with openings of 1, 2.5, and 5 mm² and 0.6 M NaCl + NaOH, pH 10 with ambient aeration at room

- temperature for 24 h at $\eta_H = -800$ mV (-1632 mV_{SCE}). a) SKP potential line scan vs. distance in x with area diameter of pre-charging noted by dotted lines. b) SKP potential area scan vs. distance in x and y for 1mm² sample with area of pre-charging noted by dotted lines. 286
- Figure 94. SKP potential line scans in 57% RH humid air across H pre-charged zones in UNS S46500 a) as annealed/CT and b) H900 temper. Samples were pre-charged by cathodic polarization in an electrochemical flat cell with a 1 cm² opening and 0.6 M NaCl + NaOH, pH 10 with ambient aeration at room temperature for 24 h at $\eta_H = -150$ to -1000 mV (-982 to -1832 mV_{SCE}). 287
- Figure 95. SKP potential line scans in 57% RH humid air across H pre-charged zones in UNS K92580 peak aged. Samples were pre-charged by cathodic polarization in an electrochemical flat cell with a 1 cm² opening and 0.6 M NaCl + NaOH, pH 10 with ambient aeration at room temperature for 24 h at $\eta_H = -150$ to -1000 mV (-982 to -1832 mV_{SCE}). 288
- Figure 96. SKP line scans in 57% RH humid air across H pre-charged zones in a hydrogen pre-charged sample by cathodic polarization in an electrochemical flat cell with a 1 cm² opening and 0.6 M NaCl + NaOH, pH 10 with ambient aeration at room temperature for 24 h at $\eta_H = -400$ mV (-1232 mV_{SCE}). a) UNS S46500 as annealed/CT b) UNS K92580. 289
- Figure 97. Average of SKP line scans in 57% RH humid air across H pre-charged zones in a hydrogen pre-charged sample by cathodic polarization in an electrochemical flat cell with a 1 cm² opening and 0.6 M NaCl + NaOH, pH 10 with ambient aeration at room temperature for 24 h at various η_H for a) UNS S46500 as annealed/CT b) UNS K92580. 289
- Figure 98. SKP line scans in 57% RH humid air across H pre-charged zones in a hydrogen pre-charged sample by cathodic polarization in an electrochemical flat cell with a 1 cm² opening and 0.6 M NaCl + NaOH, pH 10 with ambient aeration at room temperature for 18 h at $\eta_H = -200$ mV (-1032 mV_{SCE}) with comparison to calculated spread of C/C_o , over the post-charging measurement time (1080 min) estimated by the equation for steady state diffusion in an infinite plane and $D_{H,eff} = 3.1 \times 10^{-9}$ cm²/s. 290
- Figure 99. a) $C_{H,Diff}$ vs SKP potential in 57% RH humid air for peak aged UNS K92580 and UNS S46500 in the as annealed/CT and H900 temper. 291
- Figure 100. Predicted $C_{H,Diff}$ for measured SKP potentials of hydrogen pre-charged samples in a) UNS S46500 As Annealed/CT, b) UNS S46500 H900, and c) UNS K92580. Predictions from equations found from calibration in Figure 99. Samples pre-charged for 24 hours in 0.6 M NaCl + NaOH pH 10 in a 1cm² opening flat cell. 292
- Figure 101. SKP Φ line scans vs. penetration depth for successive times after 24 hour hydrogen charging of Fe-13Co-11Ni-3Cr-1.2Mo-0.2C-0.02Mn steel performed at $\eta_{chg} = -0.2$ V. The surface at x = zero is the hydrogen charged surface with diffusion into the sample with increasing x. A line scan from the uncharged edge is also displayed. 293

- Figure 102. Hydrogen concentration versus depth profiles based on calculations using Equation 61 given TDS measured $D_{H,eff}$ compared to measured Φ on a) UNS K92580 and b) UNS S46500 steel pre-charged 24 hours at $\eta_{chg} = -0.2$ V..... 293
- Figure 103. a) Predicted $C_{H,Diff}$ from SKP Φ line scans vs. penetration depth for successive times after 24 hour hydrogen charging of Fe-13Co-11Ni-3Cr-1.2Mo-0.2C-0.02Mn steel performed at $\eta_{chg} = -0.2$ V. The surface at $x = \text{zero}$ is the hydrogen charged surface with diffusion into the sample with increasing x . A line scan from the uncharged edge is also displayed. b) Hydrogen concentration versus depth profiles based on calibration equations from Figure 99 vs given TDS measured $D_{H,eff}$ compared to measured Φ on UNS K92580 and steel pre-charged 24 hours at $\eta_{chg} = -0.2$ V. 294
- Figure 104. $C_{x,t}$ vs. t , where lines are calculated diffusion profiles of $C_{x,t}$ vs time post-charging for the estimation of diffusion in an infinite plane with $D_{H,eff}$ of a) $1 \times 10^{-8} \text{ cm}^2/\text{s}$, b) $5 \times 10^{-9} \text{ cm}^2/\text{s}$, c) $1 \times 10^{-9} \text{ cm}^2/\text{s}$, d) $5 \times 10^{-10} \text{ cm}^2/\text{s}$, e) $1 \times 10^{-10} \text{ cm}^2/\text{s}$, and f) $5 \times 10^{-11} \text{ cm}^2/\text{s}$. Symbols represent measurements of $C_{x,t}$ taken from SKP potential measurements of the cross-sectioned sample over time at depths of 0, 0.003, 0.006, 0.009, and 0.013 cm below the charged surface. Best fit $D_{H,eff}$ between profiles c and d, where $D_{H,eff} = 1 \times 10^{-9}$ and $5 \times 10^{-10} \text{ cm}^2/\text{s}$ 295
- Figure 105. E-pH diagram for the iron-water system at 25°C assuming a concentration of iron ionic species of 0.1 M. The predicted potentials and pHs for fog, rain, and dew regimes are indicated.[63] 296
- Figure 106. $C_{H,Diff}$ egress with varying substrate (varying $D_{H,eff}$). a) $C_{H,Diff}$ vs. distance below the hydrogen charging surface is calculated using the assumption for diffusion in an infinite plane and an initial concentration of 10 wppm (1 wppm in the case of UNS G10180). $D_{H,eff}$ values used were 3.5×10^{-9} , 6.2×10^{-9} , 9×10^{-9} , and 1×10^{-7} for UNS S46500 As Annealed/CT, H900, UNS K92580, and UNS G10180, respectively. b) The limiting current density was estimated using the equation $iLH += -nFD\partial C\partial x$, where $y = \partial C\partial x$ taken over the range of 0 to 0.0025 cm (linear section)..... 297
- Figure 107. $C_{H,Diff}$ egress with varying time. $C_{H,Diff}$ vs. distance below the hydrogen charging surface is calculated using the assumption for diffusion in an infinite plane and an initial concentration of 10 wppm a) UNS S46500 As Annealed/CT, c) H900, e) UNS K92580 and g) UNS G10180 (1 wppm). $D_{H,eff}$ values used were 3.5×10^{-9} , 6.2×10^{-9} , 9×10^{-9} , and 1×10^{-7} for UNS S46500 As Annealed/CT, H900, UNS K92580, and UNS G10180, respectively. b, d, f, h) The limiting current density was estimated using the equation $iLH += -nFD\partial C\partial x$, where $y = \partial C\partial x$ taken over the range of 0 to 0.0025 cm (linear section)..... 299
- Figure 108. $C_{H,Diff}$ egress with varying C_o . $C_{H,Diff}$ vs. distance below the hydrogen charging surface is calculated using the assumption for diffusion in an infinite plane and time of 15 min a) UNS S46500 As Annealed/CT, c) H900, e) UNS K92580 and g) UNS G10180. $D_{H,eff}$ values used were 3.5×10^{-9} , 6.2×10^{-9} , 9×10^{-9} , and 1×10^{-7} for UNS S46500 As Annealed/CT, H900, UNS K92580, and UNS G10180, respectively. b, d, f, h) The limiting current density was estimated

- using the equation $i_L H^+ = -nFD\partial C\partial x$, where $y = \partial C\partial x$ x taken over the range of 0 to 0.0025 cm (linear section). 301
- Figure 109. a) $\partial C\partial x$ and b) i_L calculated vs. time using the assumption for diffusion in an infinite plane and an initial concentration of 10 wppm or 1 wppm for UNS G10180. Same assumptions apply as previously stated..... 302
- Figure 110. Oxidation current density compared to the limiting hydrogen oxidation current density vs. time. Oxidation current density was calculated from EIS fitting for a) 0.6 M NaCl + NaOH pH 10 exposures at E_{OCP} vs time and for b) a single exposure of 5 mM NaCl + NaOH pH 10 exposures. $i_{L,Hox}$ were calculated from $\partial C\partial x$ in Figure 109. 303
- Figure 111. Mixed potential theory model for UNS S46500 As Annealed/CT assuming a thin film formation in a low chloride environment (5mM) formed during SKP measurements at 57% RH. Currents for ORR, H/H^+ , and $H_2/2H^+$ were calculated using Equations 63-73 and stated assumptions, while the anodic scan was measured in 5 mM NaCl + NaOH pH 10 at a scan rate of 0.1667 mV/s from -100 mV vs E_{OCP} to 500 mV vs E_{OCP} . a) Displays both H oxidation currents, while b) only displays H/H^+ 304
- Figure 112. Mixed potential theory model for UNS S46500 H900 assuming a thin film formation in a low chloride environment (5mM) formed during SKP measurements at 57% RH. Currents for ORR, H/H^+ , and $H_2/2H^+$ were calculated using Equations 63-73 and stated assumptions, while the anodic scan was measured in 50 mM NaCl + NaOH pH 10 at a scan rate of 0.1667 mV/s from -100 mV vs E_{OCP} to 500 mV vs E_{OCP} . a) Displays both H oxidation currents, while b) only displays H/H^+ 305
- Figure 113. Mixed potential theory model for UNS K92580 assuming a thin film formation in a low chloride environment (5mM) formed during SKP measurements at 57% RH. Currents for ORR, H/H^+ , and $H_2/2H^+$ were calculated using Equations 63-73 and stated assumptions, while the anodic scan was measured in 5 mM NaCl + NaOH pH 10 at a scan rate of 0.1667 mV/s from -100 mV vs E_{OCP} to 500 mV vs E_{OCP} . a) Displays both H oxidation currents, while b) only displays H/H^+ 306
- Figure 114. Mixed potential theory model for UNS G10180 assuming a thin film formation in a low chloride environment (5mM) formed during SKP measurements at 57% RH. Currents for ORR, H/H^+ , and $H_2/2H^+$ were calculated using Equations 63-73 and stated assumptions, while the anodic scan was measured in 50 mM NaCl + NaOH pH 10 at a scan rate of 0.1667 mV/s from -100 mV vs E_{OCP} to 500 mV vs E_{OCP} . a) Displays both H oxidation currents, while b) only displays H/H^+ 307
- Figure 115. Mixed potential theory model for UNS S46500 As Annealed/CT assuming a thin film formation in a low chloride environment (5mM) formed during SKP measurements at 57% RH. Currents for ORR, H/H^+ , and $H_2/2H^+$ were calculated using Equations 63-73 and stated assumptions, while the anodic scan was measured in 5 mM NaCl + NaOH pH 10 at a scan rate of 0.1667 mV/s from -100

- mV vs E_{OCP} to 500 mV vs E_{OCP} . Calculations for ORR and H oxidation were made with pH values of 10, 8, 6, 4, and 2. For these calculations, CO_2 and CH_2 were assumed to be 10^0 atm. 308
- Figure 116. The wide span of different length scales with relation to the material, pitting, and aerosols in play in atmospheric corrosion. SOURCE: University of Virginia, CESE, courtesy of Matthew R. Begley and Richard P. Gangloff, Hongbo Cong and J.R. Scully, Atmospheric Corrosion, Christopher Leygraf and Thomas E. Graedel, and I. Cole. [63, 78, 79]. 309
- Figure 117. Schematic of a) SECM redrawn from Bard[34] and b) cell setup. 349
- Figure 118. Schematic of SECM ME tip approaching substrate surface of a conductor vs. insulator displaying a) positive vs. b) negative feedback. [34]. 349
- Figure 119. Schematic of redox competition mode with ORR as the dominant reaction occurring at the ME (ORR_{ME}/ORR_{WE}). Schematic depletion profiles of O_2 due to ORR are drawn for the oxygen in solution at the tip and at an active catalytic site for ORR on the surface. Each dotted line represents an iso-concentration line. 350
- Figure 120. Variation of salt concentration, 5, 50, and 500 mM NaCl adjusted with NaOH to a pH of 10, for solution characterization. CV on Pt ME tip. CV scanned from -1.0 to 0.5 V_{SCE} at a scan rate of 100 mV/s. The voltage of -0.8 $V_{Ag/AgCl}$ is noted as it was selected as the voltage to apply to the ME tip to induce ORR at the tip. . 351
- Figure 121. Schematic of steady state H diffusion in steel during cathodic pre-charging with the red region denoting H_{abs} . Diffusion profiles were estimated by steady state spherical diffusion with a $D_{H,eff} = 3.5 \times 10^{-9} \text{ cm}^2/\text{s}$ 351
- Figure 122. One hour E_{OCP} of a) UNS S46500 H900 and b) peak-aged UNS K92580 in 5 mM NaCl + NaOH pH 5.5 - 10 and post EIS (shown in Figure 123) anodic polarizations were acquired from -100 mV below E_{OCP} to 1 V vs E_{OCP} at a scan rate of 0.1667 mV/s in the same solution, c) UNS S46500 and d) UNS K92580. No intentional cathodic charging was applied prior to anodic polarization scans. 352
- Figure 123. EIS post one hour E_{OCP} of peak aged UNS S46500 a) Nyquist plot, c) phase angle, and e) Bode plot, and UNS K92580 b) Nyquist plot, d) phase angle, and f) Bode plot, in 5 mM NaCl + NaOH pH 5.5 - 10. No intentional cathodic charging was applied prior to EIS scans. 354
- Figure 124. i_{ox} vs. pH for UNS S46500 and UNS K92580. Samples were pre-exposed for 1 h at E_{OCP} in 5mM NaCl + NaOH pH 5.5-10 with no intentional cathodic pre-charging. EIS was acquired at the E_{OCP} with a 20 V_{rms} , 6 mV/dec and from 1 mHz to 10 kHz. No intentional cathodic charging was applied prior to EIS scans. i_{ox} was calculated from EIS fitting and determination of R_p and is plotted vs. the average limiting H oxidation current density ($i_{L,Hox}$). The average $i_{L,Hox}$ ($H \rightarrow H^+ + e^-$) values were calculated from the average of the first thirty min of $\partial C/\partial x$ values determined in Figure 43 (Ch 3). 355

- Figure 125. Variation of salt concentration, 5, 50, and 500 mM NaCl, for solution determination. A 1 h E_{OCP} for a) UNS S46500 and b) UNS K92580 followed by an anodic scan from -100 mV vs OCP at a scan rate of 0.1667 mV/s. No intentional cathodic charging was applied prior to scans. 356
- Figure 126. UNS S46500 As Annealed/CT EIS in 0.1 M NaOH, 5 mM NaCl + NaOH pH 10, 5.1 M NaCl, and 0.1 M HCl, a) Comparison of electrolytes, b) Phase plot comparison, and c) Bode plot comparison. No intentional cathodic charging was applied prior to scans. 357
- Figure 127. UNS S46500 H900 EIS in 0.1 M NaOH, 5 mM NaCl + NaOH pH 10, 5.1 M NaCl, and 0.1 M HCl, a) Comparison of electrolytes, b) Phase plot comparison, and c) Bode plot comparison. No intentional cathodic charging was applied prior to scans. 358
- Figure 128. UNS K92580 EIS in 0.1 M NaOH, 5 mM NaCl + NaOH pH 10, 5.1 M NaCl, and 0.1 M HCl, a) Comparison of electrolytes, b) Phase plot comparison, and c) Bode plot comparison. No intentional cathodic charging was applied prior to scans. 359
- Figure 129. UNS G10180 EIS in 0.1 M NaOH, 5 mM NaCl + NaOH pH 10, 5.1 M NaCl, and 0.1 M HCl, a) Comparison of electrolytes, b) Phase plot comparison, and c) Bode plot comparison. No intentional cathodic charging was applied prior to scans. 360
- Figure 130. Comparison of steels across electrolytes: a) 0.1 M NaOH, b) 5 mM NaCl + NaOH pH 10, c) 5.1 M NaCl, and d) 0.1 M HCl. No intentional cathodic charging was applied prior to scans. 361
- Figure 131. i_{ox} vs. measurement solution for UNS S46500 H900 and as annealed/CT, UNS K92580, and UNS G10180. Samples were exposed in 0.01 M HCl, 0.1 M NaOH, 5mM NaCl + NaOH pH 10, and 5.1 M NaCl with no intentional cathodic pre-charging. EIS was acquired at the E_{OCP} with a 20 V_{rms} , 6 mV/dec and from 1 mHz to 10 kHz. i_{ox} was calculated from EIS fitting and determination of R_p for samples exposed in the selected electrolytes with no intentional cathodic pre-charging and are plotted vs. the average limiting H oxidation current density ($i_{L,Hox}$). The average $i_{L,Hox}$ ($H \rightarrow H^+ + e^-$) values were calculated from the average of the first thirty min of $\partial C \partial x$ values determined in Figure 43 (Ch 3). 362
- Figure 132. Comparison of SECM measurement solutions, 5 mM NaCl + 0.01 M ferrocene methanol vs. 0.1 M NaOH + 0.01 M ferrocene methanol. Approach over epoxy at a rate of 1 $\mu m/s$ with the Pt tip held at a constant potential of +0.4 $V_{Ag/AgCl}$ shown in a) and b). The epoxy/Au sample was allowed to float at E_{OCP} during the measurement. Line scans from epoxy to Au calibration sample at a constant height of 30 μm tip to surface height in c) raw current measured and b) normalized current density (normalized to the steady state current at the tip at 0.4 $V_{Ag/AgCl}$ in each solution). 363
- Figure 133. Comparison of ME tip current above Au in epoxy in two SECM measurement solutions, a) 5 mM NaCl + 0.01 M ferrocene methanol vs. b) 0.1 M NaOH + 0.01 M ferrocene methanol. Area scans taken with the Pt tip held at a

- constant potential of $+0.4 \text{ V}_{\text{Ag/AgCl}}$ and a height of $30 \mu\text{m}$ above the same area of Au in epoxy..... 364
- Figure 134. A scans from epoxy to uncharged UNS S46500 for solution calibration. a) Feedback mode ($\text{ox}_{\text{ME/red,WE}}$) schematic, b) $5 \text{ mM NaCl} + 0.01 \text{ M ferrocene methanol}$, $30 \mu\text{m}$ height, c) Redox competition schematic, d) 0.1 M NaOH e) Redox competition ($\text{red}_{\text{ME/red,WE}}$) schematic, f) $5 \text{ mM NaCl} + \text{NaOH pH } 10$, $30 \mu\text{m}$ height, g) Redox competition ($\text{red}_{\text{ME/red,WE}}$) schematic, and h) $5 \text{ mM NaCl} + \text{NaOH pH } 10$, $100 \mu\text{m}$ height..... 366
- Figure 135. Comparison of line scans with ME tip signal for feedback diffusion mode of $\text{Fe}^{+2} \rightarrow \text{Fe}^{+3} + \text{e}^-$ (black line) and redox competition mode with ORR at the tip (blue and red lines) from Epoxy to uncharged UNS S46500 in the three different solutions, the i is normalized to the steady state current found from the respective CV on the Pt tip in each solution at the operating voltage ($+0.4 \text{ V}_{\text{Ag/AgCl}}$ for $5 \text{ mM NaCl} + 0.01 \text{ M ferrocene methanol}$ and $-0.8 \text{ V}_{\text{Ag/AgCl}}$ for 0.1 M NaOH and $5 \text{ mM NaCl} + \text{NaOH pH } 10$) 367
- Figure 136. Tip to substrate height calibration. a) CV on Pt ME in $5 \text{ mM NaCl} + \text{NaOH pH } 10$ showing ORR and b) Line scans of $i_{\text{ORR,ME}}$ for height calibration. Heights less than $30 \mu\text{m}$ are not shown as below a height of $30 \mu\text{m}$ in the current SECM setup, topography/tilt of sample creates risk of crashing tip into surface. Above $30 \mu\text{m}$ the difference in $i_{\text{ORR,ME}}$ measured above steel vs. epoxy becomes less defined. Scans were taken from epoxy to steel substrate in $5 \text{ mM NaCl} + \text{NaOH pH } 10$ with a potential of $-0.6 \text{ V}_{\text{Ag/AgCl}}$ applied to the tip, except at $100 \mu\text{m}$ distance where a voltage of $-0.8 \text{ V}_{\text{Ag/AgCl}}$ was applied to try to increase the signal. ∞ 368
- Figure 137. Initial scans of hydrogen uncharged vs. pre-charged steel in the SECM in feedback mode. a) Feedback mode ($\text{ox}_{\text{ME/red,WE}}$) for $\text{Fe}^{3+} + \text{e}^- \rightleftharpoons \text{Fe}^{2+}$ schematic, b) UNS S46500 line scans from uncharged to pre-charged steel in $5 \text{ mM NaCl} + 0.01 \text{ M ferrocene methanol}$, pre-charged for 24 h in an electrochemical flat cell in $0.6 \text{ M NaCl} + \text{NaOH pH } 10$ at $\eta_{\text{H}} = -400, -600, \text{ and } -800 \text{ mV}$ ($-1232, -1432, \text{ and } -1632 \text{ mV}_{\text{SCE}}$). 369
- Figure 138. Initial scans of hydrogen uncharged vs. pre-charged UNS S46500 H900 in the SECM in redox competition mode ($\text{red}_{\text{ME/red,WE}}$). a) Redox competition mode schematic, b) Scans post-charging time of UNS S46500 line scans from uncharged to pre-charged steel in $5 \text{ mM NaCl} + \text{NaOH pH } 10$, pre-charged for 24 h in an electrochemical flat cell in $0.6 \text{ M NaCl} + \text{NaOH pH } 10$ at $\eta_{\text{H}} = -800 \text{ mV}$ ($-1632 \text{ mV}_{\text{SCE}}$). 370
- Figure 139. Redox competition ($\text{red}_{\text{ME/red,WE}}$) scans of hydrogen uncharged vs. pre-charged UNS S46500 and UNS K92580 in the SECM. a,c,e, and g) Redox Competition schematic, As Annealed/CT UNS S46500 line scans of $i_{\text{ORR,ME}}$ vs. distance in x from steel to epoxy and epoxy to steel in b) $5 \text{ mM NaCl} + \text{NaOH pH } 10$ and d) 0.1 M NaOH , and UNS K92580 in f) $5 \text{ mM NaCl} + \text{NaOH pH } 10$ and h) 0.1 M NaOH pre-charged for 24 h in an electrochemical flat cell in $0.6 \text{ M NaCl} + \text{NaOH pH } 10$ at $\eta_{\text{H}} = -800 \text{ mV}$ ($-1632 \text{ mV}_{\text{SCE}}$). 372

- Figure 140. Redox competition ($\text{red}_{\text{ME}}/\text{red}_{\text{WE}}$) scans of hydrogen uncharged vs. precharged UNS S46500 and UNS K92580 in the SECM. a, c, and e) Redox Competition schematic. b) As Annealed/CT UNS S46500 line scans of $i_{\text{ORR,ME}}$ vs. distance in x from steel to epoxy in 0.1 M NaOH, pre-charged for 24 h in an electrochemical flat cell in 0.6 M NaCl + NaOH pH 10 at $\eta_{\text{H}} = -200, -400, -600,$ and -800 mV ($-1032, -1232, -1432,$ and -1632 mV_{SCE}), d) As Annealed/CT UNS S46500 with similar pre-charging conditions, but SECM scans in 5 mM NaCl + NaOH, pH 10, and f) UNS K92580 with similar pre-charging conditions, with SECM scans in 5 mM NaCl + NaOH, pH 10. 374
- Figure 141. CH_{diff} vs absolute value of normalized ME tip current ($i_{\text{ORR,ME}}$) in the SECM under redox competition modes ($\text{red}_{\text{ME}}/\text{red}_{\text{WE}}$) in a) 0.1 M NaOH and 5 mM NaCl + NaOH pH 10 for UNS S46500 in the as annealed/CT condition and b) in 5 mM NaCl + NaOH pH 10 for peak aged UNS K92580 and UNS S46500 in the as annealed/CT condition. $i_{\text{ORR,ME}}$ was taken as the average measured over the pre-charged line scan area. 375
- Figure 142. Redox competition ($\text{red}_{\text{ME}}/\text{red}_{\text{WE}}$) scans of hydrogen uncharged vs. pre-charged UNS S46500 in the SECM. a, and c) Redox Competition schematic. Comparison of hydrogen pre-charging time for as annealed/CT UNS S46500, line scans of $i_{\text{ORR,ME}}$ vs. distance in x from steel to epoxy in 5 mM NaCl + NaOH pH 10. Pre-charged for 24 and 48 h in an electrochemical flat cell in 0.6 M NaCl + NaOH pH 10 ambiently aerated at b) $\eta_{\text{H}} = -200$ (-1032 mV_{SCE}) and d) $\eta_{\text{H}} = -800$ (-1632 mV_{SCE}). 376
- Figure 143. Feedback diffusion mode ($\text{ox}_{\text{ME}}/\text{red}_{\text{WE}}$) scans of hydrogen uncharged vs. pre-charged UNS S46500 in the SECM. a) Feedback mode schematic, b) Scans post-charging time, 30 min and 45 min in-situ in the SECM and 3 days ex-situ in dry lab air, of UNS S46500 line scans of ME tip current vs. distance in x from uncharged to pre-charged steel in 5mM NaCl + 0.01 M ferrocene methanol, pre-charged for 24 h in an electrochemical flat cell in 0.6 M NaCl + NaOH pH 10 at $\eta_{\text{H}} = -800$ mV (-1632 mV_{SCE}). 377
- Figure 144. a) Redox Competition ($\text{red}_{\text{ME}}/\text{red}_{\text{WE}}$) schematic. b) Scans of hydrogen uncharged vs. pre-charged steel in the SECM, comparison of time post-charging for as annealed/CT UNS S46500, line scans of $i_{\text{ORR,ME}}$ vs. distance in x from steel to epoxy in 5 mM NaCl + NaOH pH 10. Pre-charged for 24 in an electrochemical flat cell in 0.6 M NaCl + NaOH pH 10 at $\eta_{\text{H}} = -800$ (-1632 mV_{SCE}). Scans taken 30 min post-charging and 3 days ex-situ post-charging exposed in dry lab air.. 378
- Figure 145. Scans of hydrogen uncharged vs. pre-charged steel in the SECM in redox competition mode with time in-situ in the SECM post-charging. a) Redox competition mode ($\text{red}_{\text{ME}}/\text{red}_{\text{WE}}$) schematic using O_2 , b) Scans post-charging time of UNS S46500 line scans from uncharged to pre-charged steel in 5mM NaCl + NaOH pH 10, pre-charged for 24 h in an electrochemical flat cell in 0.6 M NaCl + NaOH pH 10 at $\eta_{\text{H}} = -800$ mV (-1632 mV_{SCE}). 379
- Figure 146. Analytical concentration profile of O_2 depletion as the SECM ME tip approaches the steel surface (with dissolved H). The oxygen concentration fields arising from the two surfaces overlap at even 1000 μm distance. These

concentration profiles were generated using analytical expressions for estimating diffusion in an infinite plane, with known diffusion coefficients for H in UNS S46500 ($D_H = 6.2 \times 10^{-9} \text{ cm}^2/\text{s}$) and O_2 in solution ($D_{\text{O}_2} = 1.46 \times 10^{-5} \text{ cm}^2/\text{s}$). The source concentrations were assumed as fixed and the reactions were considered to be under diffusion control. The working distance used for the line scan experiments is 100 μm . [26] 380

Figure 147. Analytical concentration profiles of hemispherical H^+ transport from the H pre-charged area in solution were generated using the estimation for diffusion in an infinite plane with known diffusion coefficients for H in UNS S46500 ($D_H = 6.2 \times 10^{-9} \text{ cm}^2/\text{s}$) and H^+ in dilute aqueous solution ($D_{\text{H}^+} = 4.4 \times 10^{-5} \text{ cm}^2/\text{s}$). Diffusion times utilized were 25 h for H in the steel and 1h for H^+ in solution above the pre-charged SS. [26] 381

Figure 148. Schematic of a) Feedback diffusion ($\text{Ox}_{\text{ME/red,WE}}$) and b) Redox competition ($\text{red}_{\text{ME/red,WE}}$) above a hydrogen pre-charged steel sample. 382

Figure 149. Pourbaix diagram in water at 25°C for a) Fe and b) H. The range of passivity is indicated. [35] 383

Figure 150. Mixed potential theory model for UNS S46500 As Annealed/CT assuming diffusion limiting x in the SECM is $x = (D_{\text{O}_2}t)^{1/2}$, where t is time = 3600s and $D_{\text{O}_2} = 1.46 \times 10^{-5} \text{ cm}^2/\text{s}$. Currents for ORR, H/H^+ , and $\text{H}_2/2\text{H}^+$ were calculated using Equation from Ch 3 and stated assumptions, while the anodic scan was measured in 5 mM NaCl + NaOH pH 10 at a scan rate of 0.1667 mV/s from -100 mV vs E_{OCP} to 500 mV vs E_{OCP} . a) Displays both H oxidation currents, while b) only displays H/H^+ 384

Figure 151. Mixed potential theory model for UNS S46500 H900 assuming diffusion limiting x in the SECM is $x = (D_{\text{O}_2}t)^{1/2}$, where t is time = 3600s and $D_{\text{O}_2} = 1.46 \times 10^{-5} \text{ cm}^2/\text{s}$. Currents for ORR, H/H^+ , and $\text{H}_2/2\text{H}^+$ were calculated using Equation from Ch 3 and stated assumptions, while the anodic scan was measured in 50 mM NaCl + NaOH pH 10 at a scan rate of 0.1667 mV/s from -100 mV vs E_{OCP} to 500 mV vs E_{OCP} . a) Displays both H oxidation currents, while b) only displays H/H^+ 385

Figure 152. Mixed potential theory model for UNS K92580 assuming diffusion limiting x in the SECM is $x = (D_{\text{O}_2}t)^{1/2}$, where t is time = 3600s and $D_{\text{O}_2} = 1.46 \times 10^{-5} \text{ cm}^2/\text{s}$. Currents for ORR, H/H^+ , and $\text{H}_2/2\text{H}^+$ were calculated using Equation from Ch 3 and stated assumptions, while the anodic scan was measured in 5 mM NaCl + NaOH pH 10 at a scan rate of 0.1667 mV/s from -100 mV vs E_{OCP} to 500 mV vs E_{OCP} . a) Displays both H oxidation currents, while b) only displays H/H^+ 386

Figure 153. Mixed potential theory model for UNS G10180 assuming diffusion limiting x in the SECM is $x = (D_{\text{O}_2}t)^{1/2}$, where t is time = 3600s and $D_{\text{O}_2} = 1.46 \times 10^{-5} \text{ cm}^2/\text{s}$. Currents for ORR, H/H^+ , and $\text{H}_2/2\text{H}^+$ were calculated using Equation from Ch 3 and stated assumptions, while the anodic scan was measured in 50 mM NaCl + NaOH pH 10 at a scan rate of 0.1667 mV/s from -100 mV vs E_{OCP} to 500 mV vs E_{OCP} . a) Displays both H oxidation currents, while b) only displays H/H^+ 387

Figure 154. Schematic of droplet exposure and SKP line scan post exposure. 407

- Figure 155. Schematic of UNS S46500 H900 sample a) atmospheric pre-exposure and b) SKP scan shown on section taken around pit, post-exposure. 407
- Figure 156. Schematic of UHSS sample a) atmospheric pre-exposure and b) SECM scan area post-exposure. 408
- Figure 157. Anodic polarizations, from -100 mV vs EOCP to +500 mV vs EOCP in 5.5 pH NaCl solution at various concentrations; 0.05, 0.9, and 5.3 M NaCl, a) UNS S46500 H900 and b) peak aged UNS K92580. 408
- Figure 158. Anodic polarizations, from -100 mV vs EOCP to +500 mV vs EOCP in 3.9 M MgCl₂ adjusted to various pH; 2,5, and 8 for a) UNS S46500 H900 and b) peak aged UNS K92580. 409
- Figure 159. UNS S46500 H900 exposed to 3.9 M MgCl₂ 10 μ L droplet at 58% RH for 48 h a) optical and d) SEM image, 1 week b) optical e) SEM image, and 2 weeks c) optical and f) SEM image. A second set of SEM images of samples of UNS S46500 H900 displaying similar exposures of a) 48 h, b) 2 weeks, and c) 3 weeks. 410
- Figure 160. a) SKP line scans across an area of UNS S46500 H900 (a and c) pre-exposed for 2 and 14 days at 58% RH with a 3.9 M MgCl₂, 10 μ L droplet. Scans were taken 5 min post-exposure and 4 h post-exposure near the pit formed underneath the droplet. SKP area scan of pre-exposed UNS S46500 (b and d) H900. *NB: As the area scan takes 4 hours to complete, it is meant only as an indicator of droplet/pit location, as significant outgassing of H can occur over this time period and measurements cannot be directly correlated to H concentrations.* 411
- Figure 161. a) SKP line scans across an area of UNS S46500 as annealed/CT (a, c, and e) pre-exposed for 2, 14 and 21 days at 58% RH with a 3.9 M MgCl₂, 10 μ L droplet. Scans were taken 5 min post-exposure and 4 h post-exposure near the pit formed underneath the droplet. SKP area scan of pre-exposed UNS S46500 (b, d, and f) as annealed/CT. *NB: As the area scan takes 4 hours to complete, it is meant only as an indicator of droplet/pit location, as significant outgassing of H can occur over this time period and measurements cannot be directly correlated to H concentrations.* 412
- Figure 162. SKP area scans across an area of UNS S46500 H900 (Sample 1) pre-exposed for 14 days at 58% RH with a 3.9 M MgCl₂, 10 μ L droplet. Scans were taken a) 20 min post-exposure and b) 5 days post-exposure near the pit formed underneath the droplet. C) SKP line scans of pre-exposed UNS S46500 H900 at various times post-exposure. *NB: As the area scan takes 4 hours to complete, it is meant only as an indicator of droplet/pit location, as significant outgassing of H can occur over this time period and measurements cannot be directly correlated to H concentrations.* 414
- Figure 163. a) Example 3-D optical microscopy image of pit formed after 14 day exposure. b) Line scans into the depth of an unexposed sample, prepared and cut in the same manner as the pitted sample c) Area scan of SKP potential showing distance along pit vs. depth into sample of UNS S46500 pre-exposed with 3.9 M MgCl₂ droplet, 14 days, and 58 %RH. SKP potential is lower at edge of sample

near pit. d) Distance along the cut planar surface adjacent to the pit showing the height measured by SKP, indicating that the topography of the sample is flat. . 415

Figure 164. SKP line scans across an area of UNS S46500 H900 a) pre-exposed for 7 days at 98% RH with a 1 M HCl, 4 μ L droplet. Scans were taken 5 min post-exposure and 4 h post-exposure near the pit formed underneath the droplet. SKP area scan of pre-exposed UNS S46500 b) H900. *NB: As the area scan takes 4 hours to complete, it is meant only as an indicator of droplet location, as significant outgassing of H can occur over this time period and measurements cannot be directly correlated to H concentrations.* 416

Figure 165. SECM area scan in 5 mM NaCl + NaOH pH 10 solution, ME tip polarized to $-0.8 V_{Ag/AgCl}$, tip to sample distance of 30 μ m, of UNS S46500 As Annealed/ CT exposed to 3.9 M $MgCl_2$ 10 μ L droplet at 58 %RH for 1 week. A) Area scan, b) contour plot of $i_{ORR,ME}$, and c) optical image of pit. 417

Figure 166. SECM area scan in 5 mM NaCl + NaOH pH 10 solution, ME tip polarized to $-0.8 V_{Ag/AgCl}$, tip to sample distance of 30 μ m, of UNS S46500 As Annealed/ CT exposed to 3.9 M $MgCl_2$ 10 μ L droplet at 58 %RH for 2 weeks. A) Area scan, b) contour plot of $i_{ORR,ME}$, and c) optical image of pit. 418

Figure 167. SECM area scan in 5 mM NaCl + NaOH pH 10 solution, ME tip polarized to $-0.8 V_{Ag/AgCl}$, tip to sample distance of 30 μ m, of UNS S46500 As Annealed/ CT exposed to 3.9 M $MgCl_2$ 10 μ L droplet at 58 %RH for 3 weeks. A) Area scan, b) contour plot of $i_{ORR,ME}$, and c) optical image of pit. 419

Figure 168. Schematic of SECM modes; Hemispherical diffusion occurs far from the sample surface where $i_{ORR,ME}$ is limited by diffusion of the O_2 in the electrolyte, diffusion limited scenario occurs when the $i_{ORR,ME}$ is further limited as the tip approaches the sample surface and diffusion is decreased, imaging topography occurs when the $i_{ORR,ME}$ increases above a recess in topography as the diffusion is enhanced, and redox competition occurs when the $i_{ORR,ME}$ decreases above an active site as the tip is in competition with the surface for O_2 . Reproduced from [25]. 420

Figure 169. Schematic of H uptake and pH distribution from a pit. Spherical diffusion based on 14 day droplet exposure, formation of a 40 μ m diameter pit, and calculation for diffusion assuming a constant spherical source.[26] $D_{H,eff}$ in steel used was $6.2 \times 10^{-9} \text{ cm}^2/\text{s}$ and diffusion of H^+ in aqueous solution was $4.4 \times 10^{-5} \text{ cm}^2/\text{s}$ 421

List of Abbreviations and Symbols

ASTM	<i>American Society of Testing and Materials</i>
α	<i>Gerberich parameter: coefficient in units of MPa-m^{1/2}/atom fraction H</i>
α''	<i>Gerberich parameter: constant determined by computer simulation of the dislocation structure about the crack tip</i>
β'	<i>Gerberich parameter: constant determined by computer simulation of the dislocation structure about the crack tip</i>
C	<i>concentration</i>
C_{CRIT}	<i>crack growth rate mode parameter: critical stress-enhanced H concentration required at X_{CRIT} for damage</i>
$C_{H,Diff}$	<i>diffusible hydrogen concentration, $C_L + \sum C_{T,r}$</i>
$C_{H,Diff,crit}$	<i>the critical $C_{H,Diff}$ above which K_{TH} drops significantly</i>
$C_{H\sigma}$	<i>hydrogen concentration enhanced by crack tip stresses and reversible traps</i>
C_L	<i>lattice hydrogen concentration</i>
$C_{T,irr}$	<i>irreversibly trapped hydrogen concentration</i>
$C_{T,r}$	<i>reversibly trapped hydrogen concentration</i>
$C_{H,total}$	<i>total hydrogen concentration, $C_{H,diff} + \sum C_{T,irr}$</i>
$D_{H,eff}$	<i>trap-affected diffusivity of hydrogen</i>
D_L	<i>diffusivity of H in the lattice</i>
da/dt_{II}	<i>stage II crack growth rate</i>
EAC	<i>environmentally assisted cracking</i>
$E_{1/2}$	<i>reversible half cell potential</i>
E_{act}	<i>activation energy</i>
$E_{applied}$	<i>applied potential</i>
E_B	<i>trap site binding energy</i>
E_{corr}	<i>corrosion potential</i>
E_{couple}	<i>coupled potential</i>
E_{H/H^+}	<i>reversible potential for hydrogen (H/H^+)</i>
E_{H_2/H^+}	<i>reversible potential for hydrogen ($H_2/2H^+$)</i>
E_{OCP}	<i>open circuit potential</i>
E_p	<i>pitting potential</i>
E_{pass}	<i>passivation potential</i>
ERD	<i>elastic recoil detection</i>
η	<i>hydrogen overpotential</i>
η_{chg}	<i>hydrogen charging overpotential</i>
F	<i>Faraday's constant</i>
FPZ	<i>fracture process zone</i>

IR	<i>ohmic potential</i>
H	<i>hydrogen</i>
HE	<i>hydrogen embrittlement</i>
HEAC	<i>hydrogen environment assisted cracking</i>
HER	<i>hydrogen evolution reaction</i>
i_0	<i>exchange current density</i>
i_{an}	<i>total anodic current density</i>
i_{ca}	<i>cathodic current density</i>
i_{corr}	<i>corrosion current density</i>
i_{couple}	<i>coupled current density</i>
i_{ct} or i_H	<i>charge transfer controlled current density</i>
i_{H/H^+}	<i>hydrogen current density</i>
i_{H_2O}	<i>charge transfer controlled ORR reduction current density</i>
i_{lim}	<i>limiting current density</i>
$i_{L,Hox}$	<i>limiting current density for H oxidation</i>
$i_{ORR,ME}$	<i>ME tip current due to ORR</i>
IR	<i>ohmic potential</i>
K	<i>ratio of the rate constants for absorption and desorption</i>
k_1	<i>H discharge rate constant</i>
k_2	<i>H recombination rate</i>
K_{IG}	<i>critical Griffith stress-intensity factor for cleavage fracture without H</i>
K_{TH}	<i>threshold stress intensity</i>
LALT	<i>laboratory accelerated life test</i>
ME	<i>microelectrode</i>
NHE	<i>normal hydrogen electrode</i>
$N_{lattice}$	<i>number of interstitial octahedral sites</i>
$N_{T,i}$	<i>trap site concentration for trap site i</i>
OCP	<i>open circuit potential</i>
ORR	<i>oxygen reduction reaction</i>
$OX_{,ME/red,WE}$	<i>feedback diffusion mode SECM</i>
$\theta_{lattice}$	<i>fractional coverage of lattice sites</i>
θ_T	<i>trap enhanced hydrogen coverage</i>
$\theta_{T,i}$	<i>fractional H coverage of trap site i</i>
PREN	<i>pitting resistance equivalency number</i>
$Q_{H,abs}$	<i>charge calculated from H absorbed</i>
Q_{HER}	<i>charge due to HER</i>
Q_{mass}	<i>charge calculated by mass loss</i>
R	<i>ideal gas constant</i>
$red_{,ME/red,WE}$	<i>redox competition mode SECM</i>

RH	<i>relative humidity</i>
SCC	<i>stress corrosion cracking</i>
SCE	<i>saturated calomel electrode</i>
SECM	<i>scanning electrochemical microscope</i>
SEM	<i>scanning electron microscope</i>
SHE	<i>saturated hydrogen electrode</i>
SKP	<i>scanning Kelvin probe</i>
SKPFM	<i>scanning Kelvin probe force microscope</i>
SSRT	<i>slow strain rate test</i>
σ_H	<i>hydrostatic stress</i>
σ_{YS}	<i>yield strength</i>
T	<i>temperature</i>
t	<i>time</i>
TDS	<i>thermal desorption spectroscopy</i>
UHSS	<i>ultra-high strength steel</i>
$V_{Ag/AgCl}$	<i>potential vs. Ag/AgCl</i>
V_H	<i>H volume fraction</i>
V_{SCE}	<i>potential vs. SCE</i>
V_{NHE}	<i>potential vs. NHE</i>
x	<i>crack or crevice depth</i>
X_{crit}	<i>the critical distance ahead of the crack tip surface</i>
XRD	<i>X-ray diffraction</i>

CHAPTER 1. Introduction

1.1. Background

The high cost of corrosion degradation in aging infrastructure, combined with the need for new high-performance materials for use in increasingly severe environments, has generated a significant motivation for materials durability/ resiliency research in today's highly technological society.[1] Hydrogen embrittlement (HE), a specific form of corrosion, which can lead to hydrogen environment assisted cracking (HEAC), continues to be a large area of concern, specifically in ultra-high strength steels (UHSS) prevalent in key structural and vehicle components.[2, 3] Of particular interest are the UHSS used in landing gear for naval aircraft, such as AerMet 100 (UNS K92580) and Custom 465 (UNS S46500). These newer alloys were designed to replace previously used materials, like UNS G43406, a high strength steel that is highly susceptible to stress corrosion cracking (SCC).[4, 5] However, while new UHSS have shown to generally possess greater resistance to SCC [6], they continue to display high susceptibility to cracking due to HE in the presence of sufficient hydrogen (H) levels.[4] The resistance of these steels to HE is greatly dependent on the diffusible hydrogen concentration developed within them during either processing or subsequent exposure to environments when in service. Thus post-processing HE is dependent on the hydrogen produced in the exposure environment and the subsequent production, absorption, and trapping ability of the materials.[7]

While hydrogen production and uptake is well documented in many full immersion environments, including high strength materials under cathodic polarization[7-11], there is a lack of information regarding hydrogen in atmospheric exposure conditions. Marine aerosols, industrial pollutants, and other environmental factors, such as UV and relative humidity (RH), greatly affect atmospheric corrosion damage, where ORR (oxygen reduction) is the primary cathodic reaction.[12] However, HER (hydrogen evolution) and reduction of H_2O can also occur. Hydrogen production and uptake that occurs on a metal surface is likely affected by many of the same environmental factors that cause high environmental severity, since anodic and cathodic reactions are coupled during naturally occurring corrosion.[13] An understanding of the effects of these various exposure conditions on hydrogen production and uptake in UHSS is necessary to develop future alloys as well as to anticipate and manage the effects of environment severity on currently employed UHSS.

1.1.1. Hydrogen Detection Methods

Strongly related to this problem, and that of hydrogen environment assisted cracking, is the local spatial determination of hydrogen concentrations. Knowledge of localized hydrogen concentrations under aerosol deposition sites, droplets, crack tips, occluded sites, microstructural features, or other enhanced local sources for hydrogen production and absorption would aid in understanding HE. Unfortunately, local hydrogen detection and quantification remains a challenge.

Hydrogen concentrations and diffusion properties have been well quantified in UHSS and other pertinent engineering materials, through global measurements over the meso-length scale.[7, 14-16] The more traditional hydrogen concentration measurement tools, such as thermal desorption spectroscopy (TDS), barnacle cell, and Devanathan Stachurski permeation cell, measure hydrogen with resolution limited to typically greater than a mm length scale.[15, 17-19] As shown in Table 1, with added serial grinding/ sectioning of samples, some depth detection can be achieved through TDS[20], but these methods are typically used over larger area/ volume samples and are ideally utilized for detection of H from samples that are uniformly charged.

Techniques for spatial detection at the sub-mm length scales, specifically with lateral detection, are lacking. Significant challenges to the HE problem include detection of H at pits, cracks and at features associated with corrosion morphology produced by atmospheric exposure (Figure 1). Tritium autoradiography, nuclear reaction analysis, scanning electrochemical microscopy, microprinting to enable an on/off hydrogen assessment, rescaled pits using TDS, and elastic recoil detection have been applied for spatial H detection.[20-29] Permeation was employed for temporal resolution of H during atmospheric exposure.[30] However, these techniques were either destructive to the sample, had no or poor lateral resolution, lacked quantification of H concentrations, or did not monitor hydrogen levels in real time.

The Scanning Kelvin Probe (SKP), SKP force microscope (SKPFM), and SKP combined with TDS and secondary ion mass spectrometry are promising new methods for spatial H

detection with lateral and depth profiling (utilizing cross-sections of samples).[31-41] Recently, the SKP has detected H uptake with a modified permeation technique with backside detection through a Pd film in permeation mode during atmospheric corrosion.[42] However, these methods have not yet provided quantification of the spatial H concentration at local corrosion sites due to atmospheric uptake.

1.1.2. Atmospheric Corrosion of Ferrous Alloys in Outdoor Environments

It is important to this dissertation to begin our discussion of these steels by considering atmospheric corrosion and, to a lesser extent, field and laboratory exposures in thin films, droplets, or atmospheric conditions. Atmospheric corrosion, in both field and laboratory settings, has been fairly well quantified for uniform and pitting corrosion of steels.[43-46] Also, there exists substantial research in the correlation of atmospheric environments to laboratory accelerated life test (LALT) environments.[47] Modification of standard engineering tests, for example the ASTM B-117, with UV, ozone, etc. has helped to produce environments more similar to real world exposures.[48] When ASTM B-117 was modified with 23 ppm ozone, acceleration factors for corrosion damage from these modified LALT vs. field exposures were upwards of 20x that of severe marine environments (Daytona Beach, FL) to 120x the moderate environment (Trenton, NJ).[48] The indoor atmosphere modified with ozone was as oxidizing as natural field exposures. However, unfortunately, studies directed at better field vs. laboratory exposures correlation have often compared morphology and even corrosion products[48], but did not consider the fraction of the anodic reaction supported by proton discharge or water reduction.

The formation and precipitation of various oxides (listed in Table 2) produced on Fe alloys under environmental exposures can give an indication of the severity of the exposure and contribute to understanding lab vs. field. Oxides can also provide information as to what species were present in solution prior to the formation of the oxide.[49, 50] However, they also do not shed light on hydrogen production and uptake.

Corrosion Metrics for Atmospheric Corrosion: Often times a corrosion metric, such as mass loss, can be used as a correlation between lab and field experiments. Townsend et al. determined the effects of alloying elements on steel through mass loss due to corrosion in three industrial atmospheric field exposures; Bethlehem; PA, Pittsburgh, Pa; and Columbus, OH. Samples alloyed with P, Si, Cr, C, Cu, Ni, Sn, and Mo were more corrosion resistant, those alloyed with S had a large adverse effect, and V, Mn, Al, Co, As, and W had little to no effect.[45] Baker and Lee identified the severity of various marine environments, both natural and artificial, with mass loss in iron over time. [51] Samples exposed in more severe marine environments suffered greater mass loss compared to those in moderate marine, while for LALT samples exposed to solutions with lower wt% chloride suffered greater mass losses per exposure time compared to those with higher wt% chloride.[51] This gives one example of the difficulties in simulating and reproducing corrosion properties of natural field exposures in LALT.

Effect of Chloride on Atmospheric Corrosion: The effects of atmospheric exposure can be examined further when the corrosion rate is compared to at least one environmental

factor such as the chloride deposition density, as shown in Figure 2. For the exposures in Figure 2, the samples exposed with higher chloride deposition density suffered higher average corrosion rates. Not only does the salt deposition density affect the corrosion rate, as shown previously, but the RH dependent concentration of the salt solution formed can also influence the corrosion. RH has been shown to be a significant factor for corrosion, specifically with an effect on SCC.[52]

The chloride concentration of a solution is a significant influence on pitting in stainless steel.[53] As chloride concentration increases, the tendency toward pitting increases. This can be seen through a relationship established for AISI 304 stainless steel, where the E_p , pitting potential, is often related to the chloride concentration by:[54]

$$E_p = A + B \log[Cl^-] \quad \text{Equation 1}$$

Where A and B are constants. If E_p is equivalent to the corrosion potential, E_{corr} , then pitting is likely. Alloying additions of molybdenum and chromium increase the chloride concentration that is tolerable without initiation of pitting. Earlier work on stainless steels showed a maximum susceptibility to SCC at or near the deliquescence point for the single salt solution, where a saturated salt solution such as NaCl, CaCl₂, MgCl₂, etc. exists, while for seawater it was governed by the deliquescence point of MgCl₂. [55] Below and above these RHs, susceptibility dropped as below, the droplets dried out, and above this RH the chlorides became diluted. At the deliquescence point, the saturated

high concentration of salt existed, thus lowering E_p and establishing conditions more susceptible towards pitting.

Effect of Relative Humidity on Atmospheric Corrosion: As mentioned, another central variable in atmospheric corrosion is the relative humidity (RH), which can govern both the concentration and size of deposited aerosols present in an atmosphere. For salts in solution, an equilibrium concentration is dependent on RH, which then influences the amount of water the drop will absorb or evaporate to reach this concentration.[56, 57] Examples are given in Figure 3 for both single salts at varying RH, and for an estimation of a water layer thickness for the equilibrium concentration of NaCl solution. If the RH is varied, aerosol droplets will grow or shrink in dimensions for a given salt content in moles. Figure 3-b gives the assumed uniform water layer thickness necessary achieve the equilibrium concentration of the liquid salt solution present in the layer or drop for a given humidity and salt loading level. It must also be noted that the deliquescence points of these salts should not be taken as a limit to corrosion or corrosion damage across the samples. As shown previously by Schindelholz et al., corrosion can occur as low as 33% RH for NaCl and 11% RH for $MgCl_2$, well below their respective deliquescence points due to salt crystallization hysteresis, alteration of deliquescence points caused by the interaction of corrosion chemistry, and adsorbed or trapped electrolyte.[58] It is important to point out that if a new salt is formed between the corrosion product and existing salt solution, such as $FeCl_3$, a new deliquescence will govern the relationship of this salt with humidity.

Effect of pH on Atmospheric Corrosion: The pH of an environment can govern the thermodynamics necessary for the corrosion of a material in that exposure. For Fe, as seen from the Pourbaix diagram, the material is generally passive at higher pHs (Figure 4-a).[59] Alloying elements, such as Cr, Ni, and Mo can extend this zone of passivity (Figure 4-b-d), and therefore materials become less susceptible to general corrosion and more prone to pitting. However, at extremely low pHs, even stainless steels can exhibit general corrosion. Not only does pH affect the form of corrosion, but it also governs the hydrogen overpotential established within an environment. As pH decreases, if the potential is kept at a constant value, the overpotential η_H , and thus driving force for H production, will increase. Atmospheric gasses can also influence the development of acidity through hydrolysis and OH^- production activities.[60] Separation of anodic and cathodic sites can increase the disparity in pH as the anode develops a higher acidity while the cathode becomes more alkaline. The degree of anode cathode separation influences the resultant pH. One study showed specifically the effect of pH on atmospheric exposures of stress corrosion cracking of martensitic stainless steel.[61] Bhatt and Phelps found that as the pH of a 3 wt% NaCl solution decreased, the time to failure of the steel significantly decreased, suggesting that HE was intensified at a lower pH likely by enhanced H production and uptake.[61] At a pH of 1, hydrogen evolution from the surface of the steel sample was visibly evident, suggesting that hydrogen evolution was the principle cathodic reaction.[61] Also, the authors found that when polarized cathodically, with high cathodic current densities, the time to failure decreased, consistent with the hydrogen embrittlement mechanism.[61]

Effect of Droplets on Atmospheric Corrosion: Corrosion is dependent on conditions developed within droplets.[62] Resultant corrosion can take the form of pitting, general, or mixed corrosion, depending on alloy composition and microstructure combined with the severity of the environment (Figure 6). Different corrosion cells can be established in droplets ranging from the Evans cell in a relatively uniformly corroding material due to differential diffusion of oxygen across the droplet (Figure 6-a), to acid pits formed by the dissolution, hydrolysis, acidification and Cl^- ingress mechanisms in passivating alloys (Figure 6-b).[58, 62, 63] In stainless steels, dissolution of manganese sulfide inclusions has been correlated with the formation of an acidified environment containing sulfides or thiosulfate, and possible prevention of repassivation, thus promoting pitting.[64, 65] Within these cells, due to the drop in potential below the $E_{\text{H}^+/\text{H}_2}$ at the anodic sites, these areas can become local “hotspots” for hydrogen production and uptake.

Mixed potential theory can be applied to the establishment of differential aeration cells, such as in the case of the Evans droplet.[66] For differential aeration, initially the corrosion rate is higher at the area with high oxygen, the outer ring of a droplet (Figure 5-a). However, as the iron corrodes, the pH increases in this region due to the cathodic reaction ORR and production of OH^- , and the iron begins to passivate.[66] At the center of the droplet, with poor access to oxygen once the readily available oxygen is consumed, the pH decreases due to hydrolysis (Figure 5-b), and the increased acidity leads to increased anodic activity.[66] The mixed couple potential for the entire drop is theorized to be the same, indicated by the coupled potential, E_{couple} in Figure 5-b. However, this Evans diagram does not reflect current and potential distributions that might exist across

the drop. Moreover, local variations in potential, as seen through Scanning Kelvin Probe [67], could indicate lower potentials, as low as $E_{\text{corr,A}}$ at the droplet center while the droplet edge is at $E_{\text{corr,C}}$. In this case, $i_{\text{H}^+/\text{H}_2}$ is the dominant cathodic reaction coupled with $i_{\text{corr,A}}$ such that to a good approximation, $i_{\text{H}^+/\text{H}_2} = i_{\text{corr,A}}$. In reality, the hydrogen production rate in the acid region might range from $i_{\text{corr,A}}$ to any value along $i_{\text{H}^+/\text{H}_2}$ (from the $\frac{1}{2}$ cell reaction up to $E_{\text{corr,C}}$). The different potentials can establish locally higher hydrogen overpotentials, especially in acidified regions, thus facilitating hydrogen production and uptake within areas of the drop. The amount of H^+ produced in these regions could even be predicted with knowledge of the local pH, potential, H^+/H_2 rates, and predicted corrosion rates. In this case, $i_{\text{H}^+/\text{H}_2}$ at E_{couple} is the H_2 production rate for a droplet in the acidified zone, but at E equal to E_{couple} . According to the plot in Figure 5-b, $i_{\text{H}^+/\text{H}_2}$ would be a small percentage of the rate of corrosion given by i_{couple} under these circumstances. For a small drop, the entire system may sit at a single potential, E_{couple} . Clearly both local potential and pH must be mapped.

The droplet length scale with respect to the material length scale is also an important aspect of atmospheric corrosion and hydrogen uptake (Figure 1). Droplet size can play a role in the establishment of the electrochemical cell within the droplet. Separation of the anode and cathode within the cell is necessary for the development of an acidified zone based on the hydrolysis taking place at the anode while OH^- production occurs at the cathode. If the droplet size is significantly small ($<1 \mu\text{m}$), then a differential diffusion of oxygen across the droplet might not be significant enough to produce the Evans cell formation with an acidified zone; in this case microstructural features may dominate to

govern the details of the electrochemical cell within the drop instead of geometric zones.[68]

In stainless steels, MnS inclusion particles can become sites of initiation for pits.[65] As these inclusions can occur anywhere, the corrosion site in a pit dominated cell is not always at the center, as it is not dependent on droplet geometry. The original Evans drop only considered microstructurally homogeneous iron.[69] Therefore, whether the Evans cell dominates corrosion electrochemistry is somewhat dependent on interaction of the droplet size and the microstructural length scale.[62, 70] It was found that for NaCl (5.1 – 5.4 M) exposed at high RH on UNS G10180, for small drops of diameters $< 100\text{ }\mu\text{m}$, the surfaces passivated, whereas for drops with diameters $> 100\text{ }\mu\text{m}$, the samples actively corroded.[62] In a second study, it was found that the corrosion rate could be correlated with the droplet size, with mass loss decreasing with decreasing drop size. However this was also highly dependent on the inclusions and inclusion density of the steel.[71] Whether the Evans cell dominates corrosion electrochemistry is dependent on droplet size and the microstructural length scale of features that might alter corrosion. With regards to the global corrosion scale, droplet size plays a role in terms of uniform vs. non-uniform corrosion. The size and distribution of droplets can affect the overlap of corrosion sites, whether they are pit dominated or Evans cell, and thus effect the overlap of the H uptake and the uniformity of the H concentration. Pertaining to pitting in stainless steels, in terms of droplet liquid size, it has been found that the droplet liquid height can also affect the resultant pit morphology that forms. In a study of MgCl_2 drops on 304L stainless steel exposed at different constant RHs, it was found that pits formed

with “spiral attack” in higher liquid height drops.[72] Also, a difference was seen in the pits based on where they formed within the drop. Spiral attack was seen at the center where the droplet height was higher, and pits close to the droplet edge formed satellite pits where the drop was shallower (Figure 7).

One critical unresolved issue for the steels of interest in this dissertation is that the average mass loss rates in atmospheric corrosion for UNS G10180, UNS S45600, and UNS K92580 are undetermined. Standards, such as the ASTM G101[73] and the pitting resistance equivalency number (PREN)[53], can help provide a basis for expected corrosion susceptibility of these materials, but further investigation is necessary to understand the effect of different environments on corrosion, as well as how this corrosion in turn affects hydrogen production and uptake.

Details of Cl^- concentrations, electrolyte chemistry, relative electrochemical local potentials, and the resultant pH in droplets govern atmospheric corrosion and thus hydrogen production and uptake. Moreover, the interaction of a material and droplet determines the type and severity of corrosion.

1.1.3. Materials of Interest

AerMet 100 (UNS K92580) is a secondary hardened, martensitic, ultra-high strength steel designed for army aircraft fracture-critical components (composition and material properties are in Table 3 and Table 4).[4] It exhibits its highest toughness in the H900 temper condition (austenitized at 885°C, air-cooled, quenched in liquid nitrogen and

peak-aged at 482°C), where coherent M_2C carbides (Figure 8(b)) are formed in the martensitic structure (Figure 8(a)). The alloy has high toughness that is attributed to the microstructure of the tempered steel, formation of reverted austenite, and lack of cementite.[74]

UNS K92580 possesses high susceptibility to hydrogen embrittlement at near peak aged conditions.[10] While this alloy exhibits higher resistance to stress corrosion cracking [75], it requires an electroplated Cd coating for corrosion resistance.[76] Although this protects from corrosion, this process can introduce hydrogen into both the Cd heavy metal coating and/or steel. Yet, without such a coating, UNS K92580 is significantly susceptible to corrosion, of both general and pitting morphologies.[6, 77] Atmospheric exposures of aerosol droplets on bare UNS K92580 at the University of Virginia have shown it exhibits both Evans cell formation, as well as localized pitting under a drop.[63, 78] This may be influenced by exposure conditions and time, as discussed by Sun et. al.[77] For UNS K92580, Shedd determined diffusion controlled pit growth with an increase in pit radius with Cl^- deposition density and a increase in pit depth with exposure time (Figure 9). There was not a clear relationship established between the repassivation potential and the charge density as UNS K92580 had a tendency towards general corrosion rather than pitting.[78] Hydrogen production and uptake under cathodic polarization, similar to galvanic coupling, will be addressed and has been covered elsewhere.[79] Further studies into the formation of the electrochemical cell established on bare UNS K92580 during atmospheric corrosion are necessary to understanding

hydrogen production and uptake. This is pertinent to information at the local scale and can be further applied to knowledge of the crack tip.

Custom 465 (UNS S46500) is a martensitic, age-hardenable, stainless steel with some intrinsic corrosion resistance imparted by the passivation elements. Composition and material properties are given in Table 3 and Table 4. UNS S46500 has a PREN # of 14.63.[53] It will be studied here in both the as annealed / CT condition (solution annealed at 982°C for 1 h and cooling rapidly to room temperature, then cool treated at -73°C for 8 h and warming back to room temperature) and the H900 temper (tempered at 482°C for 4 hours and air cooled). These tempers were selected as the as annealed condition was evaluated in previous work by Shedd et al., and the H900 temper has been shown highly susceptible to HE. [78, 80] The microstructure of UNS S46500 is composed primarily of martensitic lath packets within prior austenite grains.[81, 82] UNS S46500 is used for high strength aircraft and structural components due to its age-hardenability and cold work ability. It displays a high level of strength and toughness. For example, in the H900 temper UNS S46500 has a yield strength of 1600 MPa with a fracture toughness of $60 \text{ MPa(m)}^{1/2}$. [83] The material's high strength is attributed to both the formation of martensite and fine precipitated particles, specifically coherent Ni_3Ti particles (Figure 10 (b)), during aging.[84, 85] Also, while at high austenitizing temperatures in these precipitation-strengthened martensitic stainless steels, some martensite reverts to austenite, and has been measured by XRD in the H900 temper as 4 ± 1 wt. %.[82, 84]

The benefit of UNS S46500 over other ultra-high strength steels is that a protective surface coating or metal plating is not necessary for corrosion resistance due to a higher concentration of Cr, Mo, and N contents than other martensitic stainless steels.[85-87] While the PREN is only 14.63, this does not account for the large alloying additions of Ni and Ti.[53] These steels have been used as a replacement for 304 stainless steel (PREN # of 19.6-21.6) as they have a higher pitting resistance in acidic chloride solutions.[53, 88] However, while these steels show resistance to general corrosion, martensitic precipitation-hardening stainless steels have displayed decreased pitting potentials with increased aging temperature thought to be produced by chromium depletion.[53] They have even exhibited pitting potentials at potentials less noble than 304 stainless.[53] In work by Shedd et al., it was found that UNS S46500 has diffusion controlled pit growth with a pit radius that increases with increasing salt loading density during exposure (Figure 9).[78] It is important to note here that the electrochemical cell developed during atmospheric corrosion will be passive, minimizing general corrosion, and dominated by the development of acid pits formed by the dissolution, hydrolysis, and acidification mechanism.[89] Consequently, hydrogen production and uptake will depend critically on the corrosion form.

1018 Steel (UNS G10180) is evaluated here as a representative mild carbon, lower strength steel. It is a hypoeutectic steel, with a microstructure consisting of pro-eutectic ferrite and pearlite. Its material composition and properties are given in Table 3 and Table 4 respectively. It is generally regarded as an easily weldable, plain carbon steel with a balance of toughness, strength and ductility.[90] However, it does not contain the

significant potential hydrogen trap site population that UNS K92580 and UNS S46500 possess. UNS G10180 has been found to initiate corrosion through pitting under NaCl droplets in the initial stages of atmospheric corrosion (much less than 30 min) [44], but the longer term corrosion that is established is uniform attack largely driven by ORR.[62] This general corrosion allows for formation of the Evans cell as the electrochemical cell established within droplets under atmospheric corrosion. [69] Subsequent potential and pH developed across the Evans drop are anticipated to influence the hydrogen production and uptake as a function of position in the drop.

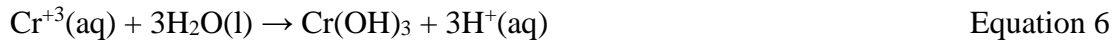
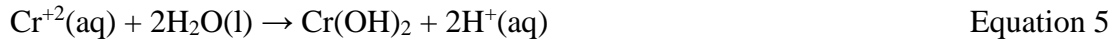
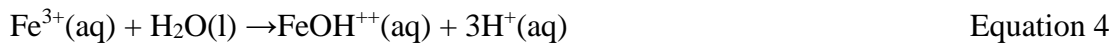
In combination with the material composition, environment can critically impact not only the amount of corrosion damage, but the morphology type, from general corrosion to pitting/crevice corrosion ranging from high aspect ratio acid pits to surface staining.[91] As shown in Figure 14, material composition, in this case in terms of wt % Cr in the alloy or PREN, can have a strong impact, and combined with environment type can greatly affect the amount and type of corrosion damage to a material. This curve has not been reproduced over a broad range of environments, but is likely to be similar in many where passivity is possible in Cr bearing alloys and Cl^- is present. It displays in general the significance of alloy-environment interaction during exposure.

1.1.4. Hydrogen Behavior and Materials

The first stage of this research requires that the transport rate of hydrogen through steel be known. This will be significant towards understanding atmospheric corrosion specifically with knowledge of both hydrogen penetration depth and lateral spread. Also

significant to this research is the understanding of the production of H in various environments, therefore, a discussion of the production of H in full immersion is pertinent to this work.

Hydrogen Production Under Full Immersion: In corrosive environments, HE under atmospheric conditions is important to the development and quality testing of UHSS. The amount of hydrogen uptake greatly influences the materials' engineering properties.[92] This amount (or concentration), however, varies widely across different environments due to a range in severity of environments. Severity in the context of this study means with respect to hydrogen production. Hydrogen can arise from a variety of sources; processing steps, electroplating, cathodic protection, and, of interest here, corrosion reactions occurring on the surface. The possible half cell and hydrolysis reactions for H production and uptake are:



It is instructive to review hydrogen production process under full immersion conditions. Hydrogen production and uptake increases with hydrogen overpotential ($E - E_{H^+/H_2}$) especially in more acidic environments, such as those found in occluded cells and crack tips. The hydrolysis reactions shown above can decrease locally the pH through H^+ production, creating environments that are even more conducive to hydrogen production (Table 5). Furthermore, this decrease in pH can be influenced by alloying content, specifically in the case of Cr^{+3} where the reaction produces large amounts of H^+ . An example of this can be seen in work by Bogar et al., where the crevice pH was measured in 3.5 wt% NaCl solution for Fe-Cr binary alloys.[93] The crevice pH was shown to decrease as the Cr content increased (Figure 11).[93]

Knowledge of the effect of full immersion environments and hydrogen production and uptake has been fairly well quantified in the case of martensitic steels.[7, 10, 18, 94-98] One method of understanding hydrogen production and uptake is through using scaling laws. In another example here, using a predictive method for H production determined that there were three general regimes in the cathodic reaction governed by charge transfer control H^+ reduction (i_{ct}), mass transfer limited H^+ reduction (i_{lim}), and charge transfer controlled H_2O reduction (i_{H_2O}) (Figure 13). They were found experimentally for UNS K92580 possesses rates defined by the following equations:[11]

$$i_{ct} (A/cm^2) = 10^{-8.28} x [H^+]^{0.39} x 10^{(-E_{1/2}/0.090)} x 10^{(-\eta/0.090)} \quad \text{Equation 9}$$

$$i_{lim} (A/cm^2) = 10^{-pH} \quad \text{Equation 10}$$

$$i_{H_2O} (A/cm^2) = 1.05 x 10^{-11} x 10^{(-E_{applied}/0.155)} \quad \text{Equation 11}$$

Where i_{ct} , i_{lim} , and i_{H_2O} are in A/cm^2 , $E_{1/2}$ is the reversible H potential for the overall reaction in V_{SCE} , η is the hydrogen overpotential in V, $E_{applied}$ is the applied potential in V_{SCE} , and $[H^+]$ is the hydrogen concentration in mol/L. These can be combined to equal the total cathodic current (i_{ca}) as a function of potential over the three regions using the following:

$$i_{ca} = \frac{i_{ct} i_{lim}}{i_{ct} + i_{lim}} + i_{H_2O} = \frac{\left(10^{-8.28} x [H^+]^{0.39} x 10^{\left(-E_{1/2} / 0.090 \right)} x 10^{(-\eta / 0.090)} \right) x (10^{-pH})}{\left(10^{-8.28} x [H^+]^{0.39} x 10^{\left(-E_{1/2} / 0.090 \right)} x 10^{(-\eta / 0.090)} \right) + (10^{-pH})} +$$

$$\left(1.05 x 10^{-11} x 10^{(-E_{applied} / 0.155)} \right) \text{ Equation 12}$$

As can be seen, the H production is affected by the pH and hydrogen overpotential.

In another study, Thomas et al. investigated the effect of overpotential on hydrogen uptake in both UNS K92580 and AISI 4130.[7] They found that for a given overpotential, UNS K92580 displayed a higher $C_{H,Diff}$ (diffusible hydrogen concentration) than AISI 4130, indicative of the higher trap density present in UNS K92580 (Figure 15).[7] Full immersion testing combined with modeling of hydrogen uptake in UNS K92580 and UNS S46500 in varying pH solutions has shown that the $C_{H,Diff}$ increases with increasing hydrogen overpotentials but is finite at zero overpotential and even at underpotentials (Figure 16).[7, 99] Also, shown are the effects of pH on hydrogen uptake, with decreasing $C_{H,Diff}$ as pH increases.

In pre-cracked specimens, crack geometry, defined by x^2/G (where x is the distance into the crack and G is the gap size) and local corrosion cells, thus formed at occluded sites in the material, are key factors in determining the extent of the effect of hydrogen uptake. In these pre-cracked specimens, the local crack tip hydrogen overpotential and pH determine local hydrogen concentration. These, in turn, are a function of the material external applied potential and geometric factors. It was found that as the hydrogen overpotential increases below the OCP, in 0.6 M NaCl, the K_{TH} also decreases.[100] However, above the OCP, hydrogen entry and a decline in K_{TH} is attributed to formation of an acidic occluded crack tips and IR drop below reversible hydrogen (Figure 17a).[100] All of these factors can be related to the root cause, $C_{H,Diff}$ at the crack tip.[101] Differences in $C_{H,Diff}$ have been shown to impact the threshold stress intensity factor of these steels. Kehler et al., found that as $C_{H,Diff}$ increased within a UHSS sample, the stress intensity threshold (K_{TH}) decreased significantly.[100] If $C_{H\sigma}$ (the stress enhanced crack tip H concentration dependent on $C_{H,Diff}$, Equation 17) was greater than the critical stress enhanced H concentration required at X_{crit} , the critical distance ahead of the crack tip surface, this led to decreased K_{TH} , however if it was less than $C_{H,\sigma}$, there is no crack growth. This same phenomenon was also confirmed by Thomas et al., showing that the $C_{H,Diff}$ has a negative effect on the threshold strength in UNS K92580 (Figure 17a).[7, 10] Figure 17b shows the effect of applied potential on a number of high strength steels, showing the effects of net cathodic polarization and anodic polarization.[99] It has to be noted, however, that these experiments were all pre-cracked specimens, and these must be distinguished from occluded sites or pits within an atmospheric drop. In the latter case, little information exists.

UNS S46500 exhibits a similar trend. $K_{I\ EAC}$ (threshold stress intensity) drops as the hydrogen overpotential increases in full immersion.[81] Thus an understanding and quantification of hydrogen concentration in a material is key to understanding the severity of HE in UHSS. In this case of atmospheric exposure of non-pre-cracked or pre-cracked material, the critical unresolved issue is hydrogen uptake in drops or exposed surfaces experiencing atmospheric corrosion. These conditions might result in high overpotentials such as -0.6 or -0.5 V_{SCE} seen in Figure 17b.

Hydrogen Uptake: In a microstructure free of traps, hydrogen diffusivity through a material can be described by perfect lattice interstitial diffusion (D_L), based on the motion of hydrogen from one interstitial site to the next vacant site and the dependence on nanostructure and atomic packing factor. In these UHSS, the D_L is affected by alloying elements and the density of reversible trap sites, thus becoming $D_{H,eff}$, the effective hydrogen diffusivity.[102, 103] The effect of alloying by Ni and Cr, two of the largest alloying elements in these UHSS, with other martensitic alloys, as compared to pure Fe, can be seen in Table 6. As Ni and Cr alloying content increase, the $D_{H,eff}$ is lowered significantly. (Table 6) This can be attributed to the introduction of hydrogen interstitial sites around the added solute atoms which differ in size and electronic interaction can function as trap sites for hydrogen.[104] Moreover, in these high strength steel microstructures; grain boundaries, dislocations, carbides, and constituent particles might serve as reversible trap sites which remain in equilibrium with interstitial sites.[105] These reversible trap sites can lower the lattice diffusion rate by capturing and releasing

interstitial hydrogen, thus creating a $D_{H,eff}$ for hydrogen through the microstructure. Irreversible trap sites, such as TiC, may also contribute to trapping effects and slower $D_{H,eff}$. [7] Typical reversible trap states found within martensitic steels include traps within the martensite microstructure (Cr or Ni in Fe), hydrogen trapped at ferrite-cementite interfaces, and hydrogen at retained austenite interfaces. Higher binding energy trap states, those considered irreversible traps, may or may not include mixed dislocation cores, grain boundaries, Cr carbides in Fe-Cr steel, various incoherent particles in Fe, and Fe-Ti-C alloy incoherent carbides. [18, 87] Reported trap states for selected alloys are shown in Table 7. Trap binding energies for PH 13-8 and UNS K92580 are given in Table 8 and Table 9. The trap enhanced hydrogen coverage, θ_T , can be determined if the trap site binding energy, E_B and the $\theta_{lattice}$ are known using the following:

$$\frac{\theta_T}{1-\theta_T} = \left(\frac{\theta_{lattice}}{1-\theta_{lattice}} \right) \exp \left(\frac{E_B}{RT} \right) \quad \text{Equation 13}$$

$D_{H,eff}$ is an important factor in predicting the time necessary for hydrogen to diffuse in the material to reach a significant concentration. [106] It can also be a qualitative signifier for the diffusible hydrogen concentration obtained in a given BCC alloy at a given interstitial lattice concentration. The ratio of D_L to $D_{H,eff}$ can be related to the ratio of $C_{H,Diff}$ to C_L as [7, 100]:

$$\frac{D_L}{D_{H,eff}} \approx \frac{C_{H,Diff}}{C_L} \quad \text{Equation 14}$$

Given C_L as a function of droplet electrochemistry and governing exposure conditions for BCC steels, the amplification to $C_{H,Diff}$ can be predicted using Equation 14. Rearranging as the following:

$$C_{H,Diff} = C_L \left(\frac{D_L}{D_{H,eff}} \right) \quad \text{Equation 15}$$

However, this is only an indicator of magnitude of $C_{H, Diff}$, as C_L and D_L will differ for a solid solution composition of an alloy as compared to the values used for pure Fe. An attempt was made to examine the relative $C_{H,Diff}$ given the different $D_{H,eff}$ for the materials of interest in this study, where $D_{H,eff}$ for UNS K92580 was taken as $3 \times 10^{-8} \text{ cm}^2/\text{s}$, for UNS S46500 the $D_{H,eff}$ was estimated from that of PH 13-8 to be $6.7 \times 10^{-9} \text{ cm}^2/\text{s}$, and for UNS G10180 $1 \times 10^{-7} \text{ cm}^2/\text{s}$ was used.[107] D_L was estimated using the D_L for pure Fe of $2.9 \times 10^{-6} \text{ cm}^2/\text{s}$, and results for $C_{H,Diff}/C_L$ are given in Table 10. As can be seen, the enhancement is >400 times for UNS S46500. Quantifying the actual concentration of hydrogen within the material is necessary to understand $D_{H,eff}$ as well as hydrogen embrittlement. The total hydrogen concentration (H atoms/ cm^3) within a material is a combination of the reversibly trapped hydrogen concentration ($C_{T,r}$), the lattice concentration of hydrogen (C_L), and the irreversibly trapped hydrogen concentration ($C_{T,irr}$). The diffusible hydrogen is the sum of $C_{T,r}$ and C_L (Equation 16).[100]

$$C_{H,Diff} = C_L + C_{T,r} = \theta_{lattice} N_{lattice} + \sum_i \theta_{T,i} N_{T,i} \quad \text{Equation 16}$$

Where, $C_{T,r}$ = reversibly trapped hydrogen (H atoms/cm³)

θ_{lattice} = fractional H coverage of lattice sites (no units)

N_{lattice} = the number of interstitial octahedral sites per cm³ (sites/cm³)

$\theta_{T,i}$ = fractional H coverage of trap site i (no units)

$N_{T,i}$ = the H trap site concentration for trap site i (sites/cm³)

The $C_{H,\text{Diff}}$ concentration level is of great importance as it is the concentration of hydrogen that can migrate towards a crack tip under stress fields, embrittling the material and significantly reducing resistance to cracking.[18, 108-110] The relationship between the diffusible concentration and the stress enhanced H concentration in the tri-axial stress field at a crack is given by the following:[111]

$$C_{H,\sigma} = C_{H,\text{Diff}} \exp\left(\frac{\sigma_H V_H}{RT}\right) \quad \text{Equation 17}$$

Where, $C_{H,\sigma}$ = stress enhanced H concentration at the crack tip (atomic fraction)

$C_{H,\text{Diff}}$ = Diffusible H concentration (atomic fraction)

σ_H = hydrostatic tensile stress causing lattice dilation (MPa)

V_H = H volume fraction (cm³/mol)

And RT has the usual meaning

As $C_{H,\text{Diff}}$ increases, so does the $C_{H,\sigma}$ which is significant to note when accounting for the effects of H on important engineering properties such as K_{TH} . One model predicts a K_{TH} for decohesion based fracture relative to the crack tip Griffith toughness for H free

cracking for brittle cracking in the presence of crack tip plasticity in the form of a specific dislocation crack tip interaction and gives the relationship:[111]

$$K_{TH} = \frac{1}{\beta'} \exp \left[\frac{(k_{IG} - \alpha C_{H,\sigma})^2}{\alpha'' \sigma_{YS}} \right] \quad \text{Equation 18}$$

Where, $(k_{IG} - \alpha C_{H,\sigma})$ = the hydrogen affected Griffith stress intensity for hydrogen embrittlement

k_{IG} = critical Griffith stress intensity factor for cleavage fracture without H

α = damage or decohesion embrittlement coefficient or potency factor in $\text{MPa(m)}^{1/2}$ / atomic fraction of H

β' and α'' = constants determined by computer simulation of the dislocation structure around a crack tip

Knowing the density and trap states (both reversible and irreversible) and concentrations within the material provides a great amount of information towards understanding the diffusible hydrogen concentration and ultimately the embrittlement susceptibility of the steel. These concepts can be extended to corrosion conditions implying that knowledge of the diffusion coefficients and trapping in high strength materials are pertinent details.

The peak aged condition of UNS K92580 produces a large density of potential trap sites, such as M_2C carbides, leading to a significantly lower $D_{H \text{ eff}}$ than typical martensite by almost an order of magnitude.[7] (Table 7) The high density or population of traps includes both reversible and irreversible types, with at least three resolvable trap states

found through TDS.(Table 7) The significant reversible trap states present are the M_2C precipitates. The primary irreversible trap states correspond to possibly martensite interfaces, austenite grain boundaries, and mixed dislocation cores as well as higher irreversible trap states due to un-dissolved metal carbides and highly mis-oriented grain boundaries.[18] The HE susceptibility of UNS K92580 in this peak-aged condition is ascribed primarily to the M_2C carbides, and the ability of the trapped hydrogen under high hydrostatic tensile stress to redistribute from such a homogeneous distribution towards the tensile tri-axial stress field of a crack tip.[18]

UNS S46500 temper conditions (between 900 and 1150 °F) typically exhibit higher SCC resistance.[83] Yet, the H900 temper displays degraded toughness in 3.5 wt% NaCl and has been shown to be vulnerable to SCC.[83, 85, 112] UNS S46500 has also been found susceptible to environment assisted cracking (EAC) through HE.[81] Samples were exposed using the rising step load technique in 0.0035 to 3.5 wt % NaCl solution in which the stress intensity threshold for EAC was found to decrease with increasing yield strength and NaCl, and the mechanism for EAC was identified as HE.[81] Prior austenite grain boundaries, interfaces between martensitic lath crystals, dislocations, and cementite ferrite interfaces often function as reversible hydrogen traps.[84] In full immersion charging in pH 8 Borate Buffer (Figure 16) UNS S46500 has shown a higher hydrogen uptake for a given hydrogen overpotential (η_H) and pH than UNS K92580, indicative of a trap rich material.[100] Embrittlement is both seen by grain boundary decohesion and by cracking along elongated martensitic laths, packets, and prior austenite grain boundaries [113] when subjected to high applied stresses and the presence of

hydrogen.[81] For UNS S46500, there has been little research on the $D_{H,eff}$ and the trapping behavior, leaving a large need/gap as an opportunity for study. [108] This gap in knowledge is also required to understand the charging time necessary to achieve uniform distribution of hydrogen in exposed samples as a function of sample dimensions and charging time.

1.1.5. Hydrogen Uptake in Pits and other Occluded Sites

Another complication to understanding atmospheric hydrogen uptake in these UHSS, is the electrochemical behavior in an occluded corrosion cell. Occluded cells are regions where a special restrictive geometry does not allow the exchange of the local electrolyte with that of the bulk. Some examples are: a pit, where a corrosion cap forms limiting connection with the bulk environment; a crevice, where the length of the crevice is diffusion limiting; or cracks, which exhibit a similar length limiting diffusion (Figure 1).[114] The crevice or crack tip scaling law, x^2/G , can be used to help describe the interaction of the geometry with the local electrolyte development, as these geometries limit access of oxygen from the bulk electrolyte to the Fe surface and allows acidification due to metal hydrolysis with limited dilution at large x^2/G . Large values of x^2/G imply a larger IR drop between the mouth and the interior. If the crevice or pit undergoes some anodic dissolution, due to metal ion hydrolysis, the tip becomes increasingly acidic and concentrated in Cl^- . Due to the IR drop, the potential becomes more negative than the reversible hydrogen potential, i.e., as x^2/G increases, the hydrogen overpotential and thus H uptake becomes more severe due to both the enhanced IR drop and the acidification which enhance the H overpotentials.(Figure 18)[100]

In cathodic polarization of the crack tip, the IR drop still exists, but the OH^- is increased. As x^2/G increases, the OH^- increases and $|\eta_{\text{H}}|$ decreases. The IR drop actually makes the cathodic polarization decrease as it decreases the $|\eta_{\text{H}}|$. Therefore, the hydrogen overpotential is not as significant as in the anodic case. The hydrogen uptake is actually favored more as x^2/G decreases in the case of net cathodic polarization. (Figure 21) The hydrogen in this case is produced both at the crack tip and on the boldly exposed surface.

The pits and crevices are in a region where hydrogen evolution is thermodynamically possible across a range of pH. An example of such electrochemical conditions for an occluded site (crack tip) is given in Figure 22. These pits, cracks, and crevices could therefore become “hotspots” for hydrogen production and uptake under the right conditions.

Switzer, through model pit experiments combined with cross sectioning and TDS measurements, established hydrogen concentration versus depth and potential within a rescaled pit in full immersion.[115] Anodic polarizations of PH 13-8 were carried out in H_2SO_4 solutions with dissolved metal ions (Fe^{+2} , Cr^{+3} , and Ni^{+2}), and 5 M H_2SO_4 to predict the potential range and possible critical current densities for the passive to active transitions (Figure 19-a). The HER current density in this potential range of $E < E_{\text{H}/\text{H}^+}$ could be predicted from cathodic $E\text{-log}(i)$ data and the pH and H overpotential using[115]:

$$i_{H^+/H_2} = (1.31 \times 10^{-4})[H^+]^{0.525} \exp(-14.45\eta_H) \quad \text{Equation 19}$$

Where i_{H^+/H_2} is in A/cm², $[H^+]$ is the hydronium in concentration in mole/L, and η_H is the H overpotential in V. Within an acidified crevice or pit, considerable H production and uptake can occur at corroding conditions near the OCP in the acid solution if the H overpotential drop in potential reaches -0.75 V_{Hg/Hg2SO4} (Figure 19-b). In Figure 19-b, 10-15 times the base H level or about 3-4 wppm H occurs at OCP 1. Switzer also established a prediction for the relationship between x_{crit}^2/G to determine if the crevice lied in a potential region where H production was possible without passivation (Figure 20). In this figure, open symbols indicate X_{crit}^2 , where $E_{H^+/H_2} > E > E_{pass}$ when $X^2 > X_{crit1}^2$ for a given G. The solid lines indicate conditions for $E_{H^+/H_2} > E_{pass} > E$ for $X^2 > X_{crit2}^2$.

For experimental verification, samples were machined with drilled holes (size determined using crevice scaling laws; x^2/G) representing varying pit sizes and were held at a range of overpotentials in 5 M H₂SO₄ plus 0.1 M Fe⁺², 0.018 M Cr⁺³, 0.01 M Ni⁺², and 0.01 M HCl solutions. Samples were exposed and charged to reach a calculated 90% through-thickness saturation and sections were sectioned to measure hydrogen uptake versus pit depth by TDS. The absorbed hydrogen concentration followed the trend of the change in overpotential within the rescaled pits, increasing as the cathodic overpotential became more negative. An example is shown in Figure 23.[116] While rescaled crevices and model pits have been employed previously for other materials and conditions [79, 116], they have not been used to evaluate the conditions presented in a drop or in any other atmospheric corrosion circumstance.

1.1.6. Hydrogen Uptake in an Atmospheric Drop (Evans Cell)

Somewhat similar to the situation occurring in an occluded corrosion cell is that of a droplet. In a droplet, an oxygen concentration cell can develop as presented by U.R. Evans.[63] In such a schematic, as described previously, the outer ring of the droplet forms the cathodic region, as it has easily attainable oxygen due to the thinness of the droplet at this area, whereas the center comprises an anodic region due to the diffusion limiting droplet height which restricts access to a renewed oxygen supply. The pH and potential in this region can be shifted towards regions in which HER is a significant or even the dominant cathodic reaction, thus producing a higher surface H concentration at the Evans cell anode for hydrogen uptake (Figure 5-b). However, this depends on a_{H^+} and the subsequent pH. This has been confirmed by a few studies with various detection methods, the first example here used a multi-electrode array. In this study, Muster et al., designed a 10 x 10 array of 500 μm diameter zinc wires and exposed these to varying sizes of seawater droplets while monitoring the coupled current density to each wire.[117] The establishment of an Evans cell was measured for larger droplets (10 μL) and the formation of mixed cells for smaller droplets (1 μL), shown in Figure 24.

Another method to examine the electrochemical cell established in a drop is the Scanning Kelvin Probe (SKP). The SKP can map the work function (SKP voltage) of a planar material spatially over small areas and has the capacity to measure the change in SKP voltage of a surface covered with a thin electrolyte film that enables electrochemical reactions, which can then be converted to the electrochemical potential and, at least

empirically, related to the mixed potential across the surface.[118, 119] Mansfeld et al. employed this phenomenon to study the effect of droplet corrosion cells on the SKP voltage derived open circuit potential of various materials.[118] Droplets were examined on carbon steel, stainless steel, galvanized steel, and aluminum (Figure 25). Scans across these droplets observed an Evans-type cell formation on the carbon steel.[118] The Evans cell formation was indicated by the potential rings formed under the drop that correlated with variations in pH measured simultaneously with pH indicators (potassium ferricyanide and phenolphthalein). In Figure 25, pink corresponds to the formation of OH^- at the cathodes at the drop exterior, while dark blue corresponds to the formation of Fe^{2+} at the anodes on the carbon steel. The potential shown was calibrated to the saturated hydrogen electrode (SHE) using measurement of the Volta potential of a Cu/CuSO_4 electrode and a correction factor established for the SKP. As the pH and potential can be determined through these measurements, local H overpotentials can be established and the local H production can be predicted. While these measurements can indicate local mixed potential likely dominated by corrosion reactions and pH across a droplet, they do not provide a direct method for spatial H detection.

Also affecting the determination of these droplet cells is the interaction with the material itself. For example, in the case of a high Cr passive alloy like UNS S46500, pitting can occur even within a droplet on stainless steel, thus establishing even more severe localized anodic sites due to local breakdown and local Cr hydrolysis producing a lower local pH. Electrochemical cells can therefore develop with Evans formation, dominated by pitting, or as a mixture, all of which result in different pH and overpotentials as a

function of position, material, and environmental severity producing variations in the hydrogen concentration readily available at the materials' surface. However, although it is easy to substantiate i_H , the determination of exact values is unknown.

1.1.7. Studies of Atmospheric Hydrogen Embrittlement

While there are fewer studies concerning the atmospheric HE of metals, there are a few precedents of interest. One example of field exposures of high strength martensitic steel 4135, shows the effects of exposure environment. High strength martensitic steel 4135 generally exhibited higher hydrogen uptake in marine exposure sites as compared to rural sites.[44] Hydrogen uptake in martensitic steels (AISI 4135 and a NIMS developed steel) was also measured, through TDS, after cyclic atmospheric corrosion testing in an LALT chamber followed by slow strain rate testing (SSRT). An inverse power law relationship was established between the notched tensile strength of hydrogen pre-charged specimens and diffusible hydrogen content, with decreasing strength for an increase in $C_{H,Diff}$ [44, 120] This relationship was further examined through atmospheric testing using cyclic corrosion tests followed by SSRT testing of notched specimens (Figure 26) with TDS measurements resulting in $C_{H,Diff} = 0.05 - 0.17$ wppm .[121] The cyclic corrosion tests were an 8 h cycle that consisted of a dry step at 50% RH for 5.75 h, a 1.75 wet step at 98% RH, and a 0.5 h salt spray step with 0.5 wt% NaCl solution spray, all of which were carried out in a chamber at 30°C. A similar procedure was carried out for field exposures, resulting in TDS measured $C_{H,Diff}$ concentrations of 0.05 – 0.35 wppm. [122]

A recent study relevant to this discussion purports to relate H concentrations with a corrosion metric, mass loss.[123] Steel was evaluated while exposed to atmospheric conditions of a moving vehicle for 7 days, and the measured H concentration (via a cylinder attached to function as an in-situ permeation cell) vs. mass loss is shown in Figure 27. As can be seen, the H concentration increases with increasing mass loss (and increasing exposure time), suggesting it might be useful as a signifier of H uptake.

These studies elucidate the importance of atmospheric HE, that significant concentrations of hydrogen can be developed through atmospheric hydrogen uptake, and that these concentrations can be detrimental to the engineering properties of these materials. Impact will depend on alloy and state of stress as well as environmental severity factors. While such a relationship was well known for full immersion exposures for more than 50 years in pre-cracked specimens,[124] it is important to note here that levels of $C_{H,Diff}$ from atmospheric exposures are proportional to those in full immersion. While they are not usually as significant as the large concentrations that can be produced by full immersion charging, atmospheric exposures, in this specific example, cyclic corrosion tests of an 8 h dry step, 5.75 h wet step, and 1.75 h salt spray step, have produced a concentration that can decrease the fracture stress of a material in half (Figure 26).[121] If these concentrations extend to values greater than $C_{H,Diff,crit}$ (the critical diffusible hydrogen concentration above which K_{TH} drops significantly, Figure 17-a), these atmospheric exposures can lead to detrimental effects on the materials' engineering properties. However, little is known about the electrochemical details of hydrogen production and uptake in droplets during atmospheric corrosion. Prior to this study, there

has been a limited number of efforts with atmospheric H uptake in droplets using permeation.[30]

1.1.8. Local Scale Investigations of Hydrogen Uptake in Atmospheric Conditions

While global measurements for determination of total hydrogen concentration (TDS, LECO, and barnacle cell) in both full immersion and atmospheric corrosion are well established at least in full immersion and will also be employed in this study [20, 79, 125], the development of local and spatial detection tools is necessary to understand the anatomy of the corrosion cell and hydrogen uptake conditions developed in aerosol droplets. Several methods would help address this issue, especially various mapping methods that can spatially explore drops.

One scientific scheme of interest for localized hydrogen detection is modified permeation cell study for aerosol droplets. Tsuru et al. have established a technique for Devanathan-Stachurski style permeation during hydrogen uptake with the entry surface open to atmospheric conditions.[30] Pure iron foil, 0.3 mm thick, with a Pd film plated on the exit surface was examined to explore the effects of a wet/dry process and the roles of water layer thickness and pH in governing the permeation current registered on the exit surface. The solutions of the droplets placed on the entry surface were 0.5 M NaCl, 0.5 M NaCl + 0.01 M Na₂SO₃, and 1-5 mM Na₂SO₃. When the rust layer was moistened on the entry surface, corrosion and metal cation (Fe²⁺) hydrolysis produced a lower pH and E_{corr} ; thus hydrogen evolution occurred on the charging surface and the H permeation current increased to a maximum of about 35 nA/cm². As the water layer dried, oxygen

diffusion increased, and E_{corr} shifted to a more noble potential. Oxygen reduction then dominated the cathodic reaction, and the pH increased. The permeation current ceased as the water layer thickness approached a certain finite value (Figure 28).[30] The dependence of a permeation current through a droplet under atmospheric conditions involving the details of the corrosion product and electrolyte layers was established through these experiments. However, these measurements require a significantly fast diffusion to produce an exit H flux above the background.

It has been shown that the work function of a metal can change due to an absorbed hydrogen concentration. [31,32,34-37,39,126] Through SKP microscopy, concentrations as low as 0.01 atomic ppm of H dissolved in the metal are detectable. [34, 37, 127] This recently developed technique enables spatial detection of H concentrations with lateral resolution limited by the tip size (for SKP about 50 μm and SKPFM 25-30 nm) and is employed to map H concentrations of pre-exposed samples both laterally and with depth detection of cross-sectioned samples.[36] For measurement, samples were scanned in the SKP in humid, ambient air as well as controlled partial pressures formed by $\text{O}_2 + \text{N}_2$ environments with backside detection of H via SKP potential measurements on a Pd film in permeation mode.[37] The change in SKP potential measured is believed to be due to the establishment of H electrode behavior formed in the thin water layer on the sample surface due to the humid air.¹ In Figure 29, an example of a permeation sample can be seen, where the sample in this case was low alloyed sheet steel galvanized with zinc and scratched. This scratch was then exposed to 0.1 M NaCl, and the exit surface, coated with Pd, was scanned by the SKP at varying time intervals.

¹ This aspect is discussed in Chapter 3.

SKP measurements have also been performed on atmospherically exposed steel but without parallel corroboration or quantification of the H concentration.[42] Backside detection on a Pd layer over steel in permeation mode showed a decrease in potential to areas exposed to pre-applied NaCl and high humidity, indicative of the hydrogen uptake within the sample. However, as this is backside detection, spatial resolution of the H concentration is lost due to the time necessary for the diffusion distance through the sample thickness and the lateral spread of H through the sample.

Utilizing the change in the SKP voltage with hydrogen content, the SKP has also been applied as a method to measure local concentration profiles and provide a local scale probe to explore $D_{H,eff}$. [26,36,128] Preliminary work in this area corroborated measurements of $D_{H,eff}$ found by TDS or SIMS with that measured by the SKP method.[36,128] Chapter 3 describes the investigation of this approach.

A second mapping technique, the scanning electrochemical microscope (SECM) enables detection of corrosion processes with spatial resolution.[129-131] When the SECM is used in tip generation/substrate collection or substrate generation/ tip collection modes, the differences in the current measured at the tip can be related to the local substrate conductivity and/or reactivity.[132,133] In Redox competition mode, the sample and microelectrode (ME) tip compete for the reduction of the component (in the case applied in this work, oxygen) present within the gap between the ME tip and sample. The current measured at the tip drops when scanned across a surface actively reducing oxygen.[134]

The SECM has previously been utilized to measure the effect of hydrogen on corrosion [135,136] and subsequent pitting susceptibility. [137] Also, the exit side of a permeation surface was characterized by an SECM to study the effect of hydrogen on the exit surface oxide. [138] While these methods explored the effect of hydrogen on anodic reactivity, no prior attempt has been made with the SECM to detect and map spatially pre-dissolved hydrogen concentration across zones of higher or lower concentrations. Chapter 4 discusses this approach.

Preliminary calibration and measurement of spatial hydrogen detection in H pre-charged UHSS in the SECM is initiated in this study as well as application of the SKP for lateral and depth detection.[27,128,139] Further development of these techniques will aid in understanding the complexities occurring at the droplet scale. Within these droplets, comprehension of the influence of localized pitting on hydrogen production and uptake is essential. It has been well established that local chemistries can differ significantly from bulk solutions in full immersion. However, carrying this same phenomenon to the droplet length scale, where a larger or infinite remote cathode is not present, is not fully understood. The techniques explored here have the potential to be extended to even smaller length scales than those reported in this presentation, such as those pertinent to crack tips and fracture process zones.

1.2. Critical Unresolved Issues

This dissertation seeks to address critical and unresolved issues framed by the above background from both an engineering as well as from a scientific/mechanistic standpoint as follows.

1.2.1. Engineering Perspective

- There exists a lack of knowledge of general corrosion characterization for these specific alloys in the atmospheric environments of interest. Therefore, the type of corrosion cell formed, believed to dictate subsequent hydrogen production and uptake, cannot be predicted.
- Hydrogen production and uptake in the majority of atmospheric environments is not understood and basic trends are unknown or not fully quantified in the ferrous materials of interest. For instance, it is unknown whether uptake is related or correlated with corrosion based mass loss even in a single environment category such as the marine atmosphere. This may be unlikely given the dominance of other cathodic reactions over HER kinetically as indicated above, but is worth exploring thermodynamically.
- There is no currently established approach or metric for relating severity of atmospheric hydrogen uptake to severity of corrosion on a convenient scale.
 - There is no known general corrosion signifier to exist, such as mass loss or pit factor, which could be used to relate hydrogen uptake to atmospheric corrosion. Mass loss, a characteristic of uniform corrosion over known time periods, has been correlated to H concentrations, in preliminary work

and may give insight into determining a simple correlation between corrosion and hydrogen production and uptake.[44, 140] However, it seems obvious that various environmental factors that increase oxidizing power, such as ozone, may or may not increase hydrogen production and uptake. The conditions are complex, for instance, an oxidizer may raise the droplet OCP but promote metal cation hydrolysis. Certainly factors that increase corrosivity have the chance to increase H production given the coupled nature of the corrosion processes.

- The effects of atmospheric environmental factors such as RH, η_H , pH, Cl^- , and O_3 on hydrogen uptake are yet to be determined.

1.2.2. Scientific Perspective

- The manner in which, and extent to which, a given atmospheric environment combined with material composition and microstructures govern the type of corrosion cell formed and can affect hydrogen uptake remains an open question and is a great opportunity for study.
 - At the local scale, i.e. in aerosol droplets, formation of Evans type cells vs. local acid pit anodes, and the subsequent effects on pH, local potential, and subsequent hydrogen overpotential can affect hydrogen production and uptake, but the degree/ magnitude of influence is unknown. The potential distribution and pH across a drop is important to determine E_{couple} at the anode. The H overpotential and production rate are difficult quantities to determine in these circumstances. The interaction of these

various electrochemical cells with material composition and microstructure and the resulting hydrogen uptake also remains a large gap in understanding of hydrogen concentrations at the local scale.

- Methods for localized hydrogen detection and quantification pertinent to atmospheric corrosion are currently lacking to identify where on a corroding surface a locally intense hydrogen uptake process occurs. Techniques at the mm or cm scale likely average corrosion rates from sites of low and high concentrations. Clearly sites of high concentrations dictate fracture properties.
 - There is a need for detection of spatial distribution of H concentrations due to controlled pre-exposure and atmospheric exposure. The capability for determination of $D_{H,eff}$ locally can provide further insight into crack predictions.
 - Furthering techniques at the sub-mm length scale for local detection will aid in improvement to the H embrittlement field, not only for determination of H uptake from atmospheric uptake, but these techniques can be applied to other pertinent occluded sites.
 - Ideally hydrogen detection and mapping is of interest across various length scales pertaining to Figure 1. These range from atmospheric corrosion dimensions, microstructural dimensions, to other dimensions.
- A comparison of the local scale predictions of hydrogen uptake to global measurements of hydrogen uptake can aid in understanding the influence of atmospheric factors specifically under these non-uniform corrosion and H production and uptake conditions. In high performance materials with passive

films, local occluded sites, and low values of $D_{H,eff}$, hydrogen is less likely to become homogenized and otherwise uniformly distributed. Therefore, the capability for local mapping is of great importance.

- Emerging SKP methods have been attempted in the permeation mode. This compromises H mapping capability in part because of hydrogen diffusion radially outward, for instance as from a point source, is much less concentrated than if mapped from the charging surface. It also creates challenges in that concentrations are lowered in the developing concentration field. The need exists to map on the H charging surface for a more direct measurement.
- The development and application of novel techniques for local H detection also requires an establishment of the effect of hydrogen on the measurement and an understanding of why/ how H detection can occur. Pertinent to the SKP and SECM are the effects of H on the SKP potential and the current measured at the SECM tip. Prior techniques for SKP have shed some light on the interaction between H and the SKP potential [33, 34], but have not discussed the necessary conditions for front side detection as they have been performed in permeation mode via backside detection. Previous SECM studies have lacked explanations for the effects of H on SECM ME tip current. There is a need to further elucidate both of these measurements to better understand the benefits and limitations of such techniques for local H detection.

With this background, the objectives associated with this dissertation work can be stated.

1.3. Objectives

This study includes both the more traditional analysis of meso-scale H uptake under atmospheric exposure conditions using TDS as well as pioneering local detection methods. The objective is to characterize and compare the effects of various LALT environments, selected field exposures, and full immersion exposures on the type of corrosion cell formed and the subsequent H uptake. This was carried out by quantification of H by more traditional approaches across a range of environments and comparing H concentrations to the mass loss over the exposure period. The goal was to provide insight into the gap in scientific understanding regarding H uptake under atmospheric exposure conditions. Broad, coarse screening was undertaken using TDS as a primary method in combination with corrosion assessments. However, given that atmospheric exposures invariably lead to non-uniform corrosion and H uptake conditions, the need for localized detection became very apparent and therefore, in this study, we explore the novel applications of the SECM and the SKP for spatial hydrogen measurements. With the SECM and SKP, the detection of spatial distribution of H concentrations from controlled pre-exposure and atmospheric exposure is possible on the pre-exposed surface or through the implementation of cross-sectional analysis. Through this work, the determination of the mechanisms governing and understanding of the hydrogen measurement concepts will be established. This is advantageous over the current applications of backside permeation methods with SKP, as it eliminates the step of through thickness diffusion and added loss of resolution. Also, the quantification of H

in the SKP can be carried out with calibration of the SKP potential with respect to known diffusible H concentrations. The application of these local scale techniques provides local and spatial information on H uptake pertinent to atmospheric corrosion previously unattainable with meso-scale techniques. An understanding of the H severity at this local scale can be expanded to the meso-scale and provide significant information on severity of atmospheric exposure environments in terms of H production and uptake.

These objectives are addressed by the following chapters:

- Chapter 2 establishes material behavior in simulated atmospheric exposures through general and local corrosion characterization in terms of mass loss, XRD, Hirox, and SEM of samples exposed in the selected atmospheric exposure environments. Electrochemical diagnostic techniques such as OCP measurements and polarization scans in environments pertinent to this study on the three alloys of interest help determine and predict the likelihood of local vs. uniform corrosion for each alloy and give an idea of some environmental factors through mixed potential theory analysis. Characterization of material-hydrogen interactions where gaps in existing knowledge occurs, including the determination of the $D_{H\text{ eff}}$ for the ultra-high strength steels evaluated in this study were established. This information was essential to assess the degree of hydrogen homogenization. This chapter also provides global characterization of hydrogen uptake in selected atmospheric environments with a broad study yielding comparisons between selected LALT, full

immersion tests, and selected field exposures. A corrosion signifier to correlate environmental severity in terms of a convenient corrosion metric was investigated. Mass loss was found to relate crudely to hydrogen uptake with respect to selected exposures such as marine atmospheres, but was a complex function of both corrosion severity and hydrogen capacity and may only be used on steels that exhibit general corrosion.

- Chapters 3 and 4 provide techniques for spatial determination of diffusible hydrogen concentrations using local scale probes. In Chapter 3 the SKP is of interest and the chapter begins with a study of the testing environment used in the SKP to determine possible factors that may limit ability to feasibly measure H concentrations. The explanation of the measurement concept for H detection in the SKP is rationalized. This chapter provides a calibration between the measured SKP potential and $C_{H,Diff}$ for samples uniformly pre-charged with known H concentrations. Factors such as RH, size of charging area, and time are explored. Also, the use of SKP for the determination of $D_{H,eff}$ compared to TDS measurements is presented. This established a possible method that if applied at a smaller length scale could identify locally enhanced $D_{H,eff}$ such as the $D_{H,eff}$ spatially near a crack tip. Finally, simulations of steady state H and H^+ diffusion are presented in an effort to explain SKP hydrogen maps around local corrosion sites such as pits.
- Chapter 4 presents a method for H detection in the SECM. The explanation of the measurement concept for H detection in the SECM is

rationalized. This chapter includes optimization of solution, potential applied to the ME tip, tip to sample height selection, scan rate, and scan size. This chapter provides a calibration between the current measured at the SECM tip and $C_{H,diff}$ for samples uniformly pre-charged with known H concentrations. Solution evaluation was carried out both through SECM experiments and electrochemical evaluation through OCP, polarization scans, EIS and CVs. Also presented in this chapter are results for samples pre-charged in the same manner as for the SKP, but with H detection in the SECM. The SECM was shown to be another method for spatial detection of H concentrations. A correlation between H pre-charged materials and the effect on ME tip current measured was determined. The effects of solutions phase transport of species used in the Redox competition mode were compared to solid state diffusion simulations.

- Chapter 5 extends towards the study of developed methods for detection of local hydrogen concentrations sites on samples pre-exposed under a limited set of plausible atmospheric conditions (in $MgCl_2$). It provides the experimental methods to apply the techniques established in Chapters 3 and 4 to analyze hydrogen uptake in simulated atmospheric pre-exposed samples. First, electrochemical analysis of conditions present in these drops was investigated to better understand the basic roles of various environmental parameters. SKP and SECM scans of samples from controlled atmospheric pre-exposures are then presented to demonstrate the application of these techniques to these types of local cells.

1.4. References

1. Koch, G.H., et al., *Corrosion Costs and Preventive Strategies in the United States*, N. International, Editor. 2002, U.S. Department of Transportation, C.C. Technologies, NACE International: Houston, TX.
2. Gangloff, R.P. and R.P. Wei, *Gaseous Hydrogen Embrittlement of High-Strength Steels*. Metallurgical Transactions a-Physical Metallurgy and Materials Science, 1977. **8**(7): p. 1043-1053.
3. Fujita, T. and Y. Yamada, *SCC and HE of iron base alloys*, in *Stress Corrosion Cracking and Hydrogen Embrittlement of Iron Base Alloys* 1977, NACE.
4. Buckley, P., B. Placzankis, J. Beatty, and R. Brown. *Characterization of the Hydrogen Embrittlement Behavior of High Strength Steels for Army Applications*. in *Corrosion 94, The Annual Conference and Corrosion Show*. 1994: NACE International.
5. Gangloff, R.P., *Hydrogen assisted cracking of high strength alloys*, in *Aluminum Co of America Alcoa Center*. 2003, Alcoa Technical Center: PA.
6. Lee, E.U., *Corrosion Behavior of Landing Gear Steel*, in *Air Vehicle and Crew Systems Technology Deoartnebt: Naval Air System Command*. 1993, Naval Air Warfare Center: Warminster, PA.
7. Thomas, R.L.S., et al., *Trap-governed hydrogen diffusivity and uptake capacity in ultrahigh-strength AERMET 100 steel*. Metallurgical and Materials Transactions a-Physical Metallurgy and Materials Science, 2002. **33**(7): p. 1991-2004.
8. Kim, C.D. and B.E. Wilde, *Kinetics of Hydrogen Absorption into Iron during Cathodic Hydrogen Evolution*. Journal of the Electrochemical Society, 1971. **118**(2): p. 202-&.
9. Bolton, K. and L.L. Shreir, *Factors affecting hydrogen absorption of high-strength steels during cathodic polarization*. Corrosion Science, 1963. **3**(1): p. 17-33.
10. Thomas, R.L.S., J.R. Scully, and R.P. Gangloff, *Internal hydrogen embrittlement of ultrahigh-strength AERMET 100 steel*. Metallurgical and Materials Transactions a-Physical Metallurgy and Materials Science, 2003. **34**(2): p. 327-344.
11. Kehler, B.A. and J.R. Scully, *Predicting the effect of applied potential on crack tip hydrogen concentration in low-alloy martensitic steels*. Corrosion, 2008. **64**(5): p. 465-477.
12. Stratmann, M. and H. Streckel, *On the Atmospheric Corrosion of Metals Which Are Covered with Thin Electrolyte Layers .1. Verification of the Experimental-Technique*. Corrosion Science, 1990. **30**(6-7): p. 681-696.
13. Leygraf, C. and T.E. Graedel, *Atmospheric corrosion*. The Electrochemical Society series. 2000, New York: Wiley-Interscience. xii, 354 p.
14. Devanathan, M.A.V. and Z. Stachurski, *The Adsorption and Diffusion of Electolytic Hydrogen in Palladium*. Proceedings of the Royal Society of London. Series A., 1962(270): p. 90-102.
15. DeLuccia, J.J. and D.A. Berman, *An Electrochemical Technique to Measure Diffusible Hydrogen in Metals (Barnacle Electrode)*, in *Electrochemical Corrosion Testing*, A.S.T.M., Editor. 1981, ASTM International: West Conshohocken, PA. p. 256-273.
16. Scully, J.R., G.A. Young, and S.W. Smith, *Hydrogen Embrittlement of Aluminum and Aluminum Based Alloys*, in *Gaseous Hydrogen Embrittlement of Materials in Energy Technologies*. 2011, Woodhead. p. 707-768.
17. Devanathan, M.A.V., Z. Stachurski, and W. Beck, *A technique for the evaluation of hydrogen embrittlement characteristics of electroplating baths*. Journal of the Electrochemical Society, 1963. **110**(8): p. 886-890.

18. Li, D.M., R.P. Gangloff, and J.R. Scully, *Hydrogen trap states in ultrahigh-strength AERMET 100 steel*. Metallurgical and Materials Transactions a-Physical Metallurgy and Materials Science, 2004. **35A**(3): p. 849-864.
19. Figueroa, D. and M.J. Robinson, *Hydrogen transport and embrittlement in 300 M and AerMet100 ultra high strength steels*. Corrosion Science, 2010. **52**(5): p. 1593-1602.
20. Switzer, M., *Use of crevice scaling laws to investigate local hydrogen uptake in rescaled model pits*, in *Materials Science and Engineering*. 2003, University of Virginia: Charlottesville.
21. Katano, G., K. Ueyama, and M. Mori, *Observation of hydrogen distribution in high-strength steel*. Journal of Materials Science, 2001. **36**(9): p. 2277-2286.
22. Otsuka, T. and T. Tanabe, *Hydrogen diffusion and trapping process around MnS precipitates in alpha Fe examined by tritium autoradiography*. Journal of Alloys and Compounds, 2007. **446**: p. 655-659.
23. Asaoka, T., et al., *Observation of Hydrogen Trapping in Fe-0.15wt-Percent Ti Alloy by High-Resolution Autoradiography*. Corrosion, 1978. **34**(2): p. 39-47.
24. Garet, M., et al., *Hydrogen trapping on non metallic inclusions in Cr-Mo low alloy steels*. Corrosion Science, 1998. **40**(7): p. 1073-1086.
25. Young, G.A. and J.R. Scully, *The effects of test temperature, temper, and alloyed copper on the hydrogen-controlled crack growth rate of an Al-Zn-Mg-(Cu) alloy*. Metallurgical and Materials Transactions a-Physical Metallurgy and Materials Science, 2002. **33**(4): p. 1167-1181.
26. Larignon, C., et al., *Investigation of Kelvin probe force microscopy efficiency for the detection of hydrogen ingress by cathodic charging in an aluminium alloy*. Scripta Materialia, 2013. **68**(7): p. 479-482.
27. Schaller, R.F., et al., *Spatially resolved mapping of the relative concentration of dissolved hydrogen using the scanning electrochemical microscope*. Electrochemistry Communications, 2015. **51**: p. 54-58.
28. Ovejero-García, J., *Hydrogen microprint technique in the study of hydrogen in steels*. Journal of Materials Science, 1985. **20**(7): p. 2623-2629.
29. Madden, S., *The Effects of Permanganate and Other Selected Chemical Inhibitors on Surface and Crack Tip Corrosion*, in *Materials Science and Engineering*. 2014, University of Virginia: Charlottesville, VA.
30. Tsuru, T., et al., *Hydrogen entry into steel during atmospheric corrosion process*. Corrosion Science, 2005. **47**(10): p. 2431-2440.
31. Senoz, C., et al., *Scanning Kelvin Probe as a highly sensitive tool for detecting hydrogen permeation with high local resolution*. Electrochemistry Communications, 2011. **13**(12): p. 1542-1545.
32. Evers, S., C. Senoz, and M. Rohwerder, *Spatially resolved high sensitive measurement of hydrogen permeation by Scanning Kelvin Probe Microscopy*. Electrochimica Acta, 2013. **110**: p. 534-538.
33. Evers, S., C. Senoz, and M. Rohwerder, *Hydrogen detection in metals: a review and introduction of a Kelvin probe approach*. Science and Technology of Advanced Materials, 2013. **14**(1).
34. Evers, S. and M. Rohwerder, *The hydrogen electrode in the "dry": A Kelvin probe approach to measuring hydrogen in metals*. Electrochemistry Communications, 2012. **24**: p. 85-88.
35. Schaller, R.F. and J.R. Scully, *Measurement of effective hydrogen diffusivity using the Scanning Kelvin Probe*. Electrochemistry Communications, 2014. **40**: p. 42-44.
36. Larignon, C., et al., *Combined Kelvin probe force microscopy and secondary ion mass spectrometry for hydrogen detection in corroded 2024 aluminium alloy*. Electrochimica Acta, 2013. **110**: p. 484-490.

37. Williams, G., H.N. McMurray, and R.C. Newman, *Surface oxide reduction by hydrogen permeation through iron foil detected using a scanning Kelvin probe*. Electrochemistry Communications, 2013. **27**: p. 144-147.
38. Koyama, M., et al., *Spatially and Kinetically Resolved Mapping of Hydrogen in a Twinning-Induced Plasticity Steel by Use of Scanning Kelvin Probe Force Microscopy*. Journal of the Electrochemical Society, 2015. **162**(12): p. C638-C647.
39. Wang, G., et al., *Investigation of hydrogen evolution and enrichment by scanning Kelvin probe force microscopy*. Electrochemistry Communications, 2013. **35**: p. 100-103.
40. Li, M., et al., *The Mechanism of Hydrogen-Induced Pitting Corrosion in Duplex Stainless Steel Studied by SKPFM*. Corrosion Science, 2012. **60**: p. 76-81.
41. Schimo, G., W. Burgstaller, and A.W. Hassel, *Potentiodynamic hydrogen permeation on Palladium-Kelvin probe compared to 3D printed microelectrochemical cell*. Electrochemistry Communications, 2015. **60**: p. 208-211.
42. Nazarov, R.P., A.I. Marshakov, and A.A. Rybkina, *Iron hydrogenation under atmospheric corrosion. Studies using a scanning vibrating microscope*. Protection of Metals and Physical Chemistry of Surfaces 2015. **51**(3): p. 347-359.
43. Baker, E.A., ed. S.W. Dean and T.S. Lee, *Long-Term Corrosion Behavior of Materials in the Marine Atmosphere*, in *Degradation of Metals in the Atmosphere*, ASTM, Editor. 1988: Philadelphia. p. 125-144.
44. Li, S.J., et al., *Evaluation of delayed fracture property of outdoor-exposed high strength AISI 4135 steels*. Corrosion Science, 2010. **52**(10): p. 3198-3204.
45. Townsend, H.E., *Effects of alloying elements on the corrosion of steel in industrial atmospheres*. Corrosion, 2001. **57**(6): p. 497-501.
46. Townsend, H.E., *Atmospheric corrosion performance of quenched-and-tempered, high-strength weathering steel*. Corrosion, 2000. **56**(9): p. 883-886.
47. Boelen, B., et al., *A Literature Survey on the Development of an Accelerated Laboratory Test Method for Atmospheric Corrosion of Precoated Steel Products*. Corrosion Science, 1993. **34**(11): p. 1923-1931.
48. Wan, Y., E.N. Macha, and R.G. Kelly, *Modification of ASTM B117 Salt Spray Corrosion Test and Its Correlation to Field Measurements of Silver Corrosion*. Corrosion, 2012. **68**(3).
49. Kim, Y.J., *Characterization of the Oxide Film Formed on Type-316 Stainless-Steel in 288-Degrees-C Water in Cyclic Normal and Hydrogen Water Chemistries*. Corrosion, 1995. **51**(11): p. 849-860.
50. Rufner, J., et al., *Oxidation behavior of stainless steel 430 and 441 at 800 degrees C in single (air/air) and dual atmosphere (air/hydrogen) exposures*. International Journal of Hydrogen Energy, 2008. **33**(4): p. 1392-1398.
51. Dean, S.W. and C. Rhea, eds. *Atmospheric Corrosion of Metals: A Symposium*. Calibration of Atmospheric Corrosion Test Sites, ed. E.A. Baker and T.S. Lee. Vol. 767. 1982, American Society for Testing and Materials. 250-266.
52. S. Shoji, et al., *Effects of Relative Humidity on Atmospheric Stress Corrosion Cracking of Stainless Steels*. Corrosion Engineering, 1986. **35**(10): p. 559-565.
53. Sedriks, A.J. and Electrochemical Society, *Corrosion of stainless steels*. 2nd ed. Corrosion monograph series. 1996, New York: Wiley. xviii, 437 p.
54. Wang, J.H., C.C. Su, and Z. Szklarskasmialowska, *Effects of Cl⁻ Concentration and Temperature on Pitting of Alsl-304 Stainless-Steel*. Corrosion, 1988. **44**(10): p. 732-737.
55. Shoji, S., N. Ohnaka, *Effects of Relative Humidity and Kinds of Chlorides on Atmospheric Stress Corrosion Cracking of Stainless Steel at Room Temperature*. Corrosion Engineering, 1989. **38**(2).
56. Frazier, J.C.W., R. K. Taylor, and A. Grollman, in *Int. Critical Tables of Numerical Data*. Vol. Vol. III. 1928, New York: McGraw-Hill.

57. Chen, Z.Y., F. Cui, and R.G. Kelly, *Calculations of the cathodic current delivery capacity and stability of crevice corrosion under atmospheric environments*. Journal of the Electrochemical Society, 2008. **155**(7): p. C360-C368.
58. Schindelholz, E., L.K. Tsui, and R.G. Kelly, *Hygroscopic Particle Behavior Studied by Interdigitated Array Microelectrode Impedance Sensors*. Journal of Physical Chemistry A, 2014. **118**(1): p. 167-177.
59. Pourbaix, M., *Atlas of electrochemical equilibria in aqueous solutions*. 1974, Houston, TX: National Association of Corrosion Engineers.
60. Cole, I.S., et al., *What really controls the atmospheric corrosion of zinc? Effect of marine aerosols on atmospheric corrosion of zinc*. International Materials Reviews, 2009. **54**(3): p. 117-133.
61. Bhatt, H.J. and E.H. Phelps, *Effect of solution pH on the mechanism of stress corrosion cracking of a martensitic stainless steel*. Corrosion, 1961. **17**(9): p. 430-434.
62. Li, S.X. and L.H. Hihara, *Atmospheric-Corrosion Electrochemistry of NaCl Droplets on Carbon Steel*. Journal of the Electrochemical Society, 2012. **159**(11): p. C461-C468.
63. Evans, U.R., *The corrosion of metals*. 1924, New York,: Longmans Arnold. xi, 212 p.
64. Wranglen, G., *Pitting and Sulfide Inclusions in Steel*. Corrosion Science, 1974. **14**(5): p. 331-349.
65. Baker, M.A. and J.E. Castle, *The Initiation of Pitting Corrosion at Mns Inclusions*. Corrosion Science, 1993. **34**(4): p. 667-682.
66. Jones, D.A., *Principles and prevention of corrosion*. 2nd ed. 1996, Upper Saddle River, NJ: Prentice Hall. xvi, 572 p.
67. C. Chen, C.B.B., and F. Mansfeld, *Scanning Kelvin Probe Analysis of the Potential Distribution under Small Drops of Electrolyte*. Materials Science Forum, 1998. **289-292**: p. 181-192.
68. Azmat, N.S., et al., *Corrosion of Zn under fine size aerosols and droplets using inkjet printer deposition and optical profilometry quantification*. Corrosion Science, 2011. **53**(11): p. 3534-3541.
69. Evans, U.R., *The corrosion of metals*. 1926, London: E. Arnold & co. xvi, 259 p.
70. Li, S.X. and L.H. Hihara, *Atmospheric corrosion initiation on steel from predeposited NaCl salt particles in high humidity atmospheres*. Corrosion Engineering Science and Technology, 2010. **45**(1): p. 49-56.
71. Risteen, B.E., E. Schindelholz, and R.G. Kelly, *Marine Aerosol Drop Size Effects on the Corrosion Behavior of Low Carbon Steel and High Purity Iron*. Journal of the Electrochemical Society, 2014. **161**(14): p. C580-C586.
72. Street, S.R., et al., *Atmospheric pitting corrosion of 304L stainless steel: the role of highly concentrated chloride solutions*. Faraday Discussions, 2015. **180**: p. 251-265.
73. A.S.T.M., *Standard Guide for Estimating the Atmospheric Corrosion Resistance of Low-Alloy Steels*, in *Atmospheric Corrosion*. 2004, ASTM International: West Conshohocken, PA.
74. Ayer, R. and P.M. Machmeier, *Transmission Electron-Microscopy Examination of Hardening and Toughening Phenomena in Aermet-100*. Metallurgical Transactions a-Physical Metallurgy and Materials Science, 1993. **24**(9): p. 1943-1955.
75. Corporation, C.T., *Aermet 100TM Data Sheet*. 1992: Reading, PA.
76. Boodey, J.B., and V. S. Agarwala. *Hydrogen in Metals: Cadmium Plated Steel*. in *Corrosion 87/224, NACE*. 1987. Houston, TX.
77. Sun, M., et al., *Electrochemical and Initial Corrosion Behavior of Ultrahigh Strength Steel by Scanning Kelvin Probe*. Journal of Materials Engineering and Performance, 2013. **22**(3): p. 815-822.

78. Shedd, M., *Modeling and Measurement of the Maximum Pit Size on Ferrous Alloys Exposed to Atmospheric Conditions*, in *Materials Science and Engineering*. 2012, University of Virginia: Charlottesville, VA. p. 155.
79. al-Ghamdi, S., Scully, J.R., *Electrochemical Mitigation of Hydrogen Environment Embrittlement of Ultra-high Strength AerMet™ 100*. Diss. University of Virginia, 2010.
80. *Alloy Data - Custom 465*. 1996, Carpenter Technology Corporation: Reading PA.
81. Lee, E.U., et al., *Environment-Assisted Cracking in Custom 465 Stainless Steel*. Metallurgical and Materials Transactions a-Physical Metallurgy and Materials Science, 2011. **42A**(2): p. 415-423.
82. Ifergane, S., Sabatani, E., Carmeli, B., Barkay, Z., Ezersky, V., Beeri, O., and Eliaz, N., *Hydrogen diffusivity measurement and microstructural characterization of Custom 465 stainless steel*. Electrochimica Acta, 2015. **178**: p. 494-503.
83. *Alloy Data - Custom 465 All*. 1996, C.T. Corporation: Reading, PA.
84. Garrison, W.M., and Moody, N.R., *Hydrogen Embrittlement of High Strength Steels*, in *Gaseous Hydrogen Embrittlement of Materials in Energy Technologies*, R.P. Gangloff, and Somerday, B., Editor. 2012, Woodhead Publishing Ltd.: Cambridge. p. 421-492.
85. Scully, J.R., *Effects of Stress - Environment Assisted Cracking*, in *LaQue*. 2013, University of Virginia: Charlottesville, VA.
86. Song, Q.M., and Wert, D., *State of the Art Stainless Steel Provides Improved Properties for Widely Varying Applications*. Advanced Materials Research, 2012. **413**: p. 341-346.
87. Gangloff, R.P. and B.P. Somerday, *Gaseous hydrogen embrittlement of materials in energy technologies*. Woodhead Publishing in materials. 2012, Cambridge, UK, Philadelphia, PA: Woodhead Publishing.
88. Schilke, P.W., et al., *Advanced Materials Propel Progress in Land-Based Gas-Turbines*. Advanced Materials & Processes, 1992. **141**(4): p. 22-30.
89. Galvele, J.R., *Transport Processes and Mechanism of Pitting of Metals*. Journal of the Electrochemical Society, 1976. **123**(4): p. 464-474.
90. *AISI 1018 Mild/Low Carbon Steel*. 2013 [cited 2013 July 3].
91. Kearns, J.R., M.J. Johnson, P.J. Park, *The Corrosion of Stainless Steels in the Atmosphere*, in *Degradation of Metals in the Atmosphere*. 1988, American Society for Testing and Materials: Philadelphia, PA. p. 35-51.
92. Bernstein, I.M., A.W. Thompson, and Metallurgical Society of AIME. Physical Metallurgy Committee., *Hydrogen effects in metals : proceedings of the Third International Conference on Effect of Hydrogen on Behavior of Materials sponsored by the Physical Metallurgy and Mechanical Metallurgy committees of the Metallurgical Society of AIME ... [et al.]*, Moran, Wyoming, August 26-31, 1980. Conference proceedings / the Metallurgical Society of AIME. 1981, Warrendale, Pa.: Metallurgical Society of AIME. xiv, 1059 p.
93. Bogar, F.D. and C.T. Fujii, *Solution Chemistry in Crevices on Fe-Cr Binary Alloys*. 1974, Naval Research Lab: Washington, D.C.
94. Frappart, S., et al., *Hydrogen trapping in martensitic steel investigated using electrochemical permeation and thermal desorption spectroscopy*. Scripta Materialia, 2011. **65**(10): p. 859-862.
95. Fuchigami, H., H. Minami, and M. Nagumo, *Effect of grain size on the susceptibility of martensitic steel to hydrogen-related failure*. Philosophical Magazine Letters, 2006. **86**(1): p. 21-29.
96. Frappart, S., et al., *Hydrogen solubility, diffusivity and trapping in tempered Fe-C-Cr martensitic steel under various mechanical stress states*. Materials Science and Engineering a-Structural Materials Properties Microstructure and Processing, 2012. **534**: p. 384-393.

97. Turnbull, A., M.W. Carroll, and D.H. Ferriss, *Analysis of Hydrogen Diffusion and Trapping in a 13-Percent Chromium Martensitic Stainless-Steel*. Acta Metallurgica, 1989. **37**(7): p. 2039-2046.
98. Scully, J.R., et al., *The Influence of Palladium on the Hydrogen-Assisted Cracking Resistance of PH-13-8 Mo Stainless-Steel*. Metallurgical Transactions a-Physical Metallurgy and Materials Science, 1991. **22**(10): p. 2429-2444.
99. Kehler, B.A. and J.R. Scully, *Predicting the effect of applied potential on crack tip hydrogen concentration in low-alloy martensitic steels (Reprinted from Proceedings of the CORROSION/2007 research topical symposium "Advances in Environmentally Assisted Cracking", 2007)*. Corrosion, 2008. **64**(5): p. 465-477.
100. Kehler, B.A., *Modeling and Experiments to Explain the Potential Dependency of an UHSS to Hydrogen Environment Assisted Cracking*, in *Materials Science and Engineering*. 2008, University of Virginia: Charlottesville.
101. Parkins, R.N., et al., *Hydrogen Gas Evolution from Cathodically Protected Surfaces*. Corrosion, 1985. **41**(7): p. 389-397.
102. Kumnick, A.J. and H.H. Johnson, *Hydrogen Transport through Annealed and Deformed Armco Iron*. Metallurgical Transactions, 1974. **5**(5): p. 1199-1206.
103. Hinotani, S., Y. Ohmori, and F. Terasaki, *Effects of Fe₃C and Mo₂C Precipitation on Hydrogen Diffusivity and Hydrogen Embrittlement in Iron-Alloys*. Materials Science and Engineering, 1985. **76**(1-2): p. 57-69.
104. Hagi, H., *Effect of Substitutional Alloying Elements (Al, Si, V, Cr, Mn, Co, Ni, Mo) on the Diffusion-Coefficient of Hydrogen in Alpha-Iron*. Journal of the Japan Institute of Metals, 1991. **55**(12): p. 1283-1290.
105. Wei, F.G., and Tsuzaki, K., *Hydrogen Trapping Phenomena in Martensitic Steels*, in *Gaseous Hydrogen Embrittlement of Materials in Energy Technologies*, R.P. Gangloff, and Somerday, B., Editor. 2012, Woodhead Publishing Ltd.: Cambridge. p. 493-525.
106. Shackelford, J.F., *Introduction to materials science for engineers*. 5th ed. 2000, Upper Saddle River, N.J.: Prentice Hall. xvii, 877 p.
107. Fisher, D.J., *Hydrogen Diffusion in Metals, A 30 Year Retrospective*. 1999, Zurich, Switzerland: Scitec Publications Limited.
108. Eliaz, N., et al., *Characteristics of hydrogen embrittlement, stress corrosion cracking and tempered martensite embrittlement in high-strength steels*. Engineering Failure Analysis, 2002. **9**(2): p. 167-184.
109. Lee, Y. and R.P. Gangloff, *Measurement and modeling of hydrogen environment-assisted cracking of ultra-high-strength steel*. Metallurgical and Materials Transactions a-Physical Metallurgy and Materials Science, 2007. **38A**(13): p. 2174-2190.
110. Lee, E.U., H. Sanders, and B. Sarkar. *Stress Corrosion Cracking of High Strength Steels*. in *Tri-Service Conf. on Corrosion*. 2000. Aberdeen, MD: Army Research Laboratory.
111. Gerberich, W.W., et al., *Crack-Growth from Internal Hydrogen - Temperature and Microstructural Effects in 4340 Steel*. Metallurgical Transactions a-Physical Metallurgy and Materials Science, 1988. **19**(5): p. 1319-1334.
112. Martin, J.W. and J.M. Dahl, *High strength stainless alloy resists stress corrosion cracking*. Advanced Materials & Processes, 1998. **153**(3): p. 37-39.
113. Truman, J.E., *Stress-corrosion cracking of martensitic and ferritic stainless steels*. International Metals Reviews, 1981. **6**: p. 301-349.
114. McCafferty, E., *Introduction to corrosion science*. 2010, New York: Springer. xvi, 575 p.
115. Scully, J.R., M. Switzer, and J.S. Lee. *Crevice Scaling Laws to Investigate Local Hydrogen Uptake in Rescaled Model Occluded Sites*. in *Second International Conference on Environment Induced Cracking of Metals (EICM-2)*. Banff, Alberta, CA.

116. Switzer, M.A., *Use of Crevice Scaling Laws to Investigate Local Hydrogen Uptake in Rescaled Model Pits*, in *Materials Science and Engineering*. 2003, University of Virginia: Charlottesville, VA.
117. Muster, T.H., et al., *The atmospheric corrosion of zinc: The effects of salt concentration, droplet size and droplet shape*. *Electrochimica Acta*, 2011. **56**(4): p. 1866-1873.
118. Chen, C., C.B. Breslin, and F. Mansfeld, *Scanning Kelvin probe analysis of the potential distribution under small drops of electrolyte*. *Materials and Corrosion-Werkstoffe Und Korrosion*, 1998. **49**(8): p. 569-575.
119. Prosek, T., et al., *Corrosion mechanism of model zinc-magnesium alloys in atmospheric conditions*. *Corrosion Science*, 2008. **50**(8): p. 2216-2231.
120. Akiyama, E., et al., *Studies of Evaluation of Hydrogen Embrittlement Property of High-Strength Steels with Consideration of the Effect of Atmospheric Corrosion*. *Metallurgical and Materials Transactions a-Physical Metallurgy and Materials Science*, 2013. **44A**(3): p. 1290-1300.
121. Li, S.J., et al., *Evaluation of susceptibility of high strength steels to delayed fracture by using cyclic corrosion test and slow strain rate test*. *Corrosion Science*, 2010. **52**(5): p. 1660-1667.
122. Li, S.J., et al., *Hydrogen embrittlement property of a 1700-MPa-class ultrahigh-strength tempered martensitic steel*. *Science and Technology of Advanced Materials*, 2010. **11**(2).
123. Ootsuka, S., et al., *Evaluation of hydrogen absorption into steel in automobile moving environments*. *Corrosion Science*, 2015. **98**: p. 430-437.
124. Troiano, A.R., *The role of hydrogen and other interstitials in the mechanical behavior of metals*. *Trans. ASM*, 1960. **52**(1): p. 54-80.
125. Kehler, B.A., *Modeling and Experiments to Explain the Potential Dependency of an UHSS to Hydrogen Environment Assisted Cracking*, in *Materials Science and Engineering*. 2008, University of Virginia: Charlottesville. p. 296.
126. Evers, S., C. Senoz, and M. Rohwerder, *Hydrogen detection in metals: a review and introduction of a Kelvin probe approach*. *Science and Technology of Advanced Materials*, 2013. **14**(1): p. 014201.
127. Blucher, D.B., et al., *Scanning Kelvin Probe force microscopy - A useful tool for studying atmospheric corrosion of MgAl alloys in situ*. *Journal of the Electrochemical Society*, 2004. **151**(12): p. B621-B626.
128. Schaller, R. and J.R. Scully, *Measurement of Effective Hydrogen Diffusivity Using the Scanning Kelvin Probe*. *Electrochemistry Communications*, 2014. **40**(March): p. 42-44.
129. Wipf, D.O., *Initiation and Study of Localized Corrosion by Scanning Electrochemical Microscopy*. *Colloids and Surfaces a-Physicochemical and Engineering Aspects*, 1994. **93**: p. 251-261.
130. Zhu, Y.Y. and D.E. Williams, *Scanning electrochemical microscopic observation of a precursor state to pitting corrosion of stainless steel*. *Journal of the Electrochemical Society*, 1997. **144**(3): p. L43-L45.
131. Yin, Y.H., et al., *In situ characterization of localized corrosion of stainless steel by scanning electrochemical microscope*. *Applied Surface Science*, 2009. **255**(22): p. 9193-9199.
132. Bastos, A.C., et al., *Imaging concentration profiles of redox-active species in open-circuit corrosion processes with the scanning electrochemical microscope*. *Electrochemistry Communications*, 2004. **6**(11): p. 1212-1215.
133. Bard, A.J., et al., *Chemical Imaging of Surfaces with the Scanning Electrochemical Microscope*. *Science*, 1991. **254**(5028): p. 68-74.
134. Eckhard, K., et al., *Redox competition mode of scanning electrochemical microscopy (RC-SECM) for visualisation of local catalytic activity*. *Physical Chemistry Chemical Physics*, 2006. **8**(45): p. 5359-5365.

135. Unwin, P.R. and A.J. Bard, *Scanning Electrochemical Microscopy: Scanning Electrochemical Microscope Induced Desorption - a New Technique for the Measurement of Adsorption Desorption-Kinetics and Surface-Diffusion Rates at the Solid Liquid Interface*. Journal of Physical Chemistry, 1992. **96**(12): p. 5035-5045.
136. Tefashe, U.M., et al., *Local flux of hydrogen from magnesium alloy corrosion investigated by scanning electrochemical microscopy*. Journal of Electroanalytical Chemistry, 2014. **720-721**(April): p. 121-127.
137. Yuan, Y.A., et al., *Study of the effects of hydrogen on the pitting processes of X70 carbon steel with SECM*. Electrochemistry Communications, 2010. **12**(12): p. 1804-1807.
138. Modiano, S., et al., *Changes on iron electrode surface during hydrogen permeation in borate buffer solution*. Electrochimica Acta, 2008. **53**(10): p. 3670-3679.
139. Schaller, R.F. and J.R. Scully, *Spatial determination of diffusible hydrogen concentrations proximate to pits in a Fe-Cr-Ni-Mo steel using the Scanning Kelvin Probe*. Submitted to Electrochemistry Communications, 2015.
140. Lan, T.T.N., et al., *Atmospheric corrosion of carbon steel under field exposure in the southern part of Vietnam*. Corrosion Science, 2006. **48**(1): p. 179-192.
141. Nagata, S., et al., *Depth Resolution and Recoil Cross-Section for Analyzing Hydrogen in Solids Using Elastic Recoil Detection with He-4 Beam*. Nuclear Instruments & Methods in Physics Research Section B-Beam Interactions with Materials and Atoms, 1985. **6**(3): p. 533-537.
142. Pioszak, G., *Hydrogen Assisted Cracking of Ultra-High Strength Steels*, in *Materials Science and Engineering*. 2015, University of Virginia: Charlottesville, VA.
143. Tahara, A. and Y. Hayashi, *Measurements of Permeation of Hydrogen Isotopes through Alpha-Iron by the Oscillating Pressure Method*. Journal of the Japan Institute of Metals, 1985. **49**(4): p. 248-252.
144. Hayashi, Y., H. Hagi, and A. Tahara, *Diffusion-Coefficients of Hydrogen and Deuterium in Iron Determined by Permeation with Gas, Ion and Electrochemical Charging*. Zeitschrift Fur Physikalische Chemie Neue Folge, 1989. **164**: p. 815-820.
145. Veniali, F. and Z. Szklarskasmialowska, *A Study of the Diffusion and Trapping of Hydrogen in Fe-3cr and Fe-5cr Alloys*. Materials Chemistry and Physics, 1986. **15**(6): p. 545-557.
146. Goltsov, V.A., Geld, P.V., Kosheleva, V.J., Simakov, J.P., *THE RATE OF PENETRATION OF DEUTERIUM AND HYDROGEN INTO STEEL AND ALLOYS AT ELEVATED TEMPERATURES*. Uchen. Zap. Permsk. Univ., 1968. **194**: p. 110-116.
147. Tseng, C.H., W.Y. Wei, and J.K. Wu, *Electrochemical Methods for Studying Hydrogen Diffusivity, Permeability, and Solubility in Aisi-420 and Aisi-430 Stainless-Steels*. Materials Science and Technology, 1989. **5**(12): p. 1236-1239.
148. Onishi, I., Kikuta, Y., Araki, T., Tanichi, F., and Fujii, T., *Fundamental Research on the Behavior of Hydrogen in Steel (Part 2): Effects of microstructure on occludability of hydrogen in steel*. Yosetu Gakkaishi, 1967. **36**(11): p. 1188-93.
149. Xu, J., et al., *Hydrogen Permeation and Diffusion in a 0.2c-13cr Martensitic Stainless-Steel*. Scripta Metallurgica Et Materialia, 1993. **29**(7): p. 925-930.
150. Scully, J.R., et al., *The Influence of Palladium on the Hydrogen-Assisted Cracking Resistance of Ph-13-8 Mo Stainless-Steel*. Metallurgical Transactions a-Physical Metallurgy and Materials Science, 1991. **22**(10): p. 2429-2444.
151. Scully, J.R., et al., *The Influence of Palladium on the Hydrogen-Assisted Cracking Resistance of PH 13-8 Mo Stainless Steel*. Metallurgical Transactions a-Physical Metallurgy and Materials Science, 1990. **22A**.
152. Shirley, A.I. and C.K. Hall, *Trapping of Hydrogen by Substitutional and Interstitial Impurities in Alpha-Iron*. Scripta Metallurgica, 1983. **17**(8): p. 1003-1008.

153. Hirth, J.P., *Effects of hydrogen on the properties of iron and steel*. Metallurgical Transactions A, 1980. **11A**(6): p. 861-890.
154. Chen, C.G. and H.K. Birnbaum, *Low-Temperature H-O and H-N Relaxations - Confirmation of Flynn-Stoneham Tunneling Theory*. Physica Status Solidi A - Applied Research, 1976. **36**(2): p. 687-692.
155. Lee, J.Y., J.L. Lee, and W.Y. Choo. *Thermal analysis of trapped hydrogen in AISI 4340 steel*. in *Current Solutions to Hydrogen Problems in Steels*. 1982: ASM.
156. Pound, B.G., *The Application of a Diffusion-Trapping Model for Hydrogen Ingress in High-Strength Alloys*. Corrosion, 1989. **45**(1): p. 18-25.
157. Wang, M. and P.G. Shewmon, in *Hydrogen Embrittlement: Prevention and Control*, L. Raymond, Editor. 1988, ASTM: Philadelphia. p. 117-124.
158. Gibala, R. *Hydrogen-defect interactions in iron-base alloys*. in *Stress Corrosion Cracking and Hydrogen Embrittlement of Iron Base Alloys*. 1977: NACE.
159. Bernstein, I.M., *Effect of Hydrogen on Deformation of Iron*. Scripta Metallurgica, 1974. **8**(4): p. 343-350.
160. Asaoka, T., et al., *Quantitative study of the hydrogen trapping characteristics in an iron-0.15% titanium ferrite by high-resolution autoradiography and degassing at different temperatures*. Scripta Metallurgica, 1977. **11**(6): p. 467-472.
161. Myers, S.M., S.T. Picraux, and R.E. Stoltz, *Defect Trapping of Ion-Implanted Deuterium in Fe*. Journal of Applied Physics, 1979. **50**(9): p. 5710-5719.
162. Myers, S.M., S.T. Picraux, and R.E. Stoltz, *Deep Deuterium Traps in Y-Implanted Fe*. Applied Physics Letters, 1980. **37**(2): p. 168-170.
163. Scully, J.R., et al., *The influence of palladium on the hydrogen-assisted cracking resistance of PH 13-8 Mo stainless steel*. Metallurgical Transactions A, 1991. **22A**(10): p. 2429-2444.
164. Council, N.R., ed. *Research Opportunities in Corrosion Science and Engineering*. 2011, The National Academies Press: Washington D.C.
165. Feliu, S., M. Morcillo, and B. Chico, *Effect of distance from sea on atmospheric corrosion rate*. Corrosion, 1999. **55**(9): p. 883-891.
166. Dahotre, N.B. and K. Mukherjee, *Development of Microstructure in Laser Surface Alloying of Steel with Chromium*. Journal of Materials Science, 1990. **25**(1B): p. 445-454.
167. Tyler, P.S., M. Levy, and L. Raymond, *Investigation of the Conditions for Crack-Propagation and Arrest under Cathodic Polarization by Rising Step Load Bend Testing*. Corrosion, 1991. **47**(2): p. 82-87.
168. Smith, J.A., M.H. Peterson, and B.F. Brown, *Electrochemical Conditions at Tip of an Advancing Stress Corrosion Crack in Aisi-4340 Steel*. Corrosion, 1970. **26**(12): p. 539-&.
169. Scully, J.R., M. A. Switzer, *Investigation of Local Hydrogen Uptake in Rescaled Model Occluded Site using Crevice Scaling Laws*. 2005, University of Virginia: Charlottesville, Va.

1.5. Tables:

Table 1. Comparison of absorbed H concentration detection and quantification characterization techniques in metallic materials with advantages and disadvantages.

Technique	Diffusible H Concentration	Total H Concentration	Lateral Resolution	Depth Resolution	Temporal Resolution	Detection Limit (wt. ppm)
Barnacle Cell	Yes	No	No, > mm scale	Possible via serial grinding	No	2
Permeation	Yes	Possible	No, > mm scale	No	Yes	2
TDS	Yes	Possible	No	Possible via serial grinding	No	~0.01 – 0.05
NRA	No	Yes	3 mm	0.01 μm via energy loss	No	~4 for Al
FIB/SIMS	No	Possible	<0.1 μm	~0.01 μm via sputtering	No	(~1000) depending on the instrument
LECO	No	Yes	N/A	Possible via serial grinding	No	~1
SKP/SKPFM	Yes	No	Yes, Tip dependent (SKP: 100s μm scale, SKPFM: <30nm)	Possible via cross sectioning	Yes	0.01
SECM	Yes	No	Yes, ME tip dependent (μm scale)	Possible	Yes	unestablished
ERD	No	Yes	Limited to beam size (1mm ²)	Yes	No	0.1 at % [141]

TDS (Thermal Desorption Spectroscopy), NRA (Nuclear Resolution Analysis), FIB/SIMS (focused ion beam/ secondary ion mass spectrometry), LECO (Inert Gas Fusion Thermal Conductivity), SKP/SKPFM (Scanning Kelvin Probe/ Forced Microscopy), SECM (Scanning Electrochemical Microscopy), and ERD (Elastic Recoil Detection).

Table 2. Oxides and Hydroxides found on corroded iron.[13]

Oxides and Hydroxides	Valence	Crystal System	Formula
Ferrous hydroxide	2	Hex	$\text{Fe}(\text{OH})_2$
Magnetite	2,3	Cub	Fe_3O_4
Green Rust I	2,3	Trig, hex, rhom	$\text{Fe}^{\text{II}}\text{Fe}^{\text{III}}\text{O}_x(\text{OH})_y$
Green Rust II	2,3	Hex	$\text{Fe}^{\text{II}}\text{Fe}^{\text{III}}\text{O}_x(\text{OH})_y$
Maghemite	3	Trig	$\delta\text{-Fe}_2\text{O}_3$
Ferric Oxide (h)	3	Hex	$\text{Fe}_2\text{O}_3 \cdot \text{H}_2\text{O}$
Ferric hydroxide	3	Cub	$\text{Fe}(\text{OH})_3$
Goethite	3	Orth	$\alpha\text{-FeOOH}$
Akaganite	3	Tetrag	$\beta\text{-FeOOH}$
Lepidocrocite	3	Otrh	$\delta\text{-FeOOH}$
Feroxyhyte	3	Hex	$\delta\text{-FeOOH}$

Table 3. Chemical Composition (wt%) of UNS S46500 Stainless Steel, UNS K92580, and UNS G10180.[75, 83, 142]

	Fe	C	Mn	Si	P	S	Cr	Ni	Mo	N	Ti	Co
UNS S46500	Bal.	0.005	0.02	0.02	0.002	0.002	11.50	11.04	0.94	0.002	1.54	-
UNS K92580	Bal.	0.23	0.019	0.016	0.001	0.0008	2.78	10.89	1.21	-	0.01	12.8
UNS G10180	Bal.	0.15	0.7	0.15-0.3	0.04	0.05	-	-	-	-	-	-

	W	Al	As	Sn	Sb	La	Ce
UNS S46500	0.7	0.1	0.0019	0.0001	0.0006	<0.0001	<0.0001
UNS K92580	-	-	0.0008	0.0009	0.0001	0.0016	0.0039
UNS G10180	-	-	-	-	-	-	-

Table 4. Mechanical Properties of UNS S46500 Stainless Steel, as-annealed / CT and H900 Temper, UNS K92580 Peak-Aged, and UNS G10180.[75, 83, 90]

Temper	Yield Strength	Tensile Strength	Elongation	Reduction of area	HRC Reported	HRC Measured
UNS S46500: As-annealed/ CT	772 MPa = 112 ksi	951 MPa = 138 ksi	20%	75%	29.5	32.5 ± 0.5
UNS S46500: H900	1703 MPa = 247 ksi	1779 MPa = 258 ksi	14%	51%	50	50.5 ± 0.5
UNS K92580: Peak-Aged	1724 MPa = 250 ksi	1965 MPa = 285 ksi	14%	65%	54	-
UNS G10180	370 MPa	440 MPa = 63.8 ksi	15%	40%	N/A	-

Table 5. Hydrolysis reactions with expressions for the equilibrium pH.[114]

Reaction	Equilibrium pH	pH of 1 M Solution
$\text{Fe}^{2+} + \text{H}_2\text{O} \rightarrow \text{FeOH}^+ + \text{H}^+$	$\text{pH} = 4.75 - 0.500\log [\text{Fe}^{2+}]$	4.75
$\text{Fe}^{2+} + 2\text{H}_2\text{O} \rightarrow \text{Fe}(\text{OH})_2 + 2\text{H}^+$	$\text{pH} = 6.64 - 0.500\log [\text{Fe}^{2+}]$	6.64
$\text{Fe}^{3+} + \text{H}_2\text{O} \rightarrow \text{FeOH}^{++} + 3\text{H}^+$	$\text{pH} = 1.61 - 0.333\log [\text{Fe}^{3+}]$	1.61
$\text{Cr}^{2+} + 2\text{H}_2\text{O} \rightarrow \text{Cr}(\text{OH})_2 + 2\text{H}^+$	$\text{pH} = 5.50 - 0.500\log [\text{Cr}^{2+}]$	5.50
$\text{Cr}^{3+} + 3\text{H}_2\text{O} \rightarrow \text{Cr}(\text{OH})_3 + 3\text{H}^+$	$\text{pH} = 1.60 - 0.333\log [\text{Cr}^{3+}]$	1.60
$\text{Ni}^{2+} + 2\text{H}_2\text{O} \rightarrow \text{Ni}(\text{OH})_2 + 2\text{H}^+$	$\text{pH} = 6.09 - 0.500\log [\text{Ni}^{2+}]$	6.09

Table 6. Calculated room temperature $D_{H,eff}$ data for iron, iron with primary alloying elements for the UHSS of interest, a martensitic Cr alloy, martensite, martensitic stainless steel, PH 13-8, and UNS K92580.

Material	Room T $D_{H,eff}$	Reference
Fe (BCC)	$2.9 \times 10^{-6} \text{ cm}^2/\text{s}$	[143]
	$8.16 \times 10^{-6} \text{ cm}^2/\text{s}$	[144]
Fe + varying wt% Ni (FCC or BCC)	0.98 wt % Ni = $9 \times 10^{-9} \text{ cm}^2/\text{s}$	[104]
	2.06 wt % Ni = $8 \times 10^{-9} \text{ cm}^2/\text{s}$	[104]
	3 wt% Ni = $6 \times 10^{-9} \text{ cm}^2/\text{s}$	[104]
Fe+ varying wt% Cr (BCC)	3 wt% Cr = $5.5 \times 10^{-5} \text{ cm}^2/\text{s}$	[145]
	5 wt% Cr = $2.8 \times 10^{-5} \text{ cm}^2/\text{s}$	[145]
	13wt% Cr = $2.78 \times 10^{-10} \text{ cm}^2/\text{s}$	[146]
AISI 420 (martensitic Cr alloy) (BCT)	$2.06 \times 10^{-11} \text{ cm}^2/\text{s}$	[147]
Martensite (0.5 wt% C Steel) (BCT)	$2.5 \times 10^{-7} \text{ cm}^2/\text{s}$	[148]
0.2 C – 13 Cr wt% Martensitic Stainless Steel	$2.78 \times 10^{-10} \text{ cm}^2/\text{s}$	[149]
PH 13-8 Mo (Aged) (BCC Martensite)	$6.7 \pm 0.7 \times 10^{-9} \text{ cm}^2/\text{s}$	[150]
UNS K92580 (peak Aged)	$3 \times 10^{-8} \text{ cm}^2/\text{s}$	[7]
UNS S46500 (H900)	$1.8 \times 10^{-9} \text{ cm}^2/\text{s}$	[82]

Table 7. Typical hydrogen trap binding energies reported for ferrous alloys (kJ/mol).

Alloy	Peak 1a : Substitutional Ni, Cr in Fe	Peak 1b: Coherent M2C carbides	Peak 2: Grain boundaries, incoherent interfaces, martensite/martensite lath interfaces, martensite packet boundaries, martensite/precipitated austenite interfaces , and prior-austenite grain boundaries	Peak 3: Undissolved metal carbides, highly mis- oriented grain boundaries
AerMet 100 as- quenched[18]	8.9	11.6	62.2	89.1
AerMet 100 aged[18]	-	11.4	61.3	89.9
	Cr, β Ni-Al, Mo	Dislocation cores, grain boundaries	MnS inclusions, interphase interfaces	-
PH 13-8[151]	26.1-27.1	30-32	70-71.8	-
	Cementite-ferrite interface, spheroidized cementite-ferrite interface	Dislocation	TiC precipitates	-
QT 0.2 C Steel[87]	19, 23	28.2	87-95	-
	-	Retained austenite	-	-
0.23-0.93 %C Steel[87]	-	49	-	-
Custom 465	Unknown	-	-	-

Table 8. Trap site binding energies and densities for precipitation hardened martensitic stainless steel (Fe-8.5Ni-12.7Cr-2.18Mo-1.13Al-0.036C-0.1Mn wt%).[125]

Trap Site	E_B (kJ/mol)	Trap Site Density (sites/cm ³)		Reference
		PH 13-8 Aged	PH 13-8 Solutionized	
Cr	26	7×10^{21}	7×10^{21}	[152]
Mo	27.1	7×10^{20}	7×10^{20}	[152]
C	3.3	4×10^{18}	4×10^{18}	[153, 154]
Ni	-11.6	6×10^{21}	6×10^{21}	[152]
Pd	-1.0	2.3×10^{20}	2.3×10^{20}	[152]
MnS inclusion	71.8	1×10^{12}	1×10^{12}	[155, 156]
Interphase interfaces	70	--		[153]
Microvoid	46.9	6×10^{15}	6×10^{15}	[155, 157]
Dislocation Elastic	20	4×10^{19}	4×10^{20}	[153, 158]
Dislocation screw-core	30	4×10^{19}	4×10^{20}	[102, 153]
Dislocation mixed-core	30	1×10^{18}	4.6×10^{19}	[102, 153]
Grain boundary	32	2.6×10^{17}	2.6×10^{17}	[155, 159, 160]
Vacancies	46	5×10^{14}	5×10^{14}	[161, 162]
PdAl	34	2.3×10^{20}	--	[163]
β -NiAl	27	5×10^{20}	--	[163]

Table 9. Trap site binding energies and densities reported for UNS K92580.[125]

Trap Site	E_B (kJ/mol)	Trap Site Density (atoms/cm ³)
Substitutional Solute Atoms	11.4-11.6 \pm 0.2	1.44-1.49 $\times 10^{20}$
Coherent M ₂ C Carbides		
Incoherent Interfaces		
Grain Boundaries	61.3-62.2 \pm 0.3	1.52-3.03 $\times 10^{18}$
Mixed Dislocation Cores		
Incoherent Particles		
Undissolved Metal Carbides	89.1-89.9 \pm 0.3	1.52-4.55 $\times 10^{18}$
Highly Misoriented Boundaries		

Table 10. Estimated ratio of $C_{H,Diff}$ to C_L based on probable $D_{H,eff}$.

$D_{H,eff}$ (cm ² /s)	$C_{H,Diff} / C_L^*$
UNS K92580: 3×10^{-8}	96.7
UNS S46500: 6.7×10^{-9}	432.8
UNS G10180: 1×10^{-7}	29

$$* \frac{C_{H,Diff}}{C_L} = \frac{D_L}{D_{H,eff}}$$

1.6. Figures:

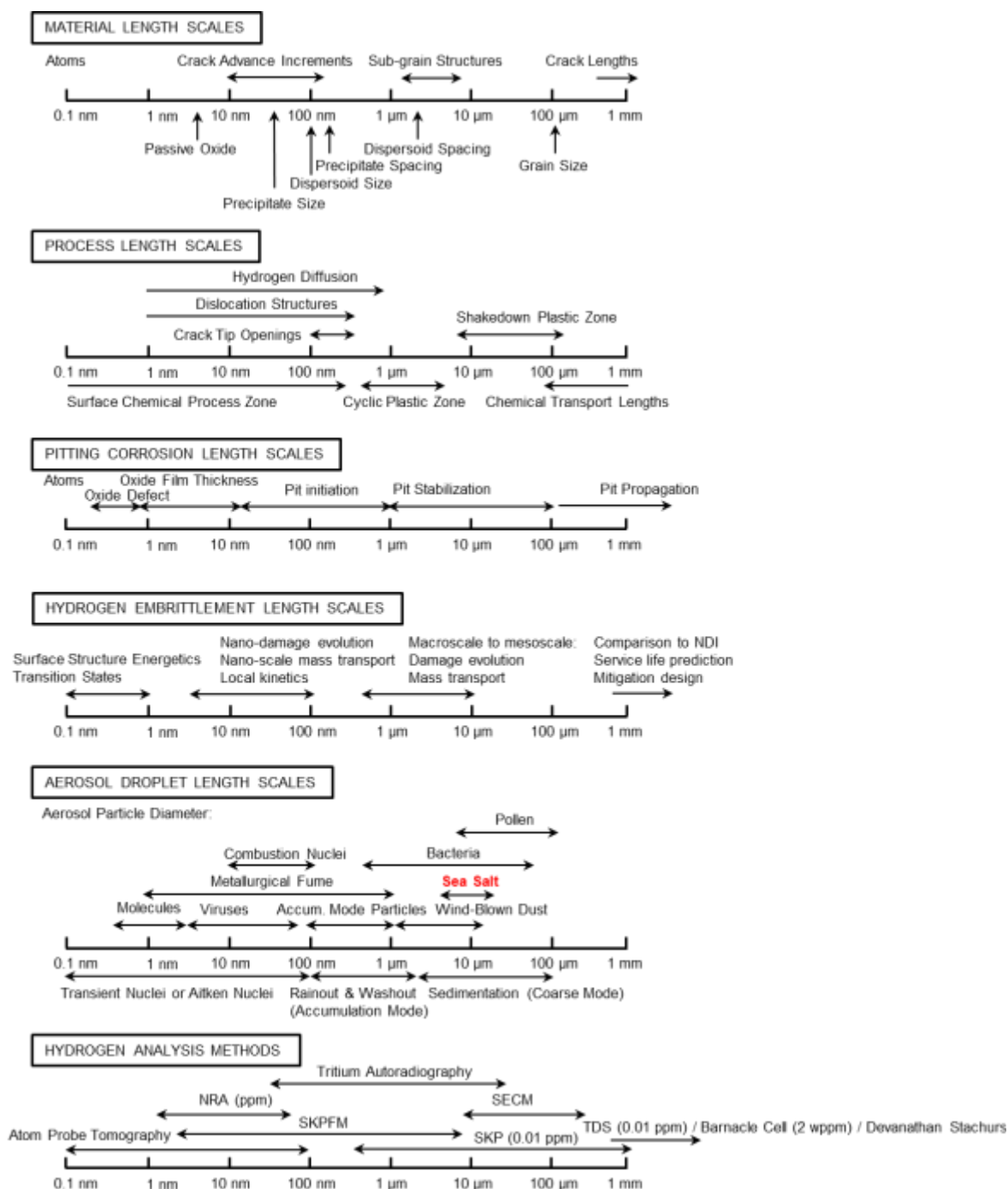


Figure 1. The wide span of different length scales with relation to the material, pitting, and aerosols pertinent to atmospheric corrosion. SOURCE: University of Virginia, CESE, courtesy of Matthew R. Begley and Richard P. Gangloff, Hongbo Cong and J.R. Scully, Atmospheric Corrosion, Christopher Leygraf and Thomas E. Graedel, and I. Cole. [13, 60, 164]

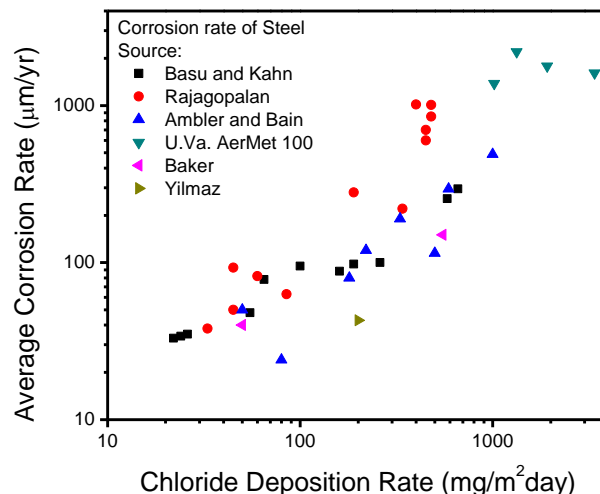


Figure 2. Average corrosion rate vs. chloride deposition rate for a range of studies of steels exposed under atmospheric field exposure conditions. Data compiled from various sources with UNS K92580 exposures at U.Va.[165]

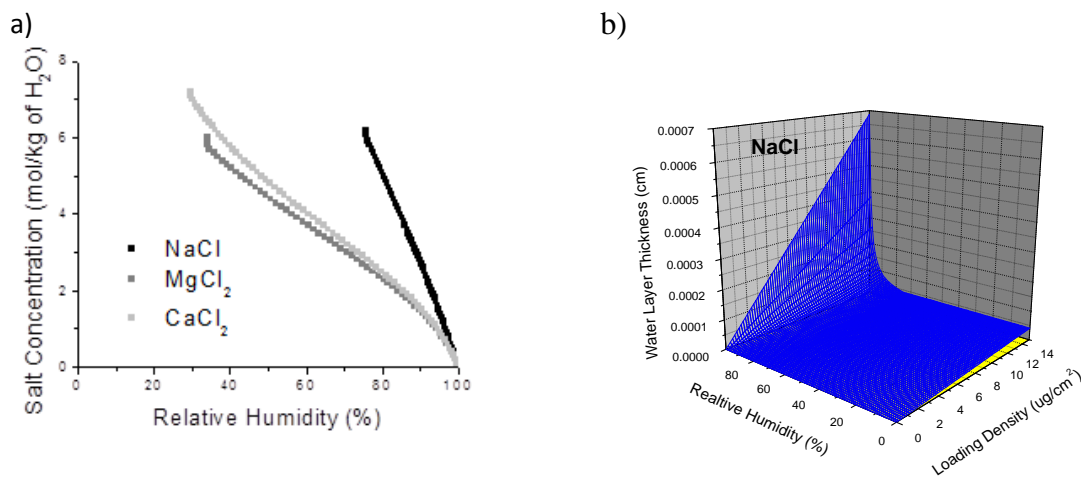


Figure 3. a) Equilibrium salt concentration for NaCl, MgCl₂, and CaCl₂ formed in an H₂O droplet with respect to relative humidity and 25 °C, [56, 57] and b) Calculated theoretically assumed uniform water layer thickness for varied RH and sodium chloride deposition densities ranging from 0 to 15 μg/cm² (field exposures have exhibited ranges from 0.22 to 10 μg/cm²/day for rural to severe marine sites[43, 44]) at room temperature assuming equilibrium salt level and perfect wetting. [55, 63]

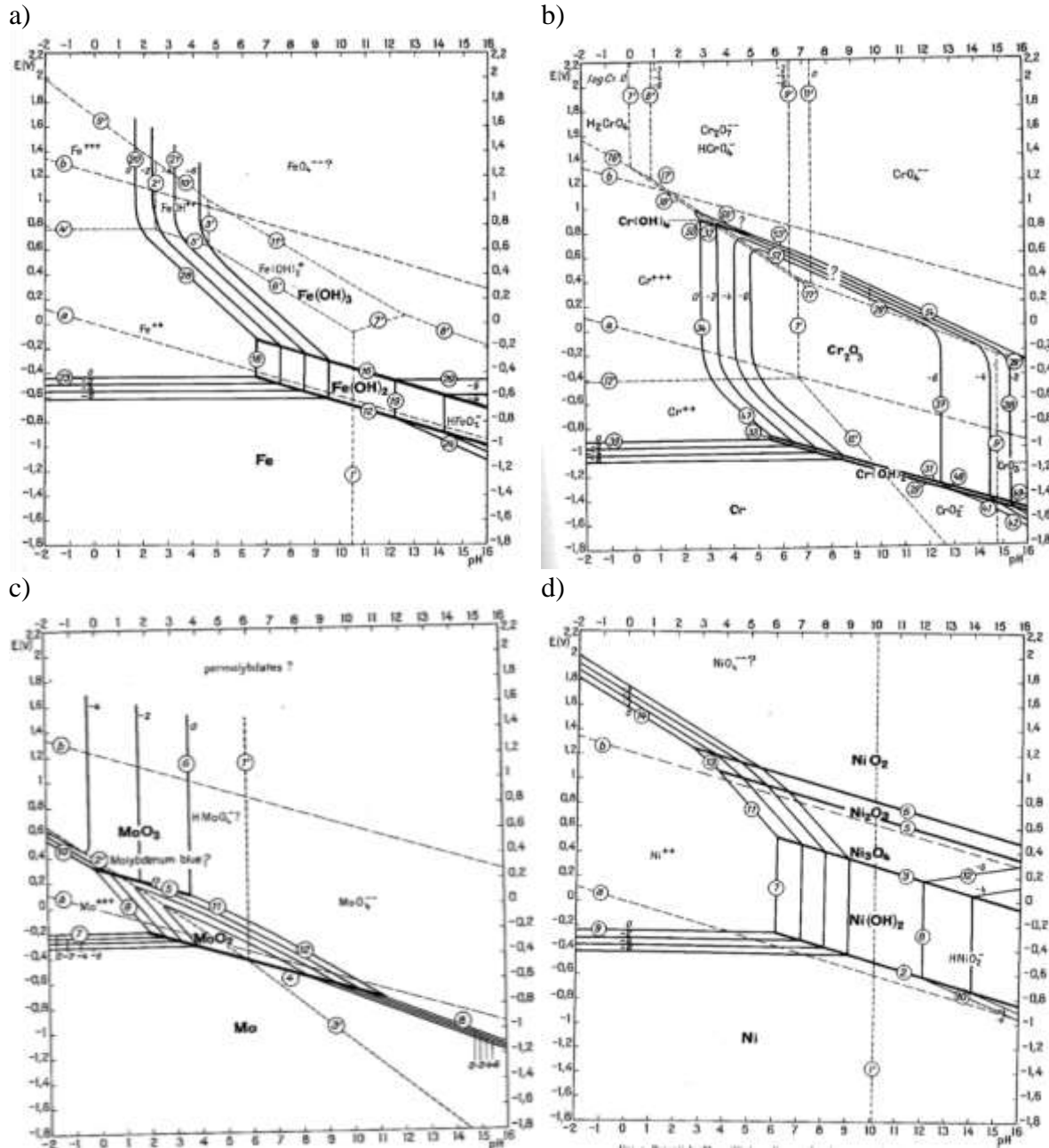


Figure 4. Pourbaix diagram in water at 25°C for a) Fe, b) Cr, c) Mo, and d) Ni. The range of passivity is indicated.[59]

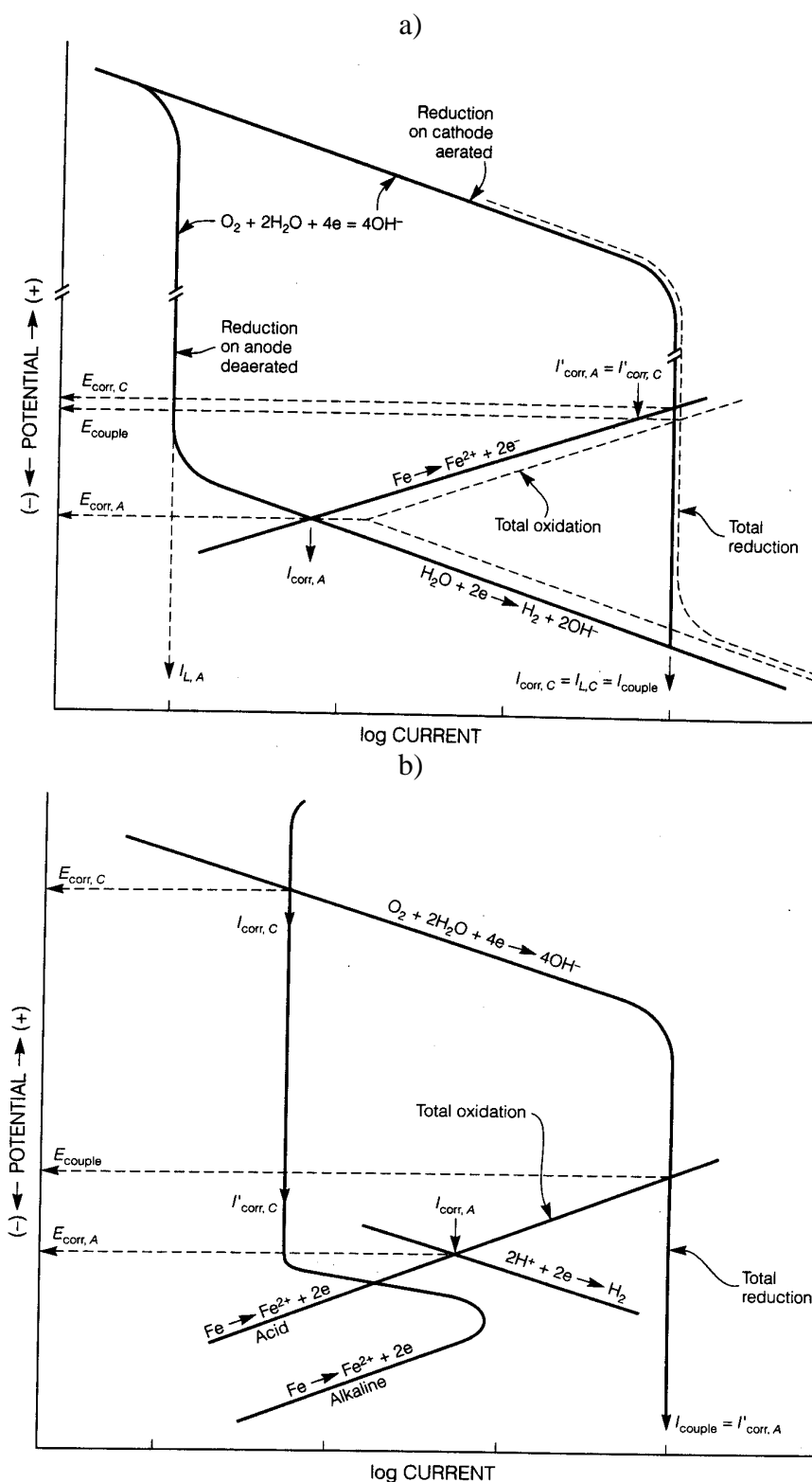


Figure 5. Mixed potential analysis of a differential aeration cell on identical iron electrodes with equal area a) assuming uniform constant solution concentration and b) with passivated cathode and acidified anode.[66]

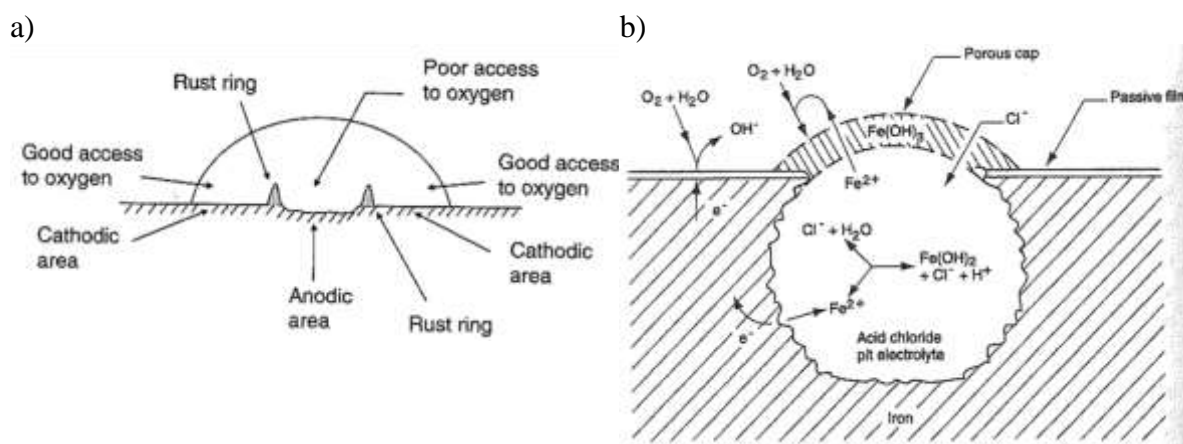


Figure 6. a) The Evans water drop experiment schematic [10, 114] and b) Schematic of process occurring at an actively growing pit in iron. [66]

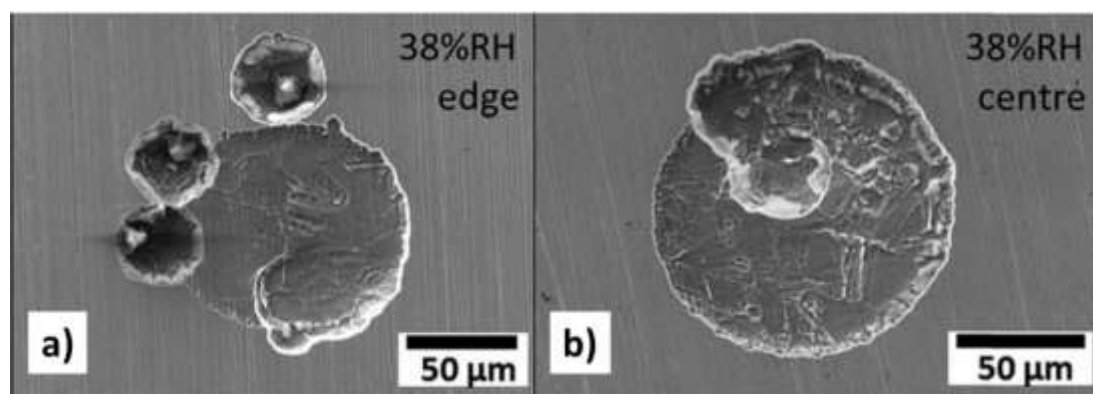


Figure 7. Pit morphologies produced in $MgCl_2$ $750 \mu g/cm^2$ exposures on 304L Stainless steel at 38% RH for 24 h and 30°C at a) edge of droplet displaying satellite pits and b) center of droplet displaying spiral attack.[72]

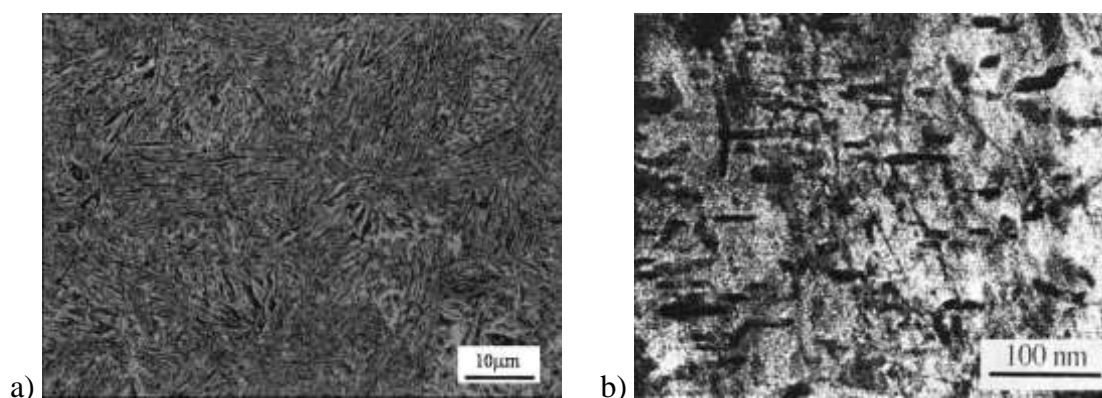


Figure 8. Scanning electron micrograph and Transmission electron micrograph of microstructural features in UNS K92580: a) martensite laths and b) coherent M_2C carbides.[74] Copyright permission obtained from Copyright Clearance Center.

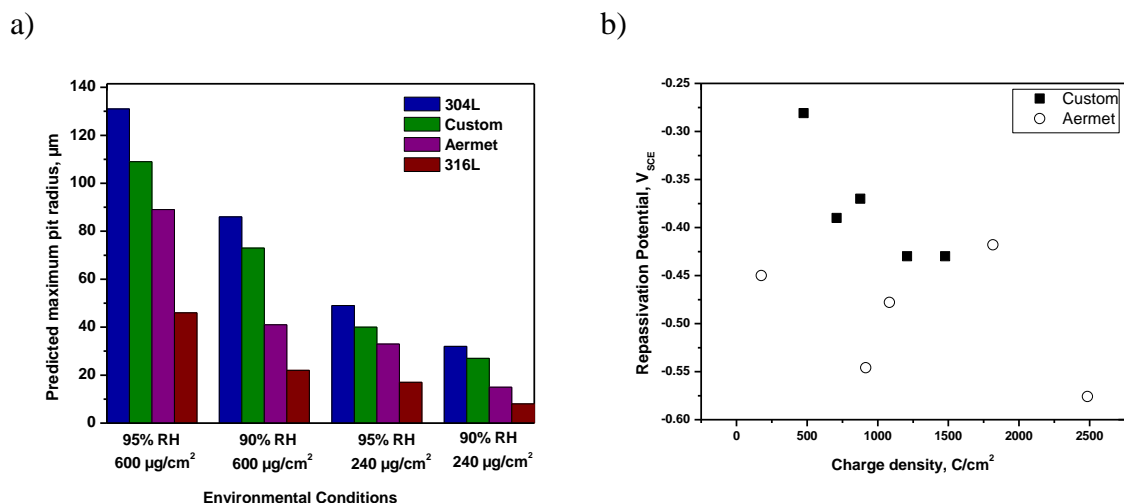


Figure 9. a) 304 L SS, UNS S46500, UNS K92580 and 316L predicted maximum pit radii from the Kelly Shedd model. NaCl loading densities of exposures were 240 or 600 $\mu\text{g}/\text{cm}^2$ exposed at 90 or 95% RH. b) Repassivation potential vs charge density for UNS S46500 and UNS K92580 exposed in 0.6 M sodium chloride.[78]

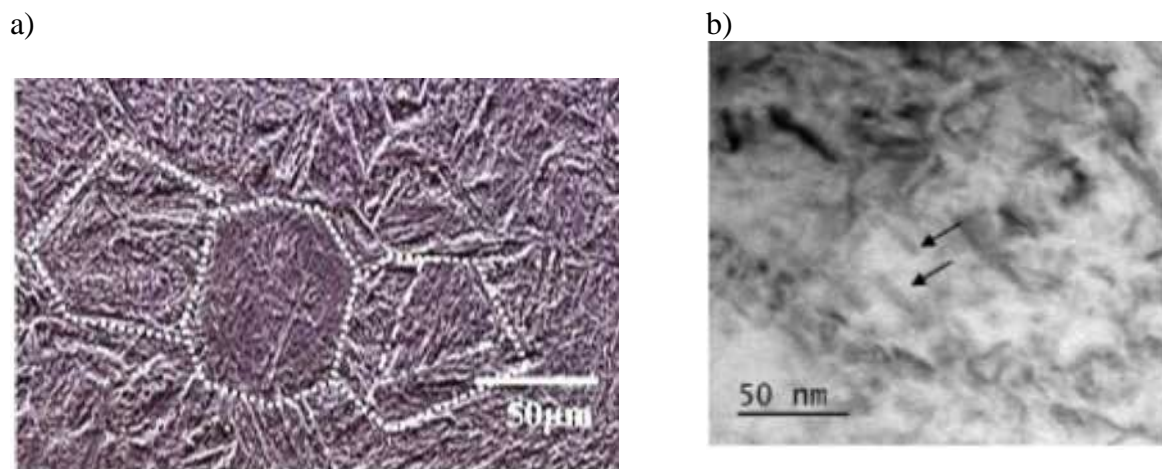


Figure 10. Scanning electron micrograph and Transmission electron micrograph of microstructural features in UNS S46500: a) banded martensite packets and b) Ni_3Ti Precipitates.[82] Copyright permission obtained from Copyright Clearance Center.

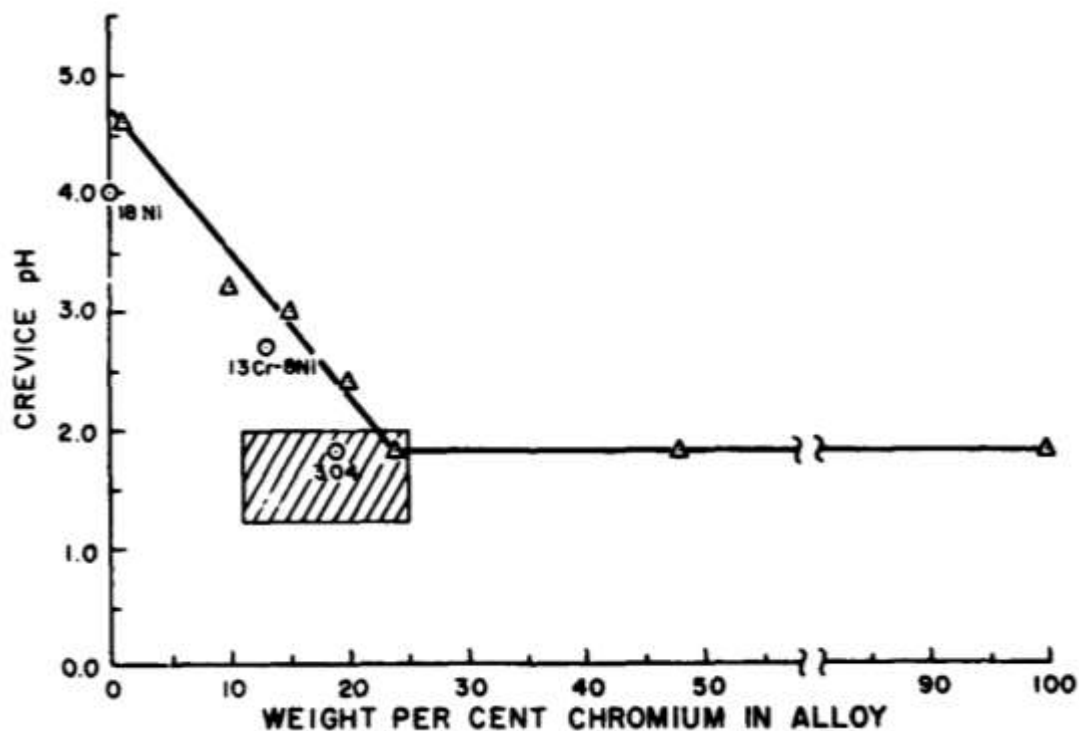


Figure 11. pH measured for crevices on Fe-Cr binary alloys with varying Cr composition, triangles: held at +0.300 V in 3.5 wt% NaCl Solution for 5 hours, and hatched region: samples exposed for 10 months to natural sea water at NRL Key West.[93]

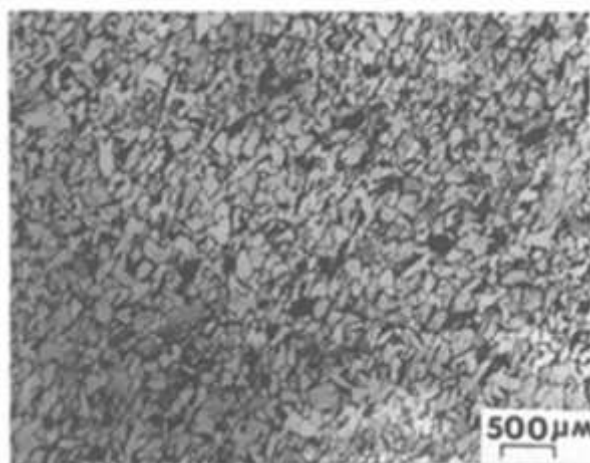


Figure 12. Optical image of UNS G10180 etched with 60mL H₂O + 40 mL HCl + 10 mL HNO₃. [166] Copyright permission obtained from Copyright Clearance Center.

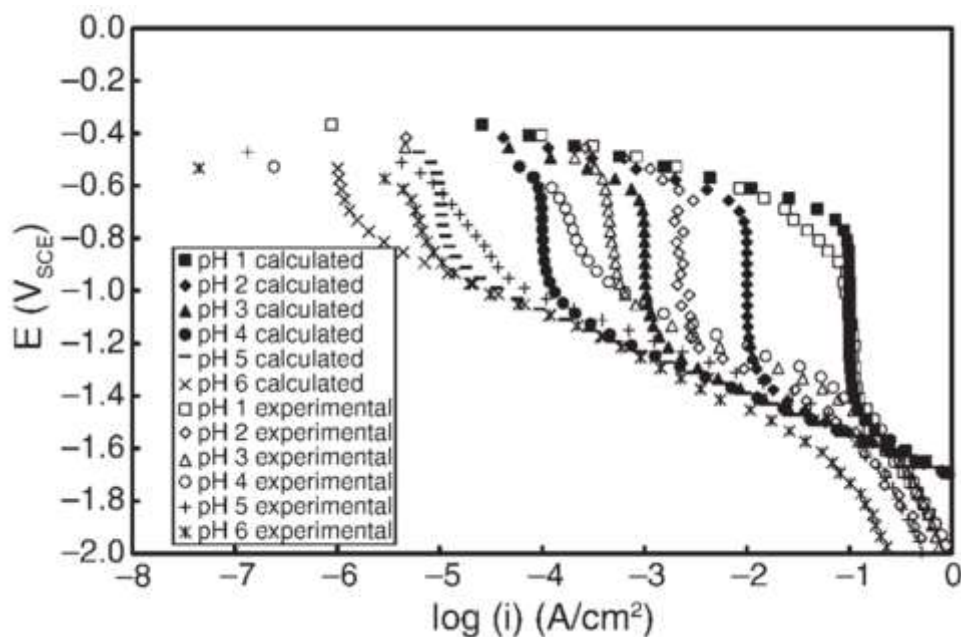


Figure 13. Cathodic polarization data, experimental and calculated, for UNS K92580. Polarization scans were acquired at 0.167 mV/s in deaerated 0.6 M Cl^- electrolytes adjusted to pH of 1 and 6 and depict HER in 3 regimes. [100]

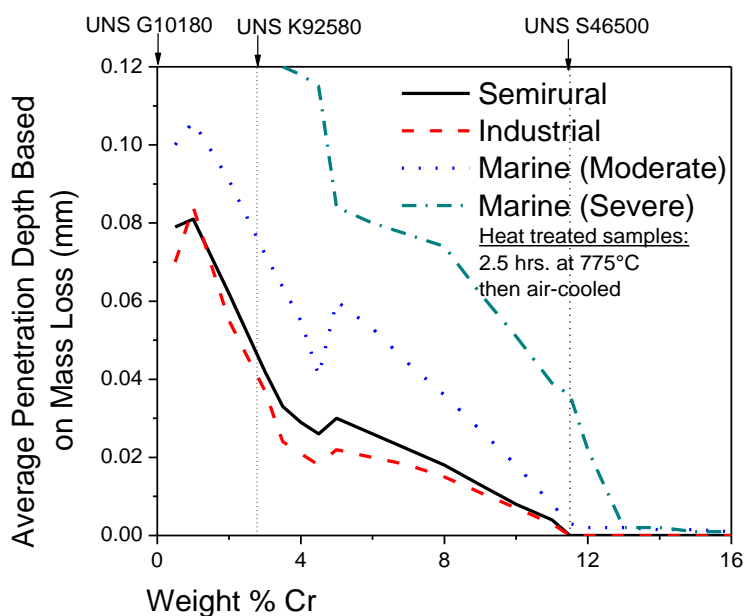


Figure 14. Corrosion vs. Cr content showing weight loss for steels exposed for four years in either semirural, industrial, moderate marine, or severe marine atmospheres with a salt loading density ranging from 2 – 150 mg $\text{NaCl}/\text{m}^2\text{d}$. [91] Copyright permission obtained from Copyright Clearance Center.

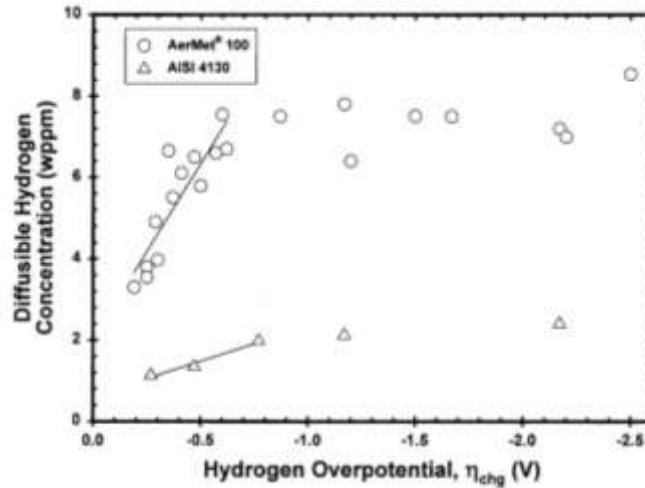


Figure 15. $C_{H-D_{diff}}$ values vs. hydrogen overpotential for UNS K92580 and AISI 4130. H pre-charged in saturated $Ca(OH)_2$ at 23°C. $C_{H,D_{diff}}$ values were calculated by the barnacle cell method.[7] Copyright permission obtained from Copyright Clearance Center.

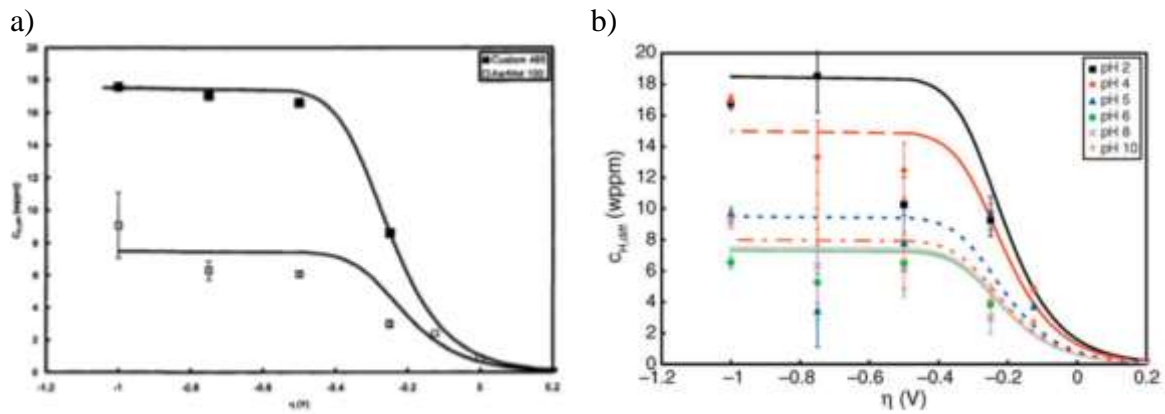


Figure 16. $C_{H-D_{diff}}$ values vs. hydrogen overpotential a) UNS S46500 H900 H pre-charged in pH 8 borate buffer. $C_{H,diff}$ values were calculated by the barnacle cell method using a D_{Heff} of $1.9 \times 10^{-8} \text{ cm}^2/\text{s}$. Results for UNS K92580 in pH 8 borate buffer are shown for comparison and b) reaction rate mechanism model results for UNS K92580 showing the relationship between $C_{H-D_{diff}}$, η_H , as well as pH.[100]

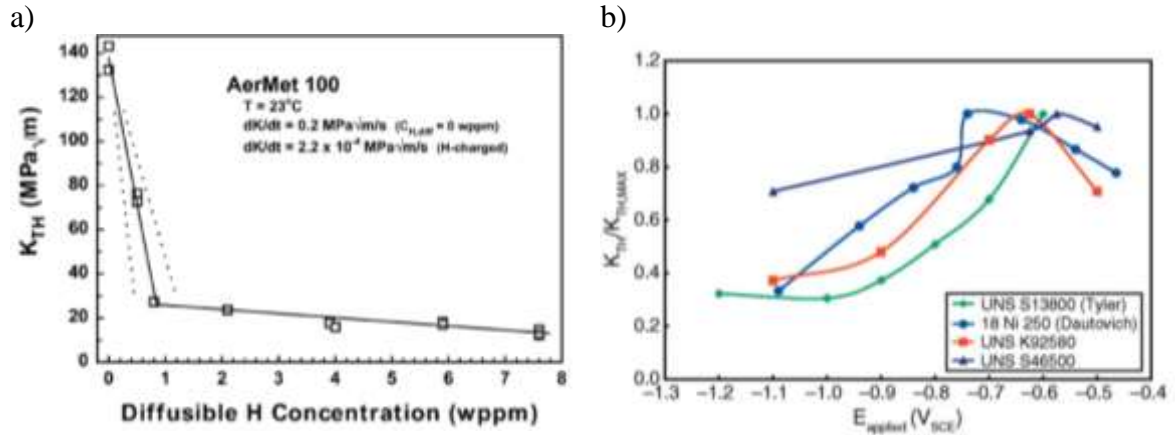


Figure 17. a) Threshold stress intensity for internal hydrogen embrittlement, K_{TH} , with a constant dK/dt of $2.2 \times 10^{-4} \text{ MPa}\sqrt{\text{m/s}}$ and varying diffusible H concentration. [10] b) Normalized K_{TH} vs E_{applied} for four high-strength steels (PH 13-8, 18 Ni 250, UNS K92580, and UNS S46500) where Kehler et al. employed the relationship of $x^2 = 2.82G$. [99, 109, 167] Copyright permission obtained from Copyright Clearance Center.

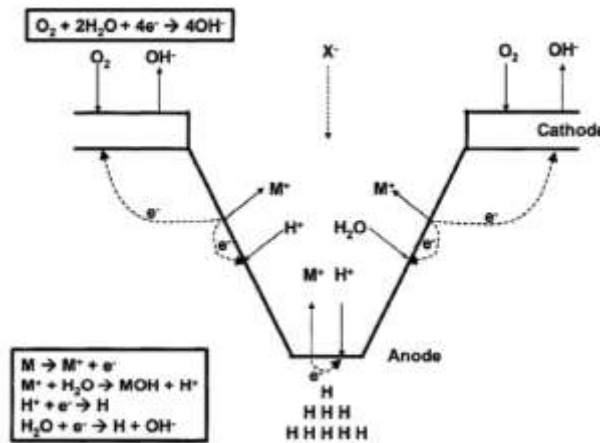


Figure 18. Schematic of electrochemical conditions at a crack tip/ pit due to anodic polarization. [100]

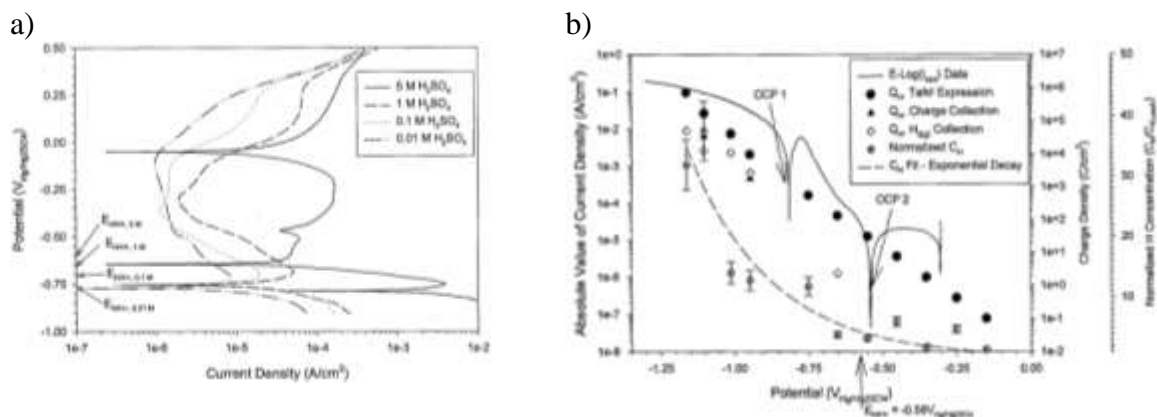


Figure 19. a) Anodic polarization scans of PH 13-8 Mo in deaerated solutions of H_2SO_4 with 0.1 M Fe^{+2} , 0.018 M Cr^{+3} , and 0.01 M Ni^{+2} . b) Polarization data for solutions of dissolved salts and deaerated 5 M H_2SO_4 with C_H vs potential for bulk charged, planar PH 13-8 Mo.[115]

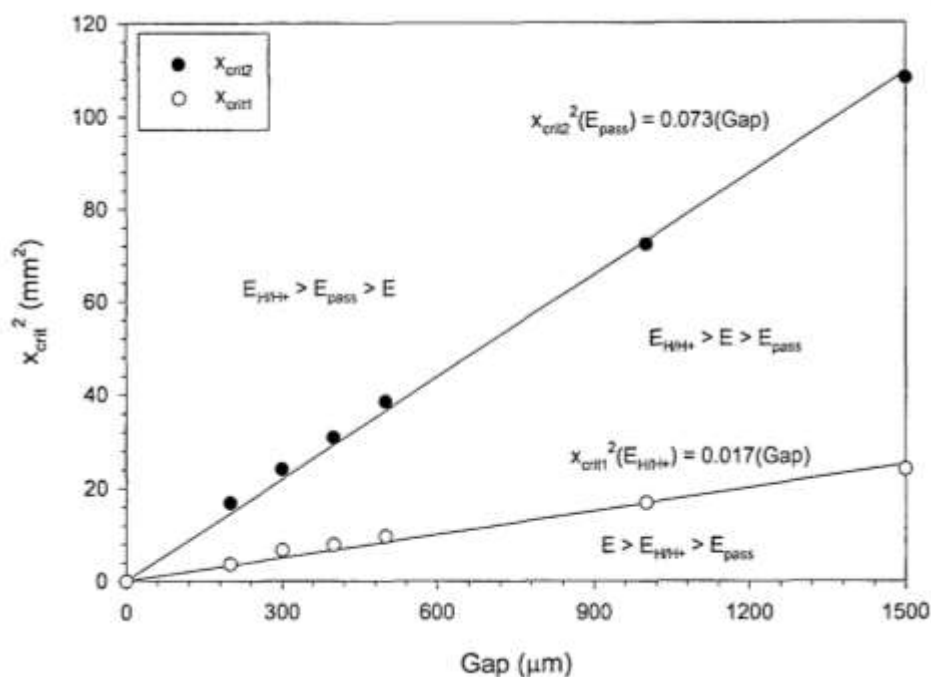


Figure 20. X_{crit}^2 vs gap data. Three regions are displayed, $E_{H/H^+} > E_{pass} > E$ where no passivation occurs but H is produced, $E_{H/H^+} > E > E_{pass}$ where H is produced but it is passive, and $E > E_{H/H^+} > E_{pass}$ where no H is produced.[115]

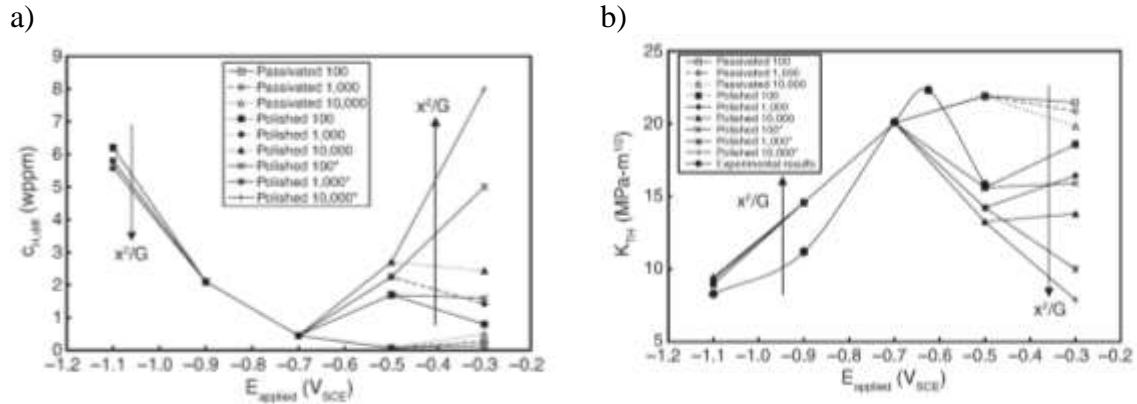


Figure 21. Example of effect of x^2/G for anodic and cathodic polarizations, a) $C_{H,diff}$ vs. $E_{applied}$ for a range of x^2/G values for UNS K92580 charged in 0.6 M NaCl solution, bulk pH calculated using the minimum pH (i.e., average minus one standard deviation) for passivated and polished surfaces. b) Predicted K_{TH} vs applied potential for UNS K92580 using the Gerberich micromechanical model where predicted values were calculated assuming $\alpha = 1.0$ MPa·m^{0.5}/atom fraction H and $k_{IG} = 0.72$ MPa·m^{1/2}. [100]

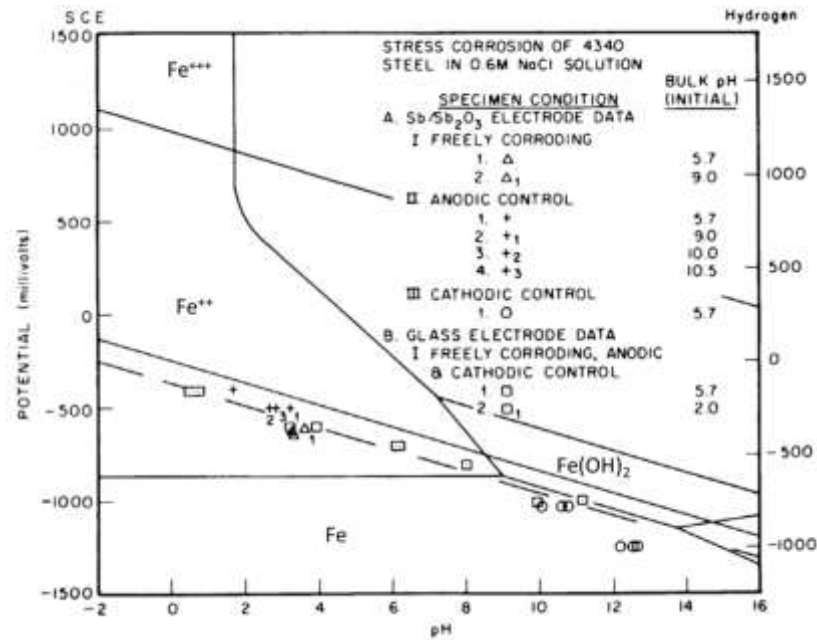


Figure 22. An example Pourbaix diagram for conditions of a propagating crack in 4340 Steel in 0.6 M NaCl solution. [168]

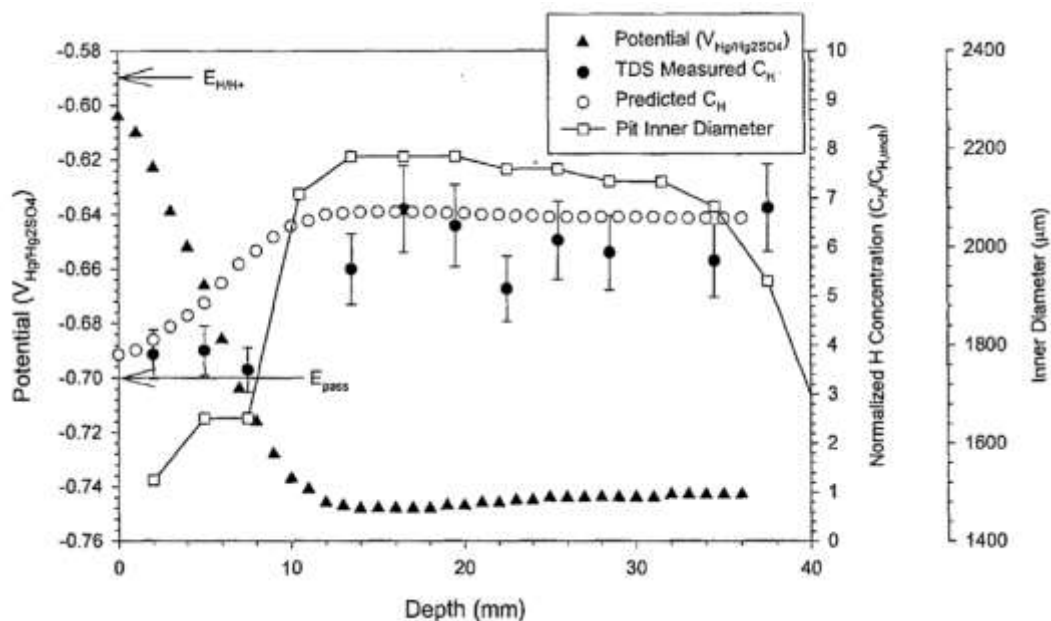


Figure 23. Potential, C_H and pit diameter versus pit depth from a rescaled experimental pit, 1500 μm diameter by 40 mm depth cylinder, which was exposed to 5 M H_2SO_4 + dissolved metal ions. $E_{\text{app}} = -0.60 \text{ V Hg/Hg}_2\text{SO}_4$. [169]

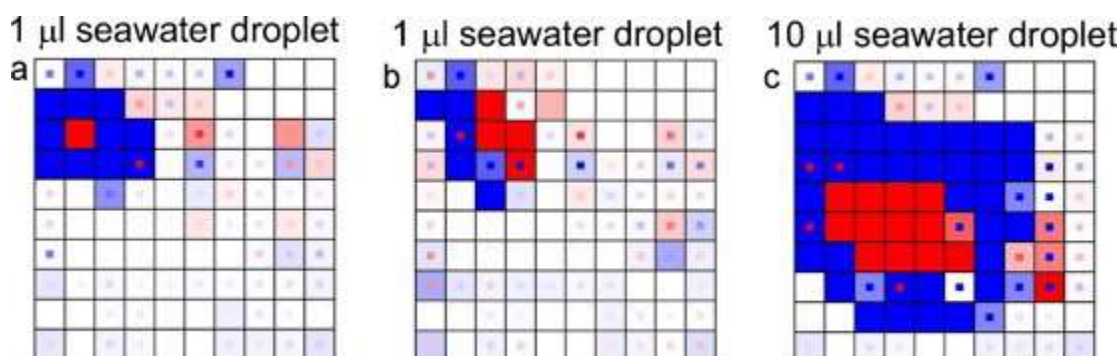
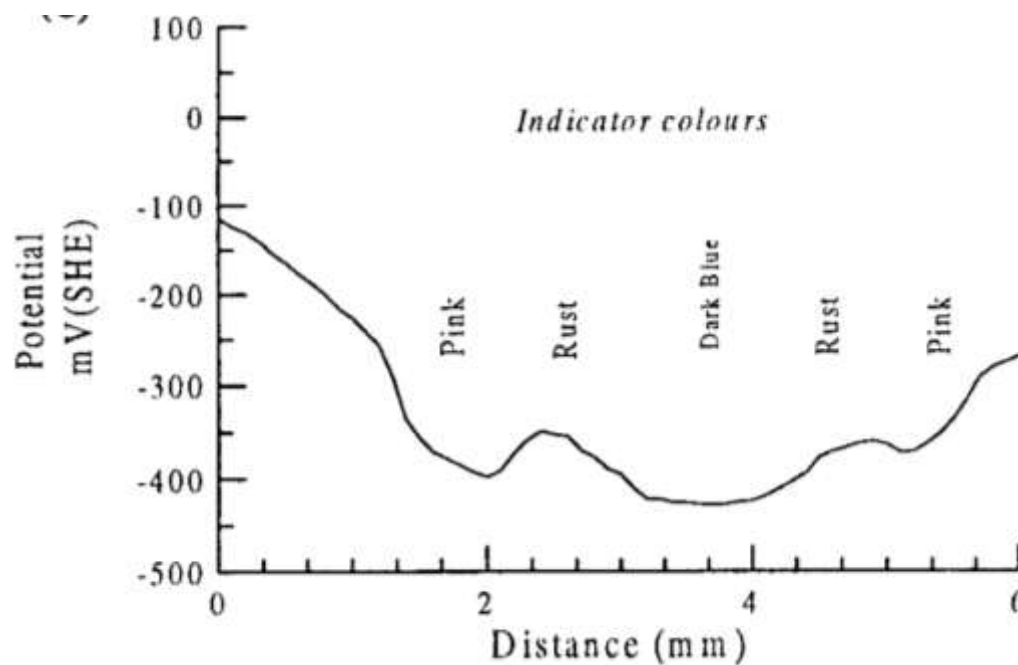
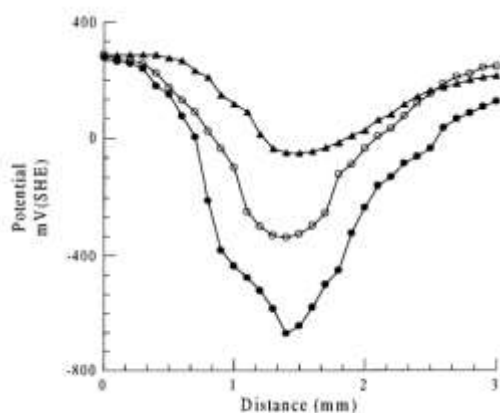


Figure 24. Current densities observed for Zinc wires in-situ during repeat experiments with 1 μL seawater droplet exposures (a and b), and c) a 10 μL seawater droplet. The strong color intensities indicate the areas covered by the droplets. [117] Copyright permission obtained from Copyright Clearance Center.

a)



b)



c)



Figure 25. Potential distribution across a) carbon steel sample with a 0.05 N NaCl droplet with reference to V_{SHE} . Colors indicated by pH indicators potassium ferricyanide and phenolphthalein (pink indicating formation of OH^- and blue indication formation of Fe^{2+}), thus the anode is the central area with a cathodic outer ring. b) SS 316 with a 0.5 M NaCl droplet after 30 min (closed circle), 2 h (open circle), and 18 h (closed triangle). c) Galvanized steel with a 0.5 g/L NaCl droplet.[118]

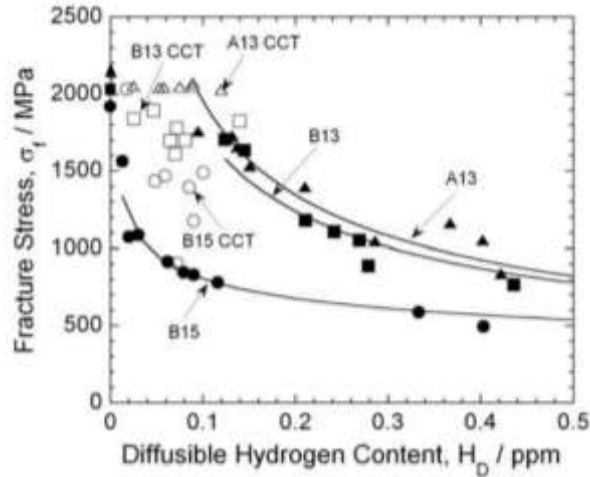


Figure 26. Fracture stress vs. hydrogen content for hydrogen pre-charged steels (solid symbols) and steels corroded by cyclic atmospheric corrosion tests (open symbols). Diffusible H concentration was determined through TDS. [121] Copyright permission obtained from Copyright Clearance Center.

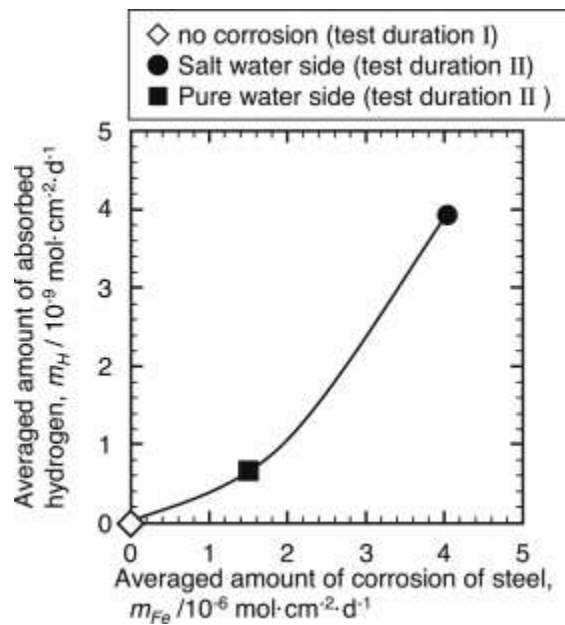


Figure 27. Comparison of the average H absorbed to the average mass loss per day for a 7 day driving atmospheric exposure test of steel (Fe-0.02C-0.01Si-0.15Mn-0.01P- \leq 0.01S wt%). [123] Copyright permission obtained from Copyright Clearance Center.

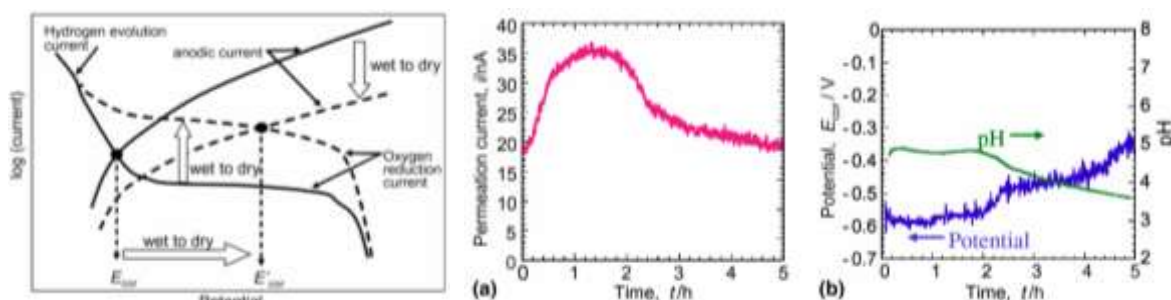


Figure 28. Schematic of the polarization diagram for a rusted and wetted surface of steel that changes to a dry surface developed by Tsuru et.al and actual measurements during drying of a) permeation current and b) pH and potential for 0.5M NaCl solution. [30] Copyright permission obtained from Copyright Clearance Center.

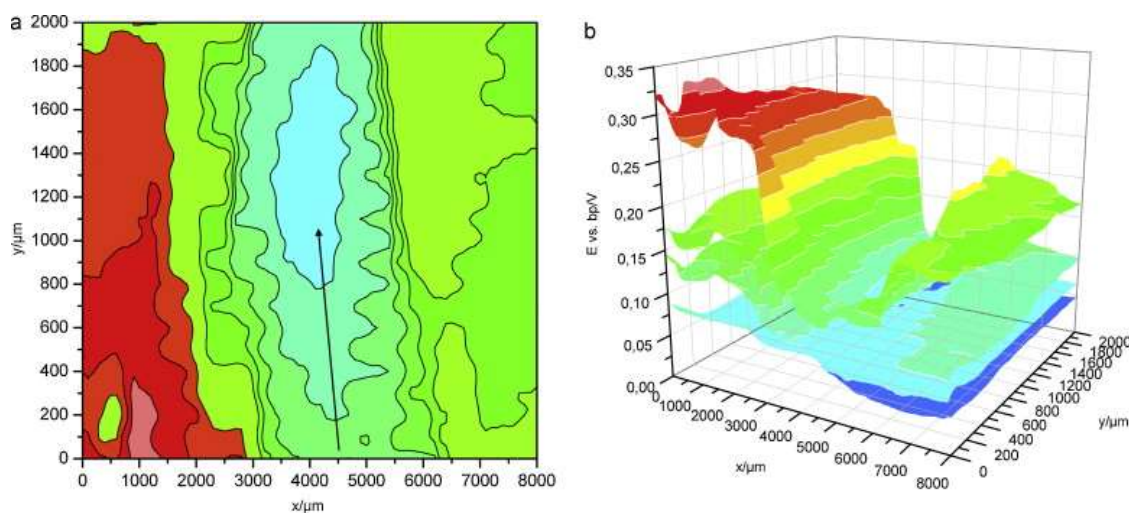


Figure 29. a) SKP potential map of the Pd coated (100 mm) exit side of the galvanized steel sample. The sample was scribed on the entry side and exposed to 0.1 M NaCl aqueous electrolyte. b) Potential maps with time: the top map is 1 h, 3 h, 4 h and 15 h is the bottom map. With time, the hydrogen rich scribe at the back side disappears or becomes uniformly charged.[32] Potentials measured in the SKP are reported referenced vs. the onset of the binary point (bp). Copyright permission obtained from Copyright Clearance Center.

CHAPTER 2. Characterization of Hydrogen Uptake in UHSS in Selected Full Immersion, Atmospheric, and LALT Environments

2.1. Abstract

The effects of standardized laboratory, customized laboratory atmospheric environments, and field exposures on hydrogen uptake in two martensitic ultra-high strength steels, a secondary age hardened alloy Aermet 100 (UNS K92580 Fe-3Cr-11Ni-13Co-1.2Mo; wt%) and an age-hardenable, stainless steel alloy Custom 465 (UNS S46500 Fe-11Ni-12Cr-1Mo-0.005C-0.02Mn; wt%) were compared to a low strength carbon steel, 1018 (UNS G10180 Fe-0.15C-0.7 Mn-0.15Si; wt%). A variety of environmental exposure scenarios were considered including full immersion, ASTM B-117 salt fog and modified salt fog, salt spray deposition, and salt printing followed by high relative humidity exposure. Each was characterized by Cl^- deposition density measurements. Global hydrogen absorption levels were established through thermal desorption spectroscopy (TDS) measurements. These results were compared to mass loss tests to create a connection between the severity of field environments and lab accelerated life test (LALT) environments towards corrosion and to establish a method to determine a “corrosion intensity factor”, in this case based on diffusible and total hydrogen contents instead of general corrosion. This enables direct comparison between atmospheric, field, and full immersion testing in terms of the severity of hydrogen uptake expressed in terms of a diffusible H concentration ($C_{\text{H,Diff}}$), a key parameter in hydrogen embrittlement. Future work should consider further development of this corrosion intensity factor for determination of environmental severity based on hydrogen uptake. However, the lack of uniform charging was an issue in using greater than mm-scale detection techniques, such as the TDS, due to the non-uniform corrosion and subsequent H uptake conditions. Local

scale and sub-mm hydrogen assessment methods are recommended for UHSS with slow diffusion rates.

2.2. Introduction and Background

Presently, many components of military and mass transportation vehicles, landing gear, turbine blades, and fasteners, are constructed of high performance alloys. These UHSS have been designed for both high yield strength and high fracture toughness.[1] For parts composed of ferrous, nickel and/or aluminum-based alloy materials, exposure to atmospheric corrosion, and high stress (often locally greater than their yield strengths) can result in hydrogen production, absorption, and stress field accumulation. Most of these ultra-high strength class of steels were not designed to provide intrinsic corrosion resistance. They rely on metallic coatings for improved corrosion resistance. Federally mandated replacement of environmentally hazardous heavy metals prevalent in these protective coatings has driven interest in designing ultra-high strength alloys with improved intrinsic corrosion resistance in an effort to eliminate these hazardous materials.[2] New alloys, specifically ferrous martensitic stainless steels, may exhibit a modest resistance to Cl^- induced localized corrosion, however can still be highly susceptible to localized attack such as crevice corrosion or pitting. General and/or local corrosion can lead to hydrogen production and uptake which can lead to hydrogen environment assisted cracking (HEAC). Thus, hydrogen embrittlement under atmospheric exposure conditions has become increasingly important to the development of these alloys, especially at UHSS levels. Materials may be screened for hydrogen embrittlement susceptibility through LALT or field exposures of stressed tensile

samples.[3] However, the trapped and diffusible hydrogen concentrations, the underlying cause of HEAC, are not usually determined during these exposures. Therefore, there is currently no way to relate the environmental severity of LALT to field conditions, particularly in the case of hydrogen embrittlement results.

As discussed in the introduction, atmospheric environmental severity factors including temperature, relative humidity, salt deposition, and droplet size influence the corrosion rate of steels. [4] These factors vary widely for different geographical regions, thus corrosion rates differ across the globe. Laboratory atmospheric testing has demonstrated the influence on corrosion rates by factors such as relative humidity, introduction of components, and chloride content.[5] Vernon et al. presented a study of steel with the influence of RH on the corrosion rate. Also, various pollutants, such as SO₂ and CO₂, with trace amounts in supersaturated environments have an effect on corrosion rates. [5] Environments containing SO₂ increased the appearance of rust on the steels in atmospheres above RH of 50% whereas environments containing CO₂ had the opposite effect; CO₂ actually suppressed corrosion of the steels. This is believed to be due to a modification of the gel structure of the primary hydroxide. [5] While these, and other studies,[6-9] provide a general indication of the corrosion of steel under various atmospheric environments, very few provide an indication of the amount of H production and uptake [10-12] and still fewer provide insight into the mechanisms and environmental factors that affect H production and uptake in these UHSS.

Atmospheric corrosion, in both field and laboratory settings, has been fairly well quantified for general corrosion of steels.[7-9, 13] As discussed in Chapter 1, there exists substantial research in the correlation of atmospheric environments to LALT environments. Modification of standard engineering tests, for example the ASTM B-117, with UV, Ozone, and varying electrolyte has helped to produce environments that better mimic conditions of real world exposures with acceleration factors of up to 20 to 120x.[14]

To determine these acceleration factors, oftentimes a corrosion metric, such as mass loss, can be used as a correlation between lab and field experiments. Standards have been developed for low alloy steels using mass loss as a corrosion predictor.[15] ASTM G-101, provides two methods of prediction for corrosion rates of a specific steel, the first, based on short term exposures in a specific site and extrapolation to a long term rate, and the second, an equation, based on the alloying elements of a specific steel, to be used as a predictor for general corrosion rate.[15] For each prediction, different analyses are applied, the first is based on data collected by Larabee and Coburn, where an equation has been developed to determine a “corrosion resistance index”. The second prediction involves data collected by Townsend et al. for three different exposure sites.[15] From this data, and the chemical composition of a low alloy steel, constants can be determined for a particular alloy that can then be applied to predict corrosion rate, mass loss, and time to a given mass loss as well as establish a predictive index. These constants, A and B, are computed as follows:

$$A = a_o + \sum a_i x_i \quad \text{Equation 20}$$

and

$$B = b_o + \sum b_i x_i \quad \text{Equation 21}$$

$$\log C = \log A + B \log t \quad \text{Equation 22}$$

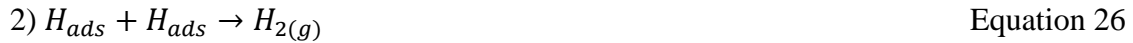
Where, A and B are constants in the corrosion exponential loss function (Equation 22), a_o and b_o are constants for the three industrial locations used for exposures by Townsend, a_i and b_i are constants for each alloying element given for each of the three industrial locations, and x_i is the individual component amount per alloy. The constants, A and B, determined for each alloy, based on composition and the data collected by Townsend, can then be used in various forms of Equation 22 to determine corrosion rates, times, and depths, where C is the corrosion mass loss or penetration and t, the time. While both methods provide predictions for corrosion rates of low alloy steels in atmospheric environments, they do not account for different environmental influences nor provide any indication of H uptake in these environments. Also, they cannot be applied to the materials of interest here as the alloying contents are outside the maximum compositions accounted for in these predictions.

For materials such as UNS S46500, that exhibit pitting rather than general corrosion, a predictive factor in terms of corrosion severity will likely not be based on mass loss. Instead, the PREN (pitting resistance equivalency number) may give a better indication of the materials resistance to acid pitting corrosion which would be a source of H.

$$\text{PREN} = 1 \times \text{wt\%Cr} + 3.3 \times \text{wt\%Mo} + 16 \times \text{wt\%Ni} \quad \text{Equation 23}$$

However, this number, again does not account for environmental conditions, nor give an indication of H uptake.

Alloy composition is greatly significant to atmospheric corrosion rate. However, environmental factors also play a large role. The effects of these varying environments and material interaction influence the following reactions that promote hydrogen embrittlement.



The main factors that influence hydrogen uptake are; an increase in percent corrosion, local acidification increasing the amount of the hydrogen evolution reaction (HER) in addition to the oxygen reduction reaction (ORR), the HER production rate, the adsorbed and absorbed hydrogen, and any role of a specific chemical species to promote recombination poison which affects the competition between Equations 25 or 26 and 27.[16]

Corrosion damage morphology of the material from atmospheric exposure can lead to both stress concentrations and the $C_{H,Diff}$ that are key factors in determining the effect of hydrogen uptake on fracture toughness. Investigations of $C_{H,Diff}$ have established the role of diffusible hydrogen and that it has a strong inverse effect on the threshold stress intensity and the notched tensile strength of these steels. [16-18]

Thus far, minimal studies have been performed to investigate atmospheric hydrogen uptake in high performance alloys.[10, 11] As seen, there exists a large amount of data collected on the corrosion damage of these types of materials in various atmospheric experiments. [19] Yet, there is only a nominal amount of hydrogen data for selected environments shown in Table 11 and a great lack of atmospheric hydrogen uptake data. Moreover, a trap rich UHSS, such as the materials of interest to this dissertation, will acquire a much greater hydrogen concentration in the presence of a given level of atomic hydrogen produced from H_2O and H^+ reduction.[17] It is necessary to study the effects of atmospheric environments to create a connection between the environmental severity of field exposures for these alloys and LALTs that could simulate field environments from the hydrogen embrittlement susceptibility view point.

The aim of this Chapter is to explore the establishment of a severity metric for a range of standard and customized laboratory atmospheric exposures as compared to selected field exposures with respect to hydrogen uptake. It is also of broad interest to identify atmospheric environment corrosion modes in accelerated laboratory testing that produce damage similar to that experienced in the field, as compared to the traditional full

immersion testing. Moreover, the same thinking must be extended to ascertaining diffusible hydrogen levels in field vs. lab. One testable hypothesis is that diffusible H content scales with corrosion rate. This premise has been applied previously, however only to a very limited sample set.[20] Through this, there is hope to establish a way to cross-reference between atmospheric (or field exposure), full immersion, and conventional LALT exposure environments. This cross referencing will allow for a standard between the two methodologies and enable a system for quality and life testing of these materials that will be based more closely to real failure rates.

2.3. Experimental Procedures

2.3.1. Materials

The material compositions for the secondary-hardened martensitic steels and carbon steel are given in Table 12 and material properties in Table 13. Samples of UNS K92580 were tested in the peak-aged condition, UNS S46500, was tested in both the solution annealed and cold treated (as annealed/CT) and the H900 temper (tempered at 482°C for 4 hours and air cooled) and UNS G10180 was tested in the as-received condition.

2.3.2. Full Immersion Corrosion Characterization

For preparation for electrochemical testing, samples were ground to 600 grit SiC paper, rinsed with DI water, dried with compressed air, and degreased in acetone. All tests were performed in an electrochemical flat cell with a 1 cm² opening, a PtNb mesh counter electrode, and a saturated calomel electrode (SCE) as a reference. Electrochemical testing consisted of a 1 h open circuit potential (E_{OCP}) followed by a potentiodynamic

scan. For anodic potentiodynamic polarizations, the scans began at -30 mV vs E_{OCP} and were taken at a scan rate of 0.1667 mV/s to 0.5 V_{SCE} in ambiently aerated 0.05 M, 0.9 M, and 5.3 M NaCl. Cathodic potentiodynamic scans were taken from +30 mV vs E_{OCP} and scanned at a rate of 0.1667 mV/s to -2 V_{SCE} in the same solutions. Chloride concentrations were chosen to give a range in order of magnitude of Cl⁻ in solution and were comparable to concentrations set by constant RH applied later for atmospheric testing. A second set of electrochemical polarizations were conducted under deaerated conditions, where the solution was deaerated for one hour prior to use with N₂. The cell was deaerated for five minutes prior to testing and nitrogen was continuously bubbled through the cell throughout testing to maintain the deaerated conditions. Samples were also tested in deaerated MgCl₂ solutions for comparison with concentrations of 0.4 M, 0.9 M, and 5.4 M MgCl₂.

2.3.3. TDS Characterization of Material-Hydrogen Interactions

Prior to exposure testing it was necessary to establish the effective hydrogen diffusivity ($D_{H,eff}$) for the materials of interest in order to calculate proper exposure length times to generate significant hydrogen concentrations in the materials. TDS analysis (described below and in Figure 30) was applied using two methods to determine $D_{H,eff}$. For the first method, TDS saturation tests, 500 μ m thick samples were cut from UNS S46500 as annealed/CT and the H900 temper. Samples were then ground to 600 grit followed by ultrasonic degreasing in methanol, and were hydrogen charged by cathodic polarization. The UNS S46500 stainless steel samples were charged at room temperature and a hydrogen overpotential ($\eta_{chg} = E_{applied} - E_{R_{H^+/H}}$) of -1.0 V (-1.74 V_{SCE}) for 1 to 122

hours in pH 8.4 in 0.0214 M $\text{Na}_2\text{B}_4\text{O}_7 \cdot 10\text{H}_2\text{O}$ + 0.1144 M H_3BO_3 buffered solution prepared with Millipore water. The counter electrode for electrochemical charging was platinum-coated titanium mesh.

The hydrogen charging for isothermal TDS samples (0.28 mm thick or thinner) was conducted in the same manner, but at a hydrogen overpotential of -0.80 V for 14 days in pH 10, 0.6 M NaCl + NaOH solution with the pH value of the solution adjusted daily.

Hydrogen uptake measurements were determined utilizing TDS. The TDS system (in Figure 30) was configured of an ultra-high vacuum (UHV) detection chamber (maintained at about 10^{-7} Torr) connected to a high vacuum load lock chamber which has the capability to be pumped down to 10^{-4} Torr. A sample was inserted into the load lock, the vacuums equilibrated, but not allowed to exceed 1×10^{-6} Torr, and the sample was lowered into the UHV chamber so as not to disturb the chamber pressure of the detection area. The sample was then heated by a programmable resistive furnace. H_2 gas was released and the partial pressure of H_2 was measured by the mass to charge signals versus time collected by a quadrupole mass spectrometer. The partial pressure was then compared to a time temperature profile that was collected simultaneously while heating the sample (ramp rate test) or compared to time while held at a single temperature (isothermal test).

For ramp rate tests, as shown in previous work, the total hydrogen concentration can be calculated by integrating the hydrogen thermal desorption rate over the temperature range

sampled.[21] This rate can be found from the change in hydrogen partial pressure and given in the following equation if instantaneous pumping rates are well known [22]:

$$\frac{dC_H}{dt} = \frac{MW_{H_2}}{R \cdot M_{sample}} \left(v \frac{dp_{H_2}}{dt} + F_{p,H_2} \right) \frac{1}{T} \quad \text{Equation 28}$$

Where,

$\frac{dC_H}{dt}$ =	H concentration desorption rate (g H/g sample · min)	$\frac{dp_{H_2}}{dt}$ =	H ₂ partial pressure change rate (atm/min)
MW_{H_2} =	H ₂ molecular weight, 2.016 g/mol	F_{p,H_2} =	Instantaneous pumping rate (L·atm/min)
R =	Ideal gas constant (L·atm/mol·K)	T =	Instantaneous Temperature (K)
M_{sample} =	Sample mass (g)		
v =	Analysis chamber volume (L)		

To find the $C_{H,Total}$ (the total H concentration) the integral of the entire hydrogen thermal desorption rate profile is taken. Given uncertainties in pumping rates which are uncertain for hydrogen compared to nitrogen and argon, helium pumping rates were used as an estimation and an alternative method for hydrogen concentration was employed for all samples.[21] A recalibration multiplier found from a calibration curve of integrated $C_{H,Total}$ acquired from TDS with $C_{H,Total}$ from LECO analysis H charged under the same conditions, was used. Uniform homogenous hydrogen concentrations were used for calibration. The calibration established was for a $C_{H,Total}$ of an assumed homogeneously charged sample. For atmospherically exposed samples, no adjustment was made for the % volume of the sample that was charged vs. uncharged. This was taken into account later as discussed in the results.

For TDS saturation tests to determine $D_{H,eff}$, the partial pressure of hydrogen was compared to a time temperature profile that was collected simultaneously while heating the sample at a set ramp rate (3 °C/min). The total hydrogen concentration can be calculated by integration of the hydrogen partial pressure, as described in previous studies.[21-23] The diffusion equation solution under diffusion control in a sheet with thickness, l , and with a constant $D_{H,eff}$ can be found from:

$$\frac{M_t}{M_\infty} = 1 - \frac{8}{\pi^2} \sum_{m=0}^{\infty} \frac{1}{(2m+1)^2} \exp\{-D_{H,eff}(2m+1)^2\pi^2 t/l^2\} \quad \text{Equation 29}$$

Where M_t is the total absorbed H at time t , and M_∞ is the equilibrium absorption level at infinite time at a set overpotential, and l is the sample thickness. As samples were charged for various lengths of time, once the measured hydrogen concentrations show the samples reach saturation, the total to saturated concentrations (M_t/M_∞) can be plotted vs. the time to half saturation. This can be fit to various diffusion coefficients and a best fit for $D_{H,eff}$ can be determined.

For a second method, isothermal TDS, samples were pre-charged all at the same overpotential and same exposure times prior to TDS. They were then measured in the TDS chamber after equilibration to a set temperature and prior to insertion of the sample (150-350 °C). The partial pressure of hydrogen was plotted versus the time of exposure in the TDS; with experiments ending once all hydrogen was egressed. The sample does not equilibrate with the target temperature in the chamber instantaneously. Therefore, the time for the sample to equilibrate with the temperature set for the isothermal test has to be

taken into account. The egress half time can be used to determine $D_{H,eff}$. Egress half times were corrected assuming isothermal heating of thin charged specimens. This correction was applied by using the average heating time for the sample to reach thermal equilibrium with the chamber, found from:

$$\Delta T = \frac{x}{2\sqrt{\kappa t}} \quad \text{Equation 30}$$

Where ΔT is the change in temperature ($T_{set} - T_{25^\circ C}$), x , $\frac{1}{2}$ the sample thickness, t , the time to reach the change in temperature, and κ , the thermal diffusion coefficient, assumed here as 21 W/m·K, a value obtained for UNS S45500.[24] From this, the average time to reach equilibrium can be estimated for each temperature change. With this correction and the TDS spectra, the time to reach half egress can be found and the diffusion coefficient at each temperature can be calculated using the relationship:

$$D_{H,eff} = 0.0492l^2/t_{0.5} \quad \text{Equation 31}$$

Where l is $\frac{1}{2}$ the sample thickness and $t_{0.5}$ is the corrected time taken to achieve half egress or the corrected egress half time. The data collected at elevated temperatures can be extrapolated to determine a room-temperature diffusion coefficient using the Arrhenius relationship for diffusion and assuming it is valid for flat specimens and independent of the C_H profile during testing.[17, 25-27]

$$D_{H,eff}(T) = D_o \exp\left(-\frac{E_m^{app}}{RT}\right) \quad \text{Equation 32}$$

Where D_0 is the pre-exponential diffusion coefficient, and E_M^{app} is the apparent activation energy. For comparison to the as-annealed / CT UNS S46500, samples were heat treated to the H900 temper. Samples were prepared as mentioned previously and hydrogen charged by cathodic polarization prior to TDS. The UNS S46500 stainless steel samples were charged at room temperature and at hydrogen over-potentials of -0.2 and -0.4 V (-1.032 and -1.232 V_{SCE} respectively) for 48 hours. This was performed in pH 10 in 0.6M NaCl + NaOH solution. Hydrogen spectra were collected from TDS ramped at 5 °C/min and compared to spectra of as-annealed / CT samples charged at the same hydrogen over-potentials, as well as unexposed samples. Selected isothermal tests were conducted as described for the as annealed/ CT UNS S46500 samples for comparison.

TDS analysis of $D_{H,eff}$ was only carried out for UNS S46500 samples as, at the time of this study it had already been characterized for UNS K92580 and was reported at 3×10^{-8} cm^2/s . [28] More recent literature applying the permeation method has reported $D_{H,eff}$ values for UNS S46500 to be 1.05×10^{-8} cm^2/s for the as-annealed/ CT and 1.8×10^{-9} cm^2/s for the H900 temper.[29]

2.3.4. Sample Preparation for Environmental Exposure

The purpose of this section was to examine the H level after exposure in typical laboratory and field Cl⁻ type environments. Planar samples of UHSS and carbon steel were cut to 500 μm thicknesses. Two types of samples were prepared, one for pre-testing of salt deposition, and a second for full immersion and atmospheric exposures with and

without salt deposition. For the first set, samples were ground with SiC grinding paper and then polished to 3 μm silica polishing slurry, cleaned by sonication in soap water, degreased with acetone, and dried with compressed air. The second set, for atmospheric exposure, was prepared with grinding up to 600 grit SiC and to a thickness of 350 μm . Samples were then sonicated in soap water, degreased with acetone, and dried with compressed air. The target sample thickness was chosen based on the diffusion of hydrogen to achieve the desired saturation assuming uniform uptake. The diffusion time was estimated using the equation for a slab of infinite width and length with a thickness of $2L$. [30]

$$C_{x,t} = C_s - \frac{4C_s}{\pi} \sum_{n=0}^{\infty} \frac{(-1)^n}{2n+1} \exp\{-D_{h,eff}(2n+1)^2\pi^2 t/4l^2\} \cos \frac{(2n+1)\pi x}{2l} \quad \text{Equation 33}$$

Where, $C_{x,t}$ is the diffusible H concentration after a time t (seconds) and at some position x (cm), C_s is the concentration of diffusing species at the surface, $C_{x,t}$, and $D_{H,eff}$ is the diffusion coefficient of hydrogen.

Samples of thickness 350 μm in full immersion environments were exposed for 48 hours based on the requirements for 99% the surface hydrogen concentration at a distance of 175 μm assuming diffusion controlled uptake. For atmospherically exposed samples (versus fully immersed samples) the exposure period was increased to 10 days due to the time to initiate corrosion, the lower surface hydrogen concentrations, and possibly slow concentration dependent diffusion. [23] Calculations of H homogeneity were performed post exposure, using assumed uniformity of H concentration profiles for damage

morphology under droplets with one dominant corrosion site per drop, 40 μm diameter pits for UNS S46500 and 500 μm diameter anodic sites produced by Evans cell formation for UNS K92580 and UNS G10180, to estimate the diffusion distances of H concentrations over 10 days from such non-uniform corrosion sites distributed across a sample surface. Diffusion of H was assumed to be steady state, radial diffusion, where the $D_{\text{H,eff}}$ for UNS S46500, UNS K92580, and UNS G10180 were taken to be $6.2 \times 10^{-9} \text{ cm}^2/\text{s}$, $3 \times 10^{-8} \text{ cm}^2/\text{s}$, and $1 \times 10^{-7} \text{ cm}^2/\text{s}$ respectively.[27, 31, 32]

2.3.5. Characterization of Salt Deposition and Calibration of Salt Coverage as a Function of Deposition Mode

For exposure and pre-testing, samples were either left in their pristine state or coated with electrolyte depositions through salt printing, salt spray, or salt droplets. The different deposition methods allowed for a variation in salt density and coverage across the samples. Salt printing gave finite control with particle diameters of less than 10 μm . [33] Salt spray provided a wider range of particle sizes with an average diameter of 40 μm . Micropipetting of salt droplets provided a range of droplet sizes depending on the volume chosen for deposition, from 685 μm in diameter for a 1 μL droplet to 7000 μm for a 10 μL droplet. Salt fog tests, ASTM B-117 [34] and modified B-117 [35], provided environments more similar to thin film exposures as the samples remained constantly wetted during exposure.

For printing, samples were covered with an even coating pattern of 1M NaCl solution. A Modified COTS ink-jet printer was calibrated using a conductivity meter and calibration

solutions with known conductivities and concentrations.[33] For calibration, parafilm samples of 1cm^2 were affixed to a CD printer tray and printed using ScribusTM layout and publishing software. The CD was printed at 60% ink opacity to lessen the salt water deposition on the sample. The NaCl deposition calibration was made by immersing the parafilm squares in a known volume of pure water and measuring the change in conductivity. A plot was constructed of conductivity versus number of parafilm squares (representing print number). This was then converted to $\mu\text{g}/\text{cm}^2$ using the calibration solutions. With the known deposition rate per print, thin samples of the UHSS were then printed with 1 M NaCl solution for multiple prints to achieve the target deposition density of about $150\text{ }\mu\text{g}/\text{cm}^2$ (actually printed $161\text{ }\mu\text{g}/\text{cm}^2$). At 95% RH, if a uniform water layer rather than individual droplets was assumed to occur, this would result in a film thickness of about $16\text{ }\mu\text{m}$.

For salt spray, a simple misting chamber was used (developed by D. Mizuno). A 1 M NaCl solution was deposited using a spray bottle within an acrylic box of dimensions 40 cm wide by 60 cm long by 40 cm high. The chamber was cleaned between multiple sprays to avoid unwanted condensation dripping onto the samples. This was calibrated using the same conductivity method, except it was calculated versus spray number instead of print number. Again, knowing the deposition rate, UHSS samples were prepared through multiple sprays to achieve similar depositions as salt printing targeted for $150\text{ }\mu\text{g}/\text{cm}^2$ (actually printed $138\text{ }\mu\text{g}/\text{cm}^2$). This would result again in an average film thickness of about $16\text{ }\mu\text{m}$, if again, it was assumed that a uniform water layer formed.

For salt droplet deposition, droplet arrays were prepared using a micropipette. The pipet was attached to an X-Y controller arm and set to step about an array with spacing of 5 mm by 5 mm between droplet centers, while each droplet was manually dispensed. Twelve droplets were pipetted per sample with average area coverage of 1.5%. One microliter droplets of 1 M NaCl solution with average diameters of 685.6 μm were deposited and the average initial salt coverage was calculated. However, these droplets will grow or shrink to achieve the equilibrium salt concentration depending on the set RH. Samples of parafilm, 4 cm^2 , were coated with the same array and the average deposition was determined using the same conductivity measurement method. Once the NaCl deposition average was found, UHSS samples were prepared with this array (Figure 31) and average coverage of 220 $\mu\text{g}/\text{cm}^2$. This deposition density, if averaged out as a thin water layer, would result in a film thickness of 24 μm at 95% RH.

Salt deposition was also measured for the ASTM B-117 salt fog exposure. Parafilm samples, 4 cm^2 , were exposed in the salt fog chamber for one hour to build up a thin film of salt solution on their surface, removed, and allowed to dry. Samples were then measured using the same conductivity method as described previously. The deposition density was determined to be 178.5 $\mu\text{g}/\text{cm}^2$ of 5% NaCl solution, and would result in a film thickness of about 20 μm at 95% RH.

For outdoor atmospheric exposures, salt deposition was determined through chlorinity measurements shown in Table 14.

Pre-Exposure SEM Imaging. Prior to full immersion and atmospheric exposures, the salt deposition was characterized in a JEOL 6700F or a FEI Quanta 650 scanning electron microscope (SEM) to determine roughly the regularity or irregularity of coverage. Samples were prepared as described previously and coated using the various forms of salt deposition. One sample was also exposed to the ASTM B-117 standard [34] in the salt fog chamber for one hour, then removed. This was to determine the distribution of salt in the thin film produced in the fog chamber. All samples were allowed to dry for fifteen minutes then inserted into the microscope for imaging. The prompt imaging was necessary so that the salt deposition, rather than the corrosion product, was imaged.

Near saturation level droplets of NaCl and MgCl₂ were deposited on Si wafers along with ASW. These were allowed to dry for 15 min and energy dispersive spectroscopy (EDS) and SEM imaging was performed on the dried salts to gain a better understanding of the morphology. In general, EDS was conducted at a working distance of 10 mm and an accelerating voltage of at least 3 times the maximum characteristic peak of interest was used, typically 15 keV.

One sample each of NaCl and ASW droplets were imaged while acquiring a video in environmental-SEM mode. This allowed for rewetting and drying of the droplets with application of the Peltier stage and variable vapor pressure to study the effect of RH on the formation of the droplets. As the Peltier stage was cooled, the vapor pressure local to the sample increased, thus causing the deliquescence of salt droplets on the Si, and the

reverse process occurred upon heating, although some hysteresis was seen as the efflorescence RH is much lower than the deliquescence point.[36, 37]

2.3.6. Exposures of Steel as a Function of Salt Deposition Method

Samples were hydrogen pre-exposed in both full immersion environments and atmospheric environments. For full immersion, samples were exposed in electrochemical cells where pristine samples were hydrogen pre-charged for 48 hours. A saturated calomel electrode (SCE +0.241 vs V_{SHE}) was used as the reference electrode with a platinum mesh counter electrode. Samples were exposed to ambiently aerated 0.6 M NaCl solution and 0.15 M NaCl solution. Samples were exposed at open circuit potential or at hydrogen overpotentials of 0 V, -0.5 V, and -1 V vs. SCE for 48 hours (found from Equations 34 and 35).

$$\eta_H = E_{app} - E_r \quad \text{Equation 34}$$

$$E_r = -0.241 \text{ V (SCE)} - 0.0591 \text{ V} \times pH \quad \text{Equation 35}$$

Atmospheric exposures were carried out in different exposure chambers; a Q-fog salt spray chamber and a relative humidity chamber. The salt spray chamber is designed to conduct the ASTM B-117 Standard test [34] and could be modified to run with UV, ozone, CO₂, and various solutions. The salt solution prepared for standard ASTM B-117 was 5 parts NaCl to 95 parts water by weight percent, samples were positioned to be supported at an angle between 15° and 30°, and the pH of the collected salt solution was between 6.5 and 7.2. The temperature of the chamber was kept at 35°C and the fog was

run so that for every 80 cm² of horizontal testing area, 1 to 2mL of salt solution was collected per hour. Bare samples were placed in the chamber post-cleaning and were exposed for 10 days. Variations of salt fog exposures tested were standard ASTM B-117 (5% NaCl pH 6.9 ± 0.4) combined with 15 ppm O₃, UV, 425 ppm CO₂ or ASTM artificial seawater (pH 8.2 ± 0.3) and acidified ASTM artificial seawater (acidified with glacial acetic acid to the ASTM G-85 Annex 1 Standard [35]).

A few various chambers were used for simple relative humidity (RH) testing. One chamber could be set to RH from 0 to 95% RH and a specific temperature, a second type could be set to constant RH with saturated salts and held at lab room temperature. However, instead of exposure at an incline, samples were set horizontally in these chambers. Both bare and salt deposited samples were exposed at various RH and 25°C for ten days. At a specific RH, the concentration of NaCl in the droplets formed from salt deposition is set by the equilibrium concentration.

Salt depositions for exposures in RH chambers included those described previously, salt printing, salt spray, and salt droplets. Samples were exposed with various coverages and deposition densities to represent a wide range of atmospheric exposures.

2.3.7. Post Exposure Characterization

Thermal Desorption Spectroscopy: Prior to testing in the TDS and post exposure, samples were stored in liquid nitrogen for a maximum of five days to limit the loss of hydrogen. Samples were removed from the liquid nitrogen, cleaned by sonication in

acetone for two minutes and dried with compressed air. Any remaining corrosion products from exposures were mechanically removed before cleaning and testing in the TDS. Samples were then inserted in a quartz crucible within the load lock chamber of the TDS and remained there for fifteen to twenty minutes at room temperature while the vacuum achieved a desired level and opened slowly to reach equilibrium with the detection chamber. Total time for the post exposure samples at room temperature prior to hydrogen detection was less than 30 minutes. Samples were inserted into the chamber and heated at a ramp rate of 5 °C/min from 25°C to 550°C while the hydrogen profiles were simultaneously measured. Total hydrogen concentrations were calculated from ramp rate profiles. The TDS was calibrated using LECO thermal conductivity analysis of total Hydrogen content, 10 wppm via LECO or 22 wppm from TDS at 550°C. TDS analysis was normalized to the grams of each sample and was therefore a global measurement of the entire sample volume inserted into the TDS chamber, on average about 0.1 g.

Optical Imaging by Hirox: Post exposure corrosion products were characterized using a HIROX optical microscope with three dimensional tiling capabilities. Through this, formation of corrosion product on the surface, or pitting into the surface could be detected. Prior to imaging, exposed samples were rinsed with deionized water (to rid the surface of excess salt solution from exposure) and dried with compressed air. Samples were also imaged after mass loss testing to examine the morphology of corrosion attack.

Scanning Electron Microscopy: SEM was used for post-exposure analysis. A working distance of 10 mm with varying accelerating voltages was applied depending on the sample. Prior to imaging, exposed samples were rinsed with deionized water (to rid the surface of excess salt solution from exposure) and dried with compressed air. Determination of corrosion morphology and type of attack could be obtained.

X-ray diffraction: XRD analysis was first conducted on unexposed, pristine surfaces of samples for comparison. Post-exposure, samples were scanned in the XRD from 10 to 110 degrees at a scan rate of 2 degrees per minute using an X'pert PANalytical system. Spectra from the samples were normalized to the Fe_2O_3 2 θ peak at 47.046°.

Corrosion Rate by Mass Loss: Mass loss experiments were performed on samples for each type of exposure. Samples were prepared similarly as above, then exposed in each environment for 48 hours for full immersion or 10 days for atmospheric. Samples were weighed prior to exposure. After exposure, samples were cleaned according to the ASTM G-1 cleaning standard for corrosion products. [38] They were then weighed again and total mass loss was calculated, which was converted to mass loss per cm^2 of sample per exposure period.

2.4. Experimental Results

2.4.1. Electrochemical Characterization of the Corrosion Behavior of Materials of Interest

Electrochemical characterization of UNS S46500 in the as annealed/CT and H900 temper, UNS G10180, and UNS K92580 was carried out in aerated and deaerated environments, as well as two different electrolytes with varied chloride contents. These scans give an indication of the general corrosion behavior of these materials. Results for aerated vs. deaerated tests in NaCl are presented in Figure 32 - 35. UNS S46500 in both the as annealed/CT and H900 temper display a passive region in the anodic scans for all conditions tested, whereas UNS G10180 and UNS K92580 did not. For the aerated case in Figure 32 - 34, the E_{OCP} decreases with increasing chloride concentration, while the anodic current density increases by about an order of magnitude from the 0.05 M to 5.3 M NaCl solution. Anodic polarizations of UNS K92580 and UNS G10180 in aerated NaCl displayed a similar trend. In deaerated $MgCl_2$, for UNS S46500 in the as annealed/CT condition and UNS K92580, scans again displayed similar results (Figures 36 and 39). However, polarizations of UNS S46500 H900 and UNS G10180 in deaerated $MgCl_2$ displayed no determinable trend (Figures 37 and 38). For deaerated cathodic potentiodynamic scans, three primary regions are seen; charge transfer controlled H^+ reduction, mass transport controlled H^+ reduction, and charge transfer controlled H_2O reduction. In general, on all materials, as Cl^- increases, the current density for mass transport controlled H^+ reduction decreases, and for charge transfer controlled H_2O reduction it increases. These electrochemical experiments provide some basis for the possible electrochemical cell establishment under atmospheric exposure conditions for

these alloys, that UNS G10180 and UNS K92580 would be dominated by general corrosion, and thus establish the Evans cell, whereas UNS S46500 would be dominated by pitting. Also, some correlation to the aggressiveness of increased Cl^- concentration correlating with increased corrosion rates was observed.

2.4.2. Characterization of the Material-Hydrogen Interaction

The effective diffusion coefficient for hydrogen in as-annealed/CT UNS S46500 was found to be $3.5 \times 10^{-9} \text{ cm}^2/\text{s}$ (Figure 40) from the TDS saturation method. Calculated saturation curves for different $D_{\text{H,eff}}$ values were also plotted in the same graph with the experimental data for comparison.

The second method of isothermal TDS for the determination of $D_{\text{H,eff}}$ in UNS S46500 is shown in Figure 41. [27] The corrected time of H egress for half the total hydrogen concentration to desorb from the sample at a given temperature was determined from isothermal tests from 150 to 350 °C (Figure 41).

The data were fit using linear regression analysis, previously applied by Thomas et. al.[17], and the resulting equation of the line for UNS S46500 in the as annealed/CT condition was (Figure 42):

$$D_{\text{H,eff}} = \left(1.5 \times 10^{-4} \text{ cm}^2/\text{s}\right) \exp([27.4 \text{ kJ/mol}]/RT) \quad \text{Equation 36}$$

With these assumptions, and within a 95% confidence limit [39, 40], the $D_{H,eff}$ was found to be $2.4 \times 10^{-9} \text{ cm}^2/\text{s}$ at 23 °C and an average E_{act} of 27.4 kJ/mol for UNS S46500 in the as-annealed/ CT condition.

For hydrogen charging in 0.6 M NaCl + NaOH solution, the H900 condition resulted in almost two orders of magnitude increase in total hydrogen concentration after charging compared to the as-annealed/CT samples, as shown in Figure 43. This is indicative of the increased formation of hydrogen trap states within the tempered and aged material, for example the reverted austenite at grain boundaries and the precipitation of Ni_3Ti precipitates during aging.[29]

The determination of $D_{H,eff}$ in UNS S46500 H900 through selected isothermal TDS tests was performed. The time of H egress for half the total hydrogen concentration to desorb from the sample was measured for isothermal tests from 150 to 350 °C and plotted in Figure 44.

The Arrhenius relationship for UNS S46500 in the H900 temper is shown in Figure 45 where the data were fit using linear regression analysis, and the resulting equation of the Arrhenius data yielded:

$$D_{H,eff} = \left(1.3 \times 10^{-5} \text{ cm}^2/\text{s}\right) \exp([19.1\text{kJ/mol}]/RT) \quad \text{Equation 37}$$

With these assumptions, and within a 95% confidence limit [39, 40], the $D_{H,eff}$ was found to be $6.2 \times 10^{-9} \text{ cm}^2/\text{s}$ at 23°C and using an average E_{act} of 19.1 kJ/mol for UNS S46500 in the H900 temper.

2.4.3. Salt Deposition and Pre-Exposure Imaging

From the calibration experiments using the conductivity meter and known calibration solutions, salt printing with a 1 M NaCl solution was found to have a deposition density of $32 \text{ }\mu\text{g}/\text{cm}^2$ per printing (shown in Figure 46-a). Salt spraying of 1 M NaCl solution was found to have a deposition density of $19.7 \text{ }\mu\text{g}/\text{cm}^2$ per spray (Figure 46-b). Salt droplets of 1 M NaCl solution (spaced in a $5 \times 5 \text{ mm}$ array of $1 \text{ }\mu\text{L}$ droplets with average area coverage of 1.5%), were found to have an average deposition density of $220 \text{ }\mu\text{g}/\text{cm}^2$ (Figure 46-c). The ASTM B-117 thin film salt solution ($5\% \text{ NaCl}$ solution) produced an average deposition density of $178.5 \text{ }\mu\text{g}/\text{cm}^2$ (Figure 46-d).

The salt deposition densities developed by these methods are reported in Table 15. As a comparison, Table 15 also reports the salt density from outdoor environments assuming a linear deposition rate for 10 days or 30 days where wash off at these two time periods was assumed to limit densities. These calculations are based on the data in Table 11 for reported deposition rates.

An example of the morphology of various electrolytes deposited as droplets are shown in Figure 47. A clear difference is seen between NaCl , MgCl_2 , and ASTM artificial seawater which may have subsequent effects on the corrosion morphology and attack

produced by these salts. For the droplets exposed in environmental-SEM, selected images at times during the wetting/drying process are given in Figure 48. As can be seen, the ASW wets and dries at a lower RH than the NaCl (ASW wets at 80.7 % RH vs 92.5% and dries at 57% RH vs. 58.5%), however, as the Peltier stage involves a change in temperature, these RH values are not the same as those predicted for deliquescence at room temperature. Also, some separation of the various constituents in ASW occurs due to this wet/dry process. This is consistent with the EDS analysis of dried NaCl and ASW droplets in Figure 47.

The morphology of the dried electrolyte for salt coated samples can be seen in Figure 49. These treatments give a range of deposition coverage from small droplets (average 7 μm diameters) produced by salt printing to full coverage of the sample from a thin film produced in the ASTM B-117. These different coverages play a role in not only the corrosion morphology that results from atmospheric exposure but also the hydrogen production and uptake. Hydrogen concentration throughout a sample can be influenced by these localized corrosion spots, producing a more varied near surface concentration rather than the uniform surface concentration in full immersion hydrogen charging.

2.4.4. Corrosion Characterization

Figures 50 to 52 display the corrosion product characterization for a few example selected environments, ASTM B-117 (100 % RH), Birdwood Golf course atmospheric exposure (average 59 % RH), and ASTM artificial seawater spray exposed at 92 % RH (equilibrium single salt concentrations at this RH would be 2.2 M NaCl, 1.2 M MgCl_2 ,

and 1.3 M CaCl_2). For UNS S46500 (Figure 50), no real significant difference was seen in corrosion morphology attack. XRD confirms the retention of the body centered cubic martensitic substrate. UNS S46500 formed pits in all three exposures, thus pitting density may be a more significant factor reflecting the severity of environment than the uniform mass loss.

For UNS K92580 (Figure 51), ASTM B-117 shows the greatest amount of corrosion product, both visibly and through XRD, possibly indicative of increased severity in terms of corrosion with increased salt density. This may be an approximate indicator of increased hydrogen production. However, the increased corrosion could also be a function of increased surface coverage of electrolyte. Further analysis, such as TDS, must be undertaken to establish whether diffusible hydrogen concentration scales with mass loss.

UNS G10180 (Figure 52) displays significant corrosion product for all exposures as this is a plain carbon steel and has little intrinsic corrosion resistance. Additional studies performed with Raman and XRD displayed other oxide formations on UNS G10180 (Table 16). [41]

As non-uniform corrosion conditions were produced in these exposure environments, calculations were made to predict the produced H concentrations in terms of uniformity and overlap. For UNS S46500 a 40 μm pit was assumed as the H uptake site, whereas for UNS K92580 and UNS G10180, a 500 μm anodic site was assumed as the primary H uptake site (Figure 53). The diffusion distances for diffusion to achieve 50% of the

surface H concentration vs the initial concentrations are noted in Figure 54 as it is assumed that an overlap of the 50% concentration fields is necessary to achieve uniform charging. Examples of uniform vs. non-uniform charging for selected exposures are shown in Table 17. Spacing of corrosion sites were estimated dependent on exposure type and are listed in Table 17. As can be seen, for the UNS S46500 samples, uniformity of hydrogen concentrations is rarely produced by the atmospheric exposures tested here, whereas for UNS K92580 and UNS G10180, as they exhibit general corrosion and were modeled with a larger H uptake site (500 μm vs 40 μm), uniform $C_{\text{H,Total}}$ profiles are more likely produced.

2.4.5. Thermal Desorption Spectroscopy Analysis of Pre-exposed Samples

The results for total hydrogen concentration determined from TDS for a wide range of hydrogen pre-exposures, including LALTs, field, and full immersion pre-charging are shown in Figure 55 for all three steels. The most severe atmospheric environments tested were ASTM B-117 modified with 15 ppm ozone, ASTM B-117 modified with UV, and ASTM artificial seawater spray exposed at both low and high RH. In general these environments exhibited higher coverage of electrolyte and therefore more uniform charging could be expected. While these environments can be characterized in terms of total hydrogen concentration produced in each material there still remains a desire to obtain some sort of an indicator to forecast the severity of each exposure in terms of $C_{\text{H,total}}$.

Figure 56 displays a subset of these various exposure environments for a more direct comparison. Samples shown were exposed at Birdwood Golf Course, selected LALT including ASTM B-117 and modified salt fog, as well as full immersion exposures in 0.6 M NaCl, pH 8.3. Initial testing indicates that while the majority of atmospheric exposures (both LALT and Field) had lower H concentrations relative to full immersion exposures (with $\eta_H = -200$ mV), some produced significant H concentrations (equivalent to H concentrations produced in full immersion environments) within the materials, indicating possible severe environments for H uptake, for example the modified salt fog with 15 ppm O₃ has a significant total H concentration. There is no obvious correlation between the environments that show higher hydrogen severity for UNS K92580 and UNS S46500. This may have to do with the different forms of corrosion morphology that they exhibit, pitting vs. general corrosion, and their susceptibility to different corrosion attack. However some form for predicting environmental severity for hydrogen uptake is still desirable.

One key point to discuss is the size of the TDS test area vs. the size of the corrosion site. The active corrosion sites may be influenced by deposition density, corrosion morphology, and with respect to hydrogen uptake, the subsequent diffusion distance for H over the time period of exposure. For UNS K92580 and UNS G10180, the corrosion morphology is typically more similar to an Evans cell (Figure 60-a), whereas for UNS S46500, the corrosion is dominated by isolated pitting (Figure 60-b). Thus the H uptake may be much more localized. For example, for a 10 day exposure period, assuming the $D_{H,eff}$ previously mentioned for each alloy and estimating spherical diffusion away from

an H source of 40 μm radius, the diffusion distance would be 1700 μm for UNS K92580, 1400 μm for UNS S46500, and 3400 μm for UNS G10180 (Table 18). In comparison, the surface area of a TDS sample test size is on average about $2.5 \times 10^7 \mu\text{m}^2$ with a volume of $8.75 \times 10^9 \mu\text{m}^3$. Therefore, in the atmospheric corrosion cases, this measurement becomes an average of hydrogen from exposed and unexposed areas, possibly producing a misleading measurement of hydrogen uptake behavior across environments, especially when normalized by the mass of the entire volume of the coupon.

Selected TDS spectra for pre-exposed samples are shown in Figure 56-a and b, and the integrated total hydrogen concentration from ramp rate analysis corrected via LECO calibration for these exposures is shown in Figure 56-c and d. As mentioned previously, there is a desire to find some form of corrosion indicator or signifier to establish a correlation between H uptake and environmental severity. Corrosion analysis was performed in an attempt to relate material corrosion indicated by mass loss with H uptake. In Figure 57-a, the mass loss measured for a 10 day period, the exposure time of the samples for the selected exposures from Figure 56 are shown, and Figure 57-b again shows the total integrated H concentration for comparison.

In an attempt to correlate the mass loss with hydrogen uptake, the two were plotted versus each other in Figure 58.[20] Increased mass loss is an indicator of a more severe environment in terms of general corrosion. Since a fraction of the cathodic reaction supporting corrosion is HER (Figure 60), one assumption is that greater corrosion is an indication of conditions for greater hydrogen uptake. In UNS S46500, mass loss is not a good indicator of hydrogen absorption. This alloy exhibits high hydrogen uptake due to

local pitting and it has a high hydrogen trap capacity, all in the case of low mass loss. UNS K92580 has generally higher total hydrogen uptake concentration than UNS G10180 for a given mass loss, indicative of a trap rich alloy. However, no apparent correlation is seen between $C_{H,total}$ and mass loss for UNS K92580 or UNS G10180 (Figure 58).

Mass loss proved a viable indicator only when similar corrosion tests were carried out, as in the case of ASTM B-117 and modified salt fog. Similar exposures, as loosely defined here, simply means the exposures consisted of similar electrolyte area coverages, environment pH, and water loadings, i.e., salt spray compared to salt spray. In contrast, salt spray versus micropipetted or printed droplets does not provide a good correlation because of non-uniform charging. Samples plotted in Figure 59-a were pre-exposed in ASTM B-117 and modified salt fog environments, all of which displayed similar electrolyte surface coverages and water loadings as they were all 100 % RH fog environments. $C_{H\ Total}$ increased to a greater extent for a given corrosion mass loss for UNS K92580 versus UNS G10180 in ASTM B-117 and the modified salt fog exposures tested, indicative of a higher trap capacity. (Figure 59(b)) This is roughly indicated by the ratio of the lattice H diffusivity, D_L , to $D_{H,eff}$:

$$\frac{D_L}{D_{H,eff}} \approx \frac{C_{H,Diff}}{C_L} \quad \text{Equation 38}$$

If one were to assume the same lattice hydrogen concentration, C_L , and lattice diffusion coefficient for both ferrous alloys, from Equation 38 it is indicated that as the $D_{H,eff}$

decreases, the $C_{H,Diff}$ increases. To estimate the diffusible hydrogen concentration from the charge due to mass loss (Q_{mass}), the following was assumed: $Q_{mass} = Q_c$ (the cathodic charge), and $10\%Q_c = Q_{HER}$ (the charge due to HER), and the charge due to absorbed hydrogen is estimated to be $Q_{abs} = 10\%Q_{HER}$. From this estimation, the $C_{H,Diff}$ can be calculated by:[42]

$$C_{H,Diff} = K \frac{D_L}{D_{H,eff}} [Q_{HER}]^{1/2} \quad \text{Equation 39}$$

Where, K is the absorption coefficient, assumed to be $1 \times 10^{-7} \text{ mol/cm}^3$, $D_L = 6 \times 10^{-5} \text{ cm}^2/\text{s}$, and $D_{H,eff}$ was taken as a range between 10^{-5} and $10^{-9} \text{ cm}^2/\text{s}$. [42] From these calculations, the increased trap capacity of the UNS K92580 leads to the higher $C_{H,Diff}$ (Figure 59-c and Table 19). This will be further expanded upon in the discussion.

2.5. Discussion

In the atmospheres studied in this dissertation, corrosion was primarily due to Fe oxidation with ORR as a main cathodic reaction. In contrast, under net cathodic polarization there is limited corrosion product formation to block hydrogen uptake and the cathodic reaction is mostly uniform reduction of water to produce hydrogen across the entire surface. Therefore, in atmospheric corrosion the first issue is the amount of atomic hydrogen produced and the relative hydrogen fugacity.

2.5.1. Hydrogen Production and Uptake During Atmospheric Corrosion

In the exposures examined here, hydrogen uptake was the most extensive during cathodic polarization in full immersion. Hydrogen uptake was least extensive at E_{OCP} in full immersion (Figure 55). E_{OCP} exposure in near neutral NaCl solution likely produced corrosion of steel mainly by oxygen reduction, whereas hydrogen production is limited. Hydrogen production is further limited in atmospheric scenarios that do not produce acidic droplet chemistries or contain hydrogen absorption promoters (e.g. SO_2 , NO_x).[43]

In terms of hydrogen uptake and production in atmospheric environments, the sample exposed with $161 \mu\text{g}/\text{cm}^2$ of salt printing for a 10 day exposure exhibited a higher total hydrogen concentration, comparable to the ASTM modified B-117 exposures (Figure 55). The reason for this is uncertain, but may be related to the corrosion rates (Figure 57-a). The average calculated corrosion current density, i_{corr} , for the salt printed sample was $656.30 \mu\text{A}/\text{cm}^2$, much higher than the other LALT samples tested. If the current due to hydrogen evolution is estimated at only 10% of this total current density, the production of hydrogen on this sample is still three times higher than the LALT exposures, and therefore may be the reason for greater hydrogen uptake in this sample. The rationale for this is that hydrogen uptake in UNS K92580 is assumed to follow Equation 39, which can also be written as:

$$C_{H,Diff} = \frac{D_L}{D_{H,eff}} K \left(\frac{i_H}{k_2} \right)^{1/2} \quad \text{Equation 40}$$

Where K is the ratio of the H absorption to desorption rate constant, i_H is the charge transfer controlled current, both of which change with pH, and k_2 is the hydrogen

recombination rate.[16] Therefore precise knowledge of i_H , the exposed sample area, and the rate of H absorption are necessary to fully understand what is occurring. Small drops may be beneficial to oxygen transport which increases the corrosion rate but small size droplets limit highly acidic local region development. Most of the cathodic reaction may have been due to ORR.

In terms of hydrogen uptake, it is clear that uptake can occur in atmospheric exposure but that amounts may be limited if corrosion occurs in near neutral pH solutions. Further work must explore the role of surface pH, hydrogen production and corrosion products in limiting atmospheric uptake. It should also be noted that local corrosion cells such as highly acidic pits may produce local sites for concentrated uptake. [44] In droplet cells dominated by Evans cell formation, anode/cathode separation also plays a large role in the corrosion severity of the environment. Plausible harsh atmospheric environments for hydrogen uptake must also be considered and it stands to reason that those that promote H uptake may not be the same as those for the most severe corrosion.

2.5.2. Hydrogen Production in an Isolated Droplet

Somewhat similar to the situation occurring in an occluded corrosion cell is that of a droplet. In a droplet, an oxygen concentration cell can develop as presented by U.R. Evans (Figure 60(a)).[45] The pH and potential in this region can be shifted towards regions in which HER is a significant or even the dominant cathodic reaction, thus producing a higher surface H concentration for hydrogen uptake at the anode site in an Evans drop. The length scale of the anode/cathode separation can effect pH and potential

development within the droplet. However, also affecting the determination of these droplet cells is the interaction with the material itself. For example, in the case of a high Cr passive alloy like UNS S46500, pitting can occur even within a droplet on stainless steel, thus establishing even more severe localized anodic sites due to local breakdown and local Cr hydrolysis (Figure 60(b)). This produces a lower local pH. Electrochemical cells on steels can develop with Evans formation, as cells dominated by pitting, or as a mixture, all of which result in different pH and overpotentials as a function of position, material, and environmental severity producing variations in the i_H and the hydrogen concentration readily available at the materials' surface.

Figure 61 shows an estimation of H overpotential, pH, and potential within an Evans cell; a) shows an example of the pH map and b) examples of the hydrogen uptake vs. the pH and η_H . In c) the potential distribution is mapped across an Evans drop through SKP measurements by Mansfeld et al.[46] Given pH, E_{app} , and E_{H/H^+} , the hydrogen overpotential can be determined (Equations 34 and 35). Also, the cathodic current density due to hydrogen evolution ($i_{c, (HER)}$) can be estimated by the following:

$$i_{c, (HER)} = k_1 [H^+]^n \exp\left(\frac{2.303 \eta}{RT}\right) \quad \text{Equation 41}$$

Where k_1 is the hydrogen discharge rate constant, $[H^+]$ is the H^+ concentration in mol/cm³, n is the reaction order with respect to H^+ , η is the hydrogen overpotential, and R is the ideal gas constant. The reaction rate constant was assumed to be $10^{-8.28}$ based on data collected by Kehler for UNS K92580. [47]

The hydrogen overpotential superimposed on the droplet shown in Figure 61-c indicates that higher hydrogen uptake would be possible at the center of the droplet in the region where the pH drops to 3. This is consistent with the idea that the anodic sites become areas with lowered pH in the Evans drop and prone to local hydrogen production and uptake. This same methodology was applied to exposed UNS K92580 and UNS S46500 with 5.3 M NaCl 1 μ L droplets. For the UNS K92580 sample exposed for 900 min and 78% RH, the pH was predicted in Figure 62-a by applying the Evans cell formation seen in Figure 53-c. Calculations of η_H , i_H , and $C_{H,Diff}$ in Figure 62-b-c, display how the Evans cell formation in a droplet effects the subsequent H uptake, in that the predicted H concentration is high at the acidified center of a droplet and lower at the more alkaline cathodic edges. Figure 63 applies these same calculations to UNS S46500 with a 120 min exposure at 78% RH, except in this case, the pH was considered to be locally lower where a pit possibly formed as in Figure 53-a. However, as it is impossible to predict where a pit will occur prior to scanning, obtaining a SKP line scan affected by the pitting potential proves difficult. The SKP line scan in Figure 63-a displays a higher potential (indicative possibly of passivation) with a small dip that may indicate a possible pit or pit initiation. The local pH change was estimated to overlap with this region as a pit could be a local spot for acidification (Figure 63-a). With the calculations of η_H , i_H , and $C_{H,Diff}$ in Figure 63-b-d, it can be seen that the H concentration is locally enhanced at the site of the supposed pit. However, these values for $C_{H,Diff}$ are much lower than in the case of UNS K92580 which could be due to the short exposure time, 120 min vs. 900 min. This could also be a result of the possibility that this potential is not truly above a pit site as

positioning is performed manually through visual inspection. Over a true pit, the potential may be significantly lower, increasing the η_H and the subsequent $C_{H,Diff}$ concentration would be much higher.

One important variable to note that is not accounted for in these calculations and plots is time. The SKP potential and pH measurements are single time measurements of the specific values, yet these greatly vary with time (Figure 64). Methods such as this only give an indication of the possible H production under the instantaneous conditions produced, but do not provide information of local H uptake produced over an exposure period. However, they provide a prediction of significant H uptake areas or hotspots. While these sites can be predicted as areas with conditions conducive to high H uptake, it is necessary to develop methods for local, spatial detection of hydrogen concentrations.

2.5.3. Basis for Hydrogen Uptake in Atmospheric Exposures: Effects of Environmental Parameters

The amount of hydrogen produced is based on water and proton reduction which will be a function of pH, overpotential, and other factors. Also, there is the issue of whether the surface condition enables or inhibits H absorption. It has been speculated that the pH formed under the $Fe(OH)_2$ layer controls hydrogen production. [7] At issue is the amount of hydrogen produced in each scenario. As seen in the Hirox images in Figure 14, corrosion product formed and penetration was most severe on the surface of the UHSS samples where there was deposition of electrolyte (Cl^- coverage). For the ASTM B-117 method, this occurred across the entire sample surface, whereas for the salt drops, spray

and printing, corrosion product formed and depth of attack and concentration was greatest to regions where the salt deposition occurred (Table 15). In the ASTM B-117 test, 5% NaCl is used which produced similar salt deposition density upon drying, but the high time of wetness creates a liquid film that does not dry. However, the corrosion rate is lower than spray or printing with similar electrolyte. Salt spray and salt printing had higher overall mass loss, possibly due to the smaller droplet formations.[48, 49] The droplet would concentrate salt (2.75 M) which lowered O₂ solubility.[50] However, a small drop would enable fast oxygen transport.[16] Moreover, in these smaller droplets, small local anodic and cathodic regions form in close proximity and highly acidic anode sites may have been suppressed by cathode proximity. The small separation of anodes and cathodes could result in low resistance through the drop being low and the oxygen reduction transport distance may be small. [51] Therefore, the higher mass loss could be due to these smaller droplet sizes which favor faster ORR, but do not favor acidic sites.

The highest H uptake environment in Figure 59 is the ASTM B-117 + O₃, which is the case of an oxidizer, where the high Cl⁻, high acidity environment promotes $\text{Fe}^{2+} \rightarrow \text{Fe}^{3+}$. Ozone has been previously shown to increase corrosion rates in modified ASTM B-117.[14] It is known to be an active oxidizer, and under atmospheric conditions, a small amount can dissolve in thin films or droplets.[4] Ozone increases corrosion rates on steel when interacting with nitrogen dioxide in a thin film, a common atmospheric pollutant, and forms nitric acid at the surface.[52] Another study on Al samples exposed to atmospheric conditions with ozone has shown that it can cause a decrease in the solution pH at the surface. For a thin water film exposed for 4 weeks, 10 ppm of ozone caused a

decrease in pH to 4.1, as compared to laboratory air at 5.9.[53] This decrease in pH at the surface likely creates conditions more conducive to H production under ozone exposures, explaining why higher uptake is seen in UNS K92580 with ozone. While hydrogen content was seen to increase with the introduction of ozone, it may not always be a relevant signifier of increased hydrogen content. Some studies have seen that ozone actually reduces corrosion rates, or have seen varying corrosion rates for different concentrations of ozone.[54-56]

However, for UNS S46500, no real significant increase is seen with either. This is correlated by previous work in full immersion with ozonated 0.5 M NaCl solution, where a breakdown in the passive film of 304 SS was not seen with increased ozone concentrations, suggesting there is little effect on corrosion. The authors did note that if there was an occluded site formed, increased localized corrosion would be expected at this site under increased corrosion conditions.[57]

In the case of UV and atmospheric corrosion, some studies have shown evidence for an increase in corrosion rates of mild steel exposed with 15 $\mu\text{g}/\text{cm}^2$ of NaCl in 97% RH with the introduction of UV illumination.[58] They proposed that under such conditions, the photo generated electrons can act as strong oxidizers, increasing the corrosion rates. As the anodic and cathodic reactions are coupled, this could lead to the increased hydrogen production and uptake seen in UNS K92580.

2.5.4. Relationship Between Hydrogen Uptake and Mass Loss

As a means of determining whether a correlation exists between mass loss and hydrogen uptake across these atmospheric exposures, the Q_{mass} (charge due to corrosion) and $Q_{\text{H, abs}}$ (charge due to hydrogen absorbed, assumed to be 1-10% of $Q_{\text{H, HER}}$ the charge due to hydrogen evolution) were both calculated.[16, 23, 59] The Q_{mass} was obtained gravimetrically using Faraday's law:

$$\frac{m}{A} = \frac{Q_{\text{mass}}(E.W.)}{AF} \rightarrow \frac{Q_{\text{mass}}}{A} = \left(\frac{m}{A}\right) \frac{F}{E.W.} \quad \text{Equation 42}$$

Where m , is the change in mass, A , the area of the sample, Q_{mass} , the charge due to mass loss, F , Faraday's constant, and $E.W.$, the calculated equivalent weight. The Q_{mass} is related to the $Q_{\text{H, HER}}$ as it is equivalent to the sum of both the cathodic charge due to HER and ORR, assuming these are the dominant cathodic reactions.[60] Therefore a correlation between mass loss and hydrogen concentration might help identify atmospherically severe environments for H production and uptake. $Q_{\text{H, abs}}$ was obtained from TDS with suitable calibration. The values calculated for both Q_{mass} and $Q_{\text{H, abs}}$ for UNS G10180 and UNS K92580 are given in Table 19. An attempt was made to see if a correlation exists in Figure 65, in which the Q_{mass} vs. $Q_{\text{H, abs}}$ was plotted.

UNS K92580 exhibited a higher charge due to $C_{\text{H, Total}}$ and UNS G10180 a higher charge due to mass loss as expected, but no strong correlation is evident between Q_{mass} and $Q_{\text{H, abs}}$ from these calculations. One main issue may be that both measurements (mass loss and hydrogen uptake) were taken as global measurements, and therefore do not

account for localized corrosion and local hydrogen uptake, which is non-uniform, or differences in electrolyte coverage, or both. Also, as can be seen in both Table 19 and Figure 65, the charge due to hydrogen is on average 4 orders of magnitude lower than the charge due to corrosion. This could be due to a variety of factors. One is that $Q_{H,abs}$ was estimated using $C_{H,total}$. This does not then account for hydrogen produced by HER that is not absorbed by the material.

2.6. Future Work

The difference in corrosion morphologies, especially under atmospheric exposure conditions, and subsequent hydrogen entry will need to be accounted for in the formation of a corrosion metric as a signifier for H uptake. The hydrogen uptake across the surface can be considered in two main forms, even distribution across the surface, or localized corrosion sites, or even a combination of the two. This local vs. even distribution is key to understanding how the material is affected as a whole. However, some influences may not be observed through TDS measurements alone, as TDS is a global measurement, and cannot capture the localized influence of pitting which may have higher $C_{H,diff}$ levels whilst passive surfaces have much lower values. At pits, local H production and uptake may increase [61], but across a sample, global H measurement averages data from local regions and other areas perhaps with no hydrogen charging at all. Therefore, general atmospheric corrosion could produce locally higher measurements of H uptake than observed globally by TDS. Further local scale analysis is necessary to understand these differences.

2.7. Conclusions

- Hydrogen uptake in UHSS is influenced by both full immersion, lab accelerated and field atmospheric environments.
 - It is influenced by salt chemistry, coverage (deposition density), and other environmental factors for a given alloy.
 - Certain lab and field environments indicate H levels of significance in comparison with fully immersed samples
 - $C_{H,Total}$ is greater for a given corrosion mass loss on UNS K92580 versus UNS G10180. The explanation for this is based on trap density.
- Since environment severity can affect both corrosion rate and H uptake independently, hydrogen concentration may be difficult to predict from mass loss across a broad range of environments (with different surface coverage).
- A second issue with mass loss as an environmental severity factor for hydrogen uptake is the correlation for materials that are not prone to general corrosion, for example, UNS S46500.
- To better understand the effect of atmospheric exposures on the global scale there is a need to further explore and develop local scale detection techniques for hydrogen uptake.

2.8. References

1. Alloy Data - Custom 465 All. 1996, C.T. Corporation: Reading, PA.
2. Kinlen, P.J., Y. Ding, and D.C. Silverman, *Corrosion Protection of Mild Steel Using Sulfonic and Phosphonic Acid-Doped Polyanilines*. Corrosion, 2002. **58**(6): p. 490-497.
3. A.S.T.M., *Standard Practice for Making and Using U-Bend Stress-Corrosion Test Specimens*, in *Environmentally Influenced Cracking*. 2009, ASTM: West Conshohocken, PA.
4. Leygraf, C. and T.E. Graedel, *Atmospheric corrosion*. The Electrochemical Society series. 2000, New York: Wiley-Interscience. xii, 354 p.
5. Vernon, W.H.J., *A Laboratory Study of the Atmospheric Corrosion of Metals*. Trans. Faraday Society, 1935.
6. Baker, E.A., ed. S.W. Dean and T.S. Lee, *Long-Term Corrosion Behavior of Materials in the Marine Atmosphere*, in *Degradation of Metals in the Atmosphere*, A.S.f.T.a. Materials, Editor. 1988: Philadelphia. p. pp125-144.
7. Li, S.J., et al., *Evaluation of delayed fracture property of outdoor-exposed high strength AISI 4135 steels*. Corrosion Science, 2010. **52**(10): p. 3198-3204.
8. Townsend, H.E., *Effects of alloying elements on the corrosion of steel in industrial atmospheres*. Corrosion, 2001. **57**(6): p. 497-501.
9. Townsend, H.E., *Atmospheric corrosion performance of quenched-and-tempered, high-strength weathering steel*. Corrosion, 2000. **56**(9): p. 883-886.
10. Akiyama, E., et al., *Hydrogen entry into Fe and high strength steels under simulated atmospheric corrosion*. Electrochimica Acta, 2011. **56**(4): p. 1799-1805.
11. Akiyama, E., et al., *Evaluation of hydrogen entry into high strength steel under atmospheric corrosion*. Corrosion Science, 2010. **52**(9): p. 2758-2765.
12. Akiyama, E., et al., *Studies of Evaluation of Hydrogen Embrittlement Property of High-Strength Steels with Consideration of the Effect of Atmospheric Corrosion*. Metallurgical and Materials Transactions a-Physical Metallurgy and Materials Science, 2013. **44A**(3): p. 1290-1300.
13. Baker, E.A., ed. S.W. Dean and T.S. Lee, *Long-Term Corrosion Behavior of Materials in the Marine Atmosphere*, in *Degradation of Metals in the Atmosphere*, ASTM, Editor. 1988: Philadelphia. p. 125-144.
14. Wan, Y., E.N. Macha, and R.G. Kelly, *Modification of ASTM B117 Salt Spray Corrosion Test and Its Correlation to Field Measurements of Silver Corrosion*. Corrosion, 2012. **68**(3).
15. A.S.T.M., *Standard Guide for Estimating the Atmospheric Corrosion Resistance of Low-Alloy Steels*, in *Atmospheric Corrosion*. 2004, ASTM International: West Conshohocken, PA.
16. Kehler, B.A. and J.R. Scully, *Predicting the effect of applied potential on crack tip hydrogen concentration in low-alloy martensitic steels*. Corrosion, 2008. **64**(5): p. 465-477.
17. Thomas, R.L.S., et al., *Trap-governed hydrogen diffusivity and uptake capacity in ultrahigh-strength AERMET 100 steel*. Metallurgical and Materials Transactions a-Physical Metallurgy and Materials Science, 2002. **33**(7): p. 1991-2004.
18. Wang, M.Q., E. Akiyama, and K. Tsuzaki, *Effect of hydrogen and stress concentration on the notch tensile strength of AISI 4135 steel*. Materials Science and Engineering a-Structural Materials Properties Microstructure and Processing, 2005. **398**(1-2): p. 37-46.
19. Shackelford, J.F., *Introduction to materials science for engineers*. 5th ed. 2000, Upper Saddle River, N.J.: Prentice Hall. xvii, 877 p.
20. Ootsuka, S., et al., *Evaluation of hydrogen absorption into steel in automobile moving environments*. Corrosion Science, 2015. **98**: p. 430-437.

21. Smith, S.W., *Hydrogen Interactions and Their Correlation to the Hydrogen Embrittlement Susceptibility of Al-Li-Cu-Zr Alloys*, in *Materials Science and Engineering*. 1995, University of Virginia: Charlottesville.
22. Scully, J.R., G.A. Young, and S.W. Smith, *Hydrogen solubility, diffusion and trapping in high purity aluminum and selected Al-base alloys*. Aluminium Alloys: Their Physical and Mechanical Properties, Pts 1-3, 2000. **331-3**: p. 1583-1599.
23. al-Ghamdi, S., Scully, J.R., *Electrochemical Mitigation of Hydrogen Environment Embrittlement of Ultra-high Strength AerMet™ 100*. Diss. University of Virginia, 2010.
24. Harvey, P.D., ed. *Engineering Properties of Steel*. 1982, American Society for Metals: Metals Park, OH.
25. Shackelford, J.F., *Introduction to materials science for engineers*. 7th ed. 2009, Upper Saddle River, N.J.: Pearson Prentice Hall. xii, 533, 33, 6, 14 p.
26. Crank, J., *The mathematics of diffusion*. 2d ed. 1975, Oxford, Eng: Clarendon Press. viii, 414 p.
27. Thomas, R.L.S., et al., *Trap-governed hydrogen diffusivity and uptake capacity in ultrahigh-strength AERMET 100 steel*. Metallurgical and Materials Transactions a-Physical Metallurgy and Materials Science, 2002. **33**(7): p. 1991-2004.
28. Lee, E.U., Sandars, H., Sarkar, B. in *Proc. Tri-Service Conf. on Corrosion*. 2000. Army Research Laboratory, Aberdeen, MD.
29. Ifergane, S., Sabatani, E., Carmeli, B., Barkay, Z., Ezersky, V., Beeri, O., and Eliaz, N., *Hydrogen diffusivity measurement and microstructural characterization of Custom 465 stainless steel*. Electrochimica Acta, 2015. **178**: p. 494-503.
30. Crank, J., *The mathematics of diffusion*. 1956, Oxford,: Clarendon Press. 347 p.
31. Schaller, R.F. and J.R. Scully, *Measurement of effective hydrogen diffusivity using the Scanning Kelvin Probe*. Electrochemistry Communications, 2014. **40**: p. 42-44.
32. Luppo, M.I. and J. Ovejero-García, *The influence of microstructure on the trapping and diffusion of hydrogen in a low carbon steel*. Corrosion Science, 1991. **32**(10): p. 1125-1136.
33. Schindelholz, E. and R.G. Kelly, *Application of Inkjet Printing for Depositing Salt Prior to Atmospheric Corrosion Testing*. Electrochemical and Solid State Letters, 2010. **13**(10): p. C29-C31.
34. A.S.T.M., *Standard Practice for Operating Salt Spray Fog Apparatus*, in *Atmospheric Corrosion*, ASTM: West Conshohocken, PA.
35. A.S.T.M., *Standard Practice for Modified Salt Spray Fog Testing*, in *Atmospheric Corrosion*. 2003, ASTM: West Conshohocken, PA.
36. Biskos, G., et al., *Nanosize effect on the deliquescence and the efflorescence of sodium chloride particles*. Aerosol Science and Technology, 2006. **40**(2): p. 97-106.
37. Schindelholz, E. and R.G. Kelly, *Wetting phenomena and time of wetness in atmospheric corrosion: a review*. Corrosion Reviews, 2012. **30**(5-6): p. 135-170.
38. International, A., *ASTM G1-03 - Standard Practice for Preparing, Cleaning, and Evaluating Corrosion Test Specimens*. 2005: West Conshohocken, PA. p. 17-25.
39. International, A., *Standard Guide for Applying Statistics to Analysis of Corrosion Data*. 2004, ASTM International: West Conshohocken, PA.
40. Hayter, A.J., *Probability and statistics for engineers and scientists*. 3rd ed. 2007, Belmont, Calif.: Thomson Brooks/Cole. xviii, 812 p.
41. Tayler, M.L., et al., *Scribe Creep and Underpaint Corrosion on Ultra-High Molecular Weight Epoxy Resin Coated 1018 Steel Part 2: Scribe Creep Model as a Function of Environmental Severity Factors*. Corrosion, 2015. **71**(3): p. 326-342.
42. Kehler, B.A., *Modeling and Experiments to Explain the Potential Dependency of an UHSS to Hydrogen Environment Assisted Cracking*, in *Materials Science and Engineering*. 2008, University of Virginia: Charlottesville. p. 296.

43. Berkowitz, B.J., et al., *Hydrogen Dissociation Poisons and Hydrogen Embrittlement*. Scripta Metallurgica, 1976. **10**(10): p. 871-873.
44. Switzer, M., *Use of crevice scaling laws to investigate local hydrogen uptake in rescaled model pits*, in *Materials Science and Engineering*. 2003, University of Virginia: Charlottesville.
45. Evans, U.R., *The corrosion of metals*. 1924, New York,: Longmans Arnold. xi, 212 p.
46. C. Chen, C.B.B., and F. Mansfeld, *Scanning Kelvin Probe Analysis of the Potential Distribution under Small Drops of Electrolyte*. Materials Science Forum, 1998. **289-292**: p. 181-192.
47. Kehler, B.A., *Modeling and Experiments to Explain the Potential Dependency of an UHSS to Hydrogen Environment Assisted Cracking*, in *Materials Science and Engineering*. 2008, University of Virginia: Charlottesville. p. 296.
48. Li, S.X. and L.H. Hihara, *Atmospheric-Corrosion Electrochemistry of NaCl Droplets on Carbon Steel*. Journal of the Electrochemical Society, 2012. **159**(11): p. C461-C468.
49. Risteen, B.E., E. Schindelholtz, and R.G. Kelly, *Marine Aerosol Drop Size Effects on the Corrosion Behavior of Low Carbon Steel and High Purity Iron*. Journal of the Electrochemical Society, 2014. **161**(14): p. C580-C586.
50. Millero, F.J., F. Huang, and A.L. Laferiere, *Solubility of oxygen in the major sea salts as a function of concentration and temperature*. Marine Chemistry, 2002. **78**(4): p. 217-230.
51. Cole, I.S., et al., *What really controls the atmospheric corrosion of zinc? Effect of marine aerosols on atmospheric corrosion of zinc*. International Materials Reviews, 2009. **54**(3): p. 117-133.
52. Oesch, S., *The effect of SO₂, NO₂, NO and O₃ on the corrosion of unalloyed carbon steel and weathering steel - The results of laboratory exposures*. Corrosion Science, 1996. **38**(8): p. 1357-1368.
53. Oesch, S. and M. Faller, *Environmental effects on materials: The effect of the air pollutants SO₂, NO₂, NO and O₃ on the corrosion of copper, zinc and aluminium. A short literature survey and results of laboratory exposures*. Corrosion Science, 1997. **39**(9): p. 1505-1530.
54. Liao, J.S., et al., *Effect of ozone on corrosion behavior of mild steel in seawater*. Corrosion Science, 2012. **55**: p. 205-212.
55. Yang, B., D.A. Johnson, and S.H. Shim, *Effect of Ozone on Corrosion of Metals Used in Cooling-Towers*. Corrosion, 1993. **49**(6): p. 499-513.
56. Khullar, P. and R.G. Kelly. *Accelerated Atmospheric Corrosion Testing of Steel*. in *Electrochemistry Society*. October, 2013. San Francisco, CA.
57. Lu, H.H. and D.J. Duquette, *The Effect of Dissolved Ozone on the Corrosion Behavior of Cu-30Ni and Type-304L Stainless-Steel in 0.5 N NaCl Solutions*. Corrosion, 1990. **46**(10): p. 843-852.
58. Song, L.Y. and Z.Y. Chen, *The role of UV illumination on the NaCl-induced atmospheric corrosion of Q235 carbon steel*. Corrosion Science, 2014. **86**: p. 318-325.
59. Scully, J.R. and P.J. Moran, *Influence of Strain on the Environmental Hydrogen-Assisted Cracking of a High-Strength Steel in Sodium-Chloride Solution - Reply*. Corrosion, 1989. **45**(4): p. 318-319.
60. Stratmann, M. and H. Streckel, *On the Atmospheric Corrosion of Metals Which Are Covered with Thin Electrolyte Layers .1. Verification of the Experimental-Technique*. Corrosion Science, 1990. **30**(6-7): p. 681-696.
61. Scully, J.R., M. Switzer, and J.S. Lee. *Crevice Scaling Laws to Investigate Local Hydrogen Uptake in Rescaled Model Occluded Sites*. in *Second International Conference on Environment Induced Cracking of Metals (EICM-2)*. Banff, Alberta, CA.

62. Tayler, M.L., et al., *Scribe Creep and Underpaint Corrosion on Ultra-High Molecular Weight Epoxy Resin-Coated 1018 Steel Part 1: Comparison of Field Exposures to Standard Laboratory Accelerated Life Tests*. Corrosion, 2015. **71**(1): p. 71-91.
63. Yilmaz, A., D. Chandra, and R.B. Rebak, *Corrosion behavior of carbon steel rock bolt in simulated Yucca Mountain ground waters*. Metallurgical and Materials Transactions a-Physical Metallurgy and Materials Science, 2005. **36A**(5): p. 1097-1105.

2.9. Tables:

Table 11. Corrosion rates of carbon steels at atmospheric exposure sites and full immersion and the diffusible hydrogen concentration for these exposures.

Environment	Cl ⁻ Deposition Density	Uniform Corrosion Rate	Diffusible Hydrogen Concentration
Full Immersion	n/a	<ul style="list-style-type: none"> · 930 $\mu\text{m}/\text{year}$ (UNS G10180, 5 wt % NaCl, E_{ocp}) [62] · 350 $\mu\text{m}/\text{year}$ (UNS G10180, 5 wt % NaCl, E_{ocp}) [62] 	<ul style="list-style-type: none"> · 4.43 wppm (steel alloy UNS K92580 charged in 0.6M NaCl with $\eta_{\text{h}} = -0.5\text{V}$, 48 hours) [28] · 0.47 wppm (steel alloy UNS K92580 charged in 0.6M NaCl with $\eta_{\text{h}} = -0.2\text{V}$, 48 hours) [28] · 0.21 wppm (steel alloy UNS K92580 charged in 0.6M NaCl with $\eta_{\text{h}} = 0\text{V}$, 48 hours) [19]
Severe Atmospheric Marine Environment	· 150 mg NaCl/ m^2yr , 25-m lot [6]	· 200-900 $\mu\text{m}/\text{yr}$ (wrought iron, 25 meters from mean ocean tide and is considered to be a severely corrosive environment) [6]	· Unknown
Moderate Atmospheric Marine Environment	<ul style="list-style-type: none"> · 36 mg NaCl/ m^2d (about 13 $\text{g}/\text{m}^2\text{yr}$), Choshi [7] · 40 mg NaCl/ m^2yr, 250-m lot [6] 	<ul style="list-style-type: none"> · 20-80 $\mu\text{m}/\text{yr}$ (wrought iron, 250 meters from mean ocean tide and is a moderately corrosive environment) [6] · 287 $\mu\text{m}/\text{yr}$ 252 $\text{g}/\text{m}^2\text{y}$ (for Fe-0.2C-0.55Si-1.6Mn-0.035P-0.035S % by mass, Choshi - rural/coastal area, average temperature 14.3°C and RH 77%) [7] 	<ul style="list-style-type: none"> · 0.1 – 0.15 wppm H content (Choshi, 12 month exposure, for Fe-0.36C-0.2Si-0.75Mn-0.016P-0.017S-0.01Cu-0.02Ni-1.02Cr-0.17Mo % steel alloy by mass) [7]
Rural Atmospheric Environment	· 2.2 mg NaCl/ m^2d (about 0.803 $\text{g}/\text{m}^2\text{yr}$), Tsukuba [7]	· 161 $\mu\text{m}/\text{yr}$ or 142 $\text{g}/\text{m}^2\text{y}$ (for Fe-0.2C-0.55Si-1.6Mn-0.035P-0.035S % by mass, Tsukuba - rural/coastal area, average temperature 15.8 °C and RH 75%) [7]	· 0.06 -0.07 wppm H content (Tsukuba, 12 month exposure, for Fe-0.36C-0.2Si-0.75Mn-0.016P-0.017S-0.01Cu-0.02Ni-1.02Cr-0.17Mo % steel alloy by mass) [7]
ASTM B-117 Salt fog	· 42.84 mg/ m^2hr (about 15637 $\text{g}/\text{m}^2\text{yr}$)	<ul style="list-style-type: none"> · 200 $\mu\text{m}/\text{year}$ (for Fe- 0.44C-0.27Si-1.57Mn-0.013P-0.31S-0.19Cu-0.06Ni-0.08Cr-0.03Mo % by weight %, 1 week test) [63] · 161 $\mu\text{m}/\text{year}$ (UNS K92580, this study) · 1160 $\mu\text{m}/\text{year}$ (UNS G10180) [62] 	· Unknown
ASTM B-117 + Acetic Acid Salt fog	· 42.84 mg/ m^2hr (about 15637 $\text{g}/\text{m}^2\text{yr}$)	<ul style="list-style-type: none"> · 1372 $\mu\text{m}/\text{year}$ (UNS K92580, this study) · 3014 $\mu\text{m}/\text{year}$ (UNS G10180) [62] 	· Unknown

Table 12. Composition (wt. %).[1]

Material	Fe	C	Mn	Si	P	S	Cr	Ni	Mo	N	Ti	Co
UNS K92580 ^a	Bal.	0.23	0.019	-	-	0.0008	2.78	10.89	1.21	-	-	12.8
UNS S46500 ^b	Bal.	0.005	0.02	0.02	0.002	0.002	11.50	11.04	0.94	0.002	1.54	-
UNS G10180	Bal.	0.15	0.7	0.15-0.3	0.04	0.05	-	-	-	-	-	-

^aAerMet 100™ peak-aged obtained through Carpenter Technology^bCustom 465™ H900 temper

Table 13. Material Properties.[1]

Temper	Yield Strength	Tensile Strength	Elongation	Reduction of Area	Rockwell Hardness C
UNS K92580 peak aged	1724 MPa	1965 MPa	14 %	65 %	54
UNS S46500 Annealed/ CT	772 MPa	951 MPa	20 %	75 %	29.5
UNS S46500 H900	1703 MPa	1779 MPa	14 %	51 %	51
UNS G10180	370 MPa	440 MPa	15%	40%	N/A

Table 14. Exposure conditions at Birdwood golf course: Location: 38.04N, 78.53W

Conditions	Data Collected ^{1,2}
Avg T	15.61 °C
Avg % RH	59.04%
Avg Dew Point	14.33 T _d (°C)
Avg Precipitation	0.133 in/day
Avg Chlorinity	0.17 mg/L ($\approx 0.5 \mu\text{g}/\text{cm}^2$)

1) Atmospheric Data collected from National Weather Service Report at NOAA:

<http://www.nws.noaa.gov/climate>

2) Chlorinity Data collected from NADP VA00:

<http://nadp.sws.uiuc.edu/sites/siteinfo.asp?id=VA00&net=NTN>

Table 15. Salt density for various atmospheric exposures and environments.

Salt Deposition Method	Average Salt Density ($\mu\text{g}/\text{cm}^2$)	Average single drop area (cm^2)	Water Weight ($\mu\text{g}/\text{cm}^2$)
Salt Print (5 prints)	161	3.845×10^{-7}	0.0115
Salt Spray (7 sprays)	138	1.133×10^{-5}	0.0990
Salt Droplets (1% coverage)	220	1.960×10^{-3}	0.1245
ASTM B-117	178.5	N/A (thin film)	8246

Salt Deposition Environment	Salt Density ($\mu\text{g}/\text{cm}^2$)*	Salt Density ($\mu\text{g}/\text{cm}^2$)**	Water Weight ($\mu\text{g}/\text{cm}^2$ ***)
Severe Marine	411	1233	1208 – 3624
Moderate Marine	98 to 110	294 to 330	295-972
Rural	6	18	27-55

* Assuming a 10 day wash off period.

** Assuming a 30 day wash off period

*** Assuming an average RH of 77 % for marine environments and 75% for rural environments and a thin film morphology.

Table 16. Table of corrosion products found with XRD and Raman. X indicates that the species was found with XRD, and R indicates that it was found with Raman. [41]

Exposure	Iron (II,III) oxide Fe_3O_4	Iron (III) oxide Fe_2O_3	Iron (III) OxideHydroxide Alpha Phase $\alpha\text{-FeOOH}$	Iron (III) OxideHydroxide Beta Phase $\beta\text{-FeOOH}$	Iron (III) OxideHydroxide Gamma phase $\gamma\text{-FeOOH}$
Birdwood	-	-	-	-	X
Golf Course	-	-	-	-	-
ASTM B-117	X	-	R	-	R

Table 17. Comparison of average atmospheric droplet spacing to H concentration at the same distance as droplet spacing relative to a corrosion site. Concentration profile is assumed uniform if overlap between hydrogen uptake spots occurs at $C_{x,t}/C_o \geq 0.5$.

Exposure Type	Average Droplet Spacing (center to center)	Material		
		UNS S46500	UNS K92580	UNS G10180
		C_H Uniformity*:		
ASTM B-117 + modified	Thin film	pit density	uniform	uniform
Salt Print	46 μm	uniform	uniform	uniform
Salt Spray	163 μm	$C_{x,t}/C_o < 0.11$	uniform	uniform
Micropipetted Droplets	5 mm	$C_{x,t}/C_o < 6.0 \times 10^{-9}$	$C_{x,t}/C_o < 2.3 \times 10^{-7}$	$C_{x,t}/C_o < 0.015$

*Calculation for H diffusion made with same assumptions as **Error! Reference source not found..**

Table 18. Calculated diffusion distances for C_H equal to 90% C_o over a period of 10 days for different initial spherical H distributions. $D_{H,eff}$ used were $6.2 \times 10^{-9} \text{ cm}^2/\text{s}$, $6 \times 10^{-9} \text{ cm}^2/\text{s}$, and $1 \times 10^{-7} \text{ cm}^2/\text{s}$ for UNS S46500, UNS K92580, and UNS G10180 respectively.

Material	Diffusion distance away from a spherical source in 10 days assuming an initial concentration (C_o) of radius (μm):		
	5	40	500
UNS K92580	600	1700	6000
UNS S46500	500	1400	5000
UNS G10180	1200	3400	12100

Table 19. Calculated Q_{mass} (gravimetric) and $Q_{H,abs}$ (TDS) corrected with LECO calibration based on mass loss and $C_{H,total}$ for selected 10 day exposures. ^a

Exposure	UNS G1018		UNS K92580	
	$Q_{H,abs}$ (C/cm^2)	Q_m (C/cm^2)	$Q_{H,abs}$ (C/cm^2)	Q_m (C/cm^2)
ASTM B-117	0.05	32.6	0.05	5.9
ASTM B-117+ UV	0.07	56.7	0.25	9.6
ASTM B-117 + ASW	0.07	13.3	0.09	1.8
5.3 M NaCl 79% RH 1 μL drop array	0.01	82.8	0.06	60.4
5.3 M NaCl 79% RH 5 μL drop array	0.02	58.0	0.05	30.2
5.3 M NaCl 79% RH spray	0.02	677.4	0.06	12.1
0.9 M NaCl-99% RH spray	0.05	277.1	0.07	36.2

^a UNS S46500 not included as it does not display significant mass loss.

2.10. Figures:

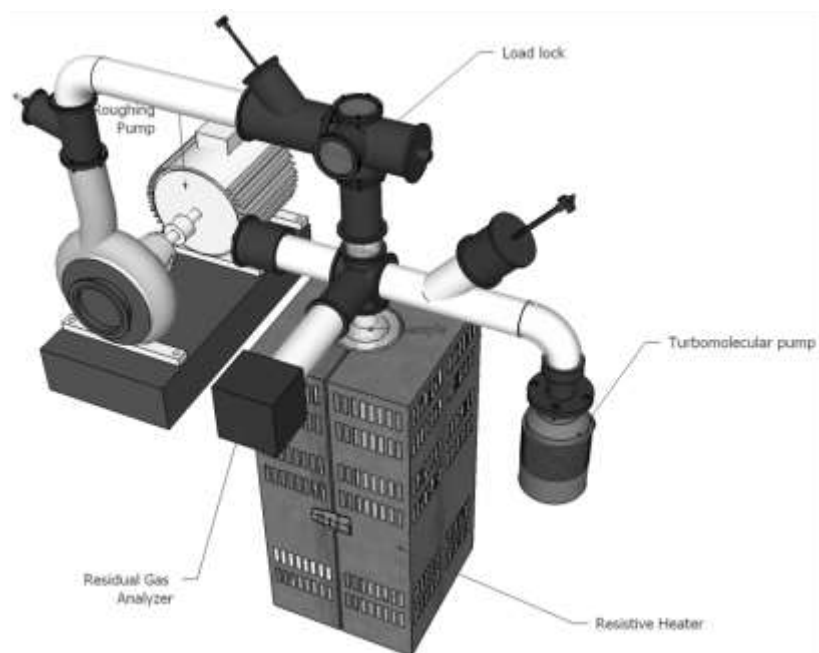


Figure 30. Thermal Desorption Spectroscopy chamber schematic

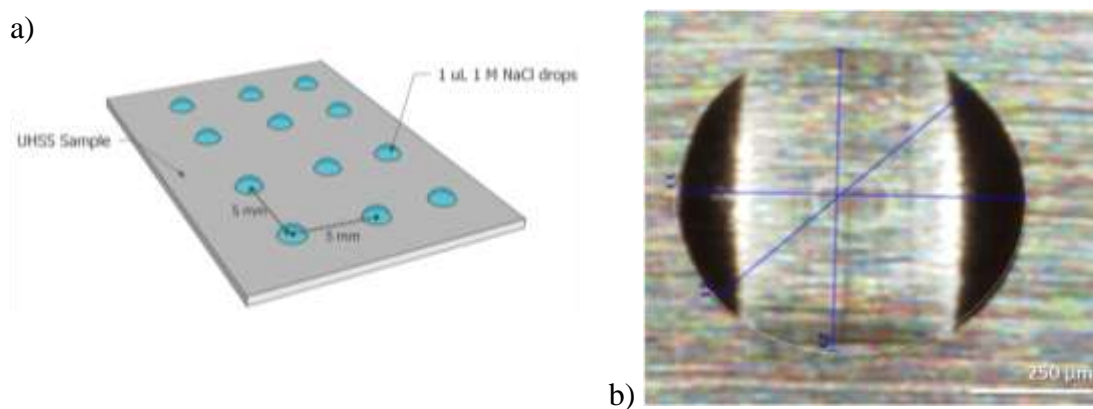
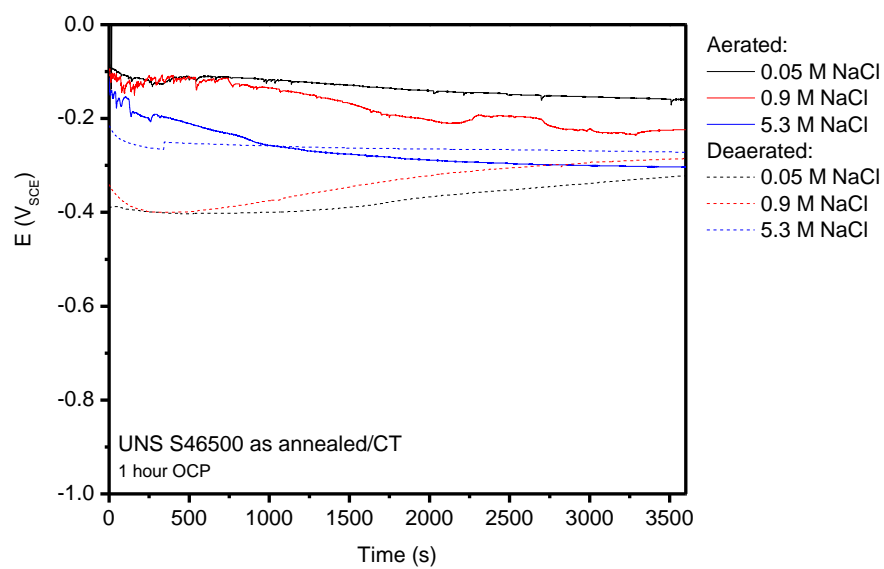
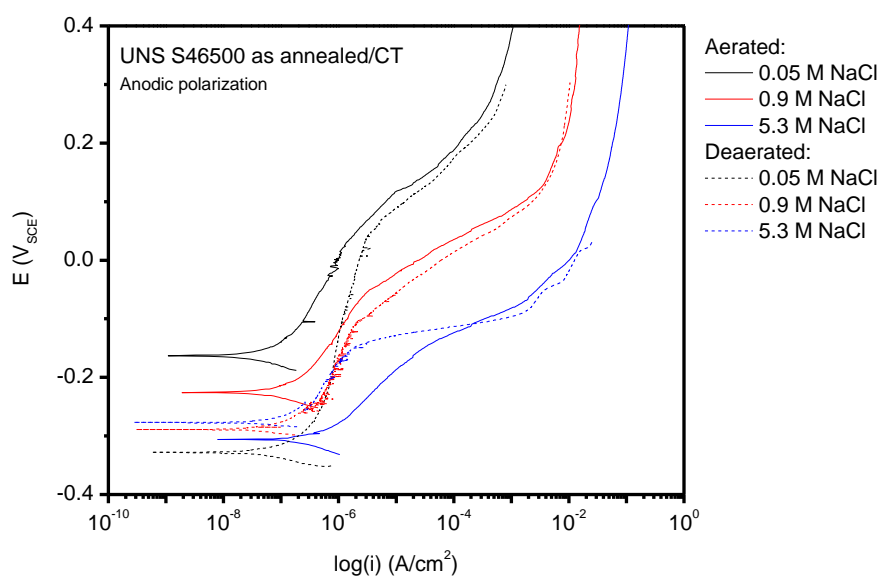


Figure 31. A) A droplet array with 5 by 5 mm spacing between droplet centers of 1 M NaCl pH 6.5 solution 1 μ L drops (average diameter of 500 μ m) on UHSS and B) a Hirox optical image of a 1M NaCl pH 6.5 droplet on UHSS sample.

a)



b)



c)

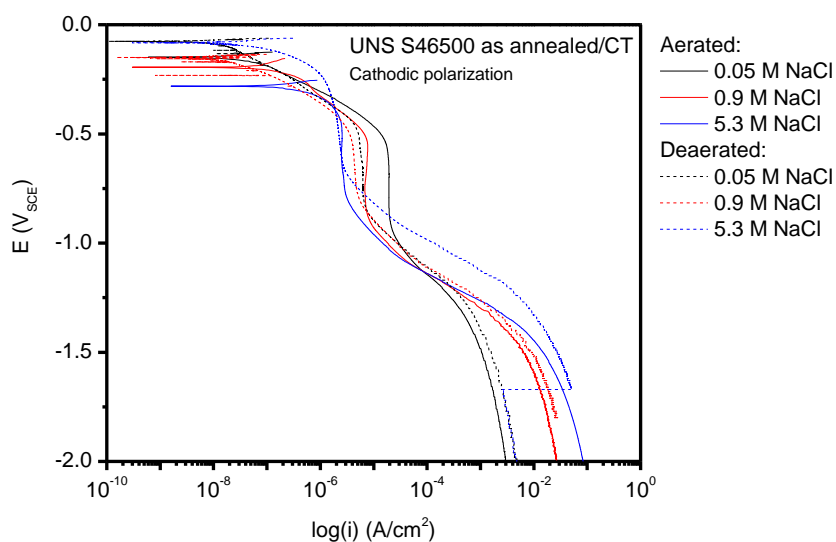
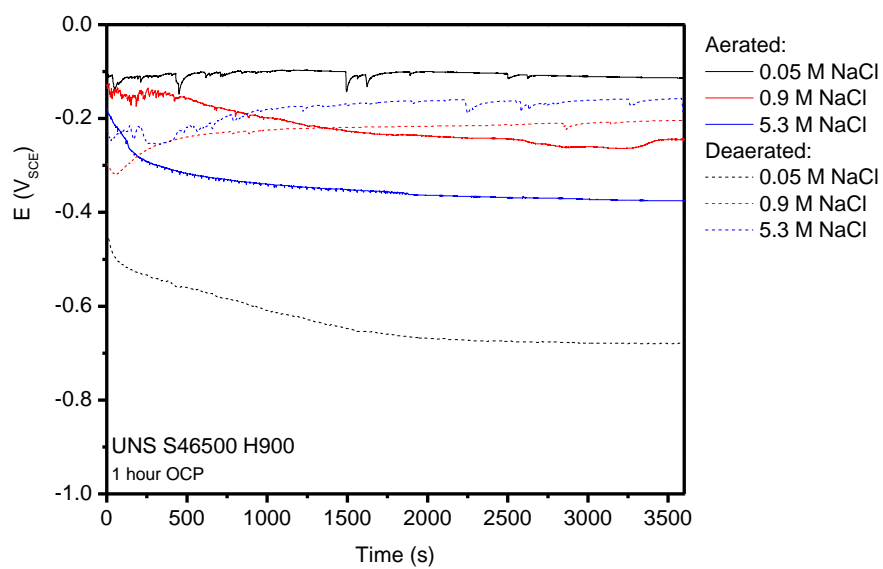
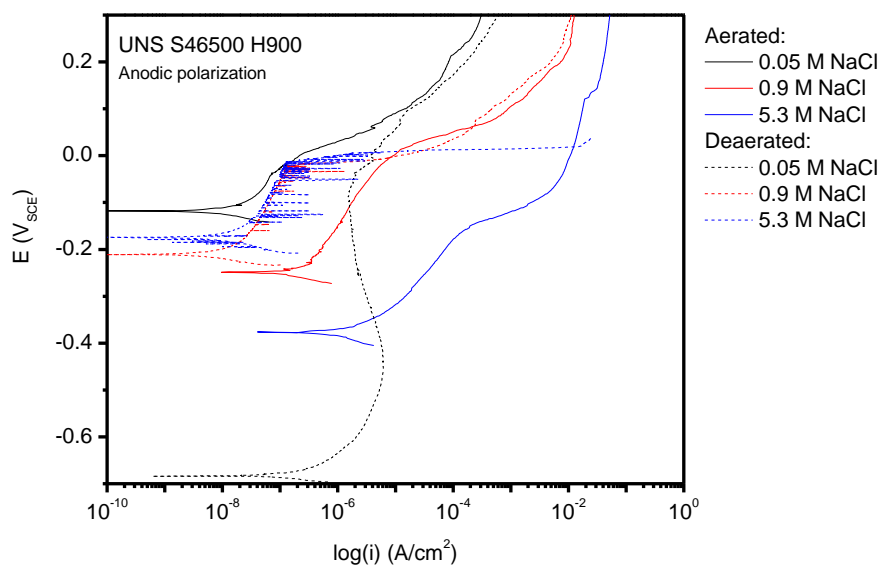


Figure 32. Electrochemical testing of UNS S46500 as annealed/CT a) 1 h E_{OCP} followed by a polarization scans either b) anodic polarizations, from -30 mV vs E_{OCP} , at a scan rate of 0.1667 mV/s to 0.5 V_{SCE} or c) cathodic polarizations, from +30 mV vs E_{OCP} , at a scan rate of 0.1667 mV/s to -2 V_{SCE} in ambiently aerated and deaerated 0.05 M, 0.9 M, and 5.3 M NaCl.

a)



b)



c)

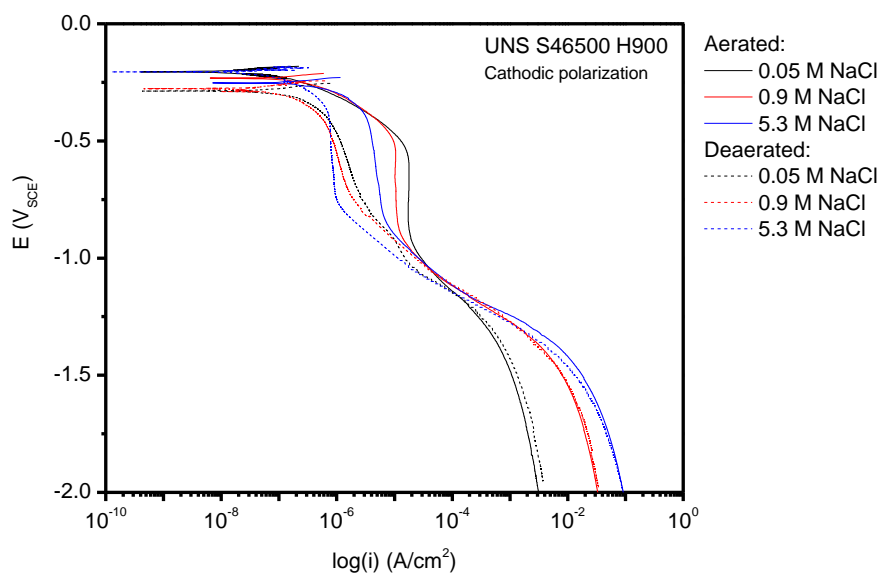
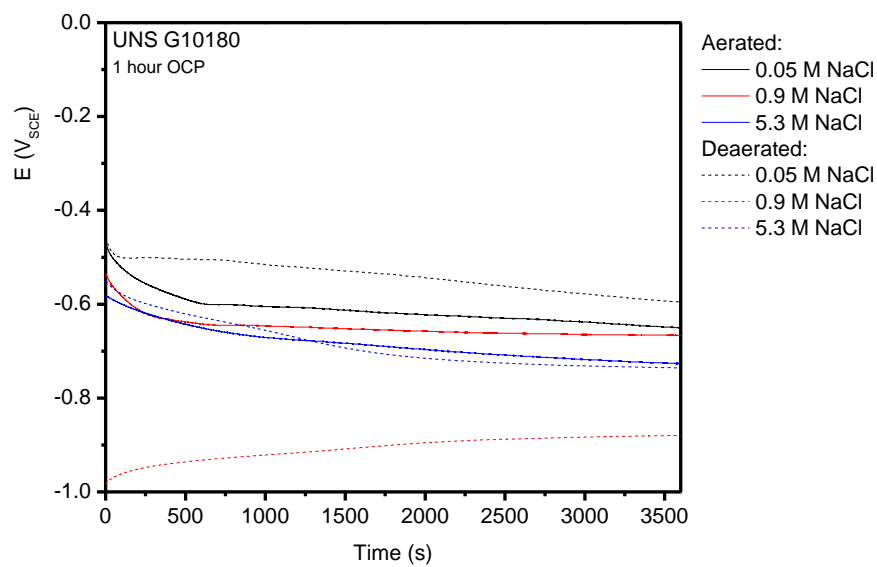
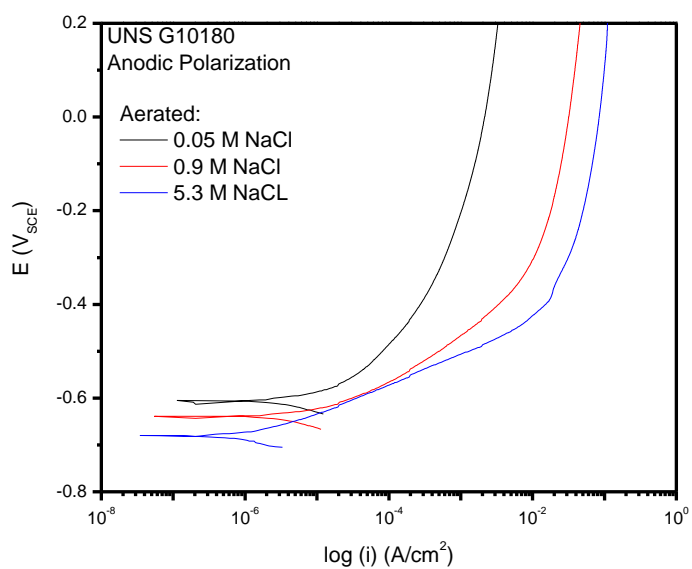


Figure 33. Electrochemical testing of UNS S46500 H900 a) 1 h E_{OCP} followed by a polarization scans either b) anodic polarizations, from -30 mV vs E_{OCP} , at a scan rate of 0.1667 mV/s to 0.5 V_{SCE} or c) cathodic polarizations, from +30 mV vs E_{OCP} , at a scan rate of 0.1667 mV/s to -2 V_{SCE} in ambiently aerated and deaerated 0.05 M, 0.9 M, and 5.3 M NaCl.

a)



b)



c)

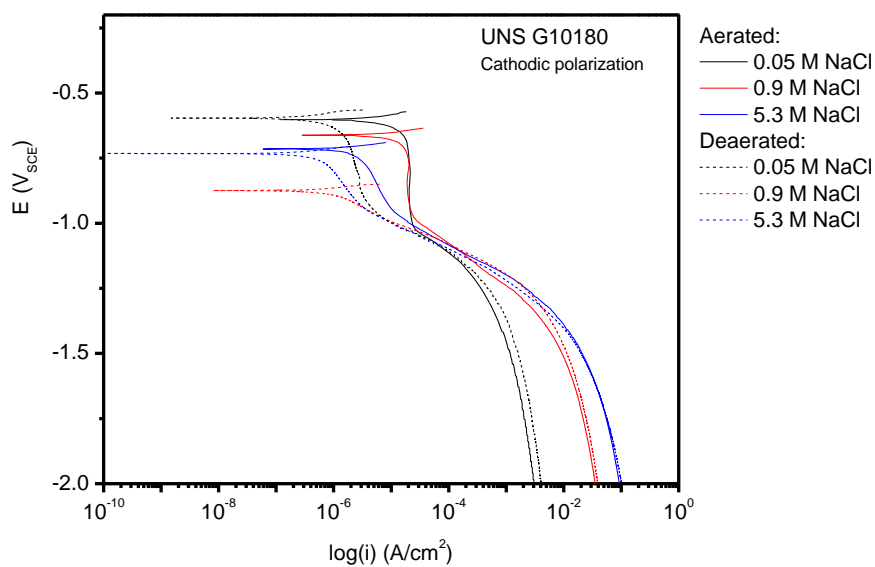
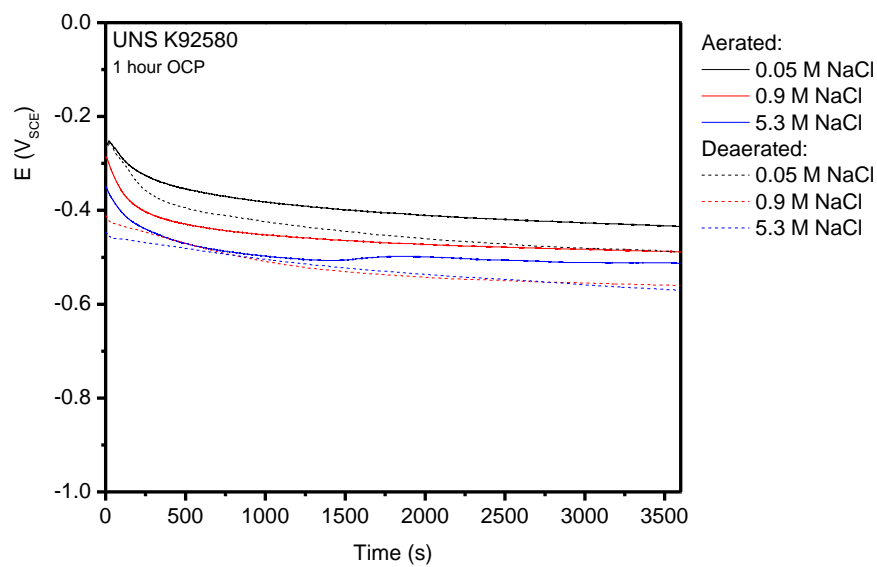
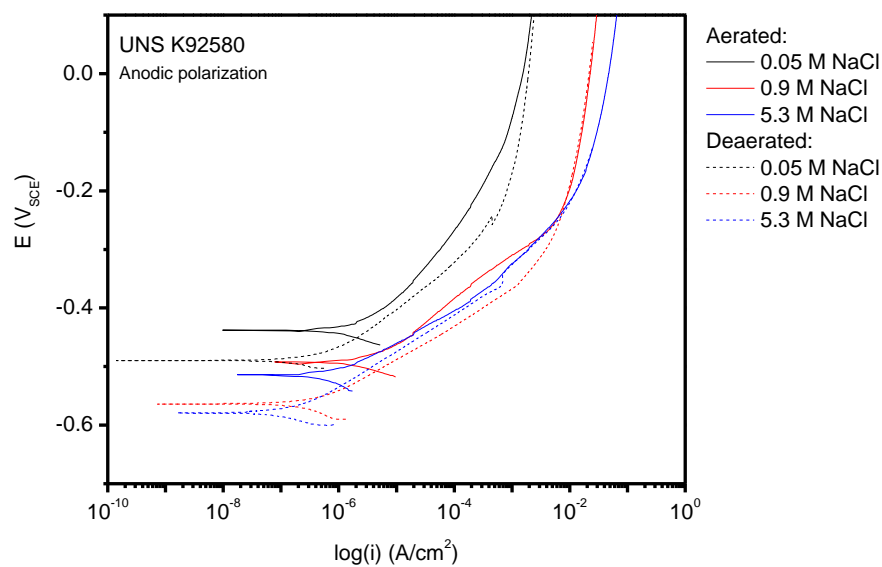


Figure 34. Electrochemical testing of UNS G10180 a) 1 h E_{OCP} followed by a polarization scans either b) anodic polarizations, from -30 mV vs E_{OCP} , at a scan rate of 0.1667 mV/s to 0.5 V_{SCE} or c) cathodic polarizations, from +30 mV vs E_{OCP} , at a scan rate of 0.1667 mV/s to -2 V_{SCE} in ambiently aerated and deaerated 0.05 M, 0.9 M, and 5.3 M NaCl.

a)



b)



c)

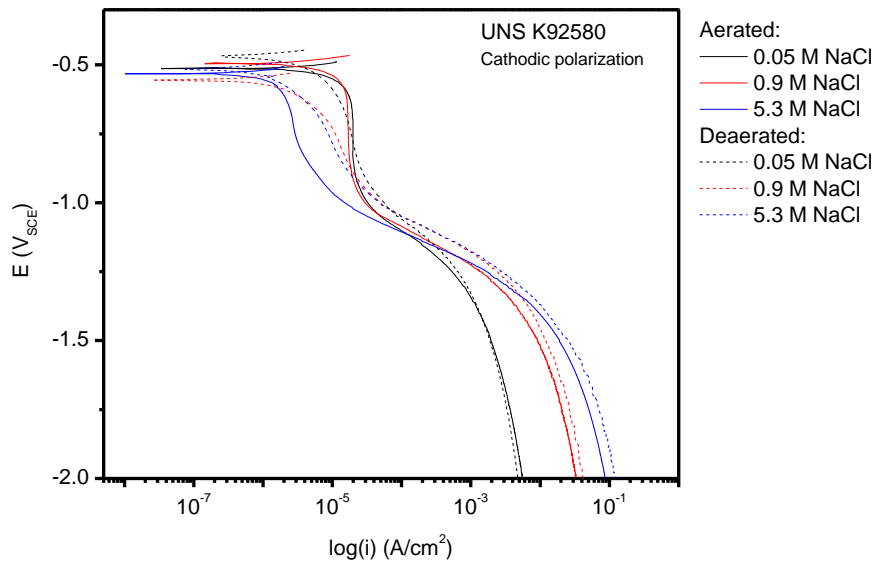
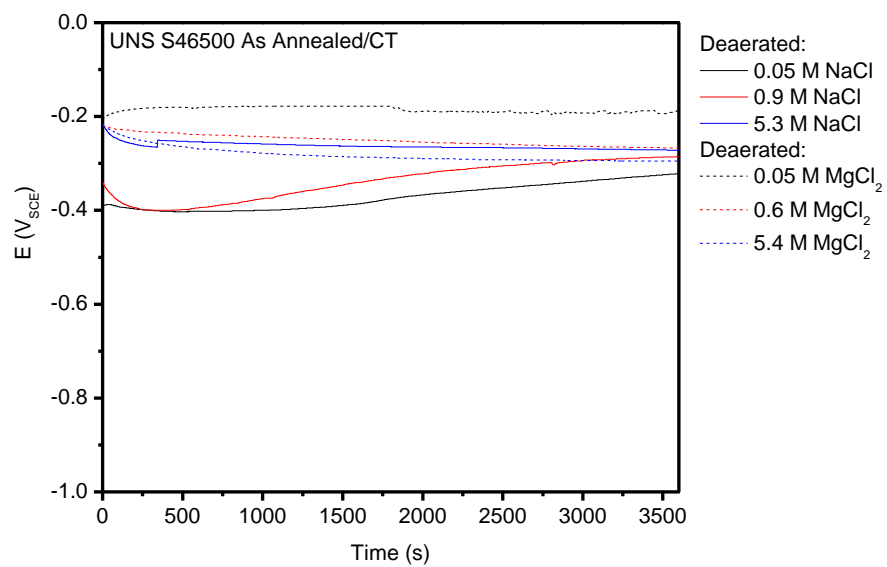
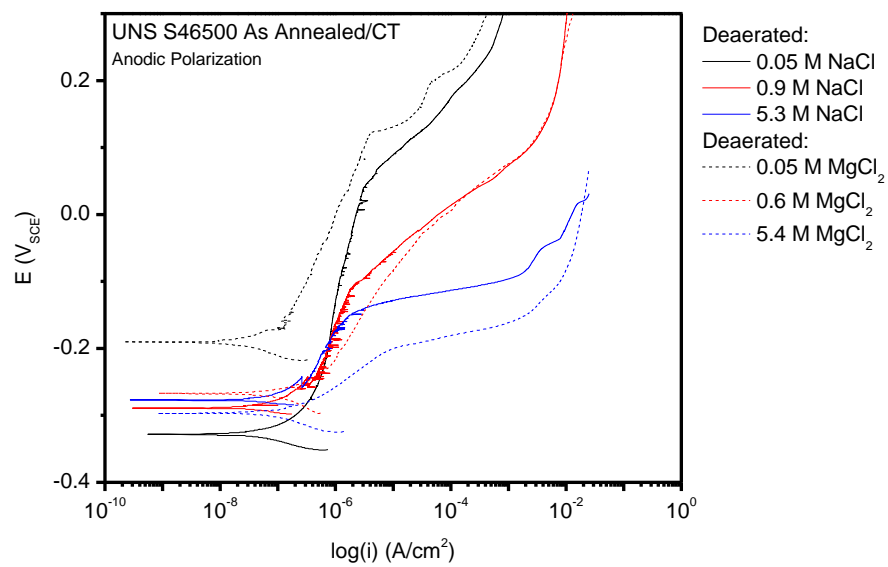


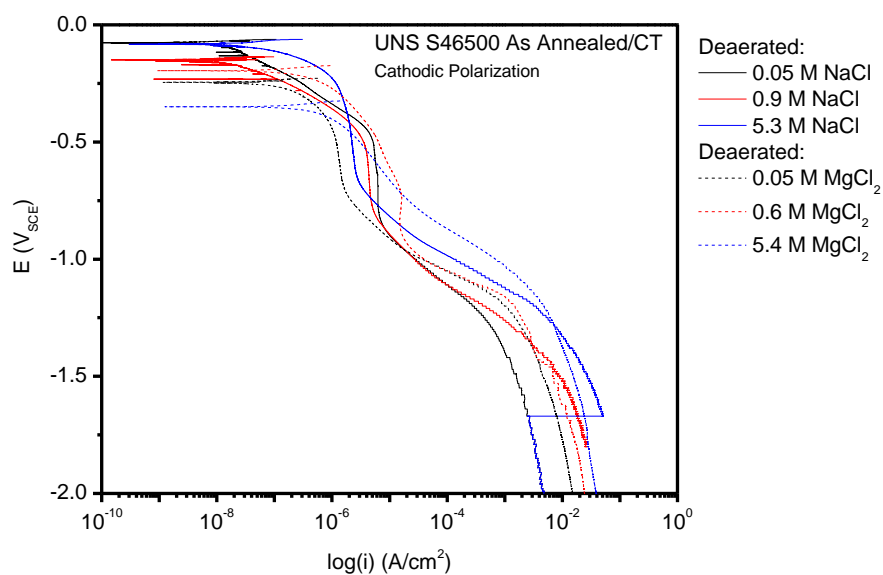
Figure 35. Electrochemical testing of UNS K92580 a) 1 h E_{OCP} followed by a polarization scans either b) anodic polarizations, from -30 mV vs E_{OCP} , at a scan rate of 0.1667 mV/s to 0.5 V_{SCE} or c) cathodic polarizations, from +30 mV vs E_{OCP} , at a scan rate of 0.1667 mV/s to -2 V_{SCE} in ambiently aerated and deaerated 0.05 M, 0.9 M, and 5.3 M NaCl.

a)



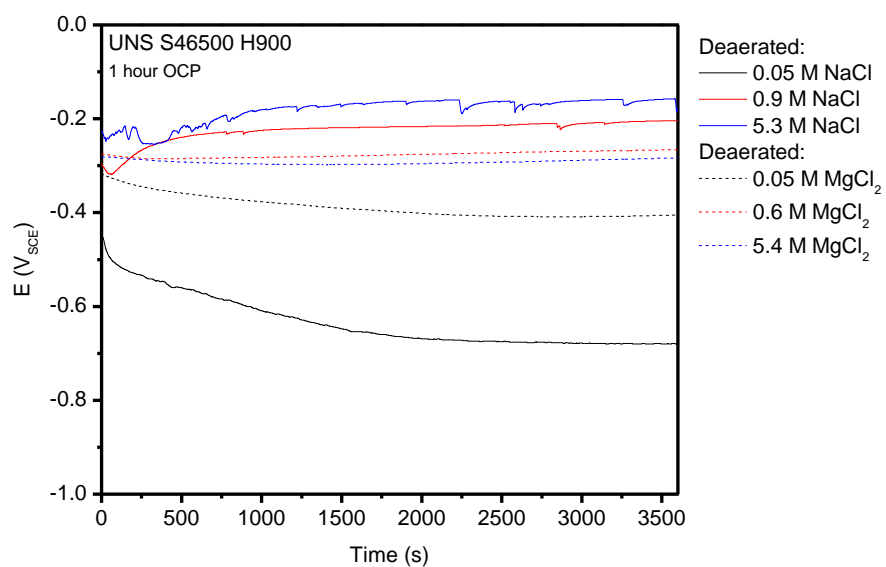
b)



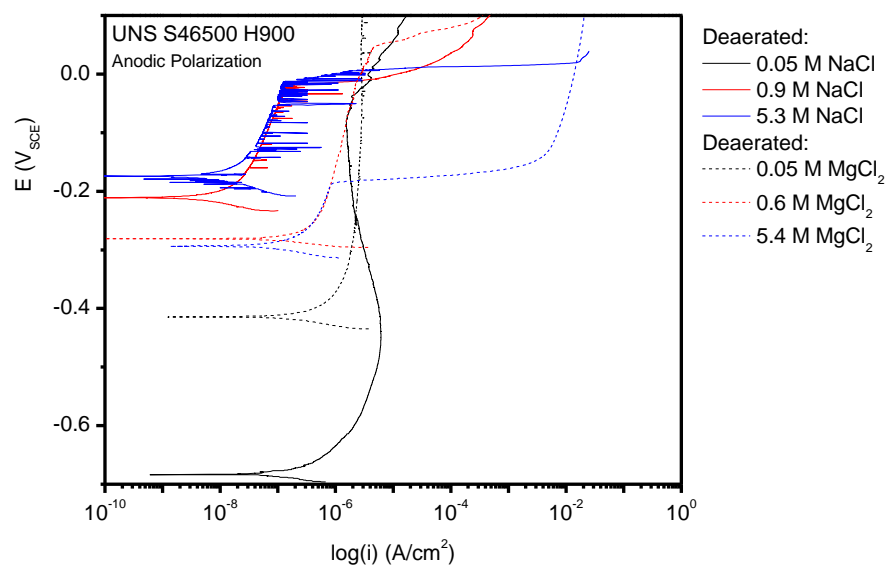


c)

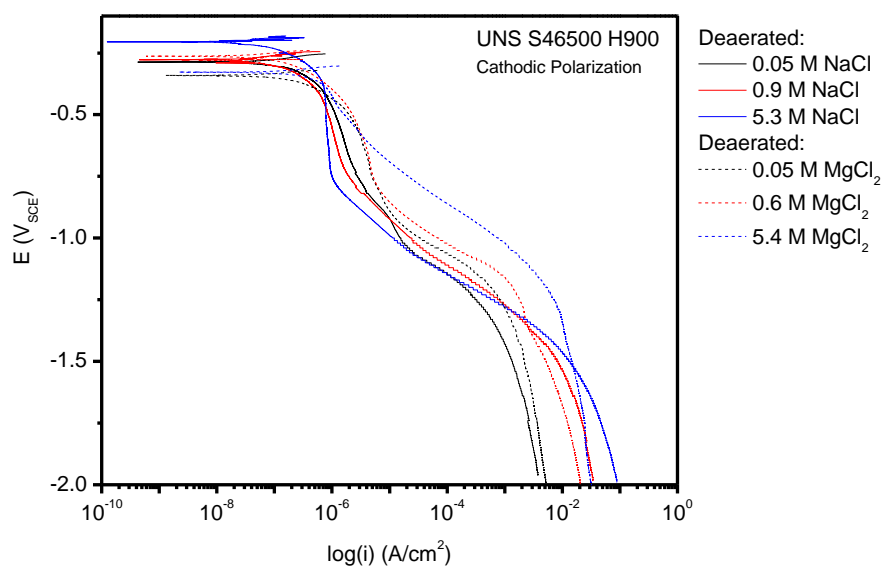
Figure 36. Electrochemical testing of UNS S46500 As Annealed/CT a) 1 h E_{OCP} followed by a polarization scans either b) anodic polarizations, from -30 mV vs E_{OCP} , at a scan rate of 0.1667 mV/s to 0.5 V_{SCE} or c) cathodic polarizations, from +30 mV vs E_{OCP} , at a scan rate of 0.1667 mV/s to -2 V_{SCE} in deaerated 0.05 M, 0.9 M, and 5.3 M NaCl and 0.05 M, 0.6 M, and 5.4 M MgCl₂.



a)

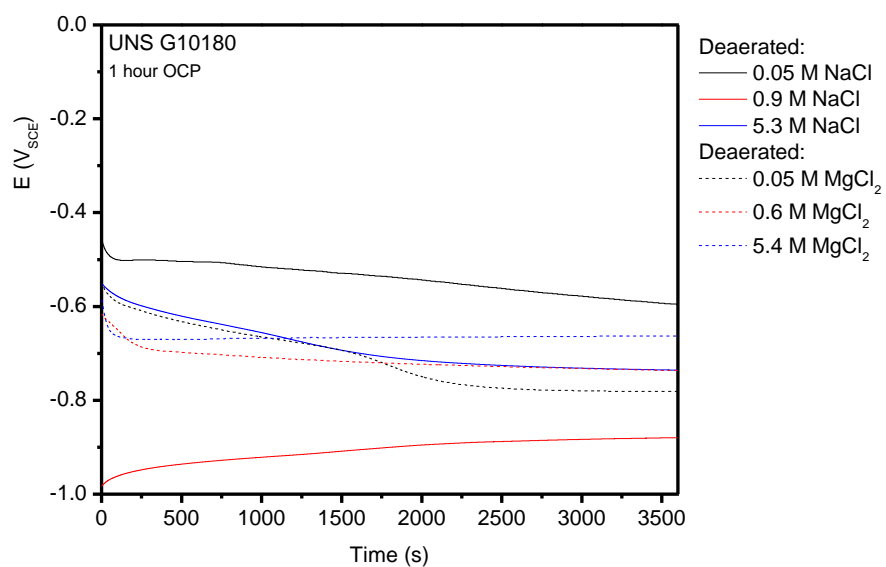


b)

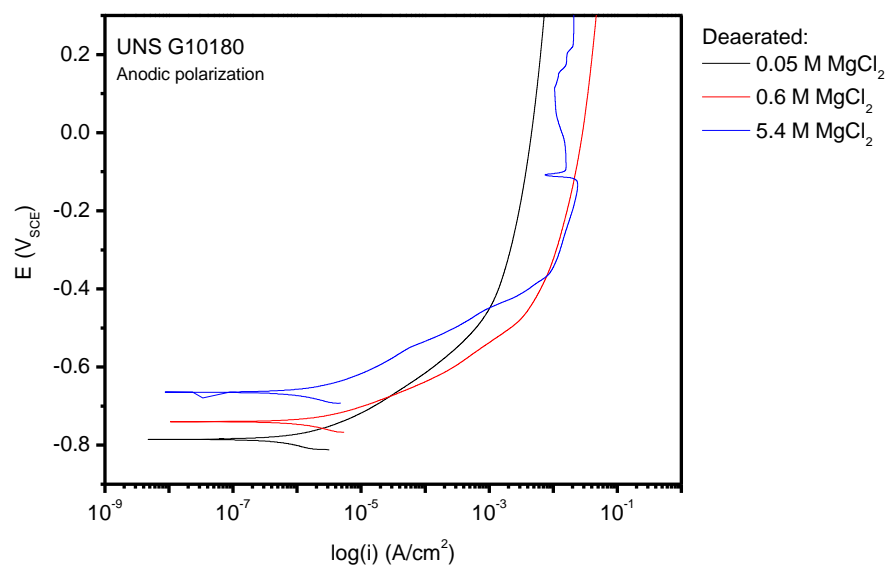


c)

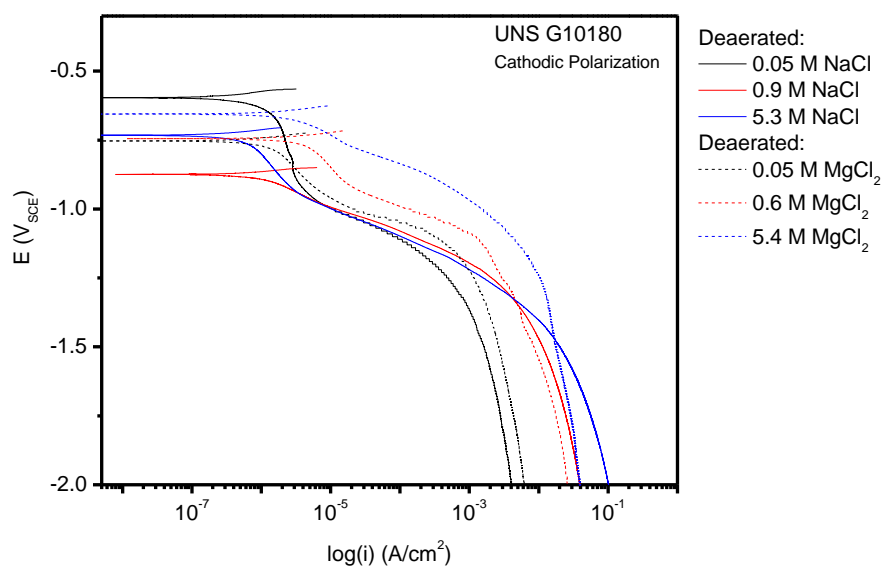
Figure 37. Electrochemical testing of UNS S46500 H900 a) 1 h E_{OCP} followed by a polarization scans either b) anodic polarizations, from -30 mV vs E_{OCP} , at a scan rate of 0.1667 mV/s to 0.5 V_{SCE} or c) cathodic polarizations, from +30 mV vs E_{OCP} , at a scan rate of 0.1667 mV/s to -2 V_{SCE} in deaerated 0.05 M, 0.9 M, and 5.3 M NaCl and 0.05 M, 0.6 M, and 5.4 M MgCl₂.



a)

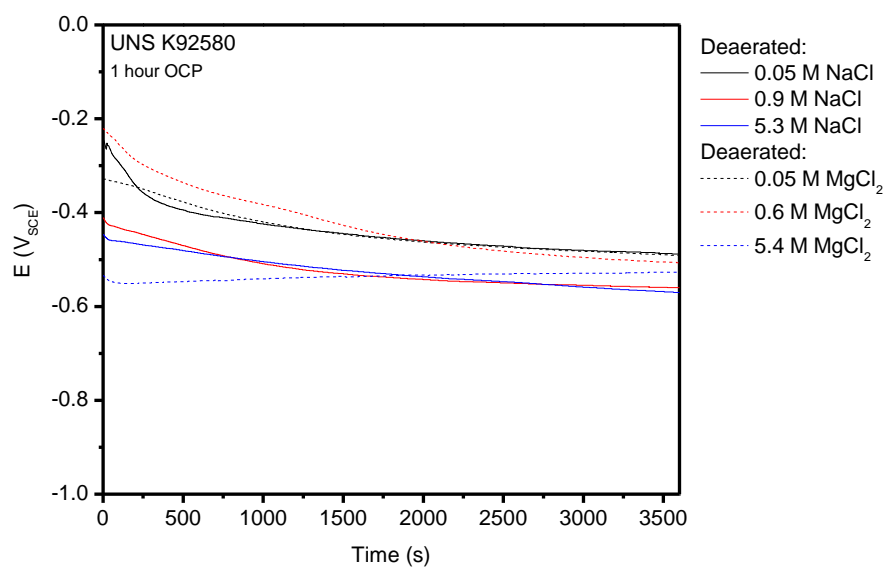


b)

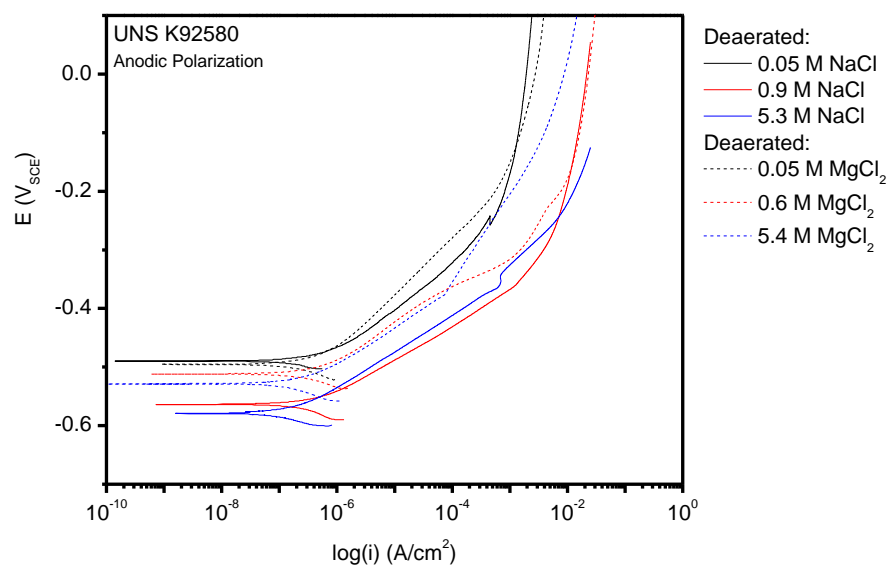


c)

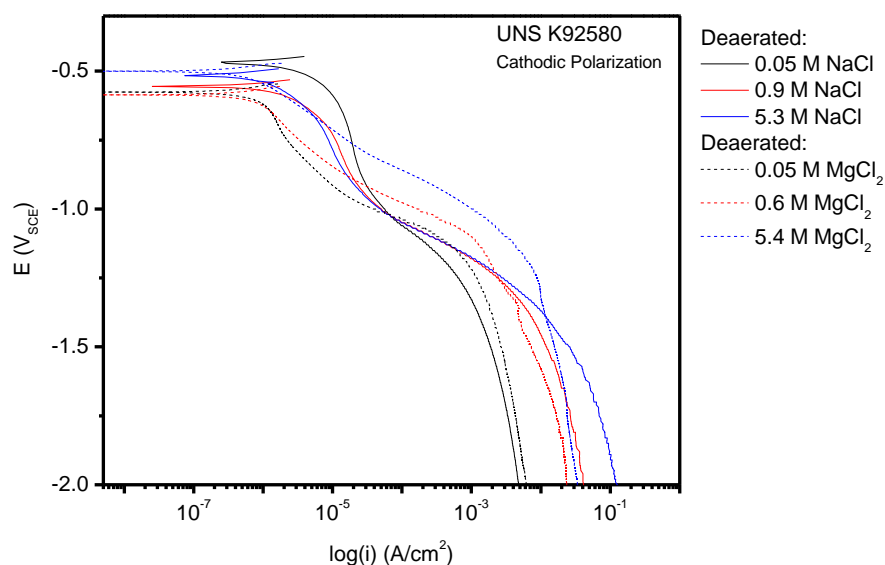
Figure 38. Electrochemical testing of UNS G10180 a) 1 h E_{OCP} followed by a polarization scans either b) anodic polarizations, from -30 mV vs E_{OCP} , at a scan rate of 0.1667 mV/s to 0.5 V_{SCE} or c) cathodic polarizations, from +30 mV vs E_{OCP} , at a scan rate of 0.1667 mV/s to -2 V_{SCE} in deaerated 0.05 M, 0.9 M, and 5.3 M NaCl and 0.05 M, 0.6 M, and 5.4 M MgCl_2 .



a)

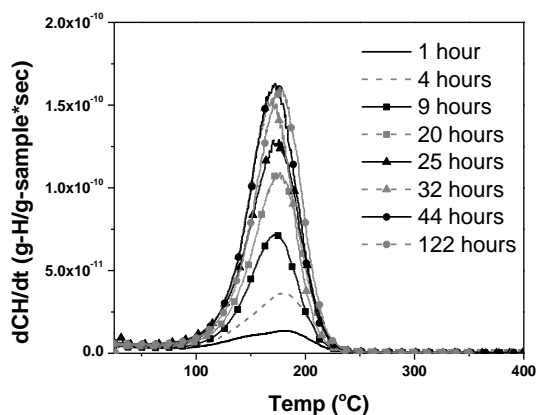


b)



c) Figure 39. Electrochemical testing of UNS K92580 a) 1 h E_{OCP} followed by a polarization scans either b) anodic polarizations, from -30 mV vs E_{OCP} , at a scan rate of 0.1667 mV/s to 0.5 V_{SCE} or c) cathodic polarizations, from +30 mV vs E_{OCP} , at a scan rate of 0.1667 mV/s to -2 V_{SCE} in deaerated 0.05 M, 0.9 M, and 5.3 M NaCl and 0.05 M, 0.6 M, and 5.4 M MgCl₂.

a)



b)

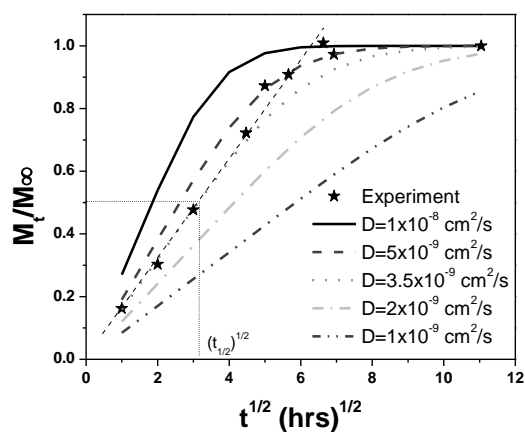


Figure 40. A) TDS ramp rate tests of charged a) hydrogen over-potential of -1.0 V (-1.74 V_{SCE}) in pH 8.5 borate buffered solution) as-annealed / CT UNS S46500, b) Calculated saturation curves assuming various diffusion coefficients (lines) plotted with experimental results from TDS ramp rate tests of as annealed/CT UNS S46500 (squares).

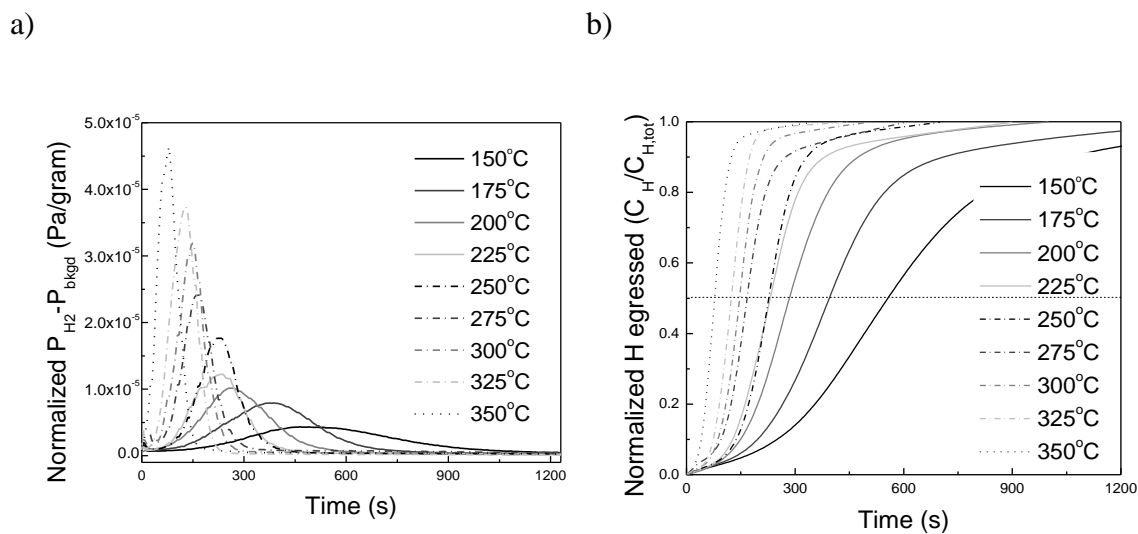


Figure 41. Isothermal TDS results at various temperatures for as-annealed / CT UNS S46500 stainless steel. a) Background subtracted H_2 pressure as a function of time, b) normalized H concentration egressed as a function of time. Specimens were H-charged for 14 days at room temperature at a hydrogen overpotential of -0.8 V in pH 10, 0.6M NaCl solution.

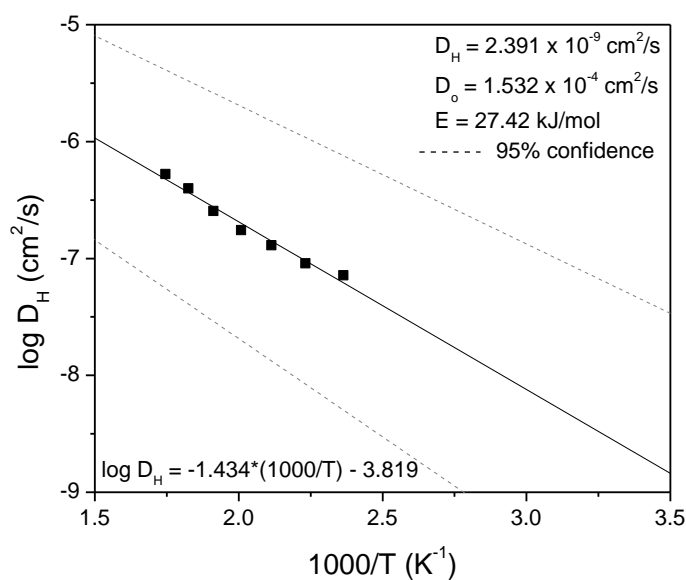


Figure 42. Arrhenius plot of D_H for as-annealed/CT UNS S46500 stainless steel, obtained from isothermal TDS tests shown with 95% confidence interval for regression indicated.

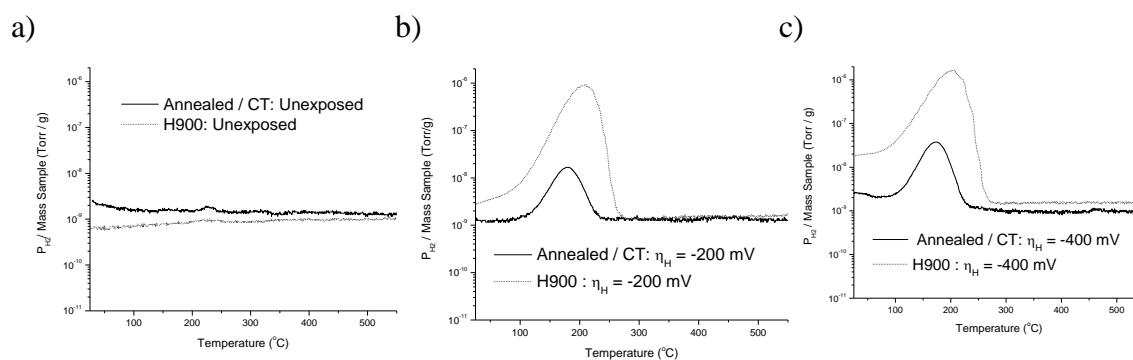


Figure 43. TDS spectra for as-annealed/CT and H900 UNS S46500 at a ramp rate of 5 °C/min for a) unexposed samples and samples charged in pH 10, 0.6 M NaCl solution for 48 hours at η_H = b) -200 mV and c) -400 mV.

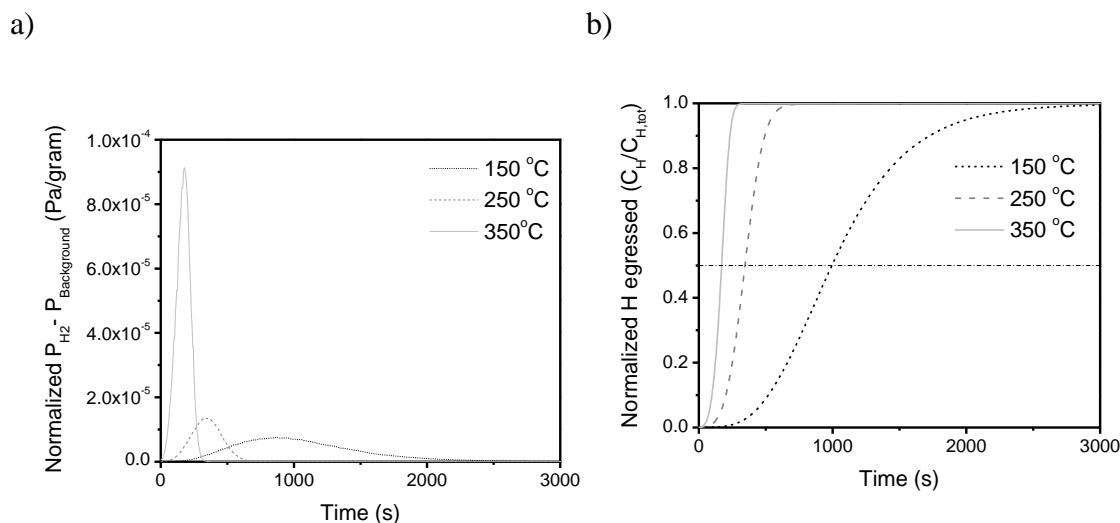


Figure 44. Isothermal TDS results at various temperatures for H900 UNS S46500 stainless steel. a) Background subtracted H_2 pressure as a function of time, b) normalized H concentration egressed as a function of time. Specimens were H-charged for 14 days at room temperature at a hydrogen overpotential of -0.8 V in pH 10, 0.6 M NaCl solution.

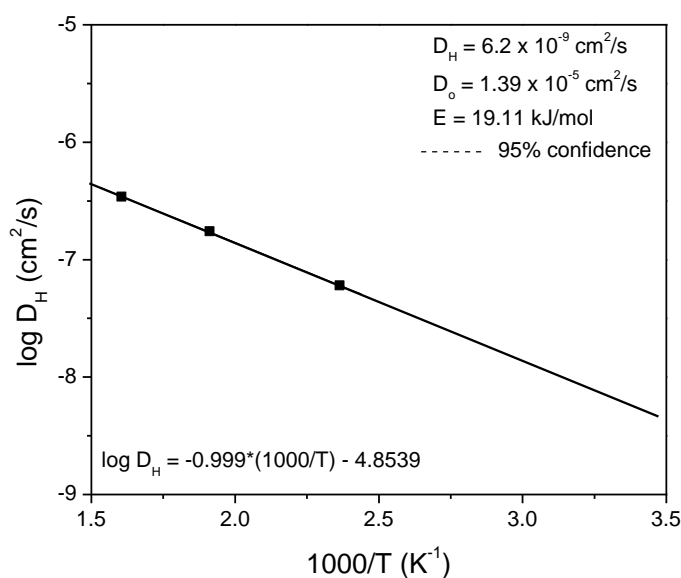


Figure 45. Arrhenius plot for H900 stainless steel, obtained from isothermal TDS tests shown with 95% confidence interval for regression. Data was corrected using an average heating time for the sample to reach the chamber temperature of 7.6 s.

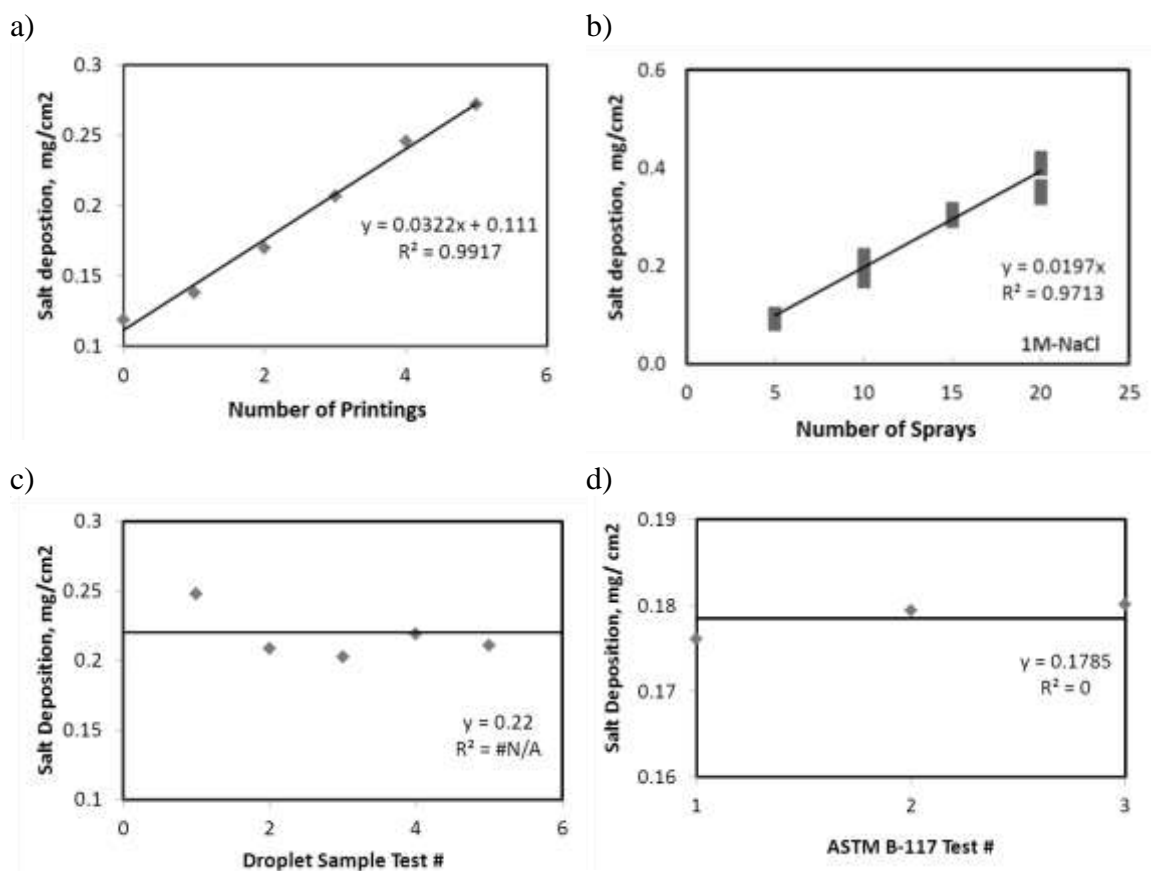


Figure 46. Calibration through conductivity measurements of average salt deposition per cm² for salt print, mist and droplets. a) Salt print, calibration was deposition versus print number, b) Salt spray, deposition versus spray number, c) Salt drops, deposition versus sample number (all samples were loaded with same number of droplets and average area coverage of 1.5 %) and d) ASTM B-117 standard versus sample number of parafilm substrates exposed for one hour.

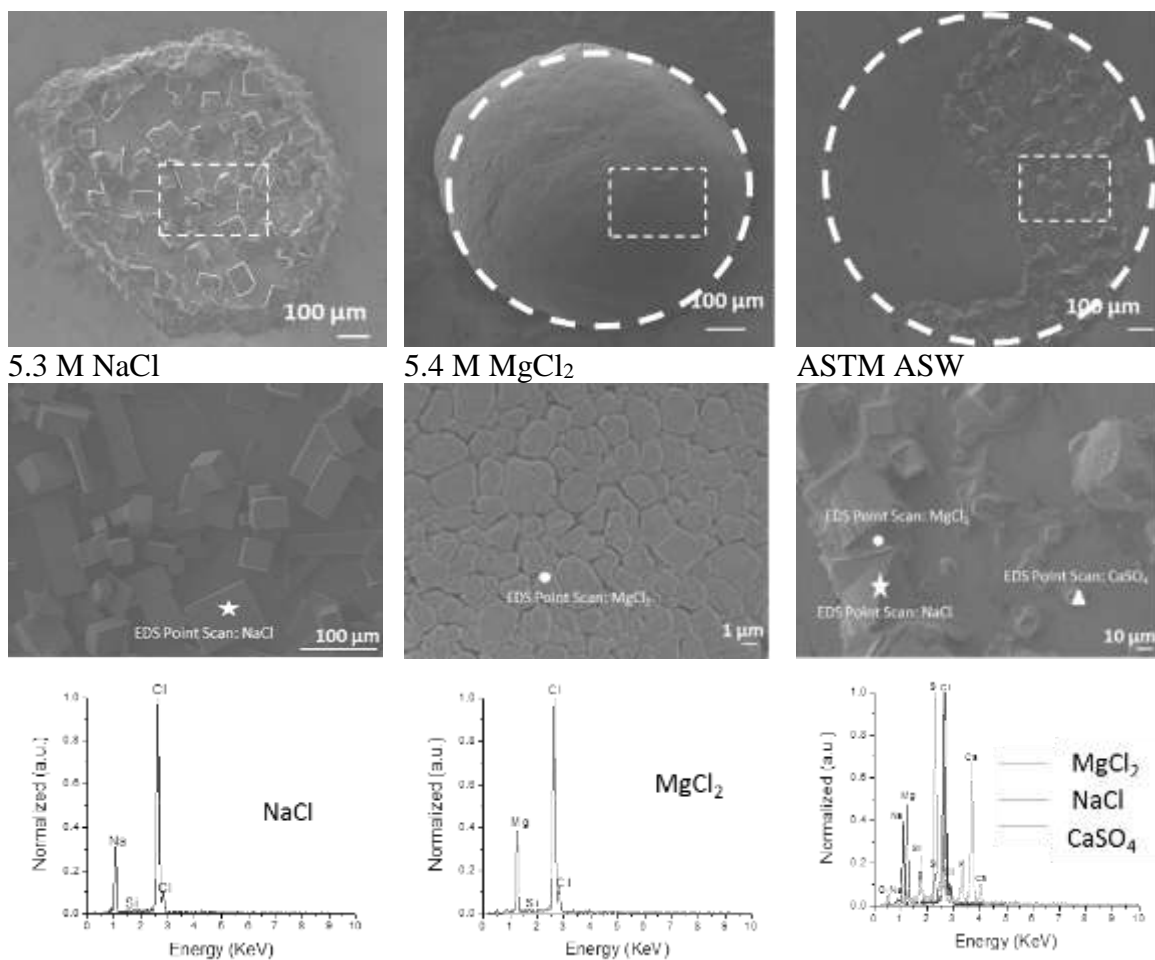
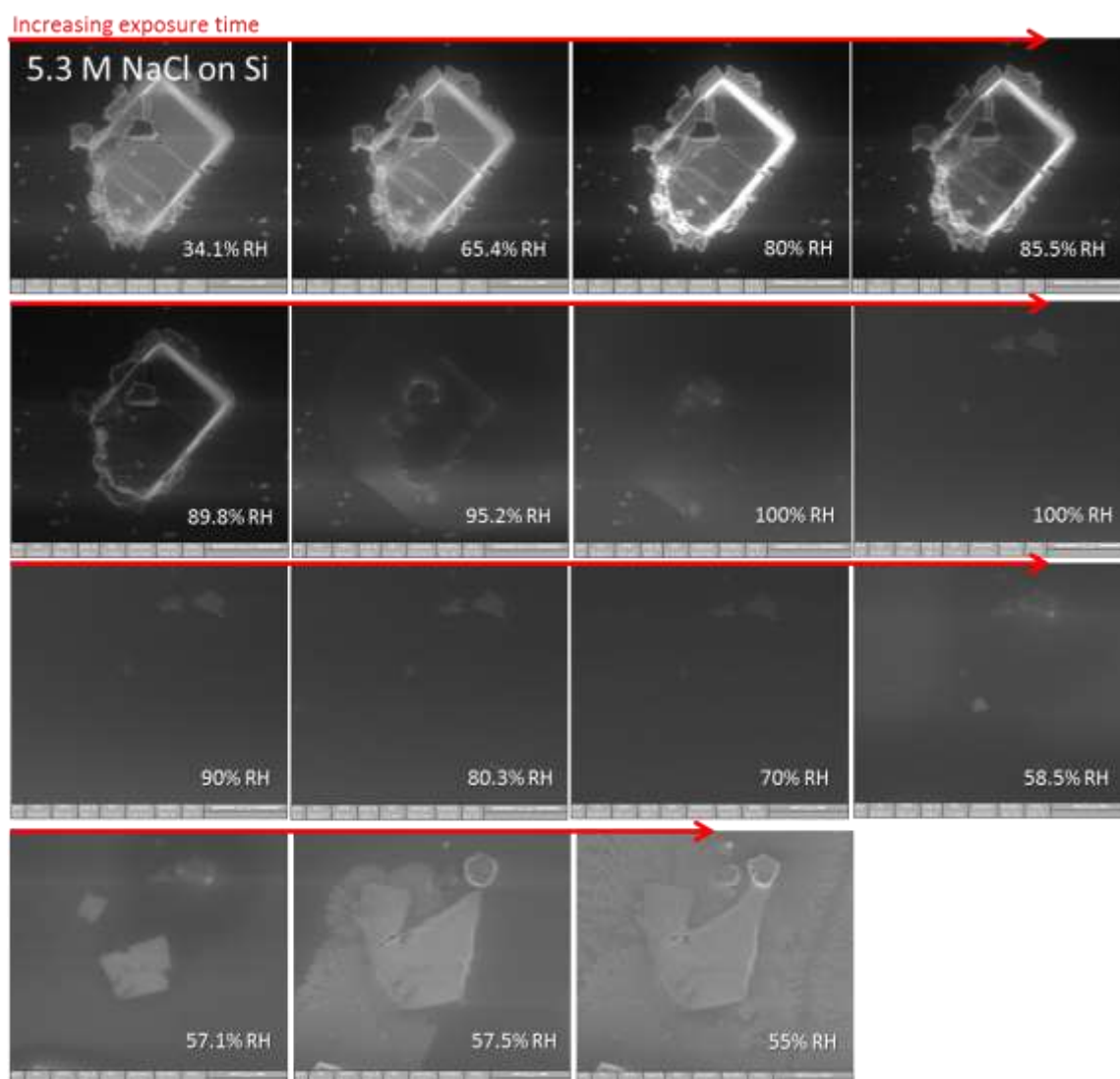


Figure 47. SEM and EDS analysis of dried 0.5 μL salt droplets on Si substrate. Concentrations are different than those discussed previously, as higher concentrations were chosen to display salt morphology.

a)



b)

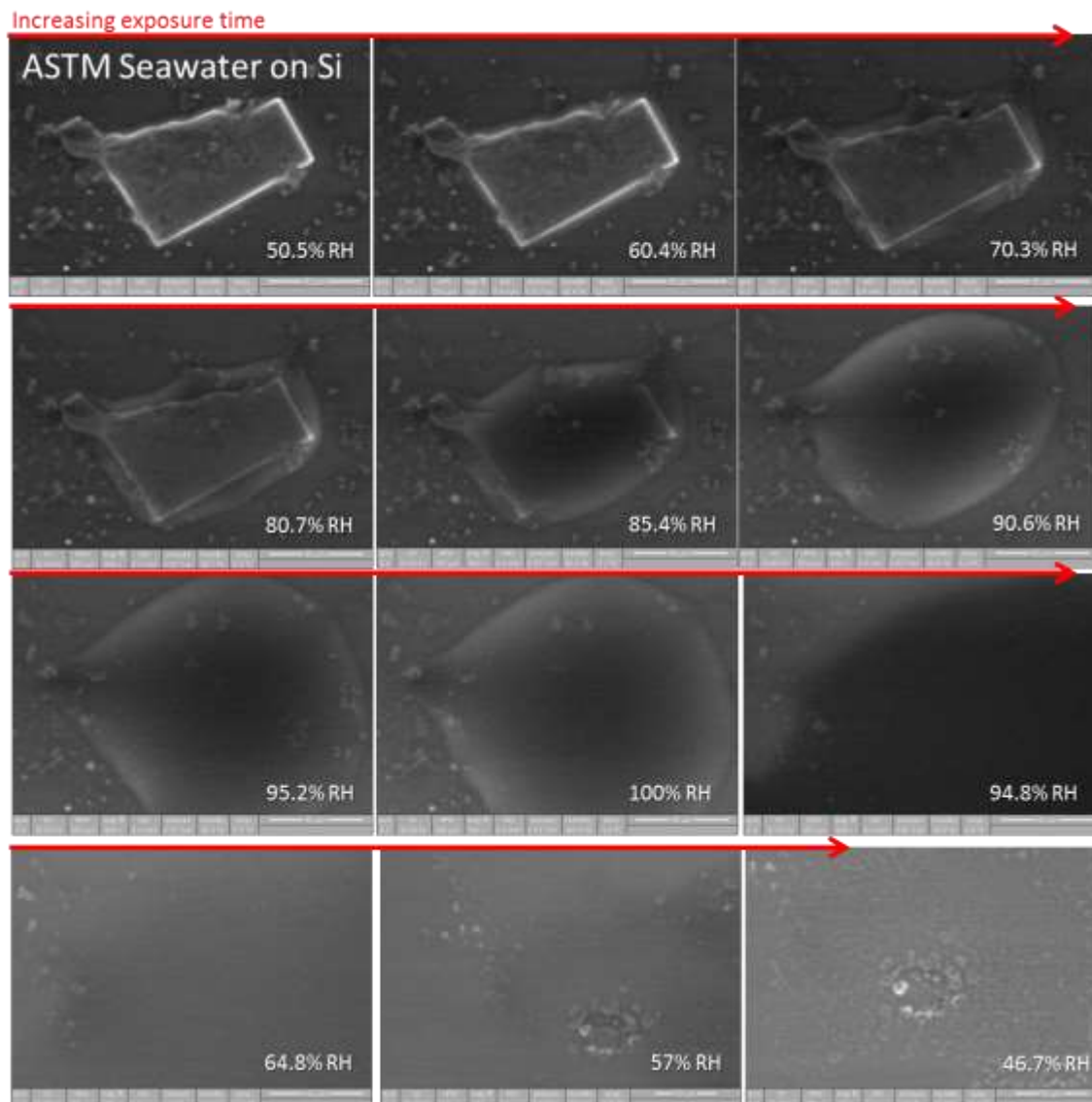


Figure 48. SEM micrographs of a) NaCl and b) ASTM Seawater on Si. Samples were exposed on a Peltier stage with dry salts and imaged while temperature was decreased at the stage. This caused an increase in localized RH as the vapor pressure condensed about the stage as the temperature decreased and evaporated as it was increased. Simultaneous imaging shows the wetting and drying cycle for both salts, but as temperature changes were involved, the deliquescence points are different from those expected at room temperature. Also, in both cases, some hysteresis is observed.

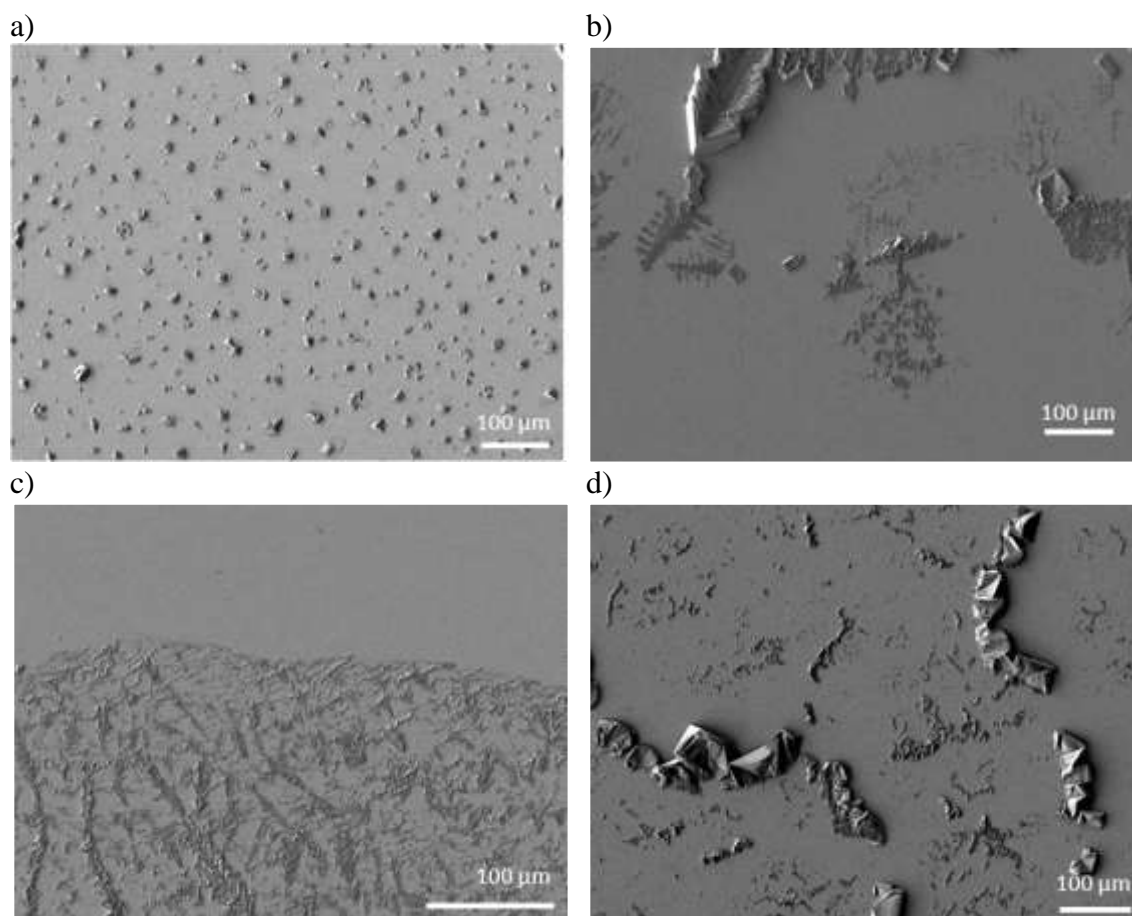


Figure 49. SEM images of unexposed samples with a) salt printing deposition of 1 M NaCl solution, producing about $161 \mu\text{g}/\text{cm}^2$ on UHSS, b) 1 M NaCl salt solution, about $138 \mu\text{g}/\text{cm}^2$ on UHSS, c) 1 M NaCl solution, about $220 \mu\text{g}/\text{cm}^2$ on UHSS, and d) ASTM-B-117 after 1 h exposure. All samples allowed to dry 15 min prior to imaging.

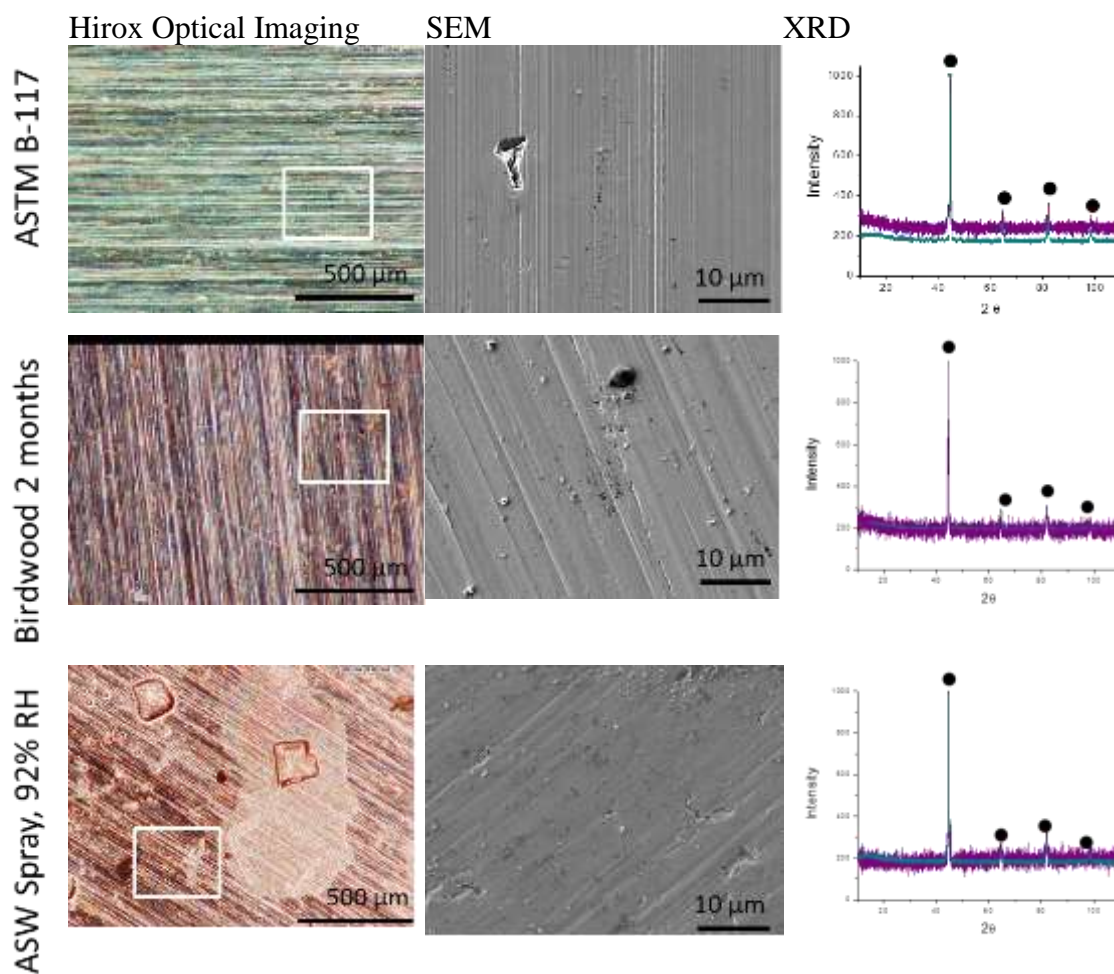
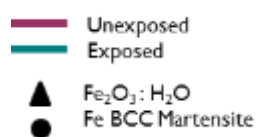


Figure 50. UNS S46500 Hirox optical imaging, SEM, and XRD of three exposure environments: ASTM B-117, Birdwood Golf course atmospheric exposure, and ASTM artificial seawater spray exposed at 92 % RH. XRD unexposed spectra shown in purple and exposed in green.



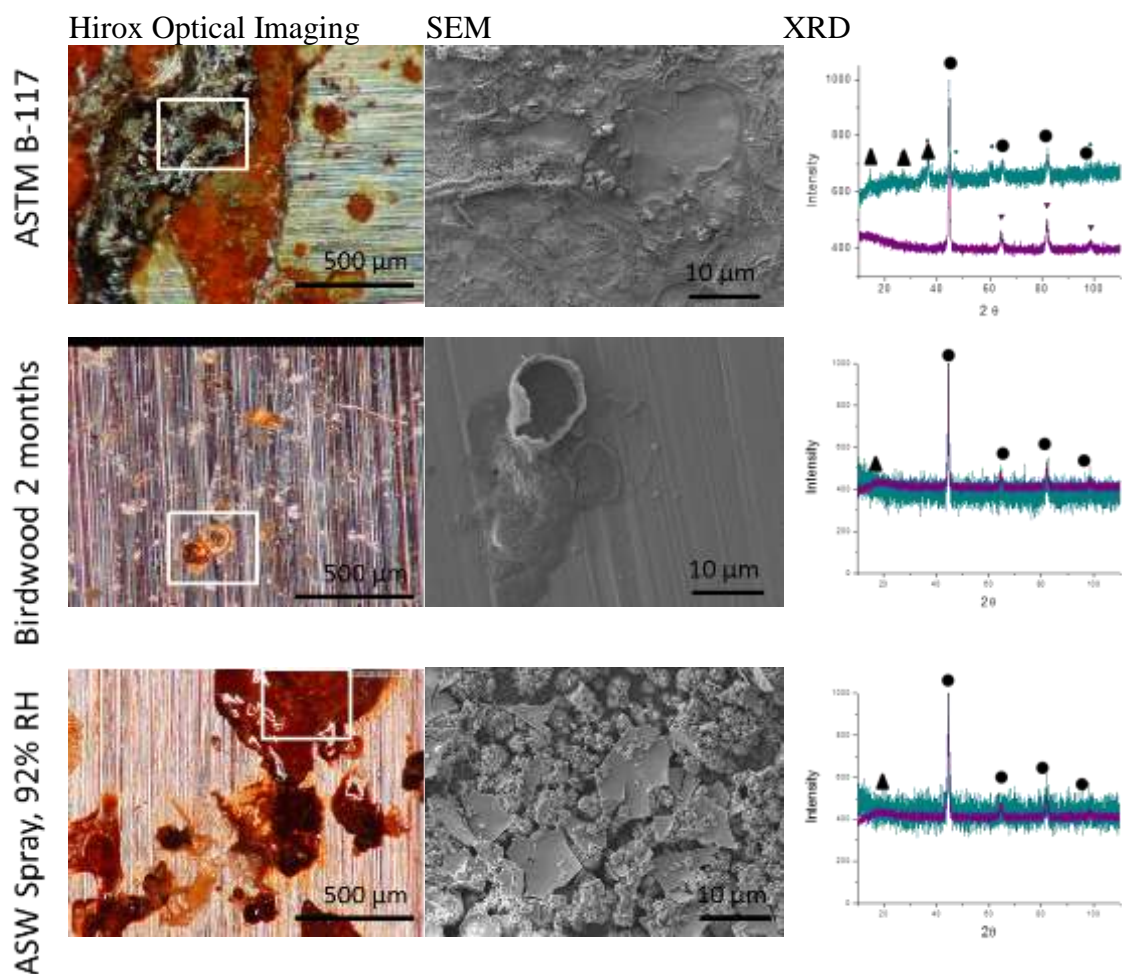
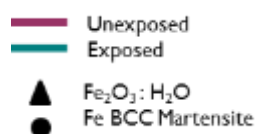


Figure 51. UNS K92580 Hirox optical imaging, SEM and XRD of three exposure environments: ASTM B-117, Bidrwood Golf course atmospheric exposure, and ASTM artificial seawater spray exposed at 92 % RH. XRD unexposed spectra shown in purple and exposed in green.



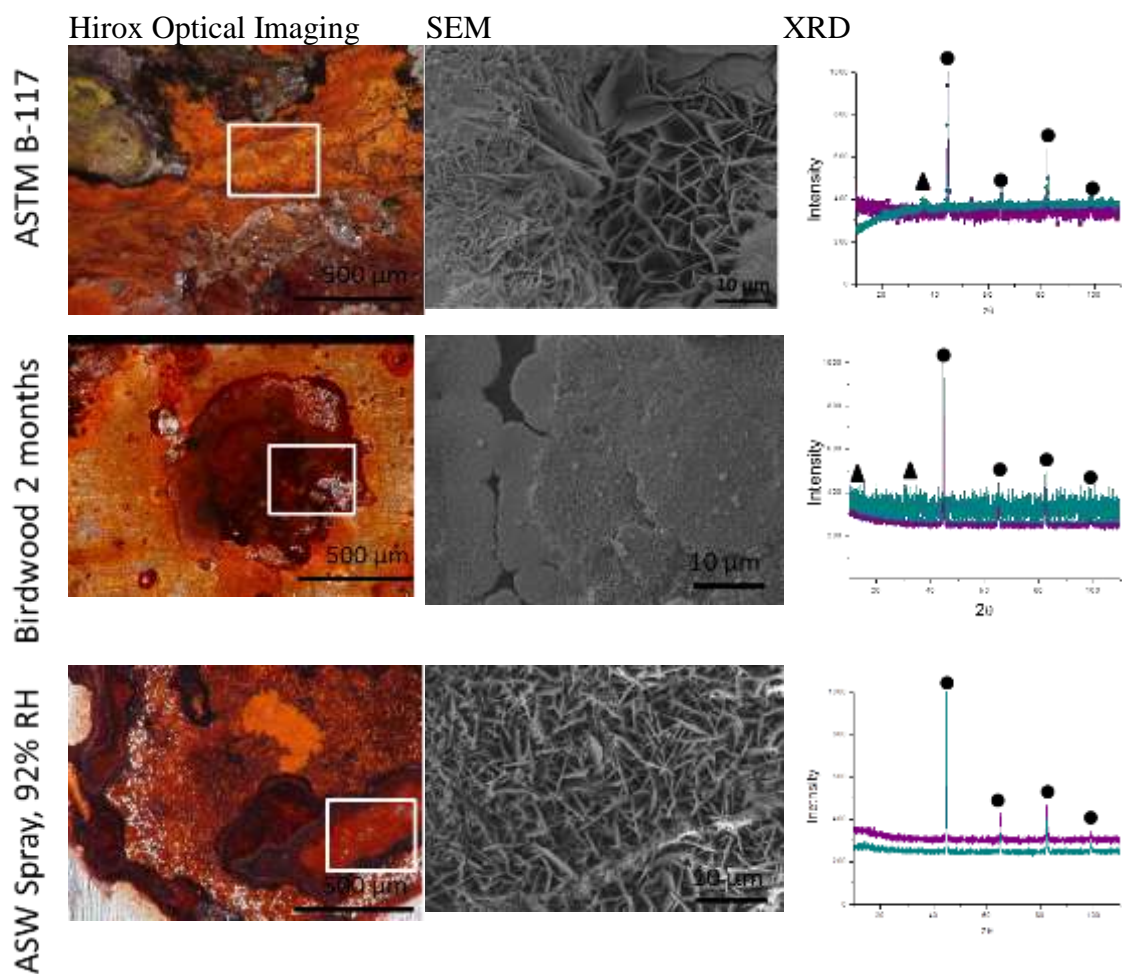
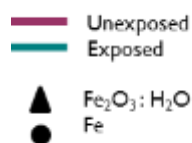


Figure 52. UNS G10180 Hirox optical imaging, SEM and XRD of three exposure environments: ASTM B-117, Bidrwood Golf course atmospheric exposure, and ASTM artificial seawater spray exposed at 92 % RH. XRD unexposed spectra shown in purple and exposed in green.



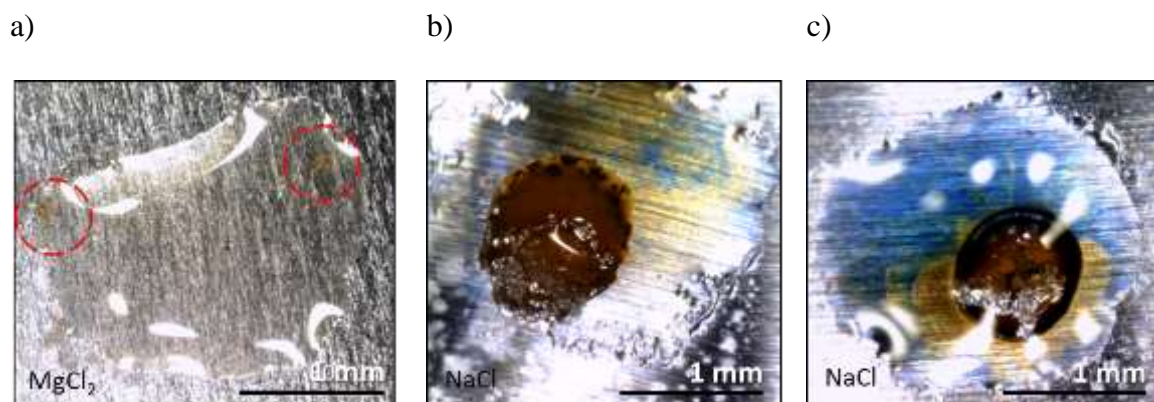


Figure 53. Example droplet exposures for 48 h at 99% RH with Universal pH indicator for a) UNS S46500, b) UNS K92580, and c) UNS G10180. Blue indicates alkaline areas, whereas orange indicates acidic areas. Droplet exposures were used to estimate size of anodic uptake areas across the various steels, 40 μm pits for UNS S46500 and 500 μm anodic areas for UNS K92580 and UNS G10180 applied for calculations in Figure 54.

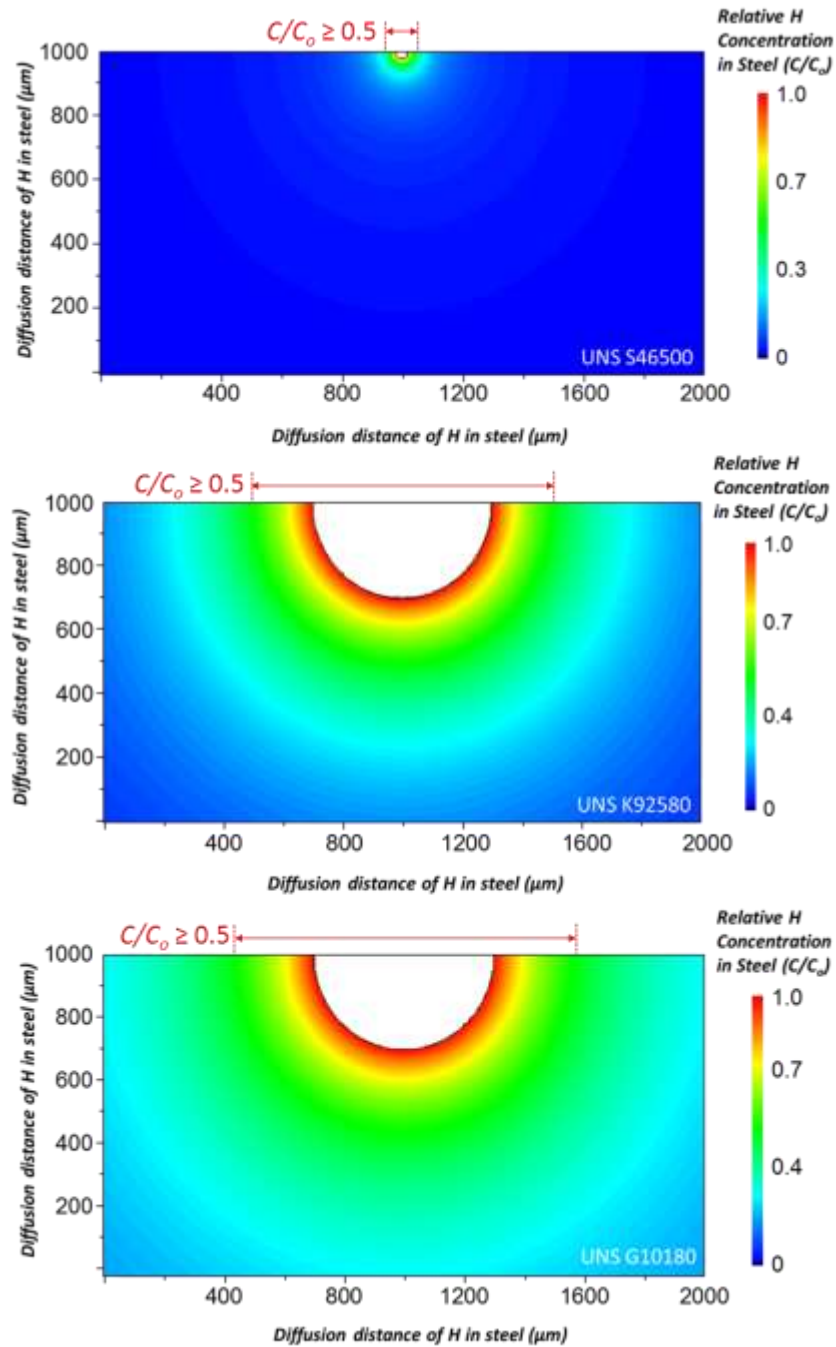


Figure 54. Relative H concentration for steady state radial diffusion of H from assumed dominant H uptake sites, for UNS S46500, assumed to be a pit of $d = 40 \mu\text{m}$, for UNS K92580 and UNS G10180, assumed to be an anodic site due to Evans cell formation of $d = 500 \mu\text{m}$. $D_{H,\text{eff}}$ assumed were $6.2 \times 10^{-9} \text{ cm}^2/\text{s}$, $6 \times 10^{-9} \text{ cm}^2/\text{s}$, and $1 \times 10^{-7} \text{ cm}^2/\text{s}$ respectively and exposure period was taken to be 10 days.

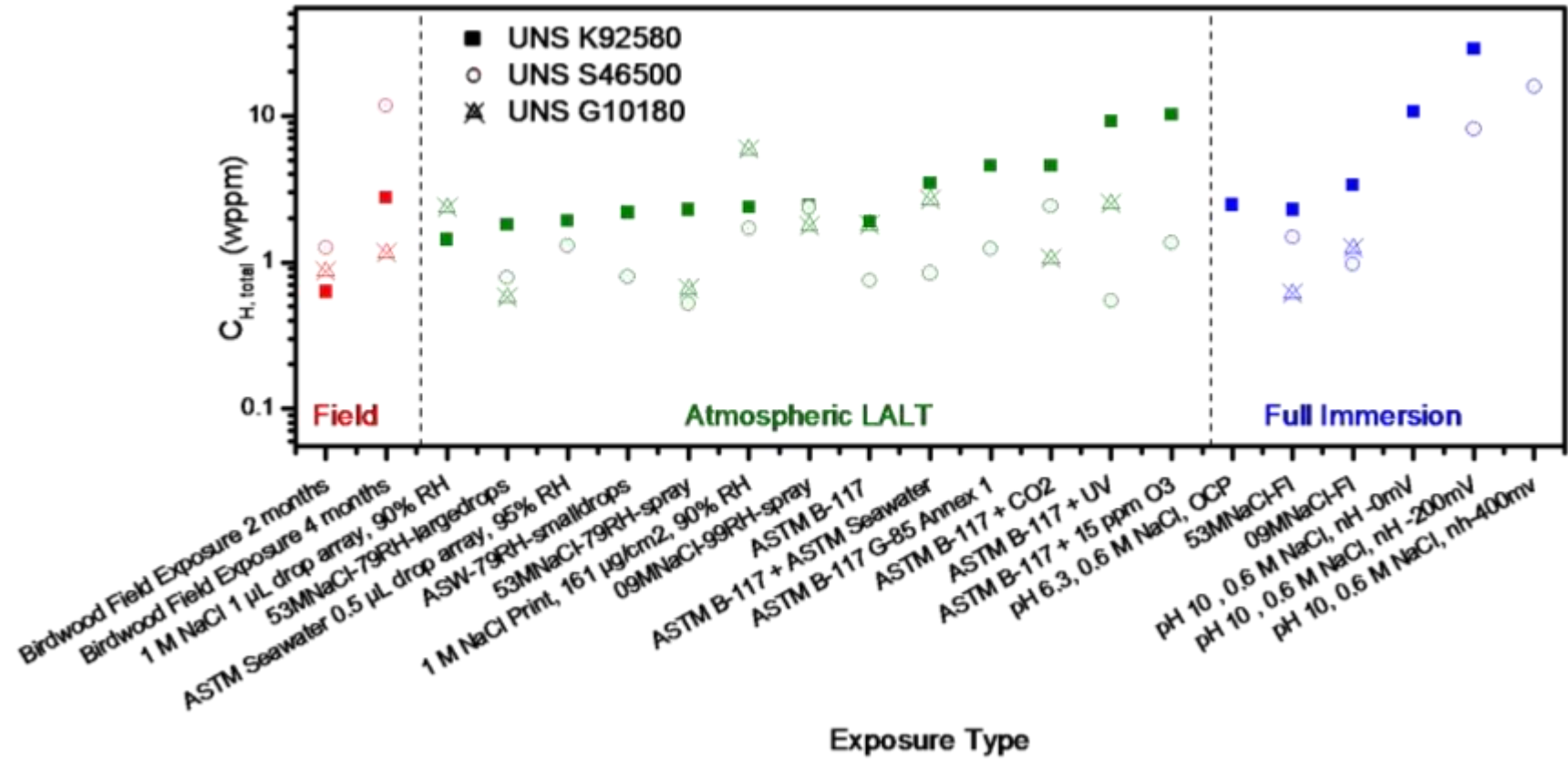


Figure 55. C_H total determined by TDS analysis for a wide range of laboratory ALTs, field, and full immersion pre-charging exposures. C_H was determined from ramped TDS and calibrated with LECO analysis.

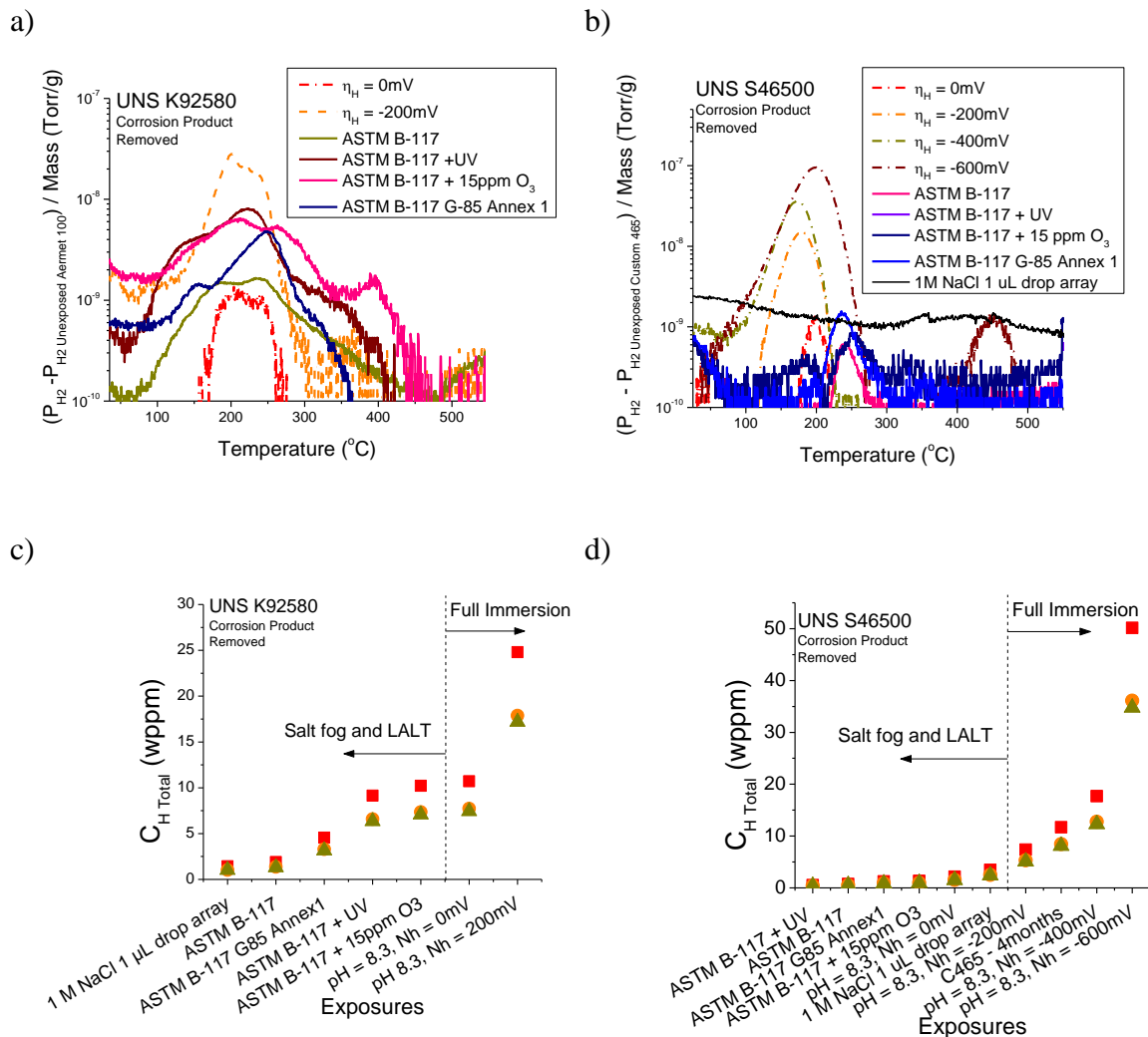


Figure 56. TDS hydrogen partial pressure spectra and CH total determined by TDS analysis for a select comparison of laboratory ALTs, field, and full immersion pre-charging exposures for UNS K92580 (a and c) and UNS S46500 (b and d). CH was determined from ramp rate TDS and calibrated with LECO analysis.

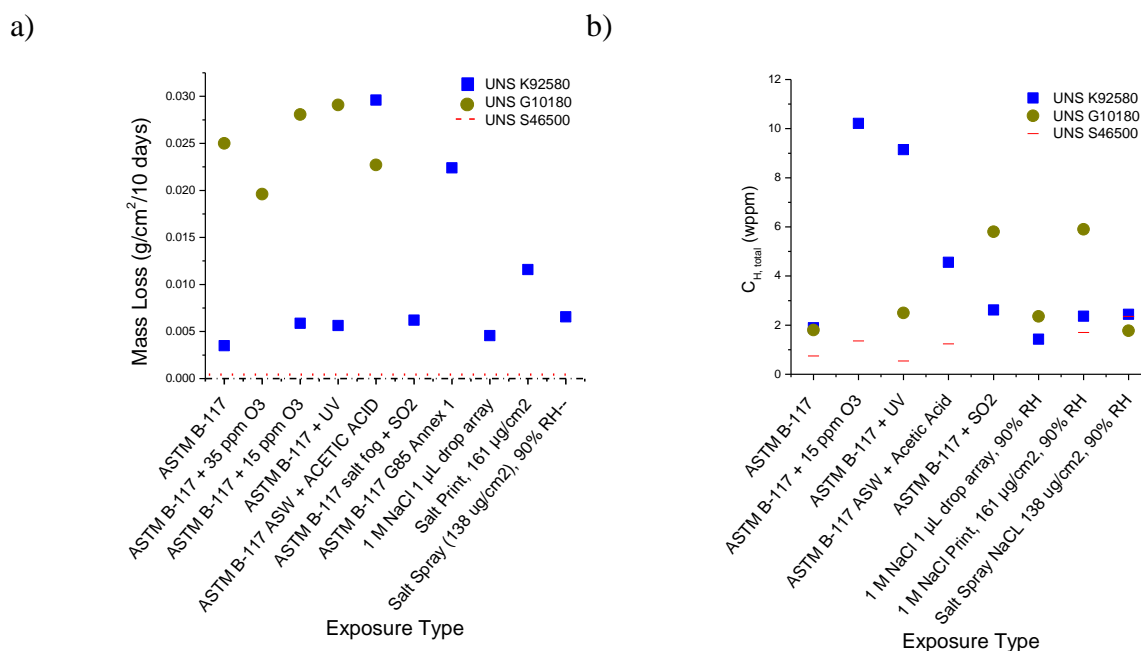


Figure 57. Selected a) mass loss and b) $C_{H, \text{total}}$ for LALT and salt fog exposures.

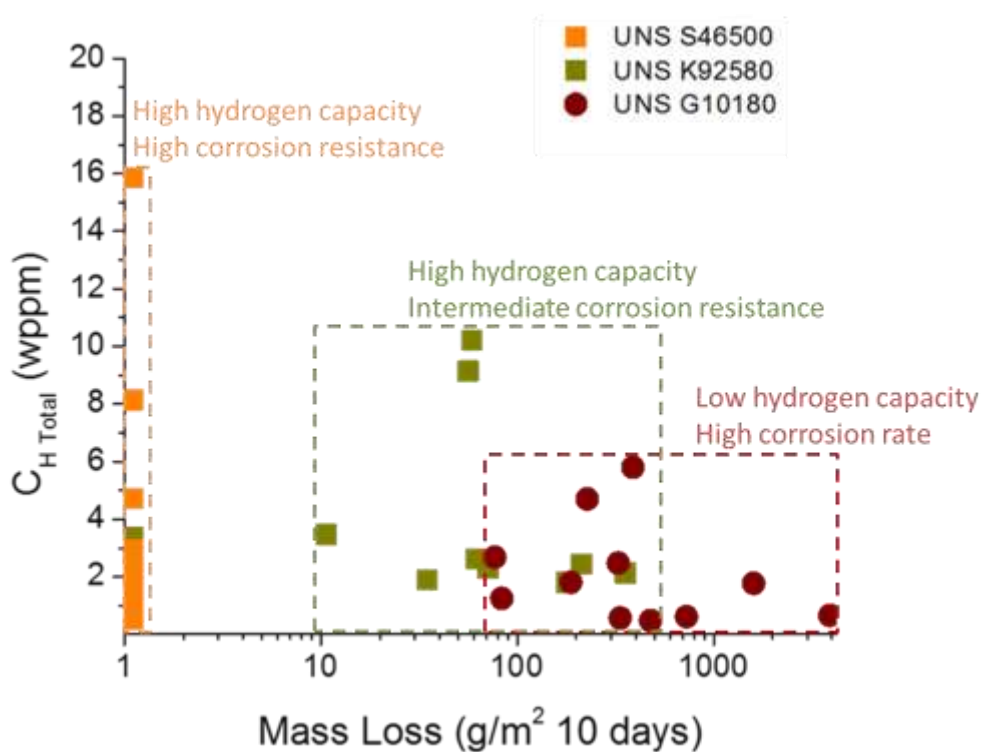


Figure 58. C_H Total vs. Mass Loss: Total hydrogen concentration vs. mass loss varies across alloy type.

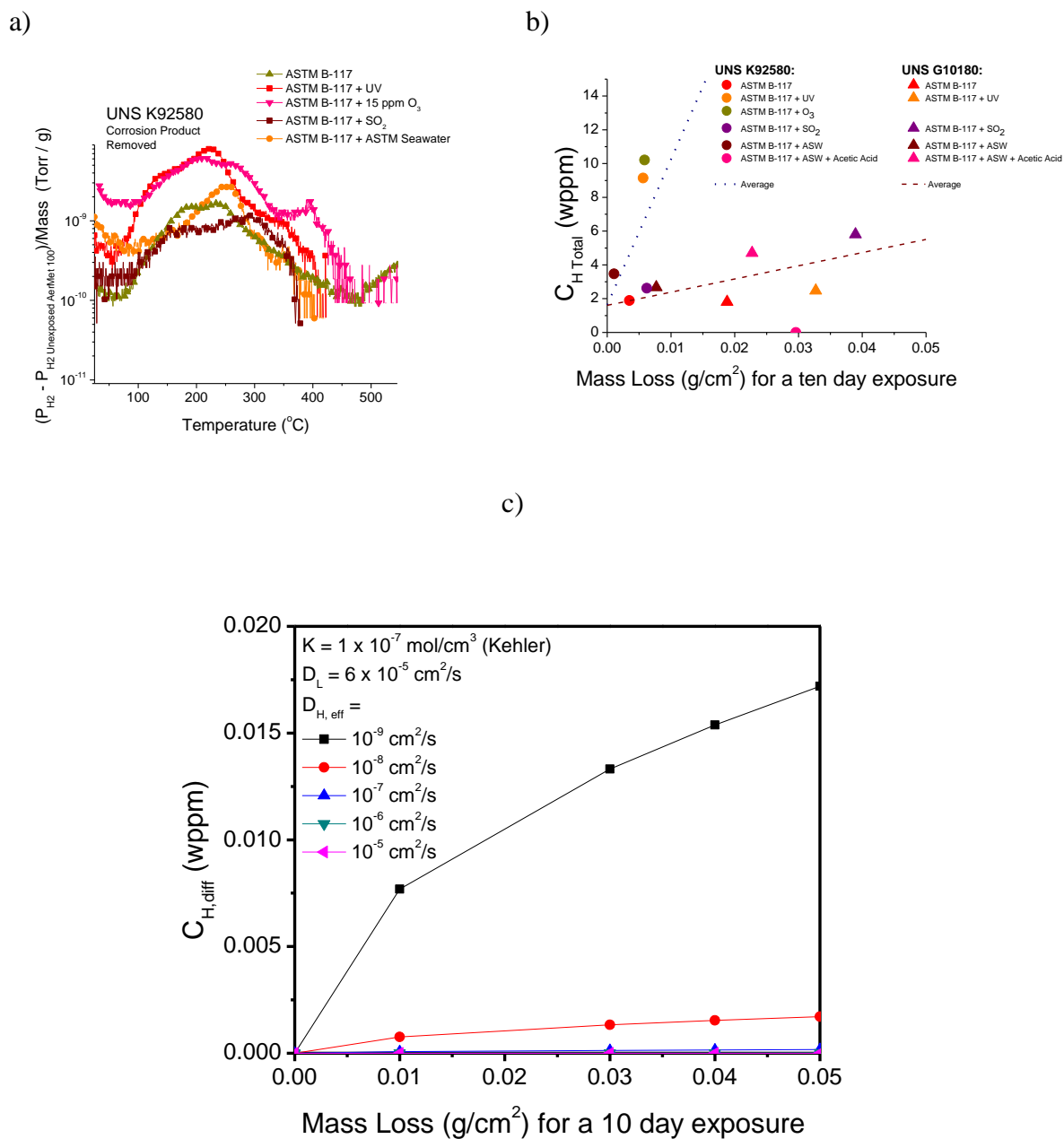


Figure 59. Within one similar environment, producing the same surface coverage, in this case ASTM –B-117 and modified B-117, $C_{H \text{ Total}}$ can be compared and scaled with mass loss. a) TDS spectra for UNS K92580 and UNS G10180 exposures, b) Estimated $C_{H,diff}$ vs. mass loss for a ten day exposure period assuming $Q_{HER} = 0 \%$ Q_C , and that $D_L = 6 \times 10^{-5} \text{ cm}^2/\text{s}$ and $K = 1 \times 10^{-7} \text{ mol/cm}^3$.

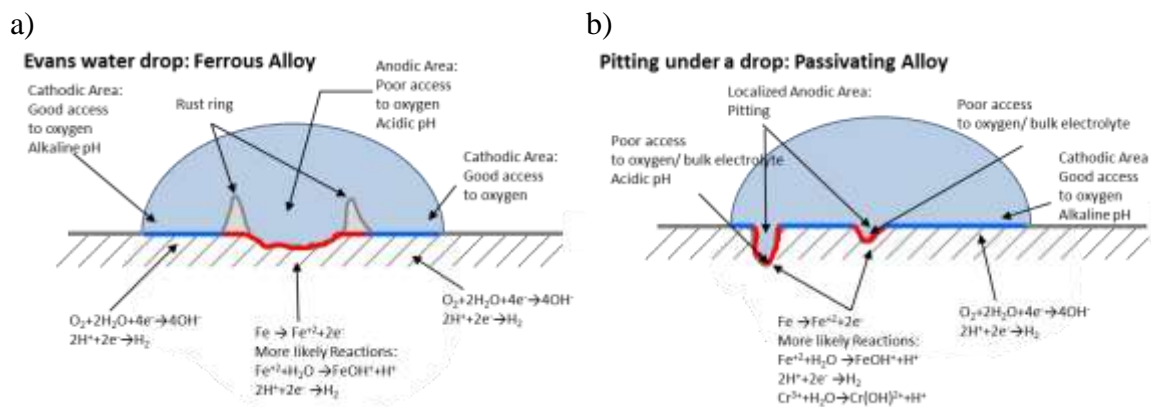


Figure 60. Schematic of a) Evans droplet cell and b) pitting droplet cell. Blue indicates alkaline pH, while red indicates acidic pH.

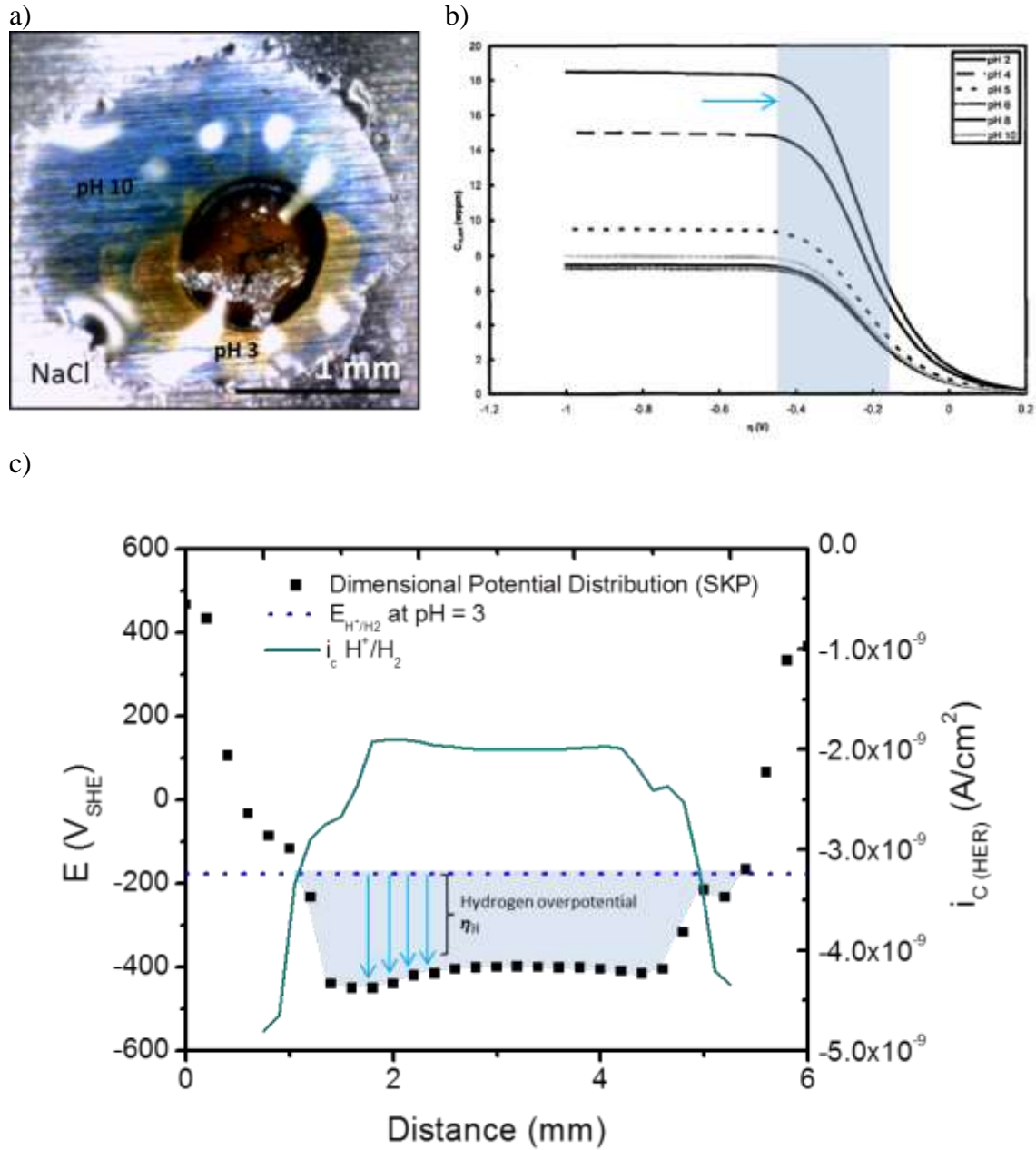
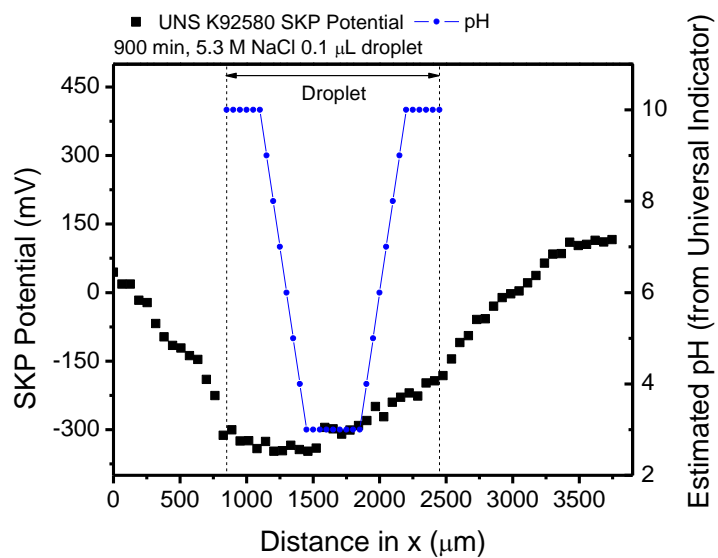
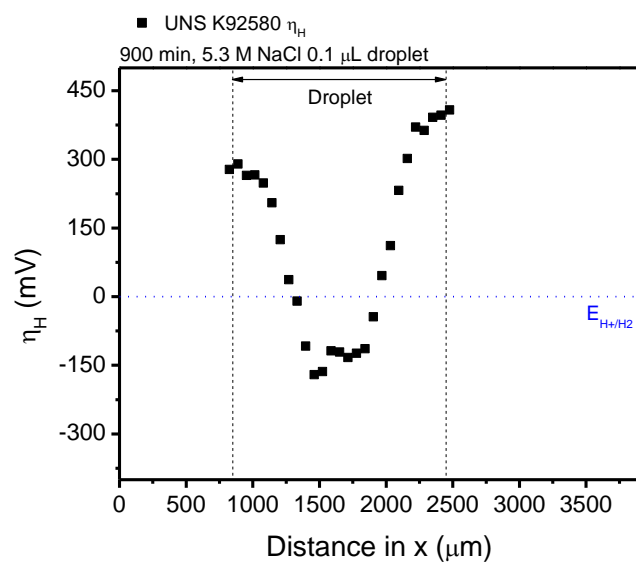


Figure 61. a) pH map of using universal indicator of NaCl droplet on carbon steel exposed for 48 h at 99% RH, indicating Evans cell formation. b) Reaction rate model results for UNS K92580 showing the relationship between $C_{H,diff}$ and η_H . Area highlighted in blue predicts the range of $C_{H,diff}$ for the overpotentials shown in c. c) SKP potential across a NaCl drop on carbon steel as measured by Mansfeld et. al.[46] Green line indicates the cathodic current density due to hydrogen and the blue shaded area represents the hydrogen overpotential.

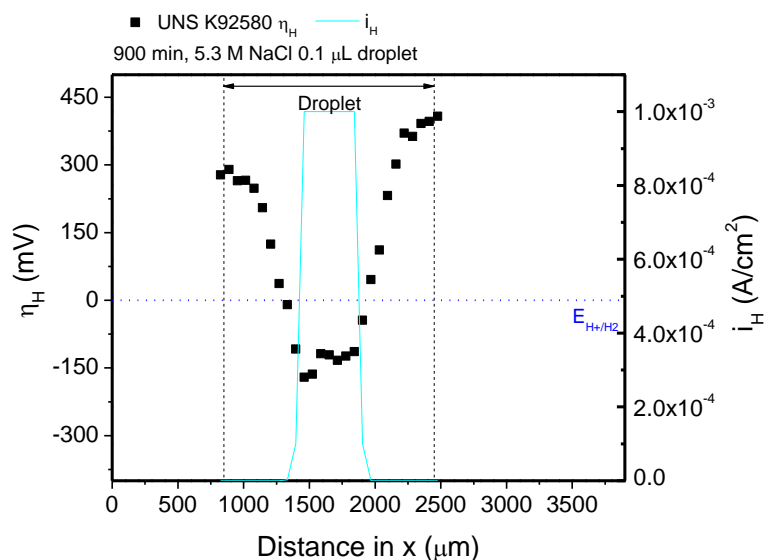
a)



b)



c)



d)

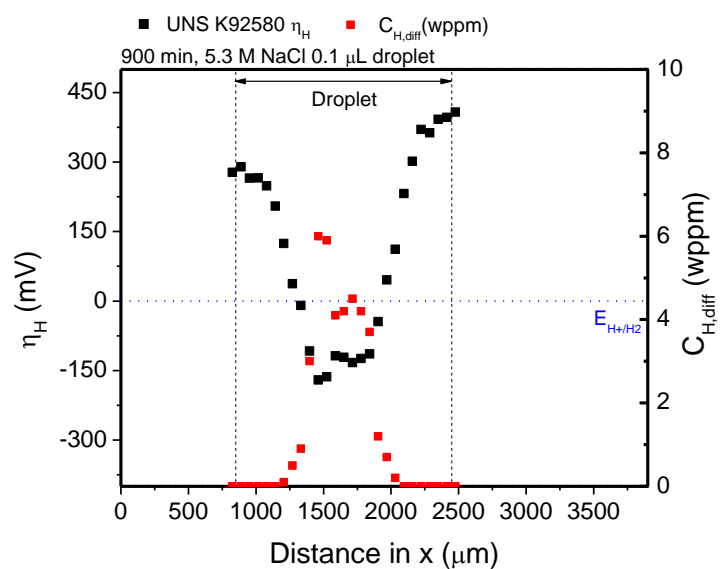
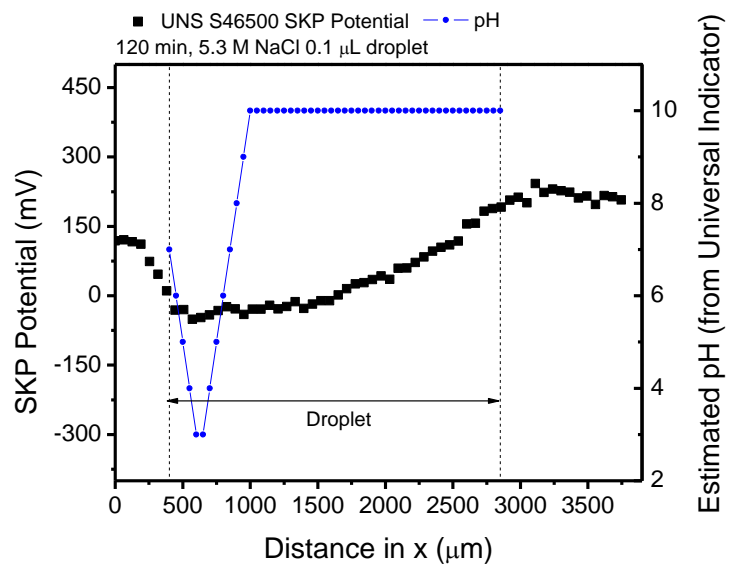
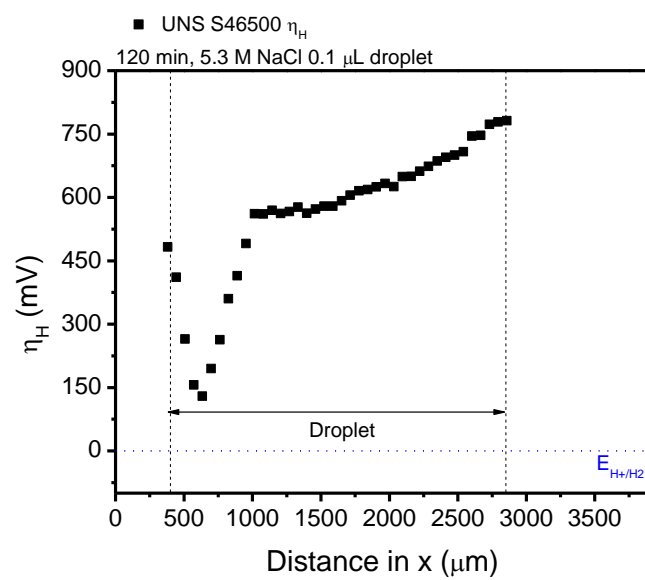


Figure 62. a) pH and potential map of UNS K92580 exposed to 5.3 M NaCl 1 μL droplet for 900 min. pH was estimated using Figure 53-c. Potential measurements were taken in the SKP. b) η_H vs distance across the droplet area calculated from SKP potential. c) η_H and i_H vs distance across drop. Green line indicates the cathodic current density due to hydrogen. d) Predicted $C_{H,diff}$ from calculated η_H and estimated pH using data for electrochemical extraction measurements for UNS K92580.[42]

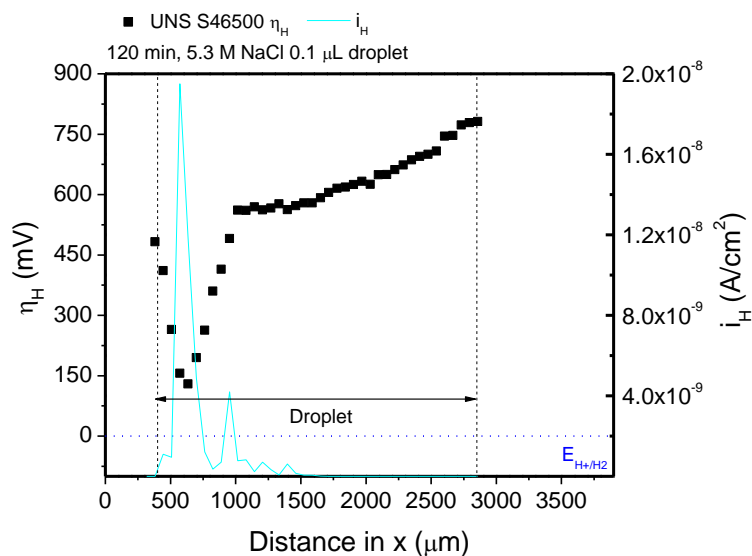
a)



b)



c)



d)

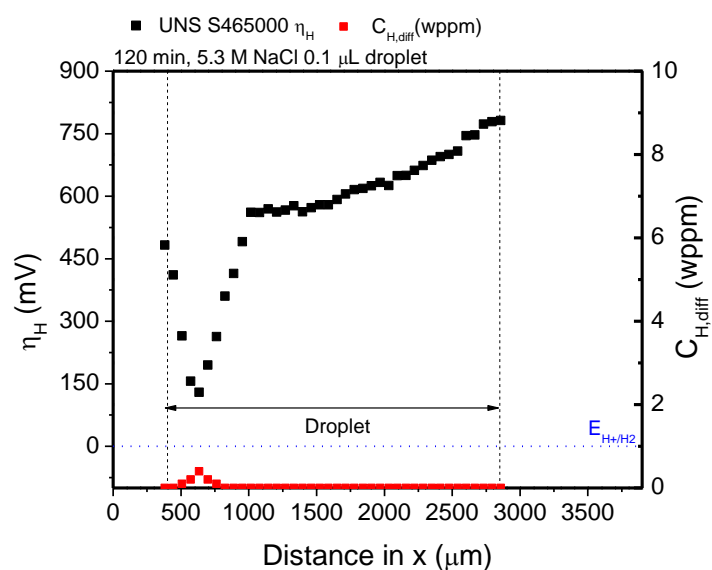
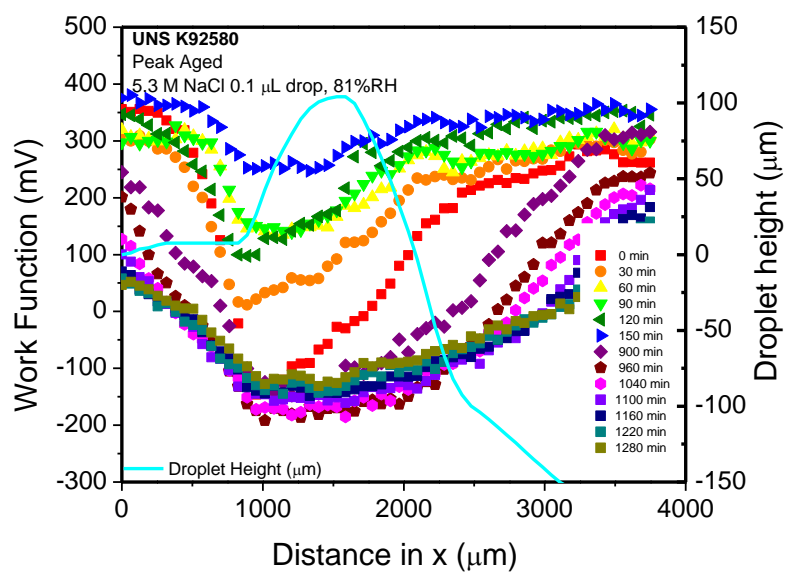
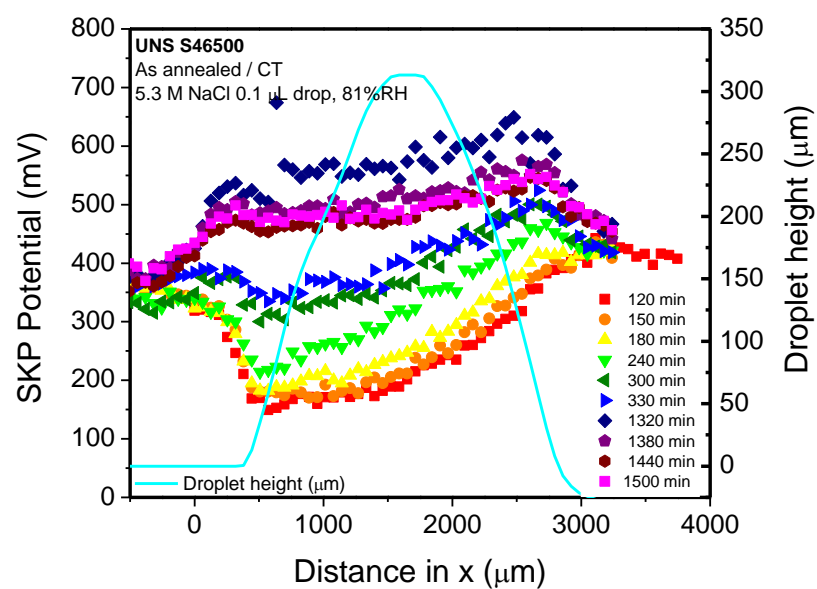


Figure 63. a) pH and potential map of UNS S46500 exposed to 5.3 M NaCl 1 μL droplet for 120 min. pH was estimated from Figure 53-a. Potential measurements were taken in the SKP. b) η_H vs distance across the droplet area calculated from SKP potential. c) η_H and i_H vs distance across drop. Green line indicates the cathodic current density due to hydrogen. d) Predicted $C_{H,diff}$ from calculated η_H and estimated pH using data for electrochemical extraction measurements for UNS S46500.[42]



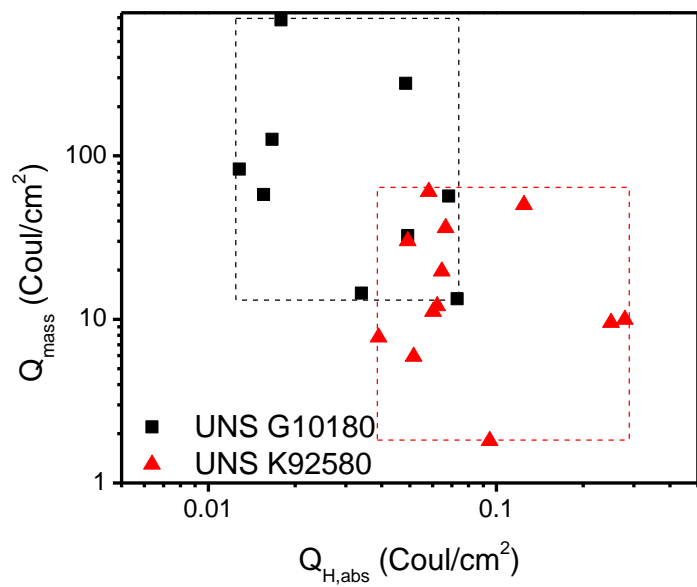
a)



b)

Figure 64. Droplet height and potential map over time of steel exposed to 5.3 M NaCl 1 μ L droplet at 78% RH. Potential measurements were taken in the scanning kelvin probe (SKP). a) peak aged UNS K92580 and b) UNS S46500 as annealed/CT.

a)



b)



Figure 65. a) Graph of calculated Q_{mass} vs. $Q_{\text{H,abs}}$ based on mass loss and $C_{\text{H,total}}$ for selected exposures. B) Schematic of relationship/quantities of different charges.[16, 23, 59]

CHAPTER 3. Spatial Determination of Diffusible Hydrogen Concentrations in UHSS from Uniform Pre-Charging Using the Scanning Kelvin Probe

3.1. Abstract

Determination of hydrogen uptake, partitioning, and trapping in ultra-high strength steels (UHSS) exposed to increasingly severe atmospheric environments is a significant topic of research interest. However techniques for local and/or spatial H determination are currently lacking. In UHSS stainless steels under atmospheric exposure, acid pits formed by the dissolution, hydrolysis, and acidification mechanism are prone to H production and uptake. Determination of such local uptake and concentration mapping is challenging on small, sub-mm, length scales. In this chapter, the scanning Kelvin probe (SKP) explored as a method for localized H detection. Two conditions of a secondary hardened martensitic stainless steel, the as annealed/CT and H900 temper of Fe-11Ni-12Cr-1Mo-0.005C-0.02Mn (wt%) were compared to a non-stainless UHSS, UNS K92580, and a low carbon steel, UNS G10180. Predetermined uniform diffusible H concentrations, quantified using electrochemical extraction methods after homogenous cathodic charging, were calibrated with changes in the surface potential measured by the SKP in humid air at 57% RH. The potential measured by the probe tip in the SKP is found to be correlated with diffusible H concentrations when the corrosion rate of the metal is significantly lower than the hydrogen oxidation current upon hydrogen egress from charged steels. At room temperature, this situation is favorable in materials with high diffusible H levels and low corrosion rates. These calibrations were then utilized to estimate diffusible H concentrations spatially proximate to atmospherically pre-exposed and pitted surfaces based on SKP line and area scans detailed in Chapter 5. The

development of these techniques adds to a suite of instruments that enable better determination of localized H uptake and may help in the future for damage prediction.

3.2. Introduction and Background

Most martensitic age-hardenable stainless alloys exhibit a much lower resistance to localized corrosion than low strength, highly alloyed stainless steels. Moreover, wetting/drying events in Cl^- environments induce pitting of stainless steels especially at or near the deliquescence point of salts.[1, 2] H production and uptake in pits formed during atmospheric exposure can result.[3] In turn, local H uptake increases diffusible H concentrations and can thus lead to H environment assisted cracking.[4] As discussed, hydrogen uptake has been fairly well quantified in full immersion environments and at the meso-scale. [5-8] However, as shown by Chapter 2, techniques for spatial detection at the sub-mm length scale, specifically lateral detection necessary for mapping H concentrations produced by droplets or in other confined spaces or volumes, are still lacking. There have been previously established studies with a variety of local scale, sub-mm techniques, but as outlined in Chapter 1, the development of techniques with local lateral detection and quantification is still lacking.[9-17]

Of interest to this chapter are a range of scanning techniques that may be possibly applied for local H detection. The scanning vibrating electrode technique (SVET), has been shown promising for interrogating the effects of H charging. Cheng et al. studied in-situ charged tensile samples of X-70 pipeline steel in near neutral pH NS4 solution.[18] Also, the SVET has the capability to detect changes in current over small areas, at the μm

scale, as evidenced by a study of pitting in 304 stainless steel in 1 M NaCl, pH 3.[19] In theory, this is a viable technique for H detection, however, currently, the SVET has not been applied for measurement of H concentrations.

The scanning electrochemical microscope (SECM), as mentioned previously, has been applied for localized detection of the effects of H pre-charging on X70 carbon steel, in-situ detection of H concentrations in an Fe foil exposed to borate buffer solution through a permeation method, and detection of localized HER on an actively corroding Mg alloy.[20-22] Issues of resolution of H detection in solutions as well as concentration dependence have not yet been explored in the SECM. The Scanning Kelvin Probe (SKP) however, has been shown a viable option for localized H detection and has been previously correlated with H concentrations. [23, 24] Advantages of the SKP over the SVET or SECM, include the ability to perform in-situ atmospheric measurements, measurements with thin films, or measurements in the “dry”.[25] Also, as will be discussed later, resolutions issues related to diffusion of H^+ in solution, as well as dragging and movement of electrolyte species and concentration alteration by the probe tip are not a concern in the SKP, as the measurement occurs without submersion of the tip in the electrolyte.

3.2.1. SKP and Corrosion Characterization

3.2.1.1. Calibration and Resolution

The SKP has been applied for quite some time as a tool to examine localized corrosion viewed through potential scans across a sample surface.[26] Stratmann developed one of the original applications of this technique for thin film analysis.[26-28] The SKP can be calibrated to a corrosion potential using a comparison of the SKP potential measured under a thin electrolyte and an OCP measurement of the same materials in the same bulk solution (Figure 66).[26] The OCP can be related to the SKP potential through understanding the basis for the SKP potential measurement. As the probe tip and the sample in the SKP are connected from the backside by a conductive wire, the Fermi level in the tip and sample are equal. The potential required to transfer an electron from the surface of the sample to the probe tip can be described in three parts, ΔE_1 , the energy to transfer an electron from the sample to the thin film electrolyte, ΔE_2 , the energy to transfer an electron from the thin film to the gas phase, and ΔE_3 , the energy to transfer an electron from the gas phase into the probe tip.[27] These energies can be described as follows:

$$\Delta E_1 = -(\mu'_e - F\phi') + (\mu_e^{El} - F\phi^{El}) \quad \text{Equation 43}$$

$$\Delta E_2 = -(\mu_e^{El} - F\Psi^{El} - FX_{El}^{Gas}) \quad \text{Equation 44}$$

$$\Delta E_3 = -A^{Tip} - F\Psi^{Tip} \quad \text{Equation 45}$$

Where, μ'_e and μ_e^{El} are the chemical potentials of the electron in the metal and electrolyte (J/mol), ϕ' and ϕ^{El} are the Galvani potentials of the electron in the metal and electrolyte (V), Ψ^{El} and Ψ^{Tip} are the Volta potentials of the electrolyte and the probe tip

(V/mol), X_{El}^{Gas} is the surface potential of the gas/electrolyte interface (V), A^{Tip} is the work function of the probe tip in a given atmosphere (eV/mol), and F is Faraday's constant (C/mol). Rearranging, these potentials sum to zero, therefore[27]:

$$\Delta\phi_{El}^M - \frac{\mu_e^M}{F} = \frac{A^{Tip}}{F} - X_{El}^{Gas} + \Delta\Psi_{El}^{Tip} \quad \text{Equation 46}$$

Where $\Delta\phi_{El}^M - \frac{\mu_e^M}{F}$ is the half cell potential ($E_{1/2}$) of the metal/electrolyte. Therefore, as:

$$E_{corr} = (E_{1/2} + \Delta E) + E_{ref} \quad \text{Equation 47}$$

Where ΔE is the difference in the half cell potential to the corrosion potential and E_{ref} is the reference electrode potential,

$$E_{corr} = \Delta\Psi_{El}^{Tip} + const. \quad \text{Equation 48}$$

As the workfunction is constant and the surface potential at the gas/electrolyte interface is small and assumed negligible, the corrosion potential can be related to the difference in Volta potentials ($\Delta\Psi_{El}^{Tip}$), which is the potential measured at the SKP tip and the addition of a constant representing the properties of the reference electrode used in corrosion measurements that allows for calibration between the corrosion potential and SKP potential.[26, 27]

In a second method, which is based on the same principle, the SKP potential was calibrated by scanning across a Cu/CuSO₄ electrode (a copper cup with a well containing saturated copper sulfate solution) prior to measurements of in-situ exposed samples. Through both methods, the SKP potential is calibrated to corrosion potentials.

With regards to resolution, the SKP is limited by the probe geometry, tip size, and the distance of the tip to the sample.[29, 30] As a circular sample area decreases, or as the mean probe tip to sample distance increases, the inability of the SKP to discern the difference between two unequal Volta potentials increases.[29] Consider a circular disk of potential V_1 surrounded by a surface potential of V_2 . When the diameter of the circular sample area is less than or equal to 0.65 times the tip to sample distance, the difference in potentials V_1 and V_2 measured by the probe tip will be underestimated by 50%, and this increases with decreasing sample area or increasing sample to tip distance.[29] A calculation can be made to estimate the difference in normalized potential between V_1 and V_2 ($V_2 - V_1 = \Delta E_{a,d}$) based on the probe tip to sample surface height, d , and the distance from the probe tip position in x to the change in the potential interface, a (Figure 67-a):[29, 31]

$$\Delta E_{a,d} = \frac{1}{2} + \frac{1}{\pi} \cdot \arctan\left(\frac{a}{d}\right) + \frac{1}{\pi} \cdot \frac{a \cdot d}{a^2 + d^2} \quad \text{Equation 49}$$

Example calculations have been made for varying d and $\Delta E_{a,d}$ vs. d values are plotted in Figure 67-b. The probe tip size is accounted for when determining the correction to the lateral spread of a measurement. The probe diameter is taken as ΔL_{50} , when two points

on the sample surface equal the difference between $\Delta E_{a,d}$ at 0.25 and 0.75 (shown on Figure 67-b) and can be calculated by:

$$\Delta L_{50} = 0.884d + 0.4D \quad \text{Equation 50}$$

Where D is the probe tip diameter. Example calculations are plotted in Figure 67-c for a range of D , and it can be seen clearly that as the diameter and tip to sample distance decrease, the correction to the lateral spread decreases. Therefore, not only is a smaller tip size advantageous for increasing SKP resolution, it aids in limiting lateral spread between two unique Volta potentials, further enhancing resolution. The sample and tip geometry and placement are essential to optimization of the SKP resolution.

3.2.1.2. Application of the SKP for Corrosion Studies

Mansfeld, et al. applied the SKP technique to the measurement of potential across atmospherically exposed droplets, where they were able to corroborate the establishment of an Evans cell across a bare steel sample.[32] Bare carbon steel was exposed to a drop of 0.05 M NaCl with pH indicator and measured in-situ in the SKP. Rings of established potential distribution correlated with areas of different pH, indicating the zones of low potential anodic acidic areas which corroborated with a blue indicator (potassium ferricyanide and phenolphthalein) due to Fe^{2+} formation at the center of the drop and a higher potential at the cathodic alkaline areas with pink indicator due to the OH^- formation near the edge of the drop.[32] Other in-situ SKP atmospheric studies have determined that anode/ cathode separation was established within 1mM to 1M NaCl

droplets on steel, zinc, and aluminum along with the variation in SKP potential with time for a 3.5 wt % NaCl droplet on AA7075.[33-35] Effects of varying RH on exposure and measurement in the SKP, shows that even below the deliquescence points of salts, corrosion can occur under NaCl particles on pure Cu.[36] Areas pre-exposed to salt, even below deliquescence conditions, exhibited a decrease in SKP potential which the authors correlated with anodically activated sites, indicating corrosion occurred at RH levels below the deliquescence point.[36] An increase in the SKP potential can also signify a growth in an oxide layer, in this case in 5% NaCl spray on an atmospherically exposed UHSS.[37] Since the SKP potential is the sum of the potential differences (Equation 48), this can include the potential difference across the oxide which is dependent on thickness, composition, and conductivity. If the contribution of the oxide layer is significant, the oxide layer can increase the SKP potential as it increases in size and conductivity decreases.[37]

With scanning Kelvin probe force microscopy (SKPFM) techniques, corrosion detection methods can be furthered to a more localized scale, from the 10 – 100 μm in the utilization of the SKP to 100 – 1000 nm length scale for SKPFM. One example of enhanced information at this localized scale established that corrosion active sites in MgCl_2 solutions at low and high RH possessed different SKPFM potentials and these were based on microstructural features for cold rolled 2205 duplex stainless steels.[38] While these methods can give insight into the establishment of the electrochemical cell under varying conditions and on different materials or presence of oxides, they do not provide details concerning the local hydrogen production and uptake. These examples of

use of the SKP and SKPFM for the study of corrosion behavior occur in situations where the potential established at the electrolyte interface is dominated by corrosion reactions and not H oxidation.

3.2.2. SKP as a Method for Local Hydrogen Characterization

As mentioned in the introduction, the SKP, SKPFM, and SKP combined with secondary ion mass spectrometry have been used as viable techniques for spatial H detection with both lateral detection and depth profiling with a H resolution of as low as 0.01 atomic ppm.[23-25, 39-43] SKP techniques have been established in a permeation mode setup, where a thin film of Pd is deposited on the exit side of a sample and the sample is either H charged or atmospherically exposed under conditions leading to hydrogen production on the entry side (Table 23). The SKP potential is measured on the Pd exit side surface, and a depression (negative shift) in the potential is correlated to increased H concentrations. With this technique, one previous study examined a scribe in galvanized steel exposed to 0.1 M NaCl (Figure 68). The SKP potential was measured on the Pd coated backside, thus the effect of H and not the galvanic couple potential between steel and zinc dominated, and a decrease in the potential near the scribe with an evolution of SKP potential with time was observed.[39] In another study the evolution of SKP potential measured with time after cathodic pre-charging of an iron foil in Na₂SO₄ solution was observed on the Pd coated backside in synthetic air at 95% RH.[42] As time increased post-charging, the change in potential between the charged and uncharged zones decreased, indicative of desorption of H from the metal. Finally, a third study explored the effects of atmospheric exposure on the evolution of the permeation SKP

potential of zinc plated iron and carbon steel with coating defects under NaCl droplets.[43] Defects were created in the zinc coating, exposed to 0.5 M NaCl droplets under atmospheric conditions at 95% RH. SKP potential measurements were taken on the reverse side, and a depression in the SKP potential was observed in the exposed area, indicating the detection of H even under atmospheric charging conditions. These studies indicate both the effects of H on the SKP potential, as well as the spatial detection capacity. SKPFM studies have expanded similar H detection techniques to a more localized scale, however it should be noted that in SKPFM, due to the reverse in the potential effects in the measurement technique, increased potential is associated with increased H concentrations. Studies have been performed using SKPFM to examine H concentrations in pre-charged Al Alloys both with lateral [14] and with depth profiling combined with secondary ion mass spectroscopy.[24] Another study applied the SKPFM for the determination of microstructure dependent adsorption of H as well as local kinetics in H charged twinning-induced plasticity austenitic stainless steel.[44] A third study explored the local H concentrations with time post-H charging at a crack tip in an 18 Ni maraging steel.[45] These SKPFM techniques display the possible application of higher resolution techniques, however, except from the examples by Rohwerder et al., there has been a lack of quantification of H concentrations and calibration of the SKP potential to known H concentrations.[25] While these SKP and SKPFM studies are at the cutting edge of employing localized hydrogen detection techniques, they have yet to be applied to atmospheric corrosion with localized H quantification.

In this chapter, the recently developed technique of SKP for spatial H detection is employed to map H concentrations for calibration of the change in the SKP potential with known $C_{H,Diff}$. Electrochemical experiments as well as calibration experiments are performed to further optimize the SKP technique. Hydrogen concentrations produced in a range of pre-charging environments were determined through the Barnacle Cell technique.[6] Similarly pre-exposed samples were then measured in the SKP under controlled RH conditions to correlate the change in potential with known H concentrations. Also examined were the effects of time post-charging, pre-charging exposure size, and the %RH of the SKP measurement environment. The SKP technique is further developed in Chapter 5 for both lateral detection across areas pre-exposed under atmospheric corrosive environments and depth detection with cross-sectioned samples when pits are formed under atmospheric exposure.

3.3. Experimental Procedures

3.3.1. Materials

The material compositions for the secondary-hardened martensitic steels are given in Table 20 and material properties in Table 21. Samples of UNS K92580 were tested in the peak-aged condition and for UNS S46500, in both the as annealed/CT and the H900 temper. One advantage of these steels for use with the SKP measurement techniques are the slow $D_{H,eff}$, ranging from $3.1 \times 10^{-9} \text{ cm}^2/\text{s}$ to $8.96 \times 10^{-9} \text{ cm}^2/\text{s}$ as determined by thermal desorption spectroscopy.[7] This enables mapping without substantial outgassing or redistribution during the transfer time from pre-exposure to initial measurements.

3.3.2. Evaluation of the Effect of Electrochemical Hydrogen Pre-charging

A range of electrochemical experiments were carried out to explore the effects of electrochemical H pre-charging on the subsequent E_{OCP} , anodic polarization, electrochemical impedance spectroscopy, as well as the effect of pH and pre-charging time. Thin sample disks, ~ 500 μm thick, were ground to SiC 1200 grit, cleaned with acetone and dried with compressed air. Samples were then inserted into an electrochemical flat cell with a 1 cm diameter opening. Initial experiments explored only the effect of pre-charging on the E_{OCP} . They were electrochemically hydrogen pre-charged by cathodic polarization at a range of $\eta_H = +200$ to -1000 mV (-0.632 to -1.832 V_{SCE}) for 30 min in 0.1 M NaOH without the presence of Cl^- to achieve a highly alkaline environment and decrease the possibility of corrosion attack. The E_{OCP} was measured for 30 min in the same solution post-charging.

A second set of samples were pre-charged both in a normal electrochemical flat cell and in a microcapillary cell (Figure 69) to explore both the effects of charging area and charging time. Samples were prepared in the same manner and pre-charged in 0.6 M NaCl solution at a natural pH of 5.5 at $\eta_H = -200$, -400 , and -800 mV (-1.032 , -1.232 , and -1.632 V_{SCE}) for 10 min and 60 min. Anodic polarizations were carried out in the same solution from 100 mV below E_{OCP} to 1 V above E_{OCP} at a scan rate of 10 mV/s after charging. The fast scan rate was selected as it displayed less noise in the microcapillary cell as well as indicating the effects of H pre-charging at short times.

A third set of samples were examined to explore the effects of pre-charging at one specific overpotential in two different solutions on both the open circuit potential (E_{OCP}) and electrochemical impedance spectroscopy (EIS) measured with time after pre-charging as shown in Table 22. Three types of exposures were characterized in two different solutions, the first with 1 hour pre-charging prior to E_{OCP} /EIS measurements, the second with a 1 hour E_{OCP} prior to E_{OCP} /EIS measurements, and the third with no initial test, only E_{OCP} /EIS measurements. The first set, pre-charged samples, were electrochemically hydrogen pre-charged in two different ambiently aerated solutions, 0.6 M NaCl + NaOH pH 10 (the solution used for electrochemical pre-charging for H measurements) or 0.6 M NaCl pH 5.5, by cathodic polarization at $\eta_H = -800$ mV (-1.632 and -1.367 V_{SCE} respectively) for 1 hour followed by 2 h E_{OCP} /EIS measurements. A second set of samples were tested with 1 h E_{OCP} in both solutions followed by 2 h E_{OCP} /EIS measurements, and a third with no prior pre-charging or E_{OCP} , only the 2 h exposure of E_{OCP} /EIS analysis in the two solutions. Post-charging, E_{OCP} , or no exposure, the open circuit potential was measured while EIS measurements were taken at E_{OCP} for $t = 0, 1, 10, 30, 60,$ and 120 min post-exposure in the same solution, experimental matrix in Table 22. Samples were scanned with an AC amplitude with V_{rms} of 20 mV in the sine sweep modes from 100 kHz to 0.1 Hz.

Finally, to examine the effect of possible local pH change on the subsequent measurement of E_{OCP} , a sample was tested in buffered solution. UNS S46500 was pre-charged for 1 h in deaerated Borate Buffer solution pH 8.4 followed by an E_{OCP}

measurement for 1 h in the same solution. This was compared to the E_{OCP} measurement in the same solution of an uncharged sample.

3.3.3. Electrochemical Impedance Spectroscopy Analysis

Analysis of EIS spectra was carried out to determine the oxidation current density (i_{ox}) for the three alloys over time. A circuit, developed previously by Al-Ghamdi for uncharged UNS K92580, was applied to fit the EIS data using Gamry Echem Analyst software.[46] The circuit consists of two Randles circuits with a resistor in series, one for the impedance across the double layer, the second for the impedance due to the oxide, and the resistor to represent the solution resistance (Figure 72). From the impedance fitting, values of oxide resistance (R_{ox}) and charge transfer resistance (R_{ct}) were determined. The oxidation current density could be calculated using the following:

$$i_{ox} = \frac{\beta_a \beta_c}{2.303 R_p (\beta_a + \beta_c)} \quad \text{Equation 51}$$

$$R_{p^{ox}, \omega \rightarrow 0} = R_{ox} + R_{ct} \quad \text{Equation 52}$$

Where β_a is the anodic Tafel slope, taken as 81.3 mV/dec, β_c is the cathodic Tafel slope of 135.4 mV/dec, and R_p^{ox} is the polarization resistance.[46] The oxidation resistance of a hydrogen pre-charged sample can be related to both the H oxidation and anodic dissolution resistance by:

$$\frac{1}{R_{p^{ox}}} = \frac{1}{R_{p^{H/H^+}}} + \frac{1}{R_{p^{Fe/Fe^{2+}}}} + \frac{1}{R_{p^{Fe^{2+}/Fe^{3+}}}} \quad \text{Equation 53}$$

Where the inverse polarization resistance for oxidation is the sum of the inverse polarization resistance for H oxidation, $R_{p_{H/H^+}}$, the inverse polarization resistance for Fe/Fe²⁺ oxidation, $R_{p_{Fe/Fe^{2+}}}$, and the inverse polarization resistance for Fe oxidation of Fe²⁺/Fe³⁺ $R_{p_{Fe^{2+}/Fe^{3+}}}$. Oxidation current densities were determined for EIS fitting of samples pre-exposed for 1 h at E_{OCP} in 0.6 M NaCl + NaOH solution pH 10 and EIS measurements taken over time, from 0 s to 120 min at E_{OCP}. A second set of EIS fitting was established for samples exposed for 1 h at E_{OCP} in 5 mM NaCl + NaOH solution pH 10. However, only a single EIS measurement was taken of each sample. Therefore, values of i_{ox} were calculated from both solution exposures for comparison.

3.3.4. Electrochemical Extraction of Hydrogen

The SKP potential was calibrated for diffusible H concentration against $C_{H,Diff}$ independently determined by electrochemical extraction.[6] A range of $C_{H,Diff}$ values were used (2 – 40 wppm). UHSS disks, 500 μ m thick were ground to 1200 grit SiC polishing paper, rinsed with DI water, dried with compressed air, and degreased with acetone. Samples were then H pre-charged potentiostatically in an electrochemical flat cell in ambient aerated, room temperature 0.6 M NaCl + NaOH, pH 10 solution for 24 hours at H overpotentials (η_H) ranging from -150 mV to -1000 mV (-982 to -1832 mV_{SCE}). A minimum of three samples were tested at each overpotential. After charging, samples were rinsed with DI water, dried with compressed air, degreased with acetone, and transferred to an electrochemical cell with a 1 cm² area opening for H extraction. Transfer time from the pre-charging cell to initiation of the experiment in the extraction cell, including deaeration of the cell, was less than 5 minutes. Samples were held

potentiostatically at a η_H of +330 mV (-649 mV_{SCE}) in 0.1 M NaOH, pH 12.5 solution, well above the Nernst potential ($E_{r, H^+/H}$) 0 mV (-979 mV_{SCE}), for 60 min to oxidize dissolved diffusible H. This current density was corrected using a background current density measured in the same manner on an uncharged sample. To calculate $C_{H,Diff}$ using the first term approximation, the following condition had to be met for each sample: $L^2/D_H \cdot t_{max} \geq 4$, where L is the sample thickness or zone of the H containing metal, $D_{H,eff}$ is the effective H diffusivity, and t_{max} is time up to which the H concentration can be calculated from the current density measured.[47] The first term solution could then be applied as follows:

$$C_{H,Diff} = \frac{i_t}{zF} \left(\frac{D_{H,eff}}{\pi t} \right)^{-1/2} \quad \text{Equation 54}$$

Where i_t is the H oxidation current density for time, t , corrected for the background current density (A/cm²), z is the H oxidation number, 1 (equiv/mole), F is Faraday's constant (C/equiv), and t is the H extraction time (s). To ensure consistency across all electrochemical extraction measurements, $C_{H,Diff}$ was calculated from the current measured 1800 s after extraction was initiated and with the previously determined $D_{H,eff}$ values of 3.1×10^{-9} cm²/s for the as annealed/ CT condition and 6.2×10^{-9} cm²/s for the H900 temper of UNS S46500.[48]

3.3.5. Measurements for SKP Calibration

3.3.5.1. Effect of Relative Humidity

For calibration of the SKP, a comparison of the SKP potential measured on various surfaces at different set RHs was carried out in air (0.16 kPa H₂O, 20.26 kPa O₂, 79.03 kPa N₂, and 0.55 kPa residual gas species).[49] The calibration block of Al and Au, as well as uncharged and pre-charged samples of UNS S46500 were examined. Samples of UNS S46500 steel were cathodically pre-charged in full immersion at η_H of -200 and -800 mV (-1032 and -1632 mV_{SCE}) in naturally aerated 0.6 M NaCl, pH 10 solution at 25°C for 24 hours. After cathodic pre-charging with H, samples were rinsed with DI water, dried with compressed air, degreased with acetone and inserted into a KP Technology Ambient Advanced SKP with a 50 μ m gold coated stainless steel tip for measurement, schematic shown in Figure 73-a. Time between removal of the sample from the pre-charging environment and measurement in the SKP was 5 min. The gradient was set to control the distance between the SKP tip and sample surface at 10 μ m. Hereafter, this method was used for all interrogations unless otherwise stated.

The RH in the SKP chamber was set to a constant level using a humidifier/dehumidifier pump and vacuum setup. The SKP voltage was acquired with time, a minimum of 10 min at a single point above each sample, Au, Al, SS, and pre-charged SS, at RHs beginning at 57% and stepped up to 60, 70, 80, and 90% RH in air (0.16 kPa H₂O, 20.26 kPa O₂, 79.03 kPa N₂, and 0.55 kPa residual gas species).[49] During this time, it is estimated that $C = 1/100 C_o$ would be achieved at a distance of 150 μ m using the estimation for steady state diffusion in an infinite plane and a $D_{H,eff} = 3.2 \times 10^{-9}$ cm²/s. As

this outgassing of the hydrogen from the steel could occur with time, a second set of pre-charged samples were investigated. For these, samples of UNS S46500 were pre-charged electrochemically in a flat cell with a 1 cm^2 opening at $\eta_{\text{H}} = -200, -600, \text{ and } -800 \text{ mV}$ ($-1032, -1432, \text{ and } -1832 \text{ mV}_{\text{SCE}}$) for 24 h in 0.6 M NaCl + NaOH pH 10 solution. Samples were removed from the pre-charging cells, cleaned, and immediately measured in the SKP at set RH. SKP line scans were taken in Cl^- free ambient lab air with an average of 3 measurements at each point, a step size of $254 \mu\text{m}$, and a total distance covered of $14986 \mu\text{m}$ (initial step taken at 0). The average time to complete each line scan was 15 min. During this time, it is estimated that $C = 1/100 C_0$ would be achieved at a distance of $80 \mu\text{m}$ using the estimation for steady state diffusion in an infinite plane and a $D_{\text{H,eff}} = 3.2 \times 10^{-9} \text{ cm}^2/\text{s}$. Line scans were taken from uncharged to pre-charged areas in 40, 60, 80, and 95 % RH in air. For further experimentation, and RH of 57% was selected as it displayed a significant trend across samples and was easiest to keep constant with the humidity pump as it was near the natural RH of the laboratory in which the SKP was located.

3.3.5.2. Effect of Pre-charging Size

To explore the effect of H pre-charging area on the SKP potential, samples were pre-charged in electrochemical cells via two methods. The first were exposed in electrochemical flat cells with a small aperture opening for comparison. Samples of UNS S46500 were pre-charged in both a 1 cm^2 opening flat cell and a 0.13 cm^2 opening flat cell at the same pre-charging overpotential of $\eta_{\text{H}} = -400 \text{ mV}$ in the conditions described previously. A second set of samples were exposed in full immersion cathodic charging.

Samples of UNS S46500 were coated with non-chromate containing stop-off lacquer prior to immersion with bare sample areas of sizes 1, 2.5, and 5 mm² open to the charging environment. Samples were pre-charged at an overpotential of $\eta_H = -800$ mV in the conditions described previously. After charging, samples were removed, cleaned (coating removed when necessary), and measured in the SKP immediately. Line scans were taken as mentioned previously from the uncharged across the pre-charged areas.

3.3.5.3. Effect of Time Post-Charging

To explore the effects of time post-charging, samples pre-charged with both small-aperture openings and the large 1 cm openings were tested. Samples were pre-charged as described previously at $\eta_H = -400$ mV (-1232 V_{SCE}) in 0.6 M NaCl + NaOH pH 10 for 24 hours. Post charging, successive line scans of the same location were taken in the same manner as described previously for both the small and large aperture pre-charged samples. The RH was kept at a constant 57% with time.

3.3.6. Calibration of the SKP Potential Versus $C_{H,Diff}$ Using Cathodically Pre-charged Samples

For calibration of the SKP, 350 μ m thick, samples of UNS S46500 and UNS K92580 steel were cathodically pre-charged in full immersion at various hydrogen overpotentials, η_H in naturally aerated 0.6 M NaCl, pH 10 solution at 25°C. Overpotentials of -150 to -1000 mV (-982 to -1832 mV_{SCE}) were applied for 24 hours, to yield measured $C_{H,Diff}$ from 3 to 40 wppm for UNS S46500 and from 1 to 20 wppm for UNS K92580.[50] A minimum of three samples were tested at each overpotential. The maximum diffusion

depth to achieve 0.01 of the surface concentration of H after 24 hours pre-charging, calculated using the assumption for diffusion in an infinite plane, was found to be 600 μm for the annealed/CT samples, 840 μm for the H900 temper, and 1000 μm for the UNS K92580 samples. The extraction depth sampled by electrochemical extraction selecting 1800 s as the extraction time was 23 and 33 μm for as annealed/CT and H900 samples, respectively. An example of calculated steady state diffusion of H over the 24 h charging period can be seen for UNS S46500 in Figure 71.

After cathodic pre-charging with H, samples were inserted into the SKP at a constant RH of 57% for measurement, schematic shown in Figure 73-a. The time between removal of the sample from exposure and the first measurement in the SKP was less than 5 minutes, during which 0.01 of the H concentration in the charged region, C_o , could be achieved by diffusion based spreading away from the initially defined pre-charged region, $\frac{1}{2} C_o \rightarrow \sqrt{(Dt)}$, over distances less than 35 μm for the as annealed/CT condition, 50 μm for the H900 temper, and 70 μm for UNS K92580. Line scans were taken on the sample from the uncharged zone, across the center of the pre-charged zone, and back to the uncharged zone, as shown in Figure 73-a and b. The distance between the SKP tip and the sample surface was controlled by a fixed gradient (fixing the tip to sample distance) between the sample and probe tip, and an average height of 5-10 μm was maintained while scanning across the sample. SKP line scans were taken in Cl^- free ambient lab air (57% RH) with an average of 3 measurements at each point, a step size of 254 μm , and a total distance covered of 14,986 μm (initial step taken at 0). The average time to complete each line scan was 15 min. Scans of pre-charged samples were compared to

uncharged, unexposed background samples. The change in the SKP potential from unexposed to pre-charged areas of the steel measured in the SKP was correlated with each previously determined $C_{H,Diff}$ level for each η_H determined by electrochemical extraction.

3.3.7. Cross-sectioning method established for estimation of $D_{H,eff}$ in selected samples

Peak-aged UNS K92580 and as annealed/CT and H900 UNS S46500 steel samples of 1.3 cm³ volume were prepared and polished in the same manner as described previously and pre-charged at a hydrogen overpotential of -0.2 V (-1.032 V_{SCE}) for 24 hours, to yield a predicted $C_{H,Diff}$ of about 3.7 wppm.[51] A penetration depth of 2000 μm perpendicular to the charging surface could be expected to achieve a diffusion limited level of 3×10^{-5} % of the surface hydrogen concentration (C_s) given $D_{H,eff} = 3 \times 10^{-8} \text{ cm}^2/\text{s}$.[51]

Post-charging, samples were immediately cross-sectioned parallel to the diffusion direction with a cut-off saw in nitrate-free coolant at room temperature. The time between removal of the sample from cutting and the first measurement in the SKP was less than 12 minutes, during which $C = \frac{1}{2} C_0$ would be achieved at a distance less than 25 μm .[51]

SKP scans, 15 min each, were taken from the charged surface along the cross-section with step size of 31.8 μm , to a depth of 1873.3 μm , and averaged over three measurements. Successive scans were acquired consecutively for 21 h in ambient air

with a relative humidity of 55% and a gas H₂ concentration of 0.55 ppmv (0.16 kPa H₂O, 20.26 kPa O₂, 79.03 kPa N₂, and 0.55 kPa residual other gaseous species).[49] Over the total 21 h sampling period, substantial outgassing can occur.

3.4. Experimental Results

3.4.1. Evaluation of the Effect of Electrochemical Hydrogen Pre-charging on Anodic Polarization and E_{OCP}

For UNS K92580 pre-charged to various overpotentials in 0.1 M NaOH, a suppression in the E_{OCP} was measured post-charging (Figure 74-c). This suppression is increased with increase in pre-charging overpotential and decreases with time post-charging (Figure 74-a and b). For all steels tested in 0.6 M NaCl + NaOH pH 10 and NaCl pH 5.5, a suppression in the E_{OCP} and increase in the anodic kinetics was seen with increasing pre-charging overpotential, possibly suggesting that these are proportional to higher H concentrations yielding a second oxidation reaction other than metal electrode dissolution (Figure 75). Secondly, increased anodic kinetics could also be due to enhanced anodic dissolution with a higher H concentration.[21, 52-57] In Figure 74 and Figure 76 - 16, it can be seen that the greatest change to E_{OCP} occurs over initial times of 5 to 10 min, depending on pre-charging time, and decreases with time. This is likely indicative of hydrogen desorption from the material with time.

3.4.2. Evaluation of the Effect of Electrochemical Hydrogen Pre-charging using EIS

For all materials, for samples H pre-charged cathodically, the polarization resistance (R_p) is initially decreased and increases again with time, indicative of a change in the overall total anodic kinetics due to H pre-charging (Figure 77 - Figure 85), and then recovers. The change with time could be due to H desorption from the material. For samples held at OCP for 1 hour prior to EIS, no significant change is seen. For samples with no prior exposure, initial EIS measurements display a lowered R_p , but no clear trend with time is displayed as with the pre-charged samples, possibly indicating that this is a measurement artifact.

3.4.3. Electrochemical Impedance Spectroscopy Analysis

Oxidation current densities established from EIS fitting are plotted vs. time in Figure 86. Hydrogen oxidation currents vs time calculated from C_H egress, as described in detail subsequently in section 3.5.3, are also plotted for comparison. For the SKP measurement to be dependent on the H concentration, i_{ox} associated with the corrosion of the material must be significantly lower than $i_{L, Hox}$. It can be seen in Figure 86, that UNS S46500 meets these requirements with almost 2 orders of magnitude difference in currents during the measurement time of the SKP. UNS K92580 still satisfies these requirements, but is more dependent on the measurement solution, i.e. the i_{ox} for UNS K92580 in 0.6 M NaCl + NaOH pH 10 is lower than the $i_{L, Hox}$, but by less than an order of magnitude, however in 5 mM NaCl + NaOH, pH 10, it is significantly lower. For UNS G10180, it is clear that

the i_{ox} could interfere with the detection of H in the SKP, as it is of the same order of magnitude and greater than the $i_{L,Hox}$ during the measurement period.

3.4.4. Effect of pre-charging: pH

Experiments showing the effect of pre-charging in an environment with a controlled buffered pH can be seen in Figure 87. As shown, the change in E_{OCP} occurs in a buffered solution and is not solely due to a change in local surface pH, such as due to the electrosorption reaction, below.



3.4.5. Electrochemical Extraction for $C_{H,Diff}$ determination: Effect of η_H and Temper

Electrochemical extraction results for $C_{H,Diff}$ for UNS S46500 in the as annealed/CT and H900 temper for various pre-charging η_H are shown in Figure 89. As expected, for increased hydrogen overpotentials, η_H , an increase in the $C_{H,Diff}$ is measured. The range for $C_{H,Diff}$ produced from these pre-charging conditions was found to be 20-40 wppm (Figure 89). For UNS K92580, electrochemical extraction results are used from previous work by Kehler et al.[50]

3.4.6. Calibration of the SKP:

3.4.6.1. Relative Humidity

Similar pre-charging experiments were performed for UNS S46500 as annealed/CT with varied RH and a select set of pre-charging conditions. The SKP potential is affected by the % RH in air (0.16 kPa H₂O, 20.26 kPa O₂, 79.03 kPa N₂, and 0.55 kPa residual gas species[49]) and increases with increasing RH (Figure 90). However, this same phenomena does not occur for noble materials, i.e. Au, which is stable across varied RH (Figure 91). Therefore, control of the RH is necessary during measurements to establish consistency for calibration as well as for application to materials with unknown H concentrations, such as those produced from atmospheric pre-exposure. As previously mentioned, 57% RH was selected for both ease of measurement as well as consistency in spread of potentials and in all experiments, O₂, N₂, residual gases are assumed constant in lab air.

3.4.6.2. Pre-charging Size

A second area of concern in the SKP is the effect of the pre-charging size on the H uptake and subsequent SKP potential measurement. An example of a small aperture cell used for pre-charging vs. the 1 cm² aperture cell is shown in Figure 92 for UNS S46500 H900 pre-charged at $\eta_H = -400$ mV for 24 h in 0.6 M NaCl + NaOH pH 10 solution. Figure 92-a displays a similar trend with time for the small aperture sample in that the SKP potential increases with time post-charging. Figure 92-b shows a slightly lower change in the SKP potential for the smaller aperture cell, possibly due to interrupted charging conditions where across such a small window, a hydrogen bubble could have built up and

temporarily blocked H uptake. While the resolution is not limited by the SKP tip at these length scales, the H pre-charging resolution is limited by the setup design. In the 24 h pre-charging time, even with a vertically positioned cell, significant bubble build up may prevent uniform charging with decreased cell aperture sizes.

A second set of samples coated with stop off lacquer and fully immersed for pre-charging with bare sample areas exposed of 1, 2.5, and 5 mm² were explored to alleviate the issues of H bubble formation in the small aperture cells and results are plotted in Figure 93. Line scans in Figure 93-a display the ability of the SKP to detect various pre-charging sizes. However, again, it is evident that issues arose in the actual pre-charging process. Line scans displayed large decreases in SKP potentials well outside the pre-charged areas for all samples. A distinct difference in the pre-charged regions between the 1 and 5 mm² line scans can be seen (Figure 93-a). However, in an area scan of the 1 mm² sample (Figure 93-b), areas well away from the pre-charged area, >2000 μm , and much larger than the expected H spread in 24 hours (C_0 is 1/100 of C_s at 590 μm in 24 h), suggest that charging has occurred through possible defects or delamination of the stop off lacquer. Further study of methods for various sizes of pre-charged areas must be undertaken for a better understanding of the effect of H pre-charged area on the SKP potential.

The resolution of the SKP can also be dependent on the ratio of the pre-charging area to the tip to sample distance. If this ratio decreases to levels near 0.65, as mentioned in the introduction, the difference in potentials measured at the probe tip can be greatly underestimated. However, as the pre-charged areas measured in this thesis are

significantly larger than the probe to sample distance, a minimum area diameter of 1 mm vs. a probe to tip height of 10 μm , this does not play a significant factor on the effect of resolution as studied here. There may however, be effects due to lateral spread as discussed in the introduction and shown in Figure 68.[29, 31]

3.4.6.3. Exposure Time After Charging Period

An example of outgassing/ desorption of H with time is shown in Figure 96, where an initial line scan was taken immediately after exposure and a second taken 71 h after exposure of a UNS S46500 as annealed/ CT sample at high η_{H} and 25 h post-exposure of UNS K92580 pre-charged at $\eta_{\text{H}} = -400 \text{ mV}$. A rise in the SKP potential with time across the pre-charged area is indicative of the H desorption with time from the material. This can be seen for various potentials in Figure 97, where the average of the change in SKP potential is plotted vs. time.

An idea of the spread in measurement of the SKP potential due to H diffusion over time is shown in Figure 98, where the edge of a pre-charged to uncharged zone is plotted with the change in relative concentration profile for the 1080 min post-charging measurement time. As can be seen, the potential spreads from the initial edge of the charged zone, which can be somewhat correlated with the spread in H concentration with time. However, this is also likely affected by the spread in H concentration during the 18 h pre-charging time, which is not accounted for in this schematic, and could explain the increased spread of H from the pre-charged area.

3.4.7. Calibration of the SKP: Electrochemically Pre-charged Samples

The average SKP line scans measured across H pre-charged zones for UNS S46500 in both the as annealed/CT and H900 temper are shown in Figure 94. Each scan is an average of measurements from at least three samples H charged at a specific pre-charging overpotential. As the SKP scanned from the uncharged to pre-charged zones across the steel, a change in the SKP potential measured was detected. This potential was shown to decrease with increasing η_H , indicative of higher $C_{H,Diff}$. For UNS K92580, SKP scans of pre-charged samples are shown in Figure 95. A slightly smaller overall change in the SKP potential is seen, as this material exhibits a lower $C_{H,Diff}$ for the same pre-charging overpotential.[58]

The line scan measurements of the SKP potential vs. the pre-charging overpotential can be combined with the electrochemical extraction measurements of $C_{H,Diff}$ vs. pre-charging overpotential to develop a calibration curve for the effect of dissolved H on the SKP potential (Figure 99). As $C_{H,Diff}$ increases, SKP potential decreases. Application of this calibration was carried out for the average values of the SKP potential vs. distance for the electrochemically pre-charged UNS S46500 as annealed/CT and H900 conditions and UNS K92580 and $C_{H,Diff}$ values are plotted in Figure 100. As discussed below, this calibration curve will not yield a unique SKP potential for a given pre-charged $C_{H,Diff}$. It is asserted in this thesis that the $C_{H,Diff}$ – SKP relationship is a unique function of material.

SKP potentials scale with increased $C_{H,Diff}$ due to the dependence of the interface potential on the H concentration. As long as the corrosion rate of the sample is low, and the H concentration significant, then the SKP potential will depend on the H oxidation at the surface, and therefore the concentration of pre-charged H within the sample.[25, 59] This concept is further elaborated upon in the discussion.

3.4.8. SKP Φ Measurements and $D_{H,eff}$ Calculations

3.4.8.1. SKP Hydrogen Concentration Distribution Calculations

$D_{H,eff}$, is a function of the $C_{H,Diff}$ which is dependent on η_{chg} , for UNS K92580 as shown by TDS. This dependence can be calculated using the following equation[51]:

$$\log(D_{H,eff}) = -0.641 \eta_{chg} - 8.14 \quad \text{Equation 59}$$

Where η_{chg} is the hydrogen overpotential used for charging. $D_{H,eff}$ is $8.96 \times 10^{-9} \text{ cm}^2/\text{s}$ at $\eta_{chg} = -0.2 \text{ V}$ (-1.032 V_{SCE}). Considering diffusion in an infinite plane, assuming that the hydrogen surface concentration is instantaneously established, is constant, and that transport is diffusion controlled, the following solution to Fick's second law describes semi-infinite transport in a flat specimen perpendicular to the flat surface [60]:

$$\frac{C_{x,t} - C_o}{C_s - C_o} = 1 - \text{erf} \frac{x}{2\sqrt{D_{H,eff}t}} \quad \text{Equation 60}$$

$$\frac{\Phi_{x,t} - \Phi_o}{\Phi_s - \Phi_o} = 1 - \text{erf} \frac{x}{2\sqrt{D_{H,eff}t}} \quad \text{Equation 61}$$

The solution to Fick's second law in this equation assumes that $D_{H,eff}$ is independent of hydrogen concentration. The equation used for estimation of $D_{H,eff}$ is based on the SKP potential (Φ) which is assumed to be proportional to $C_{H,Diff}$, as suggested by the calibration curve.[25] The following substitutions can be made; the SKP voltage due to a C_H at point, x , and time, t , ($\Phi_{x,t}$) is proportional to the diffusing hydrogen concentration ($C_{x,t}$). Similarly, Φ_o is proportional to the initial bulk concentration of hydrogen (C_o) and Φ_s is proportional to C_s . At the maximum depth measured by SKP, the Φ is dependent on C_o in the uncharged region.

A second approach to this assumes the relationships between Φ and $C_{H,Diff}$ found in the calibration curves in Figure 99. Instead of substituting Φ directly for C_H , the concentrations are first calculated from the calibration curves and then the solution for diffusion in an infinite plane is used to find $D_{H,eff}$ with the predicted $C_{H,Diff}$ values.

3.4.8.2. SKP Hydrogen Concentration Measurements: Cross-sectional Measurement and Analysis

SKP line scans of Φ are shown in Figure 101. Simultaneously plotted with the calculated graph of C_H vs. x based on Equation 61 is Φ vs. x from the uncharged cross-section of UNS K92580 sample taken at 21 h. The Φ measured from this uncharged edge is stable and equivalent to the Φ_o value for the 21 h scan in the charged area, discounting the change in Φ as an artifact of sectioning and cleaning. From the depth dependence of Φ measured along the first line scan (12 minutes post-cutting), an estimation of $D_{H,eff}$ can be made. The average of the first three Φ values (over 70 μm) nearest the charging surface

is used as Φ_s and the average of three Φ values at a depth of 2000 μm , is taken as Φ_o . The profile is plotted and compared to diffusion controlled concentration profiles obtained from a range of relevant diffusion coefficients (Figure 102-a). $D_{H,\text{eff}}$ is found to be $1 \times 10^{-8} \text{ cm}^2/\text{s}$ at positions less than 750 μm depth below the charged surface and $2.5 \times 10^{-8} \text{ cm}^2/\text{s}$ at positions greater than 750 μm . In theory, the concentration dependent $D_{H,\text{eff}}$ should be faster near the surface. The cause of this inverse relationship here is unclear.

The SKP method was also applied to UNS S46500. (Figure 102-b) $D_{H,\text{eff}}$ equal to $1.0 \times 10^{-8} \text{ cm}^2/\text{s}$ is seen with respect to x greater than 750 μm , while at shorter distances $D_{H,\text{eff}}$ is equal to $2.5 \times 10^{-8} \text{ cm}^2/\text{s}$. This corroborates fairly well with the measurements of $D_{H,\text{eff}}$ from TDS, established in Chapter 2, being $6.2 \times 10^{-9} \text{ cm}^2/\text{s}$.

The change in $D_{H,\text{eff}}$ with depth into the steel sample suggests a dependence on hydrogen concentration. [61] It is recognized that Equation 61 assumes a concentration independent $D_{H,\text{eff}}$. However, Equation 61 is a reasonable equation for a first examination especially since $D_{H,\text{eff}}$ changes only by a factor of 2.

Applying the second approach, predicted values of $C_{H,\text{Diff}}$ vs. depth into the pre-charged sample are plotted in Figure 103-a. Similarly as above, from the depth dependence of Φ measured along the first line scan (12 minutes post-cutting), an estimation of $D_{H,\text{eff}}$ can be made. The average of the first three predicted $C_{H,\text{Diff}}$ values (over 70 μm) nearest the charging surface is used as C_s and the average of three $C_{H,\text{Diff}}$ values at a depth of 2000 μm , is taken as C_o . The profile is plotted and compared to diffusion controlled

concentration profiles obtained from a range of relevant diffusion coefficients (Figure 103-b). $D_{H,eff}$ is $5 \times 10^{-9} \text{ cm}^2/\text{s}$ at positions less than $750 \text{ }\mu\text{m}$ depth below the charged surface and $1.5 \times 10^{-8} \text{ cm}^2/\text{s}$ at positions greater than $750 \text{ }\mu\text{m}$. These estimations produce $D_{H,eff}$ values slightly lower than the method above of using the SKP potential, but are still in a similar order of magnitude.

Finally, a third form of analyzing this data was carried out, predicting the $D_{H,eff}$ by measuring the SKP potential with time, and thus the H egress over time. $C_{H,Diff}$ predicted values were calculated for the first five measurements nearest the charging surface, at depths of 0, 30, 60, 90, and $130 \text{ }\mu\text{m}$. These were $C_{x,t}$ values were plotted vs. time and compared to a range of relevant diffusion coefficients. The best fit range was found to be 1×10^{-9} to $5 \times 10^{-10} \text{ cm}^2/\text{s}$, Figure 104.

This also highlights the benefits of developing SKP for $D_{H,eff}$ measurements. The ability to spatially determine $D_{H,eff}$ in phases or regions where C_H differs is lacking in the literature.

3.5. Discussion

The SKP potential was found to be dependent upon the $C_{H,Diff}$ in a pre-charged UHSS. This relationship was established for front side detection where an Fe-H electrode was formed without the application of a Pd thin film. This enables SKP H detection techniques to be better applied for spatial and lateral resolution of uptake from an exposure environment.

3.5.1. Origins of the H effect on the SKP Potential

3.5.1.1. SKP Potential and $C_{H,Diff}$

It has been shown through this work that measurements of the SKP potential above hydrogen pre-charged areas of UHSS are proportional to levels of diffusible hydrogen concentrations. The SKP measures the difference in Volta potentials between the vibrating tip and the surface potential, in this case the potential established at the surface of the thin electrolyte film formed in the humid air environment. Therefore, the potential measured by the SKP is governed by the potential established across this film, as the SKP tip potential is assumed stable. The potential at the surface of this film is influenced by the corrosion rate of the material and the hydrogen oxidation rate. As corrosion in this environment is assumed extremely slow, the potential established is due to hydrogen oxidation. At room temperature, and under no outside stresses, the hydrogen that is capable of movement within the pre-charged specimen, in response to charging at an η_H , is the diffusible concentration, rather than the total hydrogen concentration ($C_{H,Diff} + C_{H,trap}$).

3.5.1.2. Electrochemical Factors

The basis for SKP detection of H concentrations is the establishment of the H electrode at the measurement surface.[25] Previous work has shown the H electrode effect for a pre-charged palladium coated surface (Table 23), where the SKP potential measured is a logarithmic function of the H concentration during egress when sensed on the Pd coated backside of a charged 100 μm Fe foil.[25, 40] The authors state that as the hydrogen absorbed into the Pd and the hydrogen adsorbed at the surface of the Pd are in

equilibrium, therefore the potential at the surface of the thin layer, E , is governed by H activity at a rate of 60 mV/dec [25]:

$$E = E_{SHE}^o + \frac{RT}{F} \ln\left(\frac{a(H_{el}^+)}{a(H_{ad})}\right) = E^* + \frac{RT}{F} \ln\left(\frac{a(H_{el}^+)}{a(H_{Pd})}\right) \quad \text{Equation 62}$$

Where E_{SHE}^o is the potential of the hydrogen electrode, E^* is the H affected hydrogen electrode potential, $a(H_{ad})$ is the activity of adsorbed H, $a(H_{el}^+)$ is the activity of H^+ in the thin electrolyte layer, and $a(H_{Pd})$ is the activity of the absorbed H in the Pd. Studies on Pd coated Al with measurement on the uncharged side of the foil have also demonstrated similar Pd-H behavior (Table 23).[62] The addition of Pd thin films to aid in detection of H in a sample establishes a simpler measurement as Pd has a high H capacity, therefore H diffuses readily to the backside Pd thin films from the exposed or charged side of the material. As Pd is a noble material, the potential established is dependent on H oxidation rather than corrosion of Pd in the thin film. Similar behavior is expected to occur at a UHSS with H pre-charged surfaces, as shown in Figure 70, as long as a significant $C_{H,Diff}$ is present such that H oxidation occurs at a rate exceeding the corrosion rate or anodic oxidation rate where ORR and oxide reduction are the likely cathodic reactions. This situation is possible when corrosion current density (i_{corr}) \approx passive current density (i_{pass}). In the case of these martensitic stainless steels, under low corrosion passivating circumstances, the hydrogen oxidation current density (i_{Hox}) $\gg i_{corr}$.

Once the iron oxide reduction (Fe^{3+} to Fe^{2+}) occurs, the change in SKP potential reflects a Fe-H electrode as long as the reduction of Fe^{3+}/Fe^{2+} to Fe^0 sequence is not the dominant

reaction, given a low i_{corr} , i_{H} to $i_{\text{H}+}$ is the dominant anodic reaction, and ORR is the dominant cathodic reaction in a thin water layer created upon exposure to humid air. If SKP scans are measured in a constant humidity environment, for example an RH of 57%, a thin water layer is maintained at the sample surface. If it is assumed this water layer forms without any salt contamination on the surface, it is estimated to be between 1 - 7 monolayers thick at 57% RH.[63-65] However, even though samples are cleaned prior to SKP measurements, it is likely that some residual salts remain on the samples or are present in lab air from aerosol deposition.[66, 67] If it is assumed that these salts have a deposition density of 10 to 100 $\mu\text{g}/\text{cm}^2$, the water layer thickness could be much thicker than estimated above, ranging from 0.273 to 2.73 μm . This water layer is sufficiently alkaline when the metal oxide chemically reacts in the water, similar to the “dew regime” indicated on the Pourbaix diagram in Figure 105. In this case, hydrogen oxidation is assumed to be the dominant reaction. This can occur in two different reactions listed in Table 24. If both oxidation reactions occur, such that $i_{\text{H}/\text{H}+} + i_{\text{H}+/\text{H}_2} \gg i_{\text{Fe}^{2+}/\text{Fe}^{3+}}$, then the potential established is dependent upon the H desorption from the material. Therefore, an H electrode is formed and Φ is a function of C_{H} . It is important to note that this potential measured is a mixed potential with oxygen reduction occurring at the surface as well, yet the ORR is influenced by the H concentration. This will be true for UHSS where $C_{\text{H,Diff}}$ is large and the current due to H oxidation is equal to the limiting current density ($i_{\text{H}/\text{H}+} = -n\text{FDC}/x$, where x is the H depletion profile in the metal). Examples of possible limiting current densities can be seen in Figure 106 for $C_{\text{H,Diff}}$ values of 10 wppm (for UNS G10180 these were calculated with a $C_{\text{H,Diff}}$ of 1 wppm as it has a much lower H trap capacity than the quenched and tempered steels). Also, the influence of both time and

initial concentration on the limiting current density can be seen in Figure 107 and Figure 108. As initial pre-charged H concentrations increase, the limiting current density increases and thus the H oxidation in the thin film can increase, decreasing the thin film potential and in turn the SKP potential. However, these calculations also highlight the timeliness of measurements, in that as time increases post exposure the hydrogen desorbs from the alloy and limiting current density decreases thus the effect on the SKP potential decreases.

Measurements in this dissertation were taken as quickly as possible, but due to limitations in experimental setup, time between removal of samples from pre-exposure environments and initial measurement in the SKP was 5 min. Also, the average time to take a line scan was 15 min. Hydrogen can desorb from the material at room temperature in this time and the limiting current density changes over this time period (Figure 109). However, concentrations of $C_{H,Diff}$ in these high trap capacity materials were significant enough that potential at the surface was still governed by the H concentration instead of metal oxidation. In these UHSS particularly, high $C_{H,Diff}$ and low corrosion rates aided in the SKP detection.

3.5.1.3. Determination and explanation of calibration curves for ϕ dependence on

H: Calculation for H desorption and effect on SKP Potential

Calibration curves determined for the dependence of ϕ on the pre-charged H concentration were established in Figure 99. Curves were determined with a non-linear slope and a different ϕ at the same $C_{H,Diff}$. Since the ϕ is dependent upon $\frac{\partial C}{\partial x}$ at the sample

surface, the specific diffusivity of H egressing from the specific material tested influences the potential seen by the manner in which it controls $\frac{\partial C}{\partial x}$. Therefore, since $D_{H,eff}$ is different for the UNS S46500 tempers and UNS K92580, even though samples were charged to the same bulk H concentrations, a unique value of $\frac{\partial C}{\partial x}$ is obtained at the exit surface and evolves over time. This behavior would be expected (Figure 109) and thus a difference in calibration curves for the different materials with unique $D_{H,eff}$ is seen and theoretically expected. The expected non-linear relationship arises for this calibration because $\frac{\partial C}{\partial x}$ is a complex function of $D_{H,eff}$, t , and $C_{H,Diff}$.

3.5.1.4. Mixed potential theory

A further explanation of this potential dependence on H concentration can be established through mixed potential theory. For these diagrams, the following assumptions were made and equations used. The ORR activation current density, $i_{act,ORR}$, and the ORR limiting current density, $i_{L,ORR}$, along with the Nernst potential for oxygen reduction were used to calculate the oxygen reduction reaction current density, i_{ORR} .

$$i_{ORR} = \frac{i_L \cdot i_{act}}{i_L + i_{act}} \quad \text{Equation 63}$$

$$i_{act,ORR} = i_o e^{\left(\frac{-2.3\eta}{\beta_c}\right)} \quad \text{Equation 64}$$

$$i_{L,ORR} = \frac{nFD_{O_2}C_{O_2}}{\sqrt{D_{O_2}t}} = \frac{nFD_{O_2}C_{O_2}}{x} \quad \text{Equation 65}$$

$$E_{ORR} = 1.229 - 0.059pH + 0.0147 \log(P_{O_2}) \quad \text{Equation 66}$$

Where, i_0 is the exchange current density $1.7 \times 10^{-10} \text{ A/cm}^2$ [68], η is the overpotential, β_c is the Tafel slope of 60 mV/dec [68], E_{ORR} is the oxygen reduction reversible potential, P_{O_2} is the partial pressure of O_2 taken as 10, 10^0 , and 10^{-1} atm, R is the ideal gas constant, n is the number of e^- involved in the reaction, F is Faraday's constant, D_{O_2} is the diffusion coefficient of O_2 in solution of $1.46 \times 10^{-5} \text{ cm}^2/\text{s}$ [69], C_{O_2} is the concentration of O_2 in solution taken as $2.06 \times 10^{-7} \text{ mol/cm}^3$, x is the diffusion limiting distance (cm), and t is time in s. For calculations of the diffusion limiting ORR current in the SKP, the value of x was taken to be 0.005 cm, an estimate for the thin film water layer thickness formed on the sample during measurement, and $i_{\text{L,ORR}}$ calculated to be $2.3 \times 10^{-4} \text{ A/cm}^2$. The pH was assumed alkaline for SKP measurements at a pH of 10. A second limiting current density was also applied for an estimation of ORR through an atmospheric corrosion measurement. If ORR is assumed the primary cathodic reaction, then the cathodic current density will be equal to the anodic current density, i_a , due to corrosion. The i_a was calculated from a uniform corrosion rate measured for UNS G101000 exposed under isohumidity conditions, ranging from 33-90% RH, with printed NaCl, loading density of $8.6 \mu\text{g/cm}^2$, considered to be equivalent to a marine exposure, and exposed for periods up to 300 days.[70] From this data, an estimation for a corrosion rate at 57% RH was taken as $10 \mu\text{m/yr}$ and an i_a calculated to be $8.62 \times 10^{-7} \text{ A/cm}^2$. This was also then applied as a possible limiting current density for ORR as it represents a corrosion current in an atmospheric exposure environment on steel, similar to the thin film formed in the SKP at 57% RH.

For the hydrogen oxidation current calculations, two reversible electrode potentials were considered, the first for $H \rightarrow H^+ + e^-$ and the second for $H_2 \rightarrow 2H^+ + 2e^-$. For the first equation, the anodic polarization due to hydrogen oxidation, $\eta_{H^+/H}$ was calculated using the following:

$$\eta_{H^+/H} = \beta_a \log \frac{i_a}{i_o} + \frac{2.3RT}{nF} \log \left[\frac{i_L}{i_L - i_a} \right] \quad \text{Equation 67}$$

$$i_{L,H^+/H} = -nFD_{H,eff} \frac{\partial C}{\partial x} \quad \text{Equation 68}$$

$$E_o = 0 - 0.059pH - 0.0295 \log(P_{H_2}) \quad \text{Equation 69}$$

Where β_a is the Tafel constant of 0.10[71], i_o for H oxidation taken as 1×10^{-7} A/cm² [71], P_{H_2} is the partial pressure of H_2 was taken as 10^{-5} (calculated from the H partial pressure in air), 10^{-3} , 10, 10^3 , and 10^5 (taken to represent the effective H_2 or H partial pressure that would be in equilibrium with a high C_{Lattice} and $C_{H,Diff}$)[72] atm, $D_{H,eff}$ is the hydrogen trap effected diffusivity which were 3.5×10^{-9} , 6.2×10^{-9} , 9×10^{-9} , and 1×10^{-7} cm²/s for UNS S46500 As Annealed/CT, H900, UNS K92580, and UNS G10180 respectively[51], and $\frac{\partial C}{\partial x}$ is the change in concentration over the solid state distance x from H egress calculations assuming a C_o of 10 wppm wppm (1 wppm for UNS G10180) and a time of 15 min (Figure 111-Figure 114). pH again was assumed to be alkaline at a pH of 10.

To establish $\frac{\partial C}{\partial x}$, calculations for steady state diffusion of hydrogen over time in the materials of interest were made. The approximation of steady state diffusion in an infinite plane was applied:

$$C_{x,t} = C_o \operatorname{erf}\left(\frac{x}{2\sqrt{Dt}}\right) \quad \text{Equation 70}$$

Where $C_{(x,t)}$ is the concentration at distance, x and time, t , C_o is the initial concentration, and D is the diffusion coefficient (trap affected diffusivity of hydrogen). Concentration curves were calculated for SKP measurement times of 15 min and assuming an initial concentration of 10 wppm (1 wppm in the case of UNS G10180). $D_{H, \text{eff}}$ values used were 3.5×10^{-9} , 6.2×10^{-9} , 9×10^{-9} , and $1 \times 10^{-7} \text{ cm}^2/\text{s}$ for UNS S46500 As Annealed/CT, H900, UNS K92580, and UNS G10180 [51], respectively (Figure 106). As can be seen, changes in $D_{H, \text{eff}}$ influence the concentration profiles. The effects of varied times post exposure, 15 min - 24 hours, and varied initial concentrations, 2 – 10 wppm (0.1 – 1 wppm for UNS G10180) were explored in Figure 107 and Figure 108. For all samples, as time increased, the $C_{x,t}$ profiles became less steep, and therefore $\frac{\partial C}{\partial x}$ would decrease. For calculations of varied C_o , at higher initial concentrations, profiles of $C_{x,t}$ were steeper and thus $\frac{\partial C}{\partial x}$ would increase with increasing C_o . To calculate $\frac{\partial C}{\partial x}$, the slopes of concentration profiles at varied times (1 s to 60 min) were taken over the linear regions from 0 to 0.0025 cm and are plotted in Figure 109-a. From this, the limiting hydrogen oxidation current density for the conditions explored could be determined (Equations 68 and 72) and is plotted vs time in Figure 109-b.

For the second H oxidation current, the following equations were used;

$$\eta_{H_2/2H^+} = \beta_a \log \frac{i_a}{i_o} + \frac{2.3RT}{nF} \log \left[\frac{i_L}{i_L - i_a} \right] \quad \text{Equation 71}$$

$$i_{L,H_2/H^+} = -nFD_{H,eff} \frac{\partial C}{\partial x} \quad \text{Equation 72}$$

$$E_{H_2/2H^+} = 0 - 0.059pH - 0.0295 \log(P_{H_2}) \quad \text{Equation 73}$$

Where β_a is the anodic Tafel constant of 0.10 [73], i_o for H oxidation was taken as 1×10^{-6} A/cm² [73], P_{H_2} is the partial pressure of H₂ taken as 10^{-5} (calculated from the H partial pressure in air), 10^{-3} , 10^{-1} , 10^3 , and 10^5 (taken to represent the effective H₂ or H partial pressure that would be in equilibrium with a high $C_{Lattice}$ and $C_{H,Diff}$)[72] atm, $D_{H,eff}$ is the hydrogen trap effected diffusivity which were 3.5×10^{-9} , 6.2×10^{-9} , 9×10^{-9} , and 1×10^{-7} cm²/s for UNS S46500 As Annealed/CT, H900, UNS K92580, and UNS G10180 respectively[51], respectively, and $\frac{\partial C}{\partial x}$ is the change in concentration over the solid state distance x from H egress calculations assuming a C_o of 10 wppm (1 wppm for UNS G10180) and a time of 15 min. pH again was assumed alkaline at a pH of 10.

Calculated currents for ORR and H oxidation were compared to measured anodic polarization curves of the three alloys in naturally aerated 5 mM NaCl adjusted to a pH of 10 with NaOH in Evans diagrams (Figure 111-Figure 114). Scans were taken from 100 mV below E_{OCP} to 500 mV above E_{OCP} at a scan rate of 0.1667 mV/s. It can be determined from these plots that samples with pre-charged H concentrations can exhibit a

drop in potential of magnitudes up to 600-800 mV due to the H oxidation at the surface if the $i_{L,ORR}$ is assumed to be similar to that from corrosion ($8.62 \times 10^{-7} \text{ A/cm}^2$). However, in the schematics, if ORR is assumed more similar to that from the thin film calculation ($i_{L,orr} = 2.3 \times 10^{-4} \text{ A/cm}^2$) this would occur well above the OCPs of the alloys, and therefore accounts for only a few hundred mV drop, rather than those seen in measurements. Another possible factor could be that the limiting current density for ORR was calculated for too large a value. For thick electrolyte layers, this is controlled by the diffusion distance across the thin film, however, there have been some studies stating that the limiting current density in thin films is not only due to the thickness, but is further limited from the transfer of O_2 in the atmosphere to O_2 in the thin film, and is thus dependent upon the activity of O_2 in the gas phase.[28] If this further limits the ORR reaction, the corrosion potential could be lowered, and thus the effect of H oxidation would occur at further decreased coupled potentials accounting for those seen experimentally (Figure 111-Figure 114).

3.5.1.5. Mixed Potential Theory and Influence of pH

To examine the effect of possible pH change of the thin film due to H egress from the sample followed by H oxidation to H^+ , the same calculations were performed for UNS S46500 As Annealed/CT with pH values of 10, 8, 6, 4, and 2 (Figure 115). For these calculations, C_{O_2} and C_{H_2} were assumed to be 10^0 atm . While the pH change from 10 to 2 can cause a significant change in the current densities, the change in pH at the surface of the thin film could not reach the magnitudes shown in Figure 115. If it is assumed that the entire 10 wppm $C_{H,Diff}$ egresses from the sample, and thin water layer film is 0.005

cm thick with an area of 1 cm^2 , the largest pH shift that could occur would be 0.06. Even if diffusible hydrogen is estimated at 40 wppm as an initial concentration, this shift of pH can only increase by 0.54, which does not create the significant effects necessary to significantly change these current densities, and thus the potential of the thin film, as shown in Figure 115. Also, in addition to the fact that the change in magnitude of the pH is insufficient to greatly affect the coupled potential, the pH would decrease due to H egress from the samples which would only increase the reversible potential for H oxidation at the surface (Equations 74-77). This eliminates this effect as the cause responsible for the drop in SKP potential. The rise in the potential due to the pH drop is the opposite of what is seen due to the H electrode effect.

3.5.1.6. Theory of the Effect of H on the Mixed Potential

The foundations for the effect of H concentration on the mixed potential in the thin film can be explained through the effects of hydrogen activity and fugacity on the overpotential at the surface, similar to the effect seen on Pd in the SKP in Equation 62.[72, 74] The Nernst potential for H oxidation can be established through the following equation:

$$E = E_o + \frac{2.303 RT}{2F} \log \left(\frac{[H^+]}{f_{H_2}} \right) \quad \text{Equation 74}$$

Where E^o is the standard electrode potential, $[H^+]$ is the activity of H^+ and f_{H_2} is the fugacity of hydrogen. This can be related to the hydrogen overpotential η_H by:

$$\eta_H = E - (E_o - 0.0295pH) \quad \text{Equation 75}$$

And, thus

$$\eta_H = -0.0295V \log(f_{H_2}) \quad \text{Equation 76}$$

or

$$f_{H_2} = 10^{-\eta_H/0.0295} \quad \text{Equation 77}$$

Therefore, the change in an order of magnitude of the pressure of H_2 results in about a 30 mV change in the hydrogen overpotential. A hydrogen pre-charged surface with a high hydrogen concentration level would be in equilibrium with a high hydrogen fugacity, f_{H_2} on the liquid or gas phase next to the metal surface. This would be equivalent to a high hydrogen overpotential. Therefore, as the pre-charged hydrogen concentrations is increased in a material, the H fugacity in equilibrium increases, and the overpotential decreases as in Equation 77, which will be reflected in the coupled potential measured at the surface of the thin film by the SKP.

3.5.2. Limitations of H Detection in SKP

While the SKP has been shown a viable tool for localized H detection, a range of factors influence the effectiveness of this application in the current setup. The primary concern is the range and types of materials for which this technique is viable. For optimal performance, a material must possess a very low $D_{H,eff}$, high H capacity, and have high corrosion resistance. As this technique takes time, for increased localized detection, a low $D_{H,eff}$ slows the redistribution of H with measurement. Possible addition of a cooling stage may be helpful as diffusion is temperature dependent, and cooling the samples

would slow the redistribution of hydrogen within the sample. High corrosion resistance is necessary as the surface potential, taken to be the mixed coupled potential, needs to be dependent on the H concentration and oxidation, through the hydrogen oxidation reaction, rather than corrosion processes in order to determine significant effects of H. This was established for the materials of interest to this dissertation in Figure 110, where corrosion current densities for measured UNS S46500 are well below the H oxidation current density, UNS K92580 is lower, but dependent on environment, and UNS G10180 has a corrosion current density that is initially very close to the H oxidation current density and increases above it with time. This indicates the viability of the SKP as a detection method for these materials, that it is reasonable for UNS S46500 and somewhat for UNS K92580, but is not a valid method for UNS G10180 as the corrosion rate would dominate the measurements in the SKP. As mentioned a cooling stage may aid in reducing the $D_{H,eff}$ for UNS G10180 and result in a change in the $\frac{\partial C}{\partial x}$, possibly increasing the limiting $i_{H,ox}$. However, this material still has a low trap capacity and is easily susceptible to corrosion, therefore it is unlikely that a cooling stage alone will make this a viable alloy for H detection in the SKP.

3.5.2.1. Limitations of Sample Size and Time

Other factors effecting optimization of SKP measurements are sample dimensions, in that samples need to be fairly planar to achieve higher resolutions. The tip size plays a role in this, as a smaller tip increases the resolution, this was seen in calculations performed of the correction to the lateral response in Figure 67-c. However the at the signal decreases with size and thus it is necessary for the distance between tip and sample to decrease to

enhance the signal. This also increases the need for a smoothly polished planar sample surface to avoid geometry effects.[30]

Time dependence is also significant. With the current SKP, the time of measurement is limited both by the stepper motor rate and the need to control gradient adjustments. As gradient bounds are decreased a higher resolution can be achieved, however, the time to achieve a decreased gradient bound takes longer for each measurement. As mentioned previously and seen by the effect of the change in limiting current for H oxidation seen in Figure 109, the time it takes for an SKP measurement can greatly affect the dependence of the SKP potential on the hydrogen concentration. Therefore, a balance between the gradient bounds and measurement time is necessary in order to achieve a relevant H concentration measurement.

Finally, as shown previously, RH can effect potential measurements in the SKP. More advanced SKP systems have the ability not only to control RH, but also gas concentrations such as Oxygen and Nitrogen, which have also been shown to influence the SKP potential.[25, 42, 75] As the concentration of Oxygen in the atmosphere can govern the diffusion limiting current for ORR at the surface of the thin film, this could play an important role in the measurements of the SKP potential.

3.6. Future Work

Measurements from the SKP technique of spatial hydrogen detection can be used to determine the local H concentration at a pit. This can be of great significance when regarding the K_{TH} (stress intensity threshold) of a material.

$$K_{TH} = Y\sigma\sqrt{\pi a} \quad \text{Equation 78}$$

Where Y is a dimensionless geometry factor, σ is the applied stress at failure, and a is the length of a surface crack or sharp surface flaw like at a pit. It has been seen that hydrogen concentrations can greatly affect the K_{TH} of a material. [50] K_{TH} decreases with increased hydrogen concentration; therefore, the material can either fail at lower applied stress, or tolerate smaller cracks. As pit to crack transition can occur, determination of H produced at a pit in a material will give an indication of the decrease in the applied stress tolerable for that material and the possible increased susceptibility towards cracking and/or failure. Dimensions of interest (as shown previously in Ch. 1, Figure 1) in these processes are at much smaller length scales than attainable with the SKP, thus transition to measurements with SKPFM seems a likely next step.

However, further calibration and optimization of significant controllable factors in the SKP should be taken into account. For example, the relative humidity of the measurement environment can greatly affect the potential measured in the SKP (Figure 90 and Figure 91), and thus has been kept at a constant 57 % RH for all measurements

taken in this study. Future work should include further study of the effect of RH as well as the water layer thickness established on the SKP potential.

If explored further, hydrogen detection capability may be improved at an optimized RH. In other experiments, fixed O₂/H₂ gas ratios have been maintained.[75] Pd thin films have been deposited on the measurement surfaces to enhance H detection.[25]

To expand the capabilities of this technique, additional investigation into use with other alloys is necessary. The effect of not only alloy, but surface condition: morphology and roughness, should also be investigated. Calibration between the potential measured in the SKP and the diffusible hydrogen concentration is necessary for each material prior to implementation for use with atmospheric exposure assessments. Also, the SKP potential measurements can be affected by both the corrosion rate as well as the hydrogen concentration. Therefore, further research into the effect of corrosion on hydrogen measurements in the SKP is necessary for expansion of the technique to more highly corrosive alloys. Possible techniques could be used to enhance the resolution in terms of H detection, such as NaOH printing to passivate, making the exit surface more reactive to H desorption, thus possibly increasing the detection limit of the SKP.

Finally, this technique has the ability to be scaled to a measurement with increased spatial resolution through use of the SKP force microscope (SKPFM). The current work was carried out in a standard SKP with a probe tip diameter of 50 µm. Future work could not only make it possible to detect H around crack tips, such as found previously in SKPFM

[45], but, with new techniques of combining with calibration, actual quantitative H concentrations could be measured at the 100 nm length scale. Other parameters, such as local $D_{H,eff}$, could also be investigated.

3.7. Conclusions

- Hydrogen pre-charging affects the OCP and anodic kinetics of the materials of interest. Some studies have shown this could be due to enhanced anodic dissolution after H pre-charging.[52] However, hydrogen oxidation upon egress is shown here to be a major factor.
- H has an effect on the SKP potential measured on a bare ferrous alloy surface in humid air.
 - This is due to the establishment of the H electrode electrochemical cell at the surface of a H pre-charged metal. In order to observe this effect, $i_{corr} \ll i_{L,Hox}$. The mixed potential established at the surface of the thin film sensed by the SKP tip reflects the couple of H oxidation and ORR. The mixed potential is dependent upon the H desorption from the material and an H electrode is formed. Concentration, time post-charging, and diffusion coefficient for the material of interest effect $\frac{\partial C}{\partial x}$, and in turn the limiting current density of hydrogen oxidation at the surface and thus the dependence of the SKP potential on the H concentration.
 - The SKP can be utilized to map H concentrations at μm to mm spatial resolution once the SKP potential of a specific material is calibrated for known pre-charged H concentrations. As established in this chapter, this

calibration varies for different materials and different tempers dependent on their H uptake capacity, $D_{H,eff}$, and corrosion rates. Therefore, it is necessary to establish an independent calibration for each material in a specific SKP measurement environment to apply the SKP as a viable method for localized H detection.

- The SKP potential has been calibrated to a range of pre-charged H concentrations for UNS S46500 in two tempers and UNS K92580 at a specific time post charging (5 min).
- Factors governing spatial resolution, from both material and measurement tool perspectives, must be further investigated and understood to make this a readily applicable approach for spatial H detection, such as for atmospherically corroded UHSS.
- SKP volta potential mapping combined with diffusion analysis of concentration depth profiles has been demonstrated as a novel method for determination of local $D_{H,eff}$. For peak-aged UNS K92580, $D_{H,eff}$ was 1 to $2.5 \times 10^{-8} \text{ cm}^2/\text{s}$, compared to a TDS derived value of $9 \times 10^{-9} \text{ cm}^2/\text{s}$. [51] For UNS S46500 pre-charged under the same conditions, $D_{H,eff}$ was $2.5 \times 10^{-8} \text{ cm}^2/\text{s}$ at positions less than $750 \text{ }\mu\text{m}$ below the charging surface. The SKP could be applied as a novel technique to quantify hydrogen transport rates local to crack tips and microstructural traps.

3.8. References

1. Cruz, R.P.V., A. Nishikata, and T. Tsuru, *Pitting corrosion mechanism of stainless steels under wet-dry exposure in chloride-containing environments*. Corrosion Science, 1998. **40**(1): p. 125-139.
2. Cruz, R.P.V., A. Nishikata, and T. Tsuru, *AC impedance monitoring of pitting corrosion of stainless steel under a wet-dry cyclic condition in chloride-containing environment*. Corrosion Science, 1996. **38**(8): p. 1397-1406.
3. Truman, J.E., *Stress-corrosion cracking of martensitic and ferritic stainless steels*. International Metals Reviews, 1981. **6**: p. 301-349.
4. Lee, Y. and R.P. Gangloff, *Measurement and modeling of hydrogen environment-assisted cracking of ultra-high-strength steel*. Metallurgical and Materials Transactions a-Physical Metallurgy and Materials Science, 2007. **38A**(13): p. 2174-2190.
5. Devanathan, M.A.V. and Z. Stachurski, *The Adsorption and Diffusion of Electolytic Hydrogen in Palladium*. Proceedings of the Royal Society of London. Series A., 1962(270): p. 90-102.
6. DeLuccia, J.J. and D.A. Berman, *An Electrochemical Technique to Measure Diffusible Hydrogen in Metals (Barnacle Electrode)*, in *Electrochemical Corrosion Testing*, A.S.T.M., Editor. 1981, ASTM International: West Conshohocken, PA. p. 256-273.
7. Thomas, R.L.S., et al., *Trap-governed hydrogen diffusivity and uptake capacity in ultrahigh-strength AERMET 100 steel*. Metallurgical and Materials Transactions a-Physical Metallurgy and Materials Science, 2002. **33**(7): p. 1991-2004.
8. Scully, J.R., G.A. Young, and S.W. Smith, *Hydrogen solubility, diffusion and trapping in high purity aluminum and selected Al-base alloys: Aluminium Alloys: Their Physical and Mechanical Properties, Pts 1-3*. Material Science Forum, 2000. **331-337**: p. 1583-1600.
9. Katano, G., K. Ueyama, and M. Mori, *Observation of hydrogen distribution in high-strength steel*. Journal of Materials Science, 2001. **36**(9): p. 2277-2286.
10. Otsuka, T. and T. Tanabe, *Hydrogen diffusion and trapping process around MnS precipitates in alpha Fe examined by tritium autoradiography*. Journal of Alloys and Compounds, 2007. **446**: p. 655-659.
11. Asaoka, T., et al., *Observation of Hydrogen Trapping in Fe-0.15wt-Percent Ti Alloy by High-Resolution Autoradiography*. Corrosion, 1978. **34**(2): p. 39-47.
12. Garet, M., et al., *Hydrogen trapping on non metallic inclusions in Cr-Mo low alloy steels*. Corrosion Science, 1998. **40**(7): p. 1073-1086.
13. Young, G.A. and J.R. Scully, *The effects of test temperature, temper, and alloyed copper on the hydrogen-controlled crack growth rate of an Al-Zn-Mg-(Cu) alloy*. Metallurgical and Materials Transactions a-Physical Metallurgy and Materials Science, 2002. **33**(4): p. 1167-1181.
14. Larignon, C., et al., *Investigation of Kelvin probe force microscopy efficiency for the detection of hydrogen ingress by cathodic charging in an aluminium alloy*. Scripta Materialia, 2013. **68**(7): p. 479-482.
15. Ovejero-García, J., *Hydrogen microprint technique in the study of hydrogen in steels*. Journal of Materials Science, 1985. **20**(7): p. 2623-2629.
16. Switzer, M., *Use of crevice scaling laws to investigate local hydrogen uptake in rescaled model pits*, in *Materials Science and Engineering*. 2003, University of Virginia: Charlottesville.
17. Tsuru, T., et al., *Hydrogen entry into steel during atmospheric corrosion process*. Corrosion Science, 2005. **47**(10): p. 2431-2440.
18. Zhang, G.A. and Y.F. Cheng, *Micro-electrochemical characterization of corrosion of welded X70 pipeline steel in near-neutral pH solution*. Corrosion Science, 2009. **51**(8): p. 1714-1724.

19. Krawiec, H., V. Vignal, and R. Oltra, *Use of the electrochemical microcell technique and the SVET for monitoring pitting corrosion at MnS inclusions*. Electrochemistry Communications, 2004. **6**(7): p. 655-660.
20. Modiano, S., et al., *Changes on iron electrode surface during hydrogen permeation in borate buffer solution*. Electrochimica Acta, 2008. **53**(10): p. 3670-3679.
21. Yuan, Y.A., et al., *Study of the effects of hydrogen on the pitting processes of X70 carbon steel with SECM*. Electrochemistry Communications, 2010. **12**(12): p. 1804-1807.
22. Tefashe, U.M., et al., *Local flux of hydrogen from magnesium alloy corrosion investigated by scanning electrochemical microscopy*. Journal of Electroanalytical Chemistry, 2014. **720**: p. 121-127.
23. Senoz, C., et al., *Scanning Kelvin Probe as a highly sensitive tool for detecting hydrogen permeation with high local resolution*. Electrochemistry Communications, 2011. **13**(12): p. 1542-1545.
24. Larignon, C., et al., *Combined Kelvin probe force microscopy and secondary ion mass spectrometry for hydrogen detection in corroded 2024 aluminium alloy*. Electrochimica Acta, 2013. **110**: p. 484-490.
25. Evers, S. and M. Rohwerder, *The hydrogen electrode in the "dry": A Kelvin probe approach to measuring hydrogen in metals*. Electrochemistry Communications, 2012. **24**: p. 85-88.
26. Stratmann, M., *The Investigation of the Corrosion Properties of Metals, Covered with Adsorbed Electrolyte Layers - a New Experimental-Technique*. Corrosion Science, 1987. **27**(8): p. 869-872.
27. Stratmann, M. and H. Streckel, *On the Atmospheric Corrosion of Metals Which Are Covered with Thin Electrolyte Layers .1. Verification of the Experimental-Technique*. Corrosion Science, 1990. **30**(6-7): p. 681-696.
28. Stratmann, M. and H. Streckel, *On the Atmospheric Corrosion of Metals Which Are Covered with Thin Electrolyte Layers .2. Experimental Results*. Corrosion Science, 1990. **30**(6-7): p. 697-714.
29. McMurray, H.N. and G. Williams, *Probe diameter and probe-specimen distance dependence in the lateral resolution of a scanning Kelvin probe*. Journal of Applied Physics, 2002. **91**(3): p. 1673-1679.
30. Rohwerder, M. and F. Turcu, *High-resolution Kelvin probe microscopy in corrosion science: Scanning Kelvin probe force microscopy (SKPFM) versus classical scanning Kelvin probe (SKP)*. Electrochimica Acta, 2007. **53**(2): p. 290-299.
31. Wicinski, M., W. Burgstaller, and A.W. Hassel, *Lateral Resolution in Scanning Kelvin Probe Microscopy*. Corrosion Science, 2016. **104**: p. 1-8.
32. C. Chen, C.B.B., and F. Mansfeld, *Scanning Kelvin Probe Analysis of the Potential Distribution under Small Drops of Electrolyte*. Materials Science Forum, 1998. **289-292**: p. 181-192.
33. Nazarov, A. and D. Thierry, *Rate-determining reactions of atmospheric corrosion*. Electrochimica Acta, 2004. **49**(17-18): p. 2717-2724.
34. Morton, S.C. and G.S. Frankel, *Atmospheric pitting corrosion of AA7075-T6 under evaporating droplets with and without inhibitors*. Materials and Corrosion-Werkstoffe Und Korrosion, 2014. **65**(4): p. 351-361.
35. Lin, H. and G.S. Frankel, *Atmospheric Corrosion of Cu during Constant Deposition of NaCl*. Journal of the Electrochemical Society, 2013. **160**(8): p. C336-C344.
36. Chen, Z.Y., et al., *Effect of sodium chloride particles on the atmospheric corrosion of pure copper*. Corrosion, 2004. **60**(5): p. 479-491.
37. Sun, M., et al., *Electrochemical and initial corrosion behavior of ultrahigh strength steel by scanning Kelvin probe*. Journal of Materials Engineering and Performance, 2013. **22**(3): p. 815-822.

38. Ornek, C. and D.L. Engelberg, *SKPFM measured Volta potential correlated with strain localisation in microstructure to understand corrosion susceptibility of cold-rolled grade 2205 duplex stainless steel*. Corrosion Science, 2015. **99**: p. 164-171.
39. Evers, S., C. Senoz, and M. Rohwerder, *Spatially resolved high sensitive measurement of hydrogen permeation by Scanning Kelvin Probe Microscopy*. Electrochimica Acta, 2013. **110**: p. 534-538.
40. Evers, S., C. Senoz, and M. Rohwerder, *Hydrogen detection in metals: a review and introduction of a Kelvin probe approach*. Science and Technology of Advanced Materials, 2013. **14**(1).
41. Schaller, R.F. and J.R. Scully, *Measurement of effective hydrogen diffusivity using the Scanning Kelvin Probe*. Electrochemistry Communications, 2014. **40**: p. 42-44.
42. Williams, G., H.N. McMurray, and R.C. Newman, *Surface oxide reduction by hydrogen permeation through iron foil detected using a scanning Kelvin probe*. Electrochemistry Communications, 2013. **27**: p. 144-147.
43. Nazarov, R.P., A.I. Marshakov, and A.A. Rybkina, *Iron hydrogenation under atmospheric corrosion. Studies using a scanning vibrating microscope*. Protection of Metals and Physical Chemistry of Surfaces 2015. **51**(3): p. 347-359.
44. Koyama, M., et al., *Spatially and Kinetically Resolved Mapping of Hydrogen in a Twinning-Induced Plasticity Steel by Use of Scanning Kelvin Probe Force Microscopy*. Journal of the Electrochemical Society, 2015. **162**(12): p. C638-C647.
45. Wang, G., et al., *Investigation of hydrogen evolution and enrichment by scanning Kelvin probe force microscopy*. Electrochemistry Communications, 2013. **35**: p. 100-103.
46. Al-Ghamdi, S., *The Effect of Aqueous Phase Inhibitors on Mitigating Potential-Dependent Hydrogen Environment Assisted Cracking of an Ultra-High Strength Steel*, in *Materials Science and Engineering*. 2010, University of Virginia: Charlottesville.
47. DeLuccia, J.J. and D.A. Berman, *An electrochemical technique to measure diffusible hydrogen in metals (Barnacle electrode)*, in *Electrochemical Corrosion Testing*. 1981, ASTM STP. p. 256-273.
48. Schaller, R.F., et al., *Evaluation of $D_{H,eff}$ for UNS S46500 using Thermal Desorption Spectroscopy*, in *Unpublished raw data*. 2012, University of Virginia: Charlottesville.
49. Coesa, U.S., *Standard Atmosphere 1976*. 1976, US Government Printing Office: Washington, D.C.
50. Kehler, B.A. and J.R. Scully, *Predicting the effect of applied potential on crack tip hydrogen concentration in low-alloy martensitic steels*. Corrosion, 2008. **64**(5): p. 465-477.
51. Thomas, R.L.S., et al., *Trap-governed hydrogen diffusivity and uptake capacity in ultrahigh-strength AERMET 100 steel*. Metallurgical and Materials Transactions a-Physical Metallurgy and Materials Science, 2002. **33**(7): p. 1991-2004.
52. Thomas, S., et al., *The effect of absorbed hydrogen on the dissolution of steel*. Submitted to ACS Applied Materials and Interfaces, 2015.
53. Qiao, L.J. and J.L. Luo, *Hydrogen-facilitated anodic dissolution of austenitic stainless steels*. Corrosion, 1998. **54**(4): p. 281-288.
54. Ningshen, S., et al., *Hydrogen effects on the passive film formation and pitting susceptibility of nitrogen containing type 316L stainless steels*. Corrosion Science, 2006. **48**(5): p. 1106-1121.
55. Li, M.C. and Y.F. Cheng, *Mechanistic investigation of hydrogen-enhanced anodic dissolution of X-70 pipe steel and its implication on near-neutral pH SCC of pipelines*. Electrochimica Acta, 2007. **52**(28): p. 8111-8117.
56. Ejaz, A., et al., *The effects of hydrogen on anodic dissolution and passivation of iron in alkaline solutions*. Corrosion Science, 2015. **101**: p. 165-181.

57. Yu, J.G., J.L. Luo, and P.R. Norton, *Investigation of hydrogen induced pitting active sites*. *Electrochimica Acta*, 2002. **47**(25): p. 4019-4025.
58. Kehler, B.A., *Modeling and Experiments to Explain the Potential Dependency of an UHSS to Hydrogen Environment Assisted Cracking*, in *Materials Science and Engineering*. 2008, University of Virginia: Charlottesville. p. 296.
59. Schaller, R.F. and J.R. Scully, *Spatial determination of diffusible hydrogen concentrations proximate to pits in a Fe–Cr–Ni–Mo steel using the Scanning Kelvin Probe*. *Electrochemistry Communications*, 2016. **63**: p. 5-9.
60. Shackelford, J.F., *Introduction to materials science for engineers*. 5th ed. 2000, Upper Saddle River, N.J.: Prentice Hall. xvii, 877 p.
61. Fukai, Y., *The metal-hydrogen system : basic bulk properties*. Springer series in materials science. 1993, Berlin ; New York: Springer-Verlag. x, 355 p.
62. Adhikari, S., et al., *Hydrogen in aluminum during alkaline corrosion*. *Electrochimica Acta*, 2010. **55**(19): p. 5326-5331.
63. Leygraf, C. and T.E. Graedel, *Atmospheric corrosion*. The Electrochemical Society series. 2000, New York: Wiley-Interscience. xii, 354 p.
64. Lee, S. and R.W. Staehle, *Adsorption of water on copper, nickel, and iron*. *Corrosion*, 1997. **53**(1): p. 33-42.
65. Dante, J.F. and R.G. Kelly, *The Evolution of the Adsorbed Solution Layer during Atmospheric Corrosion and Its Effects on the Corrosion Rate of Copper*. *Journal of the Electrochemical Society*, 1993. **140**(7): p. 1890-1897.
66. Sinclair, J.D., L.A. Psotakelty, and C.J. Weschler, *Indoor Outdoor Ratios and Indoor Surface Accumulations of Ionic Substances at Newark, New-Jersey*. *Atmospheric Environment*, 1988. **22**(3): p. 461-469.
67. Xu, N.X., et al., *Laboratory observation of dew formation at an early stage of atmospheric corrosion of metals*. *Corrosion Science*, 2002. **44**(1): p. 163-170.
68. Parthasarathy, A., et al., *Temperature-Dependence of the Electrode-Kinetics of Oxygen Reduction at the Platinum Nafion(R) Interface - a Microelectrode Investigation*. *Journal of the Electrochemical Society*, 1992. **139**(9): p. 2530-2537.
69. Gubbins, K.E. and R.D. Walker, *The solubility and diffusivity of oxygen in electrolytic solutions*. *Journal of Electrochemical Society*, 1965. **112**(5): p. 469-471.
70. Schindelholz, E., B.E. Risteen, and R.G. Kelly, *Effect of Relative Humidity on Corrosion of Steel under Sea Salt Aerosol Proxies*. *Journal of the Electrochemical Society*, 2014. **161**(10): p. C450-C459.
71. Revie, R.W. and H.H. Uhlig, *Corrosion and corrosion control : an introduction to corrosion science and engineering*. 4th ed. 2008, Hoboken, N.J.: Wiley-Interscience. xx, 490 p.
72. Gileadi, E., E. Kirowa-Eisner, and J. Penciner, *Interfacial electrochemistry : an experimental approach*. 1975, Reading, Mass.: Addison-Wesley Pub. Co., Advanced Book Program. xviii, 525 p.
73. Jones, D.A., *Principles and prevention of corrosion*. 2nd ed. 1996, Upper Saddle River, NJ: Prentice Hall. xvi, 572 p.
74. Subramanyan, *Electrochemical Aspects of Hydrogen in Metals*, in *Comprehensive Treatise of Electrochemistry*, J.O.M. Bockris, B.E. Conway, and E. Yeager, Editors. 1991, Plenum Press: Cleveland, OH.
75. Schimo, G., W. Burgstaller, and A.W. Hassel, *Potentiodynamic hydrogen permeation on Palladium-Kelvin probe compared to 3D printed microelectrochemical cell*. *Electrochemistry Communications*, 2015. **60**: p. 208-211.
76. *Alloy Data - Custom 465 All*. 1996, C.T. Corporation: Reading, PA.

77. Nazarov, R.P., A.I. Marshakov, and A.A. Rybkina, *Iron hydrogenation under atmospheric corrosion. Studies using a scanning vibrating microscope*. Protection of Metals and Physical Chemistry of Surfaces, 2015. **51**(3): p. 347-359.
78. Cole, I.S., et al., *What really controls the atmospheric corrosion of zinc? Effect of marine aerosols on atmospheric corrosion of zinc*. International Materials Reviews, 2009. **54**(3): p. 117-133.
79. Council, N.R., ed. *Research Opportunities in Corrosion Science and Engineering*. 2011, The National Academies Press: Washington D.C.

3.9. Tables:

Table 20. UNS K92580 and UNS S46500 Composition (wt. %).[76]

Material	Fe	C	Mn	Si	P	S	Cr	Ni	Mo	N	Ti	Co
UNS K92580 ^a	Bal.	0.23	0.019	-	-	0.0008	2.78	10.89	1.21	-	-	12.8
UNS S46500 ^b	Bal.	0.005	0.02	0.02	0.002	0.002	11.50	11.04	0.94	0.002	1.54	-

^aAerMet 100™ peak-aged obtained through Carpenter Technology

^bCustom 465™ H900 temper

Table 21. UNS K92580 and UNS S46500 Material Properties.[76]

Temper	Yield Strength	Tensile Strength	Elongation	Reduction of Area	Rockwell Hardness C
UNS K92580 peak aged	1724 MPa	1965 MPa	14 %	65 %	54
UNS S46500 Annealed/CT	772 MPa	951 MPa	20 %	75 %	29.5
UNS S46500 H900	1703 MPa	1779 MPa	14 %	51 %	51

Table 22. Experimental sequence for cathodic pre-charging followed by OCP and EIS to explore effect of solution and pre-charging environments.

Sequence		Experimental Procedure										
Test 1	Pre-charge 1 h ($\eta_H = -800$ mV)	EIS post 0 min	OCP 1 min	EIS post 1 min	OCP 10 min	EIS post 10 min	OCP 30 min	EIS post 30 min	OCP 60 min	EIS post 60 min	OCP 120 min	EIS post 120 min
		EIS post 0 min	OCP 1 min	EIS post 1 min	OCP 10 min	EIS post 10 min	OCP 30 min	EIS post 30 min	OCP 60 min	EIS post 60 min	OCP 120 min	EIS post 120 min
Test 2	OCP 1 h	EIS post 0 min	OCP 1 min	EIS post 1 min	OCP 10 min	EIS post 10 min	OCP 30 min	EIS post 30 min	OCP 60 min	EIS post 60 min	OCP 120 min	EIS post 120 min
		EIS post 0 min	OCP 1 min	EIS post 1 min	OCP 10 min	EIS post 10 min	OCP 30 min	EIS post 30 min	OCP 60 min	EIS post 60 min	OCP 120 min	EIS post 120 min
Test 3	No initial test	EIS post 0 min	OCP 1 min	EIS post 1 min	OCP 10 min	EIS post 10 min	OCP 30 min	EIS post 30 min	OCP 60 min	EIS post 60 min	OCP 120 min	EIS post 120 min
		EIS post 0 min	OCP 1 min	EIS post 1 min	OCP 10 min	EIS post 10 min	OCP 30 min	EIS post 30 min	OCP 60 min	EIS post 60 min	OCP 120 min	EIS post 120 min

Table 23. SKP and SKPFM Measurements: In-situ backside H detection.

Sample	Exposure Environment	SKP Measurement Environment
25 μm Pd [25]	0.1 M H_2SO_4	Dry Nitrogen (<0.1 % RH)
25 μm Pd, 1 μm Fe, 100 nm Pd [25]	0.1 M H_2SO_4	Dry Nitrogen (<0.1 % RH)
7 μm Zn (unscribed & scribed), 0.8 mm low alloyed steel, 100 nm Pd [39]	0.1 M NaCl	Dry Nitrogen (<0.1 % RH)
300 nm Au pattern on 100 μm Pd foil[23]	unknown	Wet air 93% RH or wet N_2 93% RH
0.1 mm Pd foil [75]	Deaerated 0.1 M NaOH	Dry N_2 5.3 % RH and 0.8 Vol% O_2
Zinc plated 0.8 mm carbon steel with 5 mm defect in the zinc [77]	0.5 M NaCl droplet	Humid air 95% RH or Humid N_2 95% RH or dry air 50% RH
50 mm 2024-T351[24]	Cyclic freezing corrosion test, 8 h in RT 1 M NaCl, 16 h in air at -20°C	Lab air, 40% RH

Table 24. Possible Oxidation Reactions and Their Nernst Potentials ($\sum i_{ox} = \sum i_c = i_{ORR}$).

Cathodic Reactions	Nernst Equation(V_{SCE})
$\text{H}_2 = 2\text{H}^+ + 2\text{e}^-$	$E_{\text{H}^+/\text{H}_2} = -0.241 - 0.059\text{pH} - 0.00295\log\rho_{\text{H}_2}$
$\text{H} = \text{H}^+ + \text{e}^-$	$E_{\text{H}^+/\text{H}} = -2.106 - 0.241 - 0.059\text{pH} - 0.00295\log\rho_{\text{H}_2}$
$\text{O}_2 + 2\text{H}_2\text{O} + 4\text{e}^- = 4\text{OH}^-$	$E_{\text{O}_2/\text{OH}^-} = 1.228 - 0.241 - 0.059\text{pH} + 0.00147\log\rho_{\text{O}_2}$
$2\text{FeO} + \text{H}_2\text{O} = \text{Fe}_2\text{O}_3 + 2\text{H}^+ + 2\text{e}^-$	$E_{\text{FeO}/\text{Fe}_2\text{O}_3} = -0.057 - 0.241 - 0.059\text{pH}$
$\text{Fe}(\text{OH})_2 + \text{H}_2\text{O} + \text{Fe}(\text{OH})_3 + \text{H}^+ + \text{e}^-$	$E_{\text{Fe}(\text{OH})_2/\text{Fe}(\text{OH})_3} = 0.271 - 0.241 - 0.059\text{pH}$
$2\text{Fe}_3\text{O}_4 + \text{H}_2\text{O} = 3\text{Fe}_2\text{O}_3 + 2\text{H}^+ + 2\text{e}^-$	$E_{\text{Fe}_3\text{O}_4/\text{Fe}_2\text{O}_3} = 0.221 - 0.241 - 0.059\text{pH}$
$\text{Fe}_3\text{O}_4 + 2\text{H}_2\text{O} = 3\text{FeOOH} + \text{H}^+ + \text{e}^-$	$E_{\text{Fe}_3\text{O}_4/\text{FeOOH}} = 1.208 - 0.241 - 0.059\text{pH}$
$2\text{Cr} + 3\text{H}_2\text{O} = \text{Cr}_2\text{O}_3 + 6\text{H}^+ + 6\text{e}^-$	$E_{\text{Cr}/\text{Cr}_2\text{O}_3} = -0.654 - 0.241 - 0.059\text{pH}$
$\text{Cr} + 2\text{H}_2\text{O} = \text{CrOOH} + 3\text{H}^+ + 3\text{e}^-$	$E_{\text{Cr}/\text{CrOOH}} = -0.512 - 0.241 - 0.059\text{pH}$
$2\text{CrO} + \text{H}_2\text{O} = \text{Cr}_2\text{O}_3 + 2\text{H}^+ + 2\text{e}^-$	$E_{\text{CrO}/\text{Cr}_2\text{O}_3} = -0.785 - 0.241 - 0.059\text{pH}$
$\text{CrO} + \text{H}_2\text{O} = \text{CrOOH} + \text{H}^+ + \text{e}^-$	$E_{\text{CrO}/\text{CrOOH}} = -0.360 - 0.241 - 0.059\text{pH}$

3.10. Figures:

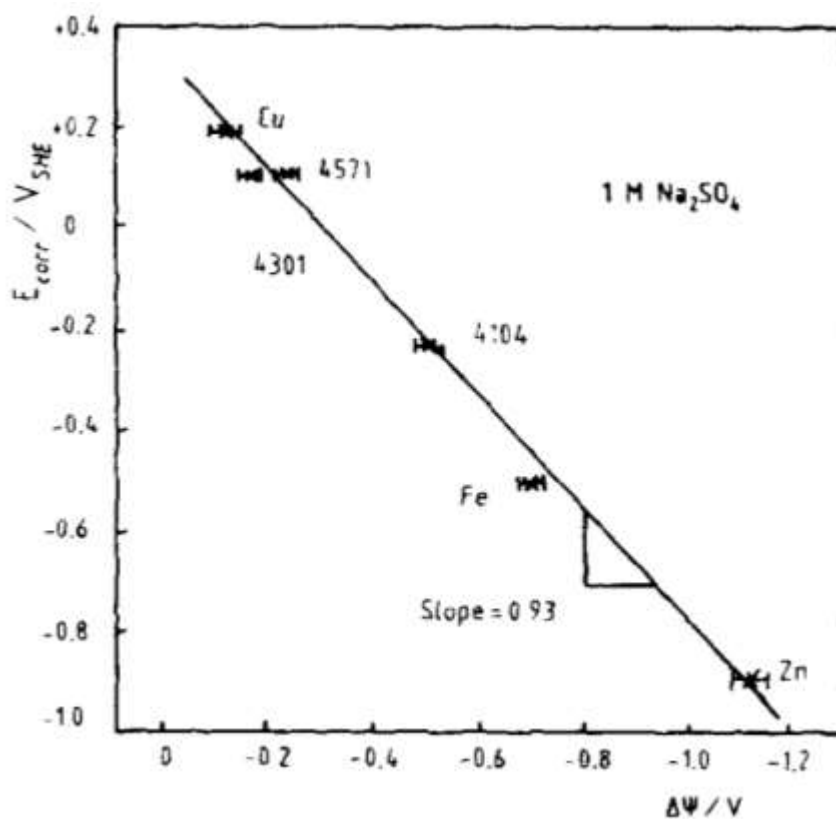


Figure 66. Calibration of the Au tip, Corrosion potential measured in bulk solution vs. the difference of the SKP potentials for different metals covered with 1 mm of 1 M Na₂SO₄. [26]

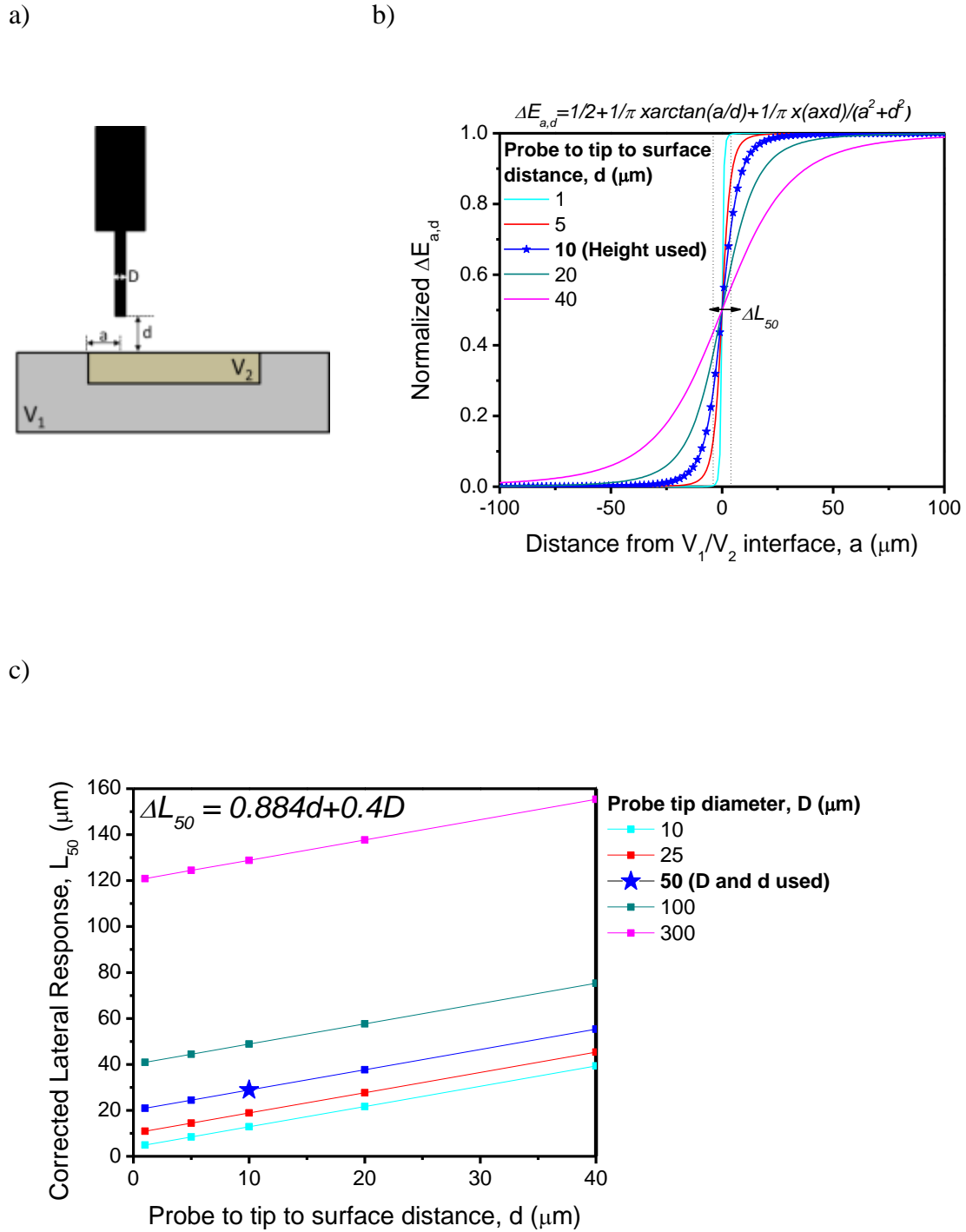


Figure 67. a) Schematic of a two potential (V_1 and V_2) sample in the SKP with a , the distance from the potential interface, d , the distance from the probe tip to sample, and D , the probe diameter noted. b) Estimation of the difference in normalized potential between V_1 and V_2 ($\Delta E_{a,d}$) based a with varied d . c) Calculation of the corrected lateral response, ΔL_{50} , based on d with varied D where the star indicates the test conditions in this study.

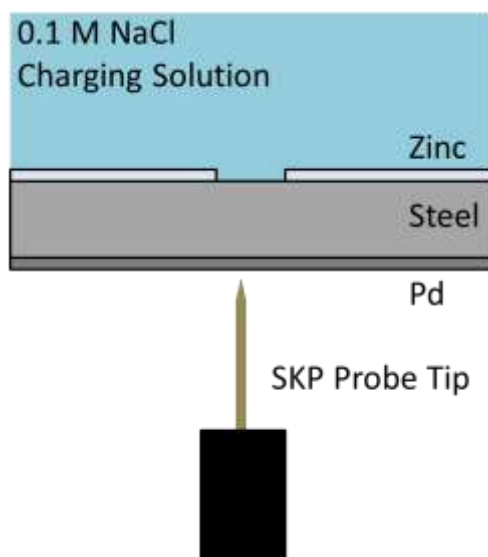


Figure 68. Schematic of SKP permeation measurement on Pd coated backside of a scribe in galvanized steel.[39]

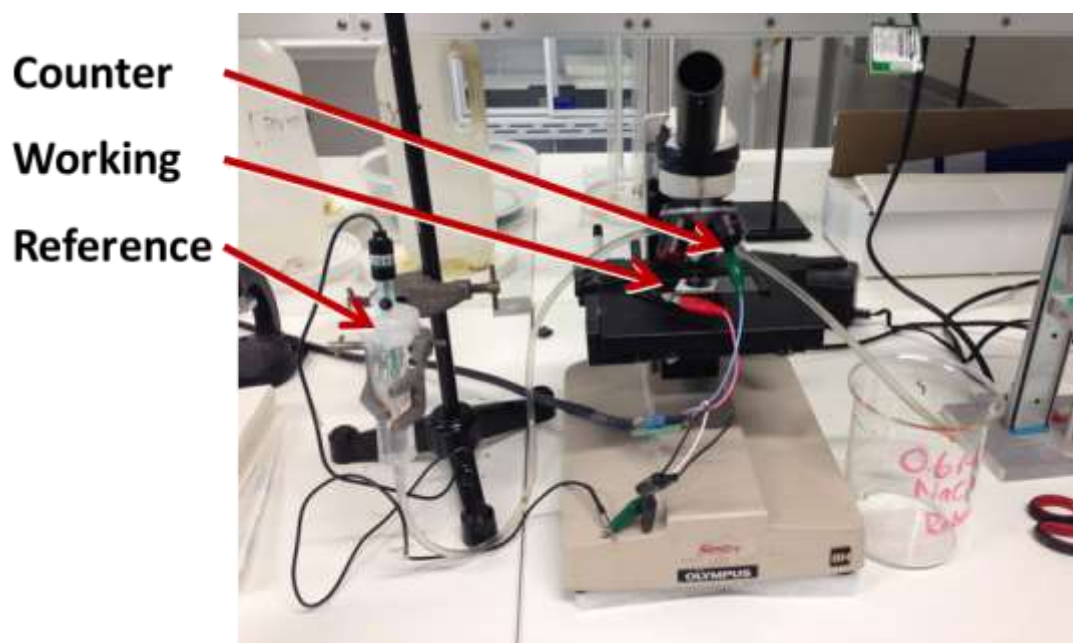


Figure 69. Image of Microcapillary cell.

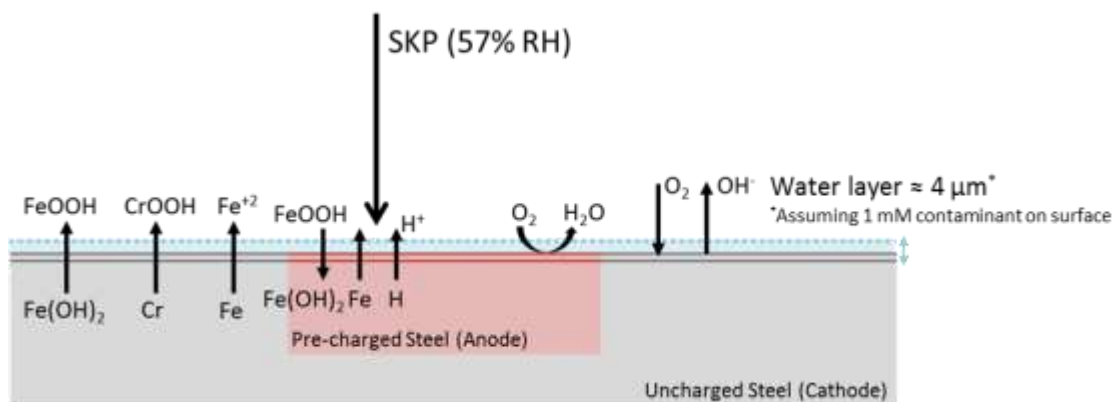


Figure 70. Schematic of the reactions during H at SKP measurement interface. The mixed potential in the red pre-charged zone represents a situation where the coupled potential is a H potential.

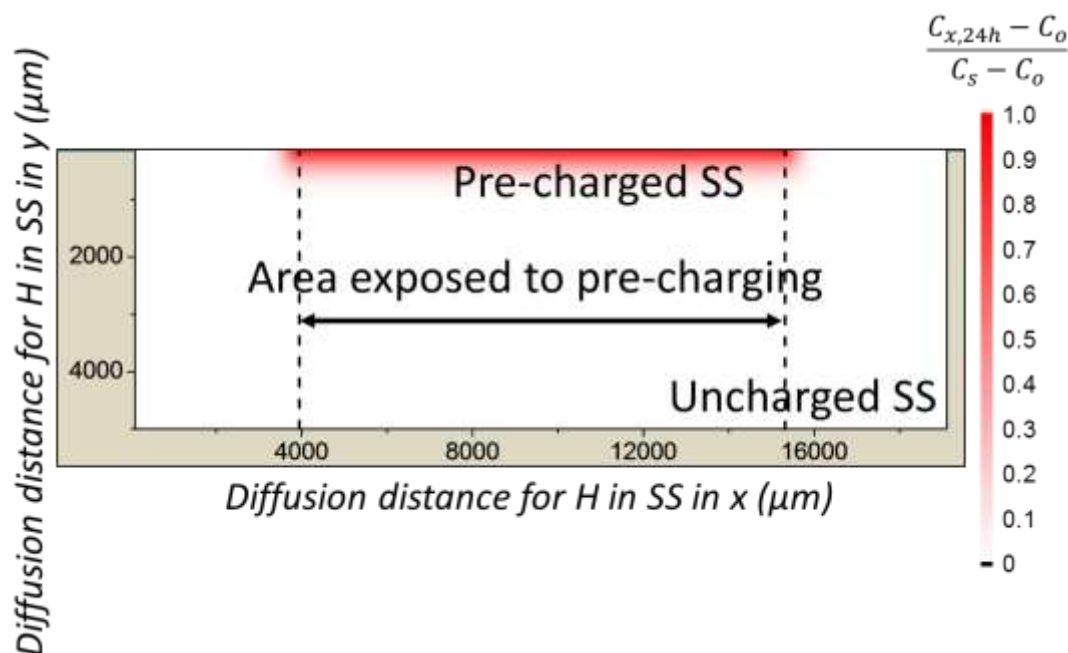


Figure 71. Example of steady state diffusion of H in UNS S46500 over the 24 h pre-charging time period.

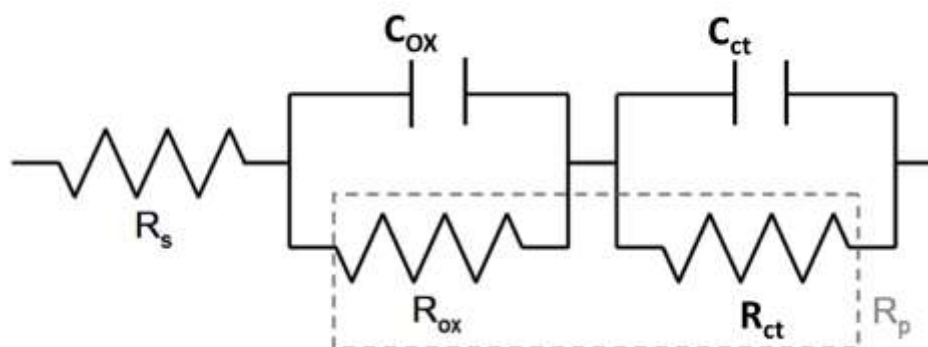
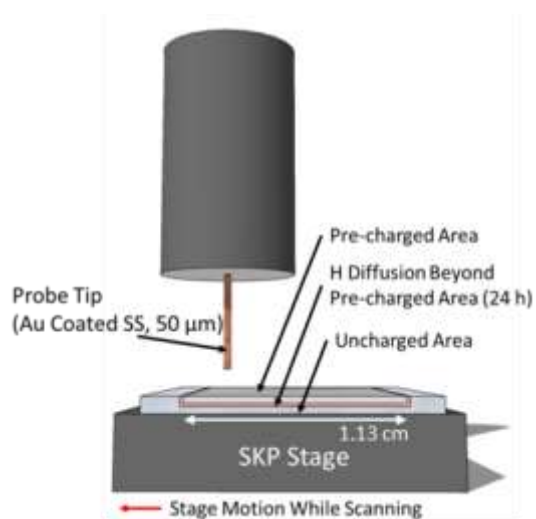


Figure 72. Model of equivalent circuit applied for EIS fitting at OCP in 0.6 M NaCl and 5 mM NaCl. [46]

a)



b)

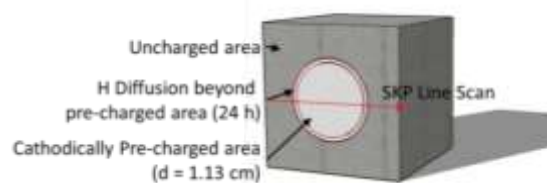


Figure 73. a) SKP stage setup and b) schematic of H pre-charged sample with position of SKP line scan.

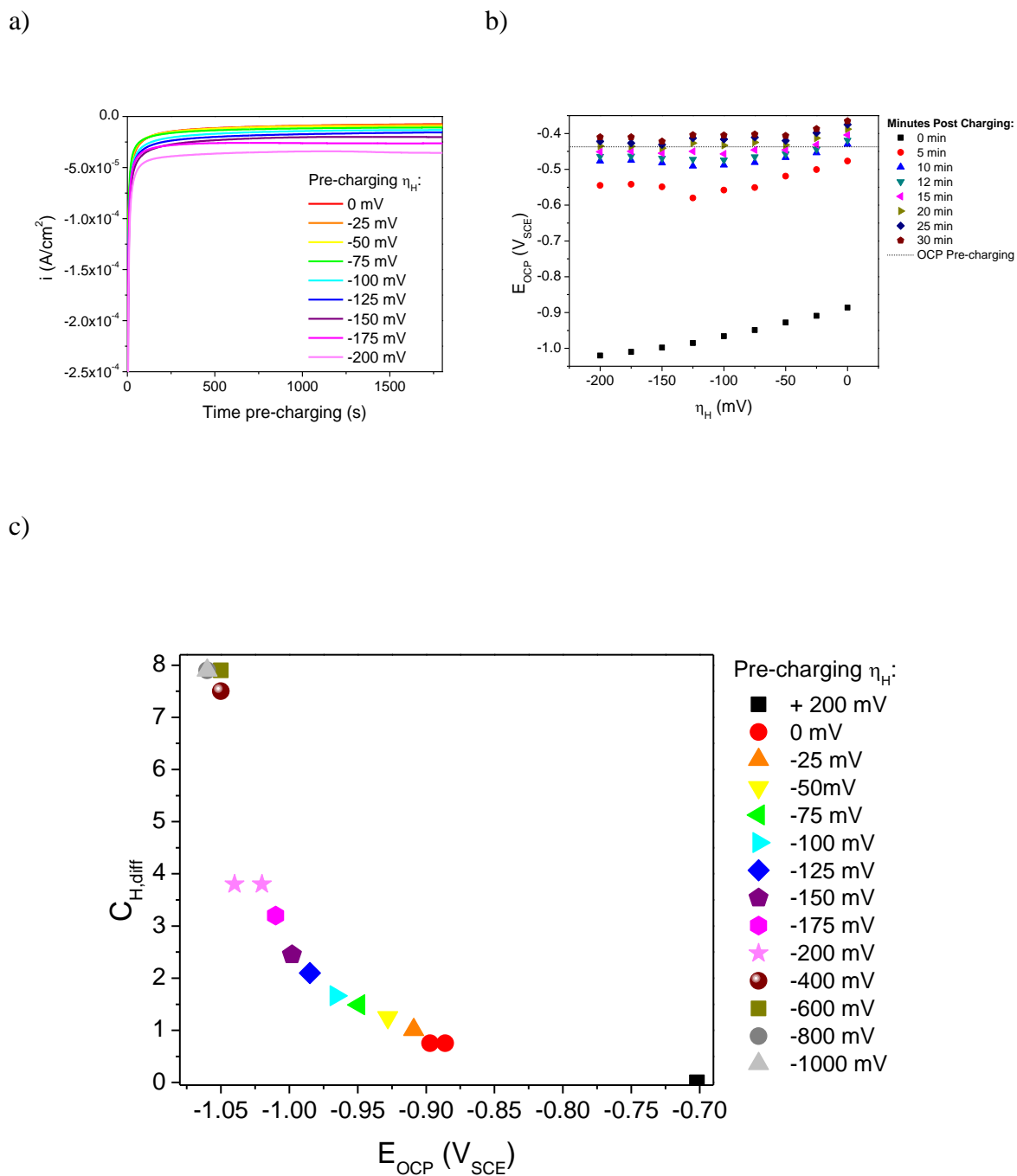
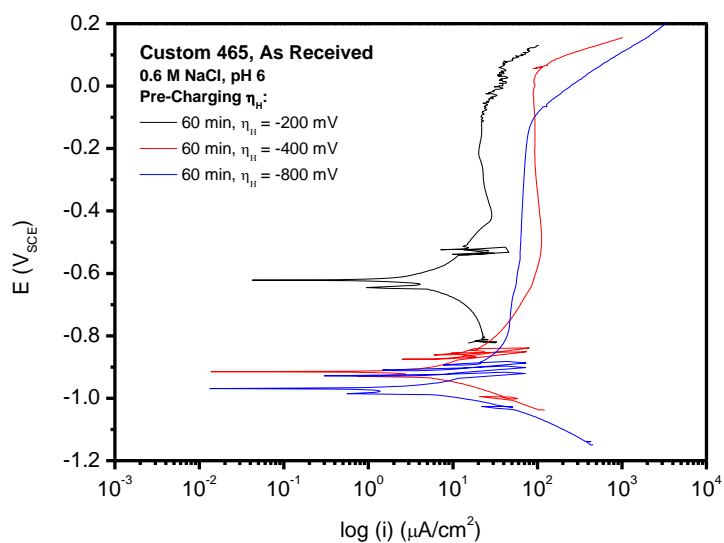
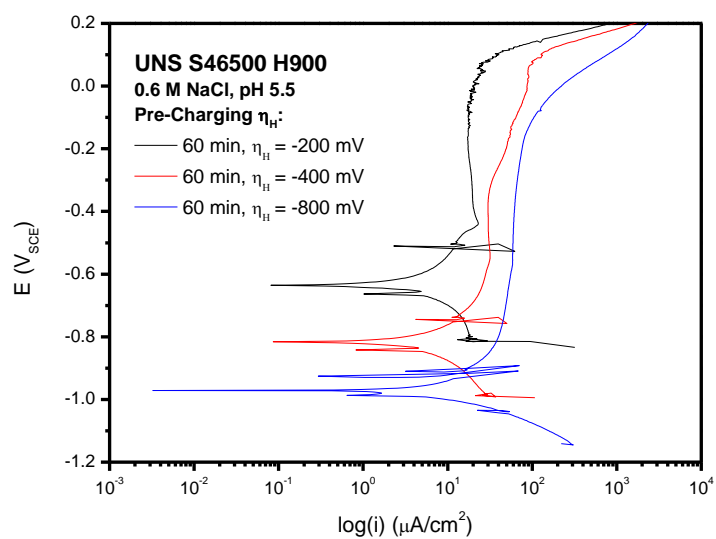


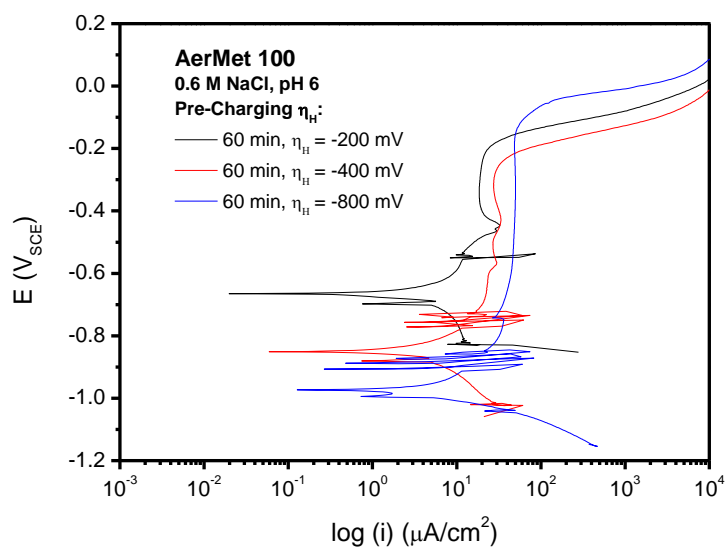
Figure 74. a) Pre-charging current densities vs. time from 30 min cathodic polarization of UNS K92580 in deaerated 0.1 M NaOH. b) E_{OCP} measured initially post-charging vs. the pre-charging overpotential in 0.1 M NaOH. c) $C_{H,diff}$ vs. E_{OCP} for UNS K92580. E_{OCP} determined from initial OCP measured post-charging for cathodic pre-charging tests, $C_{H,diff}$ determined from UNS K92580 reaction mechanism model for pH 10.[58]



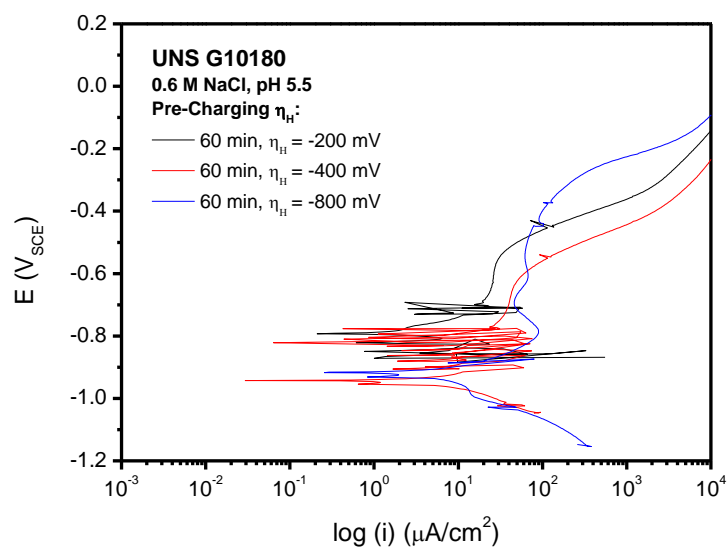
a)



b)

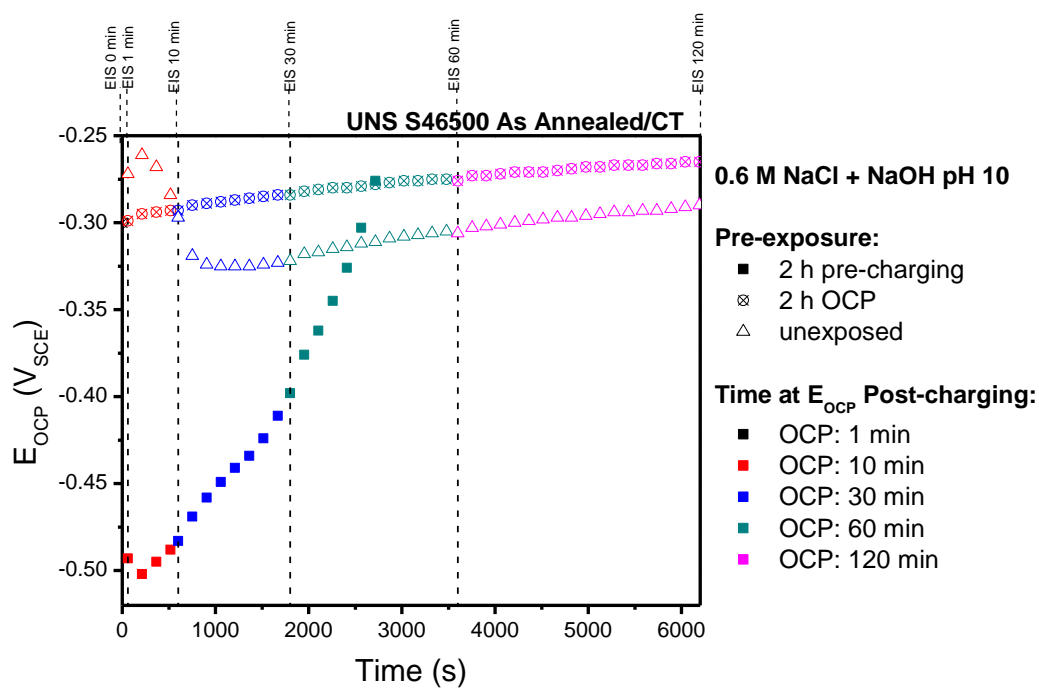


c)

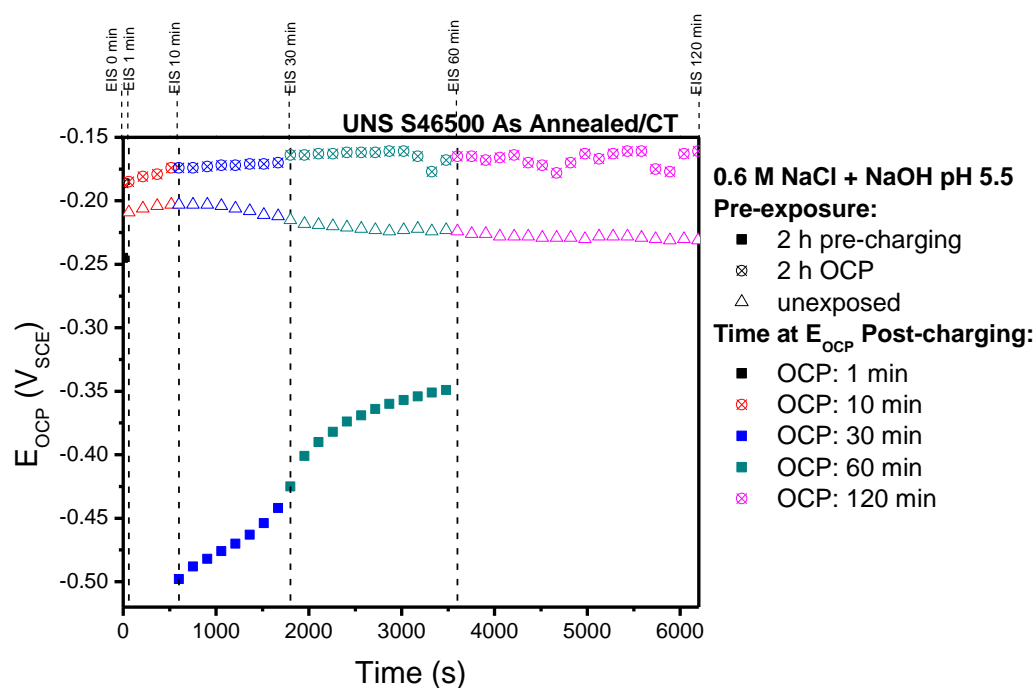


d)

Figure 75. Anodic polarizations in 0.6 M NaCl, pH 5.5. Polarizations scanned at 0.1667 mV/s from -200 mV vs. OCP to 1 V vs OCP. Scans were taken post hydrogen pre-charging for 1 h in 0.6 M NaCl + NaOH pH 10 at hydrogen overpotentials of -200, -400, and -600 mV for a) As Annealed/CT UNS S46500, b) H900 UNS S46500, c) UNS K92580, and d) UNS G10180.



a)



b)

Figure 76. E_{OCP} of As Annealed/CT UNS S46500 with 1 h hydrogen pre-charging, 1 h OCP, and no prior test a) in 0.6 M NaCl + NaOH pH 10 and b) in 0.6 M NaCl pH 5.5.

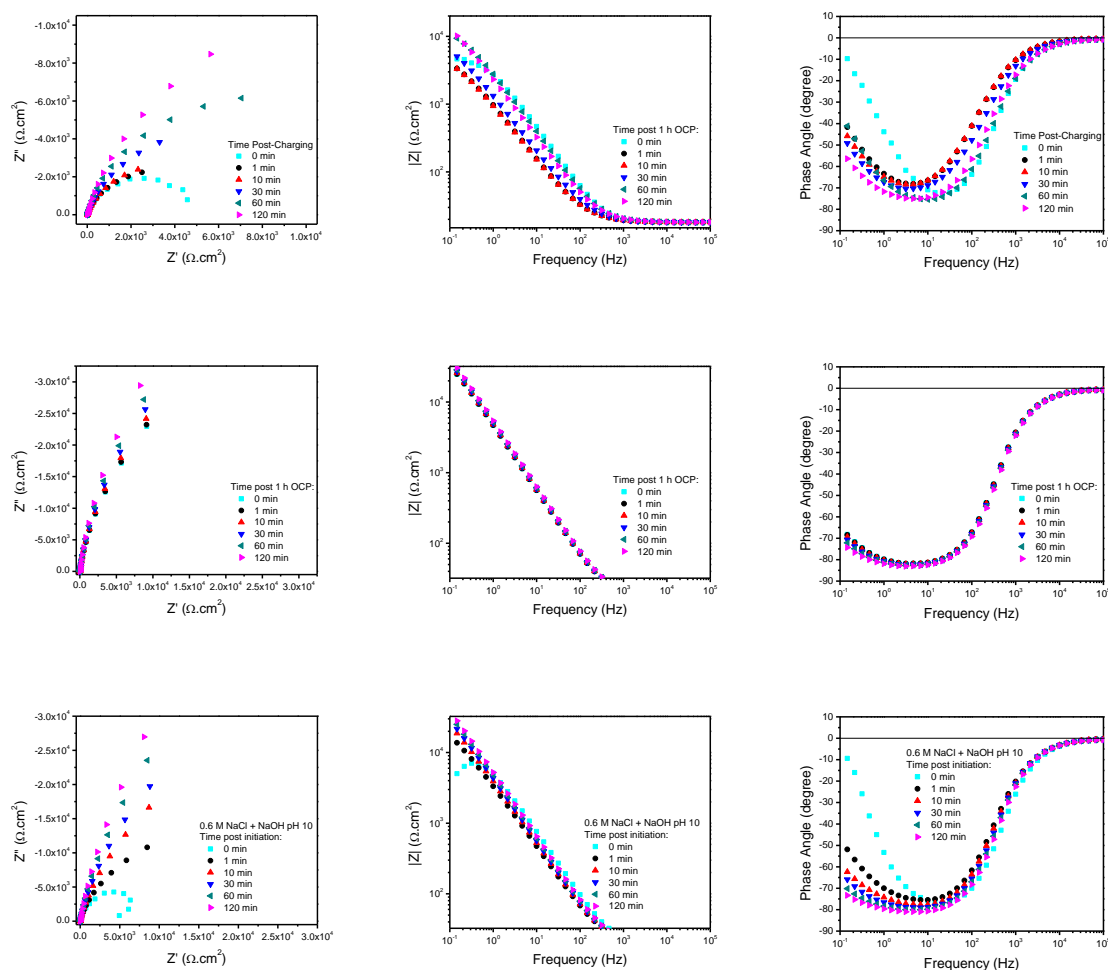


Figure 77. EIS of As Annealed/CT UNS S46500 with 1 h hydrogen pre-charging a) Nyquist, b) Bode, and c) Phase, 1 h OCP d) Nyquist, e) Bode, and f) Phase, and no prior test g) Nyquist, h) Bode, and i) Phase, in 0.6 M NaCl pH 10.

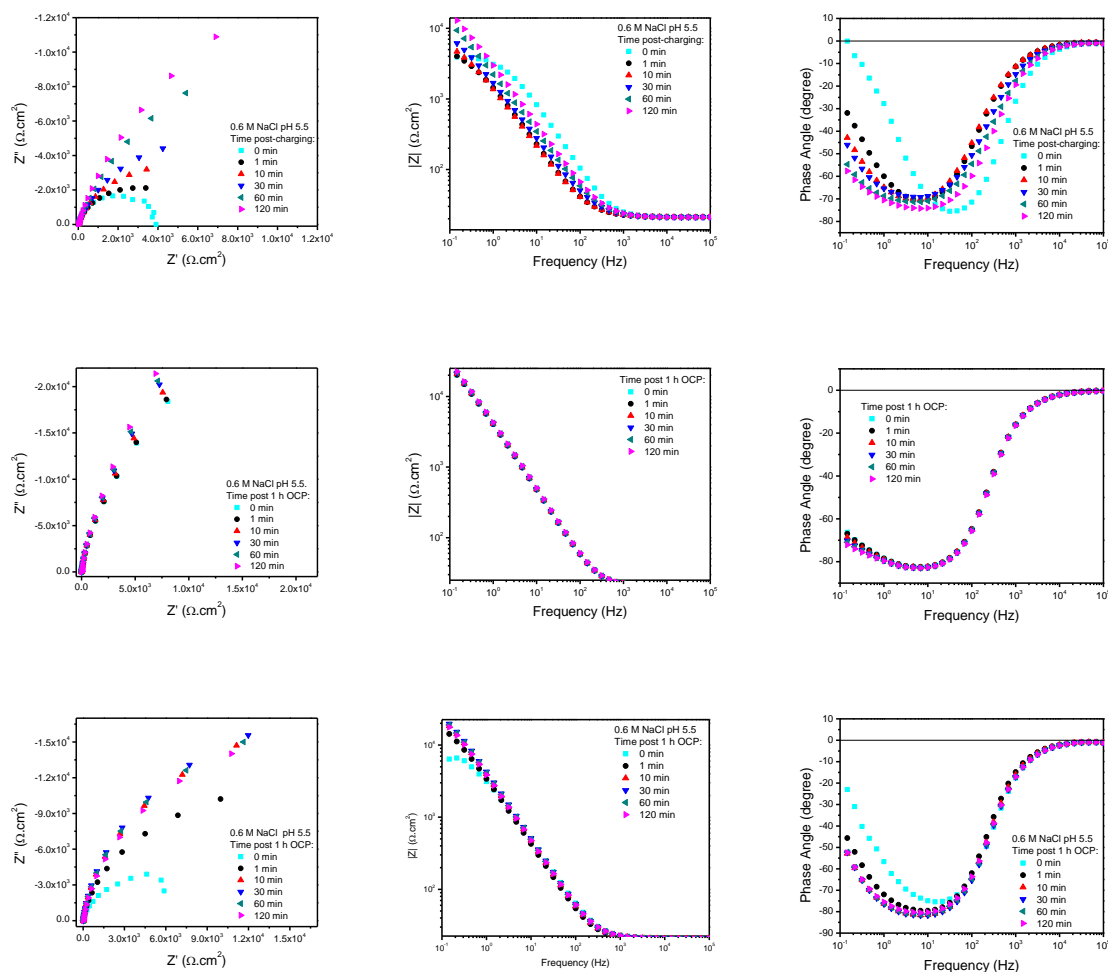
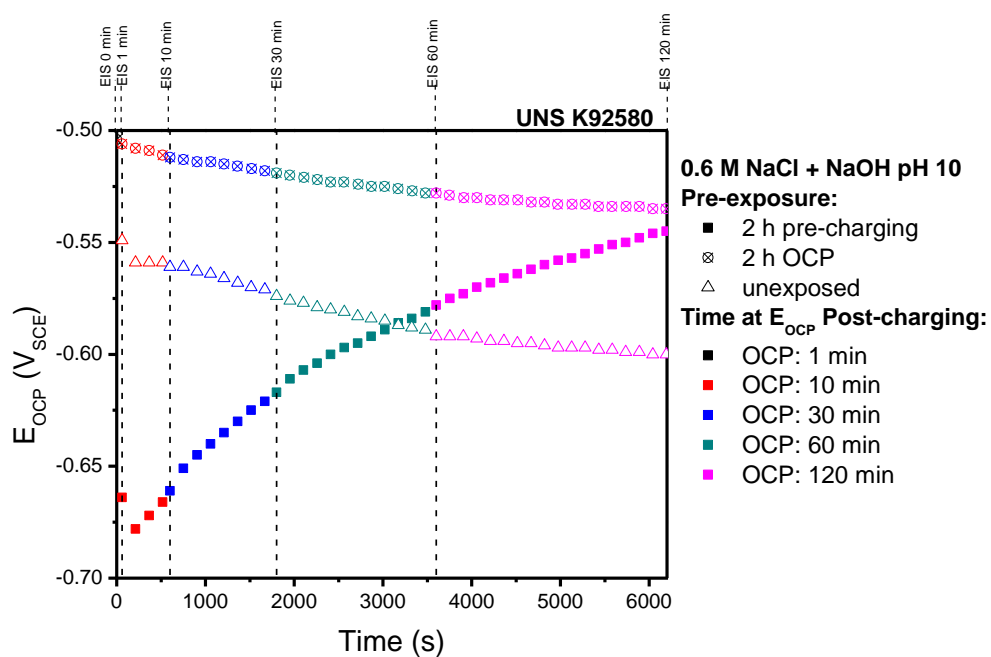
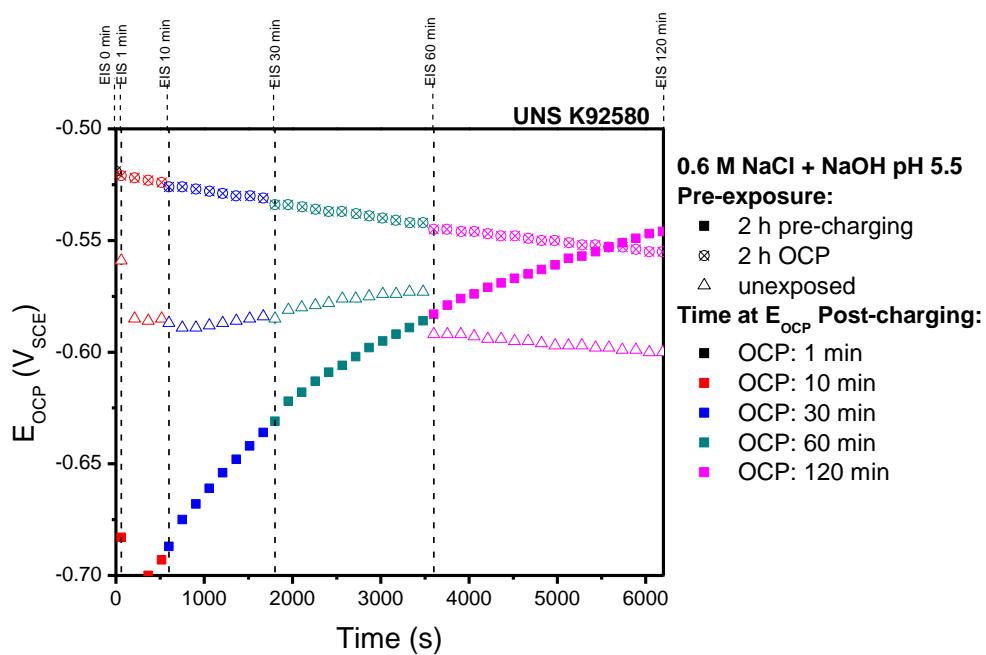


Figure 78. EIS of As Annealed/CT UNS S46500 with 1 h hydrogen pre-charging a) Nyquist, b) Bode, and c) Phase, 1 h OCP d) Nyquist, e) Bode, and f) Phase, and no prior test g) Nyquist, h) Bode, and i) Phase, in 0.6 M NaCl pH 5.5.



a)



b)

Figure 79. E_{OCP} of peak aged UNS K92580 with 1 h hydrogen pre-charging, 1 h OCP, and no prior test a) in 0.6 M NaCl + NaOH pH 10 and b) in 0.6 M NaCl pH 5.5.

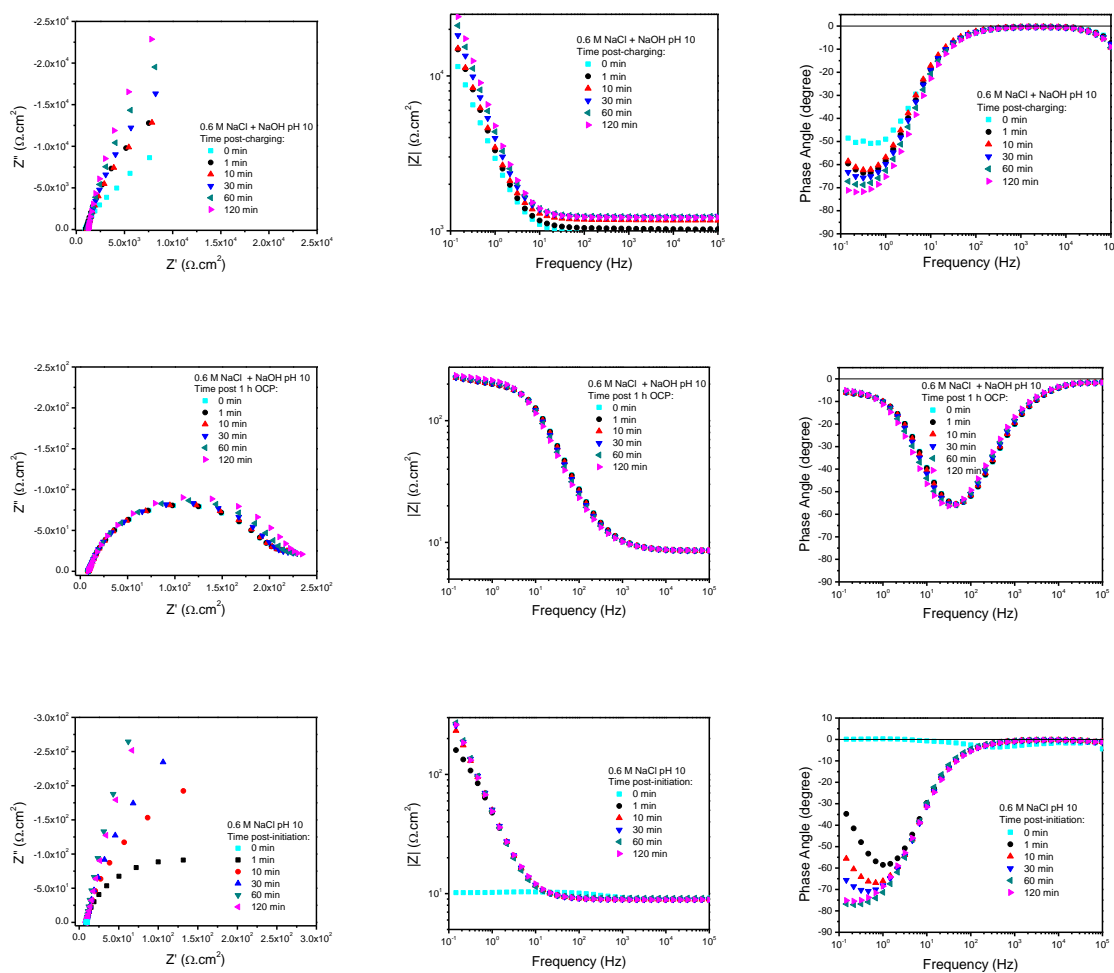


Figure 80. EIS of UNS K92580 with 1 h hydrogen pre-charging a) Nyquist, b) Bode, and c) Phase, 1 h OCP d) Nyquist, e) Bode, and f) Phase, and no prior test g) Nyquist, h) Bode, and i) Phase, in 0.6 M NaCl pH 10.

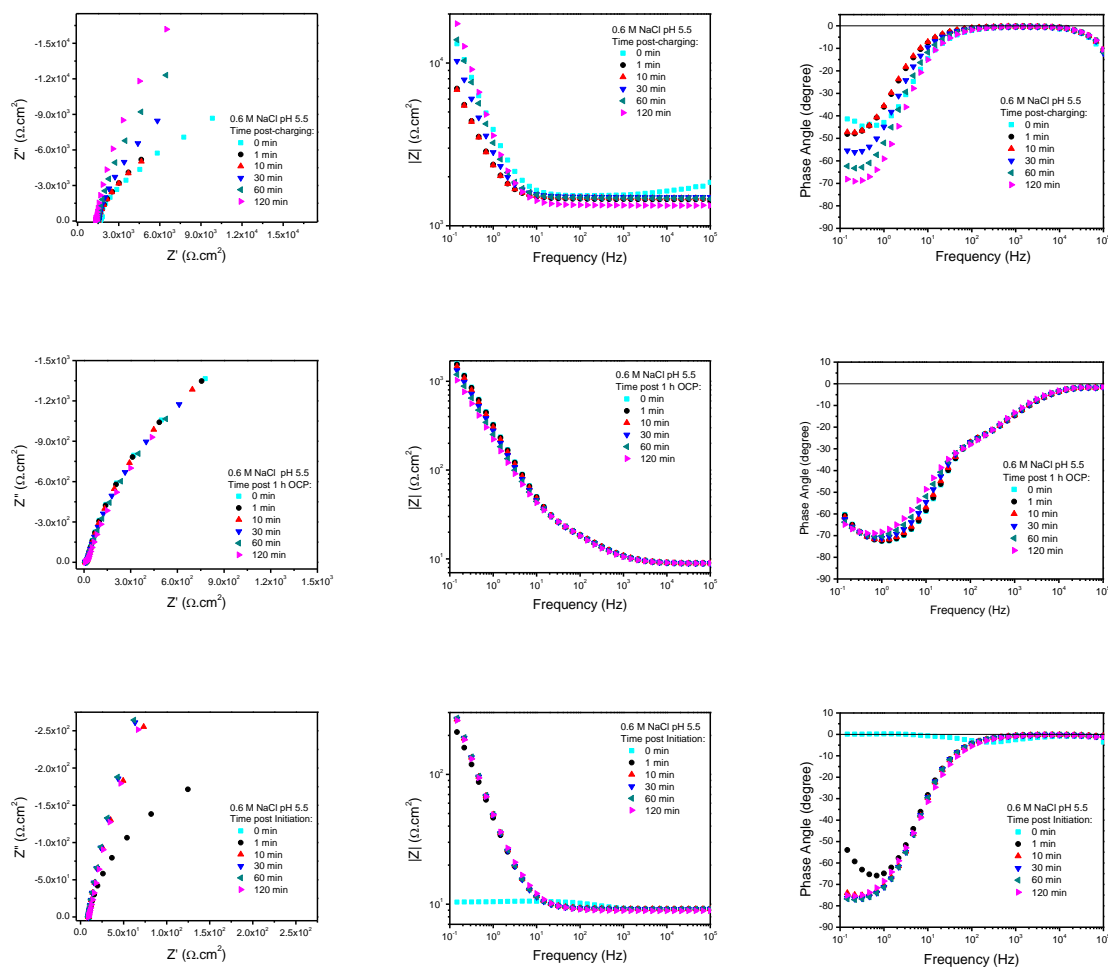
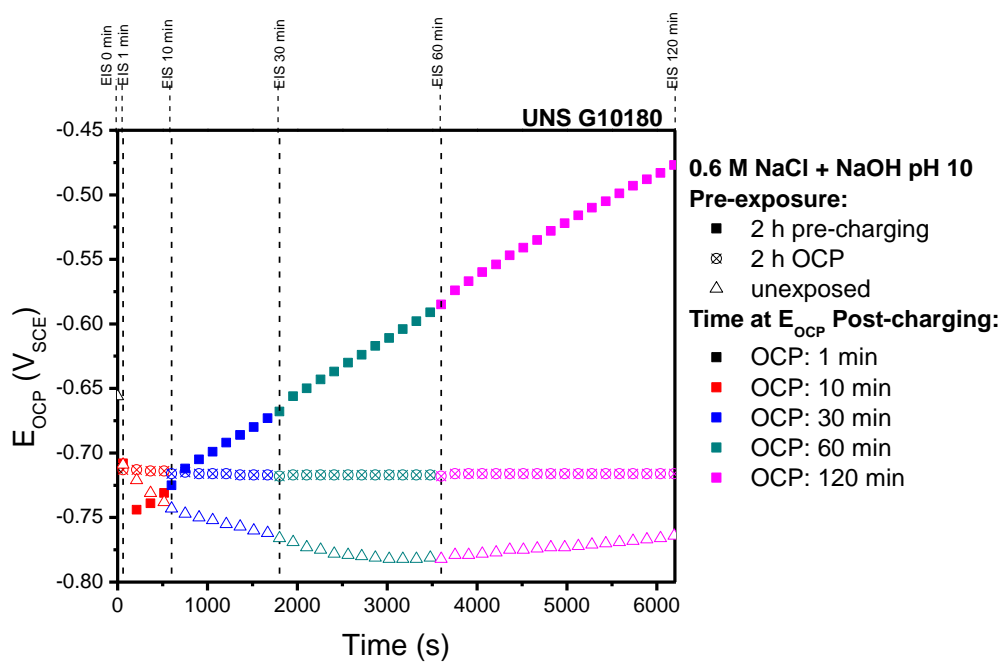
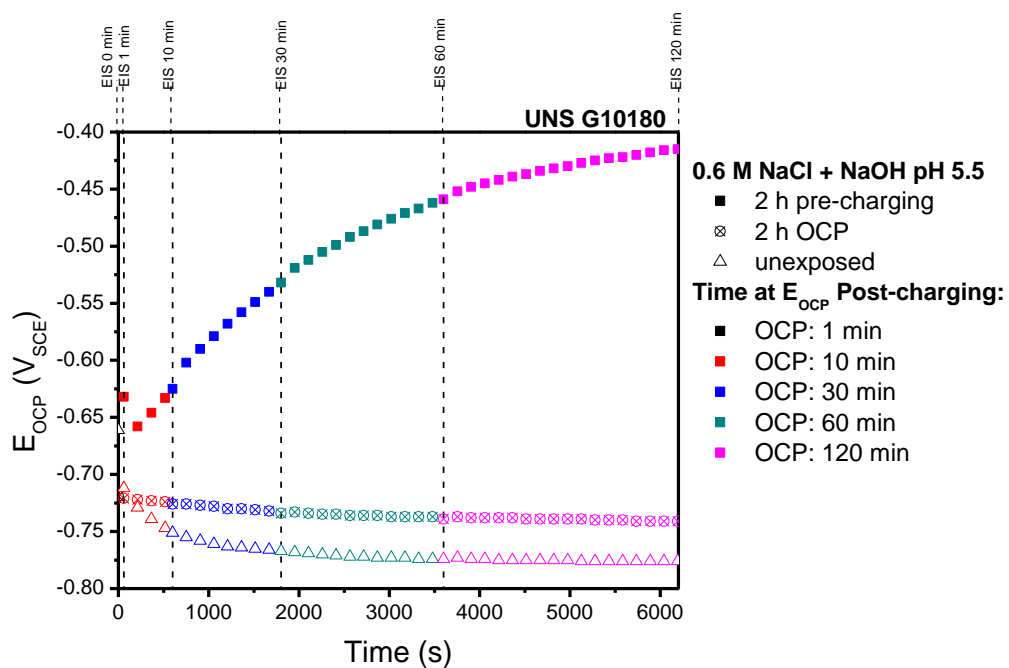


Figure 81. EIS of UNS K92580 with 1 h hydrogen pre-charging a) Nyquist, b) Bode, and c) Phase, 1 h OCP d) Nyquist, e) Bode, and f) Phase, and no prior test g) Nyquist, h) Bode, and i) Phase, in 0.6 M NaCl pH 5.5.



a)



b)

Figure 82. E_{OCP} of UNS G10180 with 1 h hydrogen pre-charging, 1 h OCP, and no prior test a) in 0.6 M NaCl + NaOH pH 10 and b) in 0.6 M NaCl pH 5.5.

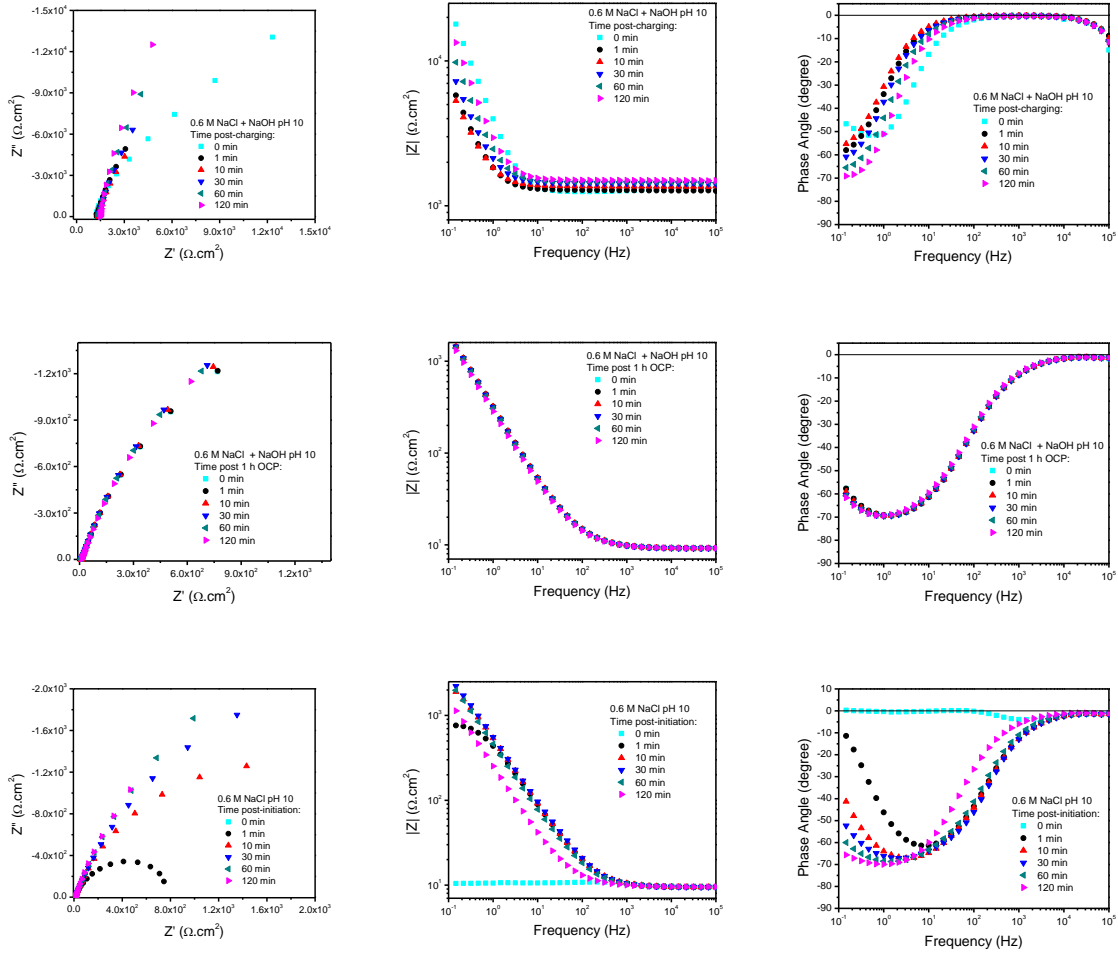


Figure 83. EIS of UNS G10180 with 1 h hydrogen pre-charging a) Nyquist, b) Bode, and c) Phase, 1 h OCP d) Nyquist, e) Bode, and f) Phase, and no prior test g) Nyquist, h) Bode, and i) Phase, in 0.6 M NaCl pH 10.

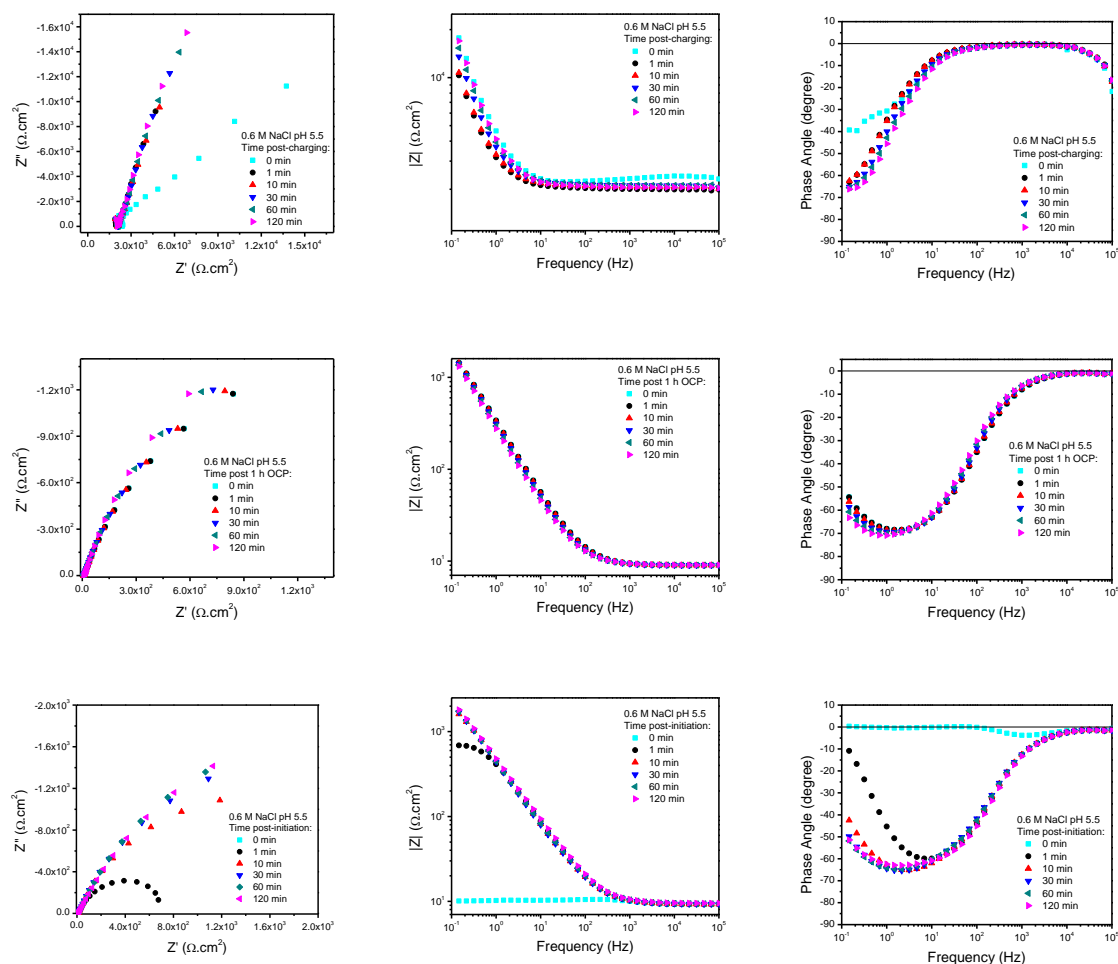


Figure 84. EIS of UNS G10180 with 1 h hydrogen pre-charging a) Nyquist, b) Bode, and c) Phase, 1 h OCP d) Nyquist, e) Bode, and f) Phase, and no prior test g) Nyquist, h) Bode, and i) Phase, in 0.6 M NaCl pH 5.5.

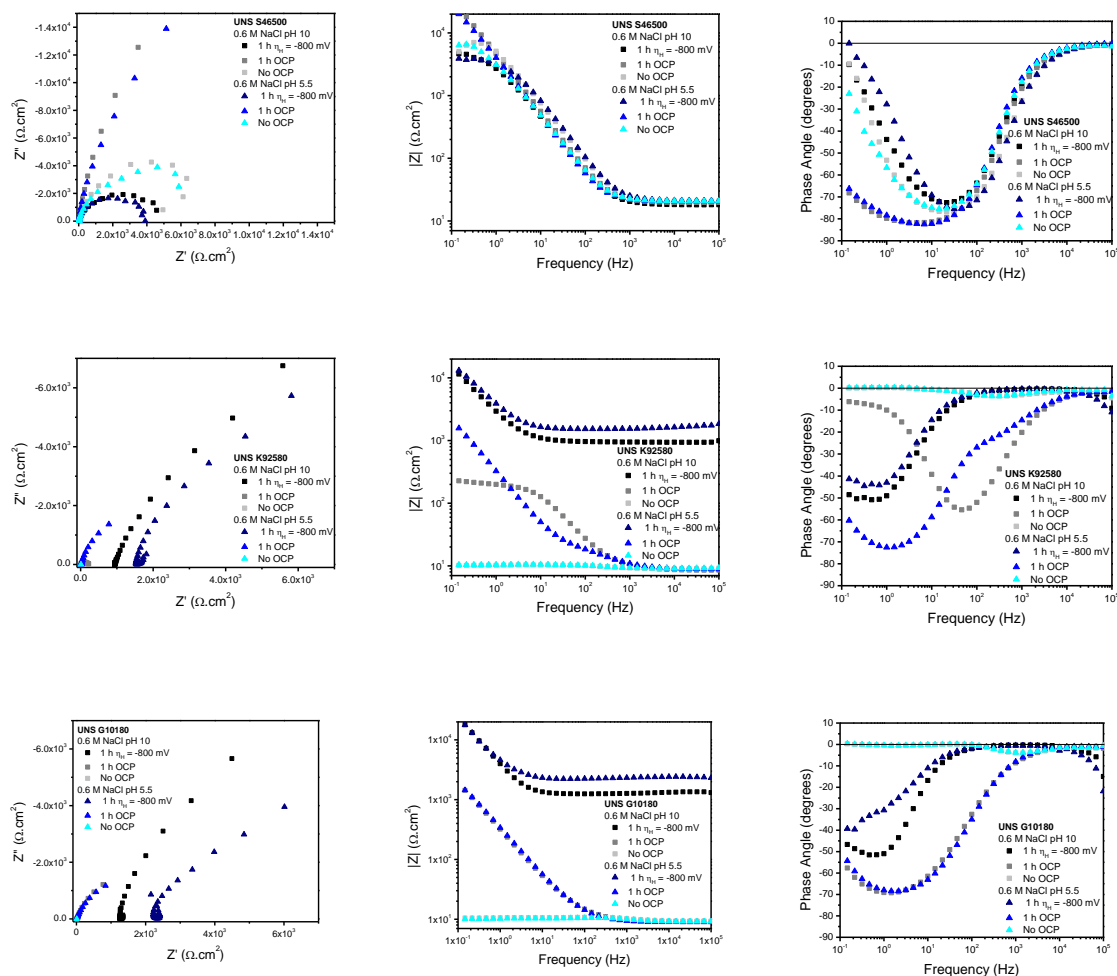


Figure 85. Summary of initial EIS taken after 1 h pre-charge, 1 h OCP, and no initial OCP in 0.6 M NaCl + NaOH, pH 5.5 and pH 10 for UNS S46500 As Annealed/CT a) Nyquist, b) Bode, and c) Phase, UNS K92580 d) Nyquist, e) Bode, and f) Phase, and UNS G10180 g) Nyquist, h) Bode, and i) Phase.

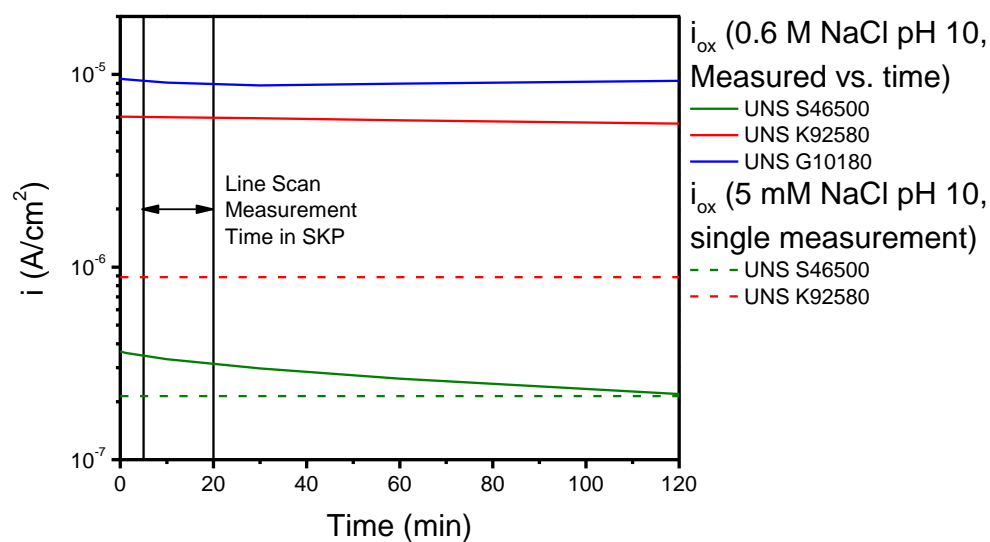
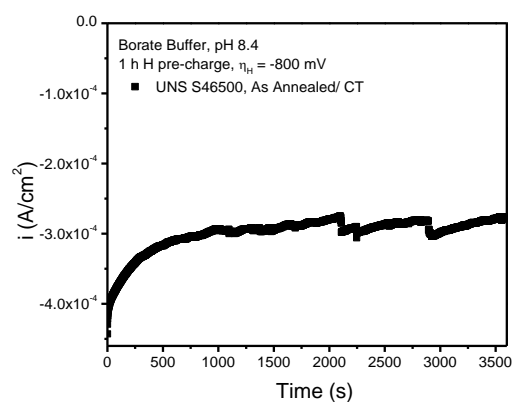


Figure 86. Oxidation current density vs. time. Oxidation current density was calculated from EIS fitting for both 0.6 M NaCl + NaOH pH 10 exposures at E_{OCP} vs time and for a single exposure of 5 mM NaCl + NaOH pH 10 exposures.

a)



b)

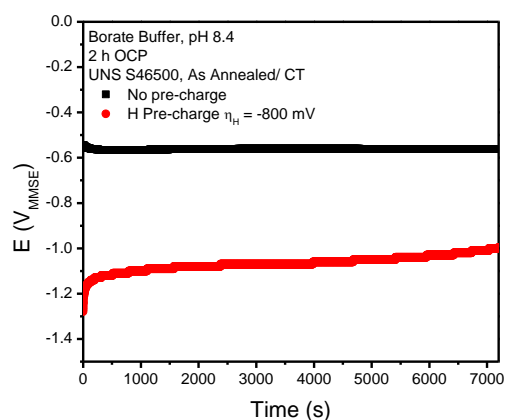
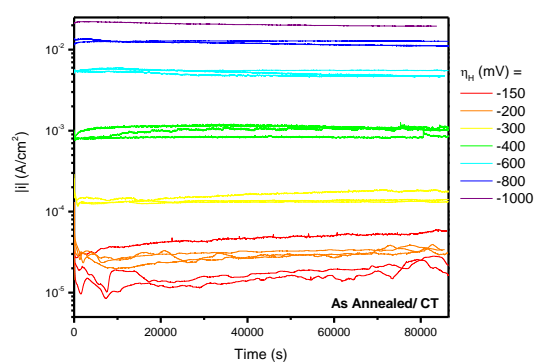
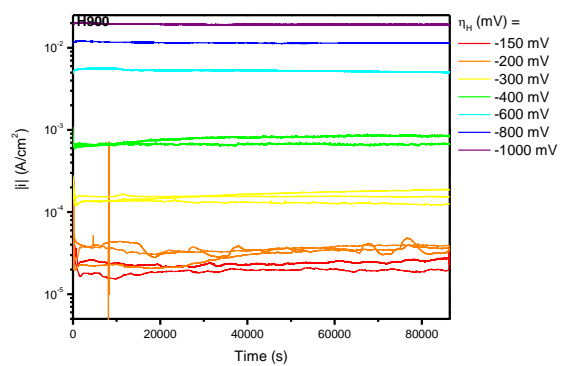


Figure 87. a) Cathodic pre-charging of As-Annealed/CT UNS S46500 in deaerated Borate Buffer solution pH 8.4 for 1 h, and b) E_{OCP} 2 h measurement in same solution for a pre-charged and uncharged sample.

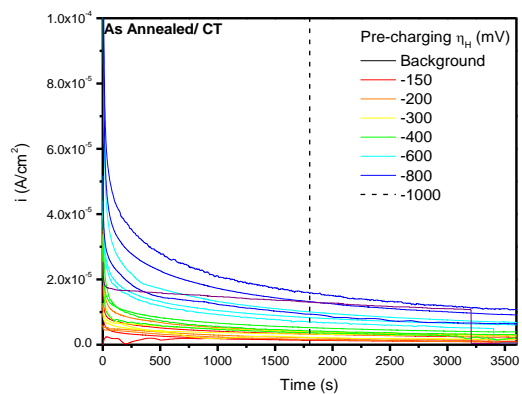
a)



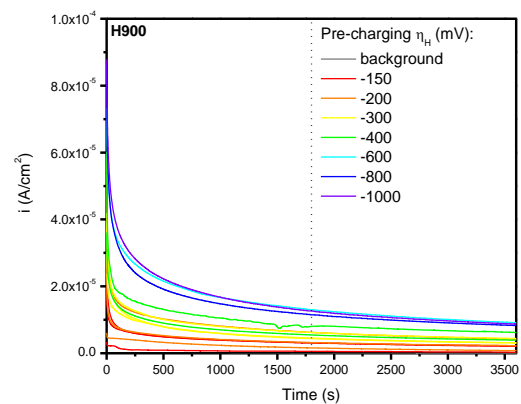
b)



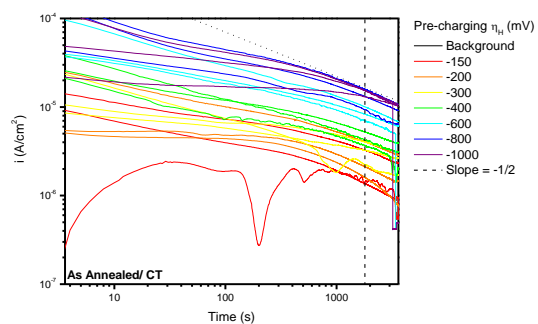
c)



d)



e)



f)

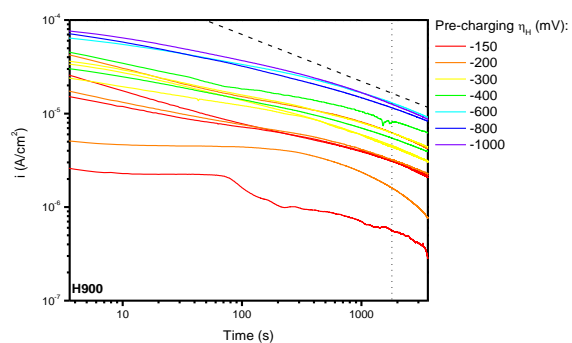


Figure 88. Pre-charging current densities in a) As Annealed/CT and b) H900 UNS S46500. UNS S46500 $C_{H,Diff}$ results from electrochemical H extraction i (A/cm^2) vs time (s) for each hydrogen overpotential (η_H), c) As Annealed/CT and d) H900. Comparison of the $\log(i)$ vs $\log(t)$ electrochemical extraction to the theoretical slope of $-1/2$ for e) As Annealed/CT and f) H900 UNS S46500.

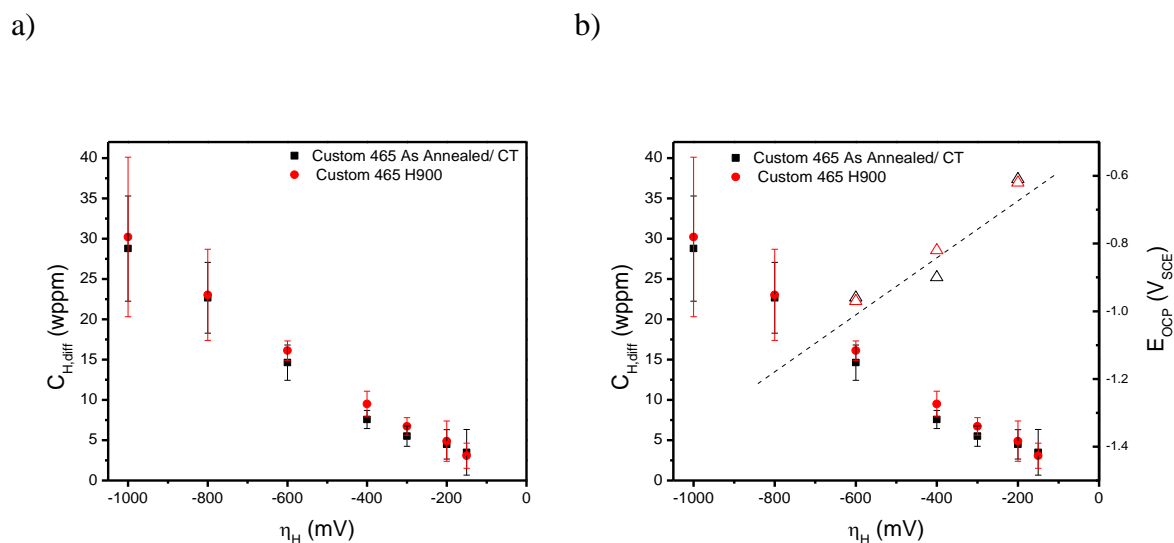
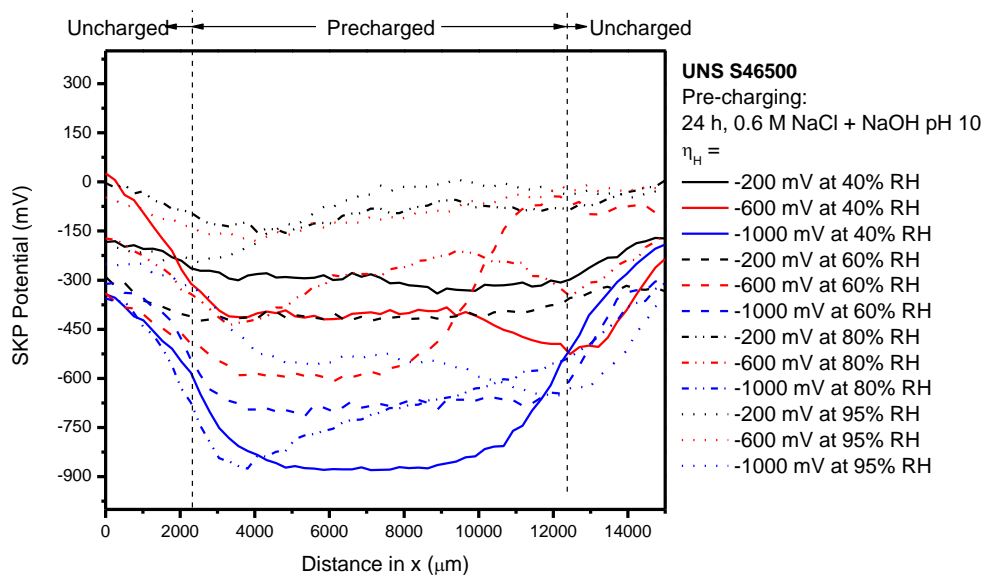
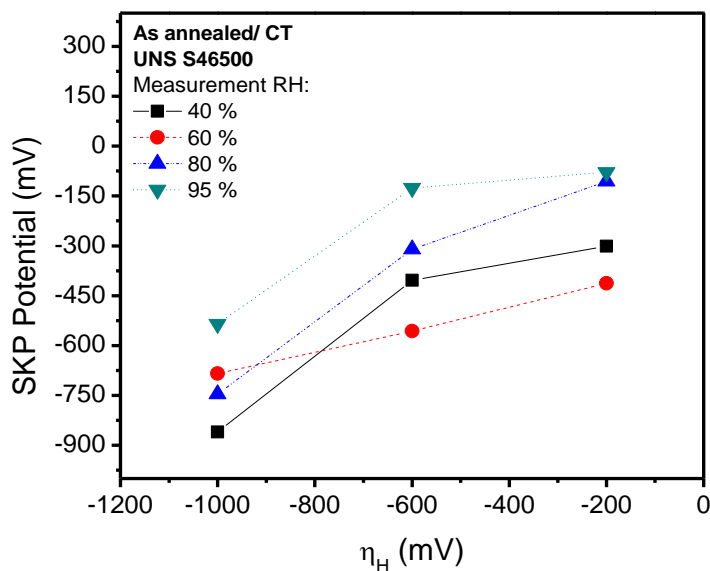


Figure 89. UNS S46500 $C_{H,Diff}$ results from electrochemical extraction. a) H extraction i (A/cm^2) vs time (s) for each hydrogen overpotential (η_H) and b) $C_{H,Diff}$ (wppm) vs. pre-charging η_H with EOCp vs. pre-charging η_H . Samples were H pre-charged in 0.6 M NaCl + NaOH, pH 10 naturally aerated room temperature solution for 24 h at $\eta_H = -150$ to -1000 mV (-982 to -1832 mV_{SCE}). Extraction occurred in 0.1 M NaOH, pH 11.75 solution at $\eta_H = +330$ mV (-605 mV_{SCE}) for 1 h. $C_{H,Diff}$ values were determined from i at 1800 s. Eocp was measured immediately post-charging in same solution for 1 hour, values shown above are those measured within the first 10 s after H charging.



a)



b)

Figure 90. a) SKP potential line scans in 40, 60, 80, and 95% RH humid air across H pre-charged zones in as annealed/CT UNS S46500. Samples were pre-charged by cathodic polarization in an electrochemical flat cell with a 1 cm^2 opening and 0.6 M NaCl + NaOH, pH 10 with ambient aeration at room temperature for 24 h at $\eta_H = -200$ to -1000 mV (-1032 to $-1832 \text{ mV}_{\text{SCE}}$). b) Pre-charging overpotential vs. SKP potential for samples H pre-charged and measured in the SKP at various RH.

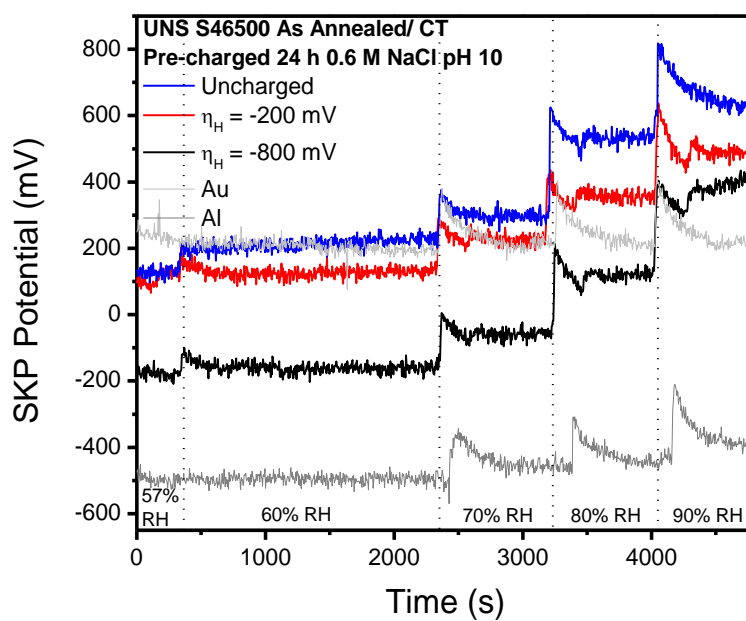
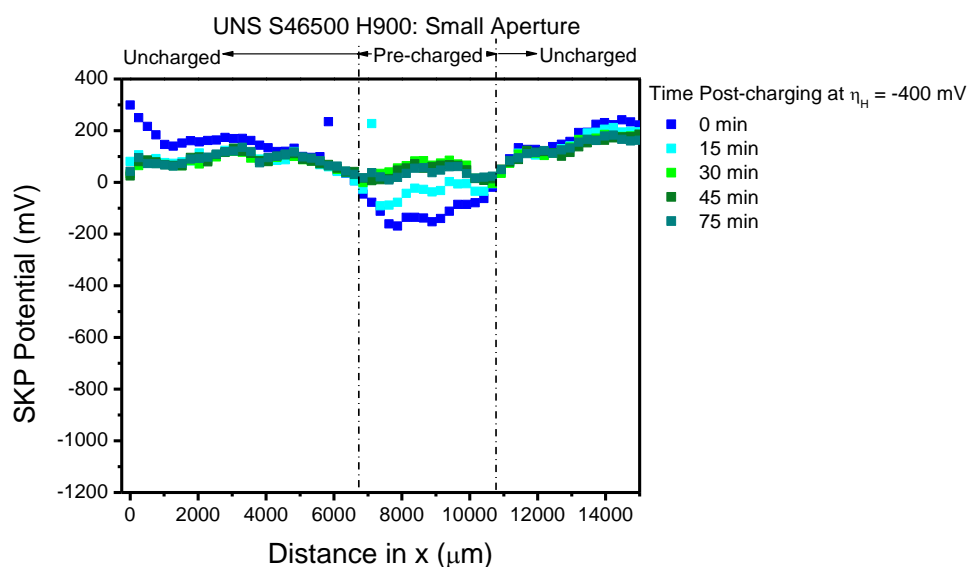
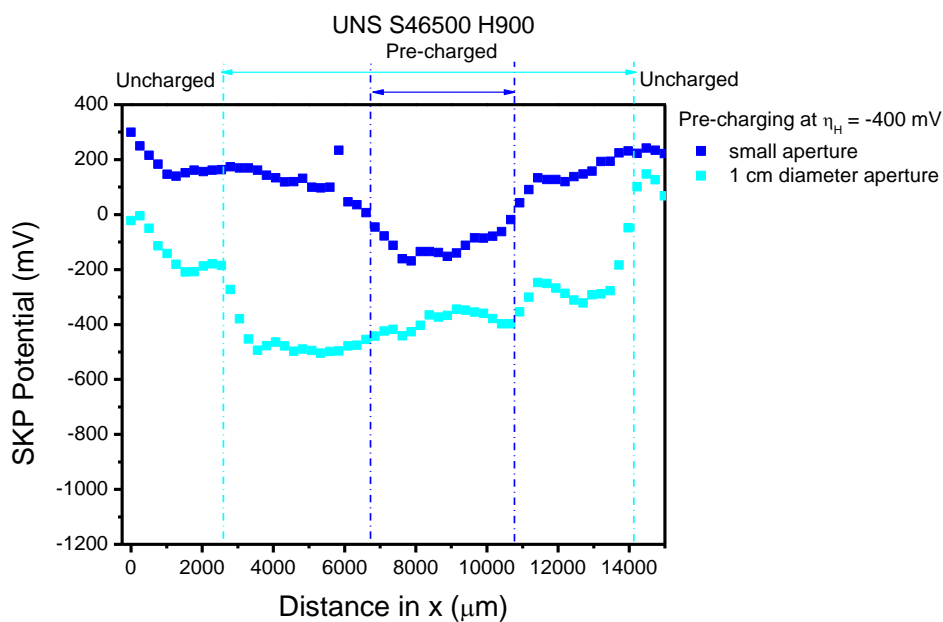


Figure 91. SKP Potential vs. time for ramped RH. Shown for the Au/Al calibration block as well as UNS S46500 in the As Annealed/ CT condition for an uncharged sample and samples H pre-charged at $\eta_H = -100$ and -800 mV for 24 h in 0.6 M NaCl + NaOH pH 10.



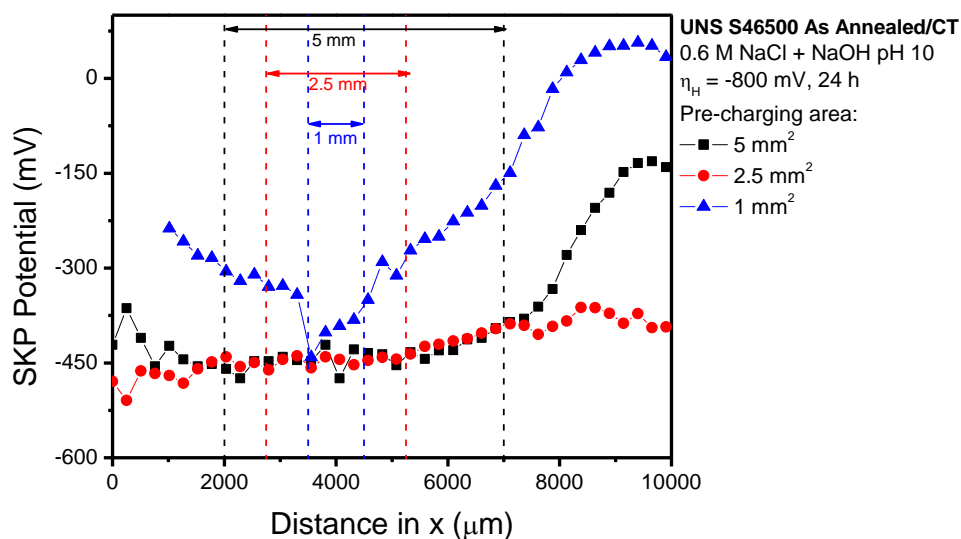
a)



b)

Figure 92. SKP potential line scans in 57% RH humid air across H pre-charged zones in as annealed/CT UNS S46500. Samples were pre-charged by cathodic polarization in an electrochemical flat cell with a 1 cm² opening and 0.6 M NaCl + NaOH, pH 10 with ambient aeration at room temperature for 24 h at $\eta_H = -400$ mV (-1232 mV_{SCE}). a) Pre-charging overpotential vs. SKP potential for samples H pre-charged in a small aperture cell and measured post-charging in the SKP at various time. b) Initial SKP line scan of small aperture and 1 cm diameter aperture pre-charged samples.

a)



b)

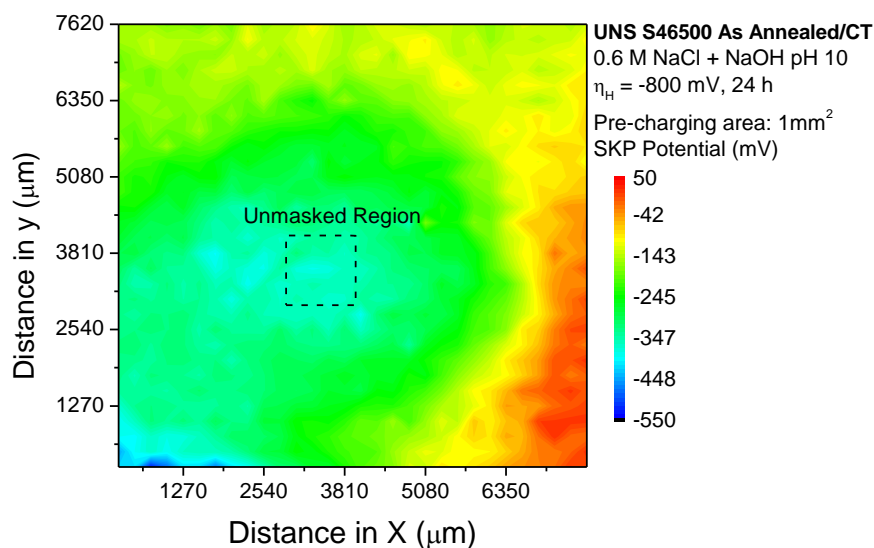
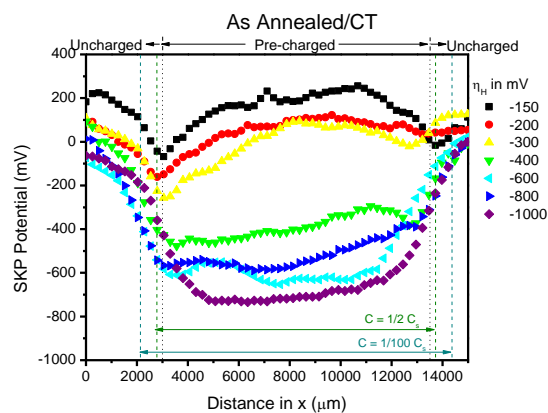


Figure 93. SKP potential line scans in 57% RH humid air across H pre-charged zones in as annealed/CT UNS S46500. Samples were pre-charged by cathodic polarization in full immersion coated with stop off lacquer with openings of 1, 2.5, and 5 mm² and 0.6 M NaCl + NaOH, pH 10 with ambient aeration at room temperature for 24 h at $\eta_H = -800$ mV (-1632 mV_{SCE}). a) SKP potential line scan vs. distance in x with area diameter of pre-charging noted by dotted lines. b) SKP potential area scan vs. distance in x and y for 1 mm² sample with area of pre-charging noted by dotted lines.

a)



b)

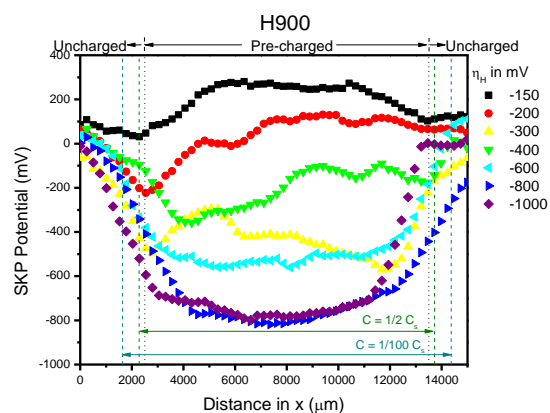


Figure 94. SKP potential line scans in 57% RH humid air across H pre-charged zones in UNS S46500 a) as annealed/CT and b) H900 temper. Samples were pre-charged by cathodic polarization in an electrochemical flat cell with a 1 cm^2 opening and 0.6 M NaCl + NaOH, pH 10 with ambient aeration at room temperature for 24 h at $\eta_H = -150$ to -1000 mV (-982 to $-1832 \text{ mV}_{\text{SCE}}$).

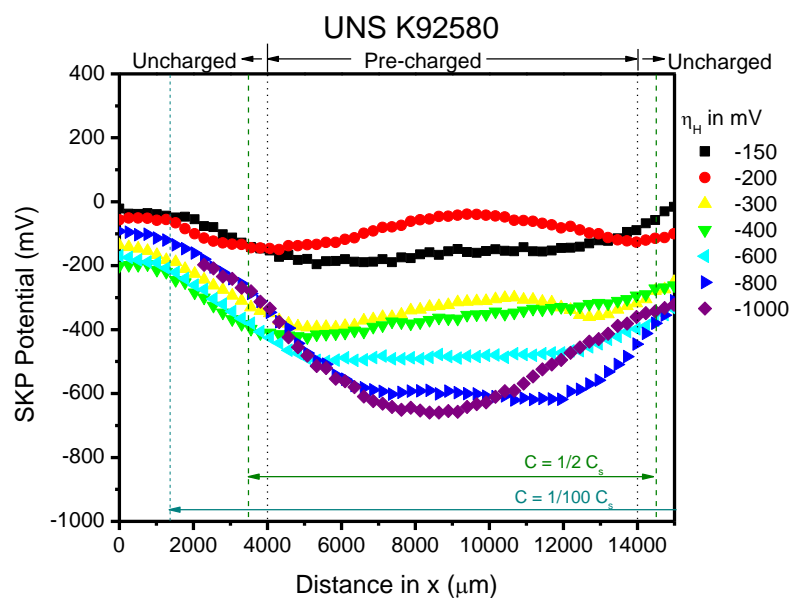
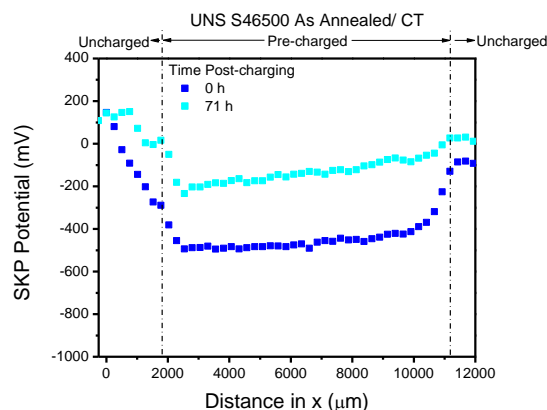


Figure 95. SKP potential line scans in 57% RH humid air across H pre-charged zones in UNS K92580 peak aged. Samples were pre-charged by cathodic polarization in an electrochemical flat cell with a 1 cm² opening and 0.6 M NaCl + NaOH, pH 10 with ambient aeration at room temperature for 24 h at $\eta_H = -150$ to -1000 mV (-982 to -1832 mV_{SCE}).

a)



b)

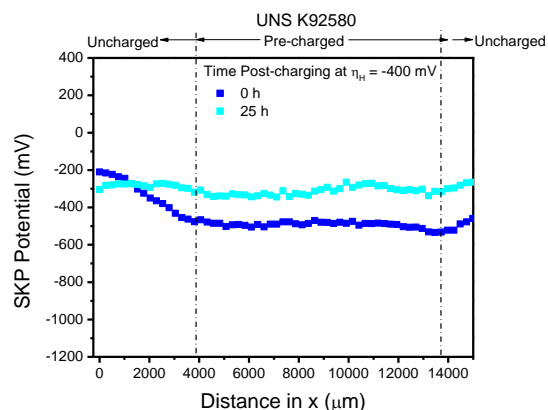
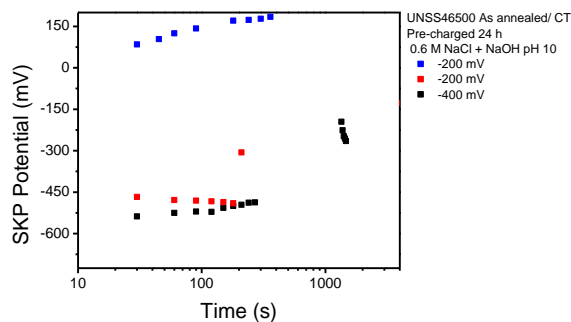


Figure 96. SKP line scans in 57% RH humid air across H pre-charged zones in a hydrogen pre-charged sample by cathodic polarization in an electrochemical flat cell with a 1 cm² opening and 0.6 M NaCl + NaOH, pH 10 with ambient aeration at room temperature for 24 h at $\eta_H = -400$ mV (-1232 mVSCE). a) UNS S46500 as annealed/CT b) UNS K92580

a)



b)

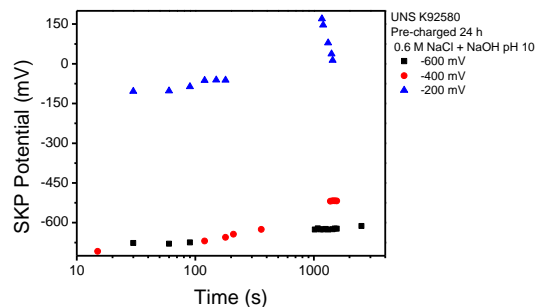


Figure 97. Average of SKP line scans in 57% RH humid air across H pre-charged zones in a hydrogen pre-charged sample by cathodic polarization in an electrochemical flat cell with a 1 cm² opening and 0.6 M NaCl + NaOH, pH 10 with ambient aeration at room temperature for 24 h at various η_H for a) UNS S46500 as annealed/CT b) UNS K92580

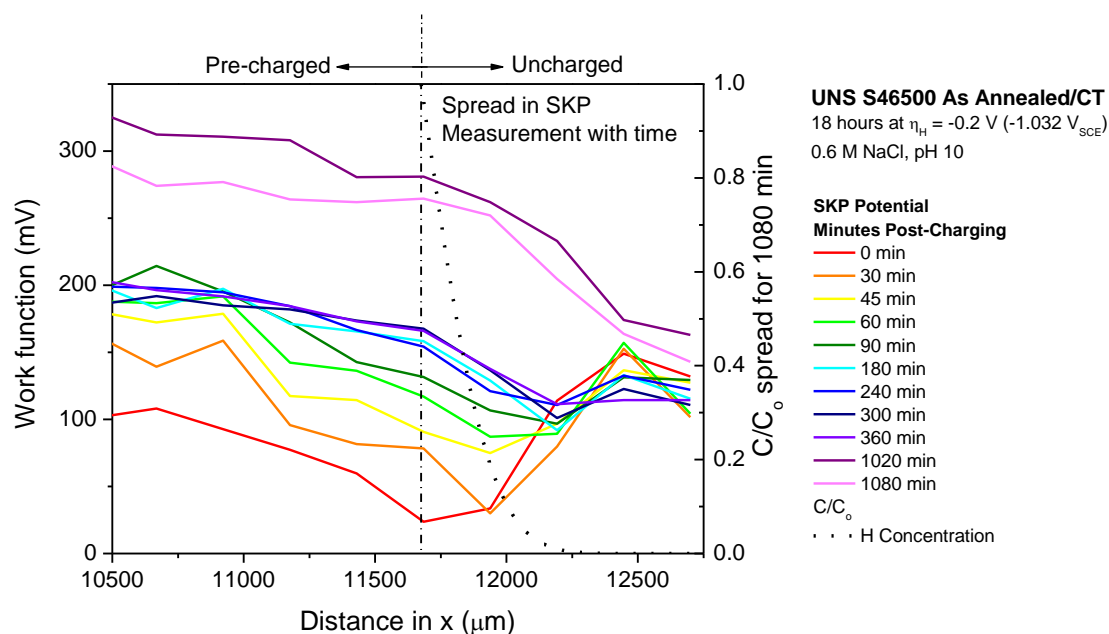


Figure 98. SKP line scans in 57% RH humid air across H pre-charged zones in a hydrogen pre-charged sample by cathodic polarization in an electrochemical flat cell with a 1 cm^2 opening and 0.6 M NaCl + NaOH, pH 10 with ambient aeration at room temperature for 18 h at $\eta_{\text{H}} = -200 \text{ mV } (-1032 \text{ mV}_{\text{SCE}})$ with comparison to calculated spread of C/C_0 , over the post-charging measurement time (1080 min) estimated by the equation for steady state diffusion in an infinite plane and $D_{\text{H,eff}} = 3.1 \times 10^{-9} \text{ cm}^2/\text{s}$.

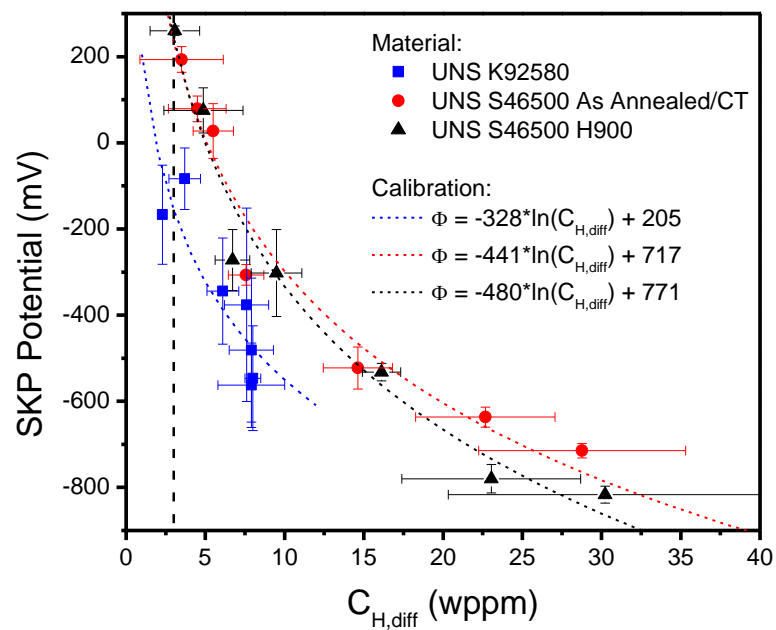


Figure 99. a) $C_{H,Diff}$ vs SKP potential in 57% RH humid air for peak aged UNS K92580 and UNS S46500 in the as annealed/CT and H900 temper.

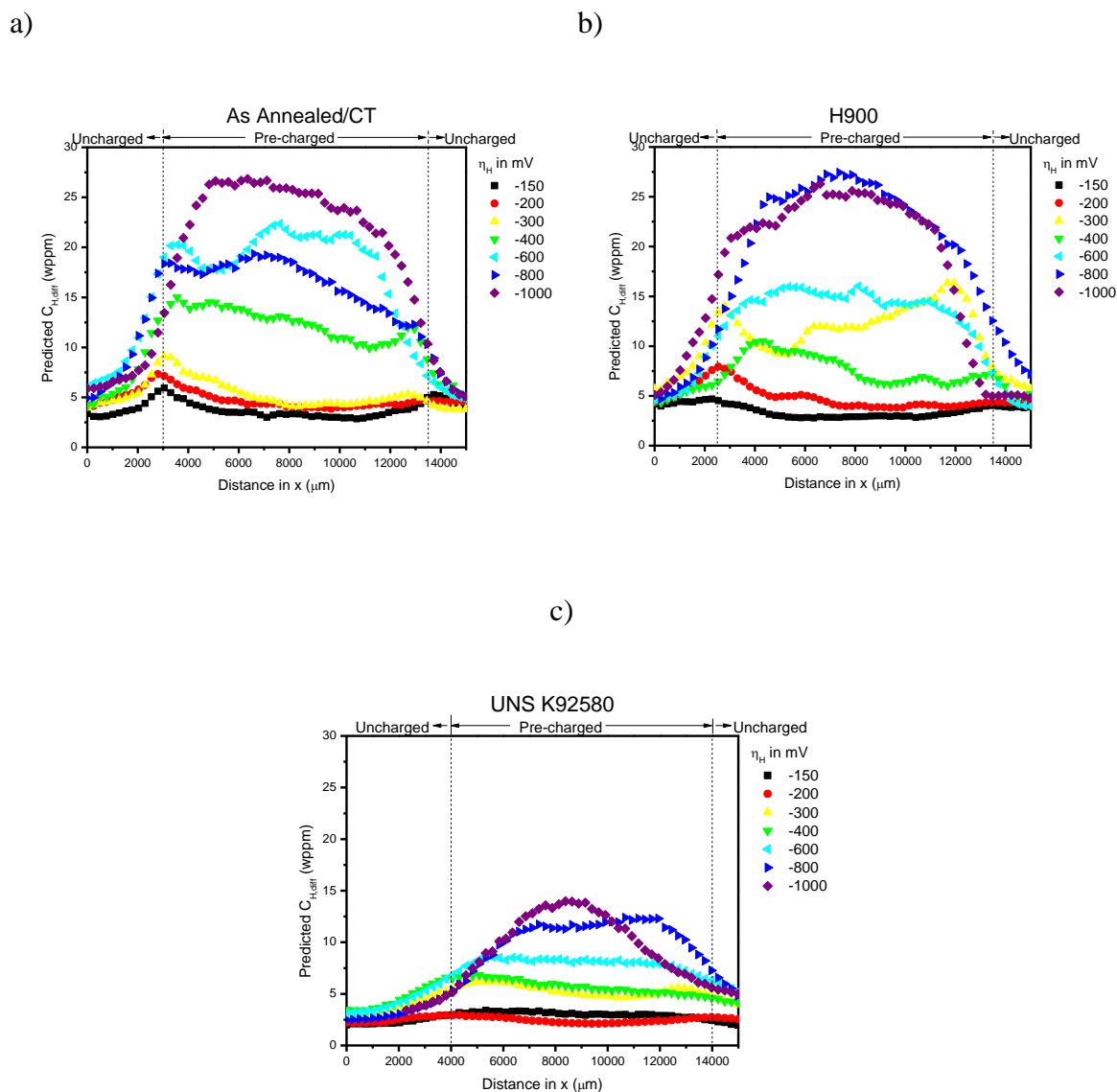


Figure 100. Predicted $C_{H,Diff}$ for measured SKP potentials of hydrogen pre-charged samples in a) UNS S46500 As Annealed/CT, b) UNS S46500 H900, and c) UNS K92580. Predictions from equations found from calibration in Figure 99. Samples pre-charged for 24 hours in 0.6 M NaCl + NaOH pH 10 in a 1cm² opening flat cell.

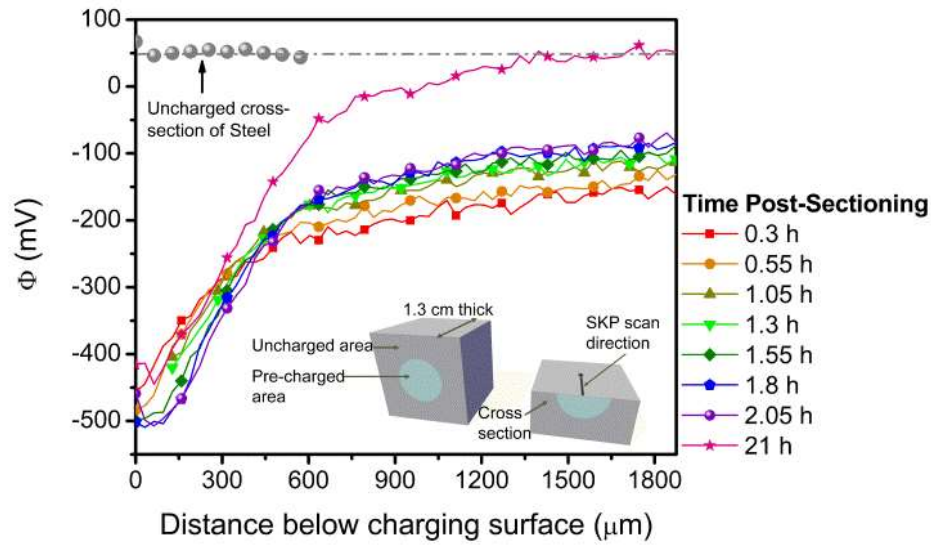


Figure 101. SKP Φ line scans vs. penetration depth for successive times after 24 hour hydrogen charging of Fe-13Co-11Ni-3Cr-1.2Mo-0.2C-0.02Mn steel performed at $\eta_{\text{chg}} = -0.2$ V. The surface at $x = 0$ is the hydrogen charged surface with diffusion into the sample with increasing x . A line scan from the uncharged edge is also displayed. [41]

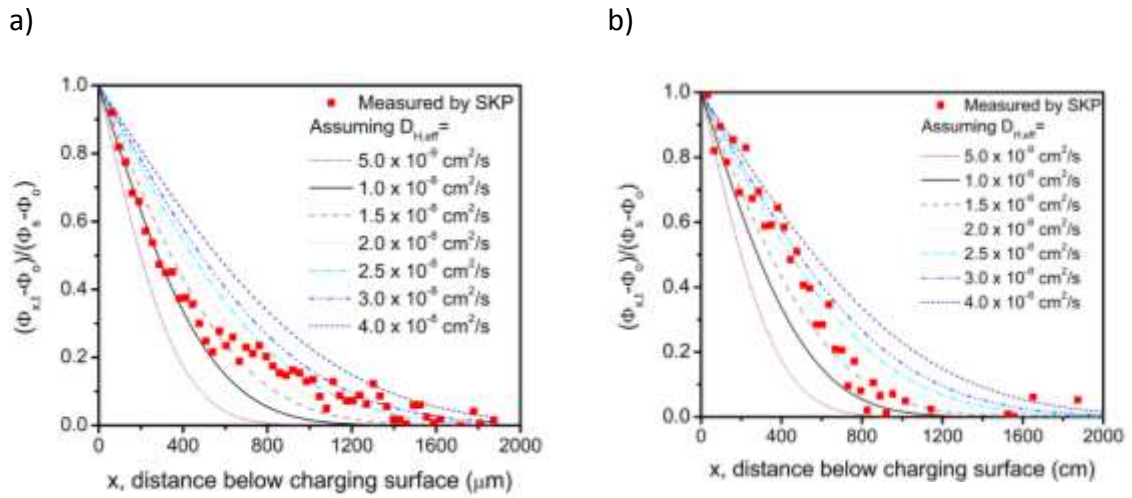
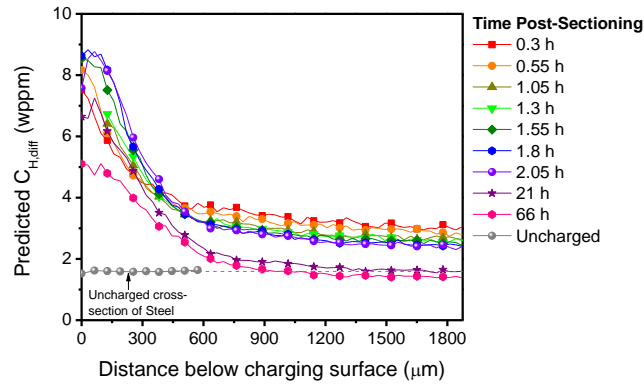


Figure 102. Hydrogen concentration versus depth profiles based on calculations using Equation 61 given TDS measured $D_{\text{H,eff}}$ compared to measured Φ on a) UNS K92580 and b) UNS S46500 steel pre-charged 24 hours at $\eta_{\text{chg}} = -0.2$ V. [41]

a)



b)

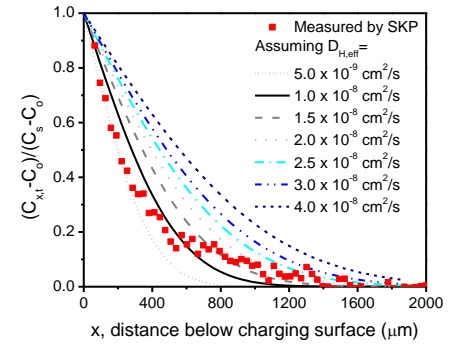


Figure 103. a) Predicted $C_{H,Diff}$ from SKP Φ line scans vs. penetration depth for successive times after 24 hour hydrogen charging of Fe-13Co-11Ni-3Cr-1.2Mo-0.2C-0.02Mn steel performed at $\eta_{chg} = -0.2$ V. The surface at $x = 0$ is the hydrogen charged surface with diffusion into the sample with increasing x . A line scan from the uncharged edge is also displayed. b) Hydrogen concentration versus depth profiles based on calibration equations from Figure 99 vs. given TDS measured $D_{H,eff}$ compared to measured Φ on UNS K92580 and steel pre-charged 24 hours at $\eta_{chg} = -0.2$ V. [41]

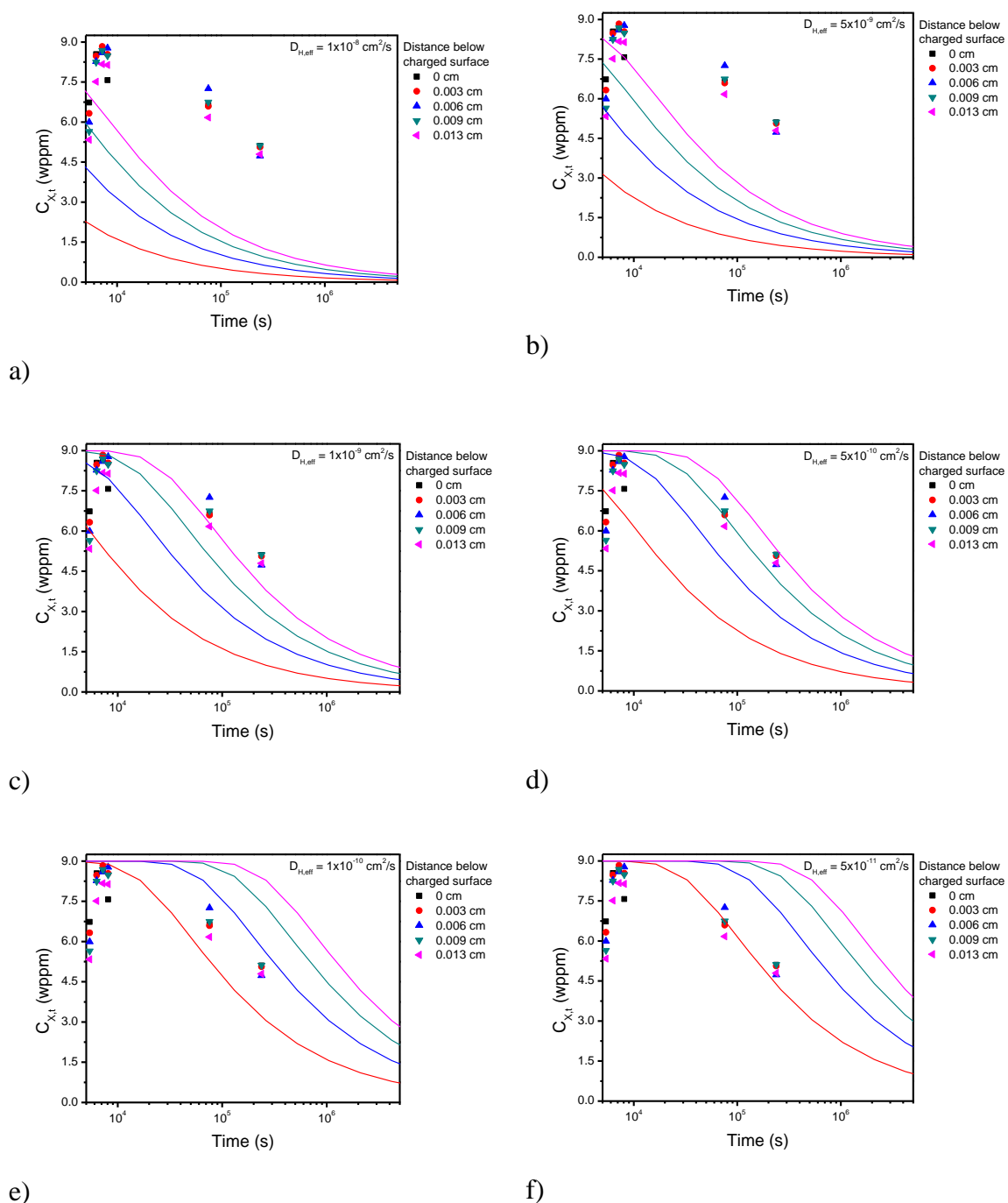


Figure 104. $C_{x,t}$ vs. t , where lines are calculated diffusion profiles of $C_{x,t}$ vs time post-charging for the estimation of diffusion in an infinite plane with $D_{H,eff}$ of a) 1×10^{-8} cm^2/s , b) 5×10^{-9} cm^2/s , c) 1×10^{-9} cm^2/s , d) 5×10^{-10} cm^2/s , e) 1×10^{-10} cm^2/s , and f) 5×10^{-11} cm^2/s . Symbols represent measurements of $C_{x,t}$ taken from SKP potential measurements of the cross-sectioned sample over time at depths of 0, 0.003, 0.006, 0.009, and 0.013 cm below the charged surface. Best fit $D_{H,eff}$ between profiles c and d, where $D_{H,eff} = 1 \times 10^{-9}$ and 5×10^{-10} cm^2/s .

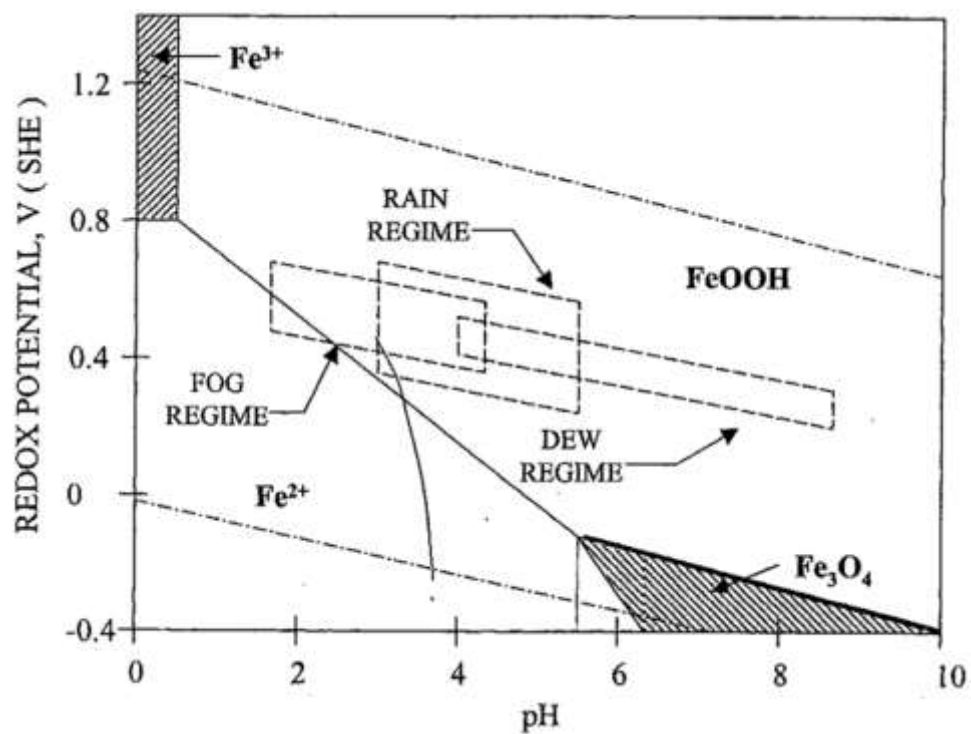
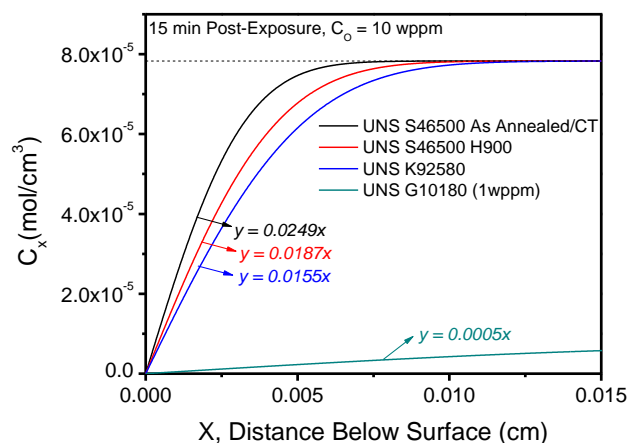


Figure 105. E-pH diagram for the iron-water system at 25°C assuming a concentration of iron ionic species of 0.1 M. The predicted potentials and pHs for fog, rain, and dew regimes are indicated.[63]

a)

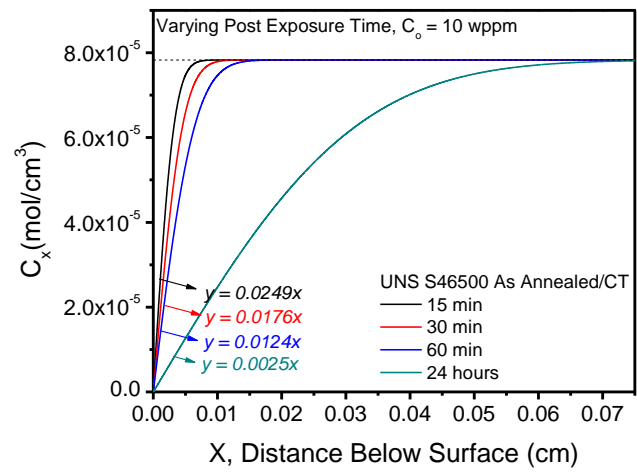


b)

Sample	i_L (A/cm ²)
UNS S46500 As Annealed/CT	8.41×10^{-6}
UNS S46500 H900	1.12×10^{-5}
UNS K92580	1.35×10^{-5}
UNS G10180 (1 wppm)	4.82×10^{-6}

Figure 106. $C_{H,Diff}$ egress with varying substrate (varying $D_{H,eff}$). a) $C_{H,Diff}$ vs. distance below the hydrogen charging surface is calculated using the assumption for diffusion in an infinite plane and an initial concentration of 10 wppm (1 wppm in the case of UNS G10180). $D_{H,eff}$ values used were 3.5×10^{-9} , 6.2×10^{-9} , 9×10^{-9} , and 1×10^{-7} for UNS S46500 As Annealed/CT, H900, UNS K92580, and UNS G10180, respectively. b) The limiting current density was estimated using the equation $i_L^{H^+} = -nFD \left(\frac{\partial C}{\partial x} \right)$, where $y = \frac{\partial C}{\partial x} x$ taken over the range of 0 to 0.0025 cm (linear section).

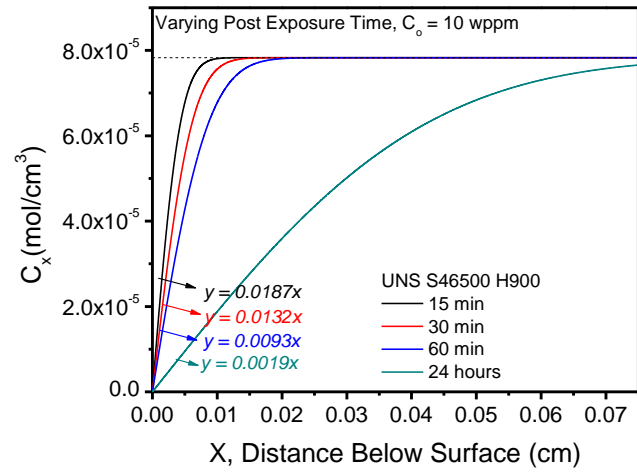
a)



b)

Time	i_L (A/cm ²)
15 min	8.41×10^{-6}
30 min	5.94×10^{-6}
60 min	4.19×10^{-6}
24 hours	8.44×10^{-7}

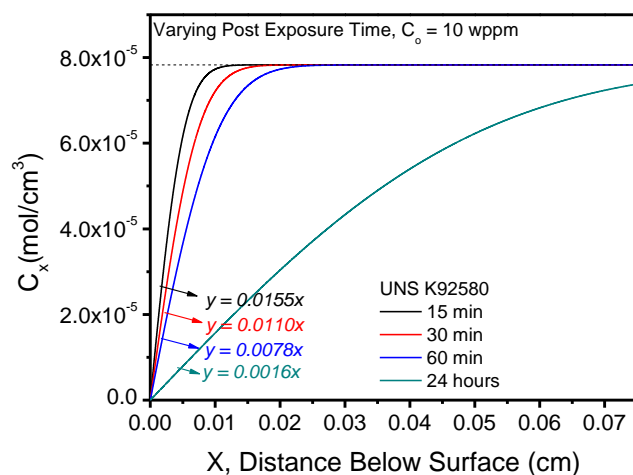
c)



d)

Time	i_L (A/cm ²)
15 min	1.12×10^{-5}
30 min	7.9×10^{-6}
60 min	5.56×10^{-6}
24 hours	1.14×10^{-6}

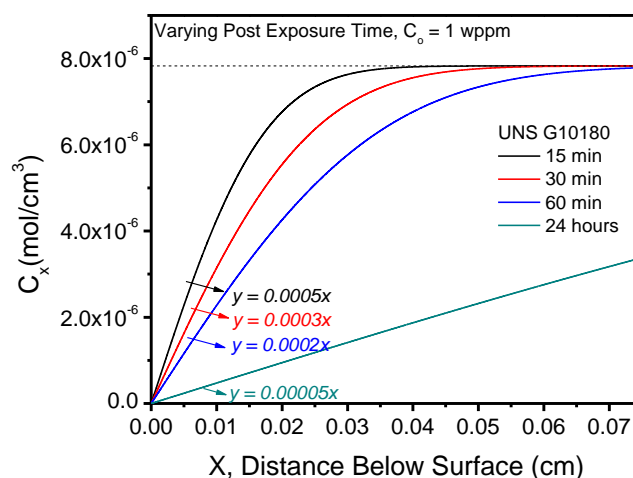
e)



f)

Time	i_L (A/cm ²)
15 min	1.35×10^{-5}
30 min	9.55×10^{-6}
60 min	6.77×10^{-6}
24 hours	1.39×10^{-6}

g)

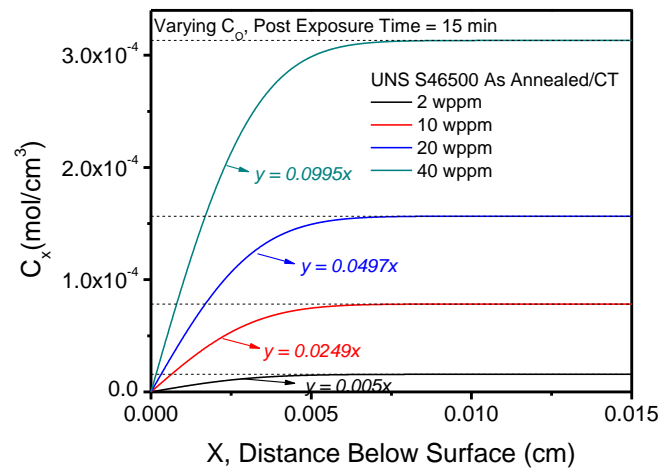


h)

Time	i_L (A/cm ²) 1 wppm
15 min	4.82×10^{-6}
30 min	2.89×10^{-6}
60 min	1.93×10^{-6}
24 hours	4.82×10^{-7}

Figure 107. $C_{H,Diff}$ egress with varying time. $C_{H,Diff}$ vs. distance below the hydrogen charging surface is calculated using the assumption for diffusion in an infinite plane and an initial concentration of 10 wppm a) UNS S46500 As Annealed/CT, c) H900, e) UNS K92580 and g) UNS G10180 (1 wppm). $D_{H,eff}$ values used were 3.5×10^{-9} , 6.2×10^{-9} , 9×10^{-9} , and 1×10^{-7} for UNS S46500 As Annealed/CT, H900, UNS K92580, and UNS G10180, respectively. b, d, f, h) The limiting current density was estimated using the equation $i_L^{H^+} = -nFD \left(\frac{\partial C}{\partial x} \right)$, where $y = \frac{\partial C}{\partial x} x$ taken over the range of 0 to 0.0025 cm (linear section).

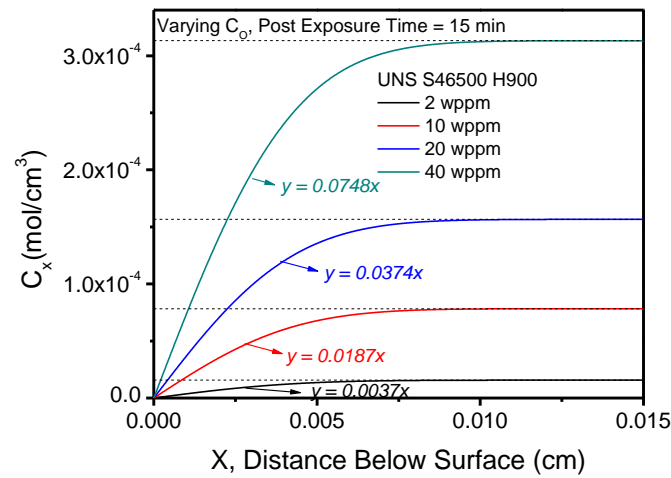
a)



b)

C_o	i_L (A/cm ²)
2 wppm	1.69×10^{-6}
10 wppm	8.41×10^{-6}
20 wppm	1.68×10^{-6}
40 wppm	3.36×10^{-5}

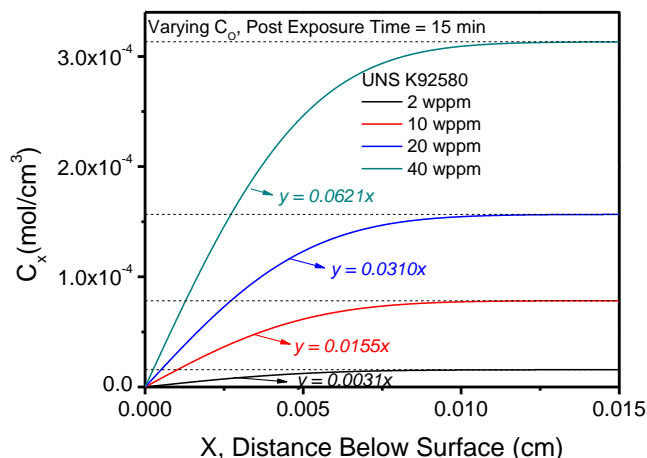
c)



d)

C_o	i_L (A/cm ²)
2 wppm	2.21×10^{-6}
10 wppm	1.12×10^{-5}
20 wppm	2.24×10^{-5}
40 wppm	4.47×10^{-5}

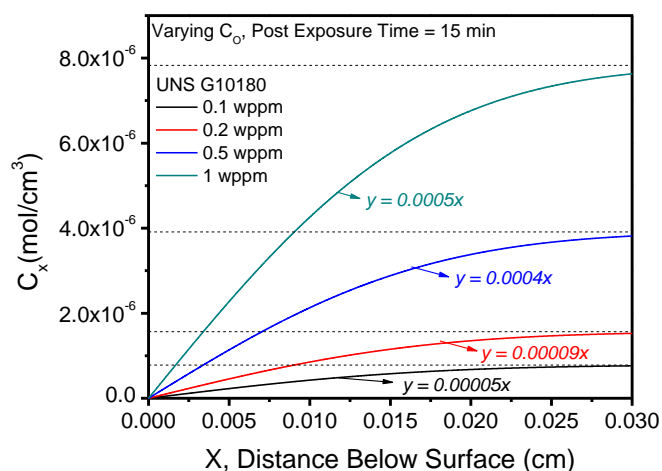
e)



f)

C_o	i_L (A/cm ²)
2 wppm	2.96×10^{-6}
10 wppm	1.35×10^{-5}
20 wppm	2.69×10^{-5}
40 wppm	5.39×10^{-5}

g)

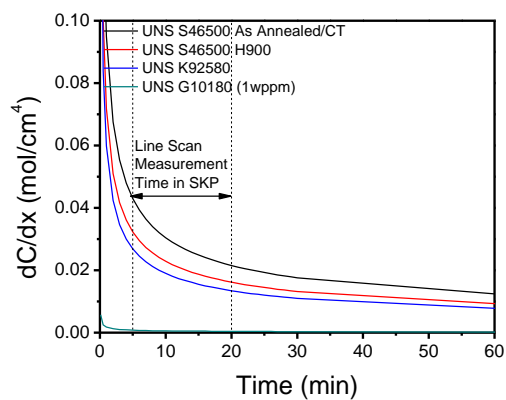


h)

C_o	i_L (A/cm ²)
0.1 wppm	4.82×10^{-7}
0.2 wppm	8.68×10^{-7}
0.5 wppm	1.93×10^{-6}
1 wppm	4.82×10^{-6}

Figure 108. $C_{H,Diff}$ egress with varying C_o . $C_{H,Diff}$ vs. distance below the hydrogen charging surface is calculated using the assumption for diffusion in an infinite plane and time of 15 min a) UNS S46500 As Annealed/CT, c) H900, e) UNS K92580 and g) UNS G10180. $D_{H,eff}$ values used were 3.5×10^{-9} , 6.2×10^{-9} , 9×10^{-9} , and 1×10^{-7} for UNS S46500 As Annealed/CT, H900, UNS K92580, and UNS G10180, respectively. b, d, f, h) The limiting current density was estimated using the equation $i_L^{H^+} = -nFD \left(\frac{\partial C}{\partial x} \right)$, where $y = \frac{\partial C}{\partial x} x$ taken over the range of 0 to 0.0025 cm (linear section).

a)



b)

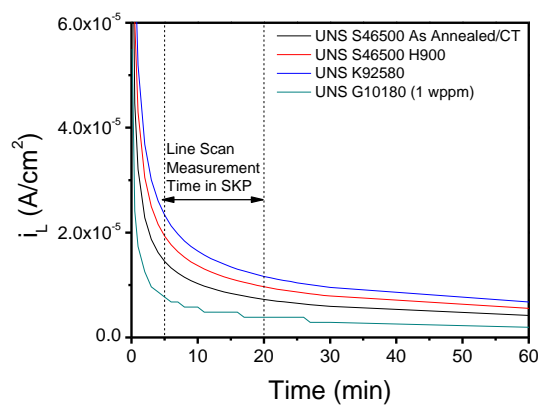
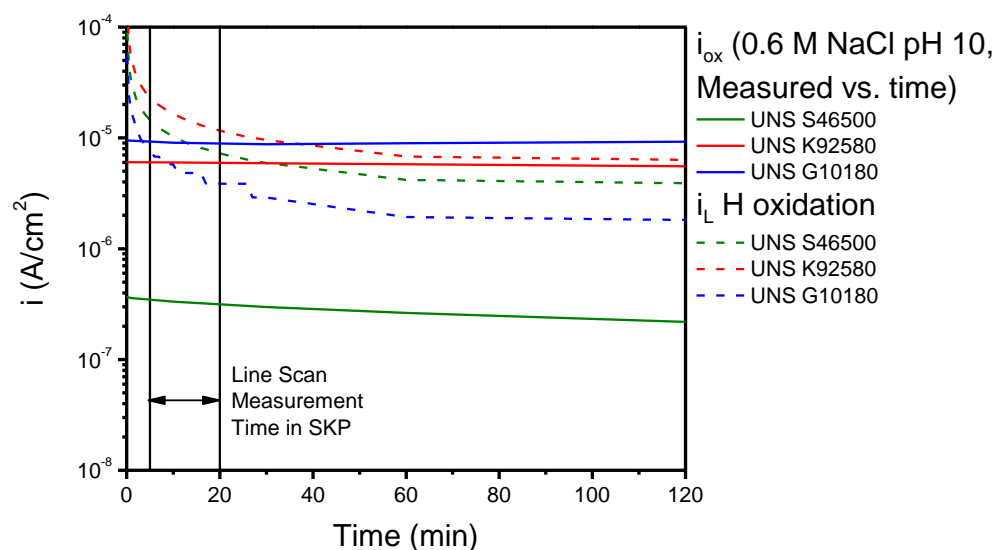


Figure 109. a) $\frac{\partial C}{\partial x}$ and b) i_L calculated vs. time using the assumption for diffusion in an infinite plane and an initial concentration of 10 wppm or 1 wppm for UNS G10180. Same assumptions apply as previously stated.

a)



b)

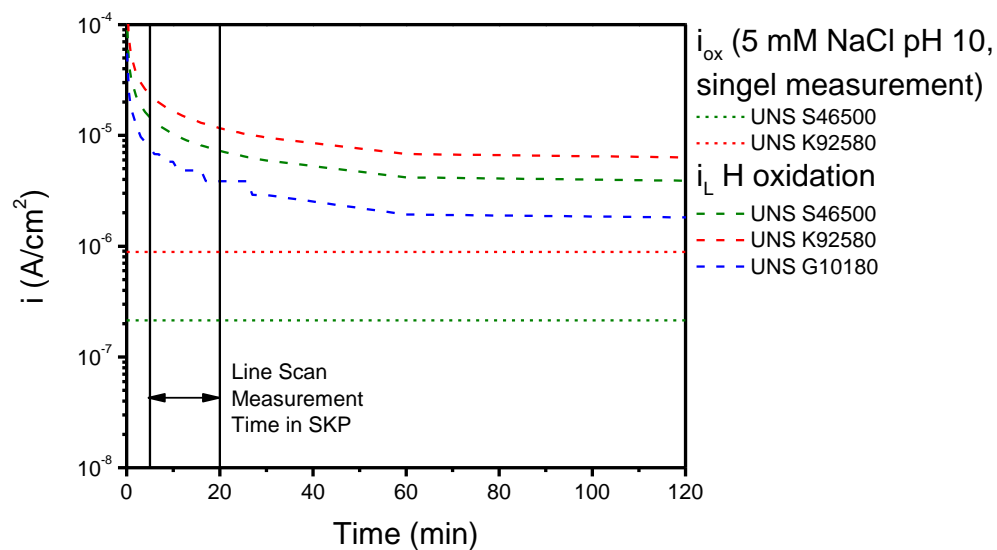
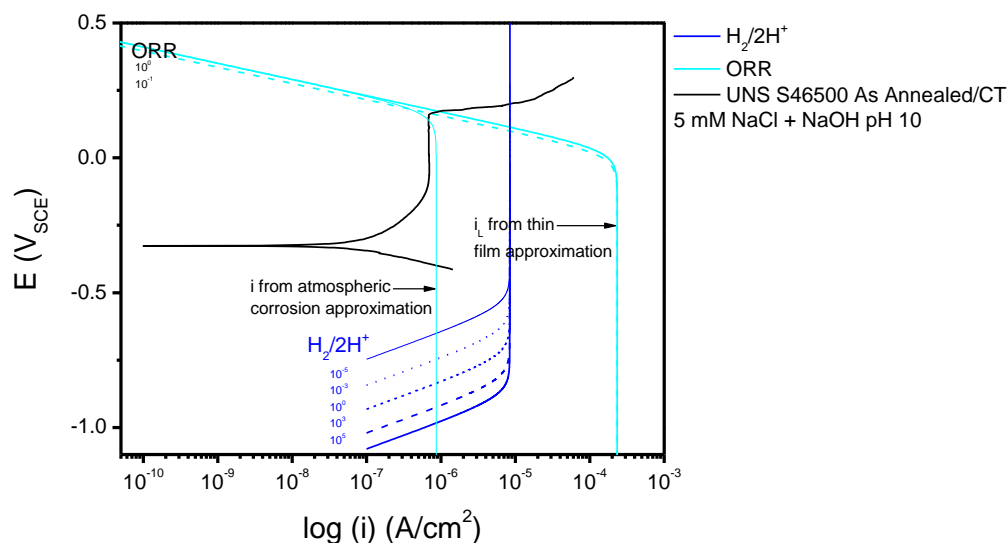
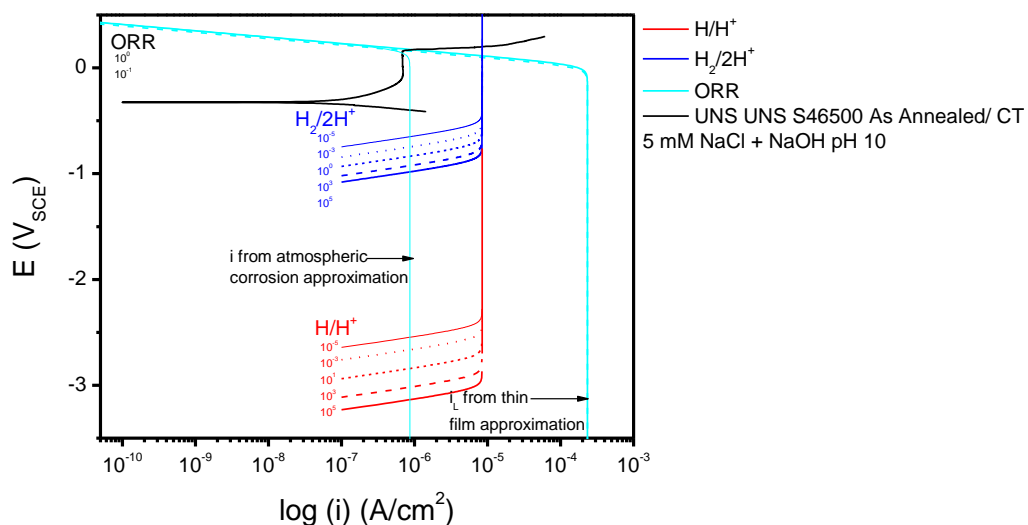


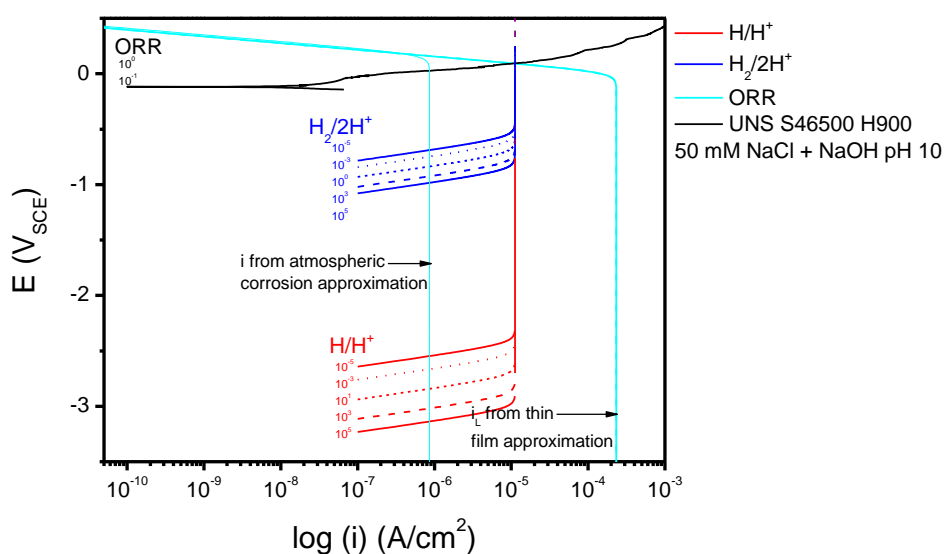
Figure 110. Oxidation current density compared to the limiting hydrogen oxidation current density vs. time. Oxidation current density was calculated from EIS fitting for a) 0.6 M NaCl + NaOH pH 10 exposures at E_{OCP} vs time and for b) a single exposure of 5 mM NaCl + NaOH pH 10 exposures. $i_{L,Hox}$ were calculated from $\frac{\partial C}{\partial x}$ in Figure 109.

a)

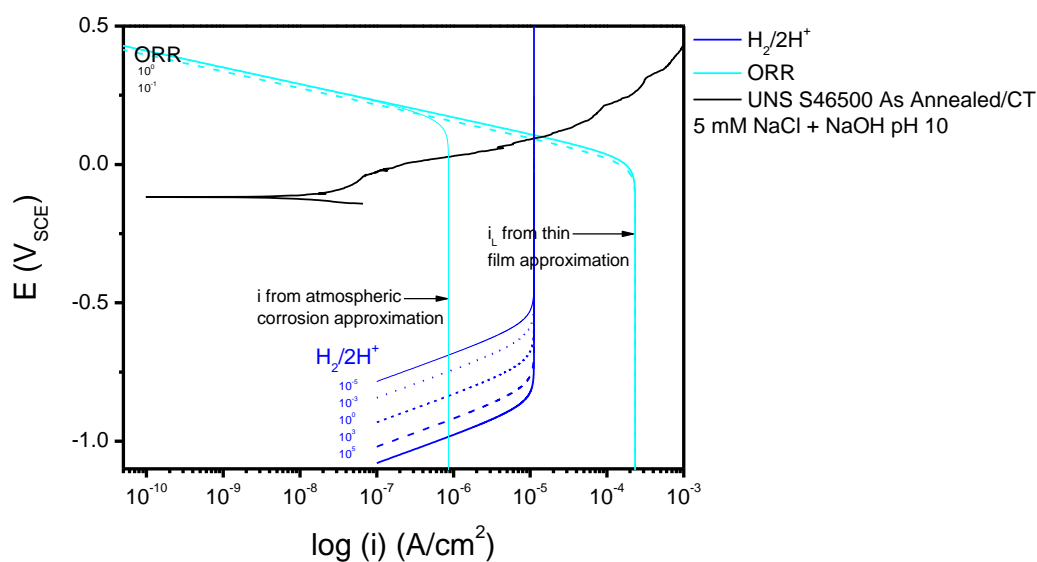


b)

Figure 111. Mixed potential theory model for UNS S46500 As Annealed/CT assuming a thin film formation in a low chloride environment (5mM) formed during SKP measurements at 57% RH. Currents for ORR, H/H^+ , and $H_2/2H^+$ were calculated using Equations 63-73 and stated assumptions, while the anodic scan was measured in 5 mM NaCl + NaOH pH 10 at a scan rate of 0.1667 mV/s from -100 mV vs E_{OCP} to 500 mV vs E_{OCP} . a) Displays both H oxidation currents, while b) only displays H/H^+ .

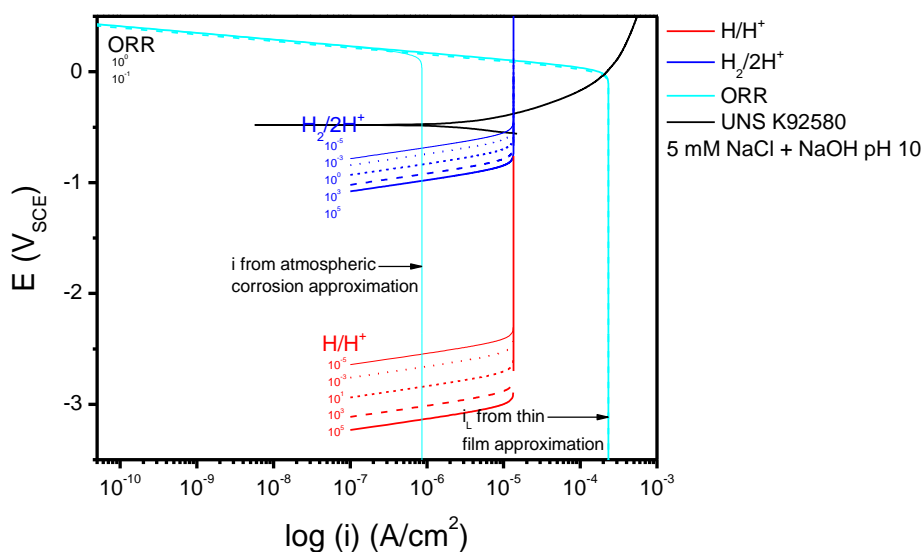


a)

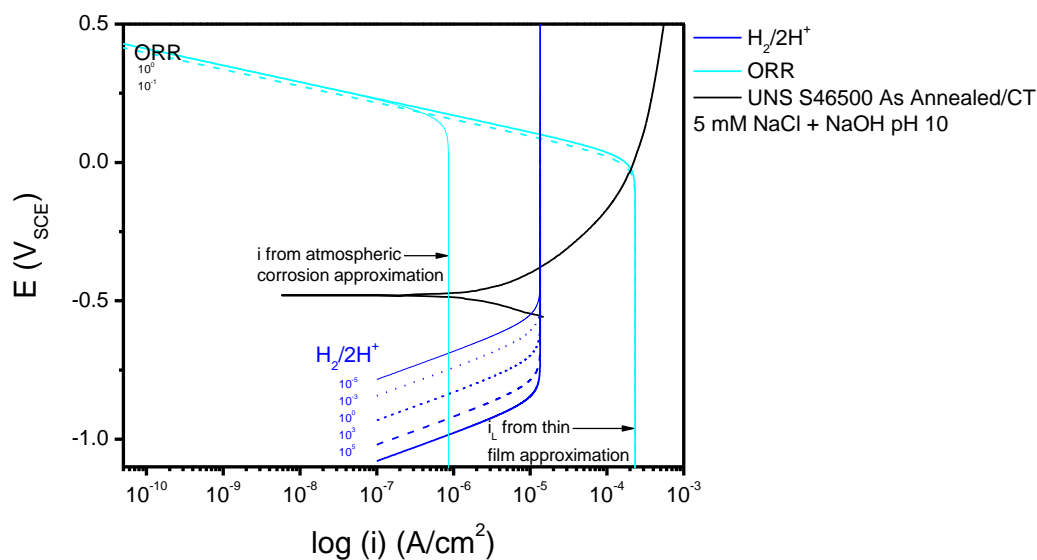


b)

Figure 112. Mixed potential theory model for UNS S46500 H900 assuming a thin film formation in a low chloride environment (5mM) formed during SKP measurements at 57% RH. Currents for ORR, H/H⁺, and H₂/2H⁺ were calculated using Equations 63-73 and stated assumptions, while the anodic scan was measured in 50 mM NaCl + NaOH pH 10 at a scan rate of 0.1667 mV/s from -100 mV vs E_{OCP} to 500 mV vs E_{OCP}. a) Displays both H oxidation currents, while b) only displays H/H⁺.

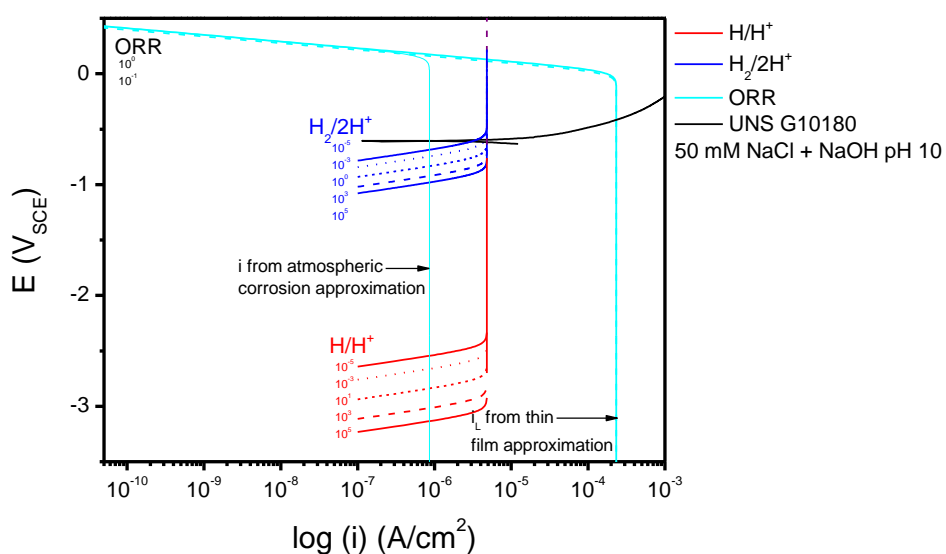


a)

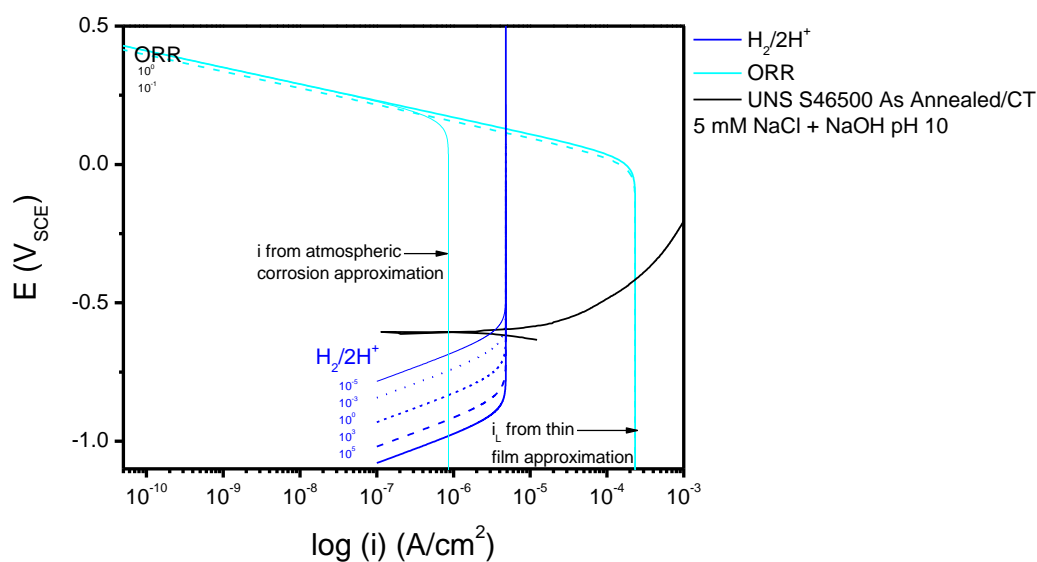


b)

Figure 113. Mixed potential theory model for UNS K92580 assuming a thin film formation in a low chloride environment (5mM) formed during SKP measurements at 57% RH. Currents for ORR, H/H^+ , and $H_2/2H^+$ were calculated using Equations 63-73 and stated assumptions, while the anodic scan was measured in 5 mM NaCl + NaOH pH 10 at a scan rate of 0.1667 mV/s from -100 mV vs E_{OCP} to 500 mV vs E_{OCP} . a) Displays both H oxidation currents, while b) only displays H/H^+ .



a)



b)

Figure 114. Mixed potential theory model for UNS G10180 assuming a thin film formation in a low chloride environment (5mM) formed during SKP measurements at 57% RH. Currents for ORR, H/H⁺, and H₂/2H⁺ were calculated using Equations 63-73 and stated assumptions, while the anodic scan was measured in 50 mM NaCl + NaOH pH 10 at a scan rate of 0.1667 mV/s from -100 mV vs E_{OCP} to 500 mV vs E_{OCP}. a) Displays both H oxidation currents, while b) only displays H/H⁺.

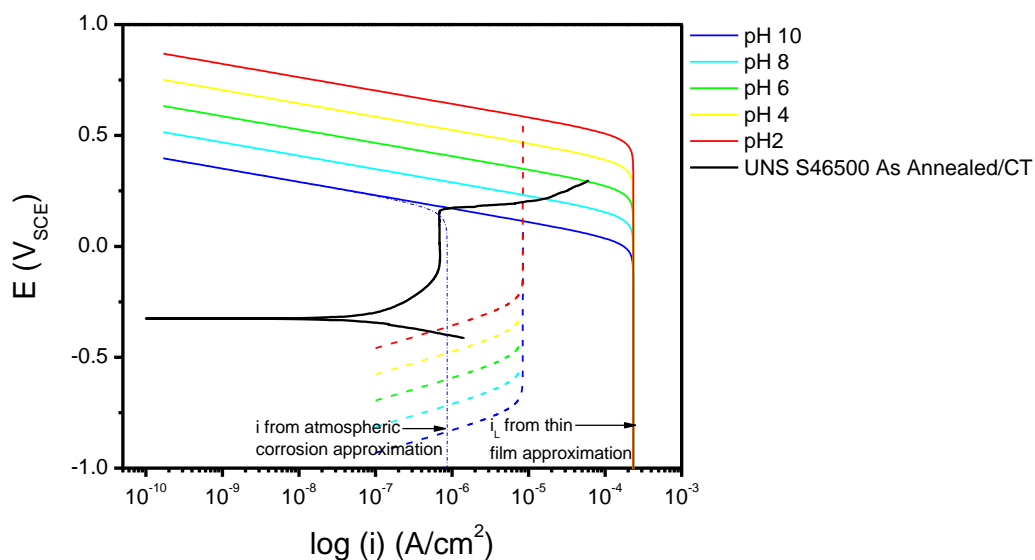


Figure 115. Mixed potential theory model for UNS S46500 As Annealed/CT assuming a thin film formation in a low chloride environment (5mM) formed during SKP measurements at 57% RH. Currents for ORR, H/H^+ , and $\text{H}_2/2\text{H}^+$ were calculated using Equations 63-73 and stated assumptions, while the anodic scan was measured in 5 mM NaCl + NaOH pH 10 at a scan rate of 0.1667 mV/s from -100 mV vs E_{OCP} to 500 mV vs E_{OCP} . Calculations for ORR and H oxidation were made with pH values of 10, 8, 6, 4, and 2. For these calculations, C_{O_2} and C_{H_2} were assumed to be 10^0 atm.

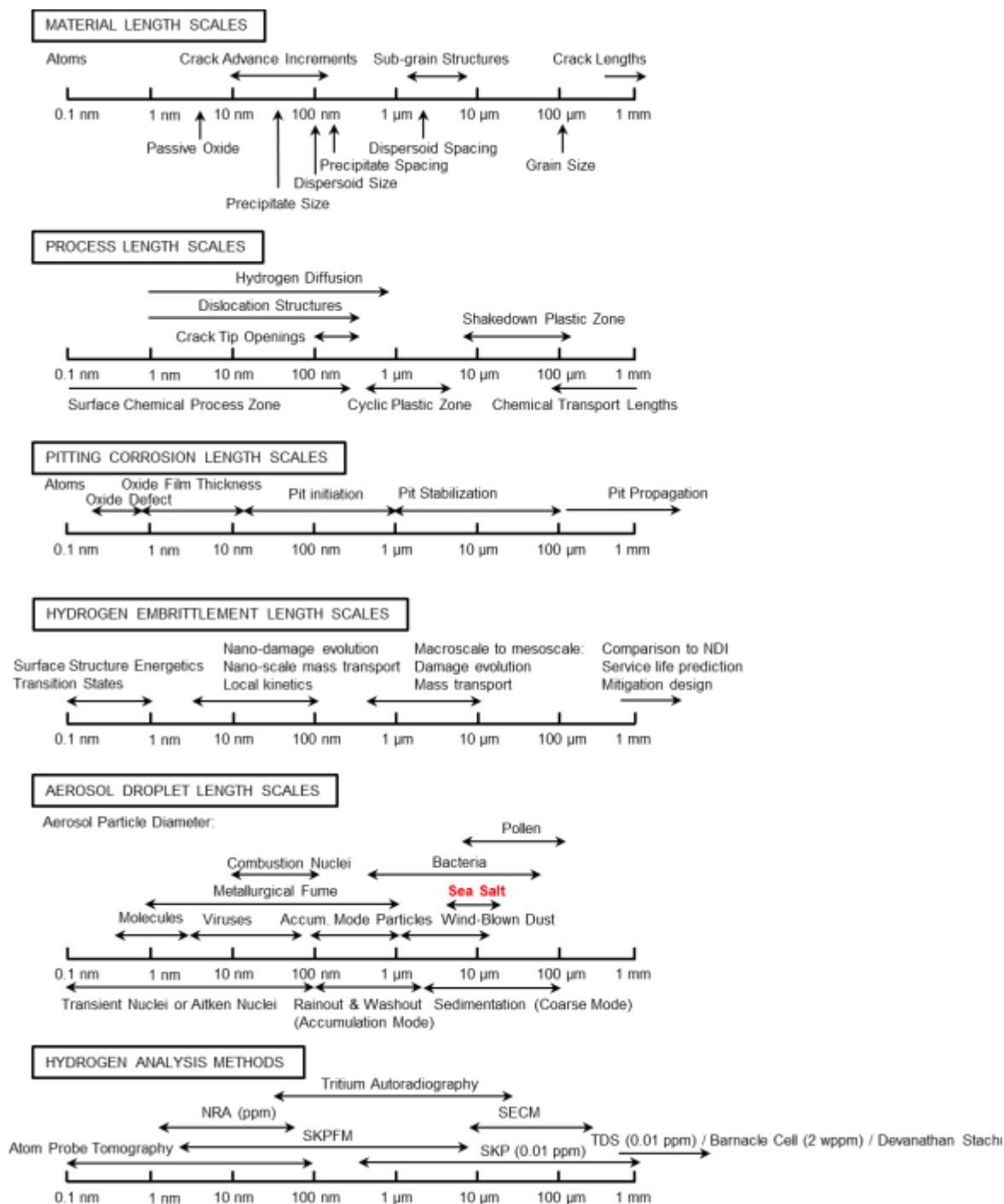


Figure 116. The wide span of different length scales with relation to the material, pitting, and aerosols in play in atmospheric corrosion. SOURCE: University of Virginia, CESE, courtesy of Matthew R. Begley and Richard P. Gangloff, Hongbo Cong and J.R. Scully, Atmospheric Corrosion, Christopher Leygraf and Thomas E. Graedel, and I. Cole. [63, 78, 79]

CHAPTER 4. Spatial Determination of Diffusible Hydrogen Concentrations in UHSS from Uniform Pre-Charging Using the Scanning Electrochemical Microscope

4.1. Abstract

Determination of hydrogen pre-charged concentrations spatially in UHSS using the scanning electrochemical microscope (SECM) is presented, similar to the study carried out in Chapter 3 with the SKP. The SECM was selected for exploration as a second spatial H detection technique as it has been established as a tool for localized corrosion and preliminary studies have explored expansion of this technique towards the detection of localized H concentrations.[1, 2] The as annealed/CT and H900 tempers of UNS S46500 were compared to UNS K92580. Predetermined uniform diffusible H concentrations, quantified using electrochemical extraction methods after homogenous cathodic charging, were examined with changes in the microelectrode (ME) probe tip current measured by the SECM in both feedback diffusion and redox competition modes. These spatial variations in current were calibrated with predetermined uniform diffusible H concentrations quantified using electrochemical extraction methods. The origins of the effects of controlling factors of the ME probe tip current are discussed. The development of these techniques adds to a suite of instruments that enable better determination of localized H uptake and may help in the future for damage prediction.

4.2. Introduction and Background

As shown in Chapter 2, techniques for spatial detection at the sub-mm length scale, specifically lateral detection necessary for mapping H concentrations produced by droplets, are lacking. The need to establish, explore, and optimize localized H detection

techniques is of great importance to furthering understanding of local H production and uptake.

4.2.1. SECM Modes and Corrosion Characterization

The SECM has been developed as a tool to explore localized corrosion in the X-Y directions across a planar sample surface. The SECM consists of a cell in which a planar sample sits below a microelectrode (ME) tip, a counter and reference electrode are shared by the ME and sample, and the ME and sample are connected to a bipotentiostat such that a bias potential can be applied to either the ME or sample, or both simultaneously (Figure 117). The tip scans in an X-Y plane parallel to the X-Y plane of a sample surface at an offset of Z. Both the probe tip and sample are immersed in solution. Typical operation modes for the SECM include, but are not limited to: feedback mode (oxidation at the ME tip/ reduction at the working electrode surface, ox_{ME}/red_{WE}) and redox competition mode (reduction at the ME tip/ in competition with reduction at the working electrode surface, red_{ME}/red_{WE}).[3-7] When the SECM is applied in feedback mode (ox_{ME}/red_{WE}), the differences in the current measured at the tip can be related to the local substrate conductivity and/or reactivity.[8] In this mode, a redox mediator, for example ferrocene methanol, is used in solutions such that the voltage selected for potentiostatic polarization of the ME Pt tip will oxidize a specific species at the tip. In the case of ferrocene methanol, $FcMeOH \rightarrow FcMeOH^{++} + e^-$ ($Fe^{+2} \rightarrow Fe^{+3} + e^-$) (Table 27). Far away from the sample, the current is based on the limiting spherical diffusion of FcMeOH to the tip. As the tip approaches an insulating surface, the FcMEOH oxidation current will decrease as the availability of the reactant decreases from the electrolyte near

the tip and is dependent on diffusion to the tip, Figure 118-b. Above an active surface, the FcMeOH^+ is reduced at suitable cathodic potentials relative to the Nernst potential for FcMeOH , thus there is a greater supply of the reactant for FcMeOH oxidation near the surface as the tip approaches and the current is increased, Figure 118-a.

A second mode of SECM operation is redox competition ($\text{red}_{\text{ME}}/\text{red}_{\text{WE}}$), in which a mediator is not used.[6, 7, 9] In this mode, the ME Pt tip is held at a potential such that ORR occurs, and again, far away from the sample surface is based on the limited O_2 spherical diffusion to the tip in the selected electrolyte. In redox competition ($\text{red}_{\text{ME}}/\text{red}_{\text{WE}}$), above an insulator, a similar behavior to feedback diffusion ($\text{OX}_{\text{ME}}/\text{red}_{\text{WE}}$) mode is seen with the tip current, in that the ME tip current drops as the tip approaches the non-reacting surface and the spherical concentration field of oxygen from the bulk electrolyte is allowed and this effects the flux of O_2 supplied to the ME. However, above a sample over which the reactant is consumed, the SECM ME tip competes with the surface for the same analyte. Thus if the surface is an active catalyst for ORR and its potential is below the Nernst potential for ORR, the ORR current at the tip is seen to further decrease as O_2 is consumed at the sample. An example of redox competition ($\text{red}_{\text{ME}}/\text{red}_{\text{WE}}$) mode is shown in Figure 119, where the oxygen diffusion profiles near the ME tip and an active site are drawn.[9] As these two profiles overlap during scanning or approach to the surface, a change in the current measured at the tip is detected.[6] These SECM modes enable detection of corrosion processes with spatial resolution.[5, 10, 11] Presented below are some specific localized corrosion studies of interest to this research.

As discussed earlier, possible hotspots for hydrogen production and uptake in the stainless UHSS could be pits produced under atmospheric exposure. Therefore, the ability of the SECM to map localized corrosion processes, specifically those pertaining to pitting and pit initiation, is important to establish prior to studying H produced or absorbed at these sites. Before discussing mapping of absorbed or adsorbed H, measurements of sites for possible H₂ evolution are discussed (pits). One example of the use of the SECM for the study of localized corrosion is the imaging of metastable pits at the open circuit potential of an austenitic stainless steel.[12] In this study, redox competition mode (red_{ME}/red_{WE}) was applied, however, the analyte of interest was Fe²⁺ which was oxidized to Fe³⁺ at the Pt ME tip via $\text{Fe}^{2+} \rightarrow \text{Fe}^{3+} + \text{e}^-$ (Table 27). The authors found that pitting occurred with the release of Fe²⁺ ions, thus enhancing the current density at the ME tip as it scanned over a pit initiation site. Ferric ions were not exploited for this method as they have a tendency to precipitate as Fe (III) oxyhydroxides and may block the probe, thus reducing sensitivity.[13] This mode in the SECM enabled imaging of metastable pitting events occurring in 0.1 M HCl in austenitic stainless steel for the first time.[13] Another example of the use of the SECM for detection of pitting applied the feedback mode (ox_{ME}/red_{WE}) combined with substrate generation to establish pitting corrosion in neutral salt solutions on 304 stainless steel.[5] In this example, the substrate was galvanostatically polarized at -80 μA while the SECM tip potential was held at +0.56 V_{Ag/AgCl} in 0.1 M NaCl solution to oxidize Fe²⁺ at the tip (Table 27). As in the example above, increased Fe²⁺ concentrations, and thus an increased ME tip current, occurred above active sites associated with pit initiation.[10]

Beyond use of the SECM for localized pitting corrosion, other studies highlight the application of the SECM for localized activity, such as the dissolution of specific species. This is pertinent here as the dissolution of species such as MnS can be initiation sites for pitting corrosion. Paik et al. were able to establish the dissolution of sulfur species on 304 stainless steel, exposed to 10 mM KI and 0.1 M NaCl, with the SECM by mapping the evolution of concentrations over time in a redox mediator.[14] In this case, potassium iodide was applied as the mediator solution in feedback diffusion mode (ox_{ME}/red_{WE}) with the tip held at +0.6 V_{Ag/AgCl} to achieve $3I^- \rightleftharpoons I_3^- + 2e^-$ as the oxidation reaction at the tip (Table 27). The authors stated that as dissolution of an MnS particle occurs, hydrosulfide or thiosulfate are produced, which react to regenerate I⁻ at the sample surface.[15] If the tip is scanned above these areas, an enhanced current density is seen as there is an increased concentration of I⁻ in the region of the dissolved MnS particle. While these studies highlight the localized detection capabilities of the SECM with both spatial and temporal mapping abilities, they do not show the capability of this technique as a viable option for localized H detection, whether that is adsorbed (H adsorbed at the sample surface), absorbed (H absorbed in the sample which occupies lattice or interstitial trap sites), or evolved hydrogen (H produced at the sample surface by corrosion processes).

4.2.2. SECM as a Method for Local Hydrogen Characterization

The use of the SECM as an instrument for localized corrosion detection has been well established, yet very few studies have highlighted the capability of the SECM for pre-charged and adsorbed or absorbed H (H_{ads} or H_{abs}) detection, and have little discussion for a mechanism for the effect of H_{abs} on the current measured at the ME Pt tip. However, the SECM has been shown a capable tool in feedback diffusion mode ($\text{OX}_{\text{ME}}/\text{red}_{\text{WE}}$) for detecting H_2 evolved at the surface through in-situ studies of corrosion of Mg alloys.[16, 17] In these studies, the ME tip was held at $-0.05 \text{ V}_{\text{Ag}/\text{AgCl}}$ in NaCl solutions such that HER occurred at the tip as it scanned above regions of H_2 evolution (Table 27). As hydrogen evolution increased at the surface, and increase in the tip current was seen.[16, 17] These methods are not directly applicable to the study of pre-charged and absorbed H concentrations, as they rely on a much higher surface concentration from H evolution for detection. Presented here are the few studies found on H effects for both pre-charged and H_{ads} or H_{abs} concentrations as well as evolved H_2 in the SECM measured on steel.

The first example explores the indirect detection of H_{ads} in a sample through the effect of H pre-charging on the initiation of pitting in the SECM.[18] In this study, samples of X70 steel were cathodically H pre-charged and subsequently measured in a corrosive environment of 0.1 M NaCl solution in the SECM to initiate pitting. The probe tip was held at a voltage of $0.6 \text{ V}_{\text{SCE}}$ to oxidize Fe^{+2} in redox competition mode ($\text{OX}_{\text{ME}}/\text{red}_{\text{WE}}$), thus more active sites with increased ME tip current were an indication of pitting initiation, and it was found that pitting increased with increasing H pre-charging current and time. The authors believed that this was due to the oxidation of the H locally at the

surface of the X70 steel which decreased the pH at the interface, slowing oxide formation and promoting pitting. A second study by Modiano et al. explored the effect of H pre-charging on the SECM tip current, however it did so in permeation mode.[1] In this study, Fe foils were measured by SECM prior to and during cathodic charging on the exit side of a Devanathan Starchuski type cell. The solution used was 0.3 M H_3BO_3 + 0.075 M $\text{Na}_2\text{B}_4\text{O}_7$ (pH 8.4) and the SECM tip was held at $-0.73\text{V}_{\text{SCE}}$ ($-0.711\text{ V}_{\text{Ag}/\text{AgCl}}$) to achieve hydrogen oxidation at the tip. As the H_{abs} concentration from the pre-charging side diffused through the sample, the authors report a drop in the resistance measured, indicating that the H permeation caused a reduction in the passive film oxide on the exit side measured by the SECM tip. This would be possible via the combination of H oxidation and Fe^{+3} reduction at the exit surface (Table 27).

In another study, Fushimi et al. explored the generation of H_2 from magnetite coupled to carbon steel in deaerated pH 3.3 sulfate solution.[2] As the magnetite was coupled to the steel, H_2 evolved at the sample surface while the ME tip was held at $0.3\text{ V}_{\text{SHE}}$ ($0.078\text{ V}_{\text{Ag}/\text{AgCl}}$) to oxidize hydrogen gas at the probe tip (Table 27), in feedback diffusion mode ($\text{OX}_{\text{ME/red,WE}}$). As the surface concentration increased, the ME tip current increased due to an increase of H_2 in solution. Therefore, concentrations of H_2 generated at the sample surface could be determined spatially as the probe tip scanned across areas of high and low generation.

While these studies begin to display the capabilities of the SECM for localized H detection, primarily H_2 and not H_{ads} or H_{abs} , further research is necessary before this

technique can be applied to atmospherically pre-exposed samples for local spatial H determination. In this chapter, the recently developed technique of SECM for spatial H detection is explored using both redox competition ($\text{red}_{\text{ME}}/\text{red}_{\text{WE}}$) and feedback mode ($\text{OX}_{\text{ME}}/\text{red}_{\text{WE}}$) to map H concentrations of samples cathodically pre-charged with known $C_{\text{H,diff}}$. Electrochemical experiments, as well as calibration experiments, are performed to further optimize the SECM technique. An explanation is given for the proposed effect of absorbed H in the working electrode on the probe tip current measured at the ME. This is further developed in Chapter 5 for detection across areas pre-exposed under atmospheric corrosive environments which produced pits.

4.3. Experimental Procedures

4.3.1. Materials

The material compositions for the secondary-hardened martensitic steels are given in Table 25 and material properties in Table 26. Samples of UNS K92580 were tested in the peak-aged condition and for UNS S46500, in the as annealed/CT and H900 conditions. As with the SKP measurement techniques, these materials are advantageous for measurement in the SECM due to their slow $D_{\text{H,eff}}$, ranging from $3.1 \times 10^{-9} \text{ cm}^2/\text{s}$ to $8.96 \times 10^{-9} \text{ cm}^2/\text{s}$ as determined by thermal desorption spectroscopy.[19] This enables mapping without substantial H outgassing or redistribution of H during the transfer time from pre-exposure to initial measurements. The average time to initial line or area scan measurements in the SECM is 30 min, during which $\frac{1}{2} C_0$ of the H concentration can diffuse 24 or 40 μm for UNS S46500 and UNS K92580 respectively.

4.3.2. Electrochemical Evaluation of SECM Measurement Environment

Prior to the measurement of H pre-charged samples in the SECM, studies were explored to ensure first, that the SECM functioned in the selected solution above a calibration sample, that this solution did not initiate corrosion rapidly on the samples of interest, and finally that the current measured at the SECM tip for a specific solution was effected by pre-charged H concentrations in the sample. Initial electrochemical experiments were performed to determine the corrosion severity of possible measurement solutions. Since the SECM is an electrochemical technique, a conductive solution is necessary; however, to avoid severe corrosion which could dominate the SECM ME tip current behavior, a high pH solution with a low Cl^- content is ideal for a ferrous alloy.[20] To study the effect of pH, E_{OCP} measurements followed by EIS and anodic polarizations were acquired. Samples of UNS S46500 As Annealed/CT and UNS K92580 were polished to 600 grit SiC, rinsed with DI water, dried with compressed air, and degreased with acetone prior to measurement. Samples were then inserted into an electrochemical flat cell with a 1 cm^2 opening, Pt-Nb Mesh counter electrode, and a SCE reference electrode. Solutions of 5 mM NaCl starting with the natural pH of 5.5 and pH adjusted to 6, 8, 9, and 10 with NaOH were tested. Measurements consisted of first, a 1 h OCP followed by EIS at OCP with $20 \text{ mV } V_{\text{rms}}$, 6 points per decade collected from 1 mHz to 100 kHz. After EIS an anodic scan was acquired from -100 mV below E_{OCP} to 1 V vs E_{OCP} at a scan rate of 0.1667 mV/s . As applied previously in Ch. 3, EIS results can be related to the oxidation current density, i_{ox} . The same model circuit as used in Ch. 3 was applied for fitting and determination of R_p . The oxidation resistance can be related to the H oxidation and anodic dissolution resistance. Oxidation current densities were determined

for EIS fitting of exposures in 5 mM NaCl starting with the natural pH of 5.5 and pH adjusted to 6, 8, 9, and 10 with NaOH. After EIS measurements, anodic polarization acquired from -100 mV below E_{OCP} to 1 V vs E_{OCP} at a scan rate of 0.1667 mV/s. No intentional cathodic pre-charging was carried out prior to these tests.

A second set of samples were assessed to explore the effects of Cl^- in the SECM electrolyte. Samples were prepared in the same manner, inserted into an electrochemical flat cell, and a 1 h OCP was collected followed by an anodic polarization acquired from -100 mV below E_{OCP} to 1 V vs E_{OCP} at a scan rate of 0.1667 mV/s. The solutions used were naturally aerated 5, 50, and 500 mM NaCl at their natural pH of about 5.5.

In a third set of electrochemical tests, EIS measurements were acquired to form a comparison of measurement solution to solutions similar to those in pre-exposure conditions, mimicking both electrochemical and atmospheric exposure conditions, as well as the measurement solution of interest. Samples of UNS S46500 in the as-annealed/CT and H900 temper, UNS K92580, and UNS G10180 were exposed. Samples were prepared in the same manner as described previously, cleaned, and inserted into an electrochemical flat cell. EIS measurements were taken at E_{OCP} with a V_{rms} of 20 mV, with 6 points acquired per decade and measured from 10 mHz to 100 kHz. Solutions tested of interest were 0.1 M NaOH, representing a non-corrosive, basic solution, 5 mM NaCl + NaOH pH 10, representing the possible SECM measurement solution, 5.1 M NaCl, representing a high chloride exposure environment, and 0.1 M HCl, representing a highly acidic environment such as one possibly produced in a pit. To compare across

solutions, i_{ox} was determined from R_p and fitting (as applied in Ch 3) of the EIS measurements. Measurements were compared to the average of the limiting H oxidation current ($i_{L,Hox}$) from C_H egress calculations. Again, no intentional cathodic pre-charging was carried out prior to these tests.

4.3.3. SECM Calibration: Determination of Optimal Measurement Electrolyte

Once solutions were electrochemically tested and established as less severe corrosion environments, such that i_{corr} was significantly lower than the i_L for H oxidation based on H egress, application of these solutions for viable measurement in the SECM was explored. Prior to each test in the SECM, the cell was set up as shown in Figure 117. Samples, mounted in epoxy and polished to 3 μm diamond paste, were cleaned with acetone, rinsed with DI water, dried with compressed air, and inserted into the SECM where they were leveled prior to measurements. The 10 μm diameter Pt ME was polished to 0.25 μm diamond paste, rinsed with DI, and dried with compressed air prior to insertion in the cell where it was flush mounted. An Ag/AgCl reference electrode and a Pt mesh counter electrode were used for all experiments. Electrolyte was introduced and a cyclic voltammogram (CV) was taken. An example set of CVs is shown in Figure 120-a with varying salt concentrations. These scans are taken to determine the steady state diffusion controlled region for the reaction of interest, in this example ORR occurring from -0.8 to -0.5 $V_{Ag/AgCl}$, the “health” of the tip, ensuring there is not contaminant on the tip causing unexpected reactions, and the stability of the solution, ensuring there is no significant contamination from corrosion product in solution, or that the solution itself is not contaminated. Unexpected peaks in the CVs, low current in the

CV measurement, or significant hysteresis between successive scans can signify an unstable or contaminated system evidenced by a non S-shape curved CV.[4] CVs were taken from -1 to 0.5 V_{Ag/AgCl} and the reverse at a scan rate of 100 mV/s, and a minimum of 3 cycles.

After the steady state region of the reaction of interest is determined in the solution, a voltage can be selected to apply to the Pt ME tip. The voltage is then held constant for the remainder of the SECM scans in that measurement.

Calibration of the SECM was necessary prior to use with UHSS samples. An Au/Epoxy sample was used for calibration in redox mediator solutions; 5 mM NaCl + 0.01 M ferrocene methanol and 0.1 M NaOH + 0.01 M ferrocene methanol in feedback mode (ox_{ME}/red_{WE}). In feedback mode, the redox species from the mediator is reduced at the tip and can be reoxidized at the substrate surface (Table 27). CVs were scanned on the Pt tip to verify the setup and probe the oxidation/reduction properties of the solution. The tip was then held at a constant voltage of +0.4 V_{Ag/AgCl} in the ferrocene methanol redox mediator as it promotes reduction of the ferrocene methanol at the tip ($FcMeOH^+_{(aq)} + e^- \rightleftharpoons FcMeOH_{(aq)}$), whereas the sample was left floating at E_{OCP} in the solution. On an insulator, such as the epoxy, FcMeOH is not reduced at the surface and FcMeOH access to the tip is limited by diffusion from the surrounding electrolyte. As the ME tip approaches an insulator surface a diffusion limited decrease in current occurs, termed negative feedback, Figure 118. When an approach curve is made, as the tip approaches the non-conductive substrate, the current will decrease. Above the Au, the current should

increase as it establishes positive feedback, where reduction of the analyte occurs at the conductive gold surface, as in these solutions, the Au E_{OCP} is expected to sit below E_0 for Fe^{+3}/Fe^{+2} . Initial experiments consisted of constructing approach curves over the epoxy area of the sample, with a scan rate in the z-direction, vertical and perpendicular to the surface (movement of the tip towards the substrate surface), of 1 $\mu m/s$. The tip reached the sample surface, with a height of “0” considered to be when the current decreased from the initial value to 30 % of this value. The ME tip was raised back above the sample and set at a constant height of 30 μm for line scans. Line scans were taken across Au to epoxy, in the x-direction parallel to the surface, at a step size of 100 μm and a scan rate of 50 $\mu m/s$. Area scans were performed in the same solutions, in the x-y directions parallel to the surface, with a step size of 100 μm and a scan rate of 50 $\mu m/s$. Results are plotted as both the raw current detected (i_{tip}) at the ME tip vs. distance (x or x-y) and as normalized current (i_{tip}/i_{∞}) vs. distance (x or x-y). The current is normalized by dividing the tip current by the average of the steady state current measured from the CV scan acquired prior to each scan setup at the ME tip considered to be i_{∞} . At the applied voltage, in these solutions +0.4 V_{Ag/AgCl}, the steady state current is averaged from the current values at +0.4 V in each of the 3 CV cycles.

Optimization was further expanded to the steel samples of interest. Samples of uncharged as annealed/CT UNS S46500 were examined first in feedback mode (ox_{ME}/red_{WE}) as carried out on the Au/Epoxy sample, and in redox competition mode (red_{ME}/red_{WE}). In the latter the tip is held at a constant potential sufficient such that ORR is the dominant reduction reaction occurring at the tip (in this study at -600 to -800

$mV_{Ag/AgCl}$), and probing the effect of surface reactions on the ORR current at the ME ($i_{ORR,ME}$). Samples were prepared as mentioned previously for electrochemical testing, inserted into the SECM, leveled, and measured in three different solutions; 5 mM NaCl + 0.01 M ferrocene methanol, 0.1 M NaOH, and 5 mM NaCl + NaOH pH 10, the first solution in feedback mode ($ox_{,ME}/red_{,WE}$), the second two in redox competition mode ($red_{,ME}/red_{,WE}$). Area scans of 4.5 by 1.5 mm were taken in the scan direction from the steel sample to the epoxy in each solution. The tip was held at a constant voltage, +0.4 $V_{Ag/AgCl}$ for 5 mM NaCl + 0.01 M ferrocene methanol ($ox_{,ME}/red_{,WE}$) and -0.8 $V_{Ag/AgCl}$ for 0.1 M NaOH ($red_{,ME}/red_{,WE}$), and -0.6 or -0.8 $V_{Ag/AgCl}$ for 5 mM NaCl + NaOH pH 10 ($red_{,ME}/red_{,WE}$), while the sample was allowed to float at E_{OCP} . The ME tip to sample height was kept at a constant 30 μm for all scans except for the 5 mM NaCl + NaOH pH 10 scan at -0.8 $V_{Ag/AgCl}$, where a height of 100 μm was also explored.

4.3.4. Measurements for SECM Calibration in the Case of H Pre-charged

Materials

Steel disks of UNS S46500 and UNS K92580, 1.9 cm in diameter and 500 μm thick, were flush mounted in epoxy, ground to 1200 grit (SiC), polished to a 3 μm diamond paste finish, rinsed with DI water, dried with compressed air, and cleaned with ethanol. For hydrogen pre-charging, steel disks were polarized cathodically for 24 h at η_H of -200, -400, -600, and -800 mV (-1032, -1232, -1432, and -1632 mV_{SCE}) in naturally aerated, room temperature 0.6 M NaCl + NaOH, pH 10 solution in an electrochemical flat cell with a 1 cm^2 opening. The diameter of the hydrogen charged area was 1.13 cm. The resulting diffusible hydrogen concentrations of 5-25 wppm were measured by

electrochemical extraction in Ch. 3 and in previous work by Kehler.[21, 22] After 24 h charging, 1/100 of the surface hydrogen concentration was achieved both at a maximum depth perpendicular to the charged surface of 840 μm and lateral spread of 840 μm radially beyond the disk diameter of 1.13 cm (Figure 121). The steel was removed from the electrochemical flat cells, rinsed with DI water, cleaned with ethanol, and dried with compressed air in 5 min. Scans were performed using a Biologic® SECM370, initiated within 30 min of removal from the pre-charging cell in both feedback diffusion mode ($\text{ox}_{\text{ME}}/\text{red}_{\text{WE}}$) and redox competition mode ($\text{red}_{\text{ME}}/\text{red}_{\text{WE}}$). During this time, 1/100 of the surface concentration of hydrogen could diffuse an additional 90 μm .

A 10 μm Pt ME tip, flush-mounted, was cleaned prior to testing by CV in 0.01 M ferrocene methanol + 5 mM NaCl solution. The ME performance was verified by standard voltammetric procedures. For feedback mode ($\text{ox}_{\text{ME}}/\text{red}_{\text{WE}}$), approach curves were acquired in the redox mediator solution to determine the optimal ME to surface height. The ME was held at +0.6 V($V_{\text{Ag}/\text{AgCl}}$) with the reduction of ferrocene methanol as the dominant reaction at the tip in the diffusion limiting regime. Line scans across the pre-charged and uncharged regions of the steel, and over the epoxy, were taken in 0.01 M ferrocene methanol + 5 mM NaCl solution with ambient aeration and quiescent stirring in order to study the effects of hydrogen on the reduction of FcMeOH at the ME tip. Line scans were utilized instead of area scans due to the short length of time required - less than 15 min per scan. The ME was scanned at a rate of 50 $\mu\text{m}/\text{s}$. The steel and ME shared a Pt counter electrode and Ag/AgCl reference electrode. The ME tip was held at 30 μm above the steel.

For redox competition mode ($\text{red}_{\text{ME}}/\text{red}_{\text{WE}}$), CVs and approach curves were at first performed in feedback mode ($\text{ox}_{\text{ME}}/\text{red}_{\text{WE}}$) with 0.01 M ferrocene methanol + 5 mM NaCl solution. After completion of the approach curves and determination of disk to ME tip height, the redox mediator was removed, the cell rinsed, and solution replaced with the 5 mM NaCl + NaOH, pH 10 without disturbing the ME to steel surface distance. The redox competition ($\text{red}_{\text{ME}}/\text{red}_{\text{WE}}$) mode was then utilized. The ME was then held at -0.7 or -0.8 $\text{V}_{\text{Ag}/\text{AgCl}}$ with ORR as the dominant electrochemical reaction at the tip. These potentials are in the diffusion limiting regime for the ORR occurring at the ME tip, while the steel floated at the open circuit potential, thus operating in redox competition mode with respect to ORR where this reaction occurred on both electrodes.[23] ORR is the principal cathodic reaction on both the ME and the steel surface under these conditions, and is limited by the diffusion of oxygen. The hemispherical O_2 concentration field of both the ME and working electrode disk shaped surfaces must overlap. The ME senses O_2 depletion by ORR taking place on the metal if positioned within the diffusional boundary layer (less than 1000 μm). [24] The limiting current density (i_{lim}) at the 10 μm ME was typically $-4 \text{ mA}/\text{cm}^2$ at -0.7 $\text{V}_{\text{Ag}/\text{AgCl}}$ without redox competition (when positioned well above the polymer).

Line scans across the pre-charged and uncharged regions of the steel, and over the epoxy, were taken in the 5 mM NaCl + NaOH, pH 10 solution with ambient aeration and quiescent stirring in order to study the effects of hydrogen on the rate of ORR occurring at the ME tip. Line scans were utilized again due to the short length of time required -

less than 15 min per scan. The ME was scanned at a rate of 50 $\mu\text{m/s}$. The steel and ME shared a Pt counter electrode and Ag/AgCl reference electrode. The ME was held 30 or 100 μm above the steel, well within the oxygen concentration field of the steel.

4.3.5. Effect of Time: Pre and Post-Hydrogen Charging

The effect of H pre-charging and post-charging time were also evaluated. Samples of UNS S46500 were pre-charged for 24 and 48 hours at overpotentials of -200 and -800 mV (-1032 and -1632 mV_{SCE}). These samples were then removed from the electrochemical flat cell, cleaned, and measured immediately in the SECM.

To examine the effect of post-charging time, samples were pre-charged at -800 mV (-1632 mV_{SCE}), removed from the electrochemical flat cell, cleaned, and immediately measured in the SECM. Following this, two explorations post-charging times were of interest; time measured in-situ in the SECM to examine the effects of H^+ and O_2 diffusion in solution and time post-charging ex-situ (in dry lab air) to examine the effects of H diffusing in the steel and possible outgassing. For the first in-situ time effect, samples were measured with consecutive line scans over the same area during exposure to the SECM electrolyte. For the ex-situ effect, samples were immediately measured in the SECM, then removed, cleaned, and allowed to sit at room temperature in dry air for 3 days. The samples were then inserted back into the SECM and line scans of the same areas were re-measured. This was performed in both feedback diffusion ($\text{ox}_{\text{ME}}/\text{red}_{\text{WE}}$) and redox competition ($\text{red}_{\text{ME}}/\text{red}_{\text{WE}}$) modes.

4.3.6. Diffusion Calculations: H^+ , H , and O_2 in Electrolyte and UHSS

To explore the effects of $H^+_{(aq)}$, $H_{(s)}$, and $O_{2(aq)}$ diffusion on the probe tip current measured, diffusion profiles were calculated for the movement with measurement time of the analytes of interest. First, the diffusion profiles of $O_{2(aq)}$ in solution, estimated as the diffusion of oxygen in water, $D_{O_2} = 1.46 \times 10^{-5} \text{ cm}^2/\text{s}$, were calculated using the assumption for steady state diffusion from a spherical source.[25] A spherical source was selected as it could be easily calculated and adjusted for a range of radii. The source concentrations were assumed fixed and the reactions were considered to be under diffusion control. These were calculated for a Pt tip above an H pre-charged surface with tip to surface separation distances of 10,000, 5,000, 2,500, and 1,000 μm to provide a schematic of diffusion profile overlap. The profiles shown are for a 30 min diffusion time, the average time it took from introduction of electrolyte in the SECM to the initial line scan measurement in the SECM. The working distances used for actual SECM line scans were 30 and 100 μm .

A second set of diffusion calculations were carried out to determine the possible steady state transport of $H_{(s)}$ in the pre-charged material and $H^+_{(aq)}$ in the SECM measurement solution. Analytical concentration profiles of hemispherical $H^+_{(aq)}$ transport from the H pre-charged area in solution were generated using the estimation for diffusion in an infinite plane with known solid state diffusion coefficients for $H_{(s)}$ in UNS S46500 ($D_H = 6.2 \times 10^{-9} \text{ cm}^2/\text{s}$) and $H^+_{(aq)}$ in dilute aqueous solution ($D_{H^+} = 4.4 \times 10^{-5} \text{ cm}^2/\text{s}$). Diffusion times utilized were 25 h for $H_{(s)}$ in the steel and 1 h for $H^+_{(aq)}$ in solution above the pre-

charged SS to represent the concentration profiles at 1 h after insertion of the sample into the SECM.[26]

4.4. Experimental Results

4.4.1. Corrosion Electrochemistry in the SECM Measurement Environment

Results for the solution analysis experiments are plotted in Figure 122 for both the E_{OCP} vs. time and anodic polarizations of 5 mM NaCl + NaOH solutions with varying pH. For both UNS S46500 and UNS K92580, as the pH decreases, the pitting incidences increase, with increased pitting in UNS K92580. Also, as the pH decreased, the E_{OCP} increased, and the passive region became smaller. From the EIS results in Figure 123, the relationship between the solution pH and corrosion rates can be established. Oxidation current densities were determined from EIS fitting of samples pre-exposed for 1 h at E_{OCP} in 5 mM NaCl + NaOH solution pH with 5.5-10. These current densities are plotted vs. pH along with the average diffusion limiting current density for H oxidation in Figure 124. While there is no clear trend for the oxidation current density vs. pH from these EIS results, it does indicate that for 5 mM NaCl adjusted to any pH in this range, the i_{ox} is significantly lower than the diffusion limiting current density for $H_{(s)}$ oxidation when $H_{(s)}$ egresses from a pre-charged steel, suggesting that they are a suitable measurement environments for $H_{(s)}$ detection (Figure 124).

A second set of electrochemical tests were acquired to determine the effect of chloride concentration, with results in Figure 125. It can be seen clearly that as chloride concentration is decreased, corrosion rate decreases for both samples. Also, in UNS

S46500, the passive region increases as chloride concentration decreases. This aids in determination of a less severe environment for SECM measurement in terms of corrosion such that again $i_{\text{corr}} \ll i_{\text{L,Hox}}$.

Finally, the comparison of selected electrolytes representing non-corrosive environments, measurement electrolyte, high chloride exposure conditions, and acidic exposure conditions are shown in Figure 130. The non-corrosive, basic conditions exhibited high polarization resistance across all samples (Figure 130-a). The high chloride concentration test conditions showed the lowest R_P values and the acidic conditions had the second lowest, indicative of highly corrosive environments (Figure 130-c and d). The EIS results for the measurement solution had significantly higher R_P values than the corrosive environments, indicating a less corrosive environment. Also, across the various samples, the UNS S46500 samples had higher resistances, than UNS K92580, and finally UNS G10180 with the lowest resistance. EIS fitting and calculation of i_{ox} from measurements in all four solutions was carried out and plotted in Figure 131. As shown in this plot, the corrosion rate of the high Cr content UNS S46500 was lower than UNS K92580 or UNS G10180 across all environments. Also, in the environment of interest for SECM measurement, 5 mM NaCl + NaOH pH 10 solution, the i_{ox} for UNS S46500 was significantly lower than $i_{\text{L,Hox}}$, the i_{ox} for UNS K92580 was somewhat higher but still significantly lower than the $i_{\text{L,Hox}}$, and the i_{ox} for UNS G10180 was much higher than the $i_{\text{L,Hox}}$. This indicated that the likelihood of obtaining significant H measurements above the influence of the corrosion rate in the measurement solution was great for UNS S46500, a little less for UNS K92580, and fairly unlikely for UNS G10180.

4.4.2. SECM Calibration and Optimization

4.4.2.1. Without H pre-charging: Feedback and Redox Competition Modes

Initial SECM experiments were established to calibrate and verify solutions. Preliminary experiments applied feedback mode SECM for verification of redox mediator solutions. Approach curves, followed by line scans, and area scans in 5mM NaCl + 0.01 M ferrocene methanol and 0.1 M NaOH + 0.01 M ferrocene methanol are plotted in Figure 132 and Figure 133. In both cases, the Pt ME tip was held at +0.4 V_{Ag/AgCl} such that the oxidation of FcMeOH ($\text{Fe}^{+2} \rightarrow \text{Fe}^{+3} + \text{e}^-$) occurred at the tip (Table 27). Both line scans exhibited diffusion controlled behavior for the $\text{Fe}^{+2} \rightarrow \text{Fe}^{+3} + \text{e}^-$ reaction, in that the current decreased at the probe tip as the ME approached the surface (Figure 132-a and b), but at a much larger reduction current range for the chloride solution. Lines scans for the raw current measurement and normalized current ($i_{\text{tip}}/i_{\infty}$) are plotted in Figure 132-c and d. Again, the magnitude of the current is much higher for the scan in the chloride containing solution. When normalized, the difference in current between the Au and epoxy region is fairly similar for both cases. In area scan of the same Au to epoxy area in each solution, the chloride containing solution exhibited better definition between regions (Figure 133). The scan taken in 0.1 M NaOH + 0.01 M ferrocene methanol solution did not display any significant difference between the Au region and epoxy, and furthermore it exhibited a degradation in the solution as the current measured at the tip decreased with time.

Further exploration of these solutions was carried out above uncharged, unexposed samples of UNS S46500 As Annealed/CT samples. Area scans from steel to epoxy were

taken in 5 mM NaCl + 0.01 M ferrocene methanol at +0.4 $V_{Ag/AgCl}$ and 30 μm , in 0.1 M NaOH solution at -0.8 $V_{Ag/AgCl}$ and 30 μm , 5 mM NaCl + NaOH pH 10 solution at -0.6 $V_{Ag/AgCl}$ and 30 μm , and 5 mM NaCl + NaOH pH 10 solution at -0.8 $V_{Ag/AgCl}$ and 100 μm are plotted in Figure 134. Again, the chloride containing solutions displayed stronger trends with increased current density differences between the steel and epoxy regions at the 30 μm tip to sample distance in Figure 135. In diffusion feedback mode this could be due to enhanced corrosion at the surface in the chloride containing solution ($Fe \rightarrow Fe^{+2} + 2e^-$), thus increasing the local Fe^{+2} concentration, and subsequently increasing the ME tip current. Tip height was further examined in the 5 mM NaCl + NaOH pH 10 solution at a potential applied at the tip of -0.8 $V_{Ag/AgCl}$. Scans from steel to epoxy at tip to sample heights of 100, 80, 50, and 30 μm are plotted in Figure 136-b. An optimal tip height of 30 μm was selected for use, as it showed the highest difference in current densities measured between the two regions. Shorter tip to sample distances were not applied, as in the current setup, issues with sample tilt and height could cause inadvertent tip contact with the electrodes.

4.4.2.2. Establishment of Effect of H Pre-Charging on SECM ME Signals

Line scans of electrochemically pre-charged samples for varied pre-charging overpotentials were acquired in three solutions, 5 mM NaCl + 0.01 M ferrocene methanol in feedback diffusion mode with the reaction at the ME tip of $FcMeOH^+_{(aq)} + e^- \rightleftharpoons FcMeOH_{(aq)}$ and 0.1 M NaOH and 5 mM NaCl + NaOH pH 10 in redox competition with the reaction at the ME tip of $O_2 + 2H_2O + 4e^- \rightleftharpoons 4OH^-$. A distinct difference in the ME tip current measured above epoxy, uncharged steel, and pre-charged steel can be

seen in all solutions (Figure 137-Figure 139). Scans for feedback diffusion mode ($i_{OX,ME}/i_{red,WE}$) in 5 mM NaCl + 0.1 M ferrocene methanol are plotted in Figure 137, where a decrease in the normalized probe tip current is seen above pre-charged areas of the sample. There is not a significant difference in the normalized current for samples pre-charged at hydrogen overpotentials of -200 and -400 mV (-1032 and -1232 mV_{SCE}), but it is significantly larger for samples pre-charged at -800 mV (-1632 mV_{SCE}). This decrease in ME tip current may be indicative of the influence of H concentrations and egress. Above a pre-charged region, as H desorbs from the material, the reduction of Fe⁺² to Fe⁰ could occur as the potential at the hydrogen charged surface is decreased by the H concentration. This effect will be discussed in detail later.

Line scans of redox competition mode ($i_{red,ME}/i_{red,WE}$) were taken on UNS S64500 and UNS K92580 in both 0.1 M NaOH and 5 mM NaCl + NaOH pH 10, pre-charged for 24 h at $\eta_H = -800$ mV (-1632 mV_{SCE}) and are plotted in Figure 138 and 23. Similar to samples tested in diffusion feedback mode, a change in $i_{ORR,ME}$ is seen from the epoxy to uncharged to pre-charged regions of the sample. As hydrogen desorbs from the material, it couples with and accelerates the ORR at the surface of the sample, thus depleting the O₂ from the solution above the pre-charged steel. As the ME tip scans through these areas the ORR reaction at the probe tip is further diffusion limited, and the $i_{ORR,ME}$ decreases. This is shown for both materials in both solutions, however, for UNS K92580, a more distinct difference from pre-charged to uncharged steel was established in the 0.1 M NaOH solution. This could be due to the interference of a corrosion current in the 5 mM NaCl + NaOH solution, as UNS K92580 is more susceptible to corrosion than UNS

S46500. Examinations of various pre-charging potentials were explored to examine possible effects of H concentrations on the $i_{\text{ORR,ME}}$. Line scans of samples pre-charged for 24 h at $\eta_{\text{H}} = -200, -400, -600, \text{ and } -800 \text{ mV}$ ($-1032, -1232, -1432, \text{ and } -1632 \text{ mV}_{\text{SCE}}$) and measured in both 0.1 M NaOH and 5 mM NaCl + NaOH pH 10 are plotted in Figure 140. In general, the decrease in normalized $i_{\text{ORR,ME}}$ scaled with increased $C_{\text{H,diff}}$. However, this was not as strong of a trend as seen between pre-charged H concentrations and measurements of the SKP potential in Ch. 3. In the SECM solution, issues with diffusion of both O_2 and H^+ in solution and stirring from movement of the probe tip may arise that effect the $i_{\text{ORR,ME}}$. Also, as can be seen in Figure 140 a and b, selection of electrolyte can also effect the $i_{\text{ORR,ME}}$. Scans taken in the 5 mM NaCl + NaOH pH 10 solution displayed a much stronger definition of $i_{\text{ORR,ME}}$ differences between the uncharged and pre-charged regions of the steel than the scans taken in 0.1 M NaOH solution.

These line scan measurements of normalized SECM ME $i_{\text{ORR,ME}}$ vs. the pre-charging overpotential can be combined with the electrochemical extraction measurements of $C_{\text{H,diff}}$ vs. pre-charging overpotential to develop a calibration curve for the effect of dissolved H on the SECM $i_{\text{ORR,ME}}$ (Figure 141). As $C_{\text{H,diff}}$ increases, the SECM $i_{\text{ORR,ME}}$ decreases. However, as shown in the calibration curves, this relationship of probe tip current to $C_{\text{H,diff}}$ is affected by measurement solution, Figure 141-a, and material type, in Figure 141-b (as in the SKP). This again highlights that these measurements are unique functions of the material type, based on corrosion rate, $D_{\text{H,eff}}$, and hydrogen trap capacity. However, in the SECM, conditions of the measurement environment and effect on

$i_{\text{ORR,ME}}$, further effect these calibration curves as they can effect both the corrosion rates at the sample surface and the diffusion of species in the electrolyte.

4.4.2.3. Effect of Time: Pre and Post-Hydrogen Charging

Experiments showing the effect of pre-charging time can be seen in Figure 142. Samples were pre-charged at both a low overpotential of $\eta_{\text{H}} = -200 \text{ mV}$ ($-1032 \text{ mV}_{\text{SCE}}$) (Figure 142-a) and a high overpotential of $\eta_{\text{H}} = -800 \text{ mV}$ ($-1632 \text{ mV}_{\text{SCE}}$) (Figure 142-b) for 24 and 48 hours. A large difference is measured for the normalized $i_{\text{ORR,ME}}$ above the sample pre-charged at -200 mV , whereas a much smaller change was seen above the sample pre-charged at -800 mV . This could be explained through the influence of $\frac{\partial C}{\partial x}$, where the sample pre-charged at -800 mV had a significantly large $\frac{\partial C}{\partial x}$ in both cases due to the high pre-charged H concentration which affects $\frac{\partial C}{\partial x}$. The sample pre-charged at -200 mV may have had an initially high $\frac{\partial C}{\partial x}$ but it decreases fairly quickly as the smaller initial concentration of hydrogen desorbed. However, pre-charging for a longer time allowed the H concentration to penetrate deeper into the sample and therefore it would take longer to desorb. This would allow for a larger $\frac{\partial C}{\partial x}$ and therefore a larger $i_{\text{L,H,ox}}$ at the measurement time in the SECM which could more strongly influence the $i_{\text{ORR,ME}}$ at the probe tip.

A second set of samples were explored to examine the effect of time and H desorption post-hydrogen charging. These were examined both ex-situ (Figure 143 and 144) and in-situ (Figure 145) in the SECM. For ex-situ samples, this was explored in both 5 mM

NaCl + 0.01 M ferrocene methanol and 5mM NaCl + NaOH pH 10 solution. A similar effect was seen in both cases, where the ME tip current that was initially low above the pre-charged region for the 30 min measurement, increased back to near the initial current value measured across the uncharged region after 72 hours post-charging. In feedback diffusion mode, a rise in the SECM ME tip current with time across the pre-charged area is indicative of the H desorption with time from the material. As there is less H oxidation at the sample surface, the possibility of the coupled reaction $\text{Fe}^{+2} + 2\text{e}^- \rightarrow \text{Fe}^0$ decreases, and the effect on the ME tip current is less, therefore the current rises. For redox competition mode, a rise in the SECM $i_{\text{ORR,ME}}$ with time across the pre-charged area is indicative of the H desorption with time from the material. There is less H oxidation at the pre-charged surface and therefore less O_2 depletion from the solution.

In the in-situ study of time post-charging, line scans are shown in Figure 145 of UNS S46500 pre-charged for 24 at an η_{H} of -800 mV (-1632 mV_{SCE}). The change in current with time at the probe tip is in part affected by the hydrogen desorption over time. However, these effects are exacerbated by the mixing of solution from tip movement above the steel disk. The line scans in Figure 145 display the effects of oxygen concentration gradients, H^+ desorption, H diffusion, and mixing due to the tip movement. This readily detectable temporal evolution is also emphasized as an indication of the ability of the SECM to provide quantification of H-effects in metals more generally.

4.4.3. Diffusion Calculations: H^+ , H, and O_2 in Electrolyte and UHSS

Diffusion calculations were performed to explore the diffusion and depletion profiles of O_2 in the solutions near the probe tip and sample surface. As mentioned ORR is the principal cathodic reaction on both the ME and the steel surface under the conditions tested in the SECM, and is limited by the diffusion of oxygen. Significant measurements of changes in $i_{ORR,ME}$ in redox competition mode (red_{ME}/red_{WE}) are due to the overlap of the diffusion profiles, such that the probe tip current competes for the same analyte as the sample surface. The analytical concentration profile of O_2 depletion as the SECM ME tip approaches the steel surface (with dissolved H) is plotted in Figure 146. The oxygen concentration fields display that the effects of both surfaces interact across distances as large as 1000 μm . Since the depletion profile extends into solution, the ME detects a “shoulder” on the hydrogen pre-charged sample that is extensive.

A second set of diffusion calculations were carried out to explore the effects of in-situ measurement in the SECM post-hydrogen charging time. While the SECM has been shown capable of mapping H pre-charged vs uncharged areas, the regions of normalized $i_{ORR,ME}$ between zones are sloped rather than sharp. These variations in $i_{ORR,ME}$ outside of the pre-charged disk diameter arise from three primary effects. The pre-charged area consumes oxygen heavily, which establishes an oxygen concentration gradient in the solution. The ME detects this O_2 concentration gradient extending from the epoxy to pre-charged area giving rise to the sloped current profile. The other effects are due to the oxygen being consumed by H which internally diffuses into the uncharged regions of the steel and by desorbed oxidized H^+ diffusing in solution above the uncharged areas. The diffusivity of H^+ is orders of magnitude faster in aqueous solutions than in the SS: 4.4 x

$10^{-5} \text{ cm}^2/\text{s}$ in solution compared to $6.2 \times 10^{-9} \text{ cm}^2/\text{s}$ for solid state transport of H in UNS S46500.[27] Thus, protons can contribute to ORR even above the uncharged areas. These effects can be exacerbated due to the mixing of solution from tip movement above the steel disk. In Figure 145 successive line scans taken 60 min after pre-charging exposure display the effects of oxygen concentration gradients, H^+ desorption, H diffusion, and mixing due to the tip movement. While H^+ only desorbs from the pre-charged area of the steel, Figure 147 displays a schematic of how H^+ diffuses in solution from the H pre-charged surface during the 60 – 75 min post-charging period. It also illustrates effects of lateral H diffusion within the stainless steel during the 24 h pre-charging and post-charging periods.

4.5. Discussion

4.5.1. Origins of the H effect on the SECM tip current

4.5.1.1. Feedback Diffusion

The normalized ME tip current above the insulating epoxy in feedback diffusion mode ($i_{\text{ox,ME/red,WE}}$) tend towards 1 as it is limited by diffusion of the FcMeOH to the probe tip as reduction reactions are not supported above the non-reactive epoxy. Above the uncharged regions of the steel, during corrosion of the steel $\text{Fe} \rightarrow \text{Fe}^{+2} + 2\text{e}^-$ occurs at the surface and the ME tip current is seen to increase as there is a higher concentration of Fe^{2+} in this region for further oxidation to occur at the ME tip. However, above a pre-charged region of the steel, the ME tip current decreases. This could be indicative of the influence of H concentrations on the probe tip current. As H desorbs from the pre-charged region and H oxidation occurs at the surface ($\text{H} \rightarrow \text{H}^+ + \text{e}^-$), the reduction of

$\text{Fe}^{+2} + 2\text{e}^- \rightarrow \text{Fe}^0$ could occur as the potential at the surface is affected by the H concentration and the associated apparent fugacity, as shown in Ch. 3 through the following relationship.

$$f_{\text{H}_2} = 10^{-\eta_{\text{H}}/0.0295} \quad \text{Equation 79}$$

Where η_{H} is the hydrogen overpotential. As H increases, the overpotential decreases, and thus the mixed potential measured at the surface decreases. As this potential decreases, the activation of the Fe^{+2} to Fe^0 is possible, as can be seen from the Pourbaix diagrams in Figure 149. The current at the ME tip would be expected to increase over time as the H desorbs from the material and corrosion dominates the surface reactions rather than H oxidation at the surface of the sample. An example of this can be seen in Figure 143.

4.5.1.2. Redox Competition

The normalized ME current ($i_{\text{ORR,ME}}$) measured above the epoxy in redox competition mode, Figure 148-b, tends towards a value of -1 as the surface does not support ORR and thus the current is limited only by close approach of the epoxy and limited diffusional access of O_2 to the ME. Above the uncharged area, O_2 is consumed both at the cathodically polarized ME and the freely corroding steel surface by ORR, Equation 80. Above the pre-charged area ORR is coupled with H oxidation, Equation 81, in addition to steel corrosion:



The $i_{ORR,ME}$ decreases above the uncharged area of the steel in proportion to the metal dissolution rate since $i_{c,ORR}$ (the cathodic reaction current density on the steel) = i_{corr} (the corrosion current density of the steel) = i_{pass} (the passive current density) of about 1-2 $\mu A/cm^2$. Above the hydrogen pre-charged area, $i_{ORR,ME}$ further decreases as the rate of the O_2/H redox couple (on the steel), given by Equations 80 and 81, exceeds $i_{c,ORR}$. The $i_{ORR,H}$ (the current density of the redox couple on the steel) is proportional to the limiting hydrogen oxidation current, $i_L^{H^+}$, in the pre-charged region, which can be calculated to be 70 $\mu A/cm^2$ for a $C_{H,diff}$ of 15 wppm and a solid state diffusion length of $10^{-3}cm$ based on a 1 h diffusion time. $i_L^{H^+}$ is much greater than i_{pass} of the steel (at 1-2 $\mu A/cm^2$), resulting in a much higher oxygen consumption by Equation 82 in the pre-charged area when compared to the uncharged area. Desorbed protons (H^+) from Equation 81 can participate in Equation 82 [28] which is again coupled to Equation 80 and steel corrosion resulting in further decrease of $i_{ORR,ME}$.



Diffusion of the H^+ through the oxide film can be ignored, as the film is thin (less than 2-3 nm) and does not control diffusion based egress.[29]

4.5.1.3. Electrochemical Factors

The basis for SECM measurements in redox competition mode is similar to that of the SKP, the establishment of the H electrode at the surface. Again, as long as the corrosion rate, i_{corr} , at the surface is sufficiently lower than the limiting H oxidation current, the $i_{\text{L,Hox}}$ at the surface will be coupled to the hydrogen oxidation rate, and therefore dependent on the H concentration. This highlights again, the significance of time in hydrogen measurements. As time increases, due to C_{H} egress, the $\frac{\partial C}{\partial x}$ will decrease and thus the $i_{\text{L,Hox}}$ decreases. As $i_{\text{L,Hox}}$ decreases, the corrosion rate of the material can influence the ORR current density established as it becomes the more dominant reaction. In the SECM, it takes significantly longer to initiate a measurement due to instrument design and setup, 30 min in the SECM vs. 5 min in the SKP. Therefore, initial $i_{\text{L,Hox}}$ values are much lower than those in the SKP, and the sensitivity of SECM measurements to corrosion is much higher.

4.5.1.4. Mixed Potential Theory

A further explanation of the SECM $i_{\text{ORR,ME}}$ on H concentration can be established through mixed potential theory associated with the hydrogen “electrode” behavior of the pre-charged steel. For these diagrams, the same equations as applied in Ch. 3 were used. However, as the SECM measurements occur in full immersion, rather than a thin film environment, and the diffusion limiting current density for ORR is different. As the diffusion of O_2 is limited by the double layer in full immersion rather than the thickness of the thin film, the following assumptions were made:

$$i_{\text{L,orr}} = \frac{nFD_{\text{O}_2}C_{\text{O}_2}}{\sqrt{D_{\text{O}_2}t}} \quad \text{Equation 83}$$

Where, n is the number of e^- involved in the reaction, F is Faraday's constant, D_{O_2} is the diffusion coefficient of O_2 in solution of $1.46 \times 10^{-5} \text{ cm}^2/\text{s}$ [30], C_{O_2} is the concentration of O_2 in solution taken as $2.06 \times 10^{-7} \text{ mol/cm}^3$, and t is time in s. For calculations of the diffusion limiting ORR current in the SECM, the time was assumed to be 60 min, as the line scan and area measurements were taken starting at 30 min, but measurement times were often much longer, 15 min to hours (for area scans). The pH was alkaline for SECM measurements as the solution was adjusted to a pH of 10.

For the hydrogen oxidation current calculations, two were made, the first for $H \rightarrow H^+ + e^-$ and the second for $H_2 \rightarrow 2H^+ + 2e^-$. Again, the equations applied for H oxidation were the same as those used for mixed potential calculations in Ch. 3. However, limiting current densities calculated from $\frac{\partial C}{\partial x}$ were calculated at times of 60 min for the SECM.

Calculated currents densities were again compared to measured anodic polarization curves of the three alloys in naturally aerated 5 mM NaCl adjusted to a pH of 10 with NaOH in Evans diagrams (Figure 150 to Figure 153). From these plots it can be seen that the effect seen on $i_{ORR,ME}$ due to the establishment of the H electrode at the surface of the sample is possible for UNS S46500 and UNS K92580. However, for UNS G10180, the H oxidation limiting current densities are much lower than the limiting current density for ORR for Evans diagram calculations made during the SECM measurement time. This suggests that the corrosion at the surface of UNS G10180 would dominate the ORR current density at the surface and the measurement at the probe tip would not be representative of local hydrogen concentrations.

4.5.2. Limitations of H detection in the SECM

While the SECM has been shown a viable method for localized H detection, in the current setup, a range of factors influence the applicability of this technique for a broader range of H measurements. As with the SKP, the primary concern is the range and types of materials for which this technique is viable. As the SECM measurements take a longer time in general than the SKP and involve full immersion of the sample in a measurement electrolyte, the $D_{H,eff}$, trap capacity, and corrosion susceptibility become even more important for achieving significant H measurements. Further exploration into other electrolytes that establish less severe corrosion conditions would be advantageous. Also, the possibility of using liquids, such that diffusion rates of O_2 and or H^+ were lowered in solution may be advantageous as they could prolong the possible measurement time and aid in resolution above the sample. Other limitations of the current setup include the approach of the tip to the sample. As the leveling of the sample and flush mounting of the SECM ME tip are performed manually, insufficient planar setups may result from user error. If this could be achieved in a mechanized way, possible tip to sample distances could be achieved at less than 30 μm and may aid in resolution issues due to diffusion of O_2 and H^+ in solution.

4.6. Future Work

The SECM has been shown a viable tool for H detection, however as this is a novel technique, there exists a wide variety of areas through which H detection could be improved. As mentioned, SECM measurement electrolyte can greatly influence the

reactions studied, but also can create possible interference to the reactions of interest, as in the case of corrosion initiation and high corrosion rates. Possible application of electrolytes that exhibit less severe corrosion environments such as NaOH in the case of steel, could aid in the detection of H concentrations over corrosion reactions occurring at the surface. This could also assist in the expansion of this technique for the exploration of various alloys. However, difficulties arise as different alloys are susceptible to different environments, thus making it challenging to determine one electrolyte for H measurement across a large range of materials.

Also, similar to the SKP, the SECM has the capability to be utilized at a much smaller length scale. SECM tips can be applied at the AFM scale, it may be possible to scale this technique at the nm rather than μm length scale. However, resolution issues due to diffusion in solution as well as mixing from tip movement would still apply, therefore nm scale resolution may not be attainable.

4.7. Conclusions

- The SECM was shown to provide a novel method for spatial detection of near surface hydrogen concentrations across bare ferrous alloy surfaces.
- The influence of a pre-dissolved concentration of hydrogen on the measured probe tip current was established using ORR as the reaction occurring at the ME tip.
 - This is due to the enhancement of the ORR reaction above pre-charged areas as H desorbs from the sample. As long as the hydrogen oxidation

current is significantly greater than the corrosion current, the $i_{\text{ORR,ME}}$ will reflect the influence of the pre-charged H concentration on ORR at the sample surface. Pre-charged H concentrations, time post-charging, corrosion rates of the samples in the measurement electrolyte, and diffusion coefficients of the samples all effect this.

- Effects of proton desorption from the steel and diffusion in solution combined with radial transport of atomic hydrogen in the metal were readily detected. Diffusion of O_2 and H^+ in solution may be greater limiting factors to resolution than probe tip diameters and sample to tip distances in the SECM.

4.8. References

1. Modiano, S., et al., *Changes on iron electrode surface during hydrogen permeation in borate buffer solution*. *Electrochimica Acta*, 2008. **53**(10): p. 3670-3679.
2. Fushimi, K., T. Yamamuro, and M. Seo, *Hydrogen generation from a single crystal magnetite coupled galvanically with a carbon steel in sulfate solution*. *Corrosion Science*, 2002. **44**(3): p. 611-623.
3. Bard, A.J., et al., *Scanning Electrochemical Microscopy - a New Technique for the Characterization and Modification of Surfaces*. *Accounts of Chemical Research*, 1990. **23**(11): p. 357-363.
4. Bard, A.J. and M.V. Mirkin, *Scanning electrochemical microscopy*. 2nd ed. 2012, Boca Raton, Fla.: CRC Press. x, 660 p.
5. Yin, Y.H., et al., *In situ characterization of localized corrosion of stainless steel by scanning electrochemical microscope*. *Applied Surface Science*, 2009. **255**(22): p. 9193-9199.
6. Eckhard, K., et al., *Redox competition mode of scanning electrochemical microscopy (RC-SECM) for visualisation of local catalytic activity*. *Physical Chemistry Chemical Physics*, 2006. **8**(45): p. 5359-5365.
7. Santana, J.J., et al., *Visualization of local degradation processes in coated metals by means of scanning electrochemical microscopy in the redox competition mode*. *Electrochimica Acta*, 2010. **55**(15): p. 4488-4494.
8. Bard, A.J., et al., *Chemical Imaging of Surfaces with the Scanning Electrochemical Microscope*. *Science*, 1991. **254**(5028): p. 68-74.
9. Bastos, A.C., et al., *Imaging concentration profiles of redox-active species in open-circuit corrosion processes with the scanning electrochemical microscope*. *Electrochemistry Communications*, 2004. **6**(11): p. 1212-1215.
10. Wipf, D.O., *Initiation and Study of Localized Corrosion by Scanning Electrochemical Microscopy*. *Colloids and Surfaces a-Physicochemical and Engineering Aspects*, 1994. **93**: p. 251-261.
11. Zhu, Y.Y. and D.E. Williams, *Scanning electrochemical microscopic observation of a precursor state to pitting corrosion of stainless steel*. *Journal of the Electrochemical Society*, 1997. **144**(3): p. L43-L45.
12. Gonzalez-Garcia, Y., et al., *Imaging metastable pits on austenitic stainless steel in situ at the open-circuit corrosion potential*. *Electrochemistry Communications*, 2004. **6**(7): p. 637-642.
13. Izquierdo, J., et al., *Imaging Local Surface Reactivity on Stainless Steels 304 and 316 in Acid Chloride Solution using Scanning Electrochemical Microscopy and the Scanning Vibrating Electrode Technique*. *Electrochimica Acta*, 2014. **134**: p. 167-175.
14. Paik, C.H., et al., *Scanning electrochemical microscopy detection of dissolved sulfur species at inclusions in stainless steel and nickel*. *Localized in-Situ Methods for Investigating Electrochemical Interfaces*, 2000. **99**(28): p. 122-130.
15. Paik, C.H., H.S. White, and R.C. Alkire, *Scanning electrochemical microscopy detection of dissolved sulfur species from inclusions in stainless steel*. *Journal of the Electrochemical Society*, 2000. **147**(11): p. 4120-4124.
16. Salleh, S.H., et al., *Enhanced hydrogen evolution on Mg (OH)(2) covered Mg surfaces*. *Electrochimica Acta*, 2015. **161**: p. 144-152.
17. Tefashe, U.M., et al., *Local flux of hydrogen from magnesium alloy corrosion investigated by scanning electrochemical microscopy*. *Journal of Electroanalytical Chemistry*, 2014. **720**: p. 121-127.
18. Yuan, Y.A., et al., *Study of the effects of hydrogen on the pitting processes of X70 carbon steel with SECM*. *Electrochemistry Communications*, 2010. **12**(12): p. 1804-1807.

19. Thomas, R.L.S., et al., *Trap-governed hydrogen diffusivity and uptake capacity in ultrahigh-strength AERMET 100 steel*. Metallurgical and Materials Transactions a-Physical Metallurgy and Materials Science, 2002. **33**(7): p. 1991-2004.
20. Pourbaix, M., *Atlas of electrochemical equilibria in aqueous solutions*. 2d English ed. 1974, Houston, Tex.: National Association of Corrosion Engineers. 644 p.
21. DeLuccia, J.J. and D.A. Berman, *An Electrochemical Technique to Measure Diffusible Hydrogen in Metals (Barnacle Electrode)*, in *Electrochemical Corrosion Testing*, A.S.T.M., Editor. 1981, ASTM International: West Conshohocken, PA. p. 256-273.
22. Kehler, B.A., *Modeling and Experiments to Explain the Potential Dependency of an UHSS to Hydrogen Environment Assisted Cracking*, in *Materials Science and Engineering*. 2008, University of Virginia: Charlottesville. p. 296.
23. Souto, R.M., Y. Gonzalez-Garcia, and S. Gonzalez, *In situ monitoring of electroactive species by using the scanning electrochemical microscope. Application to the investigation of degradation processes at defective coated metals*. Corrosion Science, 2005. **47**(12): p. 3312-3323.
24. Thomas, S., et al., *Oxygen consumption upon electrochemically polarised zinc*. Journal of Applied Electrochemistry, 2014. **44**(6): p. 747-757.
25. Crank, J., *The mathematics of diffusion*. 2d ed. 1975, Oxford, Eng: Clarendon Press. viii, 414 p.
26. Schaller, R.F., et al., *Spatially resolved mapping of the relative concentration of dissolved hydrogen using the scanning electrochemical microscope*. Electrochemistry Communications, 2015. **51**: p. 54-58.
27. Hayduk, W. and H. Laudie, *Prediction of Diffusion-Coefficients for Nonelectrolytes in Dilute Aqueous-Solutions*. AIChE Journal, 1974. **20**(3): p. 611-615.
28. Gottesfeld, S. and T.A. Zawodzinski, *Polymer electrolyte fuel cells*. Advances in electrochemical science and engineering, 1997. **5**: p. 195-302.
29. Scully, J.R., et al., *The Influence of Palladium on the Hydrogen-Assisted Cracking Resistance of PH-13-8 Mo Stainless-Steel*. Metallurgical Transactions a-Physical Metallurgy and Materials Science, 1991. **22**(10): p. 2429-2444.
30. Gubbins, K.E. and R.D. Walker, *The solubility and diffusivity of oxygen in electrolytic solutions*. Journal of Electrochemical Society, 1965. **112**(5): p. 469-471.
31. *Alloy Data - Custom 465 All*. 1996, C.T. Corporation: Reading, PA.
32. Neufeld, A.K. and A.P. O'Mullane, *Effect of the mediator in feedback mode-based SECM interrogation of indium tin-oxide and boron-doped diamond electrodes*. Journal of Solid State Electrochemistry, 2006. **10**(10): p. 808-816.
33. Souto, R.M., L. Fernandez-Merida, and S. Gonzalez, *SECM Imaging of Interfacial Processes in Defective Organic Coatings Applied on Metallic Substrates Using Oxygen as Redox Mediator*. Electroanalysis, 2009. **21**(24): p. 2640-2646.
34. Bard, A.J. and M.V. Mirkin, *Scanning Electrochemical Microscopy*. 2001: Taylor & Francis.
35. Pourbaix, M., *Atlas of electrochemical equilibria in aqueous solutions*. 1974, Houston, TX: National Association of Corrosion Engineers.

4.9. Tables:

Table 25. UNS K92580 and UNS S46500 Composition (wt. %).[31]

Material	Fe	C	Mn	Si	P	S	Cr	Ni	Mo	N	Ti	Co
UNS K92580 ^a	Bal.	0.23	0.019	-	-	0.0008	2.78	10.89	1.21	-	-	12.8
UNS S46500 ^b	Bal.	0.005	0.02	0.02	0.002	0.002	11.50	11.04	0.94	0.002	1.54	-

^aAerMet 100™ peak-aged obtained through Carpenter Technology

^bCustom 465™ H900 temper

Table 26. UNS K92580 and UNS S46500 Material Properties.[31]

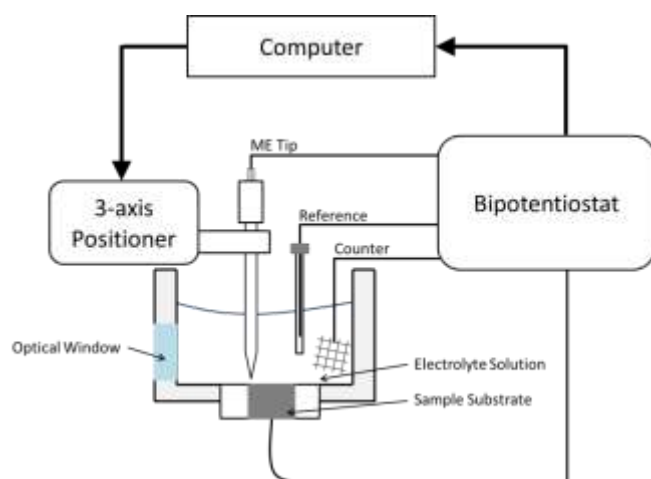
Temper	Yield Strength	Tensile Strength	Elongation	Reduction of Area	Rockwell Hardness C
UNS K92580 peak aged	1724 MPa	1965 MPa	14 %	65 %	54
UNS S46500 Annealed/CT	772 MPa	951 MPa	20 %	75 %	29.5
UNS S46500 H900	1703 MPa	1779 MPa	14 %	51 %	51

Table 27. List of Mediators and Non-Mediator Solutions and Reactions Obtained at the SECM ME Tip.[9, 15-17, 32, 33]

Mediator (Feedback Mode)	Reaction at Tip	Potential (V_{Ag/AgCl})
Ferrocene methanol (in water)	$FcMeOH^+_{(aq)} + e^- \rightleftharpoons FcMeOH_{(aq)}$ $(Fe^{3+} + e^- \rightleftharpoons Fe^{2+})$	+0.5
Potassium ferricyanide (in water)	$Fe(CN)_6^{4-} \rightleftharpoons Fe(CN)_6^{3-}_{(aq)} + e^-$ $(Fe^{2+} \rightleftharpoons Fe^{3+} + e^-)$	-0.381
Hexaamineruthenium (III) Chloride (in water)	$Ru(NH_3)_6^{2+}_{(aq)} \rightleftharpoons Ru(NH_3)_6^{3+}_{(aq)} + e^-$	-0.5
Potassium hexacyanoruthenate (II) Hydrate (in water)	$Ru(CN)_6^{3-}_{(aq)} + e^- \rightleftharpoons Ru(CN)_6^{4-}_{(aq)}$	+0.638
Potassium iodide (0.1 M NaCl + 10 mM KI solution)	$3I^- \rightleftharpoons I_3^- + 2e^-$	+0.6
Sodium chloride (0.1 – 0.6 M solution)	$H_2 \rightleftharpoons 2H^+ + 2e^-$	-0.05
Non-Mediator (Redox Competition Mode)	Reaction at Tip	Potential (V_{Ag/AgCl})
5 mM NaCl + NaOH pH 10 (aerated O ₂)	$O_2 + 2H_2O + 4e^- \rightleftharpoons 4OH^-$	-0.6 to -0.8 (applied in the literature)
0.1 M NaCl (corroding Fe electrode)	$Fe^{2+} \rightleftharpoons Fe^{3+} + e^-$	+0.6

4.10. Figures:

a)



b)

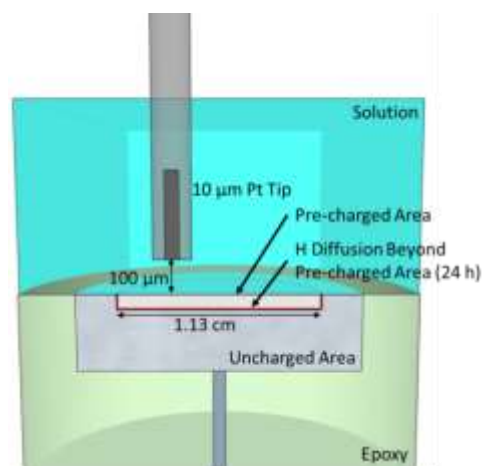


Figure 117. Schematic of a) SECM redrawn from Bard[34] and b) cell setup.

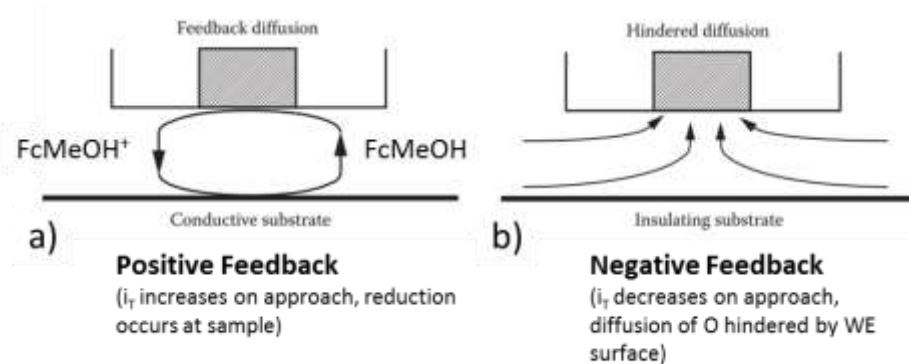


Figure 118. Schematic of SECM ME tip approaching substrate surface of a conductor vs. insulator displaying a) positive vs. b) negative feedback. [34]

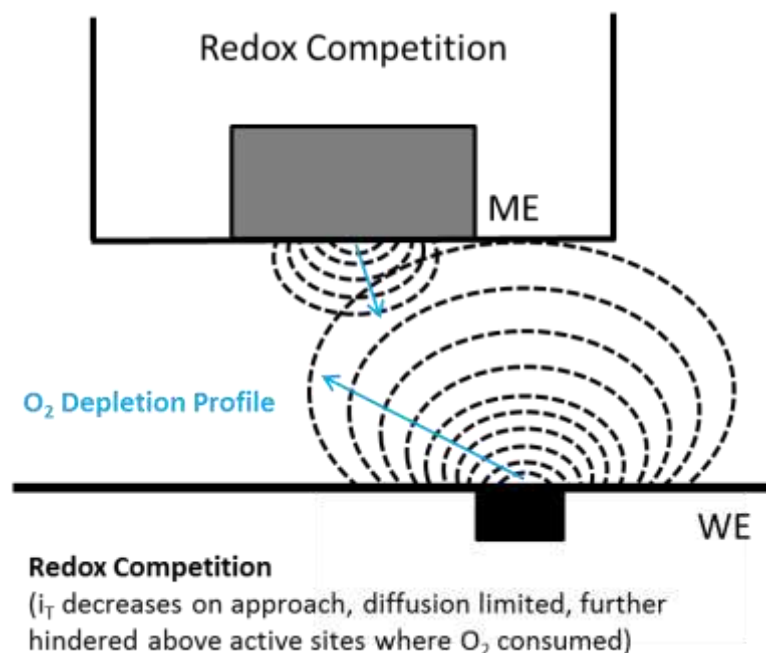


Figure 119. Schematic of redox competition mode with ORR as the dominant reaction occurring at the ME ($\text{ORR}_{\text{ME}}/\text{ORR}_{\text{WE}}$). Schematic depletion profiles of O₂ due to ORR are drawn for the oxygen in solution at the tip and at an active catalytic site for ORR on the surface. Each dotted line represents an iso-concentration line.

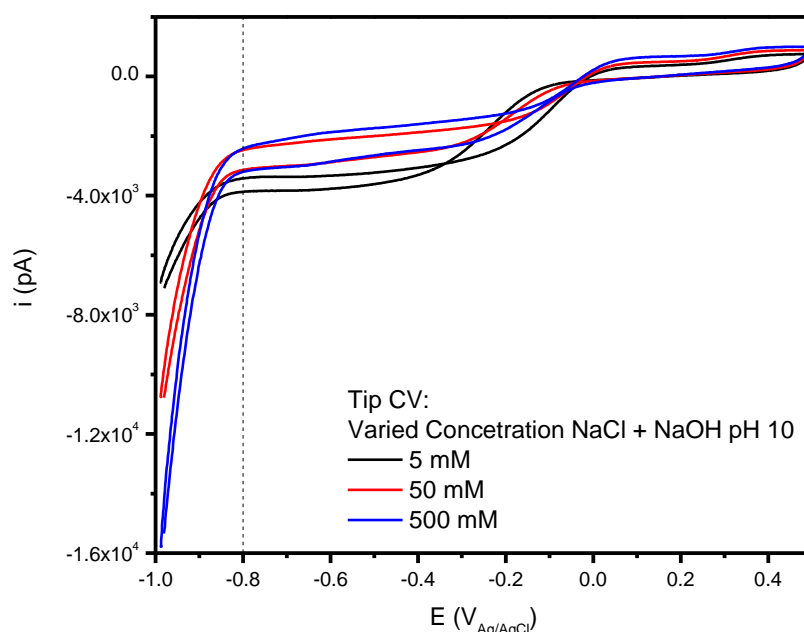


Figure 120. Variation of salt concentration, 5, 50, and 500 mM NaCl adjusted with NaOH to a pH of 10, for solution characterization. CV on Pt ME tip. CV scanned from -1.0 to 0.5 V_{SCE} at a scan rate of 100 mV/s. The voltage of -0.8 $V_{Ag/AgCl}$ is noted as it was selected as the voltage to apply to the ME tip to induce ORR at the tip.

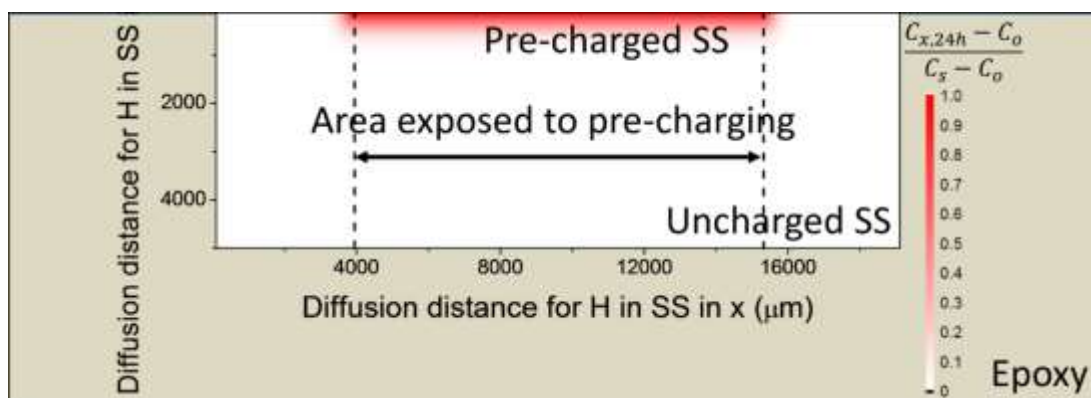


Figure 121. Schematic of steady state H diffusion in steel during cathodic pre-charging with the red region denoting H_{abs} . Diffusion profiles were estimated by steady state spherical diffusion with a $D_{H,eff} = 3.5 \times 10^{-9} \text{ cm}^2/\text{s}$.

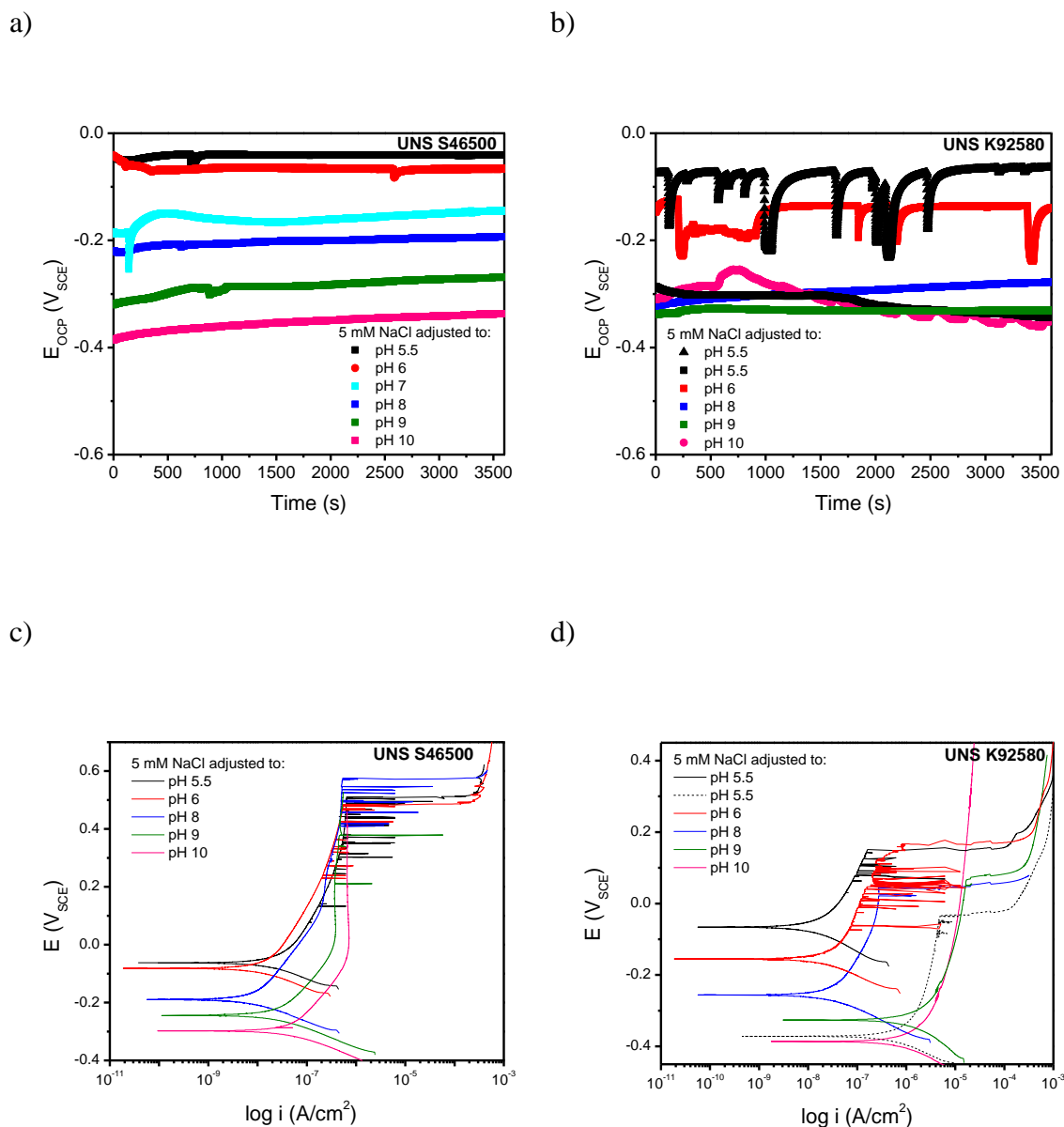
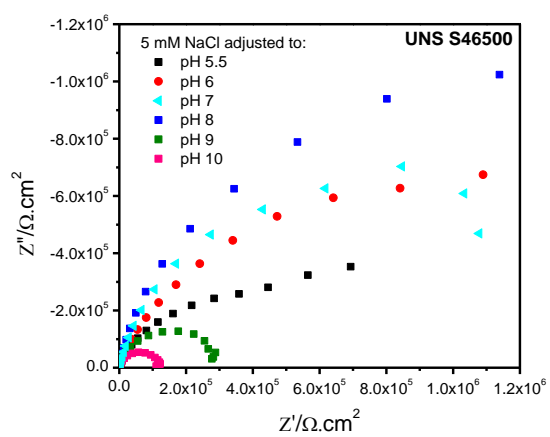
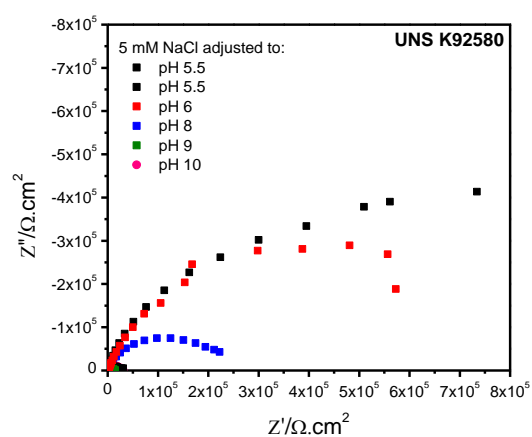


Figure 122. One hour E_{OCP} of a) UNS S46500 H900 and b) peak-aged UNS K92580 in 5 mM NaCl + NaOH pH 5.5 - 10 and post EIS (shown in Figure 123) anodic polarizations were acquired from -100 mV below E_{OCP} to 1 V vs E_{OCP} at a scan rate of 0.1667 mV/s in the same solution, c) UNS S46500 and d) UNS K92580. No intentional cathodic charging was applied prior to anodic polarization scans.

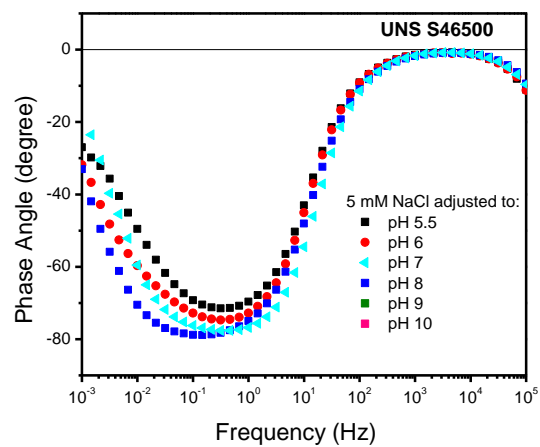
a)



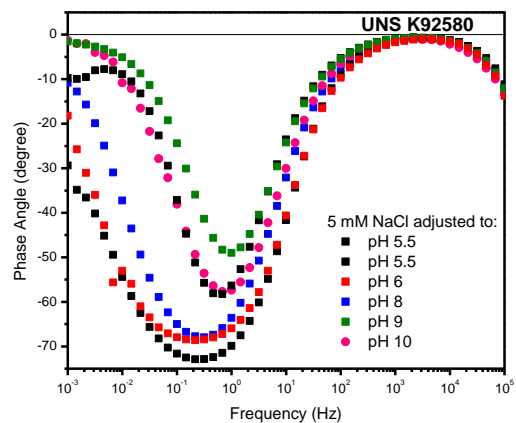
b)



c)



d)



e)

f)

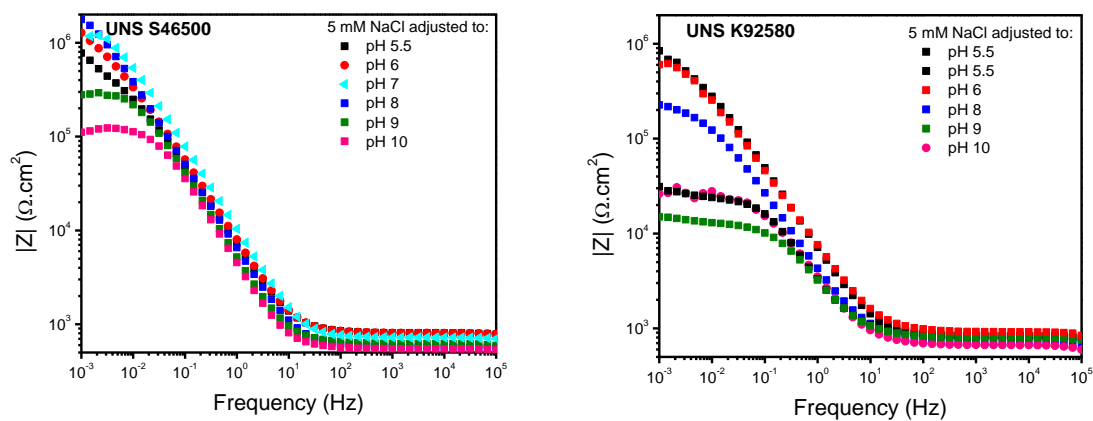


Figure 123. EIS post one hour E_{OCP} of peak aged UNS S46500 a) Nyquist plot, c) phase angle, and e) Bode plot, and UNS K92580 b) Nyquist plot, d) phase angle, and f) Bode plot, in 5 mM NaCl + NaOH pH 5.5 - 10. No intentional cathodic charging was applied prior to EIS scans.

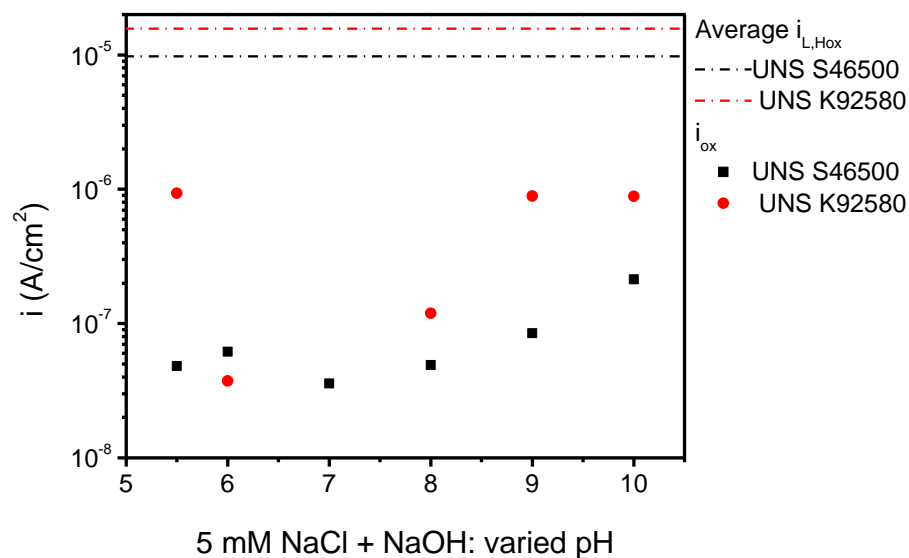


Figure 124. i_{ox} vs. pH for UNS S46500 and UNS K92580. Samples were pre-exposed for 1 h at E_{OCP} in 5mM NaCl + NaOH pH 5.5-10 with no intentional cathodic pre-charging. EIS was acquired at the E_{OCP} with a 20 V_{rms}, 6 mV/dec and from 1 mHz to 10 kHz. No intentional cathodic charging was applied prior to EIS scans. i_{ox} was calculated from EIS fitting and determination of R_p and is plotted vs. the average limiting H oxidation current density ($i_{L,Hox}$). The average $i_{L,Hox}$ ($H \rightarrow H^+ + e^-$) values were calculated from the average of the first thirty min of $\frac{\partial C}{\partial x}$ values determined in Figure 43 (Ch 3).

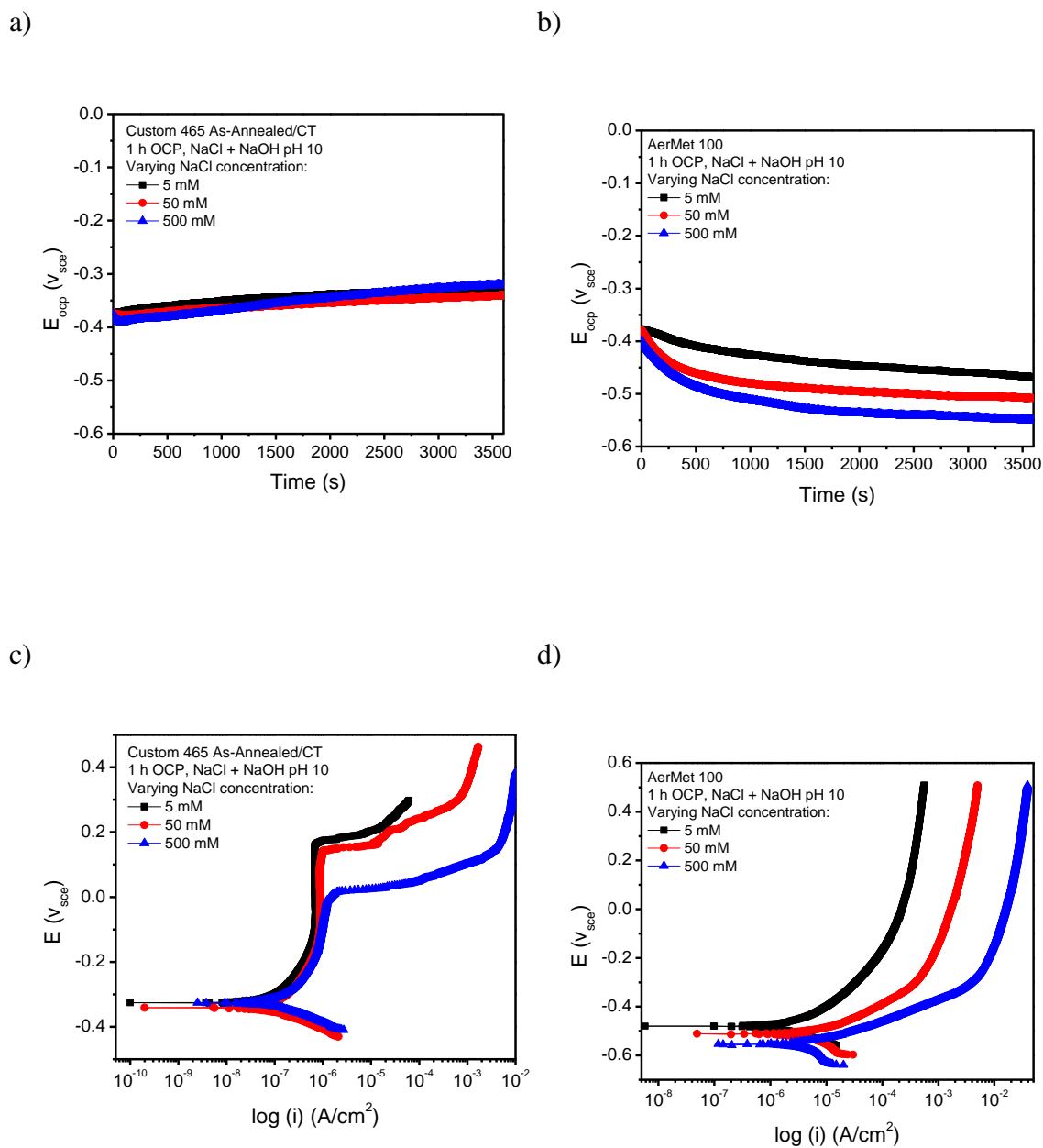


Figure 125. Variation of salt concentration, 5, 50, and 500 mM NaCl, for solution determination. A 1 h E_{OCP} for a) UNS S46500 and b) UNS K92580 followed by an anodic scan from -100 mV vs OCP at a scan rate of 0.1667 mV/s. No intentional cathodic charging was applied prior to scans.

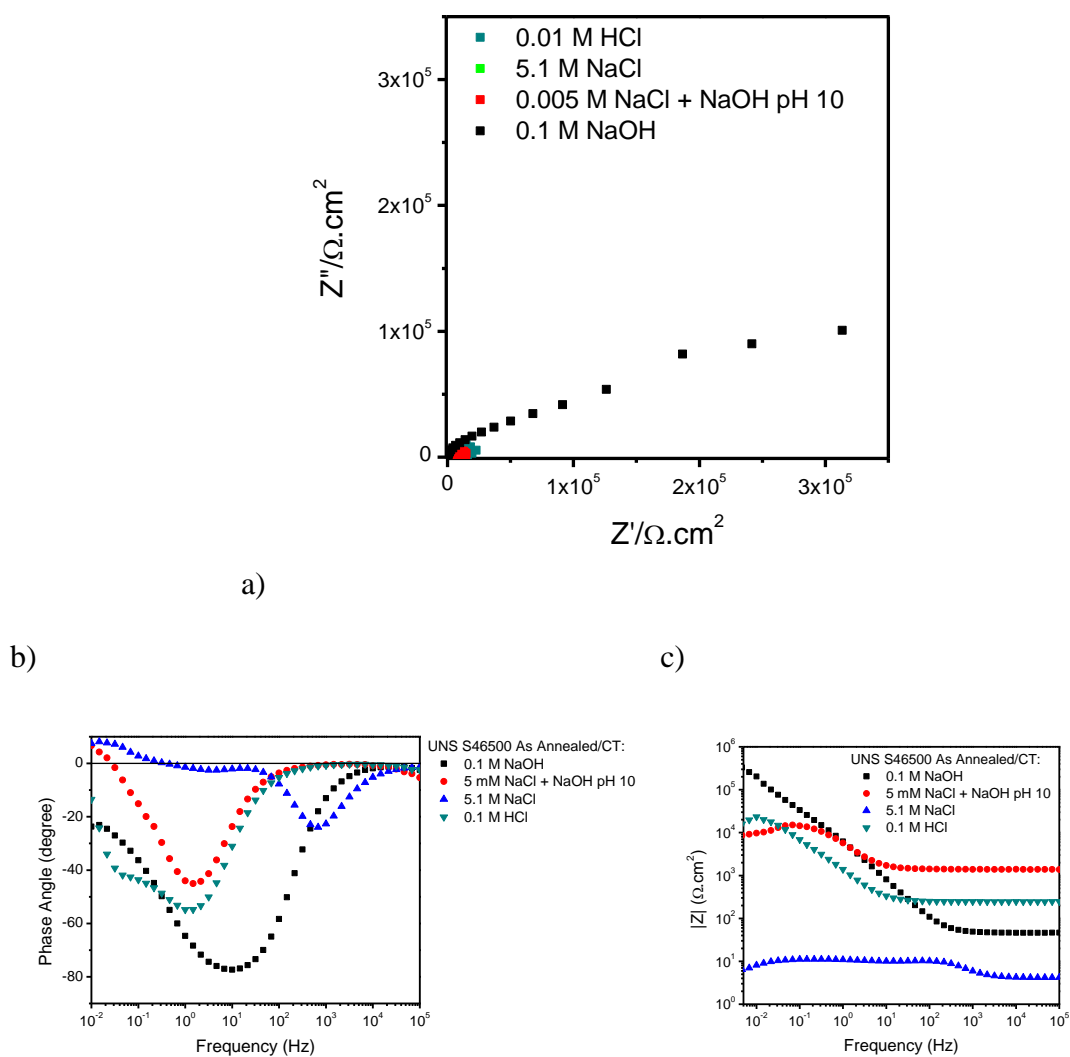


Figure 126. UNS S46500 As Annealed/CT EIS in 0.1 M NaOH, 5 mM NaCl + NaOH pH 10, 5.1 M NaCl, and 0.1 M HCl, a) Comparison of electrolytes, b) Phase plot comparison, and c) Bode plot comparison. No intentional cathodic charging was applied prior to scans.

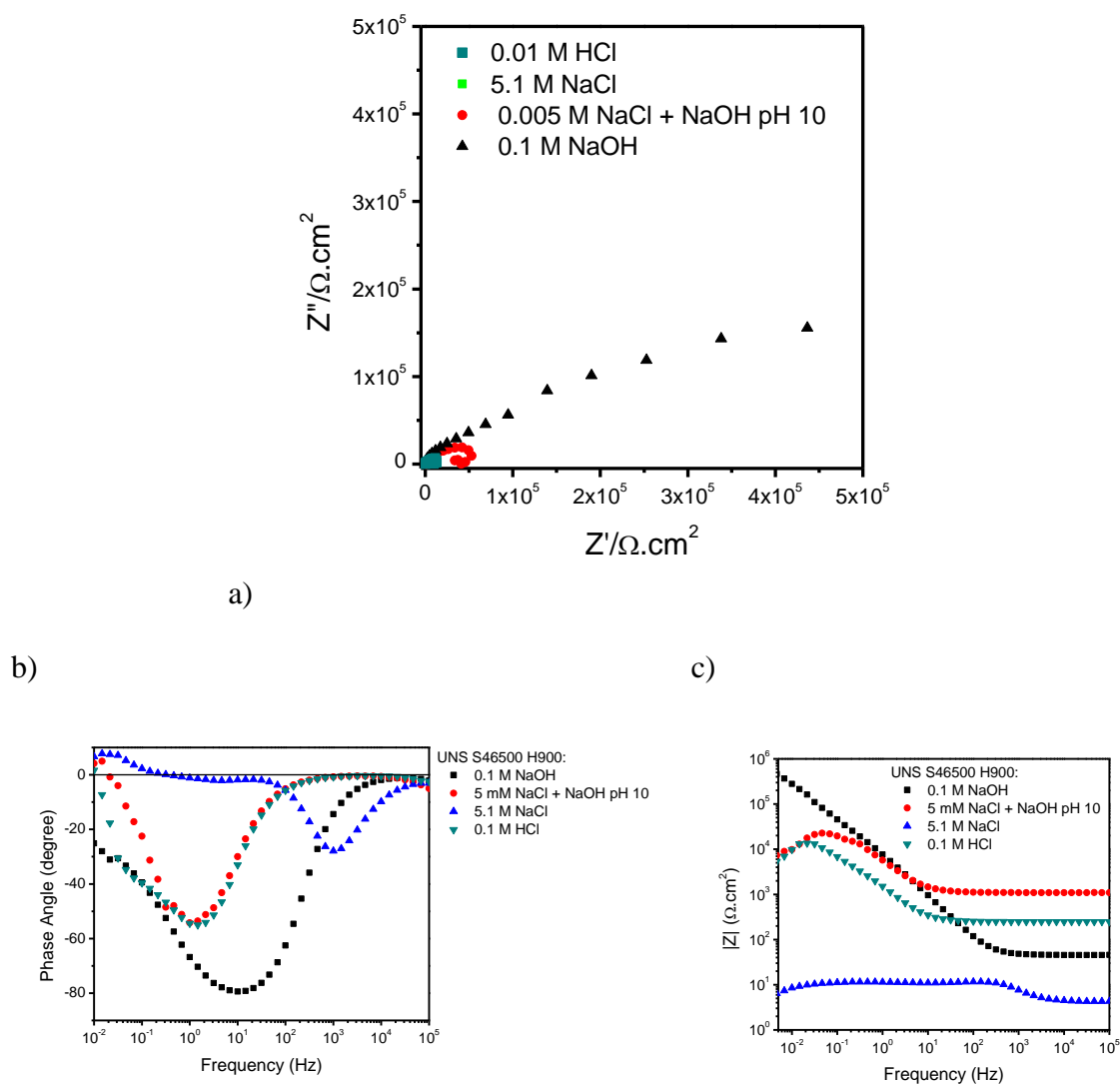
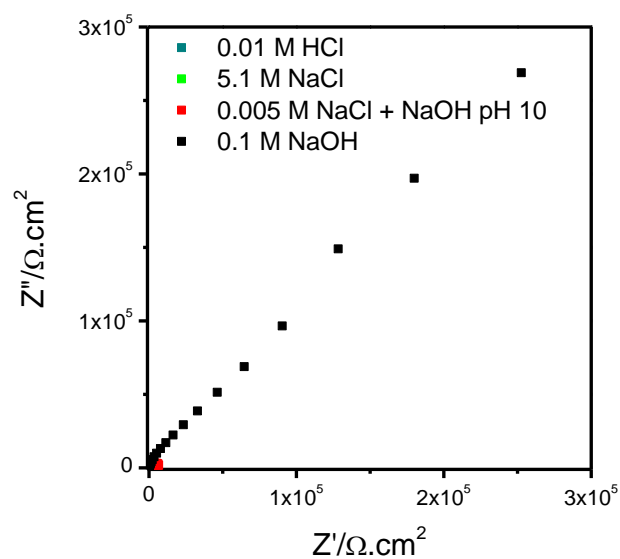
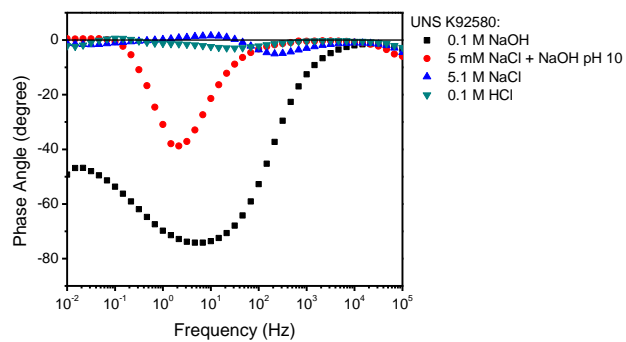


Figure 127. UNS S46500 H900 EIS in 0.1 M NaOH, 5 mM NaCl + NaOH pH 10, 5.1 M NaCl, and 0.1 M HCl, a) Comparison of electrolytes, b) Phase plot comparison, and c) Bode plot comparison. No intentional cathodic charging was applied prior to scans.

a)



b)



c)

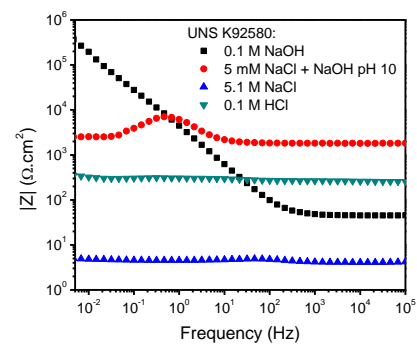
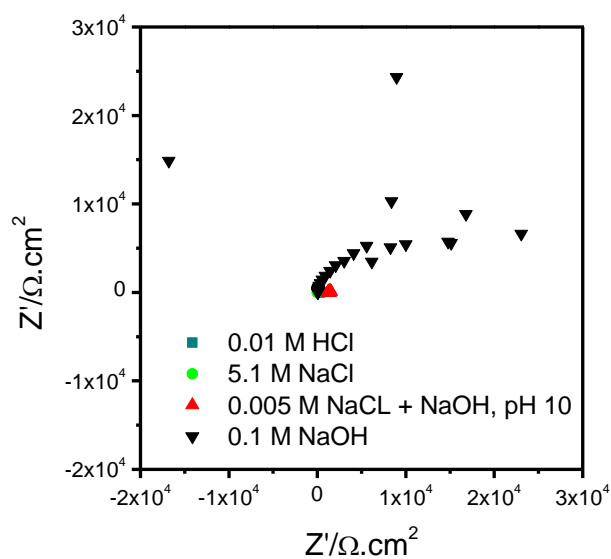
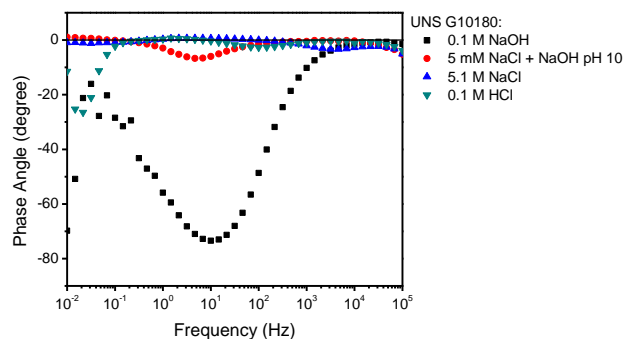


Figure 128. UNS K92580 EIS in 0.1 M NaOH, 5 mM NaCl + NaOH pH 10, 5.1 M NaCl, and 0.1 M HCl, a) Comparison of electrolytes, b) Phase plot comparison, and c) Bode plot comparison. No intentional cathodic charging was applied prior to scans.

a)



b)



c)

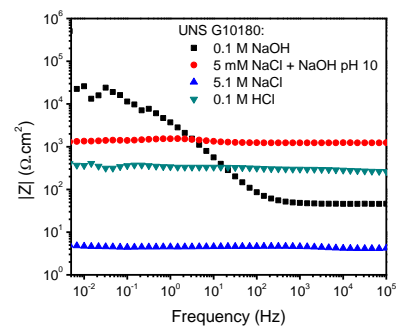
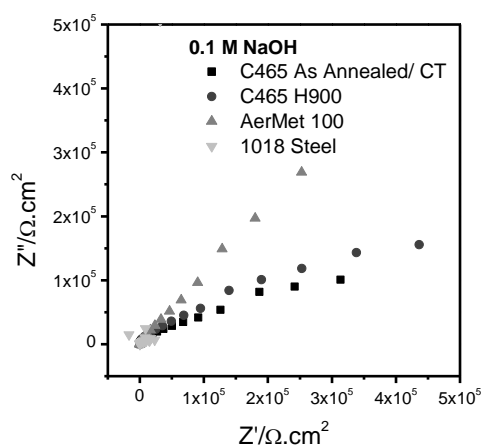
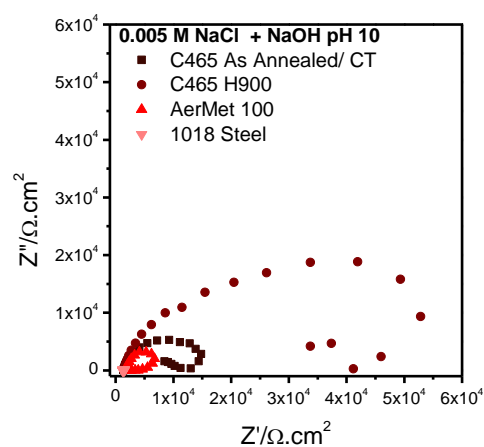


Figure 129. UNS G10180 EIS in 0.1 M NaOH, 5 mM NaCl + NaOH pH 10, 5.1 M NaCl, and 0.1 M HCl, a) Comparison of electrolytes, b) Phase plot comparison, and c) Bode plot comparison. No intentional cathodic charging was applied prior to scans.

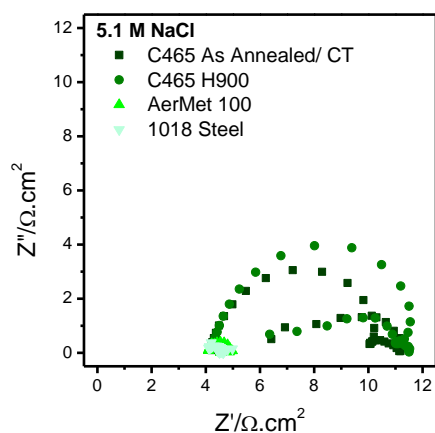
a)



b)



c)



d)

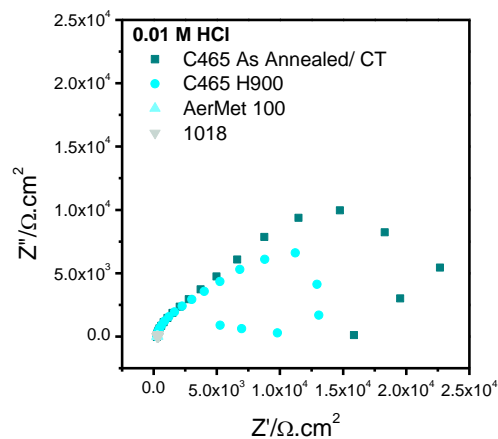


Figure 130. Comparison of steels across electrolytes: a) 0.1 M NaOH, b) 5 mM NaCl + NaOH pH 10, c) 5.1 M NaCl, and d) 0.1 M HCl. No intentional cathodic charging was applied prior to scans.

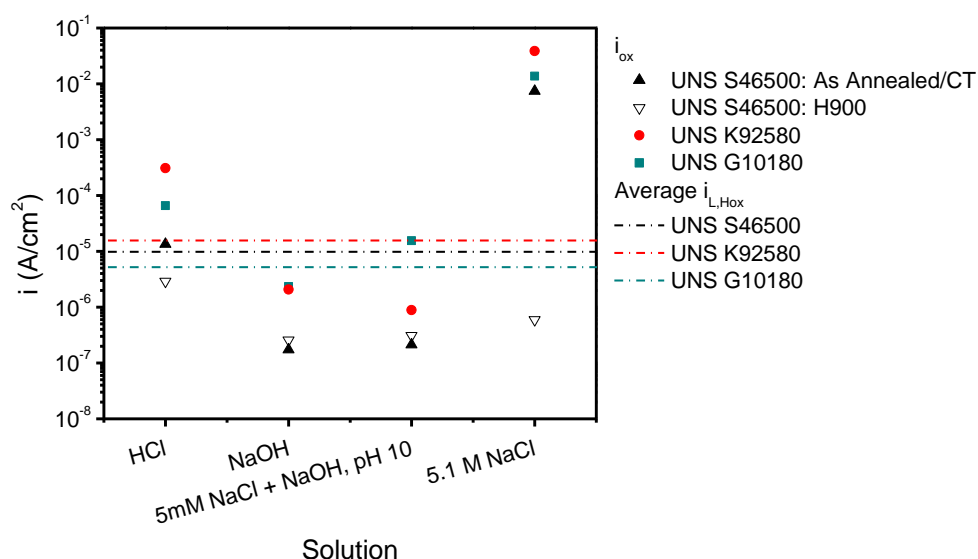


Figure 131. i_{ox} vs. measurement solution for UNS S46500 H900 and as annealed/CT, UNS K92580, and UNS G10180. Samples were exposed in 0.01 M HCl, 0.1 M NaOH, 5mM NaCl + NaOH pH 10, and 5.1 M NaCl with no intentional cathodic pre-charging. EIS was acquired at the E_{OCP} with a 20 V_{rms}, 6 mV/dec and from 1 mHz to 10 kHz. i_{ox} was calculated from EIS fitting and determination of R_p for samples exposed in the selected electrolytes with no intentional cathodic pre-charging and are plotted vs. the average limiting H oxidation current density ($i_{L,Hox}$). The average $i_{L,Hox}$ ($H \rightarrow H^+ + e^-$) values were calculated from the average of the first thirty min of $\frac{\partial C}{\partial x}$ values determined in Figure 43 (Ch 3).

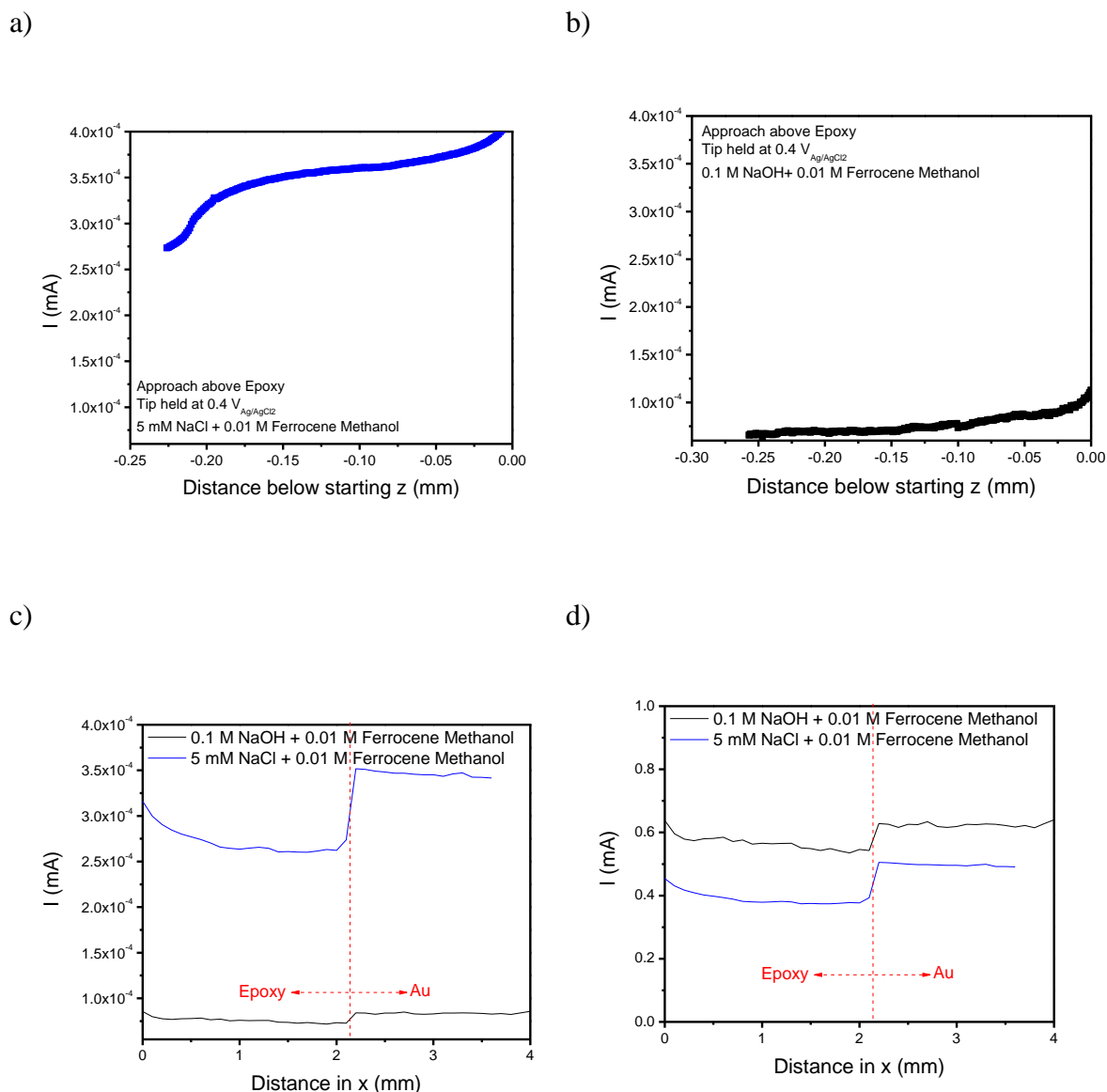
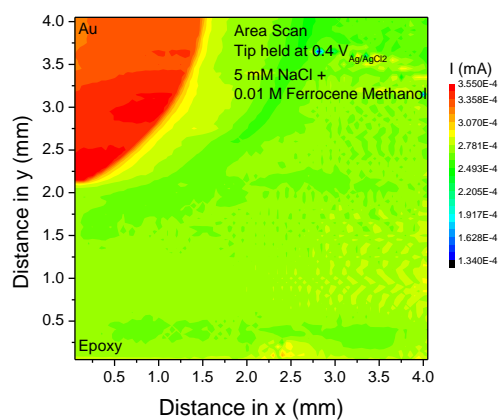


Figure 132. Comparison of SECM measurement solutions, 5 mM NaCl + 0.01 M ferrocene methanol vs. 0.1 M NaOH + 0.01 M ferrocene methanol. Approach over epoxy at a rate of $1 \mu\text{m/s}$ with the Pt tip held at a constant potential of $+0.4 V_{Ag/AgCl}$ shown in a) and b). The epoxy/Au sample was allowed to float at E_{OCP} during the measurement. Line scans from epoxy to Au calibration sample at a constant height of $30 \mu\text{m}$ tip to surface height in c) raw current measured and b) normalized current density (normalized to the steady state current at the tip at $0.4 V_{Ag/AgCl}$ in each solution).

a)



b)

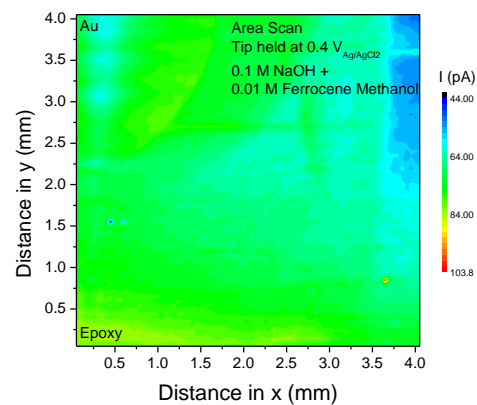
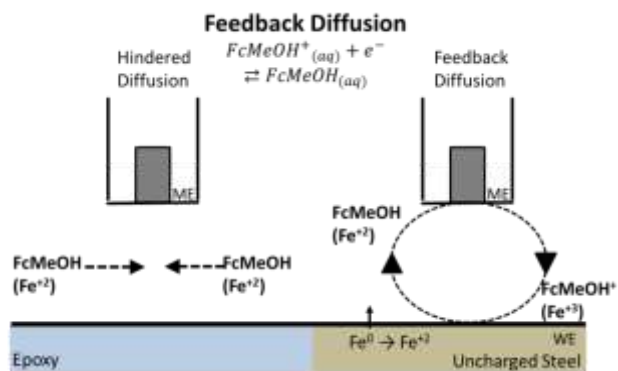
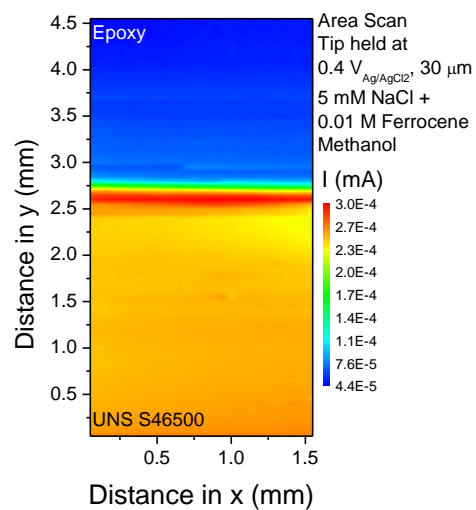


Figure 133. Comparison of ME tip current above Au in epoxy in two SECM measurement solutions, a) 5 mM NaCl + 0.01 M ferrocene methanol vs. b) 0.1 M NaOH + 0.01 M ferrocene methanol. Area scans taken with the Pt tip held at a constant potential of +0.4 V_{Ag/AgCl} and a height of 30 μ m above the same area of Au in epoxy.

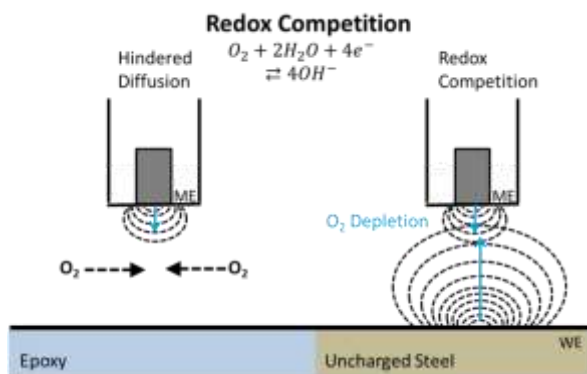
a)



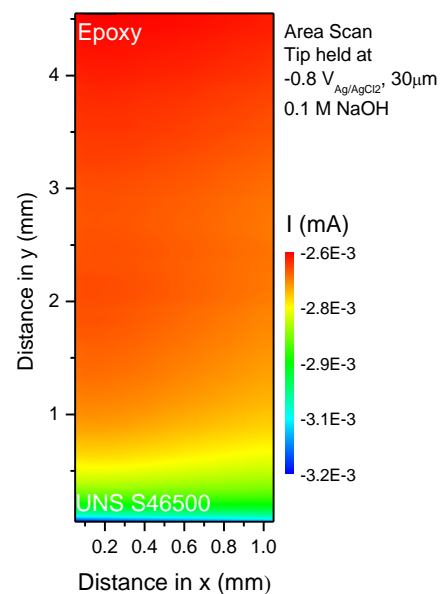
b)



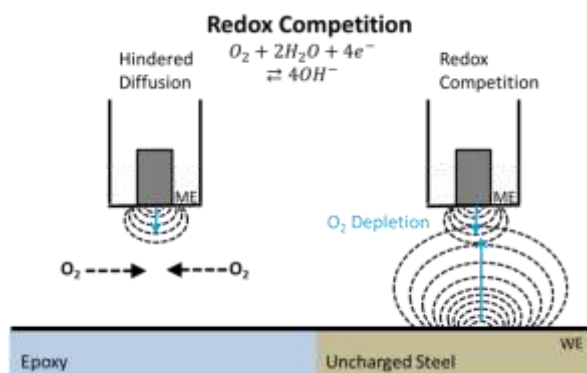
c)



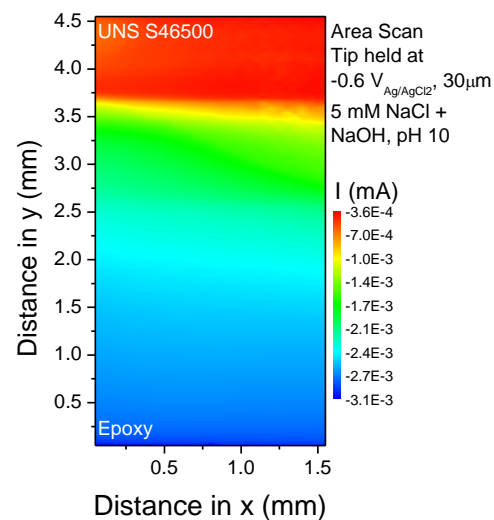
d)



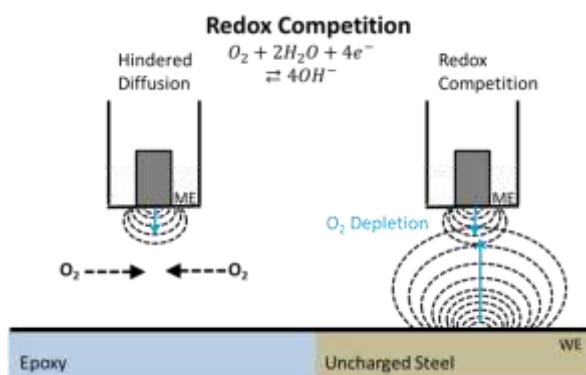
e)



f)



g)



h)

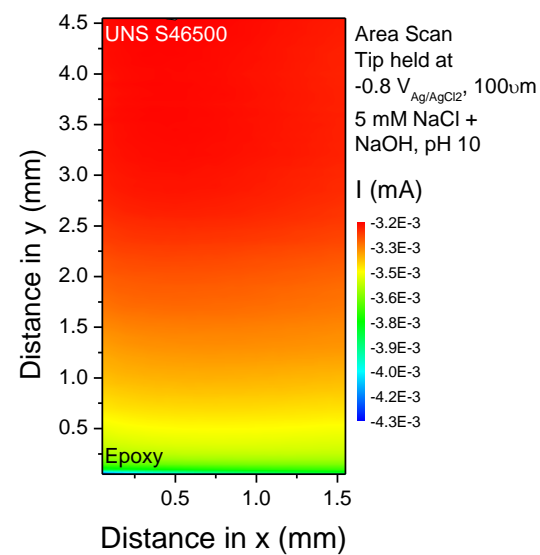


Figure 134. A scans from epoxy to uncharged UNS S46500 for solution calibration. a) Feedback mode (OX,ME/red,WE) schematic, b) 5 mM NaCl + 0.01 M ferrocene methanol,

30 μm height, c) Redox competition schematic, d) 0.1 M NaOH e) Redox competition ($\text{red}_{\text{ME}}/\text{red}_{\text{WE}}$) schematic, f) 5 mM NaCl + NaOH pH 10, 30 μm height, g) Redox competition ($\text{red}_{\text{ME}}/\text{red}_{\text{WE}}$) schematic, and h) 5 mM NaCl + NaOH pH 10, 100 μm height.

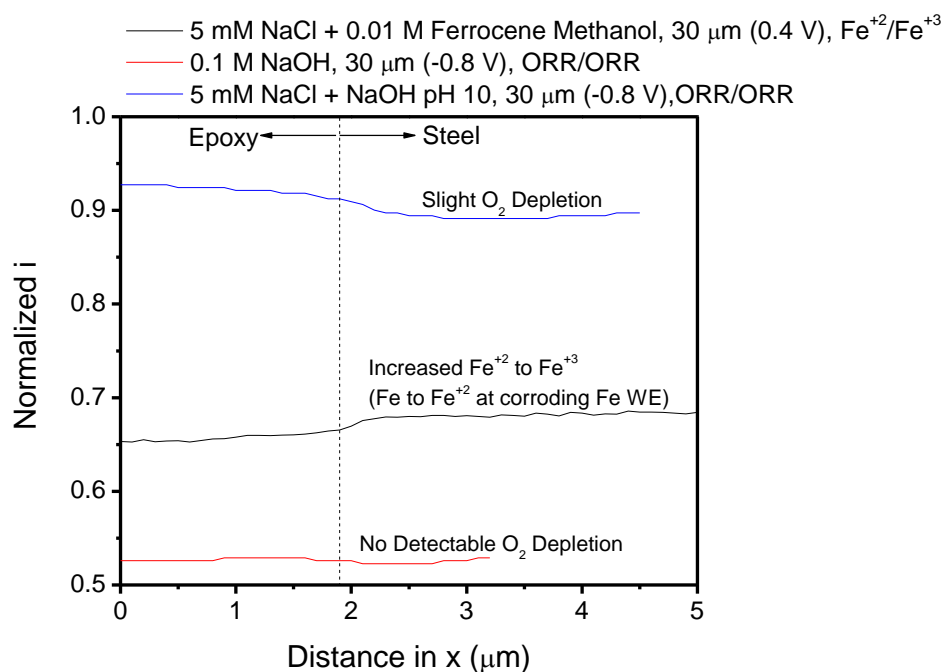


Figure 135. Comparison of line scans with ME tip signal for feedback diffusion mode of $\text{Fe}^{+2} \rightarrow \text{Fe}^{+3} + \text{e}^-$ (black line) and redox competition mode with ORR at the tip (blue and red lines) from Epoxy to uncharged UNS S46500 in the three different solutions, the i is normalized to the steady state current found from the respective CV on the Pt tip in each solution at the operating voltage ($+0.4 \text{ V}_{\text{Ag}/\text{AgCl}}$ for 5 mM NaCl + 0.01 M ferrocene methanol and $-0.8 \text{ V}_{\text{Ag}/\text{AgCl}}$ for 0.1 M NaOH and 5 mM NaCl + NaOH pH 10)

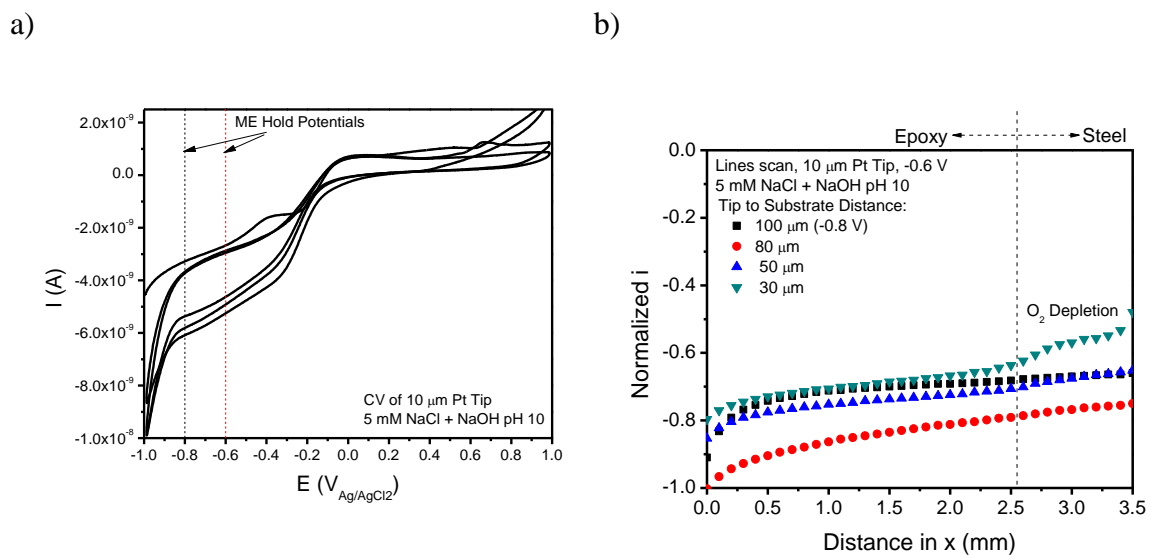


Figure 136. Tip to substrate height calibration. a) CV on Pt ME in 5 mM NaCl + NaOH pH 10 showing ORR and b) Line scans of $i_{ORR,ME}$ for height calibration. Heights less than 30 μ m are not shown as below a height of 30 μ m in the current SECM setup, topography/tilt of sample creates risk of crashing tip into surface. Above 30 μ m the difference in $i_{ORR,ME}$ measured above steel vs. epoxy becomes less defined. Scans were taken from epoxy to steel substrate in 5 mM NaCl + NaOH pH 10 with a potential of -0.6 $V_{Ag/AgCl}$ applied to the tip, except at 100 μ m distance where a voltage of -0.8 $V_{Ag/AgCl}$ was applied to try to increase the signal. ∞

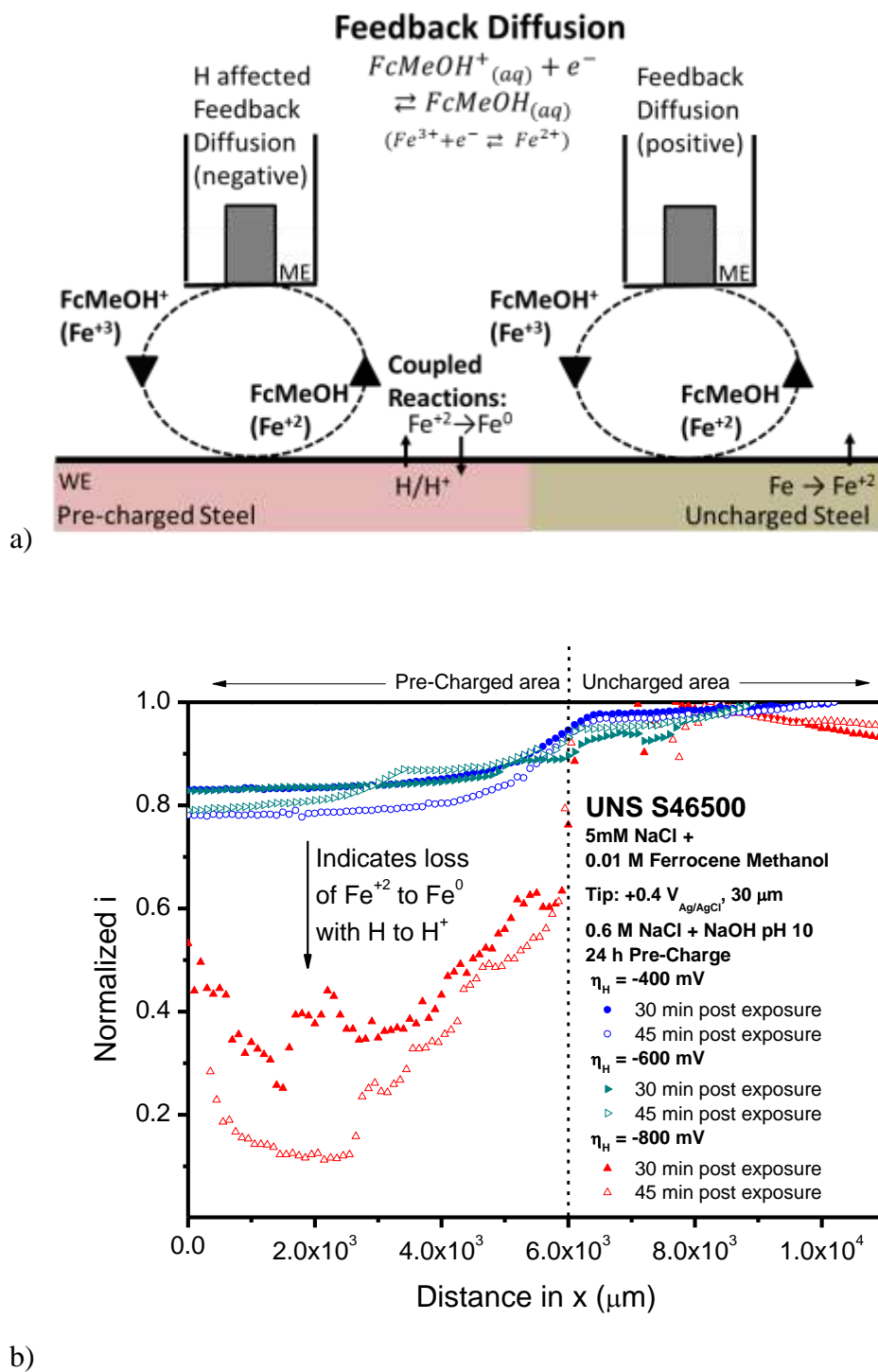


Figure 137. Initial scans of hydrogen uncharged vs. pre-charged steel in the SECM in feedback mode. a) Feedback mode (ox_{ME}/red_{WE}) for $Fe^{3+} + e^- \rightleftharpoons Fe^{2+}$ schematic, b) UNS S46500 line scans from uncharged to pre-charged steel in 5mM NaCl + 0.01 M ferrocene methanol, pre-charged for 24 h in an electrochemical flat cell in 0.6 M NaCl + NaOH pH 10 at $\eta_H = -400, -600, \text{ and } -800 \text{ mV}$ (-1232, -1432, and -1632 mV_{SCE}).

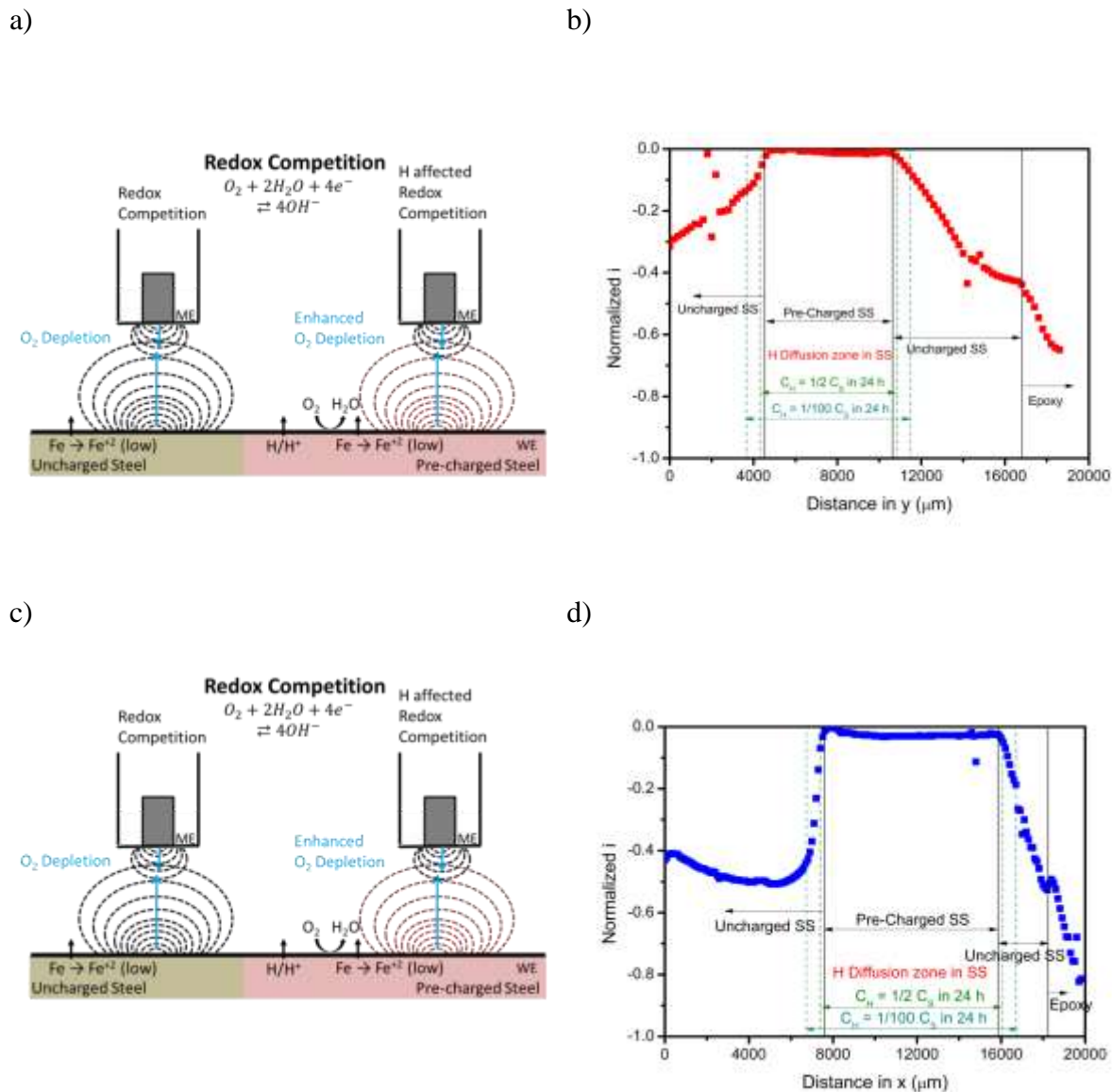
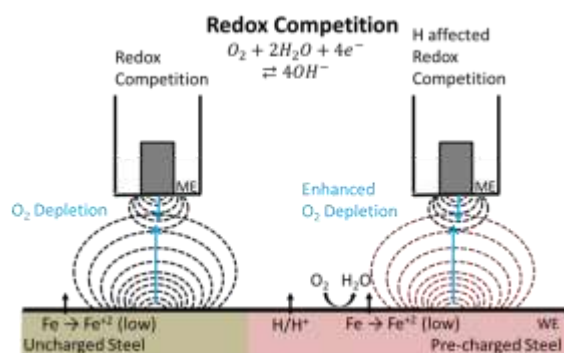
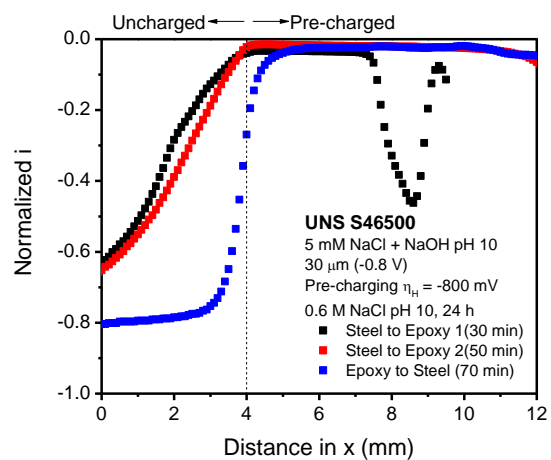


Figure 138. Initial scans of hydrogen uncharged vs. pre-charged UNS S46500 H900 in the SECM in redox competition mode (red_{ME}/red_{WE}). a) Redox competition mode schematic, b) Scans post-charging time of UNS S46500 line scans from uncharged to pre-charged steel in 5mM NaCl + NaOH pH 10, pre-charged for 24 h in an electrochemical flat cell in 0.6 M NaCl + NaOH pH 10 at $\eta_H = -800$ mV (-1632 mV_{SCE}). [26]

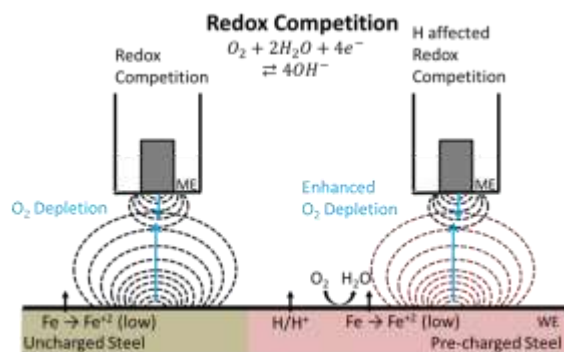
a)



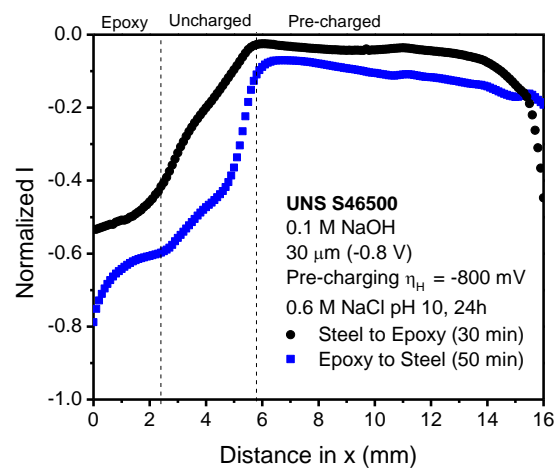
b)



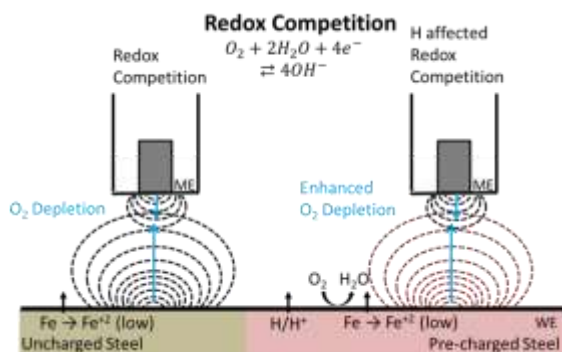
c)



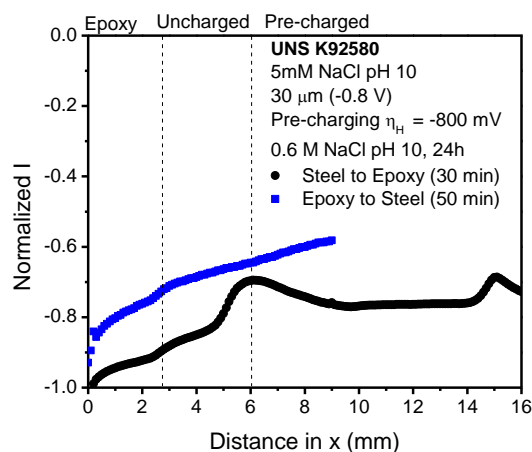
d)



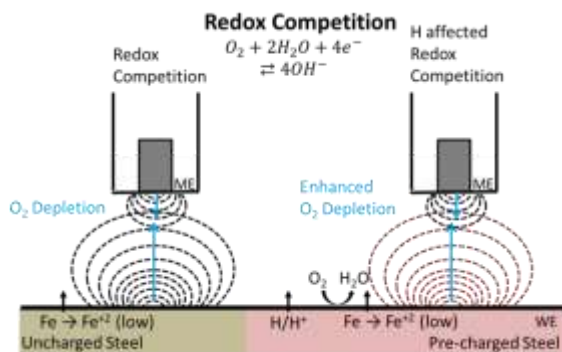
e)



f)



g)



h)

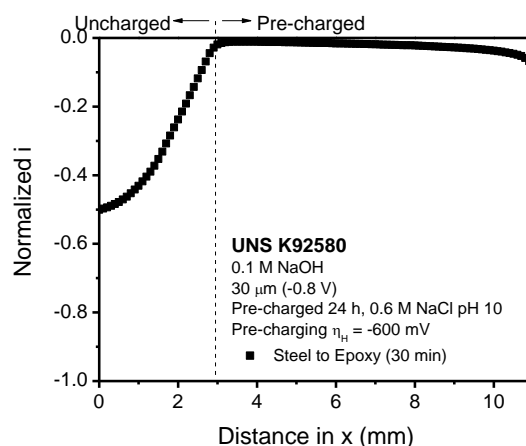
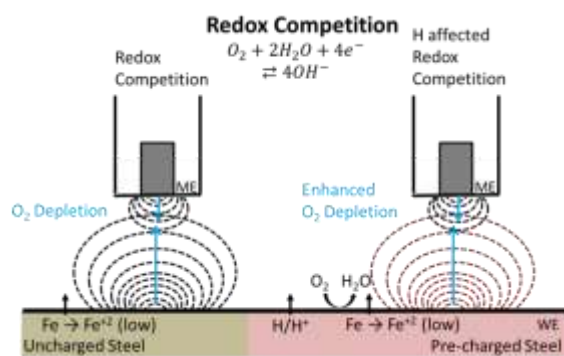
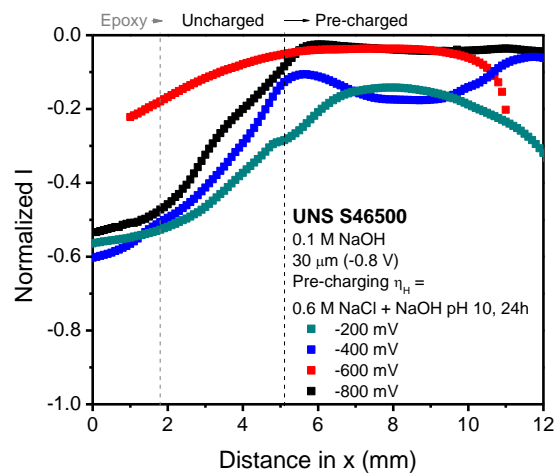


Figure 139. Redox competition (red_{ME}/red_{WE}) scans of hydrogen uncharged vs. pre-charged UNS S46500 and UNS K92580 in the SECM. a,c,e, and g) Redox Competition schematic, As Annealed/CT UNS S46500 line scans of $i_{ORR,ME}$ vs. distance in x from steel to epoxy and epoxy to steel in b) 5mM NaCl + NaOH pH 10 and d) 0.1 M NaOH, and UNS K92580 in f) 5mM NaCl + NaOH pH 10 and h) 0.1 M NaOH pre-charged for 24 h in an electrochemical flat cell in 0.6 M NaCl + NaOH pH 10 at $\eta_H = -800$ mV (-1632 mV_{SCE}).

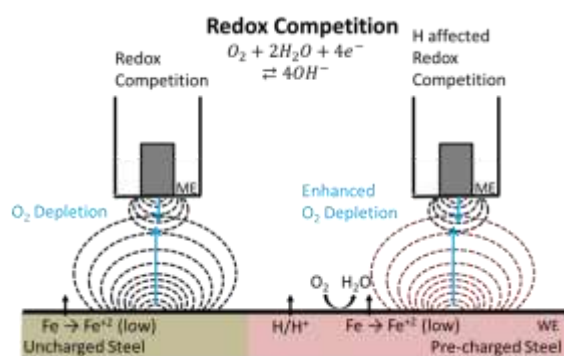
a)



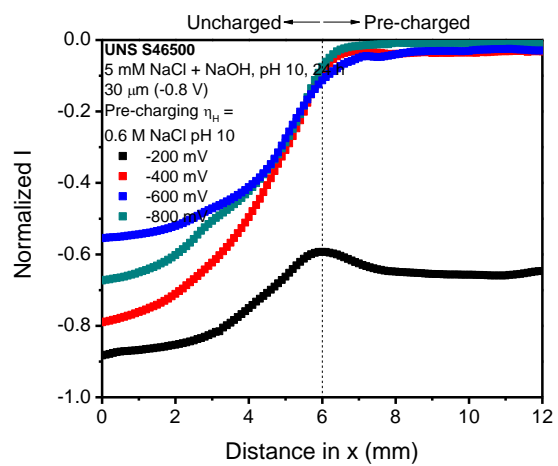
b)



c)



d)



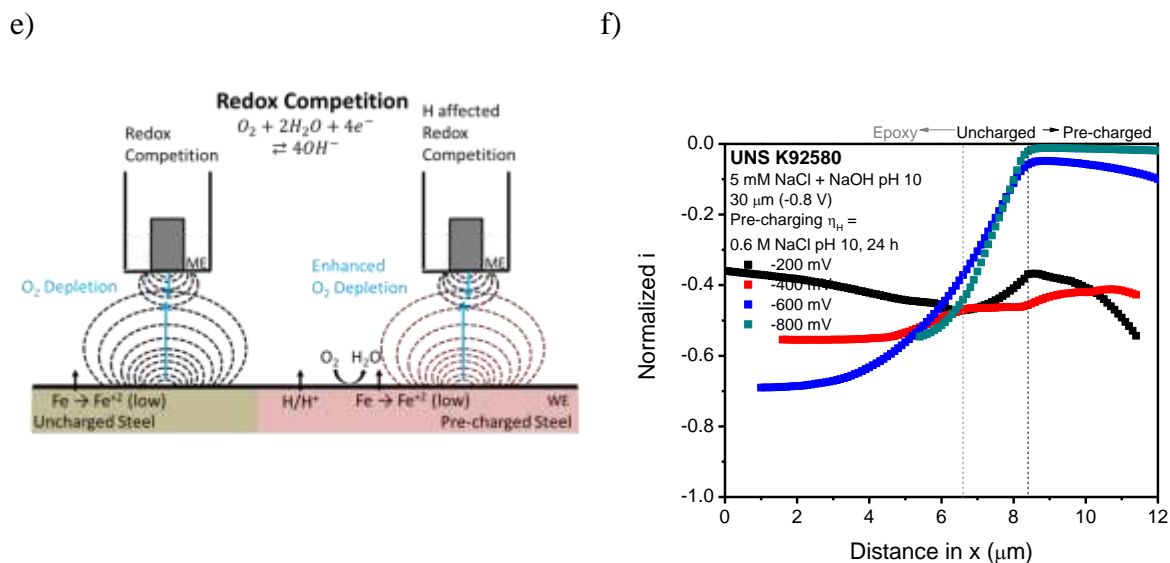


Figure 140. Redox competition (red_{ME}/red_{WE}) scans of hydrogen uncharged vs. precharged UNS S46500 and UNS K92580 in the SECM. a, c, and e) Redox Competition schematic. b) As Annealed/CT UNS S46500 line scans of $i_{ORR,ME}$ vs. distance in x from steel to epoxy in 0.1 M NaOH, pre-charged for 24 h in an electrochemical flat cell in 0.6 M NaCl + NaOH pH 10 at $\eta_H = -200, -400, -600$, and -800 mV ($-1032, -1232, -1432$, and -1632 mV_{SCE}), d) As Annealed/CT UNS S46500 with similar pre-charging conditions, but SECM scans in 5 mM NaCl + NaOH, pH 10, and f) UNS K92580 with similar pre-charging conditions, with SECM scans in 5 mM NaCl + NaOH, pH 10.

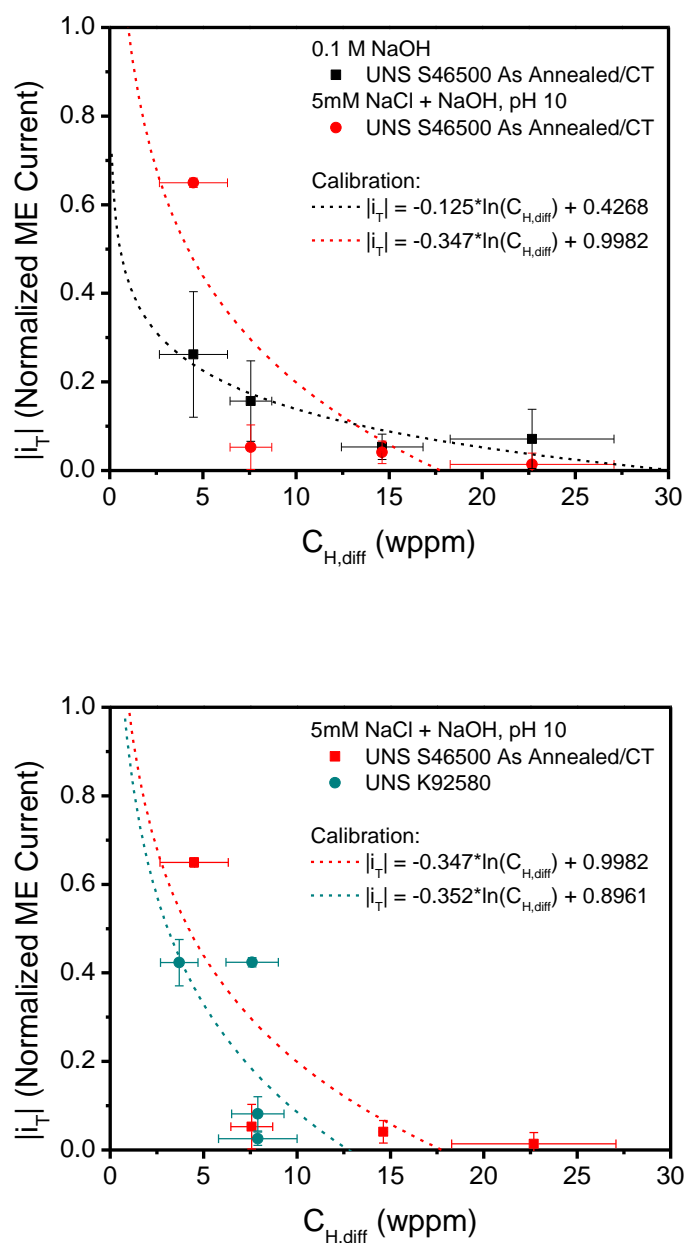


Figure 141. $C_{H,diff}$ vs absolute value of normalized ME tip current ($i_{ORR,ME}$) in the SECM under redox competition modes (red_{ME}/red_{WE}) in a) 0.1 M NaOH and 5 mM NaCl + NaOH pH 10 for UNS S46500 in the as annealed/CT condition and b) in 5 mM NaCl + NaOH pH 10 for peak aged UNS K92580 and UNS S46500 in the as annealed/CT condition. $i_{ORR,ME}$ was taken as the average measured over the pre-charged line scan area.

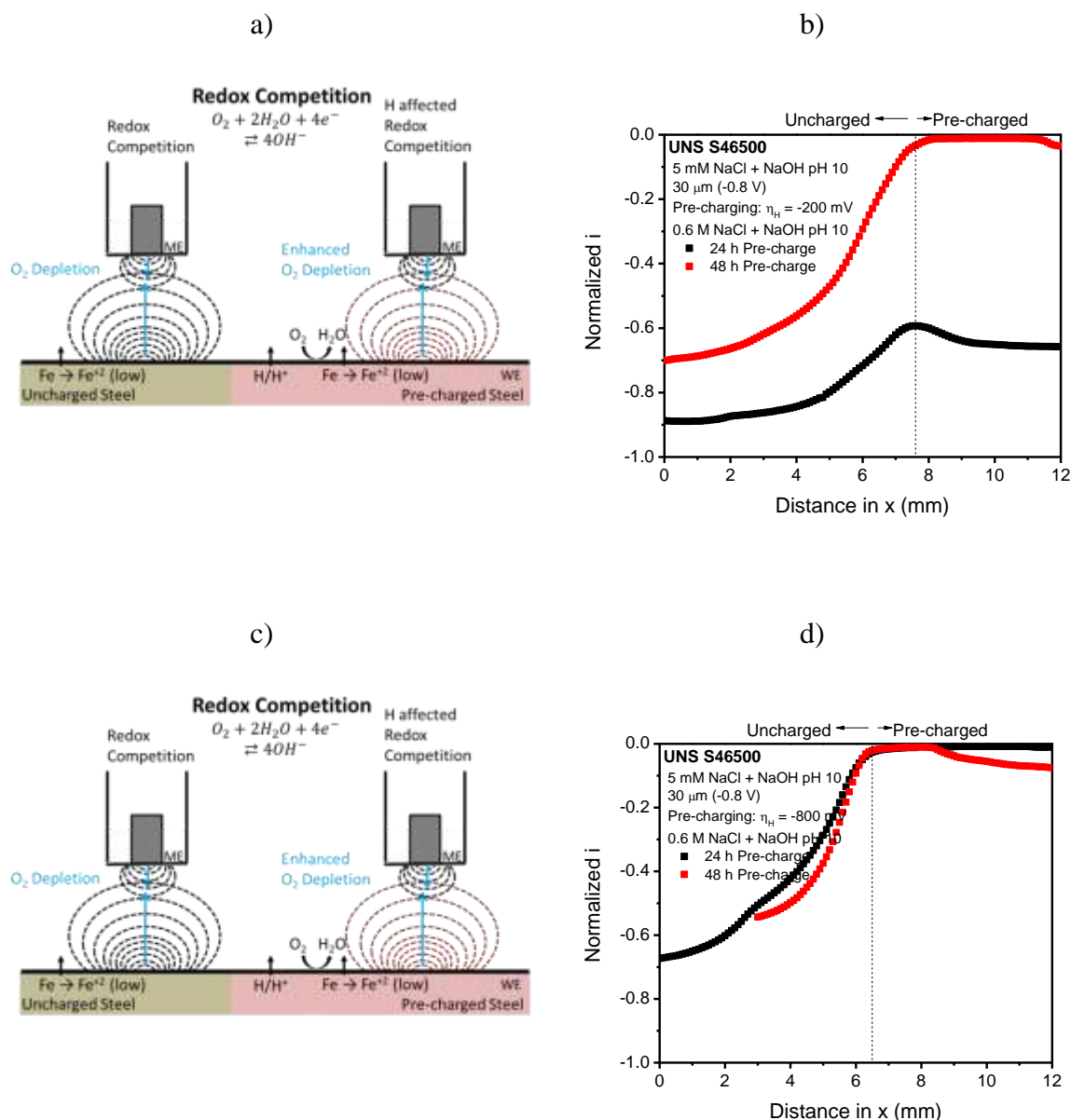


Figure 142. Redox competition (red_{ME}/red_{WE}) scans of hydrogen uncharged vs. pre-charged UNS S46500 in the SECM. a, and c) Redox Competition schematic. Comparison of hydrogen pre-charging time for as annealed/CT UNS S46500, line scans of $i_{ORR,ME}$ vs. distance in x from steel to epoxy in 5 mM NaCl + NaOH pH 10. Pre-charged for 24 and 48 h in an electrochemical flat cell in 0.6 M NaCl + NaOH pH 10 ambiently aerated at b) $\eta_H = -200$ (-1032 mV_{SCE}) and d) $\eta_H = -800$ (-1632 mV_{SCE}).

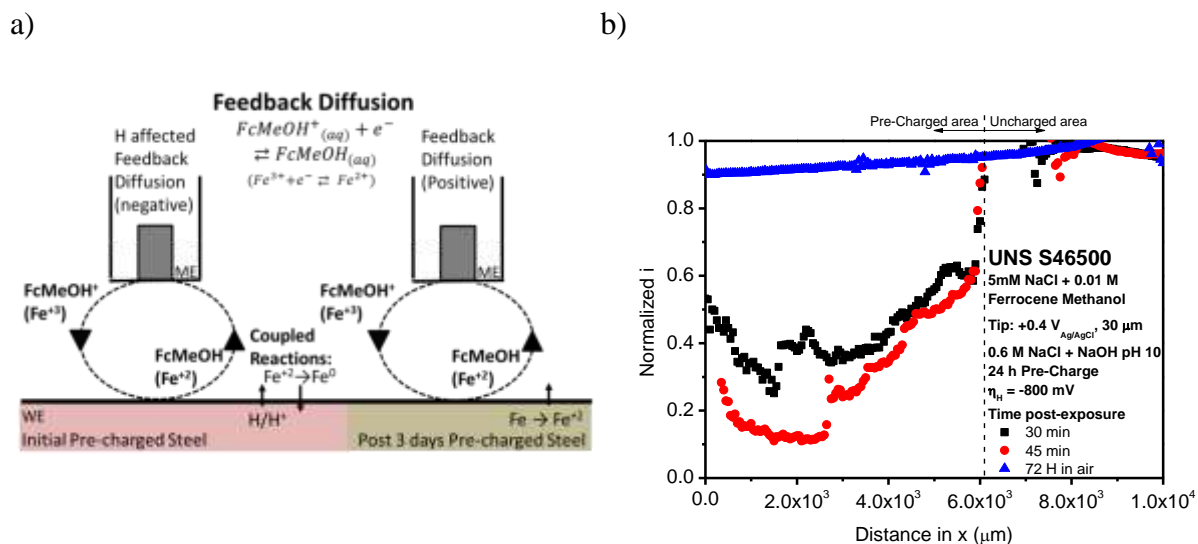


Figure 143. Feedback diffusion mode (OX_{ME}/red_{WE}) scans of hydrogen uncharged vs. pre-charged UNS S46500 in the SECM. a) Feedback mode schematic, b) Scans post-charging time, 30 min and 45 min in-situ in the SECM and 3 days ex-situ in dry lab air, of UNS S46500 line scans of ME tip current vs. distance in x from uncharged to pre-charged steel in 5mM NaCl + 0.01 M ferrocene methanol, pre-charged for 24 h in an electrochemical flat cell in 0.6 M NaCl + NaOH pH 10 at $\eta_H = -800$ mV (-1632 mV_{SCE}).

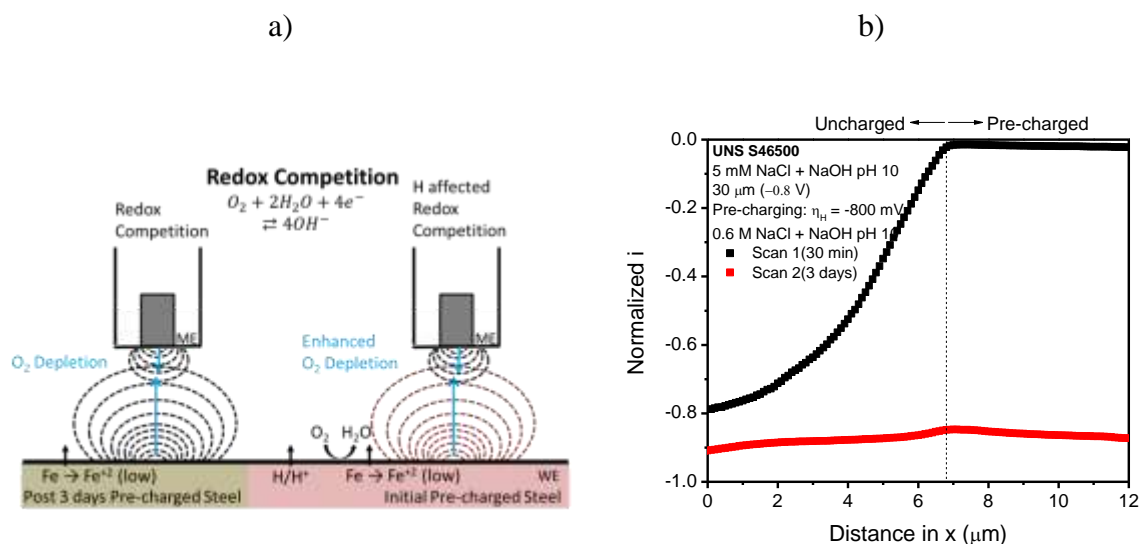
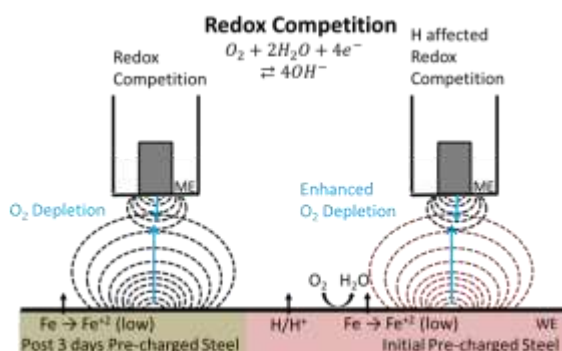


Figure 144. a) Redox Competition (red_{ME}/red_{WE}) schematic. b) Scans of hydrogen uncharged vs. pre-charged steel in the SECM, comparison of time post-charging for as annealed/CT UNS S46500, line scans of $i_{ORR,ME}$ vs. distance in x from steel to epoxy in 5 mM NaCl + NaOH pH 10. Pre-charged for 24 in an electrochemical flat cell in 0.6 M NaCl + NaOH pH 10 at $\eta_H = -800$ (-1632 mV_{SCE}). Scans taken 30 min post-charging and 3 days ex-situ post-charging exposed in dry lab air.

a)



b)

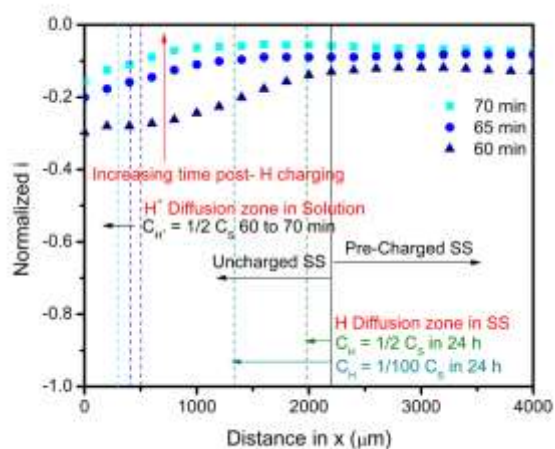


Figure 145. Scans of hydrogen uncharged vs. pre-charged steel in the SECM in redox competition mode ($\text{red}_{\text{ME}}/\text{red}_{\text{WE}}$) schematic using O_2 , b) Scans post-charging time of UNS S46500 line scans from uncharged to pre-charged steel in 5mM NaCl + NaOH pH 10, pre-charged for 24 h in an electrochemical flat cell in 0.6 M NaCl + NaOH pH 10 at $\eta_{\text{H}} = -800$ mV (-1632 mV_{SCE}). [26]

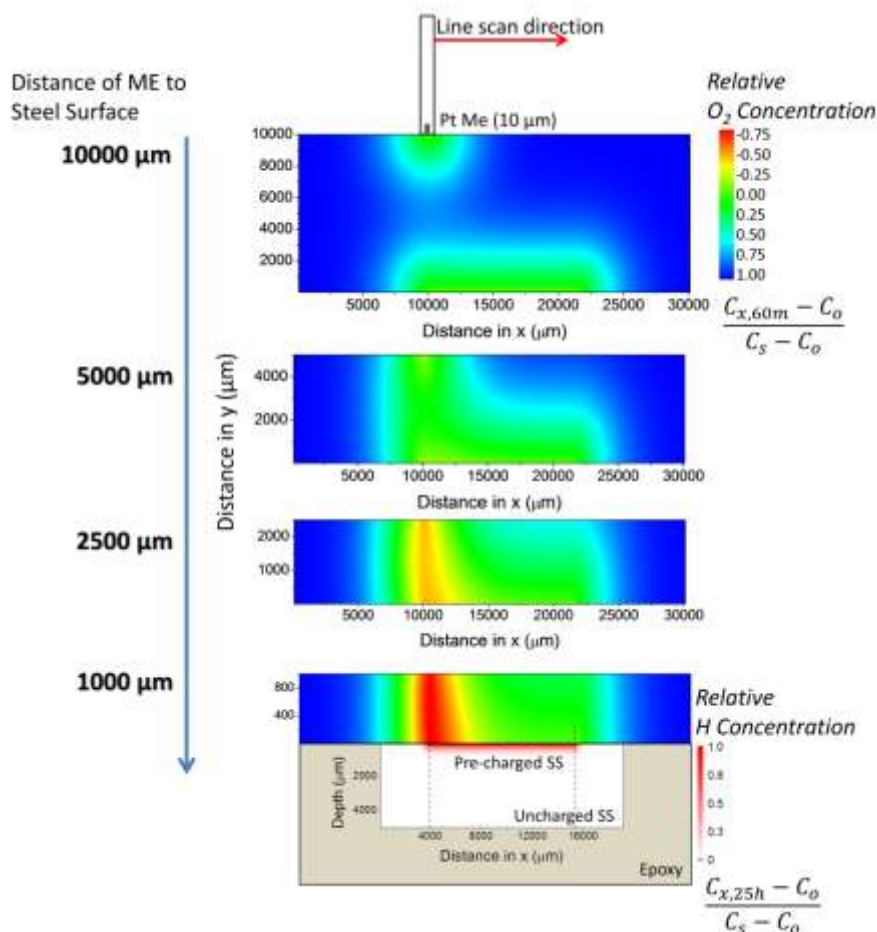


Figure 146. Analytical concentration profile of O_2 depletion as the SECM ME tip approaches the steel surface (with dissolved H). The oxygen concentration fields arising from the two surfaces overlap at even 1000 μm distance. These concentration profiles were generated using analytical expressions for estimating diffusion in an infinite plane, with known diffusion coefficients for H in UNS S46500 ($D_{\text{H}} = 6.2 \times 10^{-9} \text{ cm}^2/\text{s}$) and O_2 in solution ($D_{\text{O}_2} = 1.46 \times 10^{-5} \text{ cm}^2/\text{s}$). The source concentrations were assumed as fixed and the reactions were considered to be under diffusion control. The working distance used for the line scan experiments is 100 μm . [26]

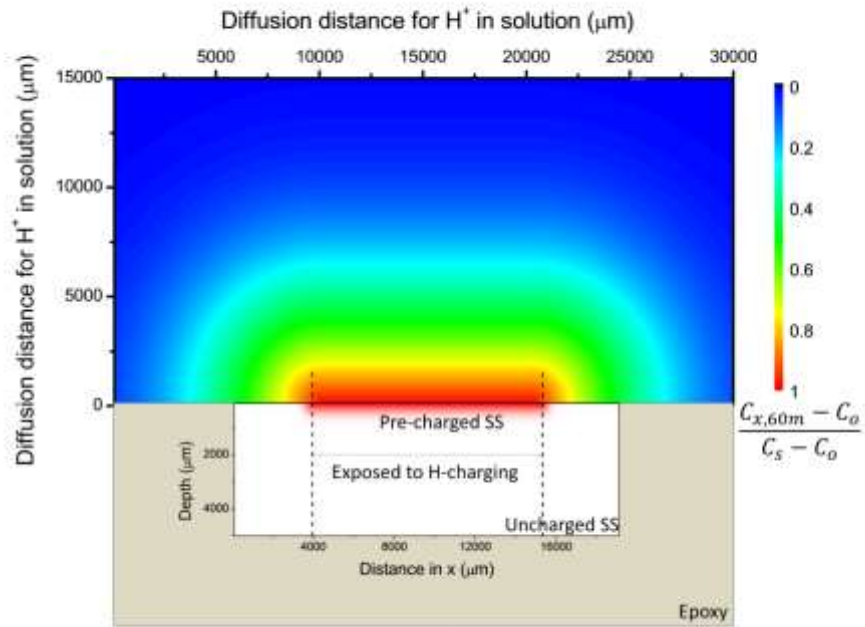
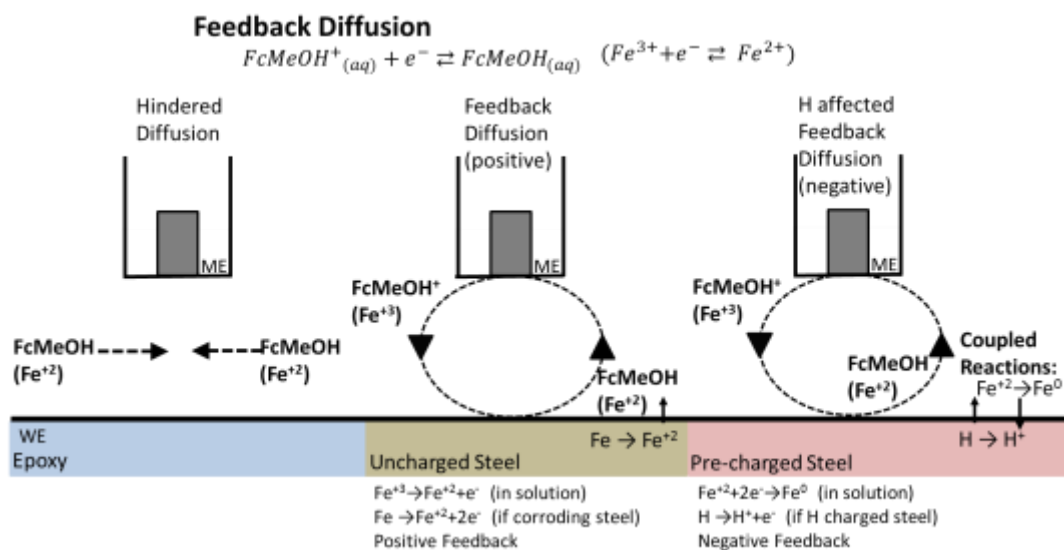
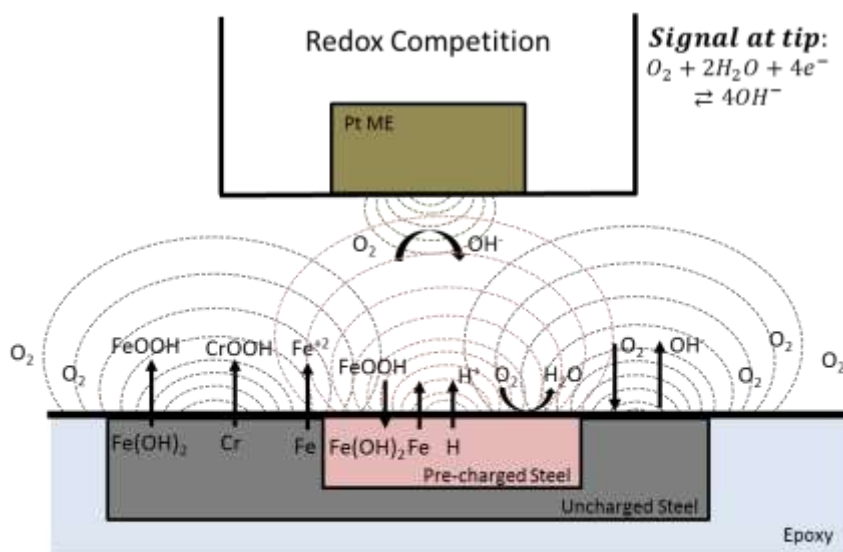


Figure 147. Analytical concentration profiles of hemispherical H^+ transport from the H pre-charged area in solution were generated using the estimation for diffusion in an infinite plane with known diffusion coefficients for H in UNS S46500 ($D_H = 6.2 \times 10^{-9} \text{ cm}^2/\text{s}$) and H^+ in dilute aqueous solution ($D_{H^+} = 4.4 \times 10^{-5} \text{ cm}^2/\text{s}$). Diffusion times utilized were 25 h for H in the steel and 1h for H^+ in solution above the pre-charged SS.[26]

a)



b)

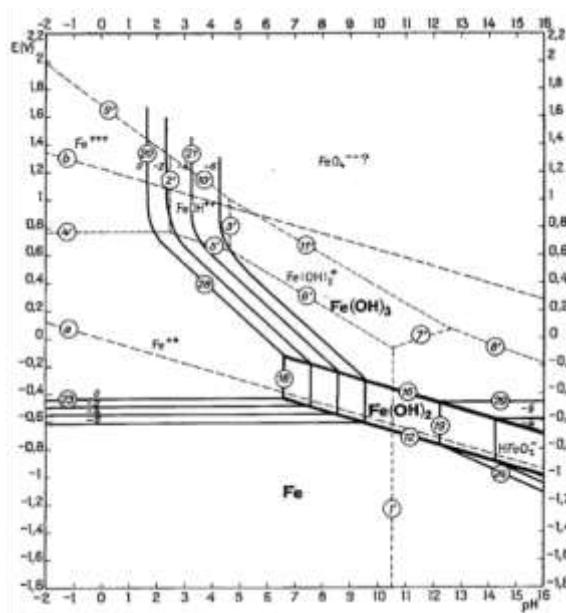


Redox Competition

(i_T decreases on approach, diffusion limited, further hindered above active sites where O_2 consumed)

Figure 148. Schematic of a) Feedback diffusion (OX_{ME}/red_{WE}) and b) Redox competition (red_{ME}/red_{WE}) above a hydrogen pre-charged steel sample.

a)



b)

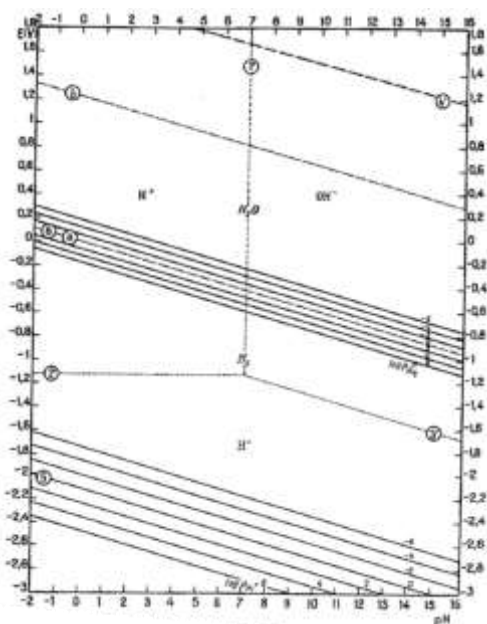
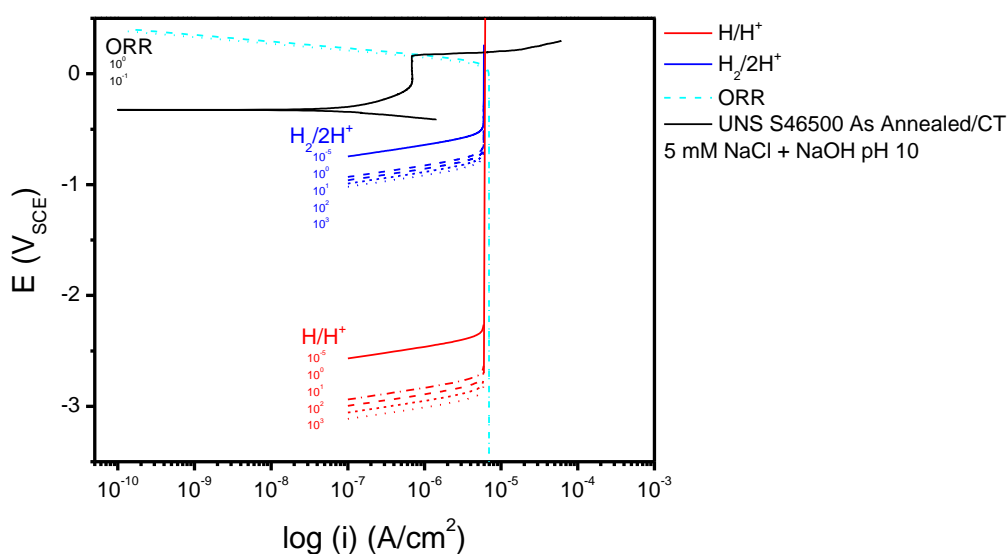
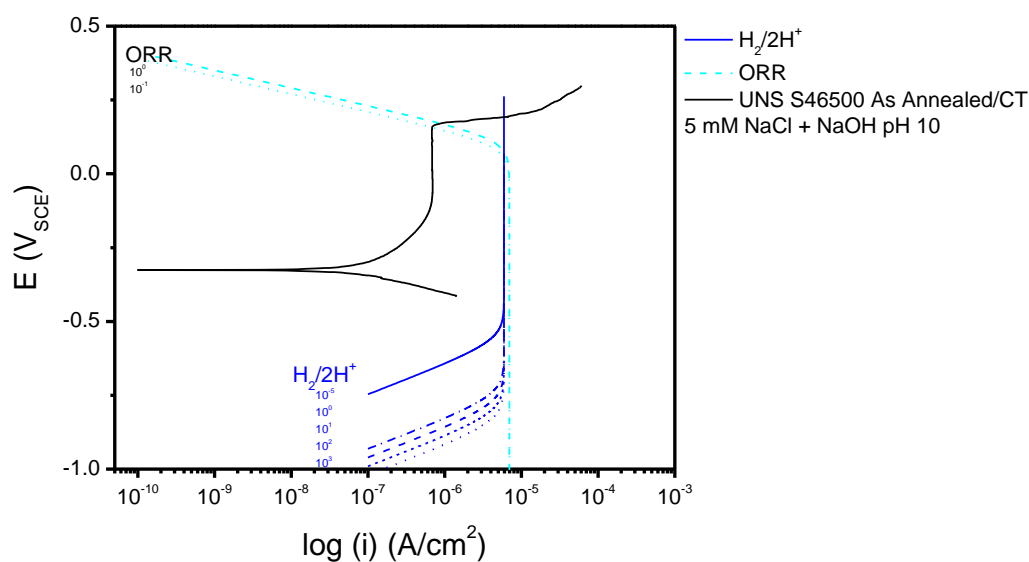


Figure 149. Pourbaix diagram in water at 25°C for a) Fe and b) H. The range of passivity is indicated.[35]

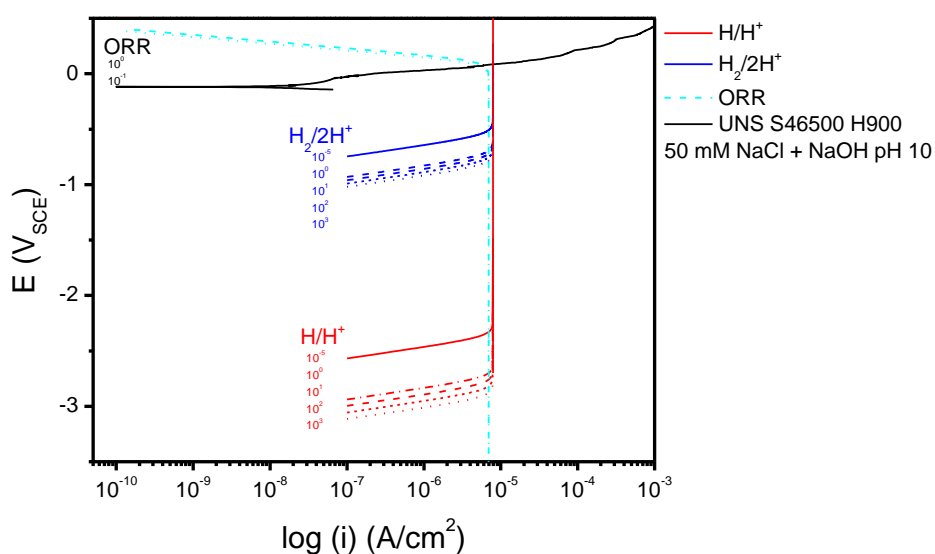


a)

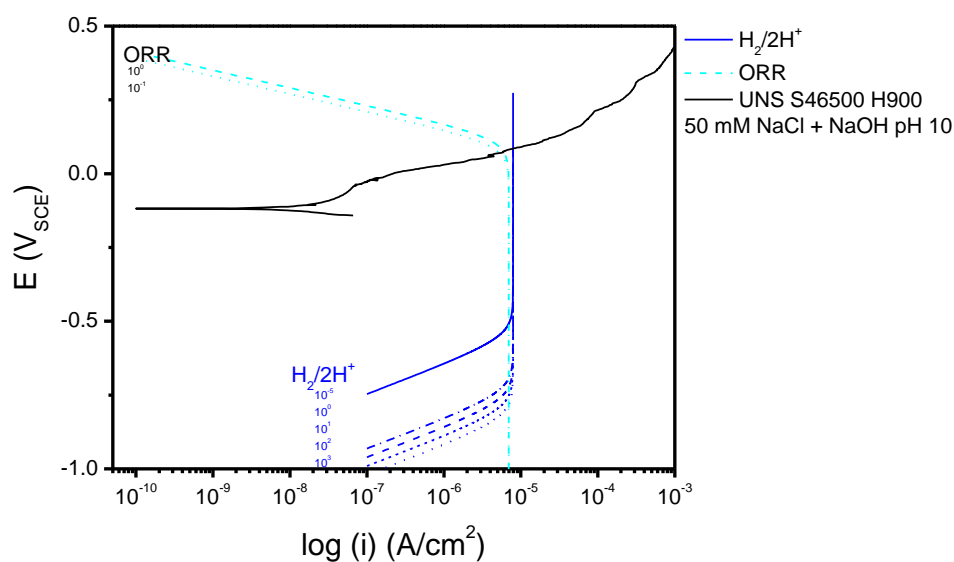


b)

Figure 150. Mixed potential theory model for UNS S46500 As Annealed/CT assuming diffusion limiting x in the SECM is $x = (D_{O_2}t)^{1/2}$, where t is time = 3600s and $D_{O_2} = 1.46 \times 10^{-5} \text{ cm}^2/\text{s}$. Currents for ORR, H/H^+ , and $\text{H}_2/2\text{H}^+$ were calculated using Equation from Ch 3 and stated assumptions, while the anodic scan was measured in 5 mM NaCl + NaOH pH 10 at a scan rate of 0.1667 mV/s from -100 mV vs E_{OCP} to 500 mV vs E_{OCP} . a) Displays both H oxidation currents, while b) only displays H/H^+ .

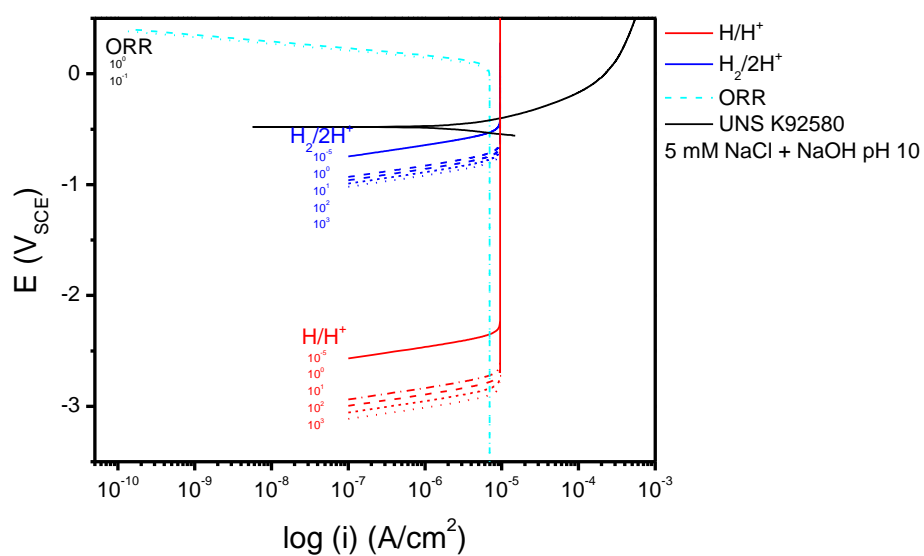


a)

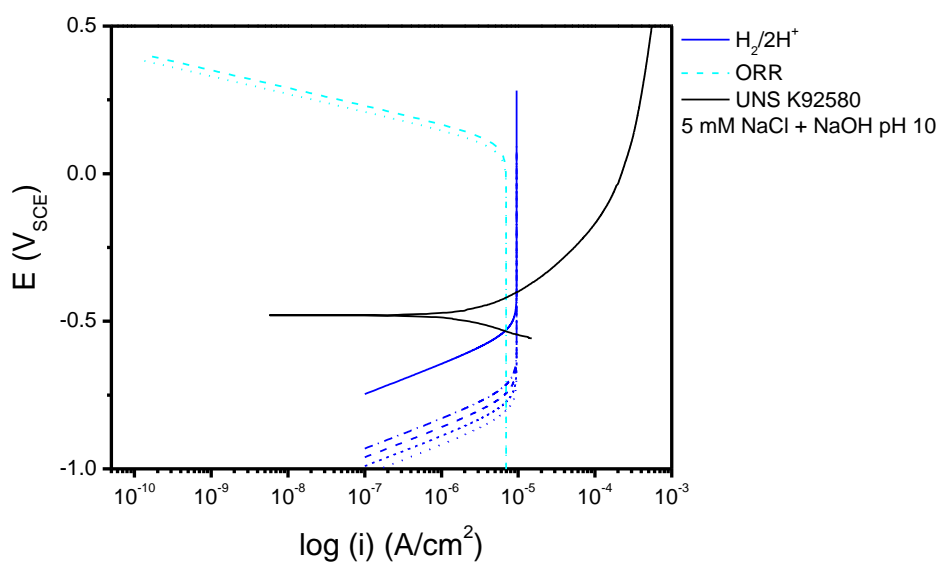


b)

Figure 151. Mixed potential theory model for UNS S46500 H900 assuming diffusion limiting x in the SECM is $x = (D_{O_2}t)^{1/2}$, where t is time = 3600s and $D_{O_2} = 1.46 \times 10^{-5} \text{ cm}^2/\text{s}$. Currents for ORR, H/H^+ , and $\text{H}_2/2\text{H}^+$ were calculated using Equation from Ch 3 and stated assumptions, while the anodic scan was measured in 50 mM NaCl + NaOH pH 10 at a scan rate of 0.1667 mV/s from -100 mV vs E_{OCP} to 500 mV vs E_{OCP} . a) Displays both H oxidation currents, while b) only displays H/H^+ .

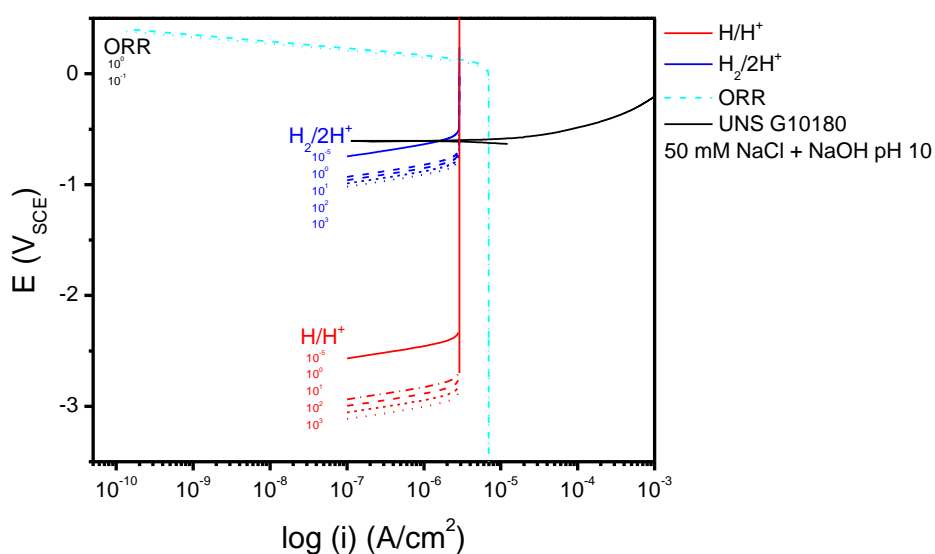


a)

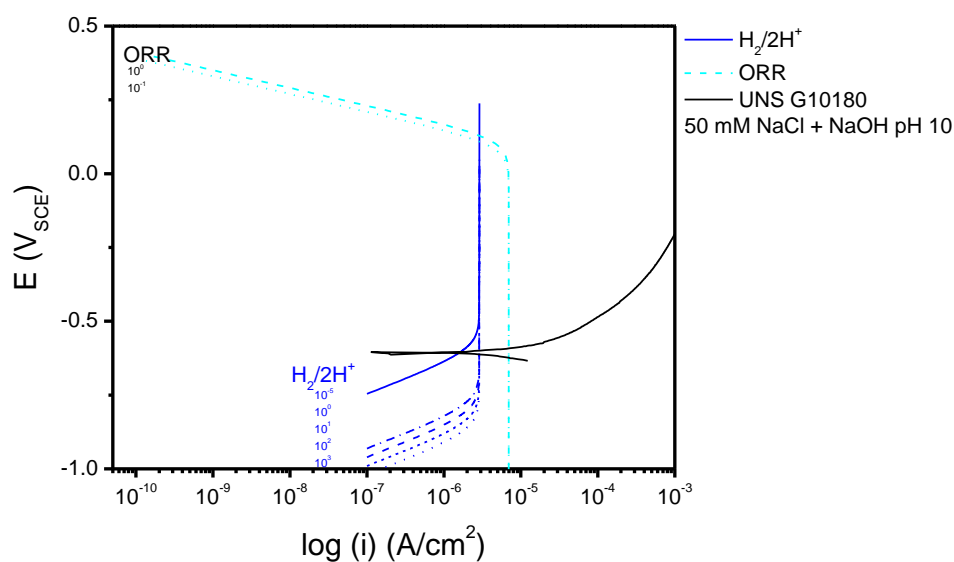


b)

Figure 152. Mixed potential theory model for UNS K92580 assuming diffusion limiting x in the SECM is $x = (D_{O_2}t)^{1/2}$, where t is time = 3600s and $D_{O_2} = 1.46 \times 10^{-5}$ cm²/s. Currents for ORR, H/H^+ , and $H_2/2H^+$ were calculated using Equation from Ch 3 and stated assumptions, while the anodic scan was measured in 5 mM NaCl + NaOH pH 10 at a scan rate of 0.1667 mV/s from -100 mV vs E_{OCP} to 500 mV vs E_{OCP} . a) Displays both H oxidation currents, while b) only displays H/H^+ .



a)



b)

Figure 153. Mixed potential theory model for UNS G10180 assuming diffusion limiting x in the SECM is $x = (D_{O_2}t)^{1/2}$, where t is time = 3600s and $D_{O_2} = 1.46 \times 10^{-5} \text{ cm}^2/\text{s}$. Currents for ORR, H/H^+ , and $H_2/2H^+$ were calculated using Equation from Ch 3 and stated assumptions, while the anodic scan was measured in 50 mM NaCl + NaOH pH 10 at a scan rate of 0.1667 mV/s from -100 mV vs E_{OCP} to 500 mV vs E_{OCP} . a) Displays both H oxidation currents, while b) only displays H/H^+ .

CHAPTER 5. Spatial determination of diffusible hydrogen concentrations proximate to pits formed under atmospheric exposure using the Scanning Kelvin Probe and Scanning Electrochemical Microscope

5.1. Abstract

In UHSS under atmospheric exposure, acid pits formed by the dissolution, hydrolysis, and acidification mechanisms are prone to hydrogen (H) production and uptake. Determination of local uptake and concentration mapping is challenging on small length scales. Diffusible H concentrations ($C_{H,diff}$) were mapped spatially, in proximity to pits formed under 3.9 M $MgCl_2$ atmospherically exposed droplets, on a stainless UHSS using a scanning Kelvin probe (SKP) and scanning electrochemical microscope (SECM). Two conditions of a secondary hardened martensitic stainless steel UNS S46500 were evaluated; the as annealed/CT and H900 temper of Fe-11Ni-12Cr-1Mo-0.005C-0.02Mn (wt%). The calibrations established in Ch 3 and Ch 4 for the comparison of pre-determined uniform diffusible H concentrations calibrated with changes in the surface potential measured by the SKP and the ME probe tip current in the SECM were utilized to estimate diffusible H concentrations spatially proximate to atmospherically pre-exposed and pitted surfaces based on SKP and SECM line and area scans. In general, as exposure time increased, a higher H concentration was detected proximate to the pit. Cross-sections of corrosion damage sites (pits) on UNS S46500 after atmospheric pre-exposure were also characterized using the SKP to determine the distribution of the H concentration along a pit perpendicular to the exposure surface. These methods establish the application of the SKP and SECM of localized H detection to atmospheric exposures.

5.2. Introduction and Background

Atmospheric corrosion of steels, in both field and laboratory settings, has been well quantified but usually focuses on general corrosion rate, morphology, and film type as a function of environmental severity.[1-4] Significant concentrations of H uptake in both field and lab accelerated life tests (LALT) have been realized.[5-7] Material composition, the environment, and exposure severity can critically impact both the amount of corrosion damage and the morphology of attack.[8] In marine atmospheric exposures, relative humidity (RH) and salt deposition density greatly influence corrosion under droplet formation.[9] RH has been shown to be a significant factor for corrosion, specifically with an effect on stress corrosion cracking (SCC).[10] Earlier work on low strength austenitic stainless steels exhibited a maximum susceptibility to SCC at the deliquescence point for the single salt solution, where a saturated salt solution such as NaCl, CaCl₂, MgCl₂, etc. exists, while for seawater it was governed by the deliquescence point of MgCl₂. [11] Corrosion in droplets can take the form of pitting, general, or mixed corrosion, depending on alloy composition and microstructure combined with the severity of the environment.[12-14] As discussed, different corrosion cells can be established in droplets ranging from the Evans cell in a uniformly corroding material such as low alloy steels to acid pits formed by the dissolution, hydrolysis, acidification, and Cl⁻ ingress mechanisms in passive film forming alloys.[12, 15, 16] Within these cells, due to the drop in potential below the H evolution reaction (HER) at the anodic sites, these areas can become “hotspots” for H production and uptake.[17]

Droplet size can also be related to the corrosion rate. Whether the Evans cell dominates, corrosion electrochemistry is somewhat dependent on droplet size and the microstructural length scale.[12, 18] It must also be noted that the deliquescence points of typical salts found in the atmosphere should not be taken as a limit to corrosion or corrosion damage across the samples. As shown by Schindelholz, et al., corrosion can occur at as low as 33 % RH for NaCl and 11 % RH for MgCl₂. [16]

Previous methods for the in-situ study of local corrosion cells during atmospheric exposure include the use of a microelectrode array to monitor, spatially, the net currents and mixed potentials established under a droplet on zinc.[19] The SKP has been employed for in-situ measurements of local mixed electrochemical potential across atmospherically exposed droplets. [20, 21] Techniques with universal pH indicator have been used to determine local pH developments.[13] However, while these measurements provide indications of local potential or pH, they do not provide a method for local or spatial H detection.

5.3. Experimental Procedures

5.3.1. Materials

The material composition for the secondary-hardened martensitic stainless steel (UNS S46500) is given in Table 28 and material properties in Table 29. Samples were tested in both the as annealed/CT and the H900 temper. One advantage of this steel for use with the SKP and SECM measurement techniques is the slow $D_{H,eff}$ for both the as-annealed and H900 temper: $3.1 \times 10^{-9} \text{ cm}^2/\text{s}$ and $6.2 \times 10^{-9} \text{ cm}^2/\text{s}$, respectively (as determined by

thermal desorption spectroscopy). This enables SKP and SECM mapping without substantial outgassing during the transfer time from pre-exposure to initial measurements in the SKP or SECM. A second advantage of UNS S46500 is the low corrosion rates it exhibits in the measurement environment. A third advantage is high $C_{H,Diff}$ due to many low energy trap states.[22]

5.3.2. Electrochemical Evaluation of Droplets

Evaluation of possible droplet electrolytes was carried out through electrochemical experiments. Anodic polarizations of naturally aerated solutions with varied concentrations and varied pH were explored on both UNS S46500 and UNS K92580. Samples of about 500 μm thickness were polished to 1200 grit SiC, rinsed with DI water, degreased with acetone, and dried with compressed air prior to insertion into a 1 cm^2 opening electrochemical flat cell. Anodic polarizations were acquired from -100 mV below E_{OCP} to 500 mV above E_{OCP} at a scan rate of 0.1667 mV/s. Electrochemical tests evaluated both varied chloride concentration solutions in naturally aerated NaCl solutions at a pH of 5.5, with 50 mM, 0.9 M, and 5.3 M and in varied pH solutions of naturally aerated 3.9 M MgCl_2 at pHs values of 2, 5, and 8.

5.3.3. Atmospheric Exposures and Imaging for Corrosion Characterization

Samples of UNS S46500 in both tempers were cut to 500 μm thick disks, ground to 1200 grit SiC polishing paper, rinsed with DI water, dried with compressed air, and degreased with acetone. For exposures, 10 μL deposited droplets of 3.9 M MgCl_2 (the equilibrium salt concentration for the exposure RH selected) were exposed for 48 h to 3 weeks, at a

constant RH of 58 % set by saturated NaBr solution.[23] Pits developed in each droplet within the first 24 h of exposure. For all samples, only one dominant pit formed per droplet was examined. This more concentrated droplet of MgCl_2 was selected for these exposures as previous experiments in this lab at the University of Virginia have shown UNS S46500 was more susceptible to form one dominant pit under these conditions. Pit size and morphology were characterized by optical imaging with 3-D capabilities as well as scanning electron microscopy (SEM).

5.3.4. SKP of Atmospherically Exposed Samples

Pre-corroded samples, exposed under the same conditions as described in section 5.3.3, were removed from the humidity chamber, corrosion products removed mechanically, rinsed with DI water, dried with compressed air, and degreased with acetone prior to measurement in the SKP. Setup and scanning in the SKP followed the procedure established in Ch. 3. Initial line scans were taken across the area exposed under the droplet and near the pit, similar to those previously described for cathodically pre-charged samples (Figure 154). After the initial line scan, an area scan was taken of the droplet area. The area scan took 4 hours to complete, and includes measurements of H outgassed areas, therefore it can only provide a qualitative image of the H uptake spatially across the area pre-exposed under a droplet. Post area scan, a second line scan was taken in the same location as the initial scan 4 h after removing the sample from its atmospheric exposure, for comparison.

To explore the effects of time post-charging, UNS S46500 H900 samples pre-exposed for 14 days were examined. Samples were pre-corroded as described previously with a 3.9 M MgCl_2 10 μL droplet. After exposure, line and area scans were taken in the same manner as above, however, a second area scan and a third line scan were taken at 5 days post-exposure. During this time the sample was kept in a dry, lab air environment.

A cross-section method was also employed with the SKP to determine the H distribution perpendicular to the atmospheric pre-exposed and pitted surface. A 2 cm thick sample of UNS S46500 in the H900 temper was prepared in the same manner and exposed for 14 days with a 3.9 M MgCl_2 droplet at 58% RH. The sample was then cleaned and sectioned parallel to the pit length. A 1 mm thick section, as shown in Figure 155, was taken around the pit. The time between removal of the sample from the atmospheric exposure and measurement in the SKP was 15 min. An area scan, 1900 μm^2 with step size of 31.75 μm , was acquired along the edge from which the pit initiated with depth into the sample, Figure 155-b. As the section was taken near, but outside of the pit, the SKP potentials measured in the area scan are not influenced by sample topography.

As a comparison of droplet electrochemical cell type, a sample of UNS S46500 was exposed to a 1 M HCl 4 μL droplet at a high humidity (98 %RH) nitrogen purged atmosphere for 1 week. This environment is expected to produce uniform corrosion rather than pitting underneath the droplet as it could easily breakdown the passive oxide on the stainless steel.

5.3.5. SECM of Atmospherically Exposed Samples

For SECM measurements, disks of UNS S46500 were flush mounted in epoxy, polished to 3 μm diamond paste, rinsed with DI water, degreased with ethanol, dried with compressed air, and exposed under atmospheric conditions as described in section 5.3.3. Pre-corroded samples were removed from the humidity chamber, corrosion products removed mechanically, rinsed with DI water, dried with compressed air, and degreased with acetone prior to measurement in the SECM. Setup and scanning in the SECM followed the procedure for redox competition mode ($\text{redox}_{\text{ME}}/\text{redox}_{\text{WE}}$) established in Ch. 4. Time between removal of the sample from pre-exposure environments and initial line or area scan measurements in the SECM was 30 min. Area scans were then taken in 5mM NaCl + NaOH solution at a pH of 10 across the area exposed under the droplet with a step size of 50 μm and an average width and length of 4 mm. Larger scans were not taken due to the physical constraints of the SECM cell and sample setup. Area scans took 2-4 hours to complete, and include measurements of H outgassed areas, therefore, as in the SKP, they can only provide a qualitative image of the H uptake. As diffusion of O_2 and H^+ in the SECM electrolyte occurs at a much faster rate than in the steel, as well as the influence of mixing from the probe tip, often only one significant area scan could be acquired per sample.

5.3.6. Diffusion modeling of H from an uptake “hot spot”

Analytical diffusion profiles were calculated to explore the effects of both H diffusion in the steel away from the pre-corroded pit, and H^+ diffusion in solution away from the pit. Calculations were made using the solution for spherical diffusion in an infinite plane,

with $D_{h,eff}$ in the steel as $6.2 \times 10^{-9} \text{ cm}^2/\text{s}$ and the diffusion of H^+ in an aqueous chloride solution to be $4.4 \times 10^{-5} \text{ cm}^2/\text{s}$. The time applied was a 14 day exposure, during which a $40 \text{ }\mu\text{m}$ hemispherical pit formed. The pit was assumed a constant spherical source of H or H^+ for these calculations.

5.4. Experimental Results

5.4.1. Electrochemical Droplet Analysis

A comparison of anodic scans in varied chloride concentration solutions of both UNS S46500 and UNS K92580 are plotted in Figure 157. As can be seen for both materials, as the chloride concentration decreases, the E_{OCP} increases. Also, the anodic dissolution increases with increasing chloride content suggesting a more severe corrosion environment. A second set of anodic polarizations investigating the effect of pH are plotted in Figure 158. For UNS S46500, as the pH decreased, the E_{OCP} was shown to decrease and the anodic current density increased. However, for UNS K92580, as pH decreased, the E_{OCP} increased. Also on UNS K92580, no significant changes in the anodic current density were seen with a change in pH in the MgCl_2 solutions.

5.4.2. Corrosion Evaluation of Droplets through Imaging

The size and morphology of pits formed under MgCl_2 droplets can be seen in the optical images and SEM micrographs in Figure 159. Pits developed under the droplets ranging in depth from about $25 \text{ }\mu\text{m}$ for 24 hour exposures to $40 \text{ }\mu\text{m}$ for 2 week exposures and diameters of about $40 \text{ }\mu\text{m}$ to $160 \text{ }\mu\text{m}$.

5.4.3. SKP of Atmospherically Pitted Samples

Line scans of atmospherically pre-exposed UNS S46500 in the as annealed/CT and H900 condition were taken at both 5 min and 4 h post-exposure period in air at 57% RH for cleaned specimens. SKP scans are shown for samples exposed for 2 and 14 days in Figure 160 and Figure 161. SKP maps were also taken, however, these are meant as an indicator, not a direct measurement, as significant outgassing of H can occur during the 4 h measurement period (Figure 160 and Figure 161). The initial scan shows a decrease in the SKP potential measured near the area of the pit, indicative of a locally enhanced H concentration. The area scan shows a similar trend as the lowest potentials are detected near the pit area and are higher beneath other locations of the droplet, as well as outside the area exposed to the droplet. The second line scan, taken 4 h post-exposure, displays a rise in SKP potential for all samples tested, specifically above the pre-charged (pre-exposed) areas, indicative of H degassing from the sample with time.

The effects of time post-exposure were explored for longer lengths of time, 5 days, and results are plotted in Figure 162. Over the 5 day period, significant changes in the potential measured away from the pit can be seen, however, near the pit, there still remains a small depression in potential, which results in an increase of the $C_{H,Diff}$ locally by about 1.8 wppm. However, this could be due to a morphological effect, possibly scanning over the pitted region as the SKP is positioned manually.

For comparison, sectioned samples were examined to determine the H profile perpendicular to the atmospherically pre-exposed surface. SKP area scans of a UNS

S46500 H900 temper sample exposed at 58 %RH for 14 days with a 10 μ L 3.9 M MgCl_2 droplet are shown in Figure 163. Both the SKP potential measured and the sample height are shown, displaying that the potential measured near the pit is unaffected by sample topography. The section was taken just outside the pit, as shown in Figure 155, such that height variations would not influence the SKP potential. The area scan of the SKP potential displays an approximately hemispherical shape to the H affected profile taken around the pit. However, this spread in SKP potential change near the pre-exposed surface suggests the H affected profile is not solely due to diffusion of H in the metal away from the pit. The change in potential along the surface could be due to the acidity spread under the droplet during exposure. Also, a second section of a sample prepared in the same manner, but not atmospherically exposed, was taken for background measurements. Line scans from the uncharged edge, into the depth of the sample are shown in Figure 163-b and display no significant changes in SKP potential measured with depth.

As comparison to an atmospherically exposed and un-pitted sample with expected H uptake, line scans of atmospherically pre-exposed UNS S46500 in the H900 condition were taken at both 5 min and 4 h after exposure to 1 M HCl droplet for 1 week. SKP line and area scans are plotted in Figure 164. Again, the SKP area map (Figure 164-b) is meant as an indicator, not a direct measurement of H as significant outgassing can occur during the measurement time period. The initial scan shows a decrease in the SKP potential measured across the area pre-exposed to the HCl droplet, indicative of enhanced H concentration. Line scans display a more uniform concentration underneath the

droplet, rather than a locally enhanced area as in the case of the pitted exposures, exemplifying the capability of the SKP to detect H from different atmospheric electrochemical cells established within droplets.

5.4.4. SECM of Atmospherically Pitted Samples

Area scans of atmospherically pre-exposed UNS S46500 in the as annealed/CT condition were taken at 30 min post-exposure period in 5 mM NaCl + NaOH pH 10 solution in redox competition mode ($i_{\text{redox,ME}}/i_{\text{redox,WE}}$) and are plotted in Figure 165 - Figure 167. SECM scans are shown for samples exposed for 7, 14, and 21 days with a 3.9 M MgCl_2 droplet. For the sample exposed at 7 days, the pitted area under the pre-exposed droplet shows an increase in normalized $i_{\text{ORR,ME}}$. However, scans of samples from droplet exposures for 2 and 3 weeks show a decrease in the $i_{\text{ORR,ME}}$. One explanation for this suggests that the morphology of the pit dominates the detection at the tip rather than the H concentration in the 1 week exposure. As the SECM scans over a pit in the surface, diffusion is enhanced by the extra electrolyte, therefore an increase in the $i_{\text{ORR,ME}}$ would be expected (Figure 168). However, as pits in these samples are considered hot spots for H uptake, the H enhanced ORR occurring at the surface of the pit, as seen in pre-charged samples in Ch. 4, would be in competition with the $i_{\text{ORR,ME}}$, and therefore a drop in current would be expected (Figure 168). The difference in behavior between the 1 week test and 2 and 3 week tests could be explained by an insufficient H concentration at the pit in the 1 week test. As the time to initial measurement in the SECM is 30 min, by the time of measurement, significant H desorption can occur such that the $i_{\text{H,ox}}$ does not dominate the reactions at the sample surface. However for the 2 and 3 week tests, as they

were exposed for longer time periods, had H retained at lower depths and thus would have an increased surface concentration of H at the time of measurement significant enough to overcome the effect on the $i_{\text{ORR,ME}}$ due to the topography and subsequent increased O_2 diffusion.

5.4.5. H Diffusion Analysis

Analytical diffusion calculations were performed to explore the movement of H within the UHSS during the exposure period and H^+ within the droplet. The diffusion rate of H^+ in solution, $4.4 \times 10^{-5} \text{ cm}^2/\text{s}$, is almost 4 orders of magnitude faster than the $D_{\text{H,eff}}$ in the steel, $6.2 \times 10^{-9} \text{ cm}^2/\text{s}$, such that over the 14 day exposure, a spread of acid Cl^- from the pit area and potential drop facilitated proton reduction and H uptake on the otherwise passive surface. The decrease in SKP potential (Φ) outside of the pitted area to a greater distance than expected in the SKP cross section in Figure 163 could be due to the acidity spread and subsequent proton reduction across the surface as seen in the analytical diffusion profile in Figure 169.

5.5. Discussion

5.5.1. Advantages/ Limitations of H Detection Atmospherically in the SKP and SECM

As discussed in chapters 3 and 4, the same advantages and disadvantages exist for measurement of pre-exposed atmospheric samples in both the SKP and SECM. However, in the previous chapters, the amount of pre-charged $C_{\text{H,Diff}}$ was controlled by electrochemical uniform pre-charging. In atmospheric exposures, this quantity is

unknown, and often flirts with detection limits in both the SKP and SECM. In both cases, the SKP and SECM were used to detect spatially local enhancement of hydrogen concentrations, displaying the advantages of these techniques over those applied previously for H research.

Another complication that arises with atmospheric exposures is the subsequent sample morphology due to corrosion and the effect this can have on both the SKP potential and the SECM probe tip current. Examples of this were seen in both studies, in the SKP, where pit morphology may have affected the SKP potential 5 days after the pre-exposure in Figure 162. In this instance, as the distance increased between the probe tip and sample surface, due to the pit, a drop in potential was seen and is more likely due to the sample morphology rather than residual H at 5 days post-exposure. Similar results were seen in the SECM where samples pre-exposed for 1 week did not display significant H concentrations to overcome the effects of topography, whereas they did for 2 and 3 week exposures (Figure 165 - Figure 167). Further research into deconvolution of the effects of topography from the H effects on either SKP potential or $i_{\text{ORR,ME}}$ in the SECM are necessary in order to obtain fully quantitative results of H concentrations from atmospheric exposures.

5.6. Future Work

As mentioned above, focus on the study of the effects of sample topography is necessary to understanding the differences in both the SKP potential and SECM $i_{\text{ORR,ME}}$ spatially across an atmospherically exposed sample. If the known and possibly calibrated

influence of these topographical effects could be established, then the true H effected profiles and area scans could be determined for each technique and quantification of H using calibration from uniformly pre-charged specimens would be more quantitatively applicable. These techniques, including H quantification, could be applied at an even more localized scale using atomic force microscopy (AFM) modified to SKPFM or SECM-AFM. Expansion to measurement of H concentrations at crack tips could greatly enhance the field of hydrogen study.

To determine a recommendation for further optimization and application of these techniques for future measurement of H uptake at the local scale, a comparison of technique type, scale resolution, H detection resolution, and modes of operation (in solution/ dry) have to be taken into consideration. H measurement techniques applied in this dissertation are compared in Table 1. As established in Chapter 2, TDS measurements applied to the local H uptake scale need a secondary validation or comparison, such as mass loss or other corrosion severity identifier, to gain significant insight into the local H production and uptake under atmospheric exposure conditions. Advantages of the SKP and SECM over the more traditional TDS, barnacle cell, and LECO methods are evident in both the local scale detection capabilities, at the micrometer vs. millimeter length scale, the ability of the SKP and SECM to map spatially local hydrogen concentrations, and as mentioned above, the ability to scale both techniques to the sub-micrometer level with the application of SKPFM or SECM-AFM. However, it is also important to note here the difficulties and drawbacks of both techniques. As discussed in detail in Chapters 3 and 4, the SKP and SECM H

measurements are highly dependent on the near surface hydrogen concentration and the corrosion rates at the surface. The SKP is somewhat advantageous over the SECM with respect to this, as measurement setup times are shorter, thus higher H concentrations are present in the sample at the time of measurement. A second advantage of the SKP over the SECM is that measurements are taken in a humid atmosphere rather than immersed in solution. Detrimental effects of the solution in the SECM include possible enhanced corrosion at the sample surface, thus increasing i_{corr} above $i_{\text{L,Hox}}$. Also, as discussed previously, H^+ and O_2 diffusion in solution combined with stirring of solution due to tip movement decrease the resolution capabilities of the SECM. Therefore, in terms of a recommendation for future H detection at the local scale, advancement and continued optimization of the SKP would be the most viable option of the methods applied in this work.

5.7. Conclusions

- The SKP can be utilized to map H concentrations with spatial resolution once the SKP potential is calibrated versus known pre-charged H concentrations.
 - H effected potentials were determined both spatially across a pre-exposed surface and with depth detection through cross sectioning.
 - Similar temporal effects on SKP potentials due to H desorption were seen in pre-exposed atmospheric samples as in H pre-charged samples in Ch. 3.
- The SECM can be utilized to map H concentrations with spatial resolution once the SECM $i_{\text{ORR,ME}}$ is calibrated versus known pre-charged H concentrations.

- Both the SKP and SECM have been applied for the detection of mapping H produced from an atmospherically pre-corroded pit.
- Further investigation into topographical effects on both the SKP potential and SECM $i_{\text{ORR,ME}}$ is necessary for H quantification of atmospherically pre-exposed samples.

5.8. References

1. Baker, E.A., ed. S.W. Dean and T.S. Lee, *Long-Term Corrosion Behavior of Materials in the Marine Atmosphere*, in *Degradation of Metals in the Atmosphere*, ASTM, Editor. 1988: Philadelphia. p. 125-144.
2. Li, S.J., et al., *Evaluation of delayed fracture property of outdoor-exposed high strength AISI 4135 steels*. Corrosion Science, 2010. **52**(10): p. 3198-3204.
3. Townsend, H.E., *Effects of alloying elements on the corrosion of steel in industrial atmospheres*. Corrosion, 2001. **57**(6): p. 497-501.
4. Townsend, H.E., *Atmospheric corrosion performance of quenched-and-tempered, high-strength weathering steel*. Corrosion, 2000. **56**(9): p. 883-886.
5. Akiyama, E., et al., *Evaluation of hydrogen entry into high strength steel under atmospheric corrosion*. Corrosion Science, 2010. **52**(9): p. 2758-2765.
6. Akiyama, E., et al., *Hydrogen entry into Fe and high strength steels under simulated atmospheric corrosion*. Electrochimica Acta, 2011. **56**(4): p. 1799-1805.
7. Schaller, R.F., S.M. Al-Ghamdi, and J.R. Scully. *Hydrogen Uptake in an Ultra-High Strength Steel Exposed to Laboratory Accelerated Life Test Environments; Preliminary Findings*. in *NACE DoD Corrosion Conference*. 2011. Palm Springs, CA.
8. Kearns, J.R., M.J. Johnson, P.J. Park, *The Corrosion of Stainless Steels in the Atmosphere*, in *Degradation of Metals in the Atmosphere*. 1988, American Society for Testing and Materials: Philadelphia, PA. p. 35-51.
9. Leygraf, C. and T.E. Graedel, *Atmospheric corrosion*. The Electrochemical Society series. 2000, New York: Wiley-Interscience. xii, 354 p.
10. S. Shoji, et al., *Effects of Relative Humidity on Atmospheric Stress Corrosion Cracking of Stainless Steels*. Corrosion Engineering, 1986. **35**(10): p. 559-565.
11. Shoji, S., N. Ohnaka, *Effects of Relative Humidity and Kinds of Chlorides on Atmospheric Stress Corrosion Cracking of Stainless Steel at Room Temperature*. Corrosion Engineering, 1989. **38**(2).
12. Li, S.X. and L.H. Hihara, *Atmospheric-Corrosion Electrochemistry of NaCl Droplets on Carbon Steel*. Journal of the Electrochemical Society, 2012. **159**(11): p. C461-C468.
13. Azmat, N.S., et al., *Corrosion of Zn under acidified marine droplets*. Corrosion Science, 2011. **53**(4): p. 1604-1615.
14. Li, S.X. and L.H. Hihara, *Atmospheric corrosion initiation on steel from predeposited NaCl salt particles in high humidity atmospheres*. Corrosion Engineering Science and Technology, 2010. **45**(1): p. 49-56.
15. Evans, U.R., *The corrosion of metals*. 1924, New York: Longmans Arnold. xi, 212 p.
16. Schindelholz, E., L.K. Tsui, and R.G. Kelly, *Hygroscopic Particle Behavior Studied by Interdigitated Array Microelectrode Impedance Sensors*. Journal of Physical Chemistry A, 2014. **118**(1): p. 167-177.
17. Switzer, M., *Use of crevice scaling laws to investigate local hydrogen uptake in rescaled model pits*, in *Materials Science and Engineering*. 2003, University of Virginia: Charlottesville.
18. Risteen, B.E., E. Schindelholz, and R.G. Kelly, *Marine Aerosol Drop Size Effects on the Corrosion Behavior of Low Carbon Steel and High Purity Iron*. Journal of the Electrochemical Society, 2014. **161**(14): p. C580-C586.
19. Muster, T.H., et al., *The atmospheric corrosion of zinc: The effects of salt concentration, droplet size and droplet shape*. Electrochimica Acta, 2011. **56**(4): p. 1866-1873.
20. Neufeld, A.K., et al., *The initiation mechanism of corrosion of zinc by sodium chloride particle deposition*. Corrosion Science, 2002. **44**(3): p. 555-572.

21. Chen, C., C.B. Breslin, and F. Mansfeld, *Scanning Kelvin probe analysis of the potential distribution under small drops of electrolyte*. Materials and Corrosion-Werkstoffe Und Korrosion, 1998. **49**(8): p. 569-575.
22. Ifergane, S., Sabatani, E., Carmeli, B., Barkay, Z., Ezersky, V., Beeri, O., and Eliaz, N., *Hydrogen diffusivity measurement and microstructural characterization of Custom 465 stainless steel*. Electrochimica Acta, 2015. **178**: p. 494-503.
23. M, A.S.T., *Standard Practice for Maintaining Constant Relative Humidity by Means of Aqueous Solutions*. 2012, ASTM International: West Conshohocken, PA.
24. *Alloy Data - Custom 465 All*. 1996, C.T. Corporation: Reading, PA.
25. Gonzalez-Garcia, Y., et al., *Scanning electrochemical microscopy for the investigation of localized degradation processes in coated metals*. Progress in Organic Coatings, 2010. **69**(2): p. 110-117.
26. Crank, J., *The mathematics of diffusion*. 1956, Oxford,: Clarendon Press. 347 p.

5.9. Tables:

Table 28. UNS S46500 Composition (wt. %).[24]

Material	Fe	C	Mn	Si	P	S	Cr	Ni	Mo	N	Ti	Co
UNS S46500 ^a	Bal.	0.005	0.02	0.02	0.002	0.002	11.50	11.04	0.94	0.002	1.54	-

^aCustom 465™ H900 temper

Table 29. UNS S46500 Material Properties.[24]

Temper	Yield Strength	Tensile Strength	Elongation	Reduction of Area	Rockwell Hardness C
UNS S46500 Annealed/CT	772 MPa	951 MPa	20 %	75 %	29.5
UNS S46500 H900	1703 MPa	1779 MPa	14 %	51 %	51

Table 30. Comparison of absorbed H concentration detection and quantification characterization techniques applied in this dissertation.

Technique	Diffusible H Concentration	Total H Concentration	Lateral Resolution	Depth Resolution	Temporal Resolution	Detection Limit (wt. ppm)
Barnacle Cell	Yes	No	No, > mm scale	Possible via serial grinding	No	2
TDS	Yes	Possible	No	Possible via serial grinding	No	~0.01 – 0.05
LECO	No	Yes	N/A	Possible via serial grinding	No	~1
SKP	Yes	No	Yes, Tip dependent (SKP: 100s μm scale, SKPFM: <30nm)	Possible via cross sectioning	Yes	0.01*
SECM	Yes	No	Yes, ME tip dependent (μm scale)	Possible	Yes	unestablished

TDS (Thermal Desorption Spectroscopy), LECO (Inert Gas Fusion Thermal Conductivity), SKP (Scanning Kelvin Probe), and SECM (Scanning Electrochemical Microscopy)

* 0.01 wppm is the detection limit in Pd. In steel, may be higher due to possible influence of corrosion at the surface.

5.10. Figures:

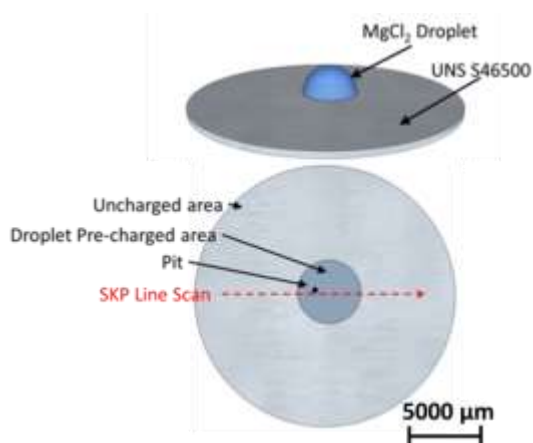


Figure 154. Schematic of droplet exposure and SKP line scan post exposure.

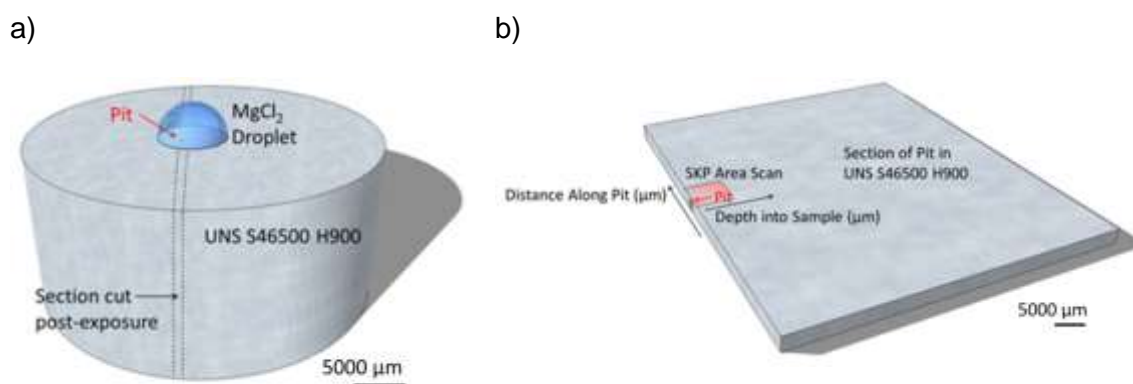


Figure 155. Schematic of UNS S46500 H900 sample a) atmospheric pre-exposure and b) SKP scan shown on section taken around pit, post-exposure.

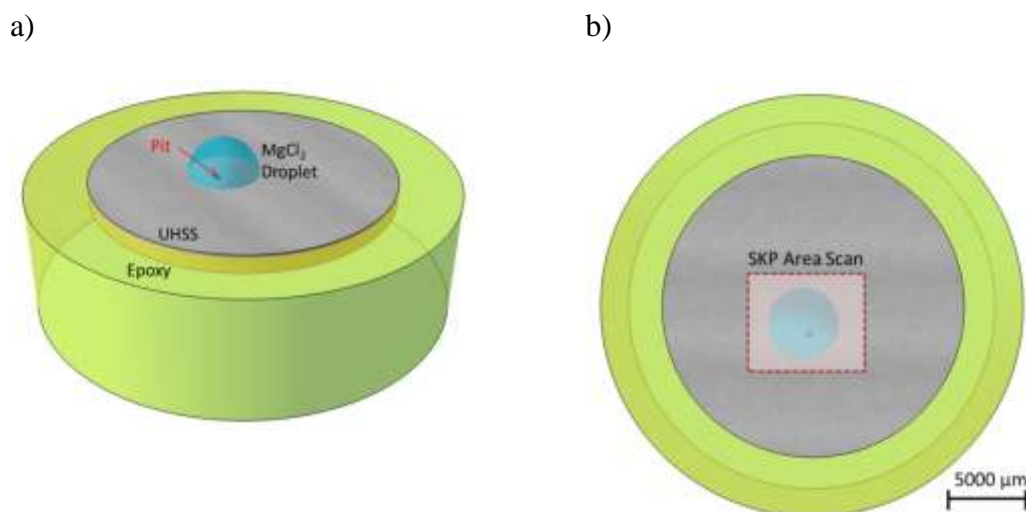


Figure 156. Schematic of UHSS sample a) atmospheric pre-exposure and b) SECM scan area post-exposure.

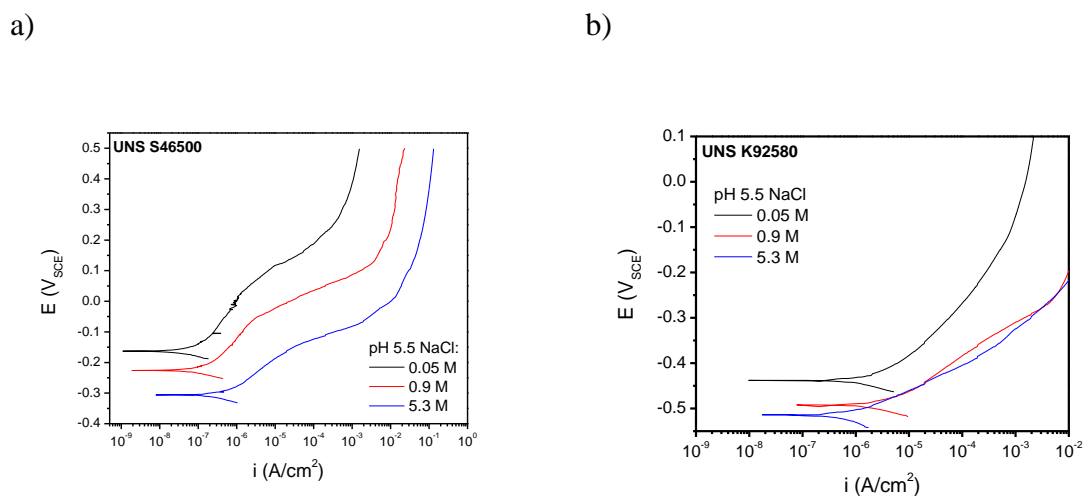
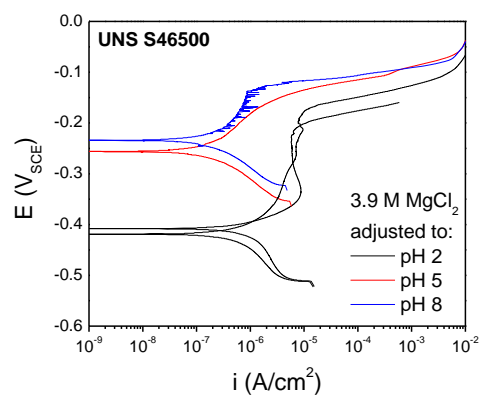


Figure 157. Anodic polarizations, from -100 mV vs EOCP to +500 mV vs EOCP in 5.5 pH NaCl solution at various concentrations; 0.05, 0.9, and 5.3 M NaCl, a) UNS S46500 H900 and b) peak aged UNS K92580.

a)



b)

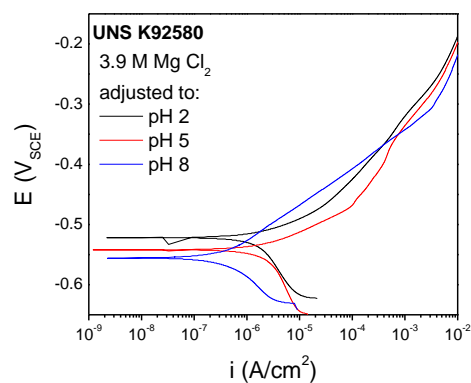


Figure 158. Anodic polarizations, from -100 mV vs E_{OCP} to +500 mV vs E_{OCP} in 3.9 M MgCl_2 adjusted to various pH; 2, 5, and 8 for a) UNS S46500 H900 and b) peak aged UNS K92580.

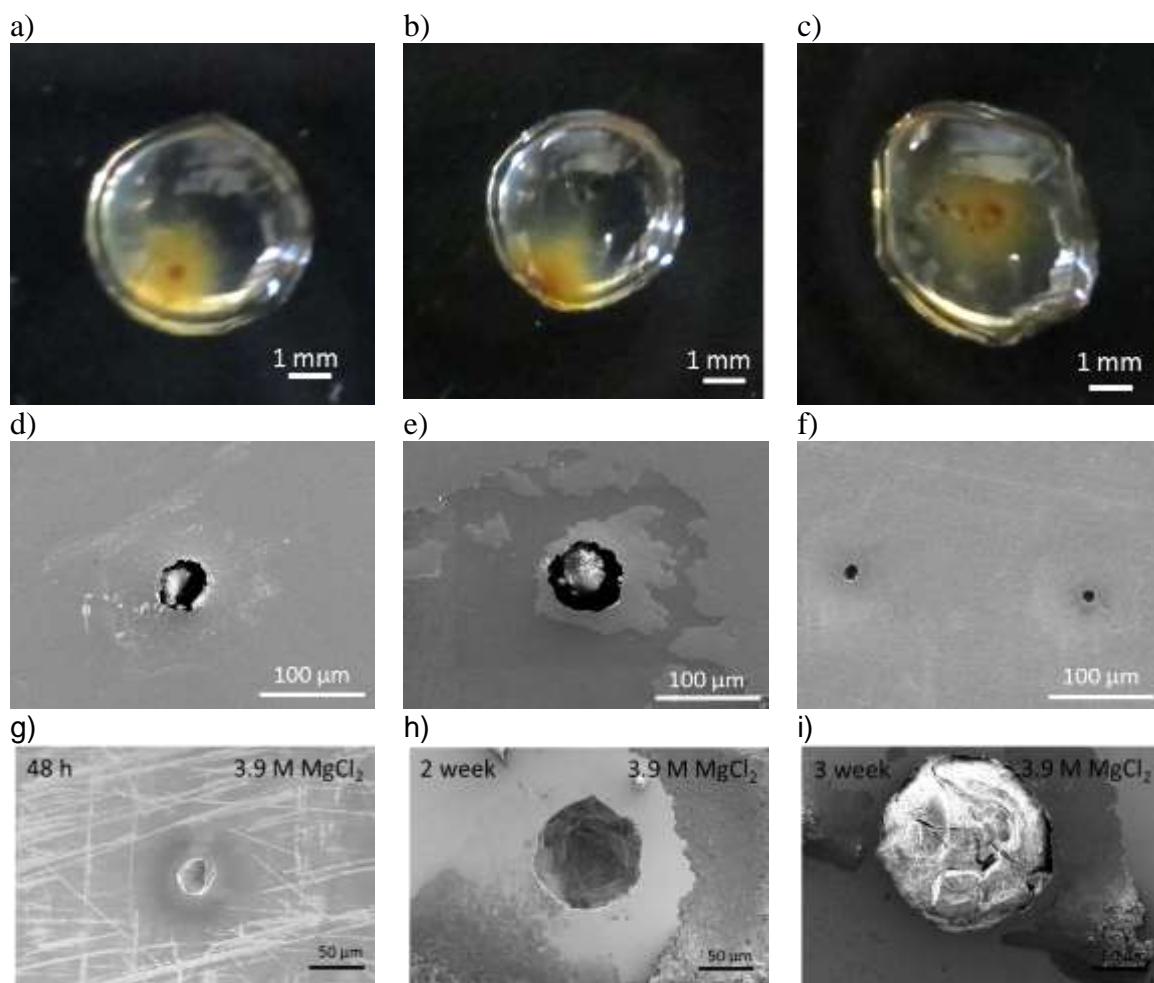


Figure 159. UNS S46500 H900 exposed to 3.9 M MgCl₂ 10 μL droplet at 58% RH for 48 h a) optical and d) SEM image, 1 week b) optical e) SEM image, and 2 weeks c) optical and f) SEM image. A second set of SEM images of samples of UNS S46500 H900 displaying similar exposures of a) 48 h, b) 2 weeks, and c) 3 weeks.

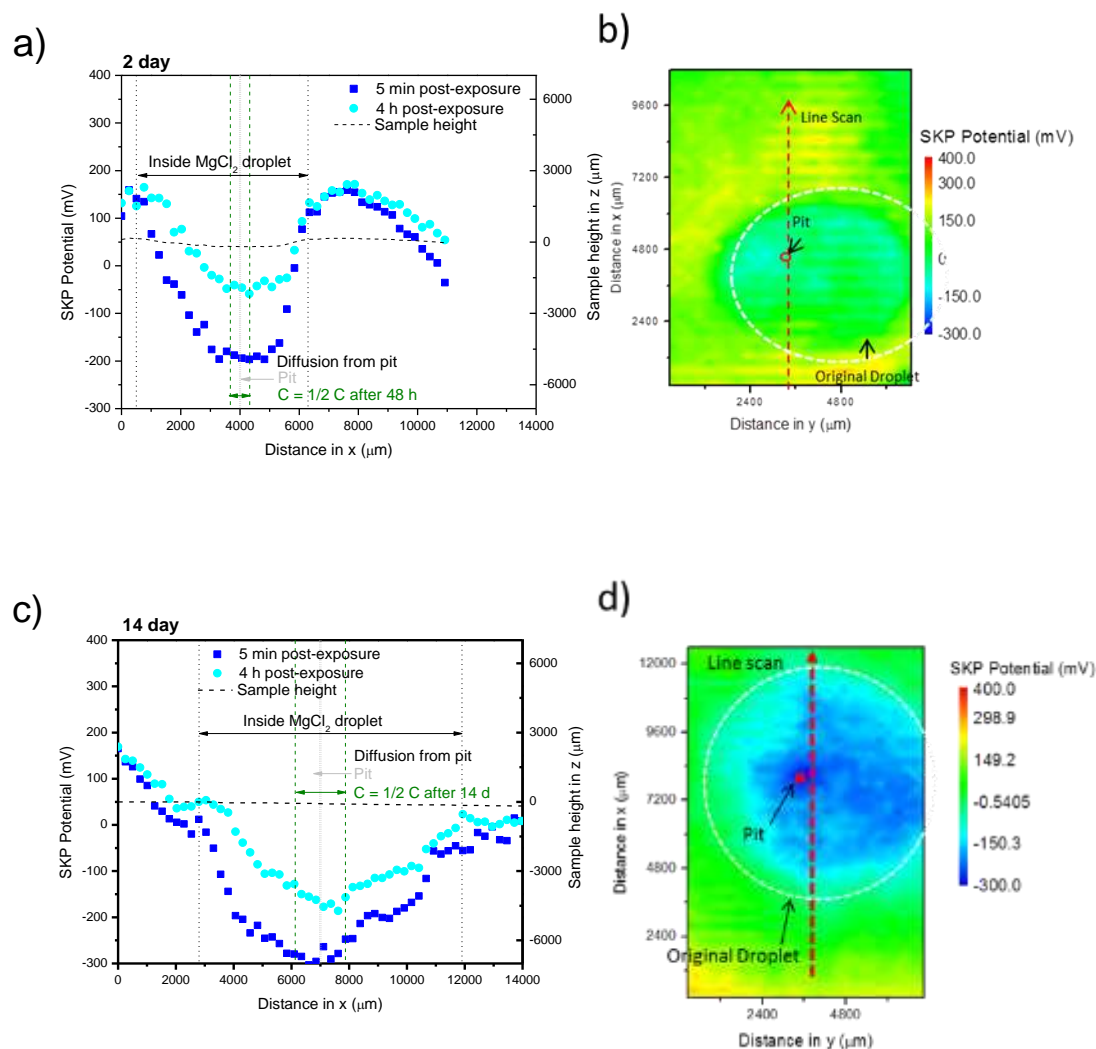


Figure 160. a) SKP line scans across an area of UNS S46500 H900 (a and c) pre-exposed for 2 and 14 days at 58% RH with a 3.9 M MgCl_2 , 10 μL droplet. Scans were taken 5 min post-exposure and 4 h post-exposure near the pit formed underneath the droplet. SKP area scan of pre-exposed UNS S46500 (b and d) H900. NB: As the area scan takes 4 hours to complete, it is meant only as an indicator of droplet/pit location, as significant outgassing of H can occur over this time period and measurements cannot be directly correlated to H concentrations.

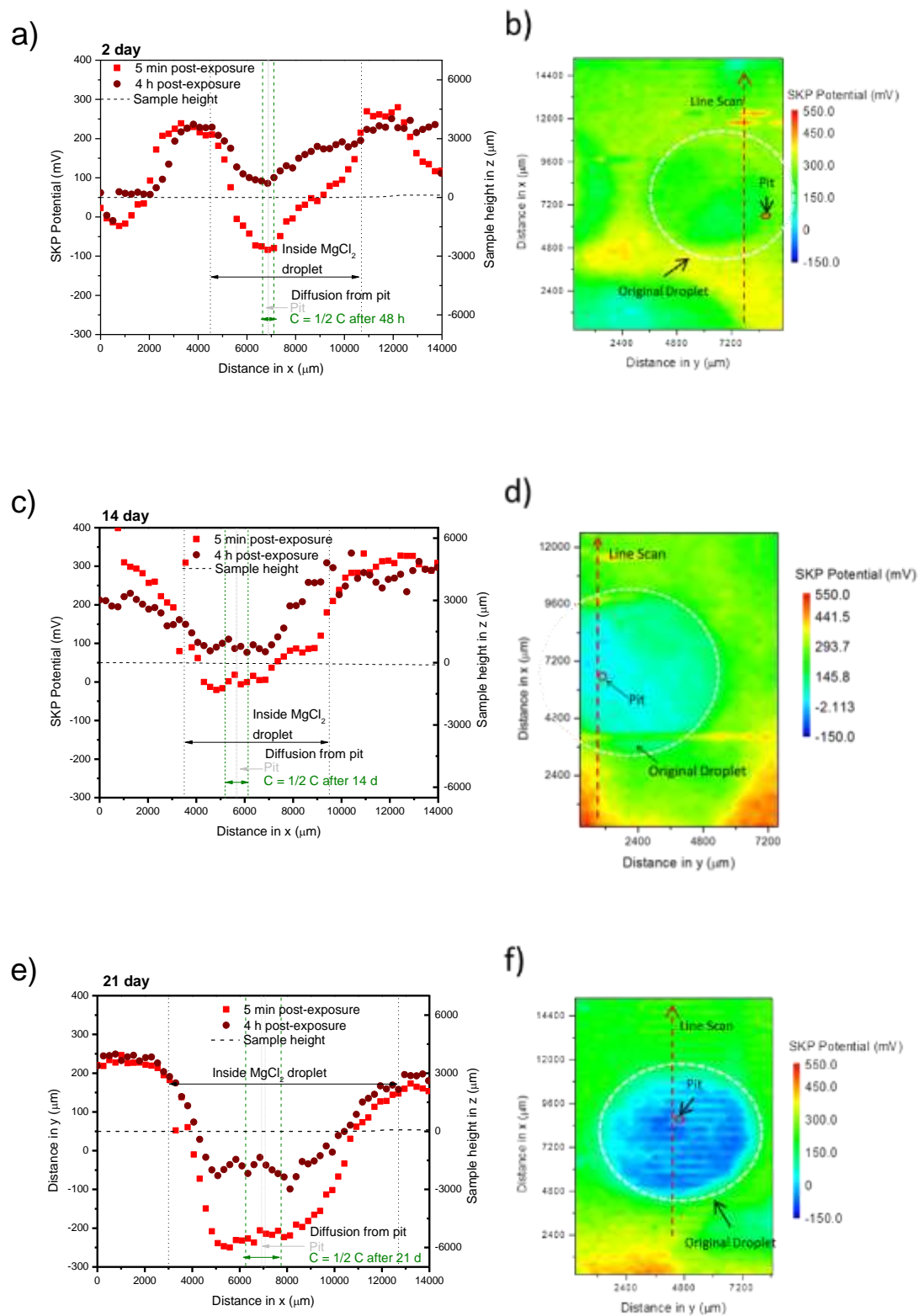


Figure 161. a) SKP line scans across an area of UNS S46500 as annealed/CT (a, c, and

e) pre-exposed for 2, 14 and 21 days at 58% RH with a 3.9 M MgCl_2 , 10 μL droplet. Scans were taken 5 min post-exposure and 4 h post-exposure near the pit formed underneath the droplet. SKP area scan of pre-exposed UNS S46500 (b, d, and f) as annealed/CT. *NB: As the area scan takes 4 hours to complete, it is meant only as an indicator of droplet/pit location, as significant outgassing of H can occur over this time period and measurements cannot be directly correlated to H concentrations.*

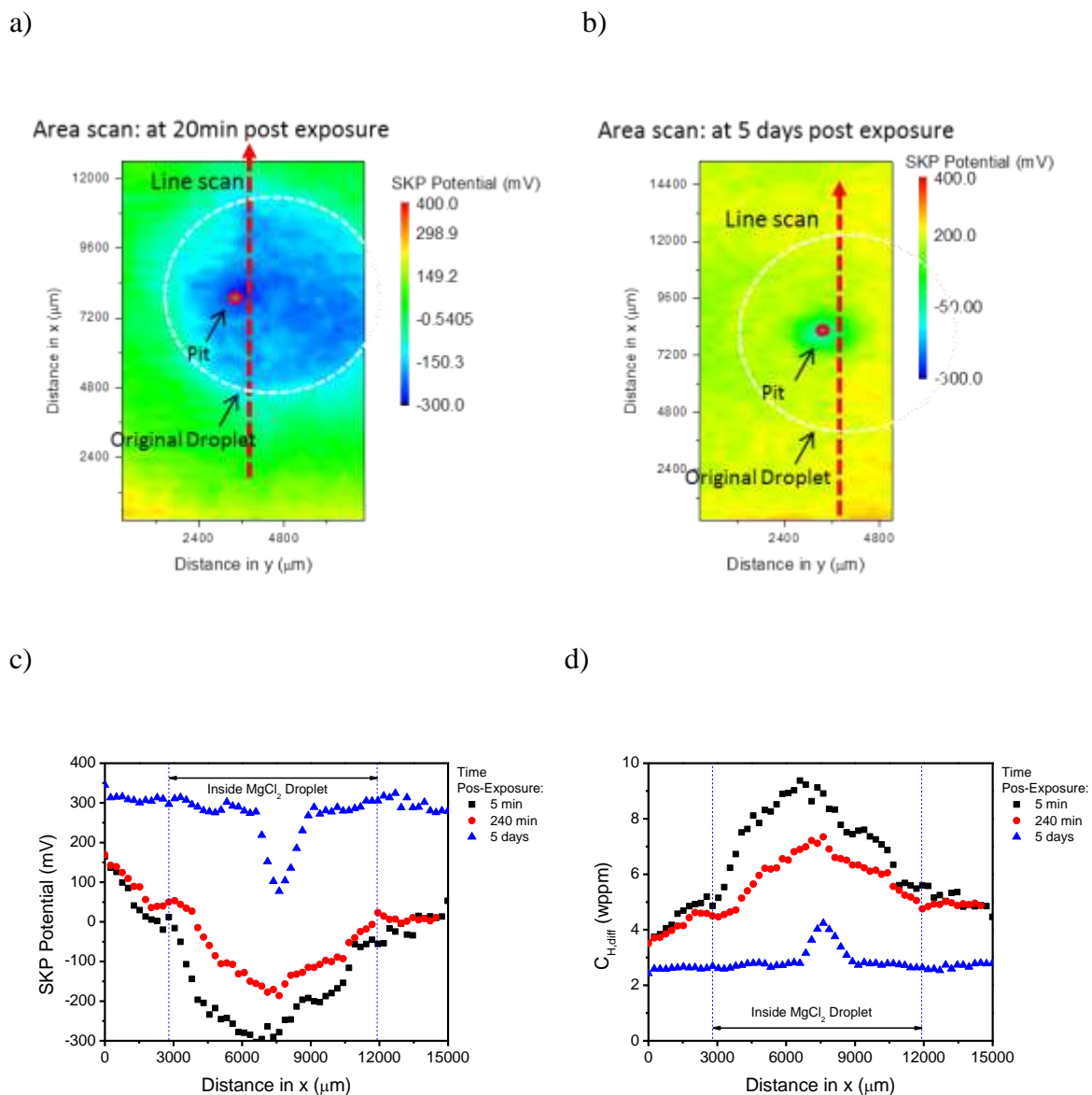


Figure 162. SKP area scans across an area of UNS S46500 H900 (Sample 1) pre-exposed for 14 days at 58% RH with a 3.9 M $MgCl_2$, 10 μL droplet. Scans were taken a) 20 min post-exposure and b) 5 days post-exposure near the pit formed underneath the droplet. C) SKP line scans of pre-exposed UNS S46500 H900 at various times post-exposure. *NB: As the area scan takes 4 hours to complete, it is meant only as an indicator of droplet/pit location, as significant outgassing of H can occur over this time period and measurements cannot be directly correlated to H concentrations.*

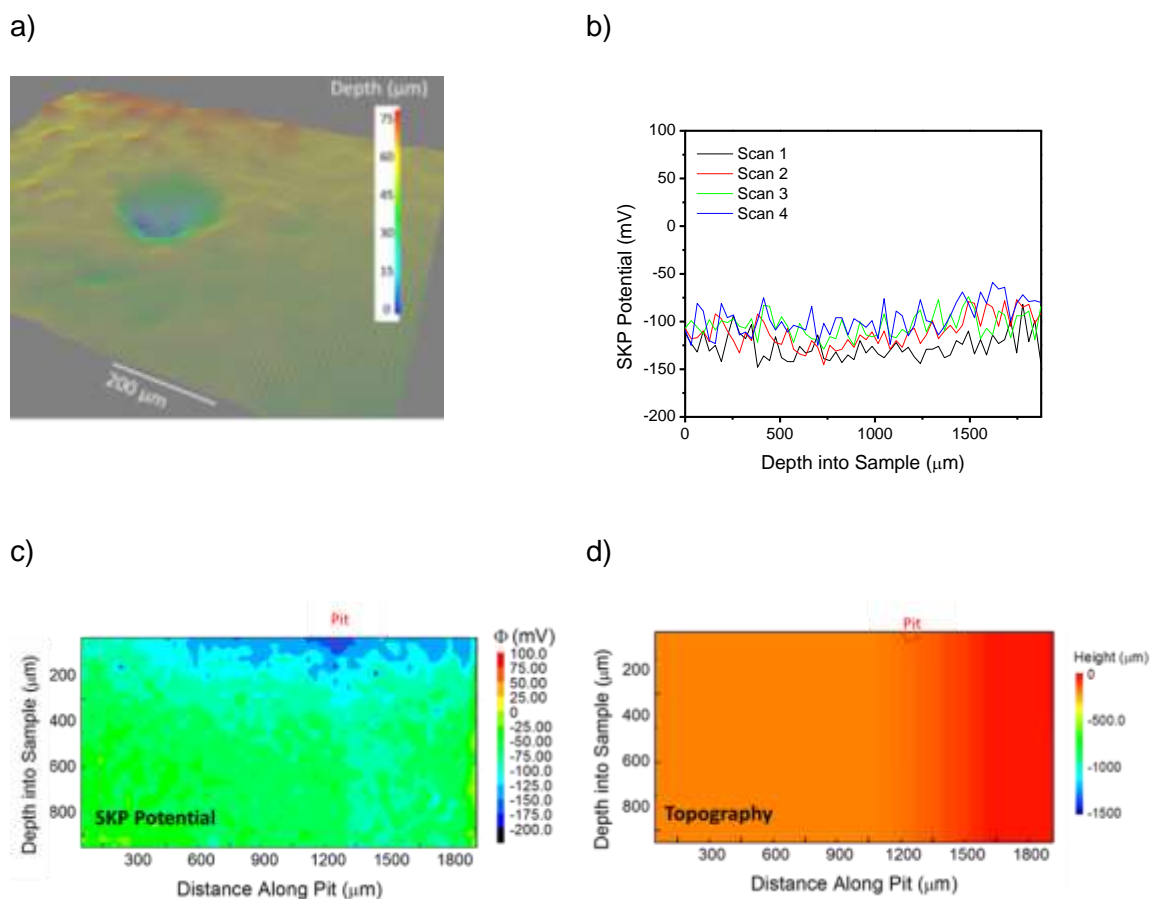


Figure 163. a) Example 3-D optical microscopy image of pit formed after 14 day exposure. b) Line scans into the depth of an unexposed sample, prepared and cut in the same manner as the pitted sample c) Area scan of SKP potential showing distance along pit vs. depth into sample of UNS S46500 pre-exposed with 3.9 M MgCl_2 droplet, 14 days, and 58 %RH. SKP potential is lower at edge of sample near pit. d) Distance along the cut planar surface adjacent to the pit showing the height measured by SKP, indicating that the topography of the sample is flat.

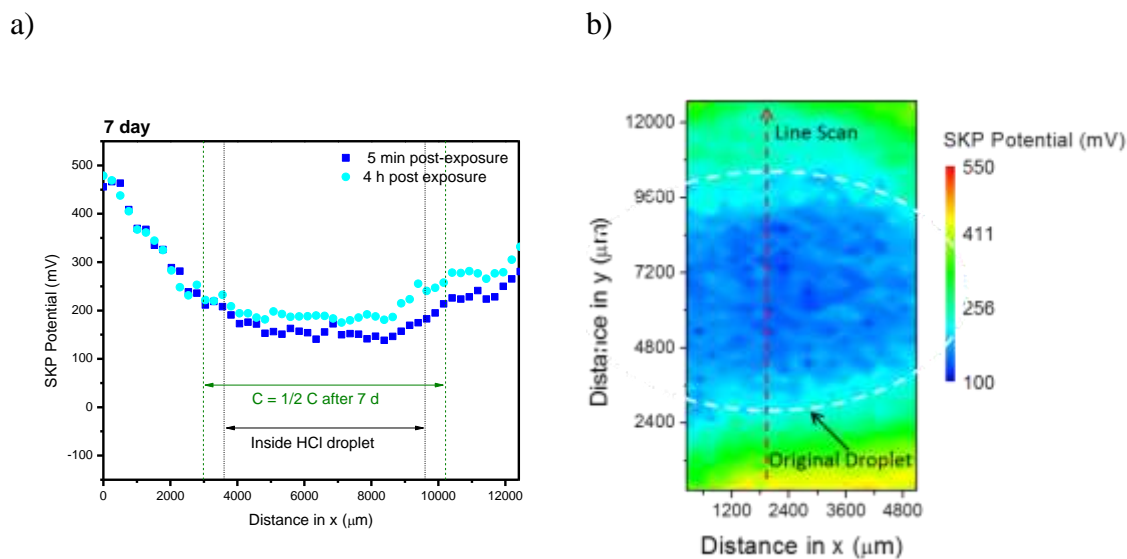
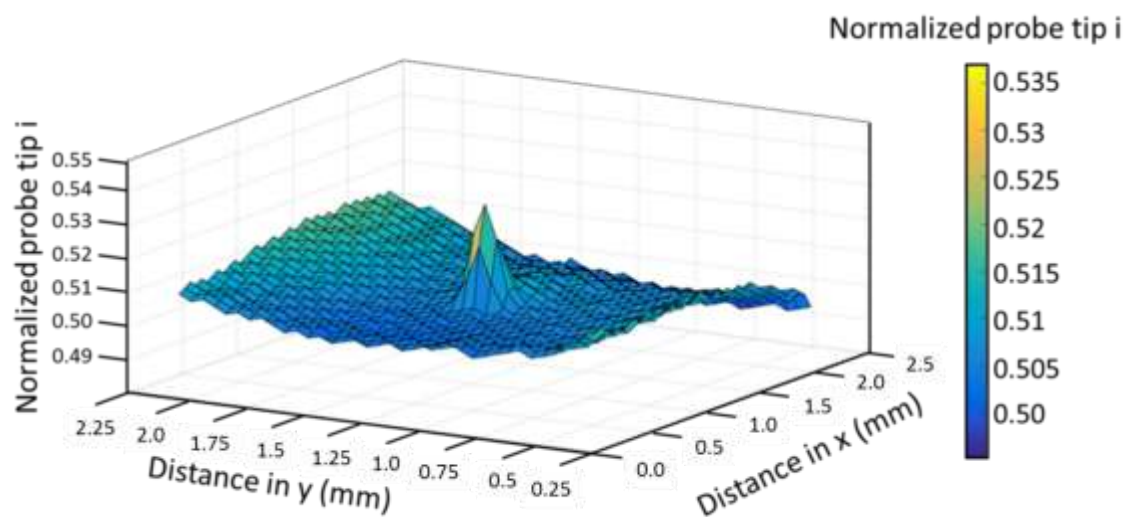
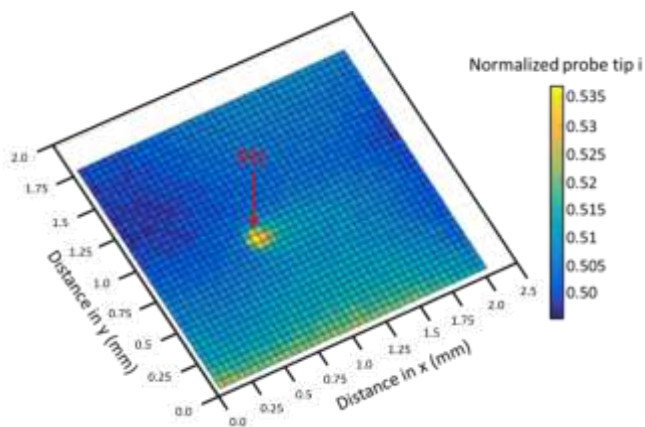


Figure 164. SKP line scans across an area of UNS S46500 H900 a) pre-exposed for 7 days at 98% RH with a 1 M HCl, 4 μL droplet. Scans were taken 5 min post-exposure and 4 h post-exposure near the pit formed underneath the droplet. SKP area scan of pre-exposed UNS S46500 b) H900. *NB: As the area scan takes 4 hours to complete, it is meant only as an indicator of droplet location, as significant outgassing of H can occur over this time period and measurements cannot be directly correlated to H concentrations.*

a)



b)



c)

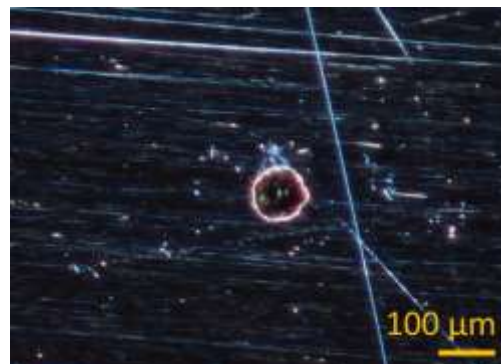
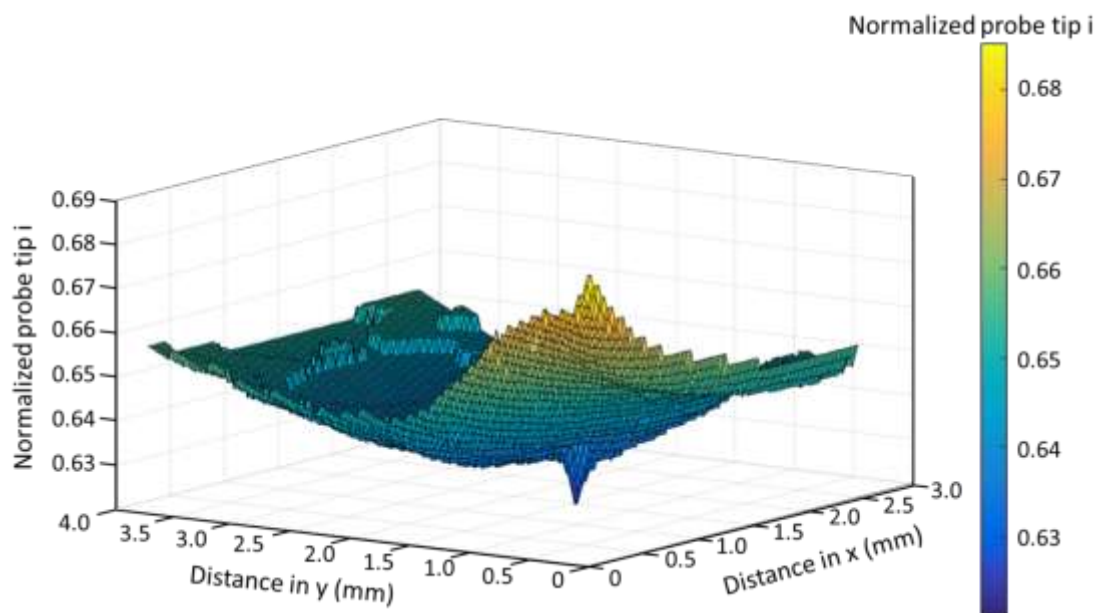
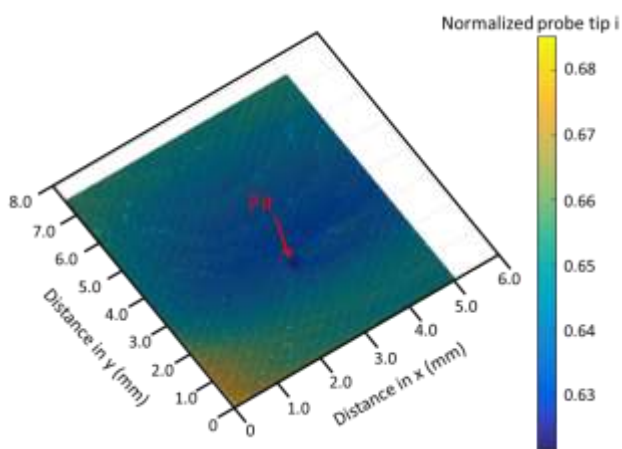


Figure 165. SECM area scan in 5 mM NaCl + NaOH pH 10 solution, ME tip polarized to $-0.8 \text{ V}_{\text{Ag}/\text{AgCl}}$, tip to sample distance of $30 \mu\text{m}$, of UNS S46500 As Annealed/ CT exposed to 3.9 M MgCl_2 10 μL droplet at 58 %RH for 1 week. A) Area scan, b) contour plot of $i_{\text{ORR,ME}}$, and c) optical image of pit.

a)



b)



c)

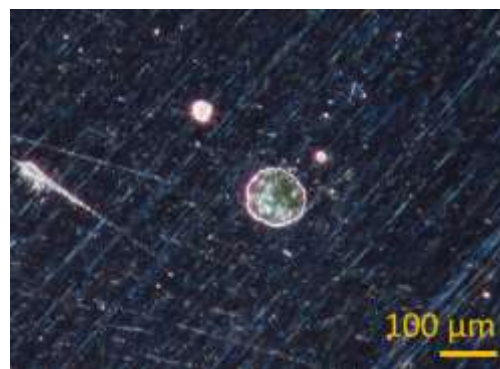
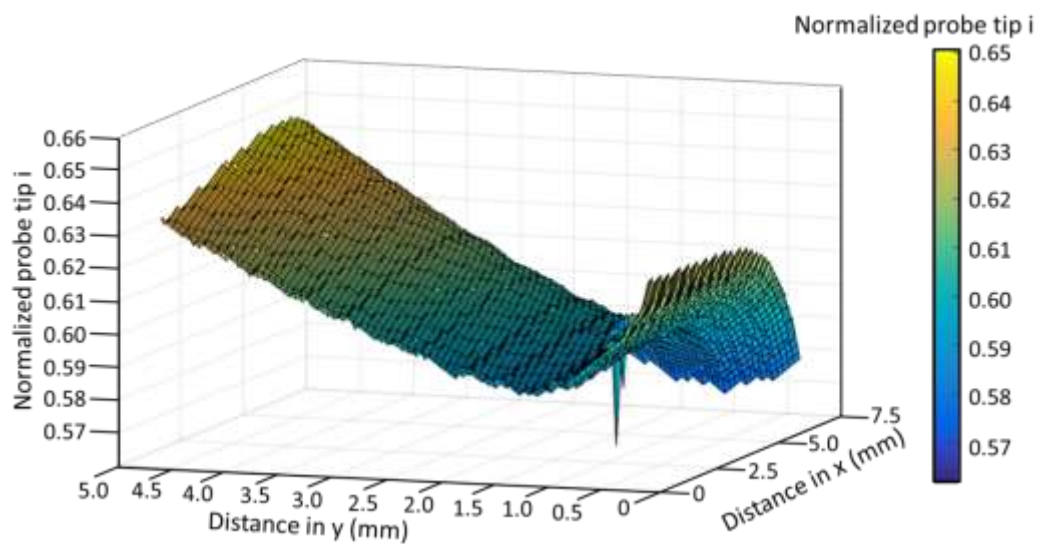
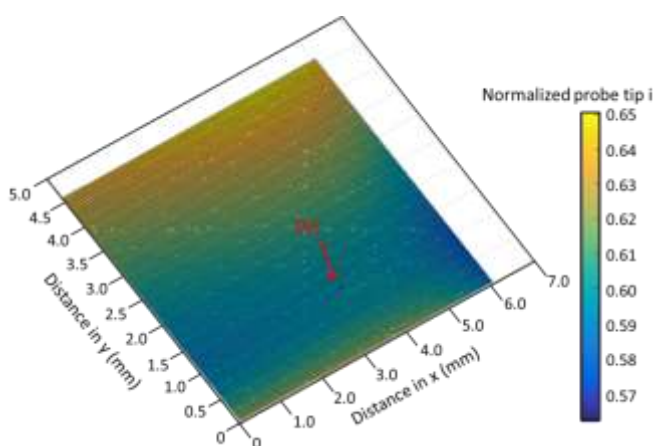


Figure 166. SECM area scan in 5 mM NaCl + NaOH pH 10 solution, ME tip polarized to $-0.8 V_{\text{Ag}/\text{AgCl}}$, tip to sample distance of 30 μm , of UNS S46500 As Annealed/ CT exposed to 3.9 M MgCl_2 10 μL droplet at 58 %RH for 2 weeks. A) Area scan, b) contour plot of $i_{\text{ORR,ME}}$, and c) optical image of pit.

a)



b)



c)

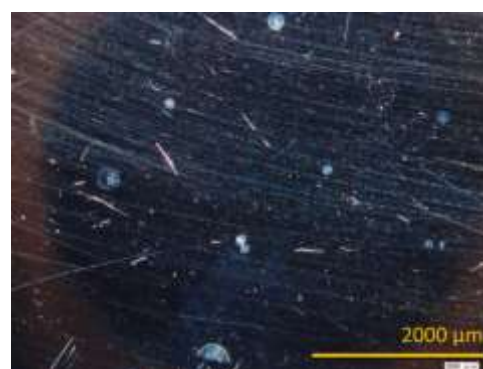


Figure 167. SECM area scan in 5 mM NaCl + NaOH pH 10 solution, ME tip polarized to $-0.8 \text{ V}_{\text{Ag}/\text{AgCl}}$, tip to sample distance of 30 μm , of UNS S46500 As Annealed/ CT exposed to 3.9 M MgCl_2 10 μL droplet at 58 %RH for 3 weeks. A) Area scan, b) contour plot of $i_{\text{ORR,ME}}$, and c) optical image of pit.

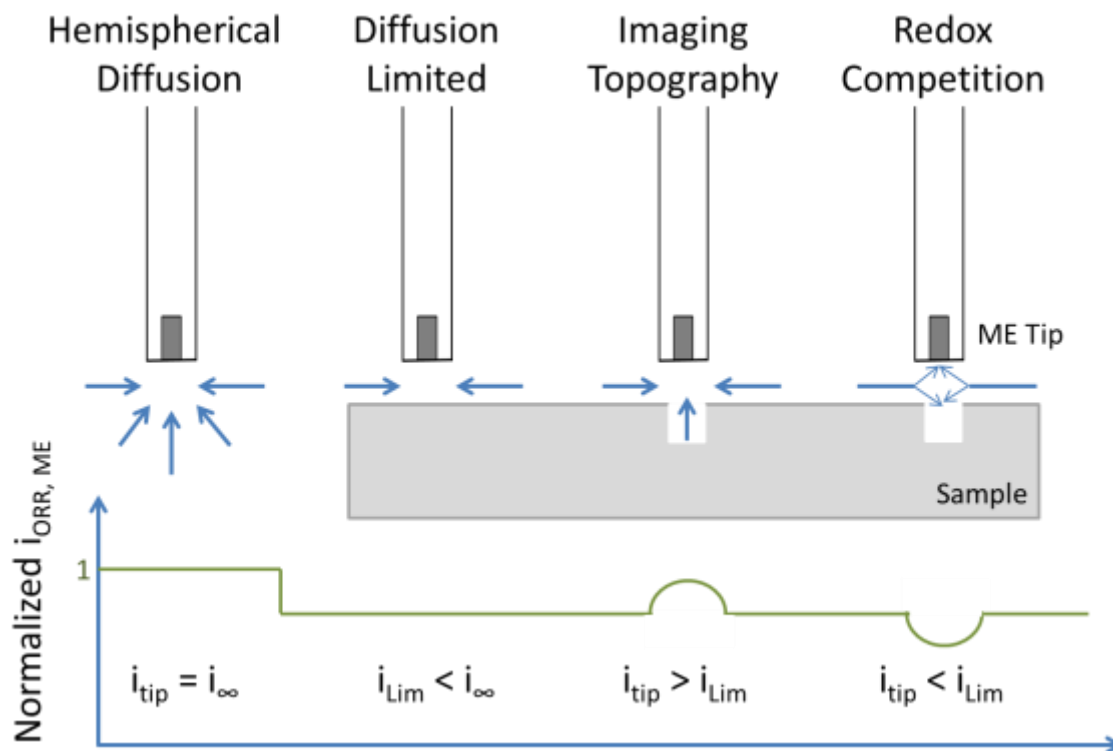


Figure 168. Schematic of SECM modes; Hemispherical diffusion occurs far from the sample surface where $i_{\text{ORR, ME}}$ is limited by diffusion of the O_2 in the electrolyte, diffusion limited scenario occurs when the $i_{\text{ORR, ME}}$ is further limited as the tip approaches the sample surface and diffusion is decreased, imaging topography occurs when the $i_{\text{ORR, ME}}$ increases above a recess in topography as the diffusion is enhanced, and redox competition occurs when the $i_{\text{ORR, ME}}$ decreases above an active site as the tip is in competition with the surface for O_2 . Reproduced from [25].

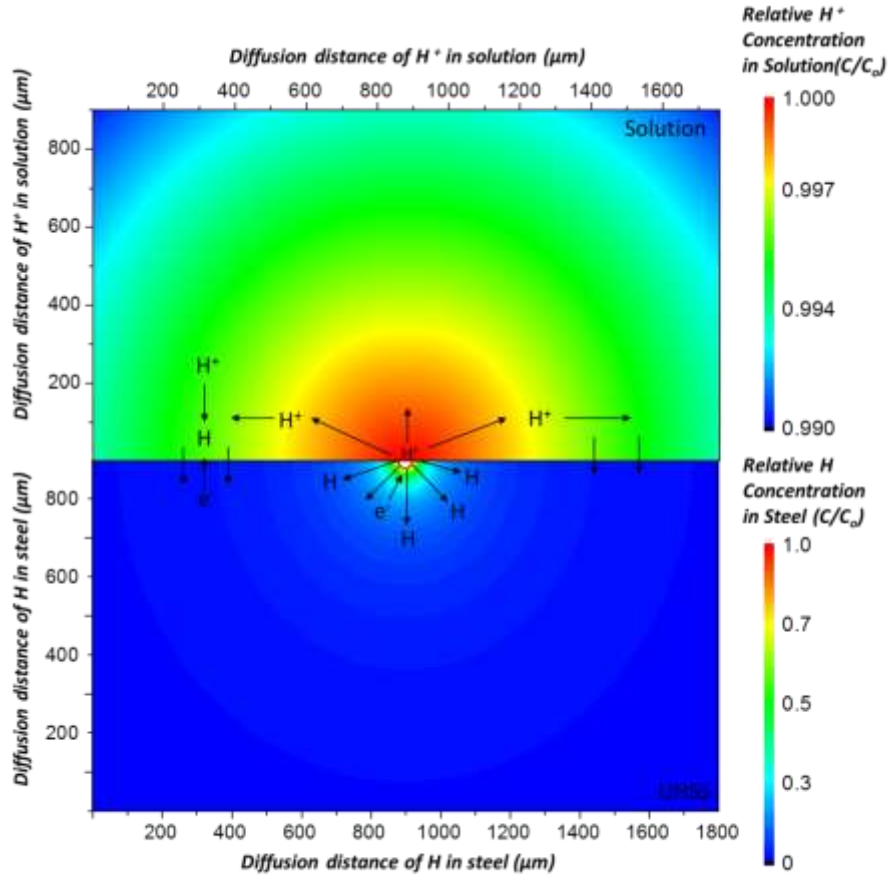


Figure 169. Schematic of H uptake and pH distribution from a pit. Spherical diffusion based on 14 day droplet exposure, formation of a 40 μm diameter pit, and calculation for diffusion assuming a constant spherical source.[26] $D_{\text{H,eff}}$ in steel used was $6.2 \times 10^{-9} \text{ cm}^2/\text{s}$ and diffusion of H^+ in aqueous solution was $4.4 \times 10^{-5} \text{ cm}^2/\text{s}$.